INFORMATION TO USERS

This manuscript has been reproduced from the microfilm master. UMI films the text directly from the original or copy submitted. Thus, some thesis and dissertation copies are in typewriter face, while others may be from any type of computer printer.

The quality of this reproduction is dependent upon the quality of the copy submitted. Broken or indistinct print, colored or poor quality illustrations and photographs, print bleedthrough, substandard margins, and improper alignment can adversely affect reproduction.

In the unlikely event that the author did not send UMI a complete manuscript and there are missing pages, these will be noted. Also, if unauthorized copyright material had to be removed, a note will indicate the deletion.

Oversize materials (e.g., maps, drawings, charts) are reproduced by sectioning the original, beginning at the upper left-hand corner and continuing from left to right in equal sections with small overlaps. Each original is also photographed in one exposure and is included in reduced form at the back of the book.

Photographs included in the original manuscript have been reproduced xerographically in this copy. Higher quality 6" x 9" black and white photographic prints are available for any photographs or illustrations appearing in this copy for an additional charge. Contact UMI directly to order.

UMI

A Bell & Howell Information Company
300 North Zeeb Road, Ann Arbor MI 48106-1346 USA
313/761-4700 800/521-0600

Université d'Ottawa · University of Ottawa

SEISMIC RETROFIT OF SLAB-ON-GIRDER STEEL BRIDGES USING DUCTILE END-DIAPHRAGMS

by

SEYED MEHDI ZAHRAI

A thesis submitted to
the School of Graduate Studies and Research
in partial fulfillment of the requirements
for the degree of

DOCTOR OF PHILOSOPHY

in Civil Engineering*

Department of Civil Engineering
University Of Ottawa
Ottawa, Canada

September 1997

* The Ph.D. in Civil Engineering Program
is a joint program with Carleton University
administered by the Ottawa-Carleton Institute for Civil Engineering

To My Wife, Faranak

ABSTRACT

Many steel bridges have suffered severe diaphragm (cross-frame) damage during recent earthquakes around the world. This can be partly explained by the absence of ductile seismic detailing provisions. Diaphragms provide an important load-path for the seismically-induced loads acting on slab-on-girder steel bridges, but their impact on seismic response is still unclear in many ways. The relative role played by intermediate and end-diaphragms in providing lateral load resistance, and the consequences of diaphragm damage on bridge seismic response have not been studied.

These bridges are also frequently supported by seismically vulnerable non-ductile substructures whose seismic retrofit can be, in many cases, a rather costly operation. Clearly, more economical and practical retrofits are desirable for such bridges. This research addresses three related issues to the seismic behavior of slab-on-girder steel highway bridges : (i) the impact of diaphragm on their seismic performance, (ii) innovative methods for their seismic retrofit and (iii) corrosion effects on the strength and ductility of their steel members.

To study the first issue, research is conducted to quantitatively investigate the impact of diaphragms on the seismic response of these steel bridges. Typical 20 m to 60 m span slab-on-girder bridges with and without diaphragms are considered and studied through elastic and

inelastic static push-over analyses. Two hand-calculation analytical models are proposed to evaluate their period, elastic response, and *PSa* at first yielding. It is shown that a small end-diaphragm stiffness is sufficient to make the entire superstructure behave as a unit in the elastic range. However, a dramatic shift in seismic behavior occurs once those end-diaphragms fail, with a sizeable period elongation, considerably larger lateral displacements and higher propensity to damage due to P-Δ effects. It is also found that the presence of intermediate diaphragms does not significantly influence the seismic performance of these bridges, both in the elastic and inelastic range.

For seismic retrofits of these bridges, this research consists of four essential parts: development of the ductile end-diaphragm concept, development of a design procedure, a series of inelastic analyses to validate the concept, and testing of full scale models for the proposed end-diaphragms to further verify the concept and to validate the proposed detailing. First, to take advantage of the benefits granted by the presence of a steel superstructure, an innovative, economical, effective and simple to implement seismic retrofit strategy, using ductile steel bridge end-diaphragms (such as shear panels, eccentrically braced frames and triangular-plate added damping and stiffness devices) has been developed. By replacing the existing steel diaphragms over abutments and piers with specially designed ductile diaphragms calibrated to yield before the strength of the substructure is reached, the substructure can be protected. Second, a step by step design procedure for ductile end-diaphragms is proposed and potential limits of application are indicated. In the third part, the DRAIN-2DX and ADINA programs are used to conduct nonlinear inelastic analyses of these retrofitted bridges and investigate their expected seismic behavior. Finally, a few specimens are designed and constructed, and a series of cyclic tests are conducted to experimentally verify the analytical models. Test results demonstrate the effectiveness of the proposed ductile end-diaphragms as effective passive energy dissipation systems in slab-on-girder steel bridges.

For the third issue, the effect of corrosion on the strength and ductility of steel members is also studied to investigate the long-term performance of the ductile end-diaphragms proposed here.

Although some past experimental studies indicate that the monotonic structural ductility of steel is not detrimentally affected by severe corrosion, no study has investigated whether such severely rusted members can reliably exhibit the stable cyclic ductile behavior necessary for seismic survival. To generate preliminary data, a few rusted pieces taken from an existing steel bridge have been subjected to numerous cycles of alternating plasticity in flexure. Specimens had up to a 60% loss of cross-sectional area due to corrosion. This limited test program revealed that, while stable hysteretic behavior comparable to that of unrusted specimen is possible, premature failure under alternating plasticity can typically develop (in spite of satisfactory ductile behavior under monotonic loading). Irregularities along the severely rusted surface apparently act as crack initiators and precipitate crack propagation throughout the section.

Acknowledgment

I am grateful to almighty god for all the blessing bestowed upon me during the process of this work and the great guidance from which I drew the strength to persevere with this research and the wisdom and ethics to live my daily life. My sincere thanks go to my supervisor, Dr. Michel Bruneau, for his guidance, encouragement, support and valuable suggestions throughout the course of this study. I would like to express my gratitude to the members of my thesis defence advisory committee. My wife's great help and patience are sincerely acknowledged. Special thanks are also extended to my parents for their support and encouragement throughout my life and studies.

The entrance scholarship provided by the Ministry of Culture and Higher Education of Iran is highly appreciated. The Natural Sciences and Engineering Research Council of Canada is acknowledged for its financial support through a Strategic Grant on the Seismic Evaluation of Existing Bridges, and a Collaborative Grant on Innovative Seismic Retrofit of Existing Bridges. The author thanks the Ministry of Ontario, and more specifically Mr. Roger Dorton, Manager, Structural Office, and Mr. Wade Young, Senior Structural Engineer, Central Region, for donation of the rusted steel bridge material used in a part of this study.

I would like to thank a few people who helped me in some parts of the experimental work: Mr. Mongi Grira, structural lab technician, for his help during the construction and testing of the specimens, Ms. Wendy Scouten for helping in the construction of specimen slabs, Mr. Madan Makasare and Mr. Brent Cotter, from machine shop of the Civil Engineering Department, for some technical support, Mr. Stephen Burke and Mr. Lowel Keith for assistance in testing some rusted pieces.

Table of Contents

Abstract i
Acknowledgment iv
Table of Contents v
List of Tables xii
List of Figures xiv
Notations xxix

CHAPTER 1

INTRODUCTION 1
1.1 Statement of the Problem 1
1.2 Research Objectives 4
1.3 Scope of Work 6
1.4 Outline of the Thesis 8

CHAPTER 2

LITERATURE REVIEW 10
2.1 Introduction 10

2.2 Reported Seismic Performance of Steel Bridges 12
2.3 Concerns and Expected Seismic Vulnerability 16
2.4 Existing Requirements for Seismic Design of Steel Bridges 17
2.5 Existing Requirements for Seismic Rehabilitation of Steel Bridges 18
2.6 Examples of Recent Seismic Rehabilitation of Steel Bridges 20
2.6.1 Small and Medium Span highway bridges 20
2.6.2 Large Span Highway Bridges 21
2.7 Summary of Research Needs 21

CHAPTER 3

IMPACT OF DIAPHRAGMS ON SEISMIC RESPONSE OF SLAB-ON-GIRDER STEEL BRIDGES 23
3.1 Introduction 23
3.2 Preliminary Information 24
3.2.1 Diaphragm Design Requirements 24
3.2.2 Description and Properties of the Selected Bridges 25
3.3 Slab-on-Girder Steel Bridges without Diaphragm 27
3.3.1 Proposed Model for Calculation of Period, Elastic Response, and *PSa* to First Yield 28
3.3.2 Ultimate Nonlinear Behavior 33
3.3.3 Effect of Web Stiffeners 34
3.4 Slab-on-Girder Steel Bridges with Effective Diaphragms 35
3.4.1 Proposed Model for Calculation of Period and Elastic Response 37
3.4.2 Numerical Examples 41
3.4.3 Ultimate Nonlinear Behavior 42
3.5 Further Observations on Seismic Behavior 43
3.6 Summary of Findings 43

CHAPTER 4

DUCTILE END-DIAPHRAGMS FOR SEISMIC RETROFIT OF SLAB-ON-GIRDER STEEL BRIDGES 44

4.1 Introduction to Seismic Retrofit 44

4.2 Preliminary Information 46

4.2.1 Description of Inelastic Computer Programs 46

4.2.2 Damping Characteristics 47

4.2.3 Earthquake Loads 47

4.3 Existing Literature on Ductile Devices in Building Structures 48

4.3.1 Triangular-plates Added Damping And Stiffness (TADAS) Device .. 48

4.3.2 Eccentrically Braced Frame (EBF) 50

4.3.2.1 Link Strength and Ductility 51

4.3.2.2 Stiffener Detailing 52

4.4 Proposed Retrofit Concept 53

4.5 Preliminary Case Studies with EBF between All Girders 55

4.6 Analytical Development 57

4.6.1 Formulation of 2-D Model 58

4.6.2 Ductility vs. Reduction Factor Strategy 63

4.7 Design Procedure 65

4.7.1 Detailed Design Procedure 66

4.8 Numerical Examples 74

4.8.1 Inelastic 2-D Push-over Analysis 75

4.8.2 Inelastic 3-D Push-over Analysis 76

4.8.3 Nonlinear Dynamic Time-History Analysis 77

4.9 Impact of Intermediate Web Stiffeners 78

4.10 Summary of Findings 79

CHAPTER 5

EXPERIMENTAL APPROACH 81
5.1 General 81
5.2 Material Properties 82
5.3 Design of Test Specimens 83
5.3.1 TADAS Specimen 85
5.3.2 EBF Specimen 86
5.3.3 SPS Specimens 87
5.4 Design of Test Foundation 88
5.5 Fabrication and Construction of Specimens 88
5.5.1 Construction of Foundation 88
5.5.2 Construction of Deck Slabs 90
5.6 Testing Set-up 91
5.6.1 Load Applicator Assembly 91
5.6.2 Reaction Frame 91
5.6.3 Lateral Restraining Frames 92
5.6.4 Lateral Support for Ductile Device 92
5.7 Instrumentation 92
5.7.1 General 92
5.7.2 Details of Strain and Displacement Measurements 93
5.7.3 Rotation and Distortion Angles Measurements 94
5.8 Loading Approach 95
5.9 Measurements Control and Monitoring 96

CHAPTER 6

OBSERVED BEHAVIOR AND EXPERIMENTAL RESULTS 97
6.1 General 97

6.2 Preliminary Tests 98
6.2.1 Web of the W200x15 SPS Device 99
6.2.2 Web of the Built-up SPS Device 99
6.2.3 EBF Link Beam Web 100
6.2.4 Girders Web Stiffeners 100
6.3 Experiment 1 (TADAS End-Diaphragm) 101
6.4 Experiment 2 (Stiffened Girders Only) 103
6.5 Experiment 3 (EBF End-Diaphragm) 104
6.6 Experiment 4 (EBF with Welded Connections) 106
6.7 Experiment 5 (Pseudodynamic Testing) 108
6.8 Experiment 6 (1st SPS End-Diaphragm) 109
6.9 Experiment 7 (2nd SPS End-Diaphragm) 111
6.10 Experiment 8 (Channel at Mid-Height) 113

CHAPTER 7

COMPARISON AND DISCUSSION OF TEST RESULTS 115
7.1 General 115
7.2 Comparison of Experimental Results with Designed Capacities 117
7.2.1 Elastic Behavior and Yield Limit 117
7.2.2 Slippage of the Connections 118
7.2.3 Material Overstrength 118
7.2.4 Post-yield Behavior 119
7.3 Hysteretic Response of the Specimens 120
7.3.1 Specimens with Ductile Diaphragms 120
7.3.1.1 Moment-Curvature Relationship 120
7.3.1.2 Shear Force-Rotation Relationship 121
7.3.2 Specimens without Diaphragm 122
7.3.3 Specimen with Channel Diaphragm 123

7.3.4 Energy Dissipation 124
7.4 Results from Other Strain Gages 125
7.4.1 Shear Strains Measured by Rosettes 125
7.4.2 Strain in Braces 127
7.4.3 Strain in Web Stiffeners 127
7.4.4 Strain in Shear Studs 128
7.5 Sideway Deflection (Sway) of the Device 128

CHAPTER 8

LONG-TERM PERFORMANCE OF DUCTILE END-DIAPHRAGMS — SEVERE CORROSION EFFECTS ON DUCTILITY OF EXISTING STEEL BRIDGES 129
8.1 Preliminary Information on Corrosion 129
8.2 Corrosion and Ductility — State-of-Knowledge 131
8.3 Non-Cyclic Material Ductility 135
8.4 Cyclic Bending Tests 137
8.4.1 Weak-axis Bending of Steel Plates 137
8.4.2 Out-of-Plane Bending of Web of Structural S-Shape 141
8.5 Some Observation on Analytical Predictions of Monotonic Load-Displacement Curve 144
8.6 Rivet Tests 146
8.6.1 Tension Test 146
8.6.2 Shear Test 147
8.7 Summary of Findings 148

CHAPTER 9

CONCLUSIONS AND DESIGN RECOMMENDATIONS 150

9.1 Conclusions 150
9.2 Practical Design Recommendations 153
9.3 Future Research 155
References 156
Tables 167
Figures 189
Appendix A: **PLASTIC FAILURE MECHANISMS — FOR STEEL BRIDGES WITHOUT DIAPHRAGM** 356
Appendix B: **DESIGN DETAILS OF TEST FOUNDATION** 360
Appendix C: **TO SCALE DRAWING DETAILS OF DUCTILE SYSTEMS** 362
Appendix D: **ADDITIONAL PLOTS OF EXPERIMENTAL RESULTS** 368

List of Tables

Table 3.1. Geometric and structural characteristics of the steel bridge considered in case studies where I_w, I_b and I_D are the moments of inertia of girder web per unit length about bridge longitudinal axis, girder bottom flange about its strong axis, and superstructure about a vertical axis, respectively 167

Table 3.2. Comparison of elastic lateral deck drift and period of steel bridges with and without web bearing stiffeners, subjected to 1g pseudo acceleration (assuming laterally simply-supported) 167

Table 3.3. Lateral periods of braced bridges obtained by proposed method and SAP90 (assuming one laterally fixed end) where ρA is the superstructure mass per unit length 168

Table 4.1. Inelastic response of the 40m span slab-on-girder bridge (braced with three EBF end-diaphragms at each end) to three different PGA levels, ξ=2%, R=3 (μ_{demand}=5) and Strain-Hardening Ratio=0.03 169

Table 4.2. Inelastic response of the 60m span slab-on-girder bridge (braced with three EBF end-diaphragms at each end) to three different *PGA* levels, ξ=2%, R=3 (μ_{demand}=5) and Strain-Hardening Ratio=0.03 170

Table 4.3. Geometric and structural characteristics of the steel bridge examples 171

Table 4.4. Design procedure for 40 m simply supported span bridge examples with target R of 3.75 172

Table 4.5. Design procedure for support diaphragms of the center 90 m span of three-span bridge examples with target R of 3 173

Table 4.6. Nonlinear inelastic response of 40 m span bridges with ductile diaphragms using Strain-Hardening ratio of 0.01 (relative displacements reported) 174
Table 5.1. Bill of materials for TADAS specimen 175
Table 5.2. Bill of materials for EBF specimen 176
Table 5.3. Bill of materials for SPS specimens 177
Table 5.4. Bill of materials for foundation, deck slabs and test set-up 178
Table 6.1. Test program for experiments 1 to 8 of the end-diaphragm specimens 180
Table 7.1. Comparison of experimental results with those predicted by the proposed analytical model for the specimens having ductile diaphragms 181
Table 7.2. Hysteretic energy values for the TADAS and the first specimen without diaphragm 182
Table 7.3. Hysteretic energy values for the EBF1 and EBF2 specimens 183
Table 7.4. Hysteretic energy values for the SPS1 and SPS2 specimens 184
Table 7.5. Hysteretic energy values for the Channel diaphragm specimen and the specimen without diaphragm tested pseudodynamically. 185
Table 8.1. Thicknesses along the gage length for rusted coupon specimens 186
Table 8.2. Thicknesses along rusted lacing plates 187
Table 8.3. Displacement Ductility and hysteretic energy values for SW-I and SW-II specimens 188
Table C.1. Bill of material provided by fabrication shop 366

List of Figures

Fig. 2.1. Restraining cables added to older existing bridges to prevent girders from falling off of their supports during earthquakes (Roberts 1992). 189

Fig. 2.2. A typical buckling of the X-configuration diaphragms on the Vun Duzen River bridge after the 1992 Mendecino earthquake (Roberts, 1992). 189

Fig. 2.3. Severe buckling of diaphragm members on the same bridge (Roberts 1992). . . . 190

Fig. 2.4. The north girder span of the same bridge; note that the restrainer cables on the left side of the girder are slack while in the right side they are taut, showing a movement to the left (Roberts 1992) 190

Fig. 2.5. Damage to seismic restrainer angle at roller bearing of the Southern bridge in the 1994 Nothridge earthquake (Astaneh-Asl et al. 1994). 191

Fig. 2.6. Bending of web stiffener at the end-diaphragm of the Northern bridge damaged in the Northridge earthquake (Astaneh-Asl et al. 1994). 191

Fig. 2.7. Fracture of diaphragm gusset plate at the east abutment of the Northern bridge damaged in the Northridge earthquake (Astaneh-Asl et al. 1994). 192

Fig. 2.8. Deformed shape of end-diaphragm due to buckling of the braces and bending of the lower horizontal member on the Old Road bridge damaged in the Northridge earthquake (Astaneh-Asl et al. 1994) 192

Fig. 2.9. Typical severe local buckling of circular steel columns after the 1995 Kobe earthquake: (a) elevation of a damaged column, (b) location of buckling and (c) close-up of fractured steel (Bruneau et al. 1996). 193

Fig. 2.10. Fracture in a rectangular steel column damaged in the Kobe earthquake: (a) global view of the column and (b) close-up view of fractured steel (Bruneau et al. 1996) 194

Fig. 2.11. Large transverse movements due to bearing failures on the Hanshin Expressway after the Kobe earthquake: (a) severe damage at the end of girders, (b) underside view showing

tear-up of diaphragm members, (c) damage at the other end of same pier and (d) close-up view indicative of lateral movement (Bruneau et al. 1996). 195
Fig. 2.12. Strengthening of diaphragm by doubling braces in a pedestrian overpass in San Francisco (Mitchell et al. 1994). 196
Fig. 2.13. Seismic retrofit of the Granville bridge in Vancouver by adding truss members (Mitchell et al. 1994). 196
Fig. 2.14. Retrofit concepts proposed for the East Bay Crossing of the Bay bridge (Astaneh-Asl 1993). 197
Fig. 2.15. Seismic retrofit measures for the Golden Gate bridge (Seim et al. 1993). 198
Fig. 3.1. Nominal end-diaphragms in existing slab-on-girder steel bridges: (a) close-up view of channel diaphragm used in a skew bridge in Ottawa, Ontario; (b) the same for another bridge in Quebec. 199
Fig. 3.2. Nominal intermediate diaphragms used in a bridge in Ottawa, Ontario 200
Fig. 3.3. Schematic of a single span simply supported bridge. 201
Fig. 3.4. Typical sliding bearings: (a) fixed bearing; (b) expansion bearing. 202
Fig. 3.5. Comparison of results for different bridges (laterally simply supported) obtained by SAP90 and proposed model: (a) lateral period; (b) lateral drift; (c) required *Psa* to bring the bridge to first yield. 203
Fig. 3.6. SAP90 deformed shapes for typical bridges without diaphragm: (a) plan view; (b) side view; and schematic of simplified model without diaphragm: (c) plan view; (d) side view 204
Fig. 3.7. Comparison of girder bottom flange displacements obtained by SAP90 and proposed model for a 20 m span bridge (simply supported laterally), respectively for girder web thickness of: (a) 8 mm; (b) 11 mm corresponding to the WWF800x184 in the original design; and (c) 20 mm. 205
Fig. 3.8. Comparison of girder bottom flange displacements obtained by SAP90 and proposed model for a 60 m span bridge (simply supported laterally), respectively for girder web thickness of: (a) 12 mm; (b) 16 mm corresponding to the WWF1600x496 in the original design; and (c) 20 mm. 206

Fig. 3.9. Rotation of girder bottom flange for the 20 m span bridge (simply supported laterally), for a normalized 100 mm of maximum transverse displacement. 207
Fig. 3.10. Rotation of girder bottom flange for the 60 m span bridge (simply supported laterally), for a normalized 100 mm of maximum transverse displacement. 207
Fig. 3.11. Comparison of girder bottom flange displacements obtained by SAP90 and proposed model for a 20 m span bridge (laterally fixed at one end), respectively for girder web thickness of: (a) 8 mm; (b) 11 mm corresponding to the WWF800x184 in the original design; and (c) 20 mm. 208
Fig. 3.12. Rotation of girder bottom flange for the 20 m span bridge (laterally fixed at one end), for a normalized 100 mm of maximum transverse displacement. 209
Fig. 3.13. ADINA modeling and deflected shapes for a 40 m span bridge without any diaphragm or web stiffeners: (a) undeformed shape (a quarter of the bridge is shown); (b) deflected shape; (c) close-up view of deformed shape near supports; (d) close-up of web deformation. 210
Fig. 3.14. Load-displacement curve for the 40 m span bridge with and without consideration of P-Δ effects. 211
Fig. 3.15. Stress vectors for the steel girders of the 40 m span bridge near end support, obtained by ADINA: (a) in the web; (b) in the flange. 211
Fig. 3.16. Stress contours for the steel girder of the 40 m span bridge near end support, obtained by SAP90. Yield lines are in agreement with the ADINA results. 212
Fig. 3.17. Impact of intermediate diaphragms on the 40 m span bridge without end-diaphragm: (a) lateral load versus midspan drift; (b) horizontal shear force in the first and second intermediate diaphragms from bridge end. 213
Fig. 3.18. Typical model (SAP90 modeling) of bridges with: (a) X-bracing at both ends; (b) intermediate X-bracing are present as well. Deck slab not shown. 214
Fig. 3.19. Schematical simplified model for bridges with end-diaphragms 215
Fig. 3.20. Lateral period versus cross-sectional area of braces for 20 m, 40 m and 60 m span bridges (laterally fixed at one end). 215
Fig. 3.21. ADINA modeling and deflected shape for a 40 m span bridge with effective

diaphragms: (a) undeformed shape (half model is shown); (b) deflected shape. . . . 216
Fig. 3.22. Inelastic results for a 40 m span bridge: (a) lateral load versus end and midspan drifts; (b) and (c) tension and compression axial forces in one pair of the diaphragm braces, respectively. Contribution resisted by flexure of the stiffened girders (per Eq. 3.26) not shown 217
Fig. 3.23. Inelastic results for a 60 m span bridge: (a) lateral load versus end and midspan drifts; (b) and (c) tension and compression axial forces in one pair of the diaphragm braces, respectively. Contribution resisted by flexure of the stiffened girders (per Eq. 3.26) not shown 218
Fig. 3.24. End views of deformed shapes for the 40 m span bridge at: (a) one end; and (b) a distance of 8 m from bridge end. 219
Fig. 4.1. Inelastic Newmark-Hall design spectra obtained for peak ground accelerations of 0.2g, 0.4g and 0.6g with 2% damping (elastic response spectra for *PGA* of 0.6g shown for comparison). 220
Fig. 4.2. Basic behavior of triangular steel plates under lateral loading (Tsai et al. 1993). . 221
Fig. 4.3. Plastic failure mechanism for a frame having Triangular-plate Added Damping And Stiffness Device (TADAS) (Tsai et al. 1993). 221
Fig. 4.4. Common configurations of Eccentrically Braced Frames (EBF). 222
Fig. 4.5. Hysteretic behavior and failure pattern of: (a) shear link without web stiffeners; (b) stiffened shear link (Kasai and Popov 1986). 222
Fig. 4.6. Shear plastic mechanism for an EBF. 223
Fig. 4.7. Inelastic behavior of proposed ductile end-diaphragms compared to that of existing steel bridges. 223
Fig. 4.8. Proposed ductile end-diaphragms of a typical 40 m span bridge with: (a) TADAS; (b) EBF; (c) SPS (other unbraced girders not shown); dotted members only if required for jacking purposes for non-seismic reasons). 224
Fig. 4.9. Ductile end-diaphragms inserted between all girders for preliminary case studies. 225
Fig. 4.10. Inelastic results for the 40 m span bridge having EBF between all girders, i.e. three panel each end, by DRAIN-2DX: (a) Lateral load; (b) bending moment in one web

stiffener at bridge end; (c) link shear force, versus deck displacement. Results for one panel shown. 226
Fig. 4.11. Inelastic results for the 60 m span bridge having EBF between all girders, i.e. three panel each end, by DRAIN-2DX: (a) Lateral load; (b) bending moment in one web stiffener at bridge end; (c) link shear force, versus deck displacement. Results for one panel shown. 227
Fig. 4.12. Inelastic time-history analysis results by DRAIN-2DX for the 40 m span bridge having EBF subjected to the El-Centro earthquake scaled to a *PGA* of 0.6g: (a) deck drift and (b) link distortion versus time. 228
Fig. 4.13. Inelastic time-history analysis results by DRAIN-2DX for the 60 m span bridge having EBF subjected to the El-Centro earthquake scaled to a *PGA* of 0.6g: (a) deck drift and (b) link distortion versus time. 229
Fig. 4.14. Ductile end-diaphragm designed for the 40 m span bridge to resist a *PGA* of 0.6g: (a) one of panels having EBF, (b) some typical connection detailing. 230
Fig. 4.15. Schematic 3-D view of the ductile end-diaphragm proposed for 2-D analytical analysis 231
Fig. 4.16. Spring modeling: (a) schematic of a typical bridge supported by a substructure including piers and foundations; (b) spring modeling of the bridge in the transverse direction; (c) simple spring model of the dual system in bridge superstructure. . . . 232
Fig. 4.17. Flexibility of the girder's bottom flange in modeling the level of fixity, based on SAP90 analyses (the rest of girders and web stiffeners not shown). 233
Fig. 4.18. Modeling of a typical slab-on-girder steel bridge using SAP90: (a) 3-D model; (b) 3-D deformed shape; (c) 2-D model; and (d) 2-D deformed shape (deformed shapes are greatly magnified for illustration purposes). 234
Fig. 4.19. Hysteretic modeling of seismic resistant systems: (a) bilinear model; (b) trilinear model 235
Fig. 4.20. Simple folw chart for proposed design procedure. 236
Fig. 4.21. Newmark-Hall and AASHTO design spectra versus the response spectra for two earthquakes, scaled to a *PGA* of 0.6g. 237

Fig. 4.22. Proposed trilinear curve for design of the TADAS for a 40 m span bridge. 237
Fig. 4.23. Proposed trilinear curve for design of the EBF for a 40 m span bridge. 238
Fig. 4.24. Proposed trilinear curve for design of the SPS for a 40 m span bridge. 238
Fig. 4.25. Lateral load and link shear force versus deck displacement respectively: (a) and (b) for the 40 m single span bridge; (c) and (d) for support diaphragm of the three span bridge (side span of 60 m and center span of 90 m), with SPS diaphragms. 239
Fig. 4.26. ADINA modeling and analysis: (a) undeformed shape; (b) deformed shape (with magnified deformations for illustration purposes); (c) and (d) close-up of deformations 240
Fig. 4.27. Inelastic 3-D analysis results for a 40 m span bridge having SPS end-diaphragms by ADINA (web stiffeners only at supports): (a) lateral load versus end and center drifts; (b) shear force in the SPS; (c) bending moment in web stiffener and (d) axial forces in braces, versus end drift. 241
Fig. 4.28. Inelastic time-history analyses for the bridges subjected to the El-Centro earthquake scaled to 0.4g (for first 10 seconds) by DRAIN-2DX: (a) deck displacement and (b) link distortion for the three span bridge with 90 m center span; (c) deck displacement and (d) link distortion for the 40 m span bridge; (e) and (f) same for bridge on stiff piers; (g) and (h) same for bridge on flexible piers 242
Fig. 4.29. Analytical hysteretic curves for the SPS implemented in the 40 m span bridge subjected to the El-Centro earthquake scaled to a *PGA* of 0.4g. 243
Fig. 4.30. Impact of intermediate web stiffeners on the proposed design procedure. 243
Fig. 4.31. Deflected shapes by ADINA for a 40 m span bridge having transverse web stiffeners at every: (a) 4 m; (b) 2 m, along the girders. 244
Fig. 4.32. Inelastic 3-D analysis results for the 40 m span bridge having SPS end-diaphragms by ADINA (web stiffeners at every 4 m): (a) lateral load versus end and center drifts; (b) bending moment in web stiffeners and (c) axial forces in braces, versus end drift. . 245
Fig. 4.33. Inelastic 3-D analysis results for a 40 m span bridge having SPS end-diaphragms by ADINA (web stiffeners at every 2 m): (a) lateral load versus end and center drifts; (b) bending moment in web stiffeners and (c) axial forces in braces, versus end drift . 246

Fig. 4.34. Inelastic 3-D analysis results for a 60 m span bridge having SPS end-diaphragms by ADINA (web stiffeners every 3 m): (a) lateral load versus end and center drifts; (b) shear force in the SPS; (c) bending moment in web stiffeners and (d) axial forces in braces, versus end drift. 247
Fig. 5.1. Drawing details for stub-girders of the specimens. 248
Fig. 5.2. Deck slab reinforcement for the designed specimens 249
Fig. 5.3. Elevation of ductile end-diaphragm specimen having TADAS. 249
Fig. 5.4. TADAS assembly designed for the TADAS specimen. 250
Fig. 5.5. Design detailing for TADAS. 251
Fig. 5.6. Bracing members for the TADAS specimen. 252
Fig. 5.7. Bottom beam and its detailing for the TADAS specimen. 253
Fig. 5.8. Trilinear curve for the TADAS specimen following the proposed design procedure. 254
Fig. 5.9. Elevation of ductile end-diaphragm specimen having EBF. 254
Fig. 5.10. Drawing details for the link beam in the EBF specimen 255
Fig. 5.11. Bracing members for the EBF specimen 256
Fig. 5.12. Trilinear curve for EBF specimen following the proposed design procedure . . . 257
Fig. 5.13. Elevation of ductile end-diaphragm SPS specimen with a W200x15 257
Fig. 5.14. Details of the first alternative SPS and its bottom beam. 258
Fig. 5.15. Elevation of ductile end-diaphragm SPS specimen with built-up section 259
Fig. 5.16. Details for the 2nd SPS alternative (bolted to the bottom beam). 259
Fig. 5.17. Bracing members for the SPS specimens. 260
Fig. 5.18. Trilinear curve for the SPS specimen following the proposed design procedure. 261
Fig. 5.19. Reinforcements for the foundation designed for testing of the specimens. 261
Fig. 5.20. Details for holes and connections of base plates and channel sections in foundation. 262
Fig. 5.21. Foundation cage and its formwork, note that one of the specimens is located in place to accurately position the anchor bolts inside the reinforced concrete foundation . 263
Fig. 5.22. Details on anchor bolts. 263

Fig. 5.23. Deck slab cage and its formwork before pouring the concrete. Four bolts are placed each side of the deck slab to be connected to load applicator beams. 264
Fig. 5.24. End plates to connect the specimen deck to the horizontal actuator. 264
Fig. 5.25. Test specimens after construction. 265
Fig. 5.26. Plan and elevation schematical views of test set-up prepared for experiments. . 266
Fig. 5.27. Photo of test set-up and load applicator beam assembly. 267
Fig. 5.28. Drawing details for load applicator beams. 268
Fig. 5.29. Light frame built with slotted angles to support Temposonic transducers and LVDTs. 269
Fig. 5.30. Instrumentation of the TADAS specimen. 270
Fig. 5.31. Instrumentation of the EBF specimen. 270
Fig. 5.32. Instrumentation of: (a) the SPS1 specimen; (b) the SPS2 specimen. 271
Fig. 5.33. Instrumentation of the Channel specimen 272
Fig. 5.34. LVDTs and Temposonic tranducer to measure deformations of the TADAS plates and rotation of bottom beam. 272
Fig. 5.35. Cyclic displacement history imposed to the specimens 272
Fig. 6.1. Preliminary tests on coupons taken from same stock as web of first SPS (W200x15), to determine the strength and ductility of provided steel: (a) first coupon; (b) second coupon. 273
Fig. 6.2. Preliminary tests on coupons taken from same stock as web of second SPS (built-up), to determine the strength and ductility of provided steel: (a) first coupon; (b) second coupon. 274
Fig. 6.3. Preliminary tests on coupons taken from link web of EBF, to determine the strength and ductility of provided steel. 275
Fig. 6.4. Preliminary tests on coupons taken from girder web stiffeners, to determine the strength and ductility of provided steel. 275
Fig. 6.5. The TADAS specimen under testing. 276
Fig. 6.6. Hysteretic curves for the TADAS specimen: (a) recorded by MTS Testar; (b) recorded by Vishay data aquisition system after data reduction. 277

Fig. 6.7. Slippage of the TADAS device base plate, also showing cracks on the whitewash of the plates particularly near the top. 278
Fig. 6.8. Small gap under the TADAS base plate on the lifted side. 278
Fig. 6.9. TADAS specimen subjected to a drift of 4% 279
Fig. 6.10. Significant slippage at the connection of the braces to the web stiffeners 279
Fig. 6.11. Local buckling observed at the bottom of the west bearing stiffener of the west girder. 280
Fig. 6.12. Rupture of the first TADAS plate near its top. 281
Fig. 6.13. More severe buckling on the west stiffener of the west girder of TADAS specimen. 282
Fig. 6.14. Ruptures in two other TADAS plates indicative of the end of testing. 282
Fig. 6.15. Cracks in web stiffeners propagating from their holes to the free edge of the stiffeners, induced during the TADAS experiment. 283
Fig. 6.16. Hysteretic curves for the first specimen without diaphragm: (a) recorded by MTS Testar; (b) recorded by Vishay data aquisition system after data reduction. 284
Fig. 6.17. Expanded and widened cracks at the stiffener holes. 285
Fig. 6.18. Fracture of the full penetration weld at the base of the west web stiffener. 286
Fig. 6.19. The specimen without diaphragm subjected to a drift of 8%. 287
Fig. 6.20. Another fracture of full penetration welds at the bottom of the girder bearing stiffeners. Experiment ended at this time when all full penetration welds were fractured. 288
Fig. 6.21. The 300 mm long stiffened shear link of the EBF end-diaphragm 289
Fig. 6.22. Hysteretic curves for the first EBF specimen: (a) recorded by MTS Testar; (b) recorded by Vishay data aquisition system after data reduction. 290
Fig. 6.23. large percentage of the applied displacements to the EBF1 specimen taken up by slip at the bolted connection of braces. 291
Fig. 6.24. Deformation of the shear link into a parallelogram bounded by the end stiffener plates and flanges of the link beam. 291
Fig. 6.25. The more severe cracks and flakes in the whitewash in the link beam web, mostly in the end panels. 292

Fig. 6.26. One of the welded connection before Experiment 4 (the EBF2 specimen). 293
Fig. 6.27. Hysteretic curves for the EBF2 specimen: (a) recorded by MTS Testar; (b) recorded by Vishay data aquisition system after data reduction. 294
Fig. 6.28. Large shear distortions of the link of the welded EBF specimen. 295
Fig. 6.29. Significant visible local buckling at the north side of the east end panel of the link 295
Fig. 6.30. Severe flange distortion in the shear link of the EBF2 specimen. 296
Fig. 6.31. Sudden twisting of the link beam of the welded EBF specimen. 297
Fig. 6.32. Fracture of the west end of the link (most visible at the top flange) due to excessive lateral deformations. 298
Fig. 6.33. Results of the pseudodynamic test of the second specimen without diaphragm subjected to the El-Centro earthquake scaled to a *PGA* of 0.085g: (a) lateral drift and (b) *PSa*, versus time; (c) hysteretic curves 299
Fig. 6.34. Results of the pseudodynamic test of the second specimen without diaphragm subjected to the El-Centro earthquake scaled to a *PGA* of 0.17g: (a) lateral drift and (b) *PSa*, versus time; (c) hysteretic curves. 300
Fig. 6.35. Results of the pseudodynamic test of the second specimen without diaphragm subjected to the actual El-Centro earthquake, i.e. scaled to a *PGA* of 0.34g: (a) lateral drift and (b) *PSa*, versus time; (c) hysteretic curves. 301
Fig. 6.36. Hysteretic curves for the SPS1 specimen: (a) recorded by MTS Testar; (b) recorded by Vishay data aquisition system after data reduction. 302
Fig. 6.37. Lateral support provided for the ductile devices 303
Fig. 6.38. SPS shear link deformation as a parallelogram bounded by the end plates and flanges. 303
Fig. 6.39. Visible buckling in the SPS1 flanges. 304
Fig. 6.40. Fracture at the base of the SPS on its north-east side and severe buckling of the SPS flange at the base on the north-west side of the panel. 304
Fig. 6.41. Fracture propagation through the web of the SPS1 specimen. 305
Fig. 6.42. Hysteretic curves for the SPS2 specimen: (a) recorded by MTS Testar; (b) recorded

by Vishay data aquisition system after data reduction. 306
Fig. 6.43. Cracks found in the whitewash of the SPS2 web a few cycles after its yielding. 307
Fig. 6.44. Little whitewash left on the SPS2 web. 307
Fig. 6.45. Fracture progressed through the entire SPS web after fracture of flange weld on the west side of the SPS2. 308
Fig. 6.46. A relatively deep channel placed at mid-height between the stub-girders (location with maximum rotation). 309
Fig. 6.47. Hysteretic curves for the Channel specimen: (a) recorded by MTS Testar; (b) recorded by Vishay data aquisition system after data reduction. 310
Fig. 6.48. Breakage beginning at the welds near the holes on the stiffener at the east top end and west lower end locations. 311
Fig. 6.49. Fractured of the weld at the bottom end of exterior stiffener on east girder of the channel specimen. 312
Fig. 6.50. Rupture of top bolt on the west side channel connection, accompanied by a huge "bang": (a) the specimen subjected to 4% drift; (b) close-up view of the ruptured bolt. 313
Fig. 6.51. Fracture of the weld at the west exterior stiffener of the channel specimen: (a) severe buckling from previous cycles; (b) close-up view of the weld rupture. 314
Fig. 6.52. The channel specimen subjected to a drift of 6%, inducing rupture of two other bolts. 315
Fig. 7.1. The predicted trilinear load-drift curve for the TADAS specimen compared to an envelope of the TADAS hysteretic curves obtained from testing. 316
Fig. 7.2. The predicted trilinear load-drift curve for the EBF1 and EBF2 specimens compared to envelopes of the EBF1 and EBF2 hysteretic curves obtained from testing. 316
Fig. 7.3. The predicted trilinear load-drift curve for the SPS1 and SPS2 specimens compared to envelopes of the TADAS hysteretic curves obtained from testing. 317
Fig. 7.4. Slippage of the stub-girders of the TADAS specimen during testing. 317
Fig. 7.5. Typical slippage of the stub-girders of the EBF specimens during testing. 318
Fig. 7.6. Typical slippage of the stub-girders of the SPS specimens during testing. 318

Fig. 7.7. Moment-curvature curves at the base of the TADAS device. 319
Fig. 7.8. Moment-curvature curves at the end of shear link in the EBF1 specimen. 319
Fig. 7.9. Moment-curvature curves at the ends of shear link in the EBF2 specimen. 320
Fig. 7.10. Moment-curvature curves at the base of the SPS1 shear link. 320
Fig. 7.11. Moment-curvature curves at the base of the SPS2 shear link. 321
Fig. 7.12. Moment-curvature curves for the bottom beams (at the location of its web stiffeners) of the TADAS specimen. 321
Fig. 7.13. Moment-curvature curves for the bottom beams (at the location of its web stiffeners) of: (a) the SPS1 specimen; (b) the SPS2 specimen. 322
Fig. 7.14. Shear-distortion curves for the TADAS device 323
Fig. 7.15. Shear-distortion curves for the EBF1 shear link. 323
Fig. 7.16. Shear-distortion curves for the EBF2 shear link 324
Fig. 7.17. Shear-distortion curves for the SPS1 shear link. 324
Fig. 7.18. Shear-distortion curves for the SPS2 shear link 325
Fig. 7.19. Comparison of the hysteretic curves for the specimen without diaphragm subjected to the El Centro earthquake scaled to *PGAs* of 0.085g, 0.17g and 0.34g. 326
Fig. 7.20. End bending moments of the channel versus drift imposed to the channel specimen: (a) at the west connection; and (b) at the east connection. 327
Fig. 7.21. Hysteretic lateral load-drift curves for: (a) the channel section only, i.e. based on its resistance to the lateral load; (b) the channel specimen. 328
Fig. 7.22. Hysteretic energies per cycle dissipated by the various specimens at different drifts. 329
Fig. 7.23. Using data from strain rosettes: (a) Mohr's circle for the strains to find the principal and maximum shear strain; (b) strain rosettes with 45° between the gages used in experiments. 329
Fig. 7.24. lateral load versus: (a) the maximum principal strain; and (b) maximum shearing strain, for the link beams of the EBF1 specimens. 330
Fig. 7.25. lateral load versus: (a) the maximum principal strain; and (b) maximum shearing strain, for the link beams of the EBF2 specimens. 331

Fig. 7.26. lateral load versus: (a) the maximum principal strain; and (b) maximum shearing strain, for the link beams of the SPS1 specimens 332
Fig. 7.27. lateral load versus: (a) the maximum principal strain; and (b) maximum shearing strain, for the link beams of the SPS2 specimens. 333
Fig. 7.28. Maximum shearing strain in bottom beam of the TADAS specimen. 334
Fig. 7.29. Maximum shearing strain in bottom beam of: (a) the SPS1; and (b) the SPS2 specimens. 335
Fig. 7.30. Strain data for: (a) one of the short angles added at the connection to the web stiffeners, (b) one of braces. 336
Fig. 7.31. Typical results for strain gages on the web stiffeners of the TADAS specimen. 337
Fig. 7.32. Typical results from strain gages on the shear studs. 337
Fig. 7.33. Typical small sideway movements for the ductile devices in the TADAS specimen. 338
Fig. 8.1. Schematic of corrosion process (Fisher et al. 1991). 339
Fig. 8.2. Corrosion pattern for typical steel bridges (bridge ends are mostly vulnerable to corrosion) (Kayser et al. 1987). 339
Fig. 8.3. Typical areas of section loss to the flanges and web of stringers (Kulicki et al. 1990). 340
Fig. 8.4. Typical condition of expansion bearings, many bolts have bent or sheared off (Kulicki et al. 1990). 340
Fig. 8.5. ASTM E8M rusted coupon specimens. 341
Fig. 8.6. Experimentally obtained tensile strength of rusted coupons compared to typical strength of unrusted A7 steel: (a) flange coupon; (b) web coupons. 342
Fig. 8.7. Experimentally obtained stress-strain relationship for rusted coupons compared to typical stress-strain curve for unrusted A7 steel. 343
Fig. 8.8. Experimentally obtained tensile strength of rusted coupons compared to their theoretical strength normalized using average and minimum thicknesses at the critical cross-section: (a) flange coupon; (b)web 1 coupon. 344

Fig. 8.9. Test set-up for 3-point bending test. 345
Fig. 8.10. Lacing plate specimen subjected to cyclic loading: (a) location of measurements; (b) loading and corresponding moment and curvature diagrams. 345
Fig. 8.11. Cyclic load-displacement relationship for plate specimen 1, first 5 cycles. 346
Fig. 8.12. Simplified hysteretic behavior of the plate specimens: (a) rusted specimen 1, for cycles 6 to failure; (b) rusted specimen 2, all cycles; (c) unrusted specimen, all cycles. . . 347
Fig. 8.13. Final state of the plate specimens and cross-width cracks: (a) global view of specimen 1 after the test; (b) cross-width cracking for specimen 1; (c) cross-width cracking for specimen 2. 348
Fig. 8.14. Close-up view of surface texture for three-point bending specimens: (a) first cracking side of specimen 1; (b) last ruptured side of specimen 2. 349
Fig. 8.15. Close-up view of other cracks of finite length parallel to the failure surface. . . . 349
Fig. 8.16. Test set-up for weak-axis bending of floorbeam's rusted web: (a) schematic view showing the set-up including the reaction column; (b) a photo of test set-up. 350
Fig. 8.17. Web thickness in the critical areas where cracking happened for two specimens 351
Fig. 8.18. Hysteretic curves for floorbeam web specimen 1 (SW-I). 351
Fig. 8.19. Specimen SW-I after testing (upside down), showing final crack length and opening. 352
Fig. 8.20. Hysteretic load-displacement curves for floorbeam web specimen 2 (SW-II). . . 352
Fig. 8.21. Progression of cracking in specimen SW-II: (a) early cracking on east face; (b) same on west face; (c) significant crack propagation on west face. 353
Fig. 8.22. Analytical prediction of monotonic load-elongation curve for flange coupon . . 354
Fig. 8.23. Special set-up to create pure shear test conditions and insertion into an uniaxial testing machine. 354
Fig. 8.24. Rivet tested in shear: (a) deformed shape of rivet at rupture (broken pieces put back together for this photo); (b) view of rupture surface and minor corrosion on shank of rivet. 355
Fig. A.1. Main yield line pattern for slab-on-girder bridges 358
Fig. A.2. Another yield line pattern for slab-on-girder bridges 359

Fig. B.1. Critical loading for the foundation design (cantilever part) 360
Fig. B.2. Location of different holes provided for the test foundation 361
Fig. C.1. To scale drawing of SPS - W section 362
Fig. C.2. To scale drawing of SPS - built-up section 363
Fig. C.3. Section views of the SPS devices 363
Fig. C.4. To scale drawing of EBF system 364
Fig. C.5. To scale drawing of TADAS device 364
Fig. C.6. Details of TADAS Device 365
Fig. D.1. Lateral load versus strain close to the free edge at: (a) top; and (b) bottom of the web stiffeners of the east girder of the TADAS specimen. 368
Fig. D.2. Lateral load versus strain close to the free edge at: (a) and (b) top; and (c) and (d) bottom of the web stiffeners of the east girder of the TADAS specimen. 369
Fig. D.3. Lateral load versus strain at the bottom of: (a) and (b) two sides of a TADAS plate in the TADAS specimen. 370
Fig. D.4. Lateral load versus strain of: (a) and (b) the 45° rosettes attached to the link beam web in the EBF2 specimen. 371
Fig. D.5. Lateral load versus vertical deflection of: (a) west; and (b) east end of the link beam of the EBF2 specimen. 372
Fig. D.6. Lateral load versus sideway deflection of: (a) west; and (b) east ends of the link beam of the EBF2 specimen. 373
Fig. D.7. Lateral load versus strain of: (a) and (b) the 45° rosettes attached to the vertical link beam web of the SPS1 specimen. 374
Fig. D.8. Lateral load versus link beam distortion in the SPS1 specimen. 375
Fig. D.9. Lateral load versus vertical deformation at: (a) top west; and (b) top east of the vertical link beam of the SPS1 specimen. 376
Fig. D.10. Lateral load versus strain of: (a) bottom flange; and (b) top flange of the channel section of the Channel specimen at a distance of the channel depth from each end 377

Notations

A Seismic acceleration coefficient (code-specified value or from site-specific data), also cross-sectional area of the entire superstructure

A_b Cross-sectional area of braces

A_{bb} Cross-sectional area of the bottom beam

A_g Area of the stiffened girders (in stub-girder model)

A_l Cross sectional area of the link beam

$A_{s,l}$ Shear area of the link beam

a Length of the beam outside the link

B A ratio to simplify the expression for force reduction factor in presence of strain-hardening

b Lacing plate width

b_f Width of beam flange

b_T Width of TADAS plates

C Viscous Rayleigh damping matrix

C_1, C_4 Constant coefficients depending upon the boundary conditions

C_k Stiffness proportional damping ratio

C_m Mass proportional damping ratio

C_r Ratio of right to left end-diaphragm stiffnesses (K_{b2}/K_{b1}, usually 1.0)

C_s Seismic response coefficient

C_{SH} Strain-hardening ratio for reduction factor in presence of strain-hardening

C_{test} Damping coefficient for the specimen in pseudodynamic testing

d_{bb} Depth of bottom beam

d_{ch} Depth of channel section

d_{LVDT} Distance between the two LVDTs used to measure device rotation

d_l Depth of link beam

E Modulus of elasticity

E_H Hysteretic energy in each cycle

e Link length

e_{max} Maximum link length to have still a shear link

$F_{eq.max}$ Maximum equivalent lateral force applied to the entire end-diaphragm

F_u Tensile strength of steel member

F_y Yield stress of steel

f_c' 28 day target strength of concrete

g Gravitational acceleration

H Height of bridge (end-diaphragm)

h_g Height of stiffened girders

h_l height of vertical link (in SPS)

h_T Height of TADAS plates

h_T/t_T Height-to-thickness ratio of the TADAS plates

h_w Girder web height between top and bottom flanges

I_{ch} Larger moment of inertia of the channel used in channel diaphragm

I_g Moment of inertia of stiffened girders (stub-length) in the lateral direction

K_b Stiffness of lateral bracing systems at one end of bridge

K_{DD} Lateral stiffness of ductile diaphragms

ΣK_{DD} Sum of lateral stiffnesses of the ductile diaphragms

K_{EBF} Lateral stiffness of the EBF implemented as end-diaphragm of slab-on-girder bridges

K_e Equivalent stiffness of the entire bridge

K_{ends} Lateral stiffness of end-diaphragms accounting for all acting diaphragms in both ends

K_g Lateral stiffness of stiffened girder

Σk_g Sum of lateral stiffnesses of the stiffened girders

K'_g Equivalent lateral stiffness of a stiffened girder due to intermediate web stiffeners

K_{IS} lateral stiffness of intermediate web stiffeners

K_{SPS} Lateral Stiffness of SPS end-diaphragm in a slab-on-girder bridge

K_{subs} Lateral stiffness of substructure including abutments, columns, piers and foundations

K_T Theoretical elastic lateral stiffness of a TADAS device

K_{TADAS} Lateral stiffness of the TADAS implemented as end-diaphragms of slab-on-girder bridges

K_{test} Lateral stiffness of the specimen in pseudodynamic testing (7.5 kN/mm)

K^* Generalized stiffness of the bridge

K_b^* Dimensionless lateral stiffness expression of end-diaphragms, and generalized stiffness for simplified braced model

K^*_{unb} Generalized stiffness for unbraced girders

I_{bb} Moment of inertia for bottom beam

I_D Moment of inertia of entire bridge section about a vertical axis perpendicular to its deck

I_l Moment of inertia of the link beam

I_s Moment of inertia of the bearing web stiffener about the longitudinal axis of the bridge

I_w Girder web moment of inertia per unit length about the longitudinal axis of the bridge

L Bridge span length, also span length for the 3-point bending test

L_s Girder spacing

l_b Length each brace in ductile diaphragms

M Mass of entire bridge

$M_{ch.E}$ Bending moments at the east end of channel

$M_{ch.W}$ Bending moments at the west end of channel

$M_{ch.g}$ Moment in the channel at the location of the gages fixed to top and bottom flanges

M_l Bending moment at the onset of shear yielding

M_{max} Maximum bending moment in the link beam

M_y Expected yield moment capacity for lacing plates

M_p Expected plastic moment capacity for lacing plates

$M_{w,max}$ Maximum bending moment in the stiffened web

M_p^* Reduced moment capacity of the link yielding in shear

m Mass per unit length for entire bridge

$m(x)$ Distribution mass function of the bridge

m_g Girder mass per unit length

m_s Slab mass per unit length

m_{test} Equivalent mass considered for the specimen deck for pseudodynamic testing (71500 kg)

m^* Generalized mass of bridge

m^*_{unb} Generalized mass for unbraced girders

m^*_b Generalized bridge mass for the equivalent braced model

$m^*_b \ddot{u}_g$ Inertia force acting on unbraced bridges

N Length of bearing plate under the flange

N_T Number of TADAS plates

n_d Number of end-diaphragms implemented at each support

n_g Number of girders

P_e Equivalent static force acting on the braced bridges

P_{eff} Effective force acting on the generalized bridge models

P_p Plastic capacity of lacing plate in 3-point bending test

P_y Yield strength of lacing plate in 3-point bending test

PSa Pseudo-spectral acceleration

Q Stiffness ratio of ductile diaphragm to stiffened girder

R Reduction factor due to the ductile behavior

R_s Support reaction resulting from bridge lateral loading tributary to one girder

R_1, R_2 Reactions at fixed and simple supports for bridges fixed at one end

r Ratio of inelastic load level to yield strength

S Site coefficient in seismic load expression

S_s Spacing of web stiffeners

S_d Spectral displacement

T Lateral period of the bridge

T_{max} Maximum kinetic energy (Rayleih method)

t Average thickness of a lacing plate

t_f Link beam flange thickness

t_T Thickness of TADAS plates

t_w Thickness of girders' web

U Strength ratio of dual systems (corresponding to yielding of stiffened girders and device)

u(x) Lateral displacement function assumed for the bridge

$u(x,t)$ Displacement function of the bridge deck

ρ Mass density

ρA Superstructure mass per unit length

$\ddot{u}_g$ Ground motion acceleration

V Lateral load

V_b Axial compression force for which braces should be designed

V_{ch} Lateral load corresponding to the moments resisted by channel in double curvature

V_d Design shear resistance of ductile device

V_e Elastic seismic base shear resistance for one end-diaphragm (elastic lateral load)

V_{inel} Inelastic lateral load (base shear)

V_l Required shear to be resisted by link beam

$V_{l,p}$ Plastic shear capacity of a wide flange beam

V_{max} Maximum potential energy (Rayleih method)

V_p Link shear strength

V_T Shear strength of TADAS

$V_{T,p}$ Plastic strength of TADAS device

$V_{T,y}$ Yield strength of TADAS device

V_y Yield strength of ductile device

V_y' Yield strength of stiffened girders

V^+_{max} Maximum positive lateral load applied to the specimens

V_g Lateral load resistance of one stiffened girder

W Maximum expected wind force

$W_{internal}$ Internal work

$W_{external}$ External work

x Variable in a direction along the girders

x_T Horizontal displacement measured by a Temposonic transducer

$Y(x)$ Lateral displacement function for braced bridges

y_1, y_2 Vertical displacements measured by LVDTs 1 and 2, to obtain the SPS link distortion

y_{T1}, y_{T2} Vertical displacements from the Temposonic transducers at the ends of the link beam

$Z(t)$ Periodic motion function

α A dimensionless parameter to determine elastic response of bridges

β A parameter to evaluate elastic response of unbraced bridges (without diaphragm)

γ Distortion angle of the device

γ_l Link distortion angle (if no rotation at the bottom end of SPS or TADAS devices occurs)

γ_{EBF} Total link distortion angle for the EBF system

γ_{max} Maximum link deformation angle or shear strain (easily obtained by dividing the maximum relative displacements of link ends by the link length; or from strain rosettes)

γ_p Plastic distortion angle for the link

γ_{xy} Shear strain in a coordinate system

$\gamma_{p.TADAS}$ Inelastic distortion demand for a TADAS device

γ_{SPS} Total link distortion angle for the SPS device

γ_y Yield distortion angle

Δ_s Maximum deck displacement

δ Lateral displacement at the end of the TADAS plates

δ_{max} Extreme value of deck displacement

$\Delta_b(x)$ Girder bottom flange lateral displacement

$\Delta_r(x)$ Bottom flange relative lateral displacement

Δ_s Slab displacement in transverse direction

δ_e Lateral displacement that would have resulted from elastic analysis

δ_{max} Maximum lateral drift of bridge at diaphragm location

δ_y Deck drift due to yielding of ductile device

δ'_y Deck drift corresponding to yield displacement of stiffened girders

μ	Ductility
μ-R	Bilinear or trilinear relationship between ductility and reduction factor
θ	Angle of a given direction to horizontal axis
θ_b	Slope angle of braces with respect to the horizontal, x, axis
θ_{bb}	Bottom beam midspan rotations for TADAS and SPS specimens
θ_l	Rotation of link beam at its ends
θ_p	Plastic rotation angle
$\epsilon_{bb.east}$	Strain recorded in the bottom beam on the east side of the ductile device
$\epsilon_{bb.west}$	Strain recorded in the bottom beam on the west side of the ductile device
ϵ_{ch}	Average strain data from the gages attached to the top and bottom flanges of a channel
$\epsilon_{i.east}$	Strain in the *ith* brace located in the east side of specimens
$\epsilon_{i.west}$	Strain in the *ith* brace located in the west side of specimens
ϵ_{max}	Maximum axial elongations at failure for tension coupons
ϵ_x, ϵ_y	Normal strains in a coordinate system
ϵ_θ	in a direction having an angle of θ with
ϵ_{45}	Strain data obtained from the middle gage of rosette
ξ	Damping ratio
ξ_n	Damping ratio for the n*th* mode of vibrations
ω	Rotational frequency of bridge lateral excitations
ω_n	Angular frequency for the n*th* mode of vibrations
φ	Phase angle of a periodic motion
ϕ	Resistance factor (0.9)
σ_{max}	Maximum stresses in the girders web
ζ	Earthquake excitation factor

Acronyms

AASHTO	American Association of State Highways Officials
ADINA	Automatic Dynamic Incremental Nonlinear Analysis

CAN/CSA	Canadian Standard Association
EBF	Eccentrically Braced Frame
LVDT	Linear Variable Displacement Transducer
NBCC	National Building Code of Canada
OHBDC	Ontario Highway Bridge Design Code
PGA	Peak Ground Acceleration
SAP90	Structural Analysis Program (1990)
SDOF	Single-Degree-Of-Freedom
SMAW	Shielded Metal Arc Welding
SPS	Shear Panel System
TADAS	Triangular-plate Added Damping And Stiffness
UDL	Uniformly Distributed Load

CHAPTER 1

INTRODUCTION

1.1 Statement of the Problem

The seismic vulnerability of existing bridges remains an important problem, since most of these structures have been built before the first seismic-resistant provisions were enacted. As knowledge on some seismicity issues is relatively recent, the earthquake-resistant provisions of the current design standards for highway bridges are still primitive and may, in many cases, be ineffective in ensuring a satisfactory seismic performance. Recent earthquakes worldwide have demonstrated that such old structures can behave poorly under even a moderate ground excitation (Tseng and Penzien 1973; Degenkolb 1978; Douglas 1979; Priestley 1988; Lew 1990; Roberts 1992; Astaneh-Asl et al. 1994; Earthquake 1990, 1994, 1995; Mitchell et al. 1995; Bruneau et al. 1996).

An indifferent attitude existed regarding these severe deficiencies for a long time in Canada, and the necessity to address this problem was first realized only shortly before the Loma Prieta (San Francisco) earthquake of 1989, and clearly articulated following it. During that moderate earthquake of Richter Magnitude 7.0, a number of bridges failed, some as far as 100 km away from the epicentral region, at a great loss of life and with large direct and indirect costs and economic losses to the region. Three major conclusions, in a report presented to California Governor, were made after the earthquake (Earthquake 1990):

1. Many structures have been built deficiently in their earthquake resistance. This has been caused by the slow improvement of new knowledge through limited research in earthquake engineering bridge design and also the lag in putting research results into practice.

2. Loss of life and damage to currently existing substandard structures will dominate the impacts suffered in future earthquakes.

3. No extensively accepted technical standards for seismic rehabilitation of bridges exist.

These statements are equally descriptive for steel bridges in different regions worldwide. In other words, a great number of seismically deficient steel bridges also exist, and the cost to retrofit those bridges is terribly high.

Several short span steel bridges were shaken during the magnitude 6.8 Northridge earthquake of January 17, 1994, epicentered in a Northwestern suburb of Los Angeles (Astaneh-Asl et al 1994). The most common forms of damage to those steel bridges were end-diaphragm buckling and/or non-ductile fracture, cracking of the abutments caused by pounding of the expansion joints and damage to the interface between steel superstructure and concrete substructure. Damage to the diaphragms was seen only in the end-diaphragms. Astaneh-Asl et al. (1994) by analyses for one bridge showed that the earthquake inertia loads that develop in the deck are mostly transferred to the piers and abutments through the end-diaphragms. Interestingly, unpublished analyses by

the author prior to this earthquake reached the same conclusions. Astaneh-Asl et al. also suggested that:

1. The connection of steel superstructure to concrete substructure needs to be made more ductile by using special bolts and passive energy dissipators.

2. In end-diaphragms, the use steel semi-rigid connections and diaphragms with initially bent members, can improve performance and reduce seismic forces and displacements.

However, they did not provide quantitative design guidance in addition to that opinion. It is noteworthy, however, that many short span steel bridges, of less critical configurations and subjected to smaller peak ground accelerations, were unaffected by the Northridge earthquake. Moreover, steel bridges designed using post-1980 seismic-resistant standards appeared to have performed better during this earthquake, although their number is limited in California.

A large number of steel bridges were damaged by the January 17, 1995, Hyogo-ken Nanbu (Kobe, Japan) earthquake. In spite of Japan's high level of awareness, many reinforced concrete and steel bridges suffered extensive damage in the area of severe shaking (Bruneau et al. 1996). Numerous types of steel bridge failures were observed for the first time, such as: severe buckling of steel columns, brittle column failures and new types of bearing failures. This earthquake clearly demonstrated the need to design and detail steel bridges for ductile response, i.e. to dissipate energy through large inelastic deformations without significant loss of resistance during earthquake. In this perspective, the existing older infrastructures constitute the largest seismic hazards.

Canada, like many other countries, is not immune to large seismic events and has a relatively old bridge infrastructure. Earthquakes of equal or even greater intensity than those of Loma Prieta and Northridge are anticipated in many major populated Canadian regions known to be seismically active. Unfortunately, the level of awareness to the existing hazards is considerably

lower in Canada than that in California, and Canadians are unquestionably less prepared to survive an earthquake (Bruneau, 1990). Therefore, the loss of life and economic disruption due to a Canadian earthquake could be very serious, particularly in light of the little redundancy of the Canadian network of transportation links. Slab-on-girder steel bridges, of the type that has suffered damage in recent earthquakes, have been built throughout Canada and the United States. In fact they have been even more common in eastern North America, where the implementation of seismic-resistant design is more recent (or still lacking in some States).

Although it is known that diaphragms provide a main load-path for the seismic loads acting on these slab-on-girder steel bridges, their impact on seismic performance is still unclear in many ways. Research is needed to identify the respective impact of end and intermediate diaphragms on seismic response of these steel bridges.

Furthermore, for those existing steel bridges identified as seismically vulnerable, to prevent fatal potential failures in future earthquakes, seismic rehabilitation or replacement must be contemplated by the agencies responsible for the transportation systems. Using current knowledge, retrofit costs to bring bridges to current design standards are often prohibitive. There currently exists considerable knowledge on how to retrofit reinforced concrete bridges, but little knowledge on how to retrofit existing steel bridges. Effective and economical rehabilitation techniques for such bridges are highly needed. Given that many steel bridges are supported by seismically vulnerable substructures, and that substructure rehabilitation in most cases is very expensive, it would be advantageous to develop a retrofit strategy to limit or reduce the lateral loads transferred to these non-ductile existing piers and abutments.

1.2 Research Objectives

This research program is concerned with the seismic structural behavior and rehabilitation of existing steel highway slab-on-girder bridges. The general objective is to improve seismic

performance of these bridges by paying special attention to the impact of diaphragms on seismic behavior, and to develop a new retrofit strategy for these bridges, using special ductile lateral bracing systems inserted in the superstructure at some selected diaphragm locations, to avoid retrofitting the substructure. The research methodology is to analytically investigate and quantify the role of diaphragms on seismic resistance, to formulate possible innovative rehabilitation schemes to be implemented in the superstructure to limit the seismic loads transferred to the substructure, to determine the most promising ones, and to verify the results experimentally. More explicitly, the main objectives and procedures of the research work are:

1. To develop the new knowledge and analytical models of the seismic behavior of existing steel bridges having diaphragms of different stiffnesses, to identify the needs for satisfactory performance, and the consequences of existing deficiencies such as loss of diaphragm due to non-ductile response or badly rusted diaphragm braces. These models and knowledge would enable structural engineers to perform safer and more accurate analyses of individual bridges, which can lead to saving in retrofit costs and even demonstrate, in some cases, that rehabilitation may not be needed.

2. To formulate effective seismic retrofitting techniques which can be implemented in a Canadian context to mitigate the seismic hazards in slab-on-girder steel bridges, and specially to prevent substructure failure. The objective of all rehabilitation strategies is to provide a better control on seismic behavior by developing more desirable and ductile failure modes. The most efficient rehabilitation techniques that would improve the behavior of the existing bridges, to ensure that seismic safety requirements for these bridges are met, are sought throughout this research. To achieve this main objective, triangular-plate added damping and stiffness (TADAS), eccentrically braced Frame (EBF) and shear panel system (SPS) as ductile seismic retrofit techniques are introduced as end-diaphragms (over abutments, piers or other intermediate supports) in existing steel bridge superstructures. The strategy is to create special ductile diaphragms that rely on a few plates or beam segments yielding in flexure or in shear to provide excellent inelastic behavior and energy dissipation characteristics (note

that this concept can be extended to new steel bridges as well). These special ductile systems can produce stable and predictable hysteretic cyclic loops, contrary to the existing diaphragms built of concentric braces that have been widely used in steel bridges, in which pinching is usually observed in the hysteretic loops due to buckling of braces and for which yield/buckling strength is less is less accurately predictable. No research work on the implementation of such systems in bridges has been done in the past for bridges so far.

3. To analytically and experimentally investigate the proposed ductile systems for existing and new steel bridges, and to identify the potential advantages of such devices in designing steel bridges in regions of high seismicity.

4. To identify the effects of corrosion on the strength and ductility of the steel base material and steel components, to investigate whether severely rusted end-diaphragms can undergo the numerous cycles of alternating plasticity expected during an earthquake. It is noteworthy that the most vulnerable locations to corrosion are the bridge ends and supports where corrosion usually occurs as the result of deck joint leakage or the accumulation of road spray. Steel bridges in Canada are subjected to this problem due to considerable amount of salt and deicing materials used on roads in the winter.

1.3 Scope of Work

To achieve the above objectives, the following research is conducted:

1. The impact of diaphragms on seismic behavior is studied by using the SAP90, DRAIN and ADINA programs. The period of bridges in the transverse direction, maximum lateral displacement, and maximum pseudo acceleration required to cause first yielding in the bridge, are the chosen parameters of interest in that study. A few short to medium single span simply supported slab-on-girder bridges are studied by varying their geometry and structural

parameters to represent a broad range of existing steel bridges. The seismic performance and behavior of foundations and abutments, as well as soil-structure interaction, are beyond the scope of this research.

2. Analytical models to simulate the seismic behavior of steel bridges are developed to obtain the above results using hand calculations. These models can give reliable results for the displacement, and period in transverse direction for two different fundamental cases;

   (i) No end-diaphragms action, i.e. no effective bracing system in the superstructure to resist lateral loads beyond the bridge girders alone.

   (ii) With end-diaphragms (may consist of bearing web stiffeners only).

   In each case, the effect of intermediate diaphragms is also investigated.

3. TADAS, EBF and SPS are proposed as effective ductile diaphragms to resist lateral loads. A simple design procedure is developed for the proposed ductile end-diaphragms. Ductile systems are designed for simply-supported steel bridges of various spans. Then, the period of resulting bridges are calculated, and analysis is conducted for seismic forces obtained by using AASHTO (American 1994) or Newmark-Hall design spectra (Newmark and Hall 1982). Time history dynamic elastic and inelastic analyses are also carried out to validate the concept.

4. A few specimens having one ductile diaphragm connected to two stub-girders, being partial full-scale models of a 40 m span slab-on-girder bridge, are designed according to the proposed design procedure. The full-scale TADAS, EBF and SPS specimens are constructed in structural laboratory. Steel members for the specimens are provided by a fabrication shop in accordance with detailed drawings prepared for each of the components.

5. A series of cyclic tests are conducted on the specimens. Comparisons and interpretations of the obtained results follow the experimental work.

6. A few experiments on rusted components and connections are conducted, including tension tests on three rusted steel coupons, tension and shear tests on a few rusted rivets, three-point-bending test on three lacing plates and two weak-axis bending tests of a floor-beam segment. Reconstruction of a theoretical curve for a rusted coupon and comparison of ductility demand to supply is accomplished.

As knowledge on the performance of existing bridges is gained, the ability to design new seismic resistant bridges is equally enhanced. It is expected that the results of this analytical and experimental research will lead to more rational seismic resistant design guidelines for new and existing bridges in Canada and worldwide.

1.4 Outline of the Thesis

Chapter 2 reviews the literature on the seismic performance of steel bridges during past earthquakes. The existing requirements for seismic design and rehabilitation of existing steel bridges, and recent seismic retrofit of steel bridges are presented as well.

Chapter 3 investigates the effect of diaphragms on the seismic response of slab-on-girder bridges. The behavior of typical steel bridges subjected to lateral loading is investigated using the programs SAP90, DRAIN and ADINA. Some analytical models are developed to predict bridge behavior in different cases.

Chapter 4 proposes the use of TADAS, EBF and SPS in end-diaphragms of different steel bridges as effective ductile seismic retrofit techniques, to protect substructure from damage. A simple

design procedure is developed and results from inelastic analyses are presented for a few examples to verify the results obtained by the proposed model.

An experimental program is then conducted to validate the ductile diaphragm concept. Description of the test specimens, including details of their design, their predicted capacity and ductility, their construction, the required test set-up and experimental procedure, are presented in Chapter 5.

Chapter 6 explains the test observations and experimental results in details, and the obtained results are discussed, compared and interpreted against their predicted values in Chapter 7.

In Chapter 8 the effects of corrosion on the seismic performance of steel bridges are investigated. The experimental work conducted to study the effect of rust on the strength and ductility of steel members and connections is described, the results obtained are presented and their significance is discussed.

Finally, conclusions and practical recommendations are made in Chapter 9 based on the analytical and experimental findings, and some outstanding issues are identified for future research.

CHAPTER 2

LITERATURE REVIEW

2.1 Introduction

Several steel bridges have collapsed or suffered significant damage during recent earthquakes such as the 1989 Loma Prieta (Earthquake 1990), 1994 Northridge (Astaneh-Asl et al. 1994; Earthquake 1994; Mitchell et al. 1995) and 1995 Kobe earthquakes (Earthquake 1995; Bruneau et al. 1996). Historically, these earthquakes have demonstrated that the current stock of bridges is vulnerable to seismicity, sustaining damage to diaphragms, bearings, substructures and foundations, and in some cases being totally destroyed as superstructures collapse from their supporting elements. A majority of existing bridge structures were designed and constructed when the level of knowledge and awareness of seismic performance was inadequate compared with current understanding.

Although the potential seismic vulnerability of bridges has long been recognized (e.g. Tseng and Penzien 1973; Kawashima 1990), these more recent failures have triggered considerable seismic

evaluation and retrofit activities throughout North America, and generated renewed research interest on that subject. Those past earthquakes taught engineers valuable lessons about the seismic resistance of bridge structures and resulted in the development of improved seismic provisions for the design of new highway bridges. They showed that special attention must be paid to the substructures, foundations and connections of bridges superstructures, to provide the strength and ductility needed for good performance during an earthquake. Other important lessons learned from past seismic events indicate that:

- The transfer of lateral forces to the ground, by the shortest and most direct path, can essentially ensure the best seismic performance.

- Symmetry in plan is recommended to minimize rotation about a vertical axis and avoid damaging effects of torsional forces.

- Different components of a bridge must remain connected together during an earthquake.

These criteria, i.e. simplicity, symmetry and integrity, define a good structural form for ductile behavior. This is true for all bridges, including steel bridges.

However, few of the existing steel bridges were designed to resist lateral loads considering the above criteria. Recent earthquakes around the world have demonstrated that these structures can behave poorly during even a moderate ground excitation (e.g. Bruneau 1990, Filiatrault et al. 1994). Several bridge collapses have occurred as a result of seismic activity at even relatively low levels of ground motion, eg., many bridge failures in the 1989 Loma Prieta earthquake were at acceleration levels of 0.15-0.25g (Mayes et al. 1992). Consequently, many steel bridges could be damaged when subjected to an earthquake, and should therefore be evaluated and, if needed, retrofitted to ensure that the infrastructure remains undamaged or only slightly damaged after an earthquake.

2.2 Reported Seismic Performance of Steel Bridges

The moment magnitude 6.7 San Fernando earthquake of 1971 revealed many inadequacies in bridge design codes prevailing at the time. While many concrete bridges suffered extensive damage, steel bridges were few in the epicentral area. Damage to a steel bridge occurred when its simply supported girders fell off their supports because they were not tied down (Roberts 1992).

After that earthquake, research was conducted to identify the structural components and parameters that significantly affect the seismic response of bridges. The addition of longitudinal restrainer ties between adjacent parts of the superstructure at expansion joints to tie superstructure to supporting substructure (Degenkolb 1978) was found to be a necessity for most existing bridges. That research also identified the strength and distribution of bridge piers in each segment of the superstructure to be the primary factors that affect the lateral response of multiple span bridges (Tseng and Penzien 1973).

Concrete bridges supported by concrete piers having non-ductile detailing (such as insufficient amounts of spiral and lateral reinforcement, inadequate splice length and end anchorage, etc.) exhibited poor seismic behavior during that earthquake. This suggests that bridges having steel superstructures supported by similar substructures were exposed to the same vulnerabilities (although this was not mentioned in the literature).

In further studies following the San Fernando earthquake, Tseng and Penzien (1973), correlating computer analysis results with the actual behavior of bridges to improve modeling techniques, showed that linear seismic response analysis can provide a good evaluation of the maximum displacement response of a bridge structure but less accurate prediction of the internal forces in the structure. Douglas (1979) showed that the vertical stiffness of composite girder bridges can be estimated by treating them as continuously composite with a uniform effective modular ratio considered along the entire length of the bridge deck. Imbsen & Penzien (1984) showed that

collision between adjacent segments of a bridge can produce large shear forces at the superstructure-substructure connections such as bearings. They also indicated that special attention must be paid to the transverse shear restraint at expansion joints: lack of this restraint can cause a large opening in the expansion joint due to the rigid body rotation of the bridge deck about a vertical axis.

Priestley (1988) reported that non-uniform distribution of pier stiffnesses along bridges and disproportionate flexural and shear strengths of concrete piers are also important factors negatively affecting bridge response. These factors were responsible for the damage to a few concrete bridges during the 1987 Whitter earthquake.

Several elevated highways and bridges in the San Francisco Bay Area sustained serious damage, during the magnitude 7.1 Loma Prieta earthquake of October 17, 1989. Beyond the damage to concrete bridges, (most notably the collapse of the double decked Nimitz freeway in Oakland (Lew 1990)) a few steel bridges suffered damage. A large truss bridge, the East Bay Crossing of the San Francisco-Oakland Bay bridge, sustained some damage when a 15 m long segment of the bridge upper collapsed on the lower deck resulting in closure of the bridge for a month (Astaneh-Asl 1993).

Damage also occurred at the truss anchorage to the top of a pier of the San Francisco-Oakland Bay bridge due to the differential movement between various piers of this rather long bridge. Evidence of joint movement of 125 to 300 mm was visible. Roberts (1992) estimated that a force of 9000 kN was required to shear all the anchor bolts at that anchorage point and break the friction force between the bearings and the top of steel tower. Damage to the bearings of another large steel bridge, the Hayward-San Mateo Crossing, was also reported (Earthquake 1990). The Fifth Avenue/880 overpass in Oakland, which has steel multiple column single deck superstructure, was also damaged during the Loma Prieta earthquake. Damage consisted of plastic hinges at the base of some steel columns and slippage of girders on their support on top

of the columns. In some locations where plastic hinges had formed, cyclic local buckling was observed (Astaneh-Asl et al. 1993).

Caltrans had completed the first phase of a billion dollar multi-phase seismic retrofitting program for older bridges on the State Highway system. Thus, all highway bridges had been retrofitted with restrainer cables at deck joints, as shown in Fig. 2.1, and backup bumper systems constructed around the sliding bearings. This has been instrumented in limiting damage during the Loma Prieta earthquake.

A few bridges were also damaged by the April 25-26, 1992 Mendocino earthquakes. One steel truss bridge, the Van Duzen River bridge, suffered limited spalling of deck joints, minor cracking of abutment walls, and buckling of vertical and horizontal members of the wind bracing systems (Roberts 1992). Figs. 2.2 and 2.3 show buckling of the lateral bracing system on the bridge. This was also typical of all the girder spans on several bridges inspected after that earthquake. Longitudinal movement of the Van Duzen River bridge was also observed, as shown in Fig. 2.4, causing a sag on one side of restrainer cables, while the cables on the other side were taut.

The magnitude 6.7 Northridge earthquake of January 17, 1994 caused failure of bridges in the Los Angeles area. At least four steel bridges sustained some structural damage to their reinforced concrete substructure, steel diaphragms, and connections of the substructures to steel superstructure (Astaneh-Asl et al. 1994).

The Pico-Lyons overcrossing, a skew bridge of two spans about 48 m each, experienced some structural damage during the Northridge earthquake, in the areas where the substructures provide support for the steel girders. This damage consisted of anchorage failure of the girder restrainers, roller support movements, and damage to the connections of the end diaphragms. Steel girders apparently moved in the longitudinal and transverse directions, as much as 102 mm causing the bolts between the girder flange and the restrainer angles to reach the end of their slotted holes (Fig. 2.5). Further longitudinal movement pulled the restrainer angles away from the abutment

walls. Three end-diaphragms at the east abutment also suffered damage: Gusset plate connections, stiffener plate connections, and stiffener to girder web connection, buckled or fractured as shown in Figs. 2.6 and 2.7 (Astaneh-Asl et al. 1994).

Horizontal and diagonal members of the end- diaphragms above a pier of the Santa Clara River bridge, having seven simply-supported 32 m-long skewed spans, buckled during the 1994 earthquake Astaneh-Asl et al. (1994). Staggering the diaphragms was blamed for the behavior of this skew bridges. Furthermore, a gap that existed between the bottom of several stiffeners and the flange allowed out-of-plane bending and damage of the girder webs at the location of the intermediate diaphragms.

The end-diaphragms of riveted Old Road bridge, having five 25 m simply-supported spans, suffered damage as well, during the Northridge earthquake. These diaphragms brace the two main plate girders to each other. The steel angle V-braces of the end-diaphragms of spans 2,3,4, and 5 buckled as shown in Fig. 2.8. In span 1, since the end-diaphragms were solidly secured to the abutment, the entire superstructure moved together essentially as a rigid box. The fracture of some anchor bolts in shear at the pin bearing assembly of abutment was also reported (Astaneh-Asl et al. 1994). The superstructure was displaced 50 to 100 mm in both the longitudinal and transverse directions, respectively.

The ends of the Valencia bridge, having two spans of 37 m each, also moved by about 150 mm at the west abutment and 75 mm at the east abutment.

Numerous steel bridges suffered extensive damage in the January 17, 1995 Kobe (Japan) earthquake. Subsequently, most major roads and railways crossing Kobe were closed due to collapsed or severely damaged bridges. Despite past earthquakes, this seismic event occurred in an area having a large number of steel bridges. Thus, a superb opportunity was provided to investigate the behavior of these bridges of various types. Bruneau et al. (1996) reported extensive damage to steel columns: local buckling of round columns used on part of the west

Kobe expressway leading to rupture of buckled steel due to excessive inelastic deformations (Fig. 2.9), and brittle failures in some columns with no signs of local buckling (Fig. 2.10).

Bearings also suffered extensive damage, mostly after major substructure damage, although in some cases, they failed while the substructure remained unaffected. The most severe bridge failure occurred where the elevated Hanshin expressway bridge rolled over. As shown in Fig. 2.11, the longitudinal and lateral movements at its superstructure on the pier caps was up to 300 mm (Earthquake 1995). No diaphragm failures similar to those discovered during the Northridge earthquake were reported, as Japanese steel bridges appear to have strong diaphragms and effective underside lateral bracing (Bruneau et al. 1996).

2.3 Concerns and Expected Seismic Vulnerability

Based on the study of damage to steel bridges during past earthquakes and corresponding analytical work by Tseng & Penzien (1973), Degenkolb (1978), Roberts (1992) and Astaneh-Asl et al. (1994), the seismic vulnerability of these bridges can be attributed to:

- The lack of longitudinal restrainer ties between deck segments at expansion joints.

- Non-ductile piers and substructures.

- Non-ductile connections of steel superstructures to concrete substructures (For example, in the lateral direction, steel rollers may slip on their masonry plate, causing some damage to the keeper ring plates welded to the ends of each roller).

- Shear or tensile failure of threaded anchor bolts connecting bearings to the substructure (Note that ductility can be increased using special anchor bolts for which the shank is machined to

about 75% of the diameter of threaded area, making the unthreaded shank yield and elongate as a weak link).

- Non-ductile end and support-diaphragms of steel slab-on-girder superstructures and their connections.

2.4 Existing Requirements for Seismic Design of Steel Bridges

In the bridge design codes currently used in North America (e.g. Ontario, 1991), seismic force levels are specified for design but ductile detailing requirements are not specified for structural members with the exception of concrete substructures. This suggests that existing codes fail to recognize that steel bridges may need to perform in the inelastic range to withstand the design earthquake. The 1995 Kobe earthquake showed that steel bridges, so designed to resist code specified loads without ductile detailing, may have insufficient energy dissipation ability in the inelastic range to survive earthquakes (Bruneau et al. 1996).

Structural elements expected to undergo inelastic response are generally designed for inelastic design load levels obtained from dividing the elastic forces in these elements by a reduction factor, R. Contrary to building design practice, different R values can be assigned to different systems of a same bridge as well as for components and connections. Those members for which a reduction factor greater than 1 is specified require special detailing to ensure their ductile performance. However, no such detailing requirements exist at this time for elements of steel bridges and their connections.

Design requirements for diaphragms in steel bridges are few. According to current bridge design codes, steel girders with spans greater than 50 m need a system of lateral bracing located in or close to the plane of bottom flanges. These cross frames or diaphragms should be as deep as possible. In addition to the forces due to ultimate loading condition, the bracing systems must

be designed to carry a lateral load equivalent to 1% of the force in girders' compression flange at the ultimate limit state. Unless analysis shows otherwise, intermediate cross frames or diaphragms are required at intervals of 8 m or less (Ontario 1991; American 1994).

While these codes require that end-diaphragms shall be proportioned to transfer all loads in the direction transverse to the bearings (and are designed by some Transportation Departments to also serve as transfer member to lift the superstructure during future bearing repairs), nothing is stated about the role of the intermediate diaphragms. Although these diaphragms facilitate the construction process and stabilize the top compression flange of steel girders until the composite concrete slab is in place, no design recommendation nor detailing requirement is provided by the codes.

2.5 Existing Requirements for Seismic Rehabilitation of Steel Bridges

Once a Regulatory Authority has performed a preliminary study to evaluate the vulnerability of its existing bridges, using one of the available methods (e.g. Seismic 1983, Filiatrault et al. 1994), the most vulnerable bridges will be targeted for seismic retrofit.

Existing retrofit guidelines do not strictly specify how bridges are to be retrofitted. In fact, seismic rehabilitation of bridges is a relatively new activity. Some of the more common seismic retrofit procedures that have been implemented to date include:

- Strengthening or replacement of steel bracing systems (to increase the capacity of bracing members, to avoid their buckling in compression, and to enhance their end connection details to preclude brittle failure).

- Addition of longitudinal joint restrainers, transverse bearing restrainers, and vertical motion restrainers (restrainers keep the superstructure from sliding off the bearings).

- Strengthening or replacement of bearings (for certain types of bearings, like steel rocker and roller bearings that have performed poorly during past earthquakes. In these cases, the bearing can be replaced with elastomeric pads or special energy dissipating devices).

- Bearing seat extensions (permit larger relative displacements to occur at the joints without loss of support).

- Base isolation systems (reduce the real elastic forces transferred to the non-ductile substructures).

- Jacketing of reinforced concrete substructures (enhances ductility, flexural strength and shear strength of concrete piers) (Priestley et al. 1992, 1996).

This list is not exhaustive as codes and retrofit guidelines outline concepts in seismic rehabilitation that are not intended to restrict innovative designs.

Seismic isolation offers significant benefits and has been popular for steel bridges. However, it should not be considered as a panacea. Feasibility studies are required in early phases to evaluate both the technical and economic issues (Mayes et al. 1992). Moreover, seismic isolation can be expensive in some cases. For instance, to implement base isolation for an existing bridge, it is necessary to lift the girders at their supports and re-shape the abutments. The seismic rehabilitation of abutments is generally one of the most difficult and costly aspects.

In this thesis, in the same perspective of limiting seismic loads acting on bridges, ductile devices such as TADAS, EBF and SPS and other passive energy dissipators are implemented in the end-diaphragms of the bridge superstructure. This technique is relatively easier and economical as will be described later in Chapter 4.

2.6 Examples of Recent Seismic Rehabilitation of Steel Bridges

2.6.1 Small and Medium Span highway bridges

Mitchell et al. (1994) reported bracing retrofit in a support bent of a pedestrian overpass in San Francisco strengthened by doubling up on the existing single angles (Fig. 2.12). The connections were also strengthened to achieve a ductile failure mode. A major steel bracing rehabilitation was provided for the Granville and Burrard bridges in Vancouver, B.C. for which large bracing members in steel deck trusses were strengthened and the connections were modified to enhance their capacity (Fig. 2.13).

Following the Loma Prieta earthquake, a total of 238 bridges in Seattle were inspected and evaluated based on their seismic vulnerability following a field investigation to verify that the as-built structure matched the designs. Some of the retrofit concepts that were most typical for those steel bridges included (Bridge 1993):

- Replacement of inadequate lateral bracing in steel framed bents.
- Replacement of tall rocker bearings with elastomeric bearing pads on concrete pedestals.
- Installation of "girder catchers" to replace bearings.
- Installation of restrainers at expansion joints.
- Removal of hanger pins at span hinges and fixing joints at these locations.

The Eel River bridge at Robinson's Ferry, south of Eureka, California, was retrofitted in 1988 with base isolation bearings on its two 90 m-through-truss bridges, before the April 25-26 Mendocino earthquakes occurred. This retrofit detail precluded the necessity of upgrading the older piers, as the base shear forces were reduced. Rocker bearings were replaced with neoprene pads and base isolation systems (Roberts 1992). However, seismic retrofit of steel and concrete piers were deemed necessary for some other existing bridges (e.g. MacRae et al. 1990; Priestley et al. 1992, 1996).

2.6.2 Large Span Highway Bridges

Subsequently to the 1989 Loma Prieta earthquake, the seismic retrofit criterion for the East Bay Crossing of the San Francisco-Oakland Bay bridge called for maintainance of functionality through future earthquakes. The proposed seismic retrofit strategies are shown in Fig. 2.14. For the cantilever-span segment of the bridge, strengthening alone or a combination of strengthening and local semi-rigidity on the top of pier E1 (Fig. 2.14) was considered. For the 154 m and 88 m span truss segments, strengthening also was found too costly to implement. Thus, for these segments, a technique to make the structure "semi-rigid" was proposed (Astaneh-Asl 1993). This retrofit solution was considered by Caltrans for implementation for a while.

A combination of isolators and strengthening the structure were considered for the seismic retrofit of the Golden Gate suspension bridge (Fig. 2.15), after the 1989 Loma Prieta earthquake. Isolators and dampers increase the structural period and energy dissipation ability. Strengthening consisted of adding material to components and footings, and replacing members with stronger elements (Seim et al. 1993).

2.7 Summary of Research Needs

The seismic behavior of short to medium span steel bridges needs to be further studied to develop specific procedures for their seismic design and retrofit. Most of the current knowledge in earthquake-resistant bridge design is based on past studies of concrete bridges, and may require adjustments to effectively capture the seismic behavior germane to steel bridges considering the major differences in structural behavior and dynamic response of steel and concrete bridges.

At the beginning of a bridge seismic rehabilitation, it is required to decide if the calculated risk of damage or failure warrants retrofit, and if so, to what level the bridge should be retrofitted. Appropriate seismic retrofit procedures should be developed based on the results of inelastic

analyses, laboratory test data, the performance of steel bridges during past earthquakes, and engineering judgment. While structural steel is inherently a ductile material, the bridge and its components must be able to resist the highest expected seismic forces or be retrofitted to resist those forces. Retrofit concepts and systems need to be developed to avoid excessive damage in seismic events. Steel bridges should not lose their structural functions in small to moderate earthquakes and should not collapse during rare strong earthquakes.

Innovative retrofitting techniques that can prevent future seismic damage to existing steel bridges should be formulated in a format compatible with codes as much as possible to help the design bridge engineers to achieve ductile design by providing effective, economical and easy to use retrofit solutions in a variety of options.

CHAPTER 3

IMPACT OF DIAPHRAGMS ON SEISMIC RESPONSE OF SLAB-ON-GIRDER STEEL BRIDGES

3.1 Introduction

Currently, in all available literature on the seismic evaluation and/or design of bridges (e.g. Seismic 1981; Buckle et al. 1986; Ontario 1991; American 1994), when the lateral period of a slab-on-girder bridge is determined, the superstructure (deck and girders) is modeled as an equivalent beam supported on columns and/or foundation springs. The effective transverse stiffness of this equivalent beam is calculated considering that deck and girders act as a single cross-section. While this approach is acceptable for concrete bridges and box-girder superstructures, it may not be for some types of existing slab-on-girder steel bridges. Typically, in such bridges, the concrete deck slab is supported on I-shape beams interconnected by a few discrete diaphragms, and the mechanism by which the seismically-induced inertia forces at the

concrete slab level will be transmitted to the girder bearings can be quite different from that assumed by the equivalent beam analogy. The magnitude of this difference is tied to the effectiveness of the diaphragms, and can be quite large in bridges having flexible diaphragms. In this chapter, the objective is to quantitatively investigate the lateral response of slab-on-girder steel bridges subjected to seismic lateral loads for various diaphragm conditions.

Here, a particular emphasis is placed on obtaining a proper representation of the superstructure's lateral stiffness as this has a direct impact on bridge period, and consequently on the intensity of earthquake excitation felt by the superstructure, bearings and substructure. To achieve this, the behavior of bridges with and without any effective diaphragms is studied. Although the latter case may appear to be a theoretical situation, that model might be worth considering for the bridges having severely rusted diaphragms or with only nominal diaphragms (e.g. single channels bolted along their web as shown in Fig. 3.1) frequently encountered in Eastern North America. Moreover, bridges having diaphragms with non-ductile connection details can potentially become bridges without diaphragms once brittle failures develop at those connections. Comprehensive analytical expressions that capture the behavior germane to slab-on-girder steel bridges as a function of end-diaphragm characteristics are presented, and elastic and inelastic analyses are conducted to validate the proposed models.

3.2 Preliminary Information

3.2.1 Diaphragm Design Requirements

Bridge design codes require that slab-on-girder bridges be provided with end-span diaphragms as well as intermediate diaphragms (cross-frames) at a spacing of no more than 7.6 m (American 1994) or 8 m (Ontario 1991). While codes state that end-diaphragms shall be proportioned to transmit all the lateral forces to the bearings (and are designed by some Departments of Transportation to also serve as transfer members for jacks used to lift the superstructure during

future bearing replacements), nothing is said about the role of the intermediate diaphragms. Although the intermediate diaphragms facilitate the construction process and stabilize the top compression flange of girders until the composite concrete deck is in place, no design guidance nor detailing requirement is provided by the codes. In fact, even though some engineers have alleged that intermediate diaphragms can help evenly distribute the gravity and live loads among girders during service, recent research indicates otherwise (Azizinamini et al. 1995). As a result, diaphragm design has varied considerably in practice.

Diaphragms built with braces in X or chevron configurations have been popular for years, but typically exhibit features undesirable in a seismic perspective, such as connection details that will fail prior to development of brace yielding. Moreover, these braces in older bridges were often only designed to resist wind loads, and have inadequate strength to resist earthquake loads (Xanthakos 1994). Not surprisingly, buckling and/or brittle failures of end-diaphragm members have been observed in recent earthquakes (Roberts 1992; Astaneh-Asl et al. 1994).

Interestingly, a very flexible type of diaphragm has been popular in some regions of Eastern North America. As shown in Fig. 3.1 for end-diaphragms and Fig. 3.2 for intermediate diaphragms, it consists of channels only connected by their webs to the main girders. The effectiveness of such a diaphragm to transfer lateral loads is debatable. The much lower lateral stiffness by this type of diaphragm translates into a longer bridge structural period with correspondingly lower lateral forces, but larger drifts.

3.2.2 Description and Properties of the Selected Bridges

Single-span slab-on-girder steel bridges are considered for this study. As shown in Fig. 3.3, for this common simply supported type of bridge, the deck is supported by hinged bearings on one abutment and expansion bearings on the other. The idealized bearings shown in Fig. 3.3 could be of any type that restrain superstructure displacement displacement laterally while providing simple supports. One example of such bearings that has been used in short to medium span steel

bridges is the expansion and hinged types of sliding bearings shown in Fig. 3.4. The expansion type of sliding bearings consists of a top plate, a bottom plate, a bearing bar welded to the bottom plate and supporting the top plate, two rectangular steel bars welded to the top plate to preclude transverse movement, and finally anchor bolts connecting the bottom plate to concrete abutment. The hinged type additionally has two rectangular steel bars welded on the top plate to prevent longitudinal movement. Any movement of the bridge deck is generally prevented by the interaction of the rectangular bars with the bearing bar.

Although multi-span simply supported steel bridges are known to be more vulnerable to earthquakes (Dicleli and Bruneau 1995, 1996), the behavior of those more complex bridges can be modeled using the findings from the study reported here, by replacing each simply supported span with an equivalent beam whose mass and stiffness properties are selected to give the appropriate element stiffness using the equations developed hereafter.

The bridges designed by Dicleli and Bruneau (1995) are considered. To reflect the expected seismic performance of existing highway steel bridges, these bridges were designed to be in compliance with the strength requirements of the 1961 edition of the American Association of State Highways Officials (AASHO) code (American, 1961). Full composite action between the deck and steel girders was considered in design of the bridges as this case is common in existing slab-on-girder bridges. The characteristics of those bridges used in the current case study are listed in Table 3.1.

Span length and in some cases girder web thickness are taken as geometric parameters to study their effects on the seismic behavior. Knowing that existing steel bridges have commonly short to medium span, in this research bridge spans ranging from 20 m to 60 m are investigated. In all cases, 8 m wide two-lane bridges, supported by four 350W grade steel girders spaced at 2 m center-to-center are considered. The bridge deck consists of a 200 mm thick 20 MPa concrete slab topped by 70 mm of asphalt. A one meter overhang is assumed at both sides of deck.

Finally, all bridges considered in this study do not have underside bracings; this was observed to be the case for those Eastern America bridges having rather weak diaphragms.

3.3 Slab-on-Girder Steel Bridges without Diaphragm

For bridges without diaphragm, preliminary analyses revealed that the concrete deck responded as a nearly rigid member in the transverse direction, irrespectively of the pattern of the distributed lateral load applied. From the elastic analyses, it is also found that the fundamental transverse direction mode is dominant. Hence, an equivalent static UDL (uniformly distributed load) applied at deck level was deemed representative of the seismically induced inertia forces acting on this bridge structure. In the following, a generic load level corresponding to a pseudo-acceleration of 1g is considered. Obviously, all elastic analyses results presented following can be scaled as necessary.

The lateral response behavior of typical slab-on-girder steel bridges of various span lengths was first investigated using the elastic linear finite element program SAP90 (Wilson and Habibullah 1992). It is noteworthy that as far as the maximum seismic loads required to bring the bridge to first yielding are concerned, the structural behavior would be elastic linear, and therefore SAP90 can be used (results from nonlinear inelastic analyses using other computer programs are presented later). The resulting calculated first lateral period of vibration, resulting maximum drifts, as well as pseudo-spectral acceleration (*PSa*) required to produce first yielding are presented as a function of span length in Figs. 3.5a, b and c, respectively (first yield being located in the girder web as described later). These terms vary nonlinearly as a function of span length in a complex manner because they depend on many other parameters that vary in the designed bridges of different lengths.

It is noteworthy that the resulting lateral periods and maximum lateral deflections are very large compared to values typically reported for slab-on-girder bridges in the literature, reflecting the

extreme flexibility of the structural system in absence of diaphragms. A typical deflected shape is presented in Figs. 3.6a and 3.6b, where side views at support and along span show a big difference in relative displacements. Clearly, the concrete deck slab displaces laterally nearly as a rigid body, while the flexible steel girders twist and deform laterally as necessary spanning between the slab and the supports. Closer examination of the steel beams reveals that they are most severely distorted near the supports; indeed, in each girder, the bearing supports are the only points which can counteract the lateral pull of the web to bring the lower flange under the slab. This visual observation of behavior has led to formulation of the proposed model described in the following section. Note that, throughout this study, it was found preferable to model the entire bridge (i.e. all girders and full width of deck) to capture the correct seismic behavior. Furthermore, calculated stresses and strains in the concrete deck slab are small and not reported here.

3.3.1 Proposed Model for Calculation of Period, Elastic Response, and *PSa* to First Yield

Clearly, based on the above description of behavior, an appropriate model should consider the displacement of the deck slab relative to the bottom flange of girders, the web of girders providing a stiffness link between these two components. As a result, stresses in the webs vary greatly along the span. In fact, in each girder, web stresses will be largest at both ends where the bottom flange is restrained by the bearings providing a maximum web stiffness, and will be minimum at locations close to midspan corresponding to a minimum web stiffness. Figs. 3.6c and 3.6d show a schematic simplified model of this behavior for slab-on-girder steel bridges without diaphragms.

Analytical expressions to calculate the lateral period and deformations of a bridge can be developed using this model. For that purpose, since the relative displacement between the deck slab and girders lower flanges plays a key role on behavior, it is convenient to define a relative displacement term, $\Delta_r(x)$, as:

$$\Delta_r(x) = \Delta_s - \Delta_b(x) \tag{3.1}$$

where Δ_s and $\Delta_b(x)$ are the slab and girders bottom flange displacements, respectively. Since the deck slab nearly behaves as a rigid diaphragm in its plane, Δ_s is assumed to be constant in this case. In light of the above observations, the behavior of a bridge without diaphragm was found to resemble closely that of a beam on elastic foundation, and that mathematical model was adopted here. In this analogy, the girder bottom flange and web respectively play the roles of the beam on a flexible surface and the springs of uniform stiffness. Therefore, the differential equation describing the bottom flange relative lateral displacement $\Delta_r(x)$ is (Tse et al. 1963):

$$EI_b \frac{d^4\Delta_r(x)}{dx^4} = - k_w \Delta_r(x) \tag{3.2}$$

where E is modulus of elasticity, I_b is the bottom flange moment of inertia about its strong axis and k_w is the web stiffness per unit length. If the bridge deck and bottom flanges can be assumed to remain always horizontal (i.e. without rotation about the bridge's longitudinal axis), the web stiffness can be modeled as:

$$k_w = \frac{12EI_w}{h_w^3} \tag{3.3}$$

where I_w is the web moment of inertia per unit length about the longitudinal axis of the bridge, and h_w is the web height between top and bottom flanges. In reality, SAP90 analyses of the bridges under lateral seismic loading reveal that while the deck remains relatively horizontal, the bottom flanges rotate and the above assumption makes the bridge slightly too stiff, but this is of little consequence in most cases as will be demonstrated later. On the other hand, considering a rotation function for the girders bottom flange further complicates the problem. Thus, the bottom flange rotation is ignored in this study, but its impact on results is disscussed. The classical solution of Eq. 3.2 is:

$$\Delta_r(x) = C_1 \sin\beta x \sinh\beta x + C_2 \sin\beta x \cosh\beta x + C_3 \cos\beta x \sinh\beta x + C_4 \cos\beta x \cosh\beta x \tag{3.4}$$

where C_1 to C_4 are constant coefficients depending upon the boundary conditions, and β is:

$$\beta = \sqrt[4]{\frac{k_w}{4EI_b}} \tag{3.5}$$

If both ends of each bottom flange are assumed as simply supported in transverse direction, then $\Delta_r(x)$ is:

$$\Delta_r(x) = \frac{2R_s\,\beta}{k_w}\,\frac{\cosh\beta x\,\cos\beta(L-x)+\cosh\beta(L-x)\,\cos\beta x}{\sin\beta L+\sinh\beta L} \tag{3.6}$$

where R_s is the support reaction resulting from bridge lateral loading tributary to one girder (based on the UDL applied at the deck level), and L is the bridge span. To obtain the fundamental lateral structural period, the generalized mass and stiffness, m^*_{unb} and K^*_{unb}, can be computed from the following (the subscript *unb* stands for unbraced girders):

$$m^*_{unb} = \int_0^L \left((m_s + \frac{n_g m_g}{2})\,\Delta_s^2 + \frac{n_g m_g}{2}\,\Delta_b^2(x) \right) dx \tag{3.7}$$

$$K^*_{unb} = n_g \left(\int_0^L \frac{12EI_w}{h_w^3}\,\Delta_r^2(x)\,dx + \int_0^L EI_b\,\Delta_b^2(x)\,dx \right) \tag{3.8}$$

where n_g is the number of girders, m_s and m_g are slab and girder's masses per unit length, respectively. Knowing that $\Delta_r=\Delta_s$ at the supports *(x=0)*, R_s can be obtained as a function of Δ_s from Eq. 3.6. For simplicity, since mass of the girders is much smaller than that of the slab, m_g and m_s can be lumped together and:

$$m^*_{unb} = \int_0^L m\,\Delta_s^2\,dx = mL\,\Delta_s^2 = M\,\Delta_s^2 \tag{3.9}$$

where m is the bridge mass per unit length and M is the entire bridge mass. In all cases, the lateral period of the bridge is given by (for unbraced girders, with m^*_{unb} and K^*_{unb}):

$$T = 2\pi\sqrt{\frac{m^*}{K^*}} \tag{3.10}$$

The resulting periods and maximum drifts calculated according to this procedure are plotted in Figs. 3.5a and 3.5b and compare well with the more accurate SAP90 results. In percentages, the difference between the results obtained using the proposed model and SAP90 increases as span length increases. For example, the lateral period and drift obtained by the proposed model are respectively 6% and 12% less than those given by SAP90 for the 20 m span bridge, whereas these rates increase to 9% and 17% for the 60 m span bridge. Note that periods are more closely approximated by this procedure than maximum displacements (beware that the vertical axis for the period graph does not start at zero).

Figs. 3.7 and 3.8 compare the lateral displacements of the bottom flange obtained using SAP90 and the proposed procedure, for 20 m and 60 m span bridges. In each case, three different web thicknesses were considered to illustrate sensitivity of response to this parameter. Clearly, the model works better for thinner webs and shorter spans. Although not shown on any figure, this is also true for the calculated fundamental period of vibrations, but with a lesser sensitivity. For example, the difference between the periods obtained by SAP90 and the proposed model for bridges having an 8 mm girder web thickness is only 4% compared to 6% for the case with 11 mm girder web thickness.

The observed above differences are mainly a consequence of neglecting bottom flange torsional rotations in the proposed model. Figs. 3.9 and 3.10 present the torsional rotation of girder bottom flange along span length for the 20 m and 60 m span bridges, respectively. As shown in these figures, where girder bottom flange twists are normalized per 100 mm drift, maximum normalized flange twist increases along with web thickness for a given bottom flange stiffness. Thus, for a thinner web, the normalized bottom flange twist is smaller, and the results of the proposed model and SAP90 (Figs. 3.7a and 3.8a) are in better agreement.

Maximum stresses in the girders web will occur at the bridge end and can be calculated by assuming full fixity at top and bottom of the girder web. This stress is given by:

$$\sigma_{max} = \frac{M_{w,max}\, t_w}{2I_w} = \left(\frac{6EI_w}{h_w^2}\, \Delta_s \right) \frac{t_w}{2I_w} = \frac{3Et_w}{h_w^2}\, \Delta_s \qquad (3.11)$$

where $M_{w,max}$ is the maximum bending moment in the web, t_w is the girder web thickness and Δ_s refers to maximum deck displacement. This equation is used to calculate the *PSa* required to bring the bridge to first yielding. Results are presented and compared with SAP90 results in Fig. 3.5c. Neglecting bottom flange rotation is conservative in this case.

Interestingly, if the bottom flange of each girder is assumed laterally fixed at one end (which would be the case if bearings at that end were prevented from moving in the longitudinal direction of the bridge), then Eq. 3.6 describing the relative deflection $\Delta_r(x)$, would become:

$$\Delta_r(x) = \beta \frac{2R_2 \sin\beta L - R_1 \sinh\beta L}{k_w \cosh\beta L} \sin\beta x \sinh\beta x + \frac{R_1\beta}{k_w} (\sin\beta x \cosh\beta x - \cos\beta x \sinh\beta x) + \beta \frac{2R_2 \cos\beta L + R_1 \cosh\beta L}{k_w \sinh\beta L} \qquad (3.12)$$

where R_1 and R_2 are reactions at fixed and simple supports. For the new boundary conditions, Fig. 3.11 shows the lateral deflections of the bottom flange corresponding to the same three different web thicknesses considered previously for the same 20 m span bridge. The difference between the results of the proposed model and SAP90 is again due to torsional rotation of girders bottom flange. As shown in Fig. 3.12, for a thinner girder web, the normalized bottom flange twist is smaller, and the proposed model gives closer results to those obtained by SAP90 (i.e. smaller difference in Fig. 3.11a). Compared to the previous case, drifts are smaller and longer *Psa* are needed to produce the first yield. Hence, Eqs. 3.6 to 3.11 can be used conservatively if expediency is desired.

3.3.2 Ultimate Nonlinear Behavior

The program ADINA (1995) was used to investigate the nonlinear behavior of these steel bridges and the impact of P-Δ effects (second order analysis) on this ultimate behavior. Deflected shape for a 40 m span bridge is presented in Fig. 3.13, showing most severe web distortions near the ends (Fig. 3.13b). Results from push-over analyses are shown in Fig. 3.14. The nearly identical drifts obtained at the bridge ends and midspan confirm that in absence of diaphragms the entire deck moves as a rigid body.

The inelastic analysis results also reveal that, since lateral displacements are generally large in bridges without any diaphragms, P-Δ effects due to the displaced weight of the deck are significant leading to inelastic overturning and structural instability (Fig. 3.14).

A few yielding failure mechanisms were studied for these bridges to evaluate the ultimate strength, as explained in Appendix A. In these models, two yield lines of limited length were considered in each girder web near top and bottom flanges at each bridge end. A third inclined yield line completes the failure mechanisms. Although the proposed models offer capacity results close to those obtained by the ADINA inelastic push-over analyses, the yield patterns obtained by ADINA differ from those expected from the yield lines assumed in the plastic collapse mechanisms. Stress vectors in the girder web obtained by ADINA for a 40 m span bridge (Fig. 3.15) indicate that yield lines form at the top and bottom of the steel girders, while the web at mid-height remains elastic. Stress contours in the girders of the same bridge in the elastic range by SAP90 analysis, shown in Fig. 3.16, compare fairly with the stress vectors from ADINA results. Incidentally, only small maximum effective stresses develop in the concrete slab, as indicated by the previous results obtained by SAP90 in the elastic range.

Inelastic analyses also revealed that, in the absence of end-diaphragms, the presence of intermediate diaphragms does not greatly improve the seismic behavior of slab-on-girder bridges as the largest girder web distortions occur nearer to the girder supports. To illustrate this

phenomenon, a 40 m span bridge with intermediate diaphragms at every 8 m was considered. As shown in Fig. 3.17, the impact of intermediate diaphragms in resisting the lateral loads is small. Note that as shown in Figs. 3.7, 3.8 and 3.11, the girder bottom flange can deform laterally further than the bridge deck in some locations. Consequently, the shear force resultant in some intermediate diaphragms can oppose that acting in the end-diaphragms or other intermediate diaphragms (Fig. 3.17b).

3.3.3 Effect of Web Stiffeners

Typically, bearing web stiffeners are present (and needed) at the supports of steel bridge girders to prevent web crippling and web buckling under gravity loads. According to bridge codes (e.g. Ontario 1991), bearing stiffeners should be provided where the support reactions at the ultimate limit states exceed the factored compressive resistance of girder webs. These stiffeners are required to support the flanges where reactions are transferred and extend next to the flanges edge. They should be considered as compression members consisting stiffeners in two side and a central strip of the web with a length of 24 times its thickness at interior supports, and 12 times web thickness at end supports.

Most existing bridges also have numerous intermediate transverse web stiffeners equally spaced along the length of girders and added to enhance the shear resistance of these girders. In view of the structural seismic behavior described above, and recognizing the role played by the web of girders, some special considerations are necessary to account for the presence of these stiffeners.

First, without changes to the above theory, the effect of equally distributed intermediate transverse web stiffeners can be directly considered by converting each stiffened web into an equivalent unstiffened web having a thickness chosen to give an identical transverse flexural stiffness. For example, following this procedure, web stiffeners of 100x10 mm at spacing of 2 m

on both sides of 11 and 16 mm thick webs (corresponding to 20 m and 60 m span bridges), can be converted into equivalent web thicknesses of 36 and 38 mm respectively.

Second, when the bearing stiffeners at the supports are larger than the distributed intermediate web stiffeners (as they frequently are), they effectively contribute an additional stiffness at each support, essentially acting as end-diaphragms, albeit weak ones. Finite element analyses were conducted to investigate the impact of this small effective end-diaphragm action. By adding some shell members as transverse stiffeners, or alternatively changing the thickness of shell elements at bridge ends to an equivalent value, input files were rearranged.

Two plates of 100x10 were used as transverse stiffeners in 20, 30 and 40 m span bridges, and two plates of 120x12 were assumed in 50 and 60 m span bridges. Table 3.2 presents the resulting maximum displacements and lateral period of vibration in steel bridges of different spans subjected to a lateral uniformly distributed load equivalent to a pseudo acceleration of 1g at the deck level. As indicated in Table 3.2, even though relatively small bearing web stiffeners were considered, their presence has a large impact on lateral period and displacement of bridges.

As bearing stiffeners can effectively be treated as end-diaphragms, it is worthwhile to extend the above analytical study to parametrically include the stiffness contribution of end-diaphragms. This is done in the following section.

3.4 Slab-on-Girder Steel Bridges with Effective Diaphragms

In previous sections, it was clearly shown that the bridges without effective diaphragms were deficient to resist seismic loads and could even collapse during a severe earthquake due to large inelastic drifts and P-Δ effects. However, in a well designed bridge, cross frames or diaphragms at piers and abutments are generally provided. Fig. 3.18 shows a model of typical bridge braced with X-shape braces at both ends. Most codes require that the lateral bracing systems be as deep

as practicable and proportioned to permit all lateral forces to be transmitted to the bearings (Ontario 1991). Nonetheless, these lateral bracing are often designed only to provide wind-resistance.

For bridges with diaphragms, preliminary analyses revealed that the concrete deck does not respond in a rigid-body motion during seismic excitations, as is the case for bridges without diaphragm. Rather, treating the structure as a generalized single-degree-of-freedom (SDOF) system, it was found appropriate to express the transverse response displacement mode shape of the bridge, $u(x)$, by:

$$u(x) = \sin\frac{\pi x}{L} \tag{3.13}$$

where L is the span length. Then, the generalized mass, m^*_b, and stiffness, K^*_b and effective force, P_{eff} for the equivalent braced model are calculated as (Clough and Penzien 1993):

$$m_b^* = \int_0^L \frac{M}{L}\,[u(x)]^2 dx = \frac{M}{2} \tag{3.14}$$

$$K_b^* = \int_0^L EI_D \left(\frac{d^2u(x)}{dx^2}\right)^2 dx = \frac{\pi^4 EI_D}{2L^3} \tag{3.15}$$

$$P_{eff} = PSa \int_0^L \frac{M}{L}\,u(x)\,dx = PSa\;\zeta = \frac{2M}{\pi}\,PSa \tag{3.16}$$

where M is the mass of the bridge, E is the modulus of elasticity, I_D is the moment of inertia of the bridge deck about a vertical axis perpendicular to the deck, ζ is the earthquake excitation factor ($2M/\pi$), and PSa is the pseudo acceleration. The corresponding equivalent static earthquake force, P_e, acting on the real bridge is calculated as (Clough and Penzien 1993):

$$P_e = \frac{\zeta^2}{m_b^*}\,PSa = \frac{8M}{\pi^2}\,PSa \tag{3.17}$$

It is noteworthy that, for the simplified equivalent model considered above, the effective force must act on the SDOF system (instead of $m^*_b\ Psa$), and P_e on the real bridge. For instance, in a 60 m span bridge with total mass of 465000 kg, a P_e of 3700 kN, distributed along the bridge as a sine curve, is obtained due to a pseudo acceleration of 1g, while in the case without diaphragms a lateral loading of 4560 kN uniformly distributed along the bridge was previously considered for the same pseudo acceleration.

In the following, this effective force corresponding to a generic pseudo acceleration of 1g is considered, and, as before, results from elastic analyses can be linearly scaled as necessary.

3.4.1 Proposed Model for Calculation of Period and Elastic Response

In the presence of end-diaphragms, the model previously derived must be modified to properly capture the lateral response of this type of steel bridge. A new model which may account for the stiffness of end-diaphragms, in addition to all the behavior features described earlier, is schematically illustrated in Fig. 3.19.

The following mathematical approach was followed to develop an analytical expression capturing the lateral behavior of these steel bridges under transverse seismic excitation.

The differential equation of motion for the bridge deck with continuous mass, neglecting the effects of shear strain and rotary inertia, can be written as (Gorman, 1975):

$$-\frac{\partial^2 u(x,t)}{\partial t^2} = \frac{EI_D}{\rho A}\frac{\partial^4 u(x,t)}{\partial x^4} \tag{3.18}$$

where $u(x,t)$ is a displacement function of the bridge deck in terms of longitudinal distance from the support, x, and time, t, I_D is the superstructure moment of inertia (slab and girders acting as a unit) about a vertical axis perpendicular to the deck, ρ is mass density and A is the cross-sectional area of the entire superstructure. Hence, ρA corresponds to the superstructure mass

per unit length. Using a displacement function of $u(x,t)=Z(t).Y(x)$ for bridge deck, the differential equation of motion becomes:

$$- Y(x) \frac{d^2Z(t)}{dt^2} = \frac{EI_D}{\rho A} Z(t) \frac{d^4Y(x)}{dx^4} \tag{3.19}$$

This equation may be rearranged so that the left-hand side of the equality is a function of time only, while the other side is a function of distance x:

$$- \frac{1}{Z(t)} \frac{d^2Z(t)}{dt^2} = \frac{EI_D}{\rho A} \frac{1}{Y(x)} \frac{d^4Y(x)}{dx^4} \tag{3.20}$$

By making both sides equal to a constant, say ω^2, and then introducing a dimensionless parameter, α, defined as:

$$\alpha^4 = \frac{\rho A \omega^2 L^4}{EI_D} \tag{3.21}$$

the following expressions for the general solution can be developed:

$$Y(x) = C_1 \sin\alpha\frac{x}{L} + C_2 \cos\alpha\frac{x}{L} + C_3 \sinh\alpha\frac{x}{L} + C_4 \cosh\alpha\frac{x}{L} \tag{3.22}$$

$$Z(t) = \cos(\omega t - \varphi) \tag{3.23}$$

where C_1 to C_4 are the coefficients depending on boundary conditions, and φ is a phase angle of the periodic motion. For a steel bridge having end-diaphragms and assumed simply supported at both ends in the transverse direction, α can be obtained by trial and error by solving the following equality:

$$(K_b^*)^2 + \frac{\alpha^3(1+C_r)(\sinh\alpha\cos\alpha - \sin\alpha\cosh\alpha)}{2C_r\sin\alpha\sinh\alpha} K_b^* + \frac{\alpha^6(1-\cos\alpha\cosh\alpha)}{2C_r\sin\alpha\sinh\alpha} = 0 \tag{3.24}$$

where C_r is the ratio of right to left end-diaphragm stiffnesses (K_{b2}/K_{b1}, usually 1.0), and K_b^*, the dimensionless stiffness, is:

$$K_b^* = \frac{K_b L^3}{EI_D} \tag{3.25}$$

in which, K_b, the stiffness of lateral bracing systems at one end, depends on the geometry of the bridge and properties of the bearing stiffeners and diaphragm braces:

$$K_b = \sum_1^{n_g} \frac{12EI_s}{h_w^3} + \sum_1^{n_g-1} \frac{2EA_b \cos^2\theta}{l_b} \tag{3.26}$$

where I_s is the moment of inertia of the bearing web stiffener about the longitudinal axis of the bridge, n_g is the number of girders, A_b, l_b and θ are the cross-sectional area, length and slope angle of braces. It is noteworthy that, in absence of diaphragm braces, K_b would simply be the lateral stiffness of transverse bearing web stiffeners, i.e. $\Sigma 12EI_s/h_w^3$. For example, with two sided Pl. 100x10 only, in a 20 m span bridge having four girders, I_s and K_b would be $7.8\text{x}10^{-6}$ m^4 and 170 MN/m respectively. With X-shape braces of 2L100x100x10 between every two girders at bridge ends, K_b would be 1930 MN/m (neglecting the contribution of the bearing stiffners), showing that braces create the main lateral stiffness for the bridge. In this case, K_b^* would be 55.33, giving α of 2.71 (Eq. 3.24); considering I_D and ρA of 1.322 m^4 and 6300 kg/m respectively, this would correspond to a lateral period of 0.053 s (per Eq. 3.21). For the 60 m span bridge, the lateral period is increased to 0.213 s following the proposed model. In case of using 2L45x45x5 at bridge ends, lateral periods are obtained as 0.0843 s and 0.232 s, respectively for the 20 m and 60 m span bridges.

On the other hand, if the girders bottom flange lateral support conditions at one end of the simply supported bridge are considered fixed, then assuming C_r (K_{b2}/K_{b1}) to be 1.0, Eq. 3.24 becomes:

$$\frac{(K_b^*)^2}{\alpha^6}(\sinh\alpha\cos\alpha - \sin\alpha\cosh\alpha) - \frac{K_b^*}{\alpha^3}(1+3\cos\alpha\cosh\alpha) + \sin\alpha\cosh\alpha + \sinh\alpha\cos\alpha = 0 \quad (3.27)$$

For the same 20 m span bridge with 2L100x100x10 at each end, this time α would be 2.96 giving a lateral period of 0.044 s.

In all cases, the displacement at the bridge ends is given by:

$$\Delta_{end} = \frac{m\ .(PSa)}{K_{b1}+K_{b2}} \quad (3.28)$$

Rayleigh's method can be used alternatively to the proposed approach to calculate the period of these bridges, considering the bridge as a beam with continuous mass and elastic springs at the supports. This approach is a specific case of the method of generalized coordinates in which the shape function is determined based on the static displacement of structure. The maximum potential and kinetic energies, V_{max} and T_{max} can be generally integrated from following equations:

$$V_{max} = \frac{1}{2}\int_0^L m(x)g\ u(x)dx \quad , \quad T_{max} = \frac{1}{2}\omega^2\int_0^L m(x)(u(x))^2dx \quad (3.29)$$

where u(x) is lateral displacement function assumed for the bridge, L and m(x) are span length and distributed mass of the bridge, g is gravitational acceleration and ω is the transverse frequency in rad/s. By equating the two energies:

$$\omega^2 = g\frac{\int_0^L m(x)\ u(x)dx}{\int_0^L m(x)[u(x)]^2dx} \quad (3.30)$$

For a 20 m span simply supported bridge having only two web stiffeners of 100x10 size at each support, ω is computed as 57 rad/s from above formula, corresponding to a lateral period of 0.11 s. By adding 2L100x100x10 braces to the ends, the lateral period decreases to 0.052 s if simply supported laterally, and 0.043 s in presence of a fixed support. These results compare well with those of SAP90.

3.4.2 Numerical Examples

Lateral X-bracings of 2L100x100x10 were designed to act as end-diaphragms and be able to resist elastically a pseudo acceleration of 1.5g (with 50% overstrength to ensure that they remain elastic), for steel bridges with spans ranging from 20 m to 60 m. Using SAP90, the lateral period was computed for bridges with different spans, considering various X-braces as diaphragms. Note that many of the bridges' lower modes of vibration correspond to displacement response in the vertical direction: the discussion here addresses the lateral period corresponding to lateral response by preventing vibrations in vertical direction.

The preliminary analyses here have shown the considerable impact of end-diaphragm on the seismic response of steel bridges. Interestingly, severe damage to the end-diaphragms of steel bridges observed following recent earthquakes, as reported in Chapter 2, corroborate these analytical results. Table 3.3 presents the lateral periods for all braced bridges considered in this study, and compares them with the periods obtained by SAP90. As observed in this Table, the transverse period obtained by the proposed model are generally very close to those calculated by SAP90 analyses. The difference between the results is smaller for larger span bridges, because shear deformations of the concrete deck are ignored in the proposed analytical model. For the 60 m span bridge, where the shear to flexural deformation ratio is the lowest, the proposed hand-calculation analytical model offers the results closest to those obtained by SAP90 (0.213 s compared to 0.22 s).

Fig. 3.20 shows the resulting lateral period versus braces cross-sectional area, for 20 m, 40 m and 60 m span bridges. If a zero cross-sectional area is assumed for the braces, periods of 0.82 s and 1.77 s are obtained respectively for 20 m and 60 m long bridges, i.e. the same values obtained before. By using 2L45x45x5 and 2L100x100x10 X-braces, lateral periods of 0.089 s and 0.052 s are obtained for the 20 m span bridge, and 0.24 s and 0.22 s respectively, for the 60 m span bridge. It is observed that a very small end-diaphragm is sufficient to produce a large "shift" in

the period of these bridges, but that further increases in diaphragm stiffness have a marginal impact on lateral structural period.

3.4.3 Ultimate Nonlinear Behavior

Frequently, end-diaphragms have sufficient strength to remain elastic during earthquakes, and brittle damage instead occurs in the diaphragm connections or elsewhere in the structure. However, to investigate whether intermediate diaphragms can effectively contribute to lateral load resistance when end-diaphragms undergo inelastic response, inelastic push-over analyses were carried out using ADINA. Fig. 3.21 presents the deformed shape of a 40 m span bridge with effective diaphragms at both ends. As shown in this figure, braced bridge behaves laterally like a simply-supported beam, i.e. steel girders and concrete deck work as a unit.

Results are presented in Figs. 3.22 and 3.23, respectively for 40 m and 60 m span bridges having X-braces diaphragms between the girders, namely 2L65x65x6 for end-diaphragms and 2L45x45x5 for intermediate diaphragms. As shown in Figs. 3.22 and 3.23, intermediate diaphragms only take a small percentage of the total applied load, even after buckling and yielding of the end-diaphragm braces, and would remain elastic until very large ductilities develop in the end-diaphragms and at least until deck drifts in excess of 5%. Contribution of intermediate diaphragms is even less significant for the shorter bridges. This is because intermediate diaphragms are located 8 m from each other, the first one being at a greater percentage of the total span from the end in shorter bridges, and thus less likely to contribute being more remote from the zone of greater girder transverse deformation.

Note that results previously obtained for bridges without end-diaphragms and presented earlier should be used if end-diaphragms and web stiffeners are deemed incapable of effectively resisting lateral loads and developing the ductile behavior assumed here.

3.5 Further Observations on Seismic Behavior

Deformed shapes for a 40 m span bridge at one end and at a distance of 8 m from the end are shown in Fig. 3.24. It is noteworthy that even though the lateral inertia force is applied at the deck level and that supports are only provided at the level of the lower bottom flanges at the bridge end, the bridge deck rotates conversely to the direction of the resulting couple, or counterclockwise at the middle. This is due to the axisymmetric cross section of the bridge which has a shear center located above the concrete slab.

3.6 Summary of Findings

Linear elastic and nonlinear inelastic analyses were conducted to investigate the impact of diaphragms on the seismic behavior of slab-on-girder steel bridges. The results of this analytical study demonstrate that a small end-diaphragm stiffness is sufficient to make the entire superstructure behave as a unit in the elastic range. However, the above results also clearly illustrate that a dramatic shift in seismic behavior could occur once rupture of the end-diaphragms occurs, with a sizeable period elongation, considerably larger lateral displacements and higher propensity to damage due to instability and P-Δ effects. It is also found that the presence of intermediate diaphragms does not significantly influence the seismic performance of these bridges, both in the elastic and inelastic range whether end-diaphragms are present or not.

Moreover, these analyses confirmed that effective end-diaphragms constitute critical structural elements along the main seismic load path, and that they should be designed accordingly. Therefore, in new bridges, they should be designed to resist in an elastic manner the forces induced by the maximum credible earthquake. In this case, large forces are consequently transferred to the substructure elements. Alternatively, they could be designed and detailed as ductile members to preclude brittle member or connections failure. This is not warranted for intermediate diaphragms. Non-ductile end-diaphragm members and connection details in existing steel bridges should be retrofitted, recognizing their impact on seismic response.

CHAPTER 4

DUCTILE END-DIAPHRAGMS FOR SEISMIC RETROFIT OF SLAB-ON-GIRDER STEEL BRIDGES

4.1 Introduction to Seismic Retrofit

The recent Northridge and Kobe earthquakes (among many) clearly demonstrated the seismic vulnerability of steel bridges supported by non-ductile substructure elements constructed of brittle materials such as concrete and masonry. While damage to superstructure components of these bridges is also possible, mostly in the form of buckling and/or connection fracture of diaphragm braces, damage to substructure components such as abutments, piers, bearings, and others have proven to be of far greater consequences, often leading to span collapses (Roberts 1992; Astaneh-Asl et al. 1994; Bruneau et al. 1996).

Hence, when existing bridges are targeted for seismic rehabilitation, much attention is paid to these substructure elements and their seismic retrofit which can be, in many cases, a rather costly

operation. Typically, the current retrofitting practice is to either strengthen the existing non-ductile members (e.g. Seismic 1983; Buckle et al. 1986; Shirolé and Malik 1993), enhance their ductility capacity (e.g. Degenkolb 1978; Priestly et al. 1992), replace them by newer elements having more desirable properties (e.g. Buckle et al. 1986; Bridge 1993), or reduce the force demands on the vulnerable substructure elements using base isolation techniques or other structural modifications (e.g. Naeim 1989; Mayes et al. 1992; Astaneh-Asl 1993). While all these approaches are proven effective solutions, none takes advantage of the unique seismic retrofit possibilities provided when the superstructure consists of steel girders, and only the base isolation concept currently recognizes that seismic deficiency attributable to substructure weaknesses may be resolved by operating elsewhere than on the substructure itself. Moreover, all approaches can be expensive, even base isolation in those instances when significant abutments modifications and other structural changes are needed to permit large displacements at the isolation bearings and lateral load redistribution among piers (Mayes et al. 1993, 1994).

To take advantage of the benefits granted by the presence of a steel superstructure, an innovative seismic retrofit strategy using ductile steel bridge end-diaphragms is proposed here. By replacing the steel diaphragms over abutments and piers with specially designed ductile diaphragms calibrated to yield before the strength of the substructure is reached, the substructure can be protected. Past research has demonstrated the effectiveness of stiff structural frame systems simultaneously capable of stable passive seismic energy dissipation in buildings, and many such experimentally proven systems have been implemented already. Among those, eccentrically braced frames (EBF) (e.g. Roeder and Popov 1978; Malley and Popov 1983; Kasai and Popov 1986), shear panel systems (SPS) (Fehling et al. 1992; Nakashima 1995; Nakashima et al. 1995), and steel triangular-plate added damping and stiffness devices (TADAS) (Tsai et al. 1993, 1994) have received a particular attention in building applications. Still, to the author's knowledge, none of these applications has been considered to date for bridge structures. This may be partly attributable to the absence of seismic ductile steel detailing provisions in North American bridge codes.

Here, the objective is to present this economical, effective and simple to implement new rehabilitation concept for a type of steel slab-on-girder bridge widely found in North America and describe simplified analytical models as well as a step-by-step design procedure developed for three types of ductile diaphragm systems (SPS, EBF and TADAS devices). This chapter also indicates potential limits of application, and presents results from nonlinear inelastic analyses conducted to investigate the seismic behavior of these retrofitted bridges. Interestingly, these innovative diaphragms could also be implemented in new steel bridges as effective passive energy dissipation systems.

4.2 Preliminary Information

4.2.1 Description of Inelastic Computer Programs

The program DRAIN-2DX, an extended version of DRAIN-2D (Dynamic Response Analysis of Inelastic 2-Dimensional Structures), is used here for nonlinear static and dynamic analyses by an event-to-event approach (using variable time steps between 0.001 and 0.01 s), where each event corresponds to a significant change in stiffness. The event-to-event scheme, longer to run, is more reliable and permits calculation of a detailed energy balance. Energy values are computed for the static elastic-plastic work, the energy absorbed by viscous damping, the kinetic energy, and the input energy. Large energy unbalances indicate that analysis results are likely to be inaccurate (Prakash et al. 1993).

For 3D analyses, the program ADINA (1995) is used to model bridge girders by shell elements. Shear yielding can be considered directly here, while spring elements are used in DRAIN-2DX to model shear yielding of the link beam. Some input files are given in Appendix A for illustrative purposes.

4.2.2 Damping Characteristics

A viscous Rayleigh damping matrix proportional to the nodal masses and element stiffnesses can be specified for dynamic analysis:

$$C = C_m M + C_k K \tag{4.1}$$

where C_m and C_k are mass and stiffness damping ratios. Mass dependent damping introduces translational and/or rotational dampers at each node. Stiffness dependent damping introduces dampers in parallel with the elements. For mass proportional damping, the damping ratio, ξ, is inversely proportional to the frequency, ω, while for stiffness proportional damping, the damping ratio is directly proportional to the frequency. For Rayleigh damping, the equations of motion can be uncoupled (Humar 1987; Clough and Penzien 1993) using:

$$\xi_n = \frac{C_m}{2\omega_n} + \frac{C_k \omega_n}{2} \tag{4.2}$$

In this study, two frequencies, the first and the third corresponding to translational modes of vibration, were used to calculate the mass and stiffness proportional damping ratios.

4.2.3 Earthquake Loads

To determine seismic loads in preliminary case studies on end-diaphragms, the Newmark-Hall design spectra is used (Newmark and Hall 1982; Naeim 1989), as shown in Fig. 4.1, where the inelastic response spectra corresponding to peak ground acceleration, *PGA*, of 0.2g, 0.4g and 0.6g are obtained by using Newmark-Hall's amplification factors for a damping ratio of 2% (ξ=0.02). A ductility demand of 5 (μ=5) was considered to derive those inelastic design spectra. (Other methods to obtain inelastic design response spectra, such as those proposed by the NBCC (National Building Code of Canada 1990) and AASHTO (American 1994) are possible and are

used in the proposed design procedure presented later in this chapter). The inelastic base shear can be determined by:

$$V_{inel} = \frac{V_e}{R} \tag{4.3}$$

in which V_e is the elastic lateral load and R is a reduction factor due to the ductile behavior. For ductile systems proposed here, R can be assumed between 3 and 4.

4.3 Existing Literature on Ductile Devices in Building Structures

A number of approaches have been developed to improve earthquake response and damage control of buildings. These can be divided into two main groups: passive systems like energy dissipation devices and active systems which require the active participation of mechanical devices whose characteristics are made to change during the structure response based on motion measurements. Here, only the three ductile devices used in the proposed seismic retrofit of steel bridges are reviewed. Other passive energy dissipation systems (e.g. friction dampers, slotted bolted connections) exist and could be also implemented in end-diaphragms.

4.3.1 Triangular-plates Added Damping And Stiffness (TADAS) Device

The TADAS device consists of triangular plates that can be bent through many cycles of inelastic deformations without any stiffness or strength degradation or curvature concentration, because a uniform curvature forms along the height of these plates (Tsai et al. 1993).

Once an end displacement is imposed perpendicular to the plane of a triangular plate fixed at the base (Fig. 4.2), the entire height of the plate yields at the same time. If the base of the triangular plates is assumed fully fixed, using the moment-area method and ignoring shear deformation, the theoretical elastic lateral stiffness of a TADAS device, K_T, is:

$$K_T = \frac{N_T\, Eb_T\, t_T^3}{6h_T^3} \tag{4.4}$$

where E is the Young's modulus, and N_T, b_T, h_T and t_T are the number, base width, height and thickness of the triangular steel plates, respectively. The yield strength, $V_{T,y}$, and plastic strength, $V_{T,p}$, of the TADAS device are:

$$V_{T,y} = \frac{F_y\, N_T\, b_T\, t_T^2}{6h_T} \tag{4.5}$$

$$V_{T,p} = \frac{F_y\, N_T\, b_T\, t_T^2}{4h_T} \tag{4.6}$$

where F_y is the tensile yield stress. The lateral displacement at the end of the TADAS plates can be obtained by:

$$\delta = \frac{6h_T^3\, V}{Eb_T\, t_T^3} \tag{4.7}$$

and the yield displacement (i.e. at $V=V_y$), δ_y, is:

$$\delta_y = \frac{F_y\, h_T^2}{Et_T} \tag{4.8}$$

If the distortion angle, γ, of the device is assumed as the ratio of lateral displacement, δ, to the height of the triangular plate, h_T, then the yield distortion angle, γ_y, would be:

$$\gamma_y = \frac{F_y\, h_T}{Et_T} \tag{4.9}$$

It is noteworthy that, the height-to-thickness ratio, h_T/t_T, of the plates has an important influence on the stiffness and strength of the device. Clearly, the lateral stiffness of the device increases with an increase thickness or decrease in height of the plates (Eq. 4.4). In other words, to obtain a large device stiffness, a small h_T/t_T ratio is selected for the plates. The failure mechanism for a frame having a TADAS device is shown in Fig. 4.3, in which the inelastic distortion demand, $\gamma_{p,TADAS}$, for a TADAS device can be obtained:

$$\gamma_{p,TADAS} = \frac{H}{h_T}\,\theta_p \tag{4.10}$$

where H and θ_p are the height and plastic drift angle of the columns, respectively. The rotation at the base of the device and the deformation of the connecting braces should be deducted from that value to compute the true distortion of the device alone. It is clear from Eq. 4.10 that the inelastic distortion demand of TADAS device increases with a decrease in plates height.

Tsai et al. (1993) conducted a few cyclic tests on 11 welded TADAS device specimens having various h_T/t_T. A distortion capacity larger than 0.25 rad was reached at failure of the TADAS specimens. They also conducted pseudodynamic tests on a two-story steel frame with TADAS devices. A maximum upper story drift angle of 0.016 rad was reported while the frame was subjected to the El Centro earthquake scaled to a PGA of 0.31g. This corresponded to a distortion angle of 0.14 rad for the TADAS devices, i.e. much less than their plastic distortion capacity (Tsai et al. 1993, 1994)

4.3.2 Eccentrically Braced Frame (EBF)

Researchers have shown that building structures having the EBF system possess high elastic stiffness (comparable to concentric bracing systems), excellent ductility and energy dissipation capacity in the inelastic range (like moment resistant frames), and perform well under the severe cyclic loading (eg. Roeder & Popov 1978; Hjelmstad & Popov 1983; Kasai and Popov 1986; American Institute 1994). In these systems (some typical configurations are shown in Fig. 4.4),

the axial forces in the braces are transferred to the columns through shear and bending of a beam segment called a link beam (Figs. 4.4a, b and c), or to the floorbeam through a vertical member in what is called shear panel system (SPS) (Fig. 4.4d).

Experimental studies have demonstrated that link beams primarily yielding in shear (called short or shear links) are more effective energy dissipators than those primarily yielding in bending (called long or flexural links) (Hjelmstad and Popov 1984; Malley and Popov 1983). In both cases, since the lateral load-carrying capacity and ductility of EBF systems mainly depends on the link capacity and ductility, the link beam must be detailed to prevent premature link failure. Kasai and Popov 1986 experimentally showed that without an adequate number of web stiffeners, web buckling within the link leads to a loss of EBF capacity and ductility, and a premature failure, as shown in Fig. 4.5. Design issues related to EBF, such as link strength and ductility and stiffener detailing are briefly reviewed in the following.

4.3.2.1 Link Strength and Ductility

For the design considered here, the link beam should primarily yield in shear to assure good inelastic behavior and energy dissipation. Fig. 4.6 shows the shear plastic mechanism of an EBF subjected to induced by a lateral load of V at the link beam level. The maximum frame drift of δ creates a girder web rotation angle of θ_p and a link distortion angle of γ_p. From the frame geometry and plastic design, a relationship can be developed between θ_p and γ_p:

$$\gamma_p = \frac{L_s}{e}\,\theta_p \tag{4.11}$$

where L_s is the girder spacing and e is the link length. The external and internal work corresponding to this plastic mechanism are (Horne and Morris 1981):

$$W_{External} = 2\left[(\frac{V}{2})\delta\right] = V\theta_p H \quad , \quad W_{Internal} = V_l\gamma_p e \tag{4.12}$$

Substituting γ_p from Eq. 4.11 in the above internal work equation, and equating external and internal work, the required shear V_l is determined in terms of the applied lateral load V:

$$V_l = \frac{H}{L_s} V \tag{4.13}$$

in which H is the frame height. The link beam must be designed to resist this shear force, i.e. it must yield at V_l, and simultaneously a bending moment, M_l, equal to:

$$M_l = \frac{1}{2} V_l e \tag{4.14}$$

an axial force must also be simultaneously considered for same frame geometries. The beam segment next to link should be designed as a beam-column for resisting an axial force equal to the horizontal component of the axial force from the brace, and M_l, accordingly.

4.3.2.2 Stiffener Detailing

Beams subjected to concentrated loads applied to one of their flanges must be designed to prevent local crippling of the web, or overall buckling of the web at the point of load application. For an EBF, these two undesirable failure modes in the beam where the braces frame can be precluded by considering the bearing resistance of the beam, given by the minimum value from the following two equations (Canadian 1994, 1995):

$$B_r = 1.1 \phi t_w (N + 5k) F_y \tag{4.15}$$

$$B_r = 300 \phi t_w^2 \left[1 + 3 \left(\frac{N}{d_l} \right) \left(\frac{t_w}{t_f} \right)^{1.5} \right] \sqrt{\frac{F_y t_f}{t_w}} \tag{4.16}$$

where ϕ=0.9 is the resistance factor, F_y is the yield stress, N is the length of bearing plate on the flange (if any), and d_b t_w and t_f are the beam depth, web and flange thickness, respectively. If the bearing resistance obtained by above equations is less than the factored concentrated load coming from axial forces in the braces, web stiffeners must be used to increase the bearing capacity of the beam's web.

Stiffeners should have a thickness of at least $0.75t_w$ or 9.5 mm. Intermediate full-depth web stiffeners are provided when the link shear strength is controlled by V_p (or when the link strength is controlled by flexure and shear associated with the reduced moment capacity of the link, M_p^*, exceeds $0.45F_y d_l t_l$).

For link beams with a distortion angle γ of 0.06 rad at the calculated design drift, the spacing of the intermediate web stiffeners must not exceed $38t_w - d/5$. With a γ of 0.03 rad or less, it should not exceed $56t_w - d_l/5$ (Engelhardt and Popov 1989). Interpolation must be used between these values. For links with a depth of 610 mm or more, the intermediate full-depth web stiffeners, if required, must be provided on both sides of the web.

4.4 Proposed Retrofit Concept

The ductile end-diaphragm retrofit strategy proposed here was developed in a capacity design perspective. The principle of capacity design, first presented by Pauley (1977), consists of forcing all structural inelastic deformations to develop only in some judiciously selected structural elements specially detailed to absorb all seismic energy. Hence, forces in a given structure cannot exceed those present at development of the plastic mechanism, and all parts of the structure for which inelastic action is not needed for development of that mechanism do not require ductile detailing. The special ductile elements can be seen as "structural fuses", all other elements being "capacity protected". The innovative idea in the retrofit strategy proposed here is to locate these structural fuses into the end-diaphragms of steel superstructures, and thus prevent damage from

developing in the non-ductile substructural elements, foundation, and bearings (referred generically as "substructure" hereafter). To achieve this substructure protection, the special end-diaphragms must be designed and detailed such that stable hysteretic ductile behavior can develop and be sustained at a reliable pre-determined load level lower than that corresponding to the threshold of unacceptable substructure damage, as schematically illustrated in Fig. 4.7. However, a minimum diaphragm strength and stiffness must also be provided to ensure satisfactory wind resistance as well as acceptable seismic inelastic behavior (strength reduction beyond a certain level may translate into excessive ductility demands even for the most ductile systems).

Examples of how the proposed passive energy dissipation systems would be implemented in the end-diaphragms of a typical 40 m span bridge are shown in Fig. 4.8a, b and c, for a TADAS, EBF and SPS respectively. Note that steel slab-on-girder bridges have been constructed throughout North America with a broad variety of end-diaphragm types (such as angle braces, full depth plates, or small shallow web-bolted channels, to name a few), and that these diaphragms would be replaced entirely by the new ones. In that perspective, bearing stiffeners of the main girders would sometimes have to be trimmed or replaced by narrower ones for reasons described later. Also note that the top horizontal member shown in Fig. 4.8 is optional in the retrofit of composite bridges, but could be needed for stability during construction of new bridges designed with the proposed diaphragms. Likewise, to satisfy the needs of a few transportation agencies who require that diaphragms be designed to accommodate jacking forces at pre-designated points to permit lifting of the bridge during future bearing replacement or other repairs, some additional holes and gusset plates can be optionally introduced in the end-diaphragms (as shown in Fig. 4.8 by dotted members) to permit the use of temporary bracing members for that purpose.

It is noteworthy that very little structural material and labor is required to accomplish the proposed retrofit strategy, which may make it a desirable alternative even for new bridges. Moreover, after a damaging earthquake, the only structural components that might need replacement are the structural fuses, although, in many instances, since research has shown that

some of the above devices are quite capable of resisting multiple earthquakes (e.g. Whittaker et al. 1990), replacement could even be unnecessary.

Obviously, ductile systems other than the three types considered in this study are also possible, provided they comply with the aforementioned objectives. However, while concentrically braced frames can be ductile, they would not be satisfactory in this application because: (i) the actual buckling strength of the compression brace is sometimes difficult to accurately predict, (ii) this buckling load decreases in subsequent loading cycles, and (iii) their hysteretic curves typically exhibit pinching and some possible strength degradation as a function of slenderness.

Finally, effective application of this retrofit solution is limited to those bridges that do not have horizontal wind bracing connecting the bottom flanges of girders as these braces could provide an alternative load path bypassing the special ductile elements. Furthermore, this retrofit method only provides enhanced seismic resistance and substructure protection for the component of seismic excitation transverse to the bridge, and must be coupled with other devices that constrain longitudinal seismic displacements, such as simple bearings strengthening (Mander et al. 1996), rubber bumpers and the likes; transportation agencies experienced in seismic bridge retrofit have indicated that deficiencies in the longitudinal direction of these bridges are typically easier to address than those in the lateral direction (Mr. Brock Radloff, Seismic Rehabilitation Engineer, Ministry of Transportation of British Columbia, private communication).

4.5 Preliminary Case Studies with EBF between All Girders

Before a design procedure for ductile end-diaphragms is proposed, some case studies were investigated. First, it was decided to insert these end-diaphragms between all girders, as shown in Fig. 4.9. For these preliminary case studies, the bridge deck was assumed rigid which is conservative for calculation of elastic forces, i.e. the entire bridge mass is used for the equivalent elastic force level. EBF end-diaphragms were designed for the 40 m and 60 m span bridges to

resist *PGA* of 0.2g, 0.4g and 0.6g. An eccentricity, e, of 300 mm, yield strength, F_y, of 300 MPa and a damping ratio, ξ, of 2% were considered.

Figs. 4.10 and 4.11 present the resulting lateral load, moment in the stiffened girder and shear in the link beam versus deck displacement for simplified models of the 40 m and 60 m span bridges, respectively. As shown in Figs. 4.10b and 4.11b, large bending moments are induced in the girders at larger drifts mainly due to the relatively high lateral stiffness provided by the bearing stiffeners of the girders (called stiffened web on the figure). Thus, in order to prevent or postpone any flexural yielding in the girders, the width of transverse web stiffeners should be reduced to the minimum width necessary to satisfy the strength and stability requirements for bearing resistance. Although flexural yielding of the girder web stiffeners during shear yielding of the link beam can be tolerated if it does not affect stability of the girders, it is preferable that girders resist only a small portion of the lateral load because they are not intended to be the major ductile energy dissipating elements here. There is limited control on possible changes to the size of the girder web stiffeners in the seismic retrofit of steel bridges, while end-diaphragms benefit from the usual design freedom.

Five earthquakes successively scaled to *PGAs* of 0.2g, 0.4g and 0.6g, were applied to the simplified nonlinear models of the bridge in time-history analyses. Figs. 4.12 and 4.13 present displacement response respectively for the 40 m and 60 m span bridges, subjected to the El-Centro earthquake scaled to a PGA of 0.6g. Tables 4.1 and 4.2, respectively present results for the 40 m and 60 m span bridges. Elastic force level, V_e, in Tables 4.1 and 4.2 is determined by the Newmark-Hall design spectra for the design *PGA* level and calculated lateral period. The inelastic force level, V_{ineb} is obtained using a strength reduction factor, R, of 3. The first and third modal periods, corresponding to lateral vibrations are used to obtain mass and stiffness proportional damping ratios, C_m and C_k. Linear elastic spectral values, PSa and S_a, for each earthquake scaled to the design *PGA* at the lateral period of interest, are presented in these Tables. These values were also confirmed by SAP90 analyses. The extreme values of deck displacement and link rotation are δ_{max} and γ_{max}, respectively. $M_{w,max}$ is related to the maximum

moment reached in the stiffened girder. The maximum lateral force applied to the entire end-diaphragm at that time is $F_{eq,max}$.

These preliminary studies showed that for the short to medium span steel bridges considered here, it is preferable to use only one ductile diaphragm at each end-diaphragm location. When inserting ductile end-diaphragms between all girders, each ductile diaphragm required only small members and it was difficult to find a structural shape having the designated dimensions. The selected available sections were mostly stronger than required, and, as a result, the diaphragms generally found for these examples (Tables 4.1 and 4.2) only developed a small ductility demand.

Although of no influence on the numerical analyses conducted here (the key connection details were designed to verify that the proposed retrofit was practical in that perspective), brace-to-beam connections were designed as bolted connections. The beam-to-girder web connection was designed as a simple connection, with bolting the beam web directly to web stiffener. Typical details are shown in Fig. 4.14 and 4.15. Preliminary sizing of connection details also favored the use of a single ductile diaphragm at each end-diaphragm location for the slab-on-girder bridges considered in this study.

4.6 Analytical Development

To study the impact of the proposed ductile end-diaphragms on seismic behavior of steel bridges and develop analytical models of this behavior, various simply supported slab-on-girder bridges with spans from 20 m to 60 m were modeled. In this study, all static and dynamic analyses were conducted considering that bridges were subjected to earthquakes having peak-ground-acceleration (PGA) of 0.31g (amplified later to 0.4g for the effective forces, Eq. 4.19). Hence, design spectra and earthquake time history records used hereafter have been scaled accordingly.

4.6.1 Formulation of 2-D Model

To provide computational efficiency and to allow formulation of a simple design procedure (presented in a later section), a simplified 2-D model capturing the essence of the 3-D behavior of slab-on-girder bridges was developed. The availability of a 2-D model was also appealing as it made possible the use of DRAIN-2DX for the subsequent studies of seismic nonlinear behavior. The proposed simplified 2-D model, shown in Fig. 4.15, consists of the ductile end-diaphragm, a stub-length of two girders with their bearing stiffeners modeled as plane flexural members of equivalent thickness, a rigid stub of the reinforced concrete deck, and a small mass/spring subsystem located at deck level and introduced to account for the longitudinal generalized mass and stiffness effects. It is noteworthy that bearing web stiffeners provide the main lateral stiffness for girders; in other words, using a longer length of girders in stub-girder model does not make any difference in model stiffness unless intermediate web stiffeners come to the picture. The impact of intermediate web stiffeners are discussed in a later section.

Recognizing that a slab-on-girder steel bridge having effective end and intermediate diaphragms does not move laterally in a rigid-body manner during earthquakes, but rather responds elastically in a flexible manner engaging the mass and stiffness of the entire bridge superstructure, the generalized mass and stiffness can be calculated assuming a single degree of freedom (SDOF) behavior and fundamental principles of dynamics of structures (Clough and Penzien, 1993). For a simply supported bridge having end-diaphragms, the first transverse mode shape of the superstructure between supports can be represented by the following sine shape function:

$$u(x) = \sin\frac{\pi x}{L} \tag{4.17}$$

where L is the span length. Therefore, ignoring deck displacements at the bridge ends, the generalized mass, m^*, generalized stiffness, K^*, and effective force, P_{eff}, for the equivalent model are calculated as:

$$m^* = \int_0^L \frac{M}{L} (u(x))^2 \, dx = \int_0^L \frac{M}{L} \sin^2(\frac{\pi x}{L}) \, dx = \frac{M}{2} \tag{4.18a}$$

$$K^* = \int_0^L EI_D \left(\frac{d^2u(x)}{dx^2} \right)^2 dx = \int_0^L EI_D \left(\frac{\pi^2}{L^2} \sin(\frac{\pi x}{L}) \right)^2 dx = \frac{\pi^4 EI_D}{2L^3} \tag{4.18b}$$

and

$$P_{eff} = PSa \int_0^L \frac{M}{L} u(x) \, dx = \frac{2M}{\pi} PSa = \frac{4m^*}{\pi} PSa \tag{4.19}$$

where M is the mass of the entire bridge, E is the modulus of elasticity, I_D is the moment of inertia of the whole bridge section about a vertical axis perpendicular to the deck and PSa is the pseudo acceleration. The effective force given by Eq. 4.19 is used for the bridge DRAIN-2DX models. Since m^* is considered for these 2-D models, earthquake records should be amplified by 27% ($4/\pi$ in Eq. 4.19), i.e. they will be scaled to 0.4g rather than 0.31g for time-history analyses. For more accuracy, the displacement of the end-diaphragms could be considered in the above shape function particularly if the deck was very rigid compared to the end-diaphragms.

While the above 2-D model can be implemented directly for computer analyses, its simplicity makes it also suitable for hand-calculations. Indeed, recognizing that the generalized stiffness of the bridge, K^*, the lateral stiffness of the end-diaphragms, K_{ends}, and the lateral stiffness of substructure including abutments, columns, piers and foundations (Fig. 4.16a), K_{subs}, are linked together as springs in series (Fig. 4.16b and c), the equivalent stiffness of the entire bridge, K_e, could be written as:

$$K_e = \frac{1}{\frac{1}{K^*} + \frac{1}{K_{ends}} + \frac{1}{K_{subs}}} \tag{4.20}$$

For single span bridges considered here, the flexibility of substructure might be ignored in Eq. 4.20, as bridges are generally supported by stiff abutments and soil structure interaction is

beyond the scope of this research. Given that the plate girders are modeled as frame members in the 2-D model, they can potentially contribute to the lateral load resistance, and that effect must also be considered in the calculation of the end-diaphragm lateral stiffness. Thus, the diaphragm behaves as a dual system, as shown in Fig. 4.16c (two springs in parallel), and the lateral stiffness of the stiffened girders, ΣK_g, should be added to the stiffness of the ductile diaphragms, ΣK_{DD} (usually much larger than the former), to obtain the lateral stiffness of the bridge end-diaphragms accounting for all acting diaphragms in both sides, K_{ends}, i.e:

$$K_{ends} = \Sigma K_{DD} + \Sigma K_g \tag{4.21}$$

The stiffness contribution of a plate girder is obviously a function of the fixity provided to its top and bottom flanges to the deck slab and bearing respectively. For some ideal cases:

$$K_g = \frac{12E I_g}{h_g^3} \tag{4.22}$$

if full fixity is provided at both ends of the vertical frame element modeling the plate girder, where I_g is the moment of inertia of the stiffened girder (stub-length) in the lateral direction, and h_g is its height;

$$K_g = \frac{3E I_g}{h_g^3} \tag{4.23}$$

if one end is fully fixed, the other one pinned; and zero if both ends effectively behave as pin supports. Obviously, the length of girder stub to consider in this model is not so critical since the bearing stiffeners at the support contribute more significantly to the term I_g than the girder's web itself. However, the actual amount of fixity provided has a major impact and can be difficult to accurately predict. It appears reasonable to expect full fixity at the deck level in composite bridges if the shear studs originally installed to allow this composite action are closely spaced and can resist the pull-out forces resulting from the moments developed at the top of the girders under lateral seismic forces. As for fixity at the bearing level, it obviously depends on the type of bearings present. However, even when infinitely rigid bearings are present, full fixity is still

difficult to ensure due to flexibility of the flanges, as revealed by finite element analyses of subassemblies at the girder-to-bearing connection point.

It is obviously the engineer's responsibility to determine the level of fixity provided at the ends of the girders. However, contrary to conventional design, the most conservative solution is not obtained when zero fixity is assumed. Recall that the role of the diaphragms in this proposed retrofit solution is to limit the magnitude of the maximum forces that can develop in the structure, and most particularly, by capacity design principles, in the substructure. Hence, the highest possible lateral load resistance of the ductile end-diaphragm is obtained when considering full fixity at the slab and bearings (in Chapter 5). In the examples reported in a later section, a slightly less conservative assumption was adopted by considering full fixity at the deck, and zero fixity at the flexible bearings. All other possible boundary conditions would simply be variations and/or simplifications from this case (e.g. a rotational spring can be used to model the actual flange flexibility on rigid bearings (as per results of localized stiffness studies shown in Fig. 4.17).

Finally, the lateral stiffness of the ductile diaphragms, K_{DD}, depends on the type of ductile device implemented. For example, if the proposed ductile shear panel system is used, the stiffness of one such end-diaphragm in a slab-on-girder bridge, K_{SPS}, can be obtained by the general expression that accounts for axial deformation of braces and bottom beam, flexural and shear displacement of the link, rotation of bottom beam at midspan, and finally axial deformation of stiffened girders,where E is the modulus of elasticity, l_b and A_b are the length and area of each brace, θ_b is the brace's angle with the horizontal, L_s is the girder spacing, d_{bb}, A_{bb} and I_{bb} are the depth, cross sectional area and moment of inertia for the bottom beam, h_l, I_l and $A_{s,l}$ are the length, moment of inertia and shear area of the link, and H and A_g are the height and area of the stiffened girders.

$$K_{SPS} = \frac{E}{\frac{l_b}{2A_b \cos^2\theta_b} + \frac{L_s}{4A_{bb}} + \left(\frac{h_l^3}{3I_l} + \frac{2.6h_l}{A_{s,l}}\right) + \frac{L_s\,(h_l + d_{bb}/2)^2}{12I_{bb}} + \frac{H \tan^2\theta_b}{2A_g}} \qquad (4.24)$$

Similarly, lateral stiffness of the EBF and TADAS implemented as end-diaphragms of slab-on-girder bridges, K_{EBF} and K_{TADAS}, can be computed from the following expressions taking into account the axial deformation of braces and bottom beam, flexural and shear displacement of the link (for EBF), flexural deformation of TADAS device and rotation of bottom beam at midspan (for TADAS) and finally axial deformation of stiffened girders,

$$K_{EBF} = \frac{E}{\frac{l_b}{2A_b \cos^2\theta_b} + \frac{a}{2A_l} + \frac{e^2 H^2}{12 L_s I_l} + \frac{1.3e H^2}{a L_s A_{s,l}} + \frac{H \tan^2\theta_b}{2A_g}} \tag{4.25}$$

$$K_{TADAS} = \frac{E}{\frac{l_b}{2A_b \cos^2\theta_b} + \frac{L_s}{4A_{bb}} + \frac{6 h_T^3}{N_T b_T t_T^3} + \frac{L_s (h_T + d_{bb}/2)^2}{12 I_{bb}} + \frac{H \tan^2\theta_b}{2A_g}} \tag{4.26}$$

where a is the length of the beam outside the link, e, I_l, A_l and $A_{s,l}$ are the length, moment of inertia, cross sectional and shear areas of the link, N_T, h_T, b_T, and t_T are the number, height, width and thickness of the TADAS plates, and all other parameters are as defined previously. Note that some of these terms have a limited impact on the overall stiffness term, and could be simplified in some practical situations. For example, of the five terms in the denominator of Eqs. 4.24 to 4.26, the second and fifth which account for axial deformations of bottom beam and stiffened girders could be ignored, and the fourth (accounting for the rotation of bottom beam at midspan in SPS and TADAS) could have a small impact if the bottom beam was a deep and stiff beam, which is not however the case in the examples studied here.

From the above equations, the lateral period of the seismically retrofitted steel bridge, T, using the proposed ductile end-diaphragm is consequently given by the following expression:

$$T = 2\pi \sqrt{\frac{m^*}{K_e}} \tag{4.27}$$

Linear static and dynamic analyses were conducted using SAP90 (Wilson and Habibullah 1992) on 3-D and 2-D models (Fig. 4.18) of end-diaphragm structures to verify the above models of generalized mass, stiffness, lateral period and other items for reference purposes. In all cases, comparison of results and response at the diaphragms were satisfactory. A small difference of 5% or less was found between the lateral periods obtained by the two models, for bridges of 20 to 60 m spans. Difference was largest for the smaller span bridges as their shear flexibility, neglected from the model expressed by Eq. 4.17, started to contribute more significantly to the overall deck stiffness. It is noteworthy that the fundamental lateral periods for the bridges studied here were mostly in the short period range (i.e. on the constant pseudo acceleration plateau of the design spectra), with values from 0.15 to 0.3 second.

4.6.2 Ductility vs. Reduction Factor Strategy

Clearly, from the above description of the end-diaphragm stiffness, the flexural resistance of the girders can potentially contribute to the lateral load resistance of the ductile system, and even to its energy dissipation capability, depending on the relative rigidities of the components of this diaphragm. If connections at the deck slab and bearings are unlikely to be sufficiently strong to allow development of this additional bending resistance, these girders can be considered effectively pinned at their top and bottom, and these diaphragms will exhibit an ideal bilinear hysteretic behavior when subjected to severe lateral earthquake excitations. In that case as shown in Fig. 4.19a, the relationship between ductility, μ, and the force reduction factor, R, could be taken as given by the classic relationship for structures in the low period range:

$$\mu = \frac{R^2 + 1}{2} \qquad or \qquad R = \sqrt{2\mu - 1} \tag{4.28}$$

However, in the alternative situation where both the girders and ductile diaphragm element can contribute to load resistance and energy dissipation, a trilinear hysteretic model must be considered, as shown in Fig. 4.19b. In that case, the relationship between ductility and the force

reduction factor is somewhat more complex, and, if derived using principles of equal energy, could be demonstrated to be equal to:

$$R^2 = \frac{1}{r^2}\left(2U\mu - U^2(Q+1) + Q(2U-1)\right) \tag{4.29}$$

if strain hardening is neglected, where $r = V_{inel}/V_y$, $U = V_y'/V_y$ and $Q = \Sigma K_{DD}/\Sigma k_g$. V_{inel} is the inelastic lateral load resistance of the entire end-diaphragm panel, V_y' and V_y are the yield strength of stiffened girders and ductile device respectively, and K_{DD} and K_g are as defined earlier.

In presence of strain-hardening, the above equation becomes:

$$R^2 = \frac{1}{r^2}\left(C_{SH}(\mu - 1 - B) + U(2\mu - 1 - B) + B + 1\right) \tag{4.30}$$

where C_{SH} is the strain-hardening ratio and B is as following:

$$B = \frac{(U-1)(Q+1)}{C_{SH}\,Q+1} \tag{4.31}$$

In all cases, since previous studies of slab-on-girder bridges (e.g. Dicleli and Bruneau 1995) and results obtained herein indicate that the steel bridges of interest have a low fundamental period of vibration in the transverse direction, the relationship between ductility and force reduction factor is based on the principle of equal energy deemed more appropriate in the low period range. On that basis, and given that lateral stiffness of the stiffened girders is usually low compared to that of the braces and energy dissipating device (leading to a modest slope along the second part of the trilinear curve), a bilinear μ-R strategy (Eq. 4.28) was found to give good results provided an equivalent yield strength of V_{inel} is used, as shown in Fig. 4.19b. This V_{inel} is simply the actual strength of the ductile diaphragm at the lateral displacement, δ_e, that would have resulted from elastic analysis. However, in cases where the slope of the second part of the trilinear curve is relatively large and/or when V_{inel} is close to V_y', it is recommended to use Eqs. 4.29 or 4.30 instead. In all cases studied here, the former method (i.e. Eq. 4.28) was used.

Note that this reduction factor (μ-R) strategy was also verified using both push-over and dynamic time-history nonlinear inelastic analyses of the proposed end-diaphragm models subjected to different earthquake excitations (the push-over analyses also proved useful to check the trilinear monotonic non-linear inelastic force-displacement behavior of the ductile diaphragm assemblies obtained using basic structural engineering principles and hand calculations). These analyses were carried out with the DRAIN-2DX nonlinear inelastic analysis program (Prakash et al. 1993), using plastic hinge beam column elements and truss bar elements. For SPS, in addition to a flexural element, an inelastic spring was inserted to model both elastic and inelastic shear deformations. For EBF, a similar modeling strategy was used. For TADAS systems, multiple elements were used to model stiffness variations along the height of the triangular plates. As consistently done in this study, equivalent springs were inserted at the connection of girder stubs to slab to include the impact of slab flexibility (K^* in Eq. 4.20), and an equivalent web thickness for the stub girder was used to model the actual stiffened girder web. Structural steel with a yield stress of 300 MPa and a strain hardening ratio of 0.005 to 0.03 was considered. For the dynamic analyses, tributary bridge mass concentrated at each slab joint and Rayleigh damping of 2% (Clough and Penzien 1993) were also considered, using the first and the third frequencies to calculate mass and stiffness proportional damping factors.

These analyses confirmed the need to consider a trilinear force-displacement characteristic curve for the nonlinear inelastic response of the ductile diaphragms of interest (as in Fig. 4.19b), to properly account for the non-negligible impact of the girders' stiffness and yield strength on behavior over the displacement range of interest. The analyses also verified the effectiveness of the proposed reduction factor (μ-R) strategy.

4.7 Design Procedure

To achieve the desirable objective of substructure protection, ductile end-diaphragms of the type described above must be designed to be the only structural elements to yield and dissipate energy,

without ever exceeding the level of lateral load that initiates undesirable damage in the substructure. However, knowing that ductility demand and force reduction factor are intertwined, a minimum strength of the ductile diaphragms must be provided to prevent undue ductility demands on the specially detailed energy dissipating elements. In compliance with this dual design constraint philosophy, a step-by-step procedure for the design of ductile end-diaphragms is proposed. Fig. 4.20 presents a flow chart for the proposed design method, while detailed procedure is explained following. In a later section, nonlinear inelastic analyses will be used to demonstrate the satisfactory seismic performance of designs resulting from this procedure.

4.7.1 Detailed Design Procedure

In the perspective of a seismic retrofit, the necessary steps of the proposed design procedure are:

1) Determine the following basic design parameters: entire mass of the bridge, M, seismic acceleration coefficient, A (code-specified value or from site-specific data), number of girders, n_g, number of end-diaphragms implemented at each support, n_d, girder spacing, L_s, and other geometric and descriptive characteristics of the bridge. Note that for a slab-on-girder bridge having 4 girders for example, it is in theory possible to insert 3 energy dissipating ductile diaphragms at each end of a span if bracing is introduced between all girders. However, as mentioned earlier, except for very large bridges, more practical member sizes for the key components of the ductile diaphragms are obtained when a single diaphragm panel is introduced at each end of a span, irrespectively of the number of girders present.

2) Calculate the generalized mass and stiffness, m^* and K^*, by using Eqs. 4.18a and 4.18b, respectively.

3) Find the elastic seismic base shear resistance, V_e, for one end of the bridge (half of the equivalent static force, P_e, using Eq. 3.16), that would be needed if fully elastic response was desirable. Typically, design engineers would obtain this value from a code formula such as (American 1994):

$$V_e = C_s \left(\frac{8Mg}{\pi^2} \right) /2 = C_s \frac{4Mg}{\pi^2} \approx 0.4 C_s Mg \tag{4.32}$$

in which g is the gravity acceleration, and the seismic response coefficient, C_s, would be typically given by:

$$C_s = \frac{1.2 A S}{T^{2/3}} \leq 2.5A \tag{4.33}$$

where S is the site coefficient and T is the lateral period of vibration. Given the generally short period of the steel bridges of interest here, the upper C_s limit, i.e. $2.5A$, is usually suitable for preliminary design. Note that for bridges with laterally rigid deck, half of the bridge mass should be conservatively considered at each end (i.e. $0.5C_sMg$ in Eq. 4.32).

Alternatively, V_e can be calculated using a pseudo acceleration, PSa, based on a smooth design spectra representative of the average (or average-plus-one-standard-deviation) seismic demand for a set of representative earthquake records. For example, as shown in Fig. 4.21, the Newmark-Hall response spectrum (Newmark and Hall 1982), for earthquakes scaled to the required seismic demand (e.g. ground acceleration of 0.4g), can be used. In that case,

$$V_e = \frac{4M}{\pi^2} PSa \approx 0.4M\ PSa \tag{4.34}$$

4) Calculate $V_{inel} = V_e / R$, where V_{inel} is the inelastic lateral load resistance of the entire ductile diaphragm panel at the target reduction factor, and R is the force reduction factor mentioned earlier. Then verify that V_{inel} is less than the lateral load resistance of the substructure, with

a comfortable safety factor (say 2.0), thus ensuring that the principal target objective is achieved. If not, this retrofit solution may not be suitable to the problem at hand, although it may be still applicable and useful to limit the extent of the required substructure retrofit work. At this time, a maximum force reduction factor of 3.75 is proposed here to limit ductility demands within reasonable ranges (in a Limit States Design context), but somewhat higher values could be used by engineers if supported by appropriate time-history inelastic analyses and experimental evidence. Nonetheless, recall that since diaphragm damage must be prevented under wind load, the additional constraint that $V_{inel} > W$ must also be respected, where W is the maximum expected wind force to be resisted by the diaphragm.

5) Determine the design lateral load, V_d, to be resisted by the energy dissipation device (e.g. link beam or TADAS) at the target ductility level, by:

$$V_d = \frac{V_{inel} - n_g V_g}{n_d} \tag{4.35}$$

where V_g is the lateral load resistance of one stiffened girder. For trilinear hysteretic systems, determination of V_d would typically require an iterative calculation, as demonstrated in the examples in a later section. For expediency in a first iteration, V_g can be taken as its yield value (equal to $K_g \delta'_y$) or any other arbitary value for that matter, however its actual value at the specified transverse displacement (i.e. $K_g \delta_t$) should be considered if girders are found to remain in the elastic range in subsequent iterations. Note that in short bridges, V_g can be a dominant factor that could overwhelm the resistance contribution provided by the special ductile diaphragm elements. However, due to the difficulty in accurately predicting true stiffness and strength contribution of the girders due largely to uncertainties in their fixity conditions (as mentioned earlier), it is recommended in this procedure that the bearing stiffeners at the support of these girders be trimmed (or replaced) to the minimum width necessary to satisfy the strength and stability requirements. Note that in longer bridges, particularly those with a lesser number of girders per cross-section, the contribution of the girders to lateral load resistance was found to be nearly insignificant.

6) Design all structural members and connections of the ductile diaphragm, with the exception of the seismic energy dissipation device, to be able to resist forces corresponding to $1.5V_d$. For example, braces should be designed to resist an axial compression force, V_b, equal to:

$$V_b = 1.5\left(\frac{V_d}{2\cos\alpha}\right) = 0.75\frac{V_d}{\cos\alpha} \tag{4.36}$$

This 50% overstrength requirement for the members adjacent to the ductile element recognize the potential of overstrength in the specified values (i.e. uncertainties in the yield strength), strain hardening and strain rate effects, and other phenomena that may make the actual yield strength exceed the expected strength of the specially detailed ductile elements. Likewise, for the SPS and TADAS systems, the bottom beam should be designed to resist the applied moment considering a 50% overstrength of the energy dissipator, i.e. $M=1.5V_d$ (h_l or h_T) where h_l and h_T are link length and plate height as mentioned before. Moreover, for a given SPS or TADAS device, it is also advantageous to select a flexurally stiff bottom beam to minimize rigid-body rotation of the energy dissipating device and thus maximize hysteretic energy at a given lateral deck displacement.

7) Select a plate thickness, t_T, based on available plates and structure size. The two key parameters, the plastic flexural strength, V_T (corresponding to flexural yielding of triangular steel plates), and the stiffness, K_T, of a TADAS device can be determined from:

$$V_T = \frac{N_T\, b_T\, t_T^2\, F_y}{4h_T} \tag{4.37}$$

$$K_T = \frac{N_T\, Eb_T\, t_T^3}{6h_T^3} \tag{4.38}$$

where N_T, b_T, t_T and h_T are the number, base width, thickness and height of the triangular steel plates. The ratio of the above equations directly provides a relationship between h_T and t_T:

$$h_T = \sqrt{\frac{2Et_T V_T}{3F_y K_T}} \tag{4.39}$$

Here, $V_T = V_d$ and a h_T of $H/10$ to $H/12$ is recommended. To have a girder drift angle of 0.02 radian in a severe earthquake, a distortion demand of 0.2 to 0.24 Rad is required for a typical H/h_T ratio of 10 to 12, as per Eq. 4.10. Hence, if a reasonable estimate of the desirable K_T for the TADAS device is possible, t_T can be determined directly from h_T. In turn, b_T can be chosen knowing that triangular plates with aspect ratio, h_T/b_T, between 1 and 1.5 are better energy dissipators, based on experimental results (Tsai et al. 1993). Finally, N_T can then be calculated using either of Eqs. 4.37 or 4.38. Small adjustments to all parameters follow as N_T is rounded up to the nearest whole number. Incidentally, many different yet appropriate TADAS systems could be designed within these constraints. However, for EBF and SPS systems replace step 7 with the following step:

7) Design the energy dissipating device. For the devices chosen here, considerable information is available in the literature, and only the major design steps are summarized here. For example, for the link beam in an eccentrically braced diaphragm, the shear force V_l in the link is:

$$V_l = \frac{H}{L_s} V_d \tag{4.40}$$

The plastic shear capacity $V_{l,p}$ of a wide flange beam given by (American Institute 1994; Canadian 1994, 1995),

$$V_{l,p} = 0.55F_y t_w d_l \tag{4.41}$$

where F_y is the yield stress of steel, t_w is the web thickness, and d_l is the depth of the link, must be chosen greater than, but as close as possible to V_l to meet the present objectives. Note that for shallow links with thick flanges, the expression for ultimate shear strength developed by Krawinkler and Popov (1982) for joint panel zone resistance may be more

appropriate if concerned about link overstrength for substructure protection (for the examples presented here, the difference was typically less than 5%, and thus negligible). The moment simultaneously applied to the link must be less than the reduced moment capacity, M_p^*, of the link yielding in shear and equal to (Malley and Popov 1983):

$$M_p^* = t_f \, b_f \, F_y \, (d_l - t_f) \tag{4.42}$$

Since shear links are more reliable energy dissipators than flexural links (Kasai and Popov 1986; American Institute 1994), shear links are favored in the current implementation and their length is therefore limited by the equation below:

$$e < e_{max} = 1.6 \, \frac{M_p^*}{V_{l,p}} \tag{4.43}$$

To attain the desired balance, it may be necessary to adjust link length or link beam size. A link length, e, of 1/8 to 1/12 of the girder spacing, L_s, is recommended for preliminary design, the less restrictive value preferred for practical reasons (i.e. detailing constraints) in presence of closely spaced girders. Deeper link beams are also preferred as the resulting larger flexural stiffness enhances the overall stiffness of the ductile device, ensuring that its yield displacements is reached much before onset of yielding of the stiffened girders.

For a SPS, the above procedure would be followed with the obvious exception that $V_l = V_d$ and the height of panel should be limited to half of the value obtained by Eq. 4.43 since the yielding link is only in single curvature, as opposed to double curvature for the EBF. A link height of 1/8 to 1/10 of the girder depth is recommended for preliminary design.

8) Calculate the stiffness of the ductile end-diaphragm by using Eqs. 4.24, 4.25 or 4.26 as appropriate. The lateral stiffness of the stiffened girders can be obtained from Eqs. 4.22, 4.23 or other values as appropriate. Once the lateral period of the bridge, T, is computed from Eq. 4.27, go back to Step 3 to determine if C_s needs to be updated, and if so repeat all above steps until convergence.

9) For the resulting design, determine the lateral deflection of the diaphragm on a figure similar to Fig. 4.19b, and calculate the base shear resistance by each of the girders and the ductile diaphragm element. At this stage, the correct value of V_g for each girder at one end of a span can be obtained based on δ_e (if $\delta_e < \delta'_y$), as shown in Fig. 4.19b:

$$V_g = K_g \delta_e \leq V_{y,g} \tag{4.44}$$

where $\delta_e = V_e / K_{ends}$ (K_{ends} was calculated in the previous section). Then determine the actual force reduction factor, recognizing the true trilinear behavior of the total diaphragm system, by:

$$R = \frac{V_e}{V_{inel}} = \frac{V_e}{n_d V_d + n_g V_g} \tag{4.45}$$

If this value is significantly different from the original target value, (i.e. 3.75 in this case), go back to step 4 and modify the design of the device as appropriate.

10) Repeat the above process until convergence or until a nearly satisfactory value is obtained for the actual R. Following this procedure, only two or three iterations were found necessary to get acceptable final results in most cases (at least one iteration is usually required to ensure appropriateness of initial assumptions in step 5). From this final solution and actual R value, the actual displacement ductility demand can be determined from Eqs. 4.28, 4.29 or 4.30 as appropriate, and the maximum lateral drift of the bridge at the diaphragm location, δ_{max}, is:

$$\delta_{max} = \mu \delta_y \quad \text{where} \quad \delta_y = \delta_{y,d} = \frac{V_d}{K_{DD}} \tag{4.46}$$

Furthermore, as the maximum ductility capacity of shear links is commonly expressed in terms of the maximum link deformation angle, γ_{max} (easily obtained by dividing the maximum relative displacements of link ends by the link length), the maximum drift for the SPS and EBF diaphragms is respectively limited to:

$$\delta_{max} < e\ \gamma_{max} \tag{4.47}$$

$$\delta_{max} < \frac{e\ H}{L_s}\ \gamma_{max} \tag{4.48}$$

with generally accepted γ_{max} limits of 0.09 (Canadian 1994; American 1994). Note that, for the SPS diaphragms, the following alternative equation that accounts for the rotation of bottom beam at the link connection may be more accurate when this factor has an important impact:

$$\delta_{max} < e\left(\gamma_{max} + \frac{V_d\ L_s\ (h_l + d_{bb}\ /2)}{12EI_{bb}}\right) \tag{4.49}$$

Should these limits be violated, modify the link's depth and length as well as the stiffness of the EBF or SPS diaphragm as necessary, and repeat the design process. Finally, a maximum drift limit of 2% of the girder height is also suggested here, at least until experimental evidence is provided to demonstrate that higher values are acceptable.

Note that steps 4 and 6 should be repeated using the properties of the final section chosen. This is to protect against situations where large overstrength may have been introduced in the design process when larger than required members were chosen based on economic considerations.

Also, given the trilinear hysteretic nature of the ductile end-diaphragms, it is desirable to provide a rather stiff braced diaphragm assembly to prevent, or at least minimize, yielding in the main girders under transverse displacements. Since the specially detailed ductile diaphragm elements are designed to dissipate large amount of seismic energy in a stable manner, the objective is to concentrate all cyclic inelastic deformations into those elements. Ideally, the braced diaphragm assembly should be 5 to 10 times stiffer than the girders with bearing web stiffeners (even though ductility demand tends to be larger in stiffer structures). Incidentally, this can also be achieved

by making the girder's web bearing stiffeners as narrow as possible to lower their lateral stiffness and further increase the distance between the yielding threshold of the girders and that of the braced diaphragm assembly. These stiffness considerations are intended to provide safety against the risk of undesirable seismic damage in the bearing web stiffeners.

Finally, the ductile energy dissipating elements should be laterally braced at their ends to prevent out-of-plane instability. These lateral supports and their connections should be designed to resist 6% of the nominal strength of the beam flange, i.e. $0.06F_y\, t_f\, b_f$ (American Institute 1994). In addition, to prevent lateral torsional buckling of beams in the SPS, EBF, and TADAS end-diaphragms, the unsupported length, L_u, of these beams shall not exceed $200b_f/\sqrt{F_y}$ where b_f is the width of beam flange in metre and F_y is the yield strength of steel in MPa (Brockenbrough and Merrit 1995).

4.8 Numerical Examples

To illustrate the proposed design procedure, a few examples are presented. In all cases, ductile diaphragms were designed considering steel with a yield stress F_y of 300 MPa, and a code-specified seismic ground acceleration of 0.31g. The design seismic force was obtained from the AASHTO (American 1994) seismic provisions, assuming a reduction factor of 3 (corresponding to a ductility capacity, μ, of 5) or 3.75 (μ of 7.5) depending on the example. Also, SPS, EBF, and TADAS end-diaphragms were developed for each bridge configuration and geometry considered. Table 4.3 presents the characteristic properties of the three example slab-on-girder steel bridges considered: a simply supported 40 m span bridge, a 60-90-60 m continuous three-span bridge (diaphragms over continuous supports considered here), and a simply supported 40 m multi-span bridge supported by reinforced concrete bents each having four columns of 0.9 m diameter and 5 m height for the third example and 0.6 m diameter and 6 m height for the last one.

Except for the second bridge example having two girders, the energy dissipation devices were introduced only between the two interior girders of these four-girder bridges.

Details of the iterative procedure are presented in Tables 4.4 and 4.5 for each bridge example, along with final verifications that limits on ductility, maximum drift, and maximum link deformation angle have not been exceeded (note that results identical to those in Table 4.4 were obtained in the third example, even though lateral period was larger, i.e. about 0.3 sec). Strain hardening was ignored for simplicity. Figs 4.22 to 4.24 show the trilinear curves for three 40 m span bridge examples according to the proposed design procedure. Incidentally, design of the ductile energy dissipating elements proved easier for longer bridges with fewer girders, as the number of structural shapes having the desirable properties seemed to increase along with the strength requirements. Beyond the tabulated calculations, conventional design of beams, braces, stiffeners, gusset plates, bolts and miscellaneous other details intended to remain elastic would follow, and is not presented here. Note that for the examples in Tables 4.4, as suggested in step 5 of the design procedure, the width of transverse web stiffeners of the girders was reduced to the minimum necessary to satisfy the bearing requirements, thus delaying their flexural yielding and reducing their originally considerable flexural stiffness. Although flexural yielding of web stiffeners might be tolerable if it does not affect the bearing stability of the girder, it should be kept to a minimum until experimental research results can demonstrate otherwise.

4.8.1 Inelastic 2-D Push-over Analysis

Although not required by the design procedure, nonlinear static push-over analyses were conducted using the DRAIN-2DX for the examples in Tables 4.4 and 4.5 to illustrate the trilinear behavior of the resulting ductile diaphragms, and the expected extent of yielding at the design level. These analyses revealed that yielding of the device (shear yielding of link beam in SPS and EBF, and flexural yielding of plates in TADAS) were obtained at a device yield strength of 142, 102 and 142 kN, when the lateral loads reached to 161, 130 and 174 kN, respectively for SPS, EBF and TADAS implemented in the 40 m span bridge. All other members remained elastic

while the plastic shear deformation occurred in the link beam. Lateral loading was increased at load steps of 10 kN. Flexural yielding in web stiffeners was observed at a drift of 11 mm (ductility of 4 to 6) and a lateral load of 275, 242 and 283 kN, respectively for SPS, EBF and TADAS end-diaphragms.

Fig. 4.25 illustrates the total lateral load and the lateral load resisted by the link versus deck displacement for the SPS end-diaphragms used in the 40 and 90 m span bridge examples, respectively, pushed to displacement ductility of approximately 6. For the 40 m single span bridge, the lateral stiffness of the stiffened girders is not negligible compared to that of the ductile device, and the girders contribute to seismic resistance of the diaphragms as shown by the resulting trilinear curve on Fig. 4.25a. By contrast, the much taller girders in the 60-90-60 m three-span bridge do not resist a significant percentage of the lateral forces, and their flexural yielding only occurs at a very large displacement beyond the expected range of response (Fig. 4.25c and d) with a resulting bilinear load-displacement behavior over that range.

4.8.2 Inelastic 3-D Push-over Analysis

The ADINA program was used, to investigate the 3-D nonlinear behavior of the bridges having ductile end-diaphragms. Fig. 4.26b presents the deformed shape of a 40 m span bridge having SPS end-diaphragms, reflecting a large lateral stiffness similar to those previously presented for bridges having X-braces. As shown by the load versus drift relationship of Fig. 4.27a, results compare well with those obtained by DRAIN-2DX up to the point of shear yielding, δ_y, of the SPS (Fig. 4.27b). However, the 3-D analyses indicate that the stiffened girders contribute about 15% more to the lateral load resistance at a drift of δ_{max} (note that for comparison, the lateral load resisted by the stiffened girders in Fig. 4.25 should be doubled to represent full fixity at the top and bottom of the stub-girders as almost the case for Fig. 4.27). Fig. 4.27c presents the bending moment in the bearing web stiffeners. Interestingly, as shown in Fig. 4.27d, the intermediate diaphragms only play a minor role in seismic resistance of the 40 m span bridge, even at larger

ductilities of the end-diaphragm, which is consistent with the findings in Chapter 3. Stresses in the concrete slab remained small (less than 3 MPa) in all cases.

4.8.3 Nonlinear Dynamic Time-History Analysis

To validate the proposed ductile diaphragm seismic retrofit concept, the 2-D structural models of the bridges were also analyzed using nonlinear inelastic time history analyses using the DRAIN-2DX program and considering five different earthquake excitations scaled to 0.4g and applied transversely to the span direction. Note that the seismic ground acceleration of 0.31g was increased due to the model effective forces (Eq. 4.19). The 1940 El-Centro S00E, 1966 Parkfield N65E, 1971 Pacoima Dam S16E, 1988 Saguenay (St-Ferreol, longitudinal component), 1989 Loma Prieta (Corralitos 37.037N 121.883W), were considered. Rayleigh damping was used with 2% (ξ=0.02) damping assigned to the first and third fundamental lateral periods (typically, for simple span bridges, these values were 0.23 and 0.027 sec, suggesting that higher modes were of little impact on response).

Table 4.6 presents the inelastic analysis results for the 40 m span bridge examples considered, using the final member sizes for the three end-diaphragms (TADAS, EBF and SPS) obtained following the proposed design procedure. As seen in that table, for the average of all earthquakes considered, maximum ductilities and drift results remain within the expected range. Resulting inelastic time-history analyses (deck displacements and link rotations) for all bridge examples with SPS end-diaphragms subjected to the 1940 El-Centro earthquake (scaled to 0.4g) are presented in Fig. 4.28 for illustration purposes. As shown in Figs. 4.28e and 4.28f, the proposed method still works for bridges on stiff pier bents. Note that due to flexibility of the piers for the third and fourth examples, the generalized mass and stiffness would be different, i.e. worse results might be obtained indicating the weakness of the proposed design procedure for the bridges on flexible piers (Figs. 4.28g and 4.28h). Fig. 4.29 shows the hysteretic behavior for the shear link in the 40 m span bridge.

4.9 Impact of Intermediate Web Stiffeners

In the proposed design procedure and above examples, no intermediate web stiffeners were considered. However, in presence of intermediate web stiffeners (found in some existing steel bridges), the lateral stiffness, K_g, of the stiffened girders used in the above procedure should be modified. The proposed design procedure can be used as long as an equivalent lateral stiffness, K'_g, is used instead of K_g in Eq. 4.21. No closed-form solution is provided for K'_g, but Fig. 4.30 shows the non-dimensional relationship between K'_g/K_g and (K_{BS}/K_{IS}), where S_s is spacing of intermediate web stiffeners, and K_{BS} and K_{IS} are the lateral stiffnesses of bearing and intermediate web stiffeners, respectively. Fig. 4.30 was obtained by running ADINA for bridges of various spans having different intermediate web stiffeners stiffnesses and spacings.

Generally, the impact of intermediate web stiffeners on K_g can be ignored, unless large stiffeners are used at small intervals. For example, if intermediate stiffeners identical in size to the bearing web stiffeners (i.e. $K_{BS}=K_{IS}$) are used at an interval of. 0.1L, K'_g would be only 6% greater than K_g, as shown in Fig. 4.30. For stiffer web stiffeners more closely spaced along the girders, K_g and V_g should be modified. In general, the farther transverse web stiffeners are from bridge ends the smaller is their contribution to the lateral load resistance.

Deformed shapes of a 40 m span bridge subjected to lateral loads and having 100x10 transverse web stiffeners at spacing of 4 and 2 m are shown in Fig. 4.31 for comparison. The larger torsional rotation of the bridge deck in the latter case, indicates that web stiffeners at every 2 m make the bridge stiffer laterally. Figs. 4.32 and 4.33 present the inelastic analysis results for the same bridge having web stiffeners at every 4 m and 2 m, respectively. Higher lateral strength and stiffness for the latter case (Fig. 4.33a compared to Fig. 4.32a) can be justified by the large bending moments resisted by the web stiffeners, as shown in Fig. 4.33b compared to Fig. 4.32b. In both cases, the intermediate diaphragms (at 8 m and 16 m from the bridge ends) do not influence the seismic resistance. Fig. 4.34 presents the 3-D inelastic results, using ADINA, for

a 60 m span bridge having 100x10 transverse web stiffeners at every 3 m along the girders. The same SPS device as above examples was considered here. Similar results to those shown in Fig. 4.33 for 40 m span bridge were generally obtained.

4.10 Summary of Findings

An innovative strategy has been proposed for the seismic retrofit of slab-on-girder steel bridges. Taking advantage of the presence of a steel superstructure, the existing end-diaphragms of these bridges are replaced by new ductile diaphragms incorporating stable seismic energy dissipation devices. Per capacity design principles, these devices act as structural fuses calibrated to yield before the strength of the substructure is reached, thus protecting that substructure from undesirable damage. Although targeted for implementation as part of a retrofit strategy, ductile diaphragms should be equally effective in new bridges.

A simple design procedure suitable for hand calculation has been proposed, using a trilinear load-displacement relationship and a strength-versus-ductility relationship based on equal energy concepts. Nonlinear inelastic analyses suggest that the resulting designs will exhibit an appropriate ultimate cyclic seismic behavior. Longer bridges having proper end-diaphragms absorb more earthquake energy and more effective retrofits are obtained for longer bridges having a smaller number of girders.

It was also found that the stiffened girders may resist a significant portion of the lateral loads at large inelastic deformations, if transverse web stiffeners are closely spaced near the bridge ends. In such cases, the proposed ductile end-diaphragms might be less effective, and other seismic retrofits (e.g. base isolation systems) can be used to protect the substructure elements. It is noteworthy that the ductile seismic retrofits proposed here works more effectively for existing steel superstructures having relatively weak lateral stiffness.

However, while the concept is promising and appears satisfactory based on the limited analyses reported herein, more research is needed before common implementation is possible. Cyclic tests should be conducted to verify the effectiveness of the rehabilitation techniques proposed here. In particular, large scale experimental verification of the concept and expected behavior is desirable.

CHAPTER 5

EXPERIMENTAL APPROACH

5.1 General

A few ductile end-diaphragms were proposed and analytically investigated in Chapter 4. To experimentally verify the analytical study and predicted structural behavior, a series of cyclic tests were carried out on full-scale specimens, each having a ductile end-diaphragm introduced between two short segments of the girders representative of a 40 m span steel slab-on-girder bridge. In designing the specimens for this experimental investigation, the design details and recommendations developed by other researchers for these types of ductile devices were used (Tsai et al. 1993, 1994; Roeder and Popov 1978; Malley and Popov 1983; Kasai and Popov 1986; Fehling et al. 1992 and Nakashima 1995). The specimens were labeled according to their ductile end-diaphragm system; i.e. TADAS (triangular-plate added damping and stiffness device), EBF (eccentrically braced frame) and SPS (shear panel system). For the EBF and SPS specimens, two design alternatives were considered. Plans were made for modifications and retest of each specimen according to a matrix presented later. These included test with and without the ductile end-diaphragm, a pseudodynamic test and a test with a deep channel

diaphragm at mid-height of the girders. Therefore, taking into account design alternatives and retests, a total of eight cyclic tests were conducted in this experimental program.

Each specimen consisted of two 0.5 m long segments of WWF1200x333 girders, 2 m center-to-center and having 10 mm thick and 100 mm wide bearing web stiffeners on each side of the web (Fig. 5.1). A 200 mm thick reinforcement concrete deck, connected to top flange of each girder segment by 10 shear studs was poured in place during construction of the specimens. The TADAS, EBF and SPS ductile diaphragms were common in that they all had a chevron-braced frame configuration, with a bottom beam, and two double angles as diagonal braces. However, each end-diaphragm had a different energy dissipation ductile device. Details of the material properties, designed test specimens, construction procedure, test set-up and instrumentation are presented in this chapter.

5.2 Material Properties

Structural Steel

CAN/CSA G40.21-M 350W structural steel (equivalent to ASTM-A572 Grade 50) was specified for all the steel specimens ordered from the steel fabricator, as well as for the miscellaneous components used in foundation and test set-up. Nominal yield and ultimate strengths of 350 MPa and 450 MPa, respectively, were used in designing test specimens. Results obtained from preliminary tests to identify material properties of the steel received are presented in the next chapter.

Concrete

Ready mix concrete obtained from a local supplier was used for casting a foundation for the specimens three months prior to testing. A 28 day target strength, f_c', of 30 MPa, 70 mm slump,

and 10 mm maximum aggregate size for the heavily reinforced foundation was ordered from the supplier. For the concrete deck on top of the three specimens, concrete was made in the University of Ottawa concrete laboratory using a mix ratio of 4:2:1 for gravel, sand and cement, respectively and a water content of 0.5, also providing a 28 day strength of 30 MPa. In each 0.1 cubic metre batch from the concrete mixer, 57 kg of #20 and #10 gravels, 69 kg of sand and 30 kg of cement were used.

In all cases, concrete was carefully vibrated using a 40 mm (1.5") vibrator, and cured as required. A few control cylinders were also taken from different batches in case concrete strength needed to be determined at a later date. The specimens were tested between one and two months after casting.

Reinforcement Steel

Grade 400, No. 25 and 20 reinforcement rebars were used as longitudinal and transverse reinforcement in the foundation and deck of each specimen. Grade 400, No. 10 stirrups were also used for shear reinforcement of the foundation and decks.

5.3 Design of Test Specimens

All specimens were designed based on the design procedure proposed in Chapter 4 to resist a *PGA* of 0.47g (0.6g for the bridge model), indicative of severe earthquakes. The end-diaphragms were designed for a 40 m span slab-on-girder steel bridge having four steel girders spaced at intervals of 2 m. Bearing web stiffeners of 100x10 were considered on both sides of the girders web (Fig. 5.1). As recommended in the design procedure, only one ductile end-diaphragm panel was considered at each bridge end. Consequently, for the full scale tests, only the two girders connected together by a ductile diaphragm needed to be considered. Furthermore, only a short length of each girder was necessary for reasons described in the earlier chapters.

For the design procedure, a generalized tributary mass of 71500 kg at each bridge end (for lateral period calculations) and an equivalent elastic lateral load, V_e, of 1325 kN were considered for the bridge model. According to the codes recommendations (American 1994, Canadian 1995) for most structural frames, a reduction factor, R, of 3.75 was considered (corresponding to ductility ratio, μ, of 7.5 per Newmark-Hall's procedure), although a higher reduction factor might be argued to be acceptable for the ductile systems considered here. This gave an inelastic seismic force, V_{inel}, of 350 kN for each specimen to be considered for design of the ductile devices.

Full fixity was assumed during design for the connection of bottom flanges, to be more representative of the experimental conditions, although fixity condition at fixed or expansion bearings approach that of a hinge in most field conditions due to large lateral rotations that can develop at the supports. A damping ratio of 2% was used in dynamic analyses. In inelastic range, a strain-hardening ratio of 0.01 was assumed. CAN/CSA-S16.1-94 Limit State Design of Steel Structures was used to design the components (Canadian 1995). A325M 20 mm high strength bolts with a minimum tensile strength of 830 MPa were used in all connections.

Lateral loads on the specimens were applied to the 200 mm deep reinforced concrete decks. Each deck was therefore designed (Canadian portland 1995) to transfer those loads to the girders by means of 10 shear studs (130 mm long) at the top flange of each girder (Fig. 5.1). Since the vertical loads were to be applied directly to the stub girders in the test set-up as will be shown later, only lateral loads were considered in the design of deck reinforcement. Conservatively modeled as a beam-column subjected to an axial force of 525 kN and a bending moment of 78 kN-m (considering 50% overstrength), the deck was reinforced with ten longitudinal No. 20 deformed rebars symmetrically located at the top and bottom layers (Fig. 5.2). Stirrups of No. 10 deformed rebars at every 150 mm were considered to resist a shear force of 120 kN for specimens without diaphragms. This reinforcement is largely in excess of what is commonly found in bridge decks, and is a consequence of the localized lateral load application on a short length of girders in the specimen. It is expected that inelastic loads could be progressively transferred from the deck to the steel girders along longer lengths of span in actual bridges.

5.3.1 TADAS Specimen

The main component in the TADAS specimen, as shown in Fig. 5.3, is the TADAS device. Following the proposed design procedure, TADAS device stiffness, K_T, and plastic strength, V_T, of 150 kN/mm and 167 kN, respectively were found to be appropriate. Using a plate thickness, t_T, of 25 mm, the plate height, h_T, of 105 mm was then obtained. A base width, b_T, of 80 was chosen considering an aspect ratio, h_T/b_T of 1.3 for the plates. Four triangular plates were finally designed for the TADAS device from the K_T or V_T expressions. Fig. 5.4 shows the detailed drawings for the designed TADAS device. Full penetration welds were used for the connection of the TADAS plates to the 20 mm rods. At the bottom, these plates were placed in snug fitting grooves in the bottom plate and fillet welded along edges (Fig. 5.5).

All other structural members and their connections were designed to remain elastic assuming a 50% overstrength for the ductile energy dissipator device, as discussed in Chapter 4. Braces consisting of 2L65x65x5 were selected to resist the resulting 165 kN resultant force. Due to space limitation, pieces of L65x65x5 were added to connect the braces to the web stiffeners (Fig. 5.6). A W150x22 beam was designed for the bottom beam based on the calculated axial force and bending moment. Web stiffeners in that beam were added and designed to prevent any web bearing or buckling failure. As shown in Fig. 5.7, top and bottom flanges were coped on one side at the ends of the bottom beams to allow their connection to the web stiffeners of the girders. Bill of material for the TADAS specimen is presented in Table 5.1.

Nonlinear push-over and time-history analyses were carried out using DRAIN-2DX to verify the effectiveness of the resulting design. As shown in Fig. 5.8, proposed design was equivalent to a reduction factor of 3.75, corresponding to a ductility ratio of 7.5. An average displacement ductility of 7.2 was obtained for time-history analyses repeated for five different earthquake records (El-Centro S00E, Parkfield N65E, Pacoima Dam S16E, Saguenay at St-Ferreol, longitudinal component, and Loma Prieta at Corralitos 37.037N 121.883W) scaled to a *PGA* of

0.6g, which confirmed the design prediction. The lateral period of the TADAS specimen was calculated to be 0.25 s.

5.3.2 EBF Specimen

Using the proposed design procedure described in Chapter 4, a W150x14 section with a link length of 300 mm (link shear yield capacity, V_l, of 124 kN, and reduced moment capacity, M_p^*, of 30 kN-m) was chosen for the link beam. This section has a shear yield strength considerably stronger than the required value of 100 kN, but it was the closest one could get using the available rolled shape sections. The existing link shear capacity, V_l, corresponds to a shear force, V_d, of 235 kN in the ductile device. Fig. 5.9 shows the EBF specimen. Details of the EBF link beam are presented in Fig. 5.10. Braces made of 2L65x65x6 were found appropriate to resist 280 kN required to remain elastic, accounting for the possible 50% overstrength of the link, as shown in Fig. 5.11.

Stiffeners in the shear link were designed to delay and control its web buckling during large inelastic deformations. As the typical values for a/t_w ratio (a being the stiffener spacing, and t_w the link web thickness) range between 25 and 30 (Malley and Popov 1983), four two-sided 138x45x8 mm web stiffeners were welded to the web and flanges of the link beam along its length (Fig. 5.10). The list of all components needed for the EBF specimen is given in Table 5.2.

Nonlinear analyses by DRAIN-2DX confirmed the design's effectiveness, as shown in Fig. 5.12. According to the proposed design approach, a ductility ratio of 5.5 was predicted with a reduction factor of 3.2. Time-history analyses of the specimen (having a 0.23 s lateral period) revealed an expected average ductility of 5.8 for the same five given earthquake records considered previously.

5.3.3 SPS Specimens

Two design alternatives were considered. For the first specimen, a W200x15 segment was chosen for the link with a shear yield level, V_l, of 166 kN. Its cross-section was welded directly to top flange of bottom beam using full penetration welds (Fig. 5.13). Following the recommendations in the previous chapter, a vertical link height of 150 mm was used. The bending moment at the onset of shear yielding, M_l, equal to 25 kN-m, was less than the moment capacity reduced to account for the plastic shear-flexure interaction, M_p^*, equal to 36 kN-m, indicating the link beam would yield in shear. As shown in Fig. 5.14, web stiffeners of 190x45x6 mm were considered at mid-height of the vertical link to prevent buckling in the shear panel web (Malley and Popov 1983; Kasai and Popov 1986).

For the second specimen, as shown in Fig. 5.15, a 175 mm long built-up section was chosen for the link and designed to be bolted to the bottom beam. Four plates of 130x45x8 mm provided the required flexural strength, with a reduced moment capacity, M_p^*, of 40 kN-m. A two-sided 148x45x6 mm stiffener was designed at mid-height of the SPS to preclude web buckling (Fig. 5.16). All welds for this specimen were full penetration welds. Eight A325M 20 mm high strength bolts were designed to connect the built-up shear panel to the bottom beam and resist combined shear force of 245 kN and bending moment of 37 kN-m (values that consider 50% overstrength of the shear panel), in addition to taking prying action into account (Fig. 5.16). Braces of 2L65x65x5 were selected to resist 165 kN of axial forces (Fig. 5.17). Similar to the TADAS specimen, a W150x22 was provided for the bottom beam. Table 5.3 presents the list of components required for the SPS specimens.

The simplified analysis procedure presented in Chapter 4 predicted that the above designs would correspond to a force reduction factor of 3.9 and thus a ductility of 8 (Fig. 5.18). Lateral period was again 0.23 s. DRAIN-2DX nonlinear inelastic analysis results, for the same five earthquake records considered for the other specimens, gave an average ductility of 7.5.

5.4 Design of Test Foundation

The foundation, pretensioned to the strong floor of the laboratory by six 1.8 m long bolts of 64 mm, provided support for the two girders of the specimens. Due to space constraints in the structures laboratory, the foundation's west end was designed to behave as a cantilever under uplifting forces from the west girder, if any (Fig. 5.19). A large rectangular shape (2.9 m x 1.7 m) with a depth of 0.45 m was considered. To keep the foundation in the elastic range, a safety factor of 2 was used in its design. Appendix B provides more details on foundation design. Two 1100x580x50 mm base plates were designed as support for vertical actuators as per details shown in Fig. 5.20. C380x50 sections sitting on the plates and spanning across the width of the foundation were designed to transfer the vertical actuator uplift forces to the foundation in addition to act as formwork. Because of the discontinuity created in the foundation at the base of actuators, the center 0.7 m-wide longitudinal strip of the foundation was designed to resist all forces imposed by the specimens. Moreover, the potential flexural contribution of side channels was conservatively ignored. Table 5.4 presents the bill of material for the reinforcing rebars.

5.5 Fabrication and Construction of Specimens

Steel components were machined and provided by a reputable steel fabricator based on detailed drawings of the designed specimens, as provided in Appendix C. These components were later assembled in structural laboratory of the University of Ottawa. The construction of the reinforced concrete foundation and specimen decks is explained below.

5.5.1 Construction of Foundation

The foundation was heavily reinforced with No. 20 and 25 rebars for the main reinforcement and No. 10 rebars for the stirrups, in addition to C380x50 sections creating a large rectangular

reinforcement frame. As shown in Fig. 5.20, holes were made in the transverse channels to allow continuity of the top and bottom longitudinal reinforcing rebars at the continuous central longitudinal strip of the foundation. The longitudinal rebars outside of that strip were welded to the transverse channels. Two 50 mm thick 350W grade steel plates, welded to the C-channels (Figs. 5.19 and 5.20), served as a base for the vertical actuators. For this purpose, four countersink type holes of 65 mm diameter and 25 mm depth were drilled to hide the bolt heads underside of the plates so that the plates could lay flat on the strong floor. Two small steel pieces were welded around each 65 mm hole to prevent rotation of actuators bolt heads during assembly of the test set-up.

The foundation was cast in wooden forms, built from 19 mm (3/4") thick standard size plywood. As shown in Fig. 5.21, the formwork end pieces were supported by four 65x65x6 angles and 3/8" threaded rods and wooden struts to prevent bulging of these pieces during construction. To protect the wood and also act as a bond breaker, a light coat of white paint was applied on one side of the formwork pieces.

Six ABS tubes with inside diameter of 76 mm (3") were carefully placed in designated locations (915 mm apart from each other in two directions) in the foundation to allow the connection of the base to the laboratory strong floor (915 mm thick) by means of six 64 mm diameter strong bolts (grade 400 MPa, 1800 mm long). Also sixteen 40 mm diameter ABS tubes were placed in the base to provide a grid for 1.5" diameter anchor bolts for future experiments. Small wooden pieces were put at the bottom of these tubes to provide a recess to accommodate bolt heads. Fig. 5.21 shows the foundation reinforcement cage and formwork. Eight 30 mm anchor bolts with appropriate hook length (Fig. 5.22) were placed in the foundation to connect the girders bottom flanges to the base. To reduce the possible slippage of the specimens, a very small clearance of 1 mm was specified for the holes in the bottom flanges of the specimens' girders. As a result, special care was needed to ensure that all anchor bolts would remain straight and at their exact location. For this purpose, rather than using templates alone to position the anchor bolts, it was decided to put one of the specimens on the foundation cage and connect it tightly

to the anchor bolts before pouring the concrete. Also using a plywood template, four 5/8" threaded rods were placed in the foundation to allow connection of lateral support beam to the main base (Fig. 5.21).

Concrete of 30 MPa specified strength with 10 mm maximum aggregate size was supplied by a local ready mix company. Two cubic metres concrete was poured and vibrated in each foundation cage. Concrete surfaces were cured for a couple of days.

5.5.2 Construction of Deck Slabs

Each slab was cast in wooden forms, built from 19 mm (3/4 in) thick standard size plywood. Again the formwork side pieces were supported by 1/4 in threaded rods to prevent bulging during construction. To support the formwork, a frame of 4"x4" wooden pieces was prepared and connected to the bottom plywood piece. A light coat of white paint was applied on one side of the formwork pieces for wood protection. As shown in Fig. 5.23, two wooden templates, each with four 5/8" bolts were carefully placed in the slab over the girders top flanges to allow connection to load applicator beam assembly.

Two end loading plates, each with two 40 mm holes for threaded rods connections, were designed for applying lateral loads. As presented in Fig. 5.24, to connect the horizontal actuator to the slab, four 40 mm holes (300 mm apart each other) were made in the larger loading plate, itself reinforced with large steel rectangular bars to prevent plate bending. Two 40 mm ABS pipes were placed longitudinally at predetermined locations (300 mm apart from each other) in each slab to allow the connection of the plates by two 1.5" threaded rods.

For each slab, 0.3 cubic metre of 30 MPa concrete with 20 mm maximum aggregate size was made in the laboratory. Concrete was carefully placed and vibrated (using a 40 mm vibrator) around the ends of slab to prevent damage to the strain gages mounted on the shear studs.

Concrete surfaces were watered and cured for a few days. Control cylinders were taken from each concrete batch. Fig. 5.25 shows the specimens after construction of their slabs.

5.6 Testing Set-up

To apply the vertical and lateral loads to the specimens, the experimental set-up schematically shown in Fig. 5.26 was designed. This test set-up was adjusted to permit application of the maximum stroke of the horizontal actuators (i.e. ±250 mm). Fig. 5.27 shows a photo of the test set-up. In the following sections, details on the components of this set-up are presented.

5.6.1 Load Applicator Assembly

For gravity loads, a load-applicator beam assembly was designed and fabricated. This assembly consisted of a steel box connected to the vertical actuators, and two 2.25 m long W410x85 segments that transfer the loads to two 0.5 m long W200x59 sections placed on the deck slabs above the flanges of the specimens' girders (Fig. 5.28). The W200x59 pieces were connected to the slab using the 8 bolts previously embedded in the concrete deck slabs. As shown in Fig. 5.28, a few web stiffeners were welded to the W-beams to preclude web buckling or bearing failure. The bill of material for all load applicator assembly components is presented in Table 5.4.

5.6.2 Reaction Frame

A reaction frame was used to support the end of the horizontal actuator used to apply lateral loads to the specimens. This frame consisted of two triangular frames (spaced 915 mm center-to-center), each bolted to 460 mm deep supporting back to back channels (Fig. 5.26) in turn connected to the laboratory strong floor by four 64 mm diameter high strength bolts. These triangular frames were connected by a vertical 50 mm thick plate acting as a support for actuator. Cyclic lateral load was applied by a servo-controlled 1000 kN capacity MTS actuator. This

actuator, and two identical vertical ones were equipped with multi-direction swivels at each end. Two 38 mm (1.5") rods running through the sleeves cast in the specimen's deck and connected to a plate on the other side were used to pull the specimen during cyclic testing.

5.6.3 Lateral Restraining Frames

Frames were placed on each side of specimen to prevent any excessive out-of-plane movement. These frames were secured to the laboratory floor using threaded rods. However, during testing they were found to be unnecessary as no such lateral movement took place.

5.6.4 Lateral Support for Ductile Device

To prevent lateral movement of the ductile device at the center of specimens bottom beam, a lateral support stub-beam was designed and connected to 4 threaded rods cast in the foundation. Web stiffeners were welded to this beam segment and three holes were made at the levels corresponding to the bottom and top flanges of bottom beams of the specimens and the top of the ductile device.

5.7 Instrumentation

5.7.1 General

All specimens were carefully instrumented for displacement and strain measurements at the points of interest. Some displacements were measured and monitored by three Temposonic Magnetostrictive Displacement Transducers, each with a stroke of 500 mm (20") and accuracy of 0.0077 mm. Also four short Linear Variable Displacement Transducers (LVDTs), each with a stroke of 50 mm (2") and accuracy of 0.0034 mm, were used to take other displacement

readings. Light frames built with slotted angles were provided to support the LVDTs where appropriate (Fig. 5.29).

Micro-Measurements strain gages of the type EP-08-250BG-120 were generally used, except that rosettes of the type CEA-06-250UR-120 were used at a few locations. M-Bond AE-10 adhesive cured at 21°C for 6 hours under 100 kN/m^2 pressure, providing a 6% elongation capability, was used at locations where large plastic strains were expected, such as webs of the panel zones, TADAS plates, and web stiffeners. M-Bond 200, a general purpose laboratory adhesive with a 3% elongation limit was used at other locations. For all gages, a smooth surface was first created using a grinder and/or proper sand papers. The steel surface was cleaned using acidic and neutral solutions. Electrical tape was finally used to directly cover the gages, except for the gages embedded in concrete which were covered by a layer of wax, a layer of window sealant, and then electrical tape to prevent the moisture penetration into the gages. All of the gages and LVDTs were tested for proper functioning prior to testing.

Three MTS actuators were used to apply the required forces to the specimens: two for gravity loads and one for lateral loads applied in a displacement-control mode. The applied loads were recorded by means of load cells integrated to the actuators. All specimens were whitewashed to help observe the yielding patterns and their progression.

5.7.2 Details of Strain and Displacement Measurements

Figs. 5.30 to 5.33 map the instrumentation used for the various specimens. A total of 19 to 26 strain gages were used in TADAS, EBF and SPS specimens (12 gages for the specimen with a channel diaphragm). Strain gages were attached to all braces to verify that they remain elastic, and to provide a check on the resultant forces transferred to the ductile device. Gages were also mounted at critical locations to permit calculation of the bending moment, shear and axial force in various members at any time during testing. Redundancy was introduced in the instrumentation scheme in case some gages fail during the test. Strain gages were also placed in

pairs to check for any out-of-plane buckling or instability. Rosettes were used where knowledge on principal strains in components subjected to shear forces was desired (Figs. 5.30 to 5.32).

Strain gages were also installed on selected shear studs in the deck of the specimen girders, to monitor their yielding. The gages were positioned as low as possible to record the maximum strains in the shear studs.

Lateral drift at the top of each specimen, was measured by two Temposonic transducers, centered and attached to the sides of specimen's slab. The magnetic rings of the transducers were connected to a light reference frame fixed to the foundation. A third Temposonic transducer was used to measure the relative displacement of TADAS plates (Fig. 5.34) and SPS device with respect to the bottom beam. A 50 mm stroke LVDT was positioned to measure lateral movement of TADAS and SPS devices, while two 50 mm stroke LVDTs were used at the two ends of the link beam for the EBF specimen, as shown in Fig. 5.32. Finally, 50 mm stroke LVDTs were placed to measure the slippage of the girders.

5.7.3 Rotation and Distortion Angles Measurements

Bottom beam midspan rotations, θ_{bb}, for TADAS and SPS specimens were measured using two 50 mm stroke LVDTs (Fig. 5.34) spaced 175 mm and 125 mm from each other, respectively.

$$\theta_{bb} = \frac{y_1 - y_2}{d_{LVDT}} \tag{5.1}$$

where d_{LVDT} is the distance between the two LVDTs, and y_1 and y_2 are the displacements in mm measured by LVDTs 1 and 2. To measure the SPS link distortion angle, a Temposonic transducer was connected to the bottom beam using slotted angles. The total link distortion angle for the SPS device, γ_{SPS}, is obtained by:

$$\gamma_{SPS} = \gamma_1 - \theta_{bb} \tag{5.2}$$

where γ_l, the link distortion angle if no rotation at the bottom end occurs, (i.e. $\theta_{bb}=0$), is given by:

$$\gamma_l = \frac{x_T}{h_l} \tag{5.3}$$

where x_T is the displacement in mm measured by the Temposonic transducer and h_l is the vertical link length, equal to 150 mm here.

To measure the EBF link distortion angle, two Temposonic LVDTs were vertically connected to a light frame. By a similar procedure, γ_l, for the EBF is determined by:

$$\gamma_l = \frac{y_{T1} - y_{T2}}{e} \tag{5.4}$$

where y_{T1} and y_{T2} are the vertical displacements from the Temposonic transducers at the ends of the link beam and e is the link length, equal to 300 mm in this case. The rotation of bottom beam at the link ends, θ_l, can be approximately obtained by:

$$\theta_l = \frac{y_{T1}}{a} \tag{5.5}$$

where a is length of bottom beam outside the link ($a=L_s/2 - e$, where L_s is the spacing between the girders, equal to 2 m here). This θ_l, although much smaller than γ_l, must be added to γ_l, to give γ_{EBF}, that is:

$$\gamma_{EBF} = \gamma_l + \theta_l \tag{5.6}$$

5.8 Loading Approach

A constant gravity load of 350 kN (175 kN per girder) was applied to the specimens deck slabs using two vertical actuators. In an actual bridge, gravity loads are transferred from concrete deck to end supports through the girder webs. This shear stress would correspond to a uniformly increasing magnitude along the web of the girders. For the specimens tested, gravity loads could not be applied in that manner. Therefore, the gravity loads applied were chosen to be equal to

half of those that would result by integrating the shear stresses along the web of the girders. This equivalent load was selected because it created the same P-Δ effects on the specimens and actual bridge.

All specimens were tested following the same protocol. Elastic cycles were applied under force control and the inelastic cycles under displacement control. The elastic cycles gave a measure of the initial elastic stiffness needed to check any stiffness degradation in the specimens in high inelastic cycles. Lateral load reversals were applied slowly to all specimens. The cyclic displacement history imposed to each specimen, as shown in Fig. 5.35, consisted of three cycles at each of displacements of $\pm 0.5\delta_y$, $\pm\delta_y$, $\pm 2\delta_y$, $\pm 3\delta_y$, $\pm 4\delta_y$, $\pm 6\delta_y$, $\pm 8\delta_y$, etc. until failure of the specimen occurred as recommended by the ATC-24 (Applied 1992). However, it was often difficult to determine δ_y, and the cyclic displacement history was adopted to consider three cycles at drifts of ±0.25%, ±0.5%, ±0.75%, ±1%, ±1.5%, ±2%, ±3%, ±4%, etc. until failure. For each cycle, excursions westward from a point of zero lateral displacement, corresponded to positive sign for forces and displacements (pushing the specimen).

5.9 Measurements Control and Monitoring

A MTS Testar Controller and a Vishay Data Acquisition System Model 5000 were used in parallel to record the data. The MTS system collected Temposonic displacements, actuators loads and actuator displacements whenever the specimens deck slabs moved laterally more than 0.1 mm. The Vishay data acquisition system recorded all strain gage and rosette data, the lateral load and all LVDTs displacements every two seconds.

During testing, the MTS Testar Controller system checked the loading rate and magnitude, and at the same time plotted the hysteretic curves corresponding to lateral load versus displacement, allowing to monitor the structural behavior of the specimen.

CHAPTER 6

OBSERVED BEHAVIOR AND EXPERIMENTAL RESULTS

6.1 General

This chapter presents observed behavior of the specimens during testing. Eight tests in total were conducted on the specimens in different situations. The test program for these experiments is presented in Table 6.1, where information is given on gravity loads, lateral support and type of testing. A gravity load of 350 kN was applied to the specimens in all experiments except for the pseudodynamic test. For each experiment, testing was conducted at slow speed to permit close monitoring of behavior. A large number of loading cycles (typically 25 to 35) were applied to each specimen for which numerous data points (from 5000 to 30000 for the various tests) were collected due to short time intervals of data recording (every two seconds) and long duration of testing (4 to 6 hours). The loading of the specimens was controlled according to the guidelines suggested by ATC-24 as much as possible (Applied 1992).

Three cycles were generally applied to the specimens at each different lateral displacement. As mentioned earlier, westward and eastward movements were considered as positive and negative, respectively, for lateral loads and drifts. To describe the location of buckling, fracture and rupture in the components, cardinal point references were marked on all specimens (e.g. NE for north-east).

The relationship between lateral force and lateral displacement at the level of the girder deck slab, relative to the foundation was plotted in real-time during the test. Control of the experiment was driven by those results. Lateral displacements at the specimens deck level were measured by two Temposonic transducers. Lateral loads were given by the load cells built into the MTS actuators.

One observation common to nearly all tests was the large cumulative amounts of slip due to the bolted connections. The exception is the second EBF experiment for which this undesirable behavior was prevented by fillet-welding all connections.

In this chapter, only behavior and data visible during actual testing are presented. Additional test results and also the interpretation and discussion of experimental results are presented in detail in the next chapter.

6.2 Preliminary Tests

To determine the physical properties of the key steel members, particularly the shear ductility of the SPS and EBF link beam webs, a series of preliminary tests were conducted on a few coupons. Although the steel fabricator was required to provide CAN/CSA G40.21-M 350W steel, it was important to accurately identify these properties. All coupons were machined to a standard size according to ASTM E8M specifications (American 1995) with a gage length of 200 mm, and marked at 25 mm intervals along the gage length. Strain gages were also attached to these coupons to confirm that the AE10 and M-Bond 200 glues would be effective at high elongations.

Each coupon was subjected to tension in a testing machine and loaded until failure occurred. The following sections present resulting details of these tension tests for different specimens.

6.2.1 Web of the W200x15 SPS Device

A 500 mm long W200x15 taken from the same stock as the first alternative of SPS device considered, was supplied. The objective was to determine the stress-strain relationship of the provided steel and to confirm its monotonic ductility capacity, as the shear panel device was to resist many high inelastic cycles during testing. For this purpose, two steel coupons were extracted from the web of the W-section. One strain gage was attached using AE10 adhesive to the surface of one of these coupons to check the glue effectiveness and also the dial gage readings.

Both coupons yielded at about 68 kN, corresponding to 370 MPa, and failed in a ductile manner with an average maximum elongation of 44 mm in 200 mm gage length, corresponding to 22% strain elongation. Stress-strain curves for these tests are presented in Fig. 6.1, where results show a visible yield plateau for this ductile steel. An ultimate strength of 91 kN (tensile stress of 460 MPa) was obtained for the coupons. As shown in Fig. 6.1a, the strain gage data correlate well with those obtained by reading of the dial gage. The AE10 adhesive worked effectively up to 5% elongation.

6.2.2 Web of the Built-up SPS Device

To conduct the same tests for the built-up SPS device, a piece of 500x100x5 mm plate taken from the same stock as the SPS device web, was supplied. Again two steel coupons were prepared from the plate specimen. A strain gage was attached to the surface of each coupon using AE10 adhesive on one coupon and M-Bond 200 adhesive on the other.

Stress-strain relationships for both coupons are shown in Fig. 6.2. Yield and ultimate strengths of 90 kN and 108 kN (corresponding to stresses of 450 MPa and 540 MPa) were observed. The failure of these coupons was somewhat brittle (a "bang" was heard), and maximum elongation of 17 mm in 200 mm gage length was observed corresponding to a 7% elongation (Fig. 6.2a). The strain gage data for both coupons showed good agreements with data from dial gages. The AE10 adhesive was effective up to a 6.5% strain elongation before the gage peeled off the surface (Fig. 6.2a), while M-Bond 200 glue worked well up to a 4% elongation (Fig. 6.2b). In view of these results, the Mill test certificate was requested for the plate material used in that built-up SPS device. Information on that certificate indicated that the material was in compliance with the specified properties of the requested steel grade. Therefore, although the coupon results showed that the supplied material was less ductile, it was decided to test the built-up SPS specimen.

6.2.3 EBF Link Beam Web

A coupon taken from the web of the W150x14 section of the EBF link beam was also tested. Stress-strain curve for this specimen shows a ductile behavior with a visible yield plateau and failure at 44 mm elongation in 200 mm gage length, equivalent to 20% strain elongation (Fig. 6.3). Failure did not occur at the middle intervals. Yield and ultimate strengths of 73 and 97.5 kN (corresponding stresses of 450 and 580 MPa), respectively, were observed.

6.2.4 Girders Web Stiffeners

To determine the properties of the material used for the web stiffeners of the bridge girders, two coupons were prepared from the web stiffener plates. Fig. 6.4 shows a ductile stress-strain relationship for both coupons of web stiffeners. At failure, strain elongation of 24% in 200 mm gage length was observed for the coupons. Web1 coupon failed outside of the middle interval (note that, different strain elongation of 15% and 34% were recorded by 50 mm dial gage for the Web1 and Web2 coupons, respectively). Average yield and tensile stresses of 400 and 570 MPa were obtained.

6.3 Experiment 1 (TADAS End-Diaphragm)

Fig. 6.5 shows the TADAS specimen during testing. This specimen was subjected to 21 cycles of lateral loading before failure occurred at 4% drift. The final lateral load-deflection curves for the specimen are shown in Fig. 6.6. Note that the hysteretic loops experienced pinching due to connection slippage even in the early stage of loading. The experiment ended after flexural failure of three TADAS plates and local buckling of the girder web stiffeners. The maximum positive lateral load applied to the specimen, V^{+}_{max}, reached 464 kN, corresponding to a maximum drift of 45 mm, while these negative values were -450 kN and -43 mm, respectively. Although all hardware was in place to rapidly provide lateral bracing to the TADAS device at any point during the test, this was not found to be necessary. A maximum lateral movement was limited by 1 mm during testing.

The laterally applied force was considered as the initial test control parameter until specimen yielding. Three cycles were first applied 90 kN corresponding to half the estimated yield capacity of 180 kN. Note that there were gaps ranging from 1 to 2 mm between the top of each TADAS plate and their reaction point. Therefore, in each half cycle, the TADAS plates slipped to the end of these unequal gaps before being engaged to contribute to the lateral load resistance. Significant slippage was recorded by the Temposonic transducer measuring the relative displacements of the TADAS plates, and the lateral load versus displacement curves exhibited some hysteretic behavior. Because of these manufacturing errors and other slip in the bolted connections, predictions of yield displacement were inaccurate and discarded. For this reason, to reach the same lateral load of 90 kN in each loading direction, positive and negative drifts of 3.6 mm and -1.4 mm were imposed, respectively. Consequently, further cycling was done with a 1.2 mm offset taken as the new center point.

Three cycles were completed at drifts of 6.1 and -3.3 mm, at lateral loads of 125 and -130 kN respectively, corresponding to about $3/4V_y$). From 100 kN and above, the load-displacement curve flattened a bit and sharp "ping" noises were heard intermittently. Inspection of the

specimen revealed no breakages or visible damage, so it was concluded that the noise was produced by slipping in the bolted connections once the forces exceeded their friction capacity. The same behavior was observed in the other direction. Lots of noise due to bolt slippage was heard during all subsequent cycles.

Strain gages readings indicated that one TADAS plate yielded at the end of the next three cycles at drifts of 12 and -8.8 mm (i.e. approximately equal to a 1% drift), corresponding to lateral loads of 210 and -230 kN, respectively. Identification of the yield threshold of the various components was not possible from the hysteretic curve plotted during the test, shown in Fig. 6.6. Same situation was noticed after completion of a cycle at 15.3 and -12.7 mm drifts (corresponding to 250 and -290 kN lateral loads).

Strain gage data showed that all TADAS plates yielded during next cycles at 20 and -18 mm (1.5% drift), corresponding to 320 and -350 kN, with the onset of yielding at a drift of 16 mm. Fine cracks were observed in the whitewash near the top of the TADAS plates. A few vertical fine cracks were also observed in concrete slab above west girder on both sides. The slight pinching noticed in the hysteretic curves (Fig. 6.6) became proportionally less significant at the larger drifts. Testing continued in displacement control to various target drift ratios.

The TADAS plates bent noticeably during the next three cycles at displacements of 25 and -23 mm (2% drift), corresponding to 370 and -380 kN loads. Slippage of the TADAS device base plate (visible in Fig. 6.7) was measured to be ±3.5 mm during these cycles. A small gap of 2 mm was noticed under the TADAS base plate on the uplifted side (Fig. 6.8). Bolted connections still made very loud noises as slippage developed. The whitewash on the surface of TADAS plates were full of cracks (Fig. 6.7). Lateral loads of 440 and -450 kN were imposed in the next three cycles at drifts of 35 and -33 mm (about 3% drift).

Finally the specimen was subjected to drifts of 45 and -43 mm (nearly 4% drift), as shown in Fig. 6.9. Slippage occurred at various locations. Large slip at the top connection of the braces

was noticed (as revealed by exposed unpainted bare steel) in addition to some rotation of the braces with respect to their original position,, as presented in Fig. 6.10. The TADAS plates slipped in their guiding grooves; the guiding assembly also rotated noticeably. However, the slippage of the stiffened girders at the base was less than 1 mm. Some local buckling was observed at the bottom of the west bearing stiffener of the west girder, as shown in Fig. 6.11. White paint on the TADAS plates flaked off, mainly at their top. At -460 kN (on the return yield excursion of 20th cycle), a big "bang" was heard and the applied lateral load dropped to 402 kN. Inspection revealed rupture of a single TADAS plate near its top (Fig. 6.12). It was decided to continue testing until the specimen reached the target drift of 4% for this cycle. Using a ruler, an out-of-straightness of 2 mm indicating onset of buckling was noticed on the east stiffener of the east girder. The west stiffener of the west girder also experienced more severe buckling at 410 kN, as shown in Fig. 6.13. Significant strength degradation was noticed during the last yield excursion (Fig. 6.6). The experiment ended when a major "bang" was heard at an applied lateral load of -350 kN, and the MTS system safety triggers shut down power after an excessive drop in the applied load to -240 kN. Inspection of the specimen revealed ruptures in two other TADAS plates, as shown in Fig. 6.14.

6.4 Experiment 2 (Stiffened Girders Only)

After dismantling all the end-diaphragm members (i.e. TADAS, braces and bottom beam), the remaining specimen with the two stiffened girders alone was tested to failure. Damaged by the previous test, the web stiffeners had cracks propagating from their holes to the free edge of the stiffeners, as shown in Fig. 6.15. Nonetheless, 25 cycles up to a maximum drift of ±96 mm (8%) were applied before the specimen experienced severe buckling and fracture of the web stiffeners at all welded connections. Maximum positive and negative lateral load reached 165 and -180 kN, respectively. Fig. 6.16 shows the lateral load versus drift hysteretic curves for this specimen.

The first three cycles were initiated to reach a top displacement of ±6 mm (0.5% drift) in both directions, by applying 60 and -65 kN, followed by three cycles at ±12 mm (1% drift). The

specimen essentially remained elastic. Note that strain hardening of the girders during the previous test may have increased the elastic range of the specimen. Yielding started during the next three cycles at displacement of ±18 mm (1.5% drift). The hysteretic curves started to exhibit stiffness softening during the next three cycles at ±24 mm (2% drift), corresponding to 154 and -160 kN (Fig. 6.16).

Three cycles at ±36 mm (3% drift), corresponding to 165 and -180 kN lateral loads, were then completed. Some strength degradation was observed as cracks at the stiffener holes expanded and widened (Fig. 6.17). When the specimen was subjected to three cycles at ±48 mm (4% drift) and ±60 mm (5% drift), it experienced severe strength degradation due to buckling of the web stiffeners at the both top and bottom ends of each girder.

During the next three cycles at ±72 mm (6% drift), a big "bang" was heard when the full penetration weld at the base of the west web stiffener broke (Fig. 6.18) and load dropped by 16 kN. Severe buckling had developed by then at the top and bottom of those web stiffeners. Finally, the specimen was subjected to three cycles at ±96 mm (8% drift as shown in Fig. 6.19). This caused fracture of all fillet welds at the top and bottom of the girder bearing stiffeners and widening of some of the cracks at the holes of the web stiffeners (Fig. 6.20).

6.5 Experiment 3 (EBF End-Diaphragm)

The 300 mm long stiffened link of the EBF end-diaphragm is shown in Fig. 6.21. This specimen was loaded up to a 3% drift. This test was stopped prior to failure of the ductile link, to permit welding of all bolted connections and re-test. Fig. 6.22 shows the hysteretic curves obtained in the 24 cycles applied to this specimen in the first phase of its testing. In this test, a great deal of slip was observed in all bolted connections. Maximum positive and negative loads of 600 kN were imposed to the specimen.

The first three cycles were applied at displacement of ±1.5 mm and slippage was noticed to have an effect on the hysteretic loops even at this low level of lateral loads (80 kN). Inspection of the specimen revealed that the nuts of the foundation anchor bolts had become loose after application of the gravity loads and they were re-tightened. The next two sets of three cycles were completed at ±3 mm drift, corresponding to 108 and -103 kN, and then at ±4.5 mm, corresponding to 135 and -130 kN. A large percentage of the applied displacements was taken up by slip at the bolted connection of braces (Fig. 6.23). The resulting larger drifts necessary to reach yielding of the ductile device prematurely induced high strains in the girder web stiffeners.

Three cycle sets were then applied at each of ±6 and ±12 mm displacements (0.5% and 1% drifts). Loud "ping" noises due to slip at the connections, as for the TADAS specimen, were intermittently heard. Strain on rosettes attached to the web of the link exceeded yield limit during the next three cycles at ±18 mm (1.5% drift), where loads reached 400 and -330 kN. Fine cracks in the whitewash of the link beam web panels were observed after yielding of the link.

Upon increases in the lateral drift, the shear link continued to deform into a parallelogram bounded by the end stiffener plates and flanges of the link beam (Fig. 6.24). During the three cycles at a drift of ±24 mm, (2%), very high strains were observed on the link web (1.2% on rosette).

Finally, three cycles were completed at ±36 mm (3% drift) causing some minor local buckling of the flange of the link beam at the east end of the link. During these cycles, the cracks and flakes in the whitewash became more severe in the link beam web, mostly in the end panels (Fig. 6.25). The hysteretic curves obtained at this point were reasonably symmetric. It was decided to stop testing and retest to failure only after welding all connections to provide an opportunity to compare the behavior of an all welded alternatives with the original mostly bolted detail. It was judged appropriate to stop the test at a drift of 3% because buckling of the girder web stiffeners started to develop at 4% drift in the previous experiment.

6.6 Experiment 4 (EBF with Welded Connections)

To eliminate the deformations due to slip at the connections and to investigate the impact of slip on hysteretic behavior, it was decided to weld all members at all connections of the EBF diaphragm. It may also be argued that it is generally a better retrofit solution to replace bolted members with new welded components. Thus, all bolted connections were fillet-welded using a standard Meg welder (COREX 706-S) with ER70 S-6 electrodes (carbon steel gas-shielded filer metal of 0.9 mm). Fig. 6.26 shows one of these welded connections.

The specimen was subjected to 22 cycles, up to a 30 mm maximum displacement (2.5% drift), at which point the link beam failed due to sudden lateral displacement of the link. As a result of this instability, brittle fracture occurred at the west end of the link flange and buckling developed at east end of the same flange. Fig. 6.27 shows the hysteretic loops for this experiment. Maximum lateral loads of 640 and -650 kN were reached. This failure might have been prevented or delayed had lateral bracing of the link beam ends been installed. Note that this was deliberately not done, and that instruments revealed no significant lateral movements of the link until the sudden buckling that developed at this 2.5% drift.

Until specimen yielding, the applied force was considered as the test control parameter. For the first three cycles, lateral loads of 150 kN were applied resulting in a 2 mm average drift. This was estimated to be equal to half of the predicted yield capacity of 300 kN. For next three cycles, a lateral load of 300 kN was imposed in both directions, producing 4.9 mm and -3.5 mm drifts. This point was considered to correspond to yielding of the specimen.

Three cycles were completed at 6.7 and -5.8 mm ($1.5\delta_y$, 0.5% drift), corresponding to 375 kN in two directions. Some whitewash cracks were observed in the web of the shear link during these cycles.

As shown in Fig. 6.28, large shear distortions of the link became progressively more visible during the next sets of cycles at $2\delta_y$ and $3\delta_y$ (1% drift). Symmetric and full hysteretic curves developed for this ductile diaphragm as no slippage occurred contrary to the previous diaphragm test.

At ±16 mm ($4\delta_y$), corresponding to 570 and -560 kN lateral loads, lateral movements up to 2 mm were observed at the west end of the shear link. Three cycles were then completed at 24 mm ($6\delta_y$ or 2% drift), corresponding to lateral loads of 640 and -650 kN. As some strength degradation was observed on hysteretic curves, the north side of the east end panel of the link developed significant visible local buckling (Fig. 6.29) causing a slight drop in shear resistance. Sideway deflection at the west end of the link increased to 2.8 mm. Subsequently, some severe flange distortion occurred as can be seen from Fig. 6.30. Also, as shown in this figure, no more white paint was left on the link web at this point. The braces of the diaphragm were also about to yield according to strain gages data (values of 1400 $\mu\epsilon$ were recorded).

The link beam suddenly twisted (Fig. 6.31) during the first excursion toward a ±32 mm drift ($8\delta_y$). This was recorded as a 12 mm lateral movement at the east end of shear link. A big "bang" was then heard as west end of the link (most visible at the top flange) fractured due to excessive lateral deformations as shown in Fig. 6.32. The top flange of the link beam also experienced severe buckling at the east end of the shear link. During the return yielding excursion, a 22 mm lateral deflection at the west end of the link was observed. Testing stopped as the specimen had suffered fatal damage.

With the exception of the final rupture, there were no loud noises nor sign of any slippage during this experiment, confirming that the sounds heard during testing of the other non-welded specimens were attributable to slippage at the connections.

6.7 Experiment 5 (Pseudodynamic Testing)

After experiment 4, all end-diaphragm members (braces and bottom beam) of the EBF specimen were flame cut at locations close to their connections to the girders. Pseudodynamic testing was conducted on the remaining specimen having only stiffened girders. Gravity loads were not imposed here.

In pseudodynamic testing, the dynamic response is simulated in a quasi-static manner by means of a step-by-step time integration method, where the inertia and damping effects of the structure are numerically prescribed and the load-deformation characteristics are directly measured while testing the specimen. Details on the concepts underlying this testing method are available in the existing literature(e.g. Mahin et al. 1989).

A mass, m_{test} of 71500 kg (a quarter of total mass for the 40 m span bridge) was considered for the specimen deck. Pseudodynamic test of elastic free vibrations at an amplitude of ±5 mm were conducted to determine the lateral stiffness of the specimen, K_{test} as 7.5 kN/mm (37.5/5). This gave a rotational frequency, ω, of 10.2 rad/s and a lateral period, T, of 0.6 s. Using a 2% damping ratio, the damping coefficient, C_{test}, was calculated to be 0.029 kN-s/mm:

$$C_{test} = 2m_{test}\,\xi\omega \qquad (6.1)$$

The above calculated lateral stiffness differed from the theoretical value of 23 kN/mm for the girders alone. Inspection of all welds of the bearing stiffeners revealed a crack on the full penetration weld of the stiffener on the lower east side of the east girder.

The first pseudodynamic test was conducted using the El-Centro acceleration record scaled to a quarter of its original intensity, i.e. to a peak ground acceleration (*PGA*) of 0.085g. Testing was stopped after 9 seconds of ground excitation. Drift and *PSa* time histories, and hysteretic curves obtained in real time during the tests are shown in Fig. 6.33. While the specimen remained

almost in elastic range as shown in Fig. 6.33c, maximum drift of -20 mm and PSa of 0.3g were observed at 2.2 s (Figs. 6.33a and 6.33b).

The first 9 s of the El-Centro earthquake scaled to *PGA* of 0.17g was then applied to the specimen. Some local bucking of the girder web stiffeners was observed as the specimen deck reached a maximum negative drift of -37 mm at 2.2 s corresponding to a *PSa* of 0.44g (Figs. 6.34a and 6.34b). As shown in Fig. 6.34c, the specimen could dissipate some hysteretic energy.

Finally the specimen was subjected to the El-Centro earthquake with the *PGA* of 0.34g. Serious damage was noticed in the girder web stiffeners during the severe inelastic cycles. Results are presented in Fig. 6.35, where maximum drift of 55 mm and *PSa* of 0.55g were observed at 2 and 2.2 s, respectively. From the El-Centro earthquake spectra with 0.34g *PGA*, at T=0.6 s and 5% damping ratio, a *PSa* of 0.8g and S_d of 75 mm were predicted. The experimental values are smaller due to changes in the period and discrepancies between the experimental hysteretic behavior and the elastic model assumed in the theoretical spectra. Hysteretic curves for this experiment are shown in Fig. 6.35c, with visible strength and stiffness degradation. In the first excursion of the 3rd inelastic cycle, web stiffeners on the west side of west girder locally buckled. The weld at the bottom end of the same stiffener fractured during the subsequent half cycle. This damage reduced the specimen stiffness in the next cycles, as the structural period elongated visibly as shown in Figs. 6.35a and 6.35b.

6.8 Experiment 6 (1st SPS End-Diaphragm)

Prior to the test, to prevent or at least reduce the slip at bolted connections, a grout of fine sand and cement was packed into all gaps remaining in the bolt holes after inserting of the bolts. This first SPS specimen (with the W200x15 shear link) was subjected to 28 cycles of lateral loading until failure occurred at a 3% drift. The resulting hysteretic curves (Fig. 6.36) exhibited less pinching compared to those from experiments 1 and 3. The test ended with fracture through the

link at large drift and after considerable hysteretic energy dissipation. The lateral loads, V_{max}, reached 500 kN corresponding to a drift of 36 mm. As done in experiment 1, hardware to laterally support the ductile device was present but not effective as the threaded rods provided to act as lateral braces were intentionally left loose; they were to be tied during testing if needed (Fig. 6.37). However, this was not necessary, given that the maximum lateral deflection of the shear panel was 1.5 mm. Although the cement and sand inserted in the bolt holes eliminated the loud noises due to slip, no significant reduction of joint slip was observed (still 8 mm).

Three cycles were first applied at a drift of ±2.8 mm corresponding to 100 kN in both directions. The load-deflection curves showed some slip at the connections. The next three cycles were completed at ±6 mm (0.5% drift) by imposing 190 and -155 kN in the positive and negative directions. After a low pitched noise was heard at 4.5 mm, the hysteretic curve showed some fluctuations in the applied load and strain in SPS rosette dropped by 100 $\mu\epsilon$. This strain reached 1250 $\mu\epsilon$ at ±6 mm lateral displacements..

The web of the vertical shear panel yielded during the next set of cycles at ±9 mm corresponding to 260 and -230 kN lateral loads. Although strains on the SPS web were large (3000 $\mu\epsilon$), hysteretic curves remained stable. Fine cracks formed in the whitewash on web of the shear panel during the next three cycles at ±12 mm (1% drift) corresponding to 320 and -300 kN lateral forces. The hysteretic load-deflection curves started to exhibit evidence of large plastification. Measured panel rotation (almost equal to shear distortion) was about 0.02, while the strains read by the rosettes on SPS web reached 8000 $\mu\epsilon$.

At large lateral drifts, the shear panel visibly deformed as a parallelogram bounded by the end plates and flanges (Fig. 6.38). During the cycles at drifts of ±18 mm (1.5% drift) and ±21 mm, maximum loads of 400 and 420 kN were imposed. Localized severe distortions started to form in the vertical shear panel.

Three cycles were then completed at ±24 mm (2% drift) by loading the specimen up to 445 kN. Slippage made more noise during these cycles in which a maximum shear panel rotation of 6.1% was measured. As shown in Fig. 6.39, the SPS flanges started to buckle visibly in the next set of cycles at ±30 mm (2.5% drift) corresponding to lateral loading of 480 kN. Hysteretic curves were still stable with no strength degradation.

Finally the specimen was subjected to three cycles at ±36 mm (3% drift) by applying a maximum of 500 kN lateral load. In the first excursion, considerable local buckling developed in the north-east flange at the bottom end of the shear panel. Almost no whitewash was left on the SPS web. With a huge "bang", the lateral load dropped (Fig. 6.36) during the third cycle due to fracture at the base of the SPS on its north-east side and severe buckling of the SPS flange at the base on the north-west side of the panel, as shown in Fig. 6.40. Loss of lateral load resistance was noticed during the reversed yield excursion due to large fracture at N-E corner of the SPS. It was decided to apply a 4th cycle at the same drift to see if strength would drop rapidly. The experiment ended as lateral load dropped rapidly as the fracture propagated through the SPS web, as shown in Fig. 6.41. In reverse loading, it became obvious that the specimen would resist no more than 200 kN, as the SPS web was totally fractured.

6.9 Experiment 7 (2nd SPS End-Diaphragm)

As would be done after an earthquake to repair a previous damaged ductile diaphragm, the fractured SPS ductile diaphragm was unbolted and replaced by a new one. For the second SPS diaphragm (built-up shear panel bolted to the bottom beam), the same approach as in Experiment 6 was adopted for the lateral support to control probable lateral deflections of the device and sand was again inserted in the bolt holes in an attempt to reduce slippage.

As for the previous experiment, this SPS specimen was subjected to 27 cycles with a maximum drift of 3% reached when subjected to a lateral load of 460 kN. Fig. 6.42 shows the final load-

deflection curves. The specimen failed due to rupture of a weld at the base on the west side of the built-up SPS and progression of that fracture through the web. Lateral deflections measured at the shear panel were small (less than 1 mm) during the test.

Since similar results as in Experiment 6 were expected (because the SPS devices were nearly identical), decision was made to follow as much as possible the exact cyclic loading history as in experiment 6. During the first three cycles at ±3 mm drift, the nuts of the anchor bolts were found to be loose maybe due to compaction of the concrete dry pack under the girders during the previous test. Testing continued after retightening of the anchor bolts.

Three cycles were completed at ±6 mm and then at ±9 mm. Strains data from the rosette on the SPS web confirmed that the shear panel was tested symmetrically. During the next three cycles at ±12 mm (1% drift), strains of 1400 $\mu\epsilon$ were recorded on the SPS web, i.e. close to the yield strain of 1750 $\mu\epsilon$, but the hysteretic curves were still straight. The built-up link web experienced yielding during the three cycles at ±15 mm. More slip was observed compared to the previous test, as this SPS was bolted to the bottom beam instead of welded.

Slip started to make some isolated noises during the next set of cycles at ±18 mm (1.5% drift) where a shear panel rotation of 0.028 rad was obtained. The hysteretic curves started to show evidence of yielding. Cracks were found in the whitewash of the SPS web (Fig. 6.43). A loud "bang" was heard during a half-cycle near -21 mm and the applied lateral load dropped to -300 from -350 kN. Inspection of the specimen revealed no visible failure and the noise was attributed to a large slip at the base of the SPS.

The SPS experienced visible shear distortion during subsequent cycles at lateral displacements of ±24 mm (2% drift) and ±30 mm (2.5% drift). Some strength degradation was noticed during the latter set of cycles where a maximum shear panel rotation of 0.06 rad was determined. Most whitewash on the SPS web was gone by then as shown in Fig. 6.44.

During the return yield excursion of the first cycle at ±36 mm (3% drift), a huge "bang" was heard accompanied by a drop of 30 kN in the lateral load (Fig. 6.42) due to fracture of the weld between the flanges on the west side of the SPS. The experiment ended in the next cycle as another loud "bang" was heard and load dropped to -275 kN (from 380) when fracture progressed through the entire SPS web (Fig. 6.45).

6.10 Experiment 8 (Channel at Mid-Height)

This last test investigated the cyclic behavior of a diaphragm detail that has been used in many steel slab-on-girder bridges. Single channels are often the only diaphragms present between girders. They are connected either at the bottom, mid-height, or top of the girders. Clearly, these channels cannot take much transverse seismic load, particularly if they are of small depth and connected near the top or bottom of the girders. To experimentally study the maximum possible impact of such a diaphragm on lateral performance, a relatively deep channel was placed at mid-height between the stub-girders (Fig. 6.46) where maximum rotation was observed in previous tests. In this way, the channel like stub-girders was subjected to double curvature.

After dismantling the bottom beam and braces of the SPS specimen, it was decided to repair the damage suffered by the girders of the specimen in the two previous tests, i.e. broken welds and cracks around the holes in web stiffeners. Using a grinder, small grooves were made to widen all cracks to provide space for good full penetration welds. The cracked and damaged weld connections of the girder web stiffeners, were then ground out and re-welded using standard SMAW (shielded metal arc welding) with E70 electrodes.

The final hysteretic curves are presented in Fig. 6.47. The specimen was subjected to 32 cycles of loading up to a maximum drift of 6%. It suffered brittle failure due to rupture of the bolts connecting the channel to the web stiffeners and severe buckling and fracture of the girder bearing stiffeners at their base. Lateral load reached a maximum of 250 kN.

The experiment started at an approximate offset of 1 mm. The first three cycles were applied at ±1.5 mm (corresponding to 2.5 and -0.5 mm drifts), followed by sets of three cycles at each of ±3, ±4.5, ±6, ±9 and ±12 mm (the last value corresponding to 1% drift). Some slippage occurred at the channel to stiffeners connections and load-delection curves were nearly linear. Three cycles were completed at 18 mm (1.5% drift), during which the welds done near the holes on the stiffener (to seal the cracks that had developed in previous tests) started to break at the east top end and west lower end locations as shown in Fig. 6.48. This had no detrimental effect in one of the cycling direction in which the cracks closed and surfaces were in bearing contact. Further cycling at ±24 mm (2% drift) was done. However, smaller loading was needed to push the specimen to a given drift compared to pulling (210 kN rather than -230 kN).

The web stiffeners at the bottom of both exterior stiffeners experienced local buckling in the next cycles at ±30 mm (2.5% drift), causing strength degradation. A big "bang" was heard as the weld at the bottom end of exterior stiffener on east girder fractured (Fig. 6.62) during the three cycles at ±36 mm (3% drift) when a large drop in lateral load (from 240 to 200 kN, Fig. 6.47) was observed. Slip at the girders base was always less than 0.5 mm.

Rupture of top bolt on the west side channel connection, accompanied by a huge "bang", suddenly occurred and strength dropped visibly while pushing the specimen to 48 mm (4% drift), as shown in Fig. 6.50. Another "bang" with a substantial drop in strength was noticed during the return yield excursion when the weld at the west exterior stiffener fractured (Fig. 6.51). The hysteretic curves exhibited severe pinching and showed poor energy dissipation during the last cycles.

Finally, two cycles were completed at ±72 mm (6% drift, Fig. 6.52). With a huge "bang", rupture of two other high strength bolts at the channel connections (top bolt at east side and bottom bolt at west side) occurred. Lateral load dropped from 220 to 190 kN. The experiment ended after another cycle which showed the specimen had no significant lateral strength left (Fig. 6.47).

CHAPTER 7

COMPARISON AND DISCUSSION OF TEST RESULTS

7.1 General

Behavior of the tested specimens is discussed in this chapter, based on a closer analysis of the recorded data. Experimentally recorded drifts and lateral loads presented in this chapter consist of deflection and force components that can be either directly obtained or calculated from measured data. Results are discussed in the form of moment-curvature and shear-distortion relationships for the ductile devices. The hysteretic relationship and magnitude efforts in each experimental component help understand the behavior of the specimens.

The inelastic cyclic behavior of the proposed ductile seismic devices is very significant for the specimens with end-diaphragms. As a result, it is crucial to calculate and plot the shear force versus distortion for each seismic energy dissipating device. For this purpose, two methods are

used to find the shear force in the TADAS plates and shear panel, V_d, which is a fraction of the lateral load, V, applied to the specimens. The first method, the more reliable, considers the resulting component of axial forces in the braces. Four strain gages attached to the braces in each diaphragm measure strain variations during the tests. Strain gage data in each brace can be simply converted into stress and axial force, as the braces remained elastic during testing:

$$V_d = EA_b \cos\theta_b \sum_{i=1}^{2} (\epsilon_{i,east} - \epsilon_{i,west}) \tag{7.1}$$

where E is the modulus of elasticity, A_b and θ_b are the cross-sectional area and angle of braces with respect to the horizontal, respectively, and $\epsilon_{i,east}$ and $\epsilon_{i,west}$ are strains in the *ith* brace located in the east and west side of the specimen, respectively. To find the shear force in the shear link of the EBF specimen, an additional calculation is required:

$$V_{l,EBF} = V_d \frac{H}{L_s} \tag{7.2}$$

where H and L_s are the height and spacing of girders for EBF specimen.

The second method consists of summing the axial forces measured by strain gages in the bottom beam on both sides of the ductile device:

$$V_d = EA_{bb} \left(\epsilon_{bb,east} + \epsilon_{bb,west} \right) \tag{7.3}$$

where A_{bb} , $\epsilon_{bb,east}$ and $\epsilon_{bb,west}$ are respectively the cross-sectional area of the bottom beam and strains recorded in the bottom beam on the east and west side of the ductile device.

To investigate yielding and high plastic strains in key specimen members, strains are also plotted. Strain data for gages of strain rosettes are also converted into principal strains.

7.2 Comparison of Experimental Results with Designed Capacities

The predicted capacities and yield displacements for the specimens were presented in Chapter 5, while results from experimental work were presented in Chapter 6.

Table 7.1 compares the predicted capacities and corresponding displacements with experimental results for all specimens having ductile diaphragms. For a better comparison, the predicted trilinear load-drift curves for those specimens are plotted together with an envelope of their hysteretic curves obtained from testing, in Figs. 7.1 to 7.3. Reasons for differences in the elastic and inelastic ranges are discussed below.

7.2.1 Elastic Behavior and Yield Limit

During some experiments (mainly for the specimens with diaphragm), the elastic response observed differed considerably from that predicted. This was mainly due to the significant amount of slippage that developed at the connections and the overstrength of some steel members supplied for the specimens. As a result, much larger yield displacements, smaller elastic stiffnesses and slightly larger strength than expected were observed in the experimentally obtained hysteretic curves except for the welded EBF specimen for which slip was prevented.

Note that for the specimens without diaphragm, yielding also occurred at displacements slightly larger than expected, due to the slippage at the girders' base and the cracks next to the holes in the web stiffeners from earlier testing with diaphragm. Experimental results, however, showed a negligible rotation at bottom end of the stub-girders confirming the full fixity assumption at the bottom flange of stiffened girders for all specimens.

7.2.2 Slippage of the Connections

Slip at the bolted connections was frequently observed during experiments 1, 3, 6, and 7, i.e. in all tests when bolted connections were used. This slip occurred at the brace-to-girder stiffener connections, bottom beam-to-girder stiffener connections and at the connections of the ductile device to the braces and bottom beam. Table 7.1 presents these estimates of different slips at the connection of the braces, and measured slips at the device base and girders's base. Estimates of range from 1.5 mm to 16 mm. As a result of the slips, instead of yielding at 3.5 mm and 4 mm, the strain gages on TADAS and EBF1 specimens did not show evidence of yielding until much greater lateral displacements, on the order of 16 mm and 20 mm, respectively. Consequently, approximately 12.5 mm and 16 mm slips developed during experiments 1 and 3 prior to yield.

It is noteworthy that for the TADAS device, a gap of 2 mm, observed due to movement of the TADAS top bars in their grooves, added to other slips. Even though design and fabrication drawings requested a for snug fitting at that location, the fabrication shop failed to build the device with the specified groove width. This explains why the TADAS device experienced the largest slippage. Also, note that a visible yield plateau did not occur (Fig. 6.6) due to unequal gaps in the grooves. In other words, the TADAS steel plates yielded one after another instead of simultaneously.

Stub-girders also slipped at their base as shown in Figs. 7.4 to 7.6, although in most cases the slippage was smaller than 1 mm, because a very small clearance was requested for the holes in girders bottom flanges.

7.2.3 Material Overstrength

Overstrength of the provided steel was one factor contributing to the overstrength in the hysteretic curves. The material supplied by the steel company was mostly stronger than what was requested. As presented in Figs. 6.1 to 6.4, the yield and ultimate capacities of steel coupons

tested ranged from 370 to 430 MPa and from 460 to 600 MPa, respectively, compared to 350 MPa used as the design yield strength. This is an overstrength of up to about 22%. For example, a yield strength of 220 kN was predicted for the SPS specimens, while the first and second SPS specimens yielded at about 295 kN and 290 kN, respectively, showing an overstrength of about 30% for yield limit. Note that part of the observed difference can be attributed to the slippage of the specimens because the stiffened girders took more lateral loads at the larger drifts required to yield the ductile device, as explained in the previous section.

7.2.4 Post-yield Behavior

The behavior of the TADAS device and shear links (EBF or SPS) in the post-yield range is of particular importance in seismic retrofit design. In all experiments dealing with ductile diaphragms, considerable increase in lateral load due to strain-hardening as shown in Figs. 7.1 to 7.3, occurred before the development of severe buckling and/or fracture of the device (the hysteretic curves are shown in Figs. 6.6, 6.22, 6.27, 6.36, and 6.42). In fact, due to high normal and shear strains at the base (or ends) of the TADAS plates and shear links, strain-hardening occurred at a great rate after yielding, resulting in strength increase without significant loss of the global stiffness of the ductile devices.

Experimental results confirmed that the TADAS plates and link beams yielded in flexure and shear, respectively. For the TADAS specimen, a uniform curvature should have developed along the height of the triangular plates due to flexure, as explained in Chapter 4. However, curvatures were observed to be larger at the top of these plates, and failure ultimately occurred there (Fig. 6.14). In hindsight, rather stocky TADAS plates were used, with a low h_T/b_T ratios. As a result, the interaction between flexure and shear forces became non-negligible, particularly at the top (close to the rods) where the cross-sectional area is smaller. Therefore, until the interaction of shear forces and flexural moment in squat TADAS devices is fully understood, it is recommended to use a larger number of thinner triangular plates in the design of TADAS systems.

In EBF and SPS, most of the inelastic deflections are due to inelastic shear strains in the link web, i.e. a shear hinge forms in the parallelogram bounded by the flanges and stiffeners or end plates. In these cases, the link shear stiffness decreases due to progressive link web yielding. However, the second SPS specimen reached a relatively low ultimate strength due to the fracture of the full penetration fillet weld at the connection of the flanges of the built-up SPS device to its base plate. This weld was in a region of high triaxial stresses, being pulled by the flanges of the SPS and located at the apex of a plastic bent in the base plate as a result of its uplift.

7.3 Hysteretic Response of the Specimens

Tests show that the lateral load versus drift hysteretic curves for all bolted specimens are pinched due to slippage at the bolted connections upon load reversals. Nonetheless, these hysteretic curves demonstrate a ductile behavior for all specimens retrofitted with ductile diaphragms, in spite of this slippage. The hysteretic behavior of the specimens depending on their diaphragm conditions is discussed below.

7.3.1 Specimens with Ductile Diaphragms

7.3.1.1 Moment-Curvature Relationship

Moment-curvature relationships are plotted at the critical locations for all ductile devices and their bottom beams. Bending moment is obtained using the force resisted by the device, V_d, that in turn is found from strain data of gages attached to the braces. To determine curvature in each case, the strain recorded in strain gages at the extreme fiber of the critical section is divided by half the section depth.

Fig. 7.7 shows the moment-curvature curves at the base of the TADAS device that resists a maximum moment of 27 kN-m. Onset of yielding is at a curvature of 0.15 rad/m corresponding

to 18 kN-m bending moment according to strain gages on the ductile device. A maximum curvature of 1.2 rad/m is achieved leading to a curvature ductility of 8 for the TADAS device.

Moment-curvature curves at the shear link ends in the EBF1 and EBF2 specimens are plotted in Figs. 7.8 and 7.9. Yield curvature of 0.02 and 0.025 rad/m corresponding to moments of 26 and 28 kN-m are obtained from strain gage data. The maximum bending moment, M_{max}, is 43 kN-m, compared to M^*_p of 37 kN-m. Figs. 7.8 and 7.9 confirm that the link of the EBFs had started to yield in flexure in addition to shear yielding during the last high inelastic cycles. Also as shown in Figs. 7.8 and 7.9, curvature ductilities of approximately 6 and 8.5 are obtained at the shear link end for the EBF1 and EBF2, respectively.

For the bottom of the vertical link in the SPS1 and SPS2 specimens, moment-curvature results are shown in Figs. 7.10 and 7.11, respectively. Inspection of strain gages indicates that the onset of yielding is at curvatures of about 0.025 rad/m corresponding to a moment of 35 kN-m at the link base. Both devices reached an average maximum curvature of 0.25 rad/m, reflecting a curvature ductility of about 8 excluding the slip of 0.04 rad/m. The maximum bending moment of 46 kN-m exceeded the predicted reduced moment capacity, M^*_p, of 36 kN-m (Figs. 7.10 and 7.11).

Moment-curvature curves for the bottom beams of the TADAS, SPS1 and SPS2 are also plotted in Figs. 7.12, 7.13a and 7.13b, to investigate their behavior in flexure. These members remained mostly elastic as expected.

7.3.1.2 Shear Force-Rotation Relationship

Shear-distortion curves are plotted for all ductile devices, to investigate their inelastic behavior. Again shear forces are determined using the strain data from the gages on the braces. The device total distortion angle is obtained from deflection data obtained from Temposonic transducers used to measure the relative displacement in the devices.

Shear-distortion curves for the TADAS device are shown in Fig. 7.14. Pinching due to slippage of the bolted TADAS base is observed. Total slippage is about 3.5 mm at a distortion angle of 0.033 rad. Yield and ultimate shear strength are 170 kN and 255 kN, respectively, indicating a 50% overstrength in the post-yield range. From strain gage data, a lateral load of 280 kN was applied to the TADAS specimen to reach device yielding, reflecting a share of 110 kN for the stiffened girders in this case. Yield and maximum distortion angles are 0.075 rad and 0.29 rad, respectively, giving a ductility of 6 (after deducting slip). The experimental results are in agreement with the distortion ductility capacity of at least 0.25 rad, reported by Tsai et al. (1993).

Figs. 7.15 and 7.16 present the shear-distortion curves for the EBF1 and EBF2 devices, respectively. A distortion angle of 0.007 rad due to slippage can be seen in Fig. 7.15 for the EBF1 specimen. Yield and ultimate shear strength of 250 kN and 430 kN for the EBF1 device, and 260 kN and 490 kN for the EBF2 device, are obtained, respectively. Yield and maximum distortion angles of 0.007 rad and 0.055 rad for the EBF1 specimen, and 0.008 rad and 0.11 rad for the EBF2 specimen, respectively, give link rotational ductilities of 8 and 14.

The SPS1 and SPS2 devices yield at link rotations of 0.009 rad and 0.008 rad (after deducting 0.003 and 0.022 rad, respectively from the measured values to take slippage) corresponding to shear forces of 185 kN and 180 kN, These devices ultimately resisted about 300 kN. Maximum link distortion for both SPS1 and SPS2 specimens is 0.12 rad leading to link rotational ductilities of 13 to 15, respectively, as shown in Figs. 7.17 and 7.18.

7.3.2 Specimens without Diaphragm

Experimental results reveal that specimens without diaphragm can resist several cycles of lateral loading, albeit with lesser extent. However, these systems generally have less strength and dissipate less hysteretic energy. They are more flexible and fail due to severe buckling of web stiffeners and/or rupture of welds at the stiffer connections, as described in Chapter 6.

The specimen in experiment 2, resisted a maximum of 180 kN lateral loading at a drift about 40 mm, greater than what was expected. This specimen also yielded at a drift, larger than the 7.5 mm predicted for stiffened girders in Chapter 5, due to lower lateral stiffness of these stiffened girders having cracks near the holes on their web stiffeners.

The pseudodynamic testing of the second specimen without diaphragm demonstrated the vulnerability of such systems to earthquakes. Fig. 7.19 compares the hysteretic curves for the specimen subjected to the El Centro earthquake scaled to *PGAs* of 0.085g, 0.17g and 0.34g. That specimen failed due to the web stiffener buckling and weld rupture at drifts of 40 to 50 mm (corresponding to a 220 kN lateral load) when subjected to the actual El Centro earthquake (i.e. 0.34g). The re-welding of the stiffeners prior to testing increased the strength of this specimen compared to the previous specimen without diaphragm which already had a few cracks before testing.

7.3.3 Specimen with Channel Diaphragm

As presented in Chapter 6 (Fig. 6.47), the nominal diaphragm provided for the last specimen slightly improved the seismic performance, as this specimen resisted lateral loads (about 80 kN stronger than the specimen in experiment 2). However, the deep channel subjected to flexure in double curvature did not enhance ductility much, and suffered brittle bolt failure. As shown in Fig. 6.47, the specimen failed at smaller drifts (40 to 50 mm), compared to the specimens without diaphragm, due to rupture of the bolts connecting the channel to the web stiffeners. As two double curvature flexures formed along the height of each stiffened stub-girder, yielding and rupture of the web stiffeners occurred at smaller drifts (about 50% less).

To better investigate the impact of such nominal diaphragms on seismic performance, its moment-curvature relationship is plotted using data from strain gages attached to the top and bottom flanges of the channel at a distance of d_{ch} from each end. Since the strong channel (with a M_y of

240 kN-m) remained elastic during testing, the moment in the channel at the location of the gages, $M_{ch,g}$ is obtained by:

$$M_{ch,g} = \frac{2E\, I_{ch}}{d_{ch}}\, \epsilon_{ch} \tag{7.4}$$

where I_{ch}, d_{ch} and ϵ_{ch} are respectively the larger moment of inertia and depth of the channel, and the average strain data from the gages attached to the top and bottom flanges of the channel. These moments must be increased by 60% to find by extrapolation the bending moments at the channel ends. Fig. 7.20 shows the west and east end bending moments of the channel versus drift imposed to the specimen. The moment drops in this figure correspond to bolt ruptures.

The lateral load corresponding to the moments resisted by this channel, V_{ch}, during the test can be obtained by:

$$V_{ch} = \frac{M_{ch,W} + M_{ch,E}}{H} \tag{7.5}$$

where $M_{ch,W}$ and $M_{ch,E}$ are the bending moments at the channel west and east ends (as per Eq. 7.4) and H is the height of girders. The resulting lateral load resisted by the channel, versus drift curves are shown in Fig. 7.21a, where a peak value of 80 kN at about 40 mm drift was taken by the channel. This corresponds to 32% of the total lateral load applied to this specimen. Also, four major drops in strength can be seen in Fig. 7.21a each corresponding to a bolt failure.

7.3.4 Energy Dissipation

The energy dissipation of the specimens under lateral load reversals, was calculated for every displacement cycle up to failure. This cumulative hysteretic energy dissipation provides a relative measure of the performance of the various specimens. Tables 7.2 to 7.5 present the resulting dissipated energy values for all specimens subjected to lateral load reversals. Hysteretic energy in each cycle, E_H, was determined by measuring the area under the curves for that specific cycle.

As can be seen in Tables 7.2 to 7.5, the specimens without diaphragms dissipated smaller energies reflecting their relative ineffectiveness compared to those with ductile diaphragms. The welded EBF specimen dissipated a cumulative hysteretic energy more than others even ignoring the fact that it dissipated some energy in the Experiment 3. To provide a better comparison of the hysteretic energies dissipated by the various specimens, these energies per cycle, E_H, are plotted at given drifts, as shown in Fig. 7.22. This EBF specimen also dissipated a larger hysteretic energy per cycle up to its failure at about 3% drift, while the TADAS specimen dissipated more hysteretic energy per cycle at about 4% drift near its failure (Fig 7.22).

Also as expected, the nominal channel diaphragm did not significantly improve the seismic performance of the specimen, as shown by the almost identical hysteretic energy per cycle as for the specimen in experiment 2 for drifts up to 3% (i.e. 36 mm). Only at very large drift did a difference become noticeable (Fig. 7.22).

7.4 Results from Other Strain Gages

The results from strain gages on the TADAS plates, link beams and braces were used in previous sections to discuss the moment-curvature and shear-rotation relationships for these devices. Discussion on the experimental results of some selected other strain gages is presented in this section.

7.4.1 Shear Strains Measured by Rosettes

Strains from the rosettes indicated yielding and high post-yield shear strains in the regions subjected to shear forces. Shearing strains are more difficult to measure directly than normal strains and are often determined by measuring normal strains in two or three different directions. Using Mohr's circle for the strains, as shown in Fig. 7.23a, the normal strain in a direction having

an angle of θ with x axis, ϵ_θ, can be computed from the normal and shear strains in two perpendicular axes by using the following expression (Riley and Zachary 1989):

$$\epsilon_\theta = \frac{\epsilon_x + \epsilon_y}{2} + \frac{\epsilon_x - \epsilon_y}{2} \cos 2\theta + \frac{\gamma_{xy}}{2} \sin 2\theta \tag{7.6}$$

where ϵ_x, ϵ_y and γ_{xy} are the normal and shear strains in a coordinate system. Since for instrumentation of the specimens, strain rosettes with 45° between the gages were used (Fig. 7.23b), ϵ_x and ϵ_y are directly given by two gages of the rosette, and Eq. 7.6 can be arranged for γ_{xy}:

$$\gamma_{xy} = 2\left(\epsilon_{45} - \frac{\epsilon_x + \epsilon_y}{2}\right) \tag{7.7}$$

where ϵ_x, ϵ_y and ϵ_{45} are the strain data obtained from the three gages of rosette, as shown in Fig. 7.23b. Then the principal normal strains can be obtained by:

$$\epsilon_{max} = \frac{\epsilon_x + \epsilon_y}{2} + \sqrt{\left(\frac{\epsilon_x - \epsilon_y}{2}\right)^2 + \frac{\gamma_{xy}^2}{4}} \tag{7.8}$$

$$\epsilon_{min} = \frac{\epsilon_x + \epsilon_y}{2} - \sqrt{\left(\frac{\epsilon_x - \epsilon_y}{2}\right)^2 + \frac{\gamma_{xy}^2}{4}} \tag{7.9}$$

Finally, the maximum in-plane shearing strain, γ_{max}, is obtained by:

$$\gamma_{max} = \epsilon_{max} - \epsilon_{min} \tag{7.10}$$

Note that since the shear strains in the shear links in the EBF and SPS specimens exceed their elastic limit, the principal stresses cannot be determined from this data as the elasticity stress-strain transformations become invalid in the plastic range.

Figs. 7.24 to 7.27 show the lateral load versus the maximum principal strain and maximum shearing strain for the link beams of the EBF1, EBF2, SPS1 and SPS2 specimens, respectively.

Note that in most cases, the strain rosette could not reliably work after γ_{max} of 3% to 4%, due to failure of the gage adhesives. Otherwise, shear strain results identical to those in Figs. 7.15 to 7.18 for the shear distortion angles of the link beams could have been obtained.

Similar procedure was followed to find the maximum shearing strain in bottom beam of the specimens. Figs. 7.28 and 7.29 present the corresponding results for the TADAS and SPS specimens. As mostly shown in Fig. 7.29, yielding developed in a portion of the bottom beam below the SPS device. This portion of the bottom beam behaved as a shear panel, and calculations after the test revealed that its shear strength was exceeded. This possibility of shear yielding in the bottom beam had been overlooked during its design.

7.4.2 Strain in Braces

Results from strain gages on braces revealed that these members, as expected, remained elastic during testing. A peak strain of 0.13% (1300 μ) was observed during testing of the EBF2 (welded) specimen. As mentioned earlier, strain values of the braces were used to find the lateral load resisted by the ductile devices. Figs. 7.30 shows the strain results for a single angle of a brace in the EBF1 specimen. The short angles added at the connection of the braces to the girders' web stiffeners typically resisted less than 30% of the axial load in these braces, as shown in Fig. 7.30a (compared to Fig. 7.30b).

7.4.3 Strain in Web Stiffeners

Girder web stiffeners experienced yielding even in the first stages of testing for the specimens with bolted connections, due to the large slippage described earlier. Fig. 7.31 shows typical results for strain gages on web stiffeners. In critical cases, this strain on the girder web stiffener reached a maximum of 4%. As shown in Fig. 7.31 for the TADAS specimen, web stiffener started to yield at a lateral load of about 200 kN, indicating that the TADAS device at this load level resisted only small percentage of the lateral loads due to the large amount of slippage in the

bolted connections. However, note in the same figure that the post-yield slope of the hysteretic curve is high demonstrating that the TADAS device can play a major role in lateral resistance once the slip displacements are overcome.

7.4.4 Strain in Shear Studs

Shear studs were only in tension during testing. Compression due to bending moment at the girder-to-slab connection was apparently resisted by the concrete alone. Fig. 7.32 shows strain variations for a shear stud in the TADAS specimen. A maximum strain of 0.2% was observed at the bottom of shear studs. Unfortunately, most strain gages attached to shear studs suffered damage early during the tests.

7.5 Sideway Deflection (Sway) of the Device

Researchers (e.g. Tsai et al. 1993, Kasai and Popov 1986) recommended that ductile devices and the compression flange of their supporting beam be restrained against out-of-plane deflection to prevent lateral torsional buckling of the yielding devices or their bottom beam. As mentioned earlier, a lateral support system was designed but not used in those tests.

However, lateral deflections were recorded in most cases. Fig. 7.33 typically shows that only small sideway movements for the ductile devices in the specimens were recorded. In other words, all specimens without lateral support could resist their capacity as expected and dissipate a lot of energy. Although a large lateral deflection of 12 mm was observed during the test of the EBF2 when the specimen buckled sideway suddenly, this instability developed only after severe link distortions in excess of those expected during earthquakes. Nonetheless, lateral support generally improve the performance of ductile end-diaphragms and is recommended particularly for bridges with larger girder spacings.

CHAPTER 8

LONG-TERM PERFORMANCE OF DUCTILE END-DIAPHRAGMS — SEVERE CORROSION EFFECTS ON DUCTILITY OF EXISTING STEEL BRIDGES

8.1 Preliminary Information on Corrosion

Corrosion is the major cause of deterioration of steel bridges. The results of this deterioration generally range from progressive weakening of a steel bridge structure over a long time to rapid bridge failure. In answer to the growing concerns in North America on the deterioration of existing bridge infrastructures, much of it due to corrosion, this topic has received considerable attention in recent years. Significant developments have occurred to better understand the causes of corrosion, enhance the corrosion-resistance of new steel bridges, and provide structural evaluation methods to assess the safe strength of existing corroded bridges. Indeed, bridge codes now specifically require that corrosion protection in steel bridges be provided by means of either

suitable alloying elements in the steel, protective coatings, provision of extra thickness as a corrosion allowance, or other approved means, and that the type and degree of corrosion protection to be provided be indicated on the structural drawings (American 1994, Ontario 1991).

The causes and chemical process of corrosion in bridges have been described at length elsewhere (e.g. Komp 1987; Kayser et al. 1987; Kulicki et al. 1990). The corrosion process of steel is a chemical change of iron to iron oxide consequently to current flow. In other words, it is an electrochemical process similar to the situation that occurs in a battery, where oxygen and an electrolyte are needed. For the corrosion conditions mostly observed in bridge members, the electrolyte is a solution of salts or other chemical compounds in water. Ions, electrically charged particles formed by the division of salts in water, cannot carry current under dry conditions, so the presence of water is crucial for the corrosion process to occur. An aggressive environment and inadequate maintenance generally cause this corrosion (Fisher et al. 1991). Fig. 8.1 schematically illustrate the corrosion process. The consequence of corrosion is a reduction in member cross-sectional area and, in turn, strength; a reduction in the carrying capacity and structural safety.

The corrosion pattern that most commonly develop in steel bridges is the corrosion of the webs at the ends of the girder, and the corrosion of the bottom portion of the girder, along the entire length. Fig. 8.2 illustrates the typical locations where corrosion is likely to occur. Figs. 8.3 and 8.4 show examples of different kinds of corrosion penetration in a few components and connections of a steel bridge.

Previous researchers have identified at least six forms of corrosion that influence the performance of structural steels used for the construction of bridges: uniform corrosion, galvanic corrosion, crevice corrosion, pitting corrosion, stress corrosion, and corrosion fatigue (Kayser et al. 1987). Of these, uniform corrosion, with metal oxidation taking place uniformly over the entire exposed surface, is the most common and accounts for the greatest destruction of metal on a tonnage basis. Simple theories also exist to describe the mechanisms of uniform corrosion and the rate

of expected corrosion in various environments (e.g. Komp 1987). However, no theory could be found in the existing structural engineering literature commenting on the impact of corrosion on the fundamental cyclic ductility of structural steel.

8.2 Corrosion and Ductility — State-of-Knowledge

Although there is no published information on the seismic performance of severely corroded members, practicing engineers have apparently not questioned whether rusted members can still exhibit the cyclic ductile behavior and hysteretic energy dissipation capacity commonly relied upon for seismic resistance.

Some evidence seems to justify this position. First, on a material level (i.e. beyond effects resulting from the changes in cross-sectional area), metallurgical engineers involved in corrosion-related research indicate that the mechanical properties of structural steel would not be affected by corrosion damage unless: (i) the microstructure of the steel of interest is modified by the corrosion process, or; (ii) hydrogen embrittlement is introduced as a result of the electrochemical corrosion reactions. In that regard, there is no reasonable ground to believe that the crystalline structure of steel would change significantly during ordinary atmospheric corrosion, and the possibility of hydrogen embrittlement under these conditions is also considered to be very remote, except in some applications of pickling (an electrochemical process used to remove corrosion products from metal surface), electroplating, or cathodic protection, with the risk of embrittlement increasing as the strength of the steel increases (Prof. M. Tullmin, Metallurgical Engineering Department, Queen's University, personal communications).

Second, experimental studies on the behavior of corroded members, although few, indicate that the monotonic structural ductility of steel is not detrimentally affected by corrosion. For example, Fisher et al. (1991) conducted ultimate strength tests on two severely corroded bridge hangers having approximately 40% area loss and taken from an actual bridge. They found that the

hangers could resist maximum axial loads corresponding to the tensile strength calculated using the effective net area of the most rusted region of the member, while exhibiting no considerable reduction in the monotonic structural ductility of the specimens.

In that perspective, analytical structural engineering evaluation techniques reported in the literature mostly consider the impact of corrosion due to loss of material and consequent reduction of section properties (e.g. Kayser and Nowak 1989; Kulicki et al. 1991). It is recognized that the presence of severe corrosion can typically result in increased stress levels for a given load, or in larger stress ranges under cyclic loading, as well as some notable shifts in the type of ultimate failure expected as some geometric properties and failure modes are related to the square or cube of member dimensions (Kayser et al. 1987; Kayser and Nowak 1987, 1989). Some analytical studies of this effect are available in the literature. For example, Kayser et al. (1987) evaluated the effect of corrosion on two simply supported composite bridges of 18.3 m (60 ft) and 30.5 m (100 ft) spans by modeling their capacity on the basis of member strength. Using reduced component thicknesses, they calculated yield and ultimate moment capacities for various levels of corrosion, and developed relationships to express loss in moment capacity as a function of cross-sectional and thickness loss. They also reported that, due to the resulting changes in width-to-thickness ratios of flange and web, corrosion would eventually shift the failure mode of the girders from plastic flexure to elastic lateral torsional buckling. Longer span bridges were observed to perform slightly better because of their larger initial girder thicknesses. Following a similar logic, Kayser and Nowak (1989) used plate theory to develop a corrosion damage model for steel girder bridges accounting for the bearing capacity of unstiffened webs and the risk of web buckling. Conclusions similar to those of Kayser et al. (1987) were found, in the perspective of web buckling. Steel bridges constructed with web bearing stiffeners were also found to be more tolerant to poor maintenance leading to severe corrosion.

In the above studies, procedures and perceptions, the impact of severe corrosion on the cyclic ductile behavior and hysteretic energy dissipation of steel members, while not directly addressed,

is inferred to be of no worse consequences than observed for monotonic static loadings. There exists, however, some compelling reasons to undertake an experimental verification of this claim.

First, at a conceptual level, one may envision that the surface of a severely corroded structural member may have sharp irregularities that can act as crack initiators and precipitate crack propagation and failure. This has never been investigated in the seismic perspective of cyclic ductility and hysteretic energy, but this concern has received some attention by researchers concerned with high-cycle fatigue resistance. While past studies have shown that this is not a major concern in most cases, notably with weathering steel for example, it remains that a limited number of fatigue-related experiments on severely corroded members (Kulicki et al. 1990, Fisher et al. 1990, 1991) indicate that, as a result of stress concentrations introduced by rust and rust-related notches, corroded base metal and details in steel bridge components could have a lower fatigue life than unrusted steel of equivalent remaining cross-sectional area. This reduction can be important, with reported fatigue performance as low as AASHTO Fatigue Category E in the combined presence of severe corrosion notches and thickness losses in excess of 50%. For pitting corrosion, Albrecht and Simon (1981) proposed a relationship to relate pit depth to a fatigue notch factor and an equivalent corresponding fatigue category detail. The extent of this potential detrimental effects of severe corrosion on fatigue life, however, is apparently difficult to quantify and a controversial topic (Kulicki et al. 1990). Also, while being a related topic, it remains that research findings on the high-cycle fatigue issue cannot be directly extrapolated to the seismic problem.

Second, research was conducted in previous chapters to seismically retrofit steel bridges using steel-based passive energy dissipation systems. Some of these systems include special devices that can be subjected to very large local ductilities during earthquakes. These key structural members located along the critical seismic-resistance load path of those steel bridge might be severely corroded if exposed for years to aggressive corrosion environment. Questions arise as to whether they can perform as intended even if rusted by the time a major earthquake strikes (in

a distant future), and whether rust would affect their ability to survive repeated earthquakes (i.e. must they be replaced following a major earthquake).

Finally, on a pragmatic level, given the absence of experimental data on the impact of severe corrosion on the hysteretic energy dissipation capacity of steel and the potential impact this may have on the seismic resistance of steel structures, a limited testing effort would be sufficient to expediently provide, if only in a preliminary way, an answer to the problem at hand.

This chapter reports the findings from one such experimental research of limited scope, to establish whether the hysteretic energy dissipation capacity of severely corroded steel is truly comparable to that of non-corroded members. For that purpose, a small number of specimens having up to a 60% loss of cross-sectional area due to corrosion were taken from a rusted existing steel bridge recently decommissioned, and tested. Results from non-cyclic monotonic tests are first reported, to demonstrate that the corroded steel tested is indeed found to be fully ductile when tested using traditional monotonic tension tests. This is followed by results from flexural bending tests on two different types of specimens, to various level of ductility intensities. Contrary to what some engineers have alleged and expected (as explained above, and heard through various personal communications), and in spite of satisfactory ductile behavior under monotonic loading, it is found that severely corroded steel exhibits a reduced resistance to alternating plasticity (also known as low cycle fatigue). Results are presented in terms of strength, ductility, cyclic ductility, and cumulative hysteretic energy, in the perspective of seismic resistance. Some observations are also made on the difficulty in generating satisfactory analytical models to replicate the observed behaviors.

Note that other serious structural effects of corrosion on structural behavior, such as freezing of bearings (that can translate into large forces in piers, abutments, and other members), freezing of pinned joints (that may create unintended bending moments in members), and the build up of corrosion products (causing local forces and distortions transverse to the normal load carrying direction, and that have led to failures in some major bridges (Kulicki et al. 1990)), among many

other detrimental effects caused by nonuniform patterns of corrosion on bridge members, are beyond the scope of this study. However, the engineer should keep those items in mind when evaluating the seismic (or general) structural performance of an existing steel bridge. Also note that, in spite of the emphasis on bridges here, the findings reported herein are broadly applicable to similarly corroded members located in any type of structure if subjected to the same load and deformation conditions.

8.3 Non-Cyclic Material Ductility

Even though the available literature reported above suggests that a ductile non-cyclic behavior is somewhat anticipated, the material under consideration here was first tested under monotonically increasing static load to establish its non-cyclic ductility, for better comparison with the cyclic tests results presented in a subsequent section. The rusted steel specimens available for this study were obtained from a bridge constructed in Ontario in the 1950s (demolished and replaced in 1991). The original structural drawings called for medium steel, likely a CAN/CSA G40.4 structural steel (equivalent to ASTM-A7 steel) as this was the prevalent mild structural steel for buildings and bridges in those days (Kulak et al. 1995). Incidentally, all specimens taken from that decommissioned bridge exhibited uniform corrosion.

To obtain the complete stress-strain relationship for the existing rusted steel material, coupons were extracted from a severely rusted floorbeam; two were taken from the web and one from the flange, all three flame-cut in the longitudinal direction of the floorbeam. Then, they were machined in accordance with the ASTM E8M specification (American 1995) with a 200 mm (8 inch) gage length (Davis et al. 1982) with the important exception that the wide sides of the steel coupons (corresponding to the outside surfaces of the flange and web) were left unmachined to preserve their rusted surfaces. Each coupon was marked in 25 mm intervals along its gage length and mapped to have the coupon thickness measured at three points across at each interval, as shown in Fig. 8.5. Thicknesses for the entire gage length of the three coupons, measured using

a micrometer, are presented in Table 8.1. Maximum loss of cross-sectional area due to corrosion, as given by the least average thickness measured across an interval, are 61.5%, 36.2%, and 6.3% for the Flange (original thickness of 18.5 mm, as per American 1953), Web 1 and Web 2 (original thickness of 11.6 mm) coupon specimens, respectively.

For each test, the specimen was put into the testing machine and loaded until its failure. Test results are presented in Figs. 8.6 and 8.7 in terms of strength versus elongation, and stress versus strain respectively. Stresses in Fig. 8.7 were obtained by dividing the applied load by the cross-sectional area at the minimum average thickness along the gage length. Expected results for comparable unrusted specimens are also plotted in these figures, using the minimum yield strength, F_y, of 230 MPa (33 ksi), tensile strength, F_u, of 420 MPa (60 ksi), and elongation in 200 mm (8 inch) of 21% specified for that G40.4 steel (Canadian 1962). Fig. 8.6 clearly illustrates that the expected loss of strength is directly proportional to the loss in cross-sectional area (note that flange and web coupons had different original thicknesses). All coupons failed at their section of least measured cross-sectional area.

As shown in Fig. 8.7, although the yield stress threshold is not affected by the presence of corrosion, a well defined yield plateau does not exist for the severely corroded specimens. This is logical since the cross-sectional area varies continuously along the length of the specimen due to randomness in the corrosion attack. Also shown in that figure, maximum elongations at failure, ϵ_{max}, of 14.2%, 15% and 16% were obtained for the rusted coupons. This is somewhat less than the specified elongation for G40.4 (A7) steel, but this loss of ductility can be mostly attributed to slightly premature necking initiation and a shorter descending branch of the stress-strain curve past that point. Considering that maximum strengths have been reached nearly at the same strain, based on this limited study of 3 samples, the available non-cyclic material ductility can be deemed not significantly affected by the presence of corrosion, within the range of practical interest, even though it was less than the minimum specified value of 21%. Finally, although the obtained ultimate stress capacity of the flange coupon is below that of the web coupons and that of the specified strength for G40.4 (A7) steel, the difference remains within

statistical expectations, particularly when recognizing that the mean yield stress across the flanges of rolled shapes is usually lower than the corresponding value in their web (Galambos and Ravindra 1978). Also, it must be recognized that the true local minimum thickness could have been missed, or simply been beyond reach due to the finite size of the micrometer's head and coarse surface of the rusted coupons..

Theoretical strength-elongation curves for the Flange and Web 1 coupons have been derived considering both their respective average thickness and minimum thickness at the location along the gage length having the smallest cross-sectional area (absolute minimum thicknesses for the specimens, located outside of the critical section where failure occurred as shown in Table 8.1, were not considered). These are plotted in Fig. 8.8 for comparison with the experimentally obtained results. As can be observed in that figure, using the least average thickness (i.e. the least remaining area as proposed by Kulicki et al. 1990) seems a reasonable procedure, even though results can be slightly on the unconservative side.

8.4 Cyclic Bending Tests

8.4.1 Weak-axis Bending of Steel Plates

To further investigate the physical properties of rusted steel, bending tests of rusted plates were conducted. Two severely rusted lacing steel plates, taken from a built-up member of the decommissioned bridge, were subjected to cyclic flexure in a 3-point bending apparatus with a span of 360 mm, designed and constructed to provide realistic support conditions (Fig. 8.9). Two cylinder bars of 10 mm diameter were inserted into the V-shape cleavage of the supporting plates. A 200 mm wide load applicator plate with a sharp edge of 45° was used to impose loading.

Lacing plates are obviously not subjected to bending in service. However, the objective of this study is to investigate *material behavior* under alternating plasticity (i.e. not structural member behavior). As such, any rusted steel piece could have been used for these tests; lacing plates were simply very convenient to use.

For each plate, originally 76 mm (3 inch) wide and 10.5 mm (3/8 inch) thick, thickness was measured at 15 locations around the point of maximum moment, as shown in Fig. 8.10, and summarized in Table 8.2. For the first specimen, in a first phase of testing, measurements of load versus center span deflections were taken to record the cyclic hysteretic behavior of the corroded specimens. Results are presented in Fig. 8.11 for the first five inelastic cycles. Onset of yielding was observed at an applied load, P_y, of 2.15 kN, corresponding to a midspan yield deflection, δ_y, of 5.8 mm, and a yield curvature, ϕ_y, of 0.00051 rad/mm.

Using the average measured thickness at the location of maximum moment (i.e. midspan), and steel yield strength, F_Y, of 230 MPa, expected yield and plastic moments capacities, M_y and M_p, were 0.131 kN-m and 0.196 kN-m respectively, obtained by:

$$M_y = F_y \frac{bt^2}{6} \quad , \quad M_p = F_y \frac{bt^2}{4} \tag{8.1}$$

where b and t are the plate width and average thickness, respectively. Since in this case $M=PL/4$, where L is the span length for the 3-point bending test, the corresponding applied midspan loads, P_y and P_p, were calculated as 1.46 kN and 2.18 kN.

As minimum average thickness and remaining area are synonymous, this assessment of yield strength follows the procedure recommended by Kulicki et al. (1990). Likewise, midspan deflection at first yield and the corresponding yield curvature were expected to be 3.7 mm and 0.00034 rad/mm, respectively. An expected midspan deflection of 14.8 mm at the onset of strain hardening was also estimated using the theoretical moment curvature for a rectangular cross-section, a parabolically increasing curvature between the yield and plastic moments, and assuming that full plastic moment is reached at the onset of strain-hardening when a curvature equals 10 times the yield curvature as schematically shown in Fig. 8.10b.

Given the good agreement between the experimentally obtained elastic stiffness (0.37 kN/mm) and theoretical one ($48EI/L^3$=0.39 kN/mm), the differences observed between experimental and analytical yield strengths and deflections can be partly attributable to the difficulty in accurately identifying experimentally the yield point for a specimen having an irregular cross-section, as well as to possible slightly greater than specified yield strength of the plates tested. It is noteworthy that loss of strength due to corrosion is considerable here, with a remaining yield strength of 2.15 kN (1.46 kN theoretical) compared to that of the non-corroded lacing plate which would have been of approximately 3.5 kN based on the original lacing plate thickness (Ketchum 1924).

Then, to investigate the stability of these hysteretic loops under severe cyclic loading, it was decided to arbitrarily subject the specimen to 50 cycles at a maximum center deflection of 60 mm. For that specimen, this corresponded to a displacement ductility of 10.3 (i.e. 60/5.8). Statistical results by Krawinkler (1996) demonstrate that stiff structural systems can undergo a large number of inelastic excursions during severe earthquakes, but corresponding cumulative hysteretic energy demands are typically less than considered here. Nonetheless, the large ductility was selected to accumulate hysteretic energy as rapidly as possible (cycling in that particular test setup required numerous manual operations). Survival to that severe test regime would have provided confidence in the cyclic ductile capacity of rusted steel members.

In each of those large ductility cycles, a hysteretic energy of 450 kN-mm per cycle (equal to a normalized hysteretic energy, $E_H/P_y\delta_y$, of 36 per cycle) was dissipated until the 28th cycle when a "popping" noise was heard. Testing was stopped and the specimen was examined. Visible on the tension side of the member was a 5 mm long crack oriented in the width direction, approximately 1 mm wide and 1 mm deep. The crack was located approximately at mid-width, and 12 mm away from the center span. A normalized cumulative hysteretic energy of 870 had been dissipated at that point. Testing resumed and an immediate drop in capacity was observed. Upon further cycling, the crack propagated in both directions, traveling towards the edges of the member as strength degradation worsened. As seen in Fig. 8.12a, after the 32th cycle, strength had fallen by 75%; the crack had spread through thickness and nearly across the entire width of the specimen, and testing was stopped. Also note that, while the deflection history was measured

continuously for the first five cycles (as shown in Fig. 8.11), only a few measurements were taken along each hysteretic loop from the 6th cycle up to failure (Fig. 8.12) to accelerate the testing process. Hysteretic energy values reported for the lacing plate tests are thus slightly lower than those would have been obtained using Ramberg-Osgood tracing over the recorded data point.

A second nearly identical specimen was similarly tested in an attempt to reproduce the results. Immediately from the first cycle, and in each cycle, the specimen (with P_y of 1.8 kN and δ_y of 5.2 mm) was pushed to a displacement ductility of 11.5, corresponding to an hysteretic energy of 362 kN-mm (normalized hysteretic energy of 39). This time, strength degradation became noticeable during the 25th cycle as shown in Fig. 8.12b, after a cumulative normalized hysteretic energy of 960. Examination of the specimen's surface revealed that fine cracking had occurred across the width of the member about 10 mm from the center span. Crack propagation and strength degradation in the subsequent cycles followed the pattern previously established, thus validating previously obtained results. Final state of the specimens and cross-width cracks are shown in Fig. 8.13. Close-up view of the rusted specimens' surface texture in the vicinity of the crack is shown in Fig. 8.14. Fig. 8.15 illustrates other cracks of finite lengths that typically developed in parallel to the failure surface.

Information on the alternating plasticity resistance (i.e. low-cycle fatigue) of structural steel indicates that at least 1000, 100 and 20 cycles should be sustained at strains of 0.03, 0.07 and 0.15 respectively prior to failure (American 1986). These would approximately correspond to curvature ductilities of 25, 60 and 130 respectively. Hence, for the maximum curvature ductility of approximately 30 developed during this test, virgin steel should be able to sustain more than 800 cycles, and the above results thus indicate a considerable drop in low-cycle fatigue resistance. However, to confirm that the results obtained were not inadvertently influenced by the particular test setup adopted, and provide an approximate experimental comparison benchmark, a new plate of mild steel (of 300 MPa yield strength) and same width as that of the rusted plates was also tested. Its thickness was chosen to be approximately equal to the least value measured on the rusted specimens (i.e. 6.3 mm). This new steel plate was subjected to 50 inelastic cycles at a center displacement of 60 mm, corresponding to a displacement ductility of 9, curvature ductility

of 20, and cumulative hysteretic energy of 26,800 kN-mm for 50 cycles (normalized cumulative hysteretic energy of 1640) without any sign of cracking or strength reduction. Results are shown in Fig. 8.12c for comparison.

Conceptually, the above observed premature cracking under alternating plasticity can be attributed to the presence of irregularities along the rusted surface that act as crack initiators and precipitate crack propagation throughout the section. Consequently, members with large corrosion notches or more severe level and types of corrosion than considered here would likely have an even lower cracking resistance under alternating plasticity, and their contribution to seismic resistance might be of even greater concern.

8.4.2 Out-of-Plane Bending of Web of Structural S-Shape

While the above provided evidence that corrosion has a detrimental effect on the alternating plasticity resistance of structural steel, at least for the severity and type of corrosion considered, failure occurred at large displacement ductilities, after a considerable amount of hysteretic energy was dissipated. Hence, additional tests were deemed necessary to determine whether similar failures would still occur at lesser ductilities.

The severely rusted web of a 350 mm-long floorbeam segment flame-cut from the same aforementioned bridge was found to be most suitable for this next phase of testing. A simple set-up made it possible to subject the rusted web plate of this structural member to cyclic out-of-plane flexure without the need to extract any material or otherwise disturb the rusted region. As shown in Fig. 8.16, the flange of the structural shape was bolted down to a rigid steel base itself anchored to a strong reaction floor. Bolts were placed as close as possible to the web of the specimen to effectively eliminate its rotation due to flexure of the flange. A horizontally placed servo-controlled actuator connected at mid-height of the web was used to cycle the cantilevering web in flexure about its weak axis, henceforth testing the most severely rusted portion of the web which happened to be near the web-flange intersection. Moreover, by simply flipping the specimen upside-down, it was possible to also test the second most rusted part of the web, located

near the other web-flange intersection. Again, this was done as a convenient way to perform alternating plasticity tests on rusted material, and is obviously not intended to replicate actual seismic effects on a floorbeam.

Preparation of the specimen was limited to extensive grinding of the ends of the floorbeam segment to smoothen the flame-cut surfaces and eliminate the possible presence of a martensite layer there, as well as any jagged edge, notch, or any other stress raiser that could trigger crack initiation unrelated to the presence of corrosion. Prior to testing, thickness of the web in the critical areas (i.e. near the flanges) was measured with a micrometer, as shown in Fig. 8.17, and was found to vary between 6.7 and 12 mm, with average thicknesses of 9.8 and 7.5 mm at the critical section of specimens SW-I and SW-II respectively, i.e. the first and second tests of this sequence. Original unrusted web thickness was 12.3 mm (American 1953).

Instrumentation was limited to a load-cell and LVDT internal to the actuator, and 3 other LVDTs set to monitor slippage of the specimen base and rotation at the web-flange intersection (these actually revealed that none occurred). A high-resolution data acquisition system was used to record all data during the cyclic hysteretic testing of the corroded specimen. Since analytical estimates of the yield displacement proved difficult to accurately calculate, each test started by first subjecting the specimen to a few cycles of loading in search of the yield displacement, followed by a pre-programmed hysteretic displacement history constructed using this yield value.

For the first test (SW-I), yield displacement was judged to occur at 12.5 mm based on first visible evidence of hysteretic behavior on real-time plots of load-displacement curve. The hysteretic displacement history was then programmed to apply 3 cycles at each of displacements of $\pm 0.5\delta_y$, $\pm 1.0\delta_y$, $\pm 2.0\delta_y$, $\pm 3.0\delta_y$, followed by 40 cycles at $\pm 4.0\delta_y$, 20 cycles at $\pm 6.0\delta_y$, and cycling to failure at $\pm 8.0\delta_y$. This follows the spirit of the ATC-24 testing protocol (Applied 1992), albeit with more cycles at the range of inelastic deformations where alternating plasticity resistance data is sought. Loading rate was 1.0 cycle/minute.

The resulting load-displacement hysteretic curves for the first test are shown in Fig. 8.18. During testing, a drop in the applied load necessary to push the specimen to displacements of $\pm 4.0\delta_y$ was noticed during the 40th load cycle (counting from the beginning of testing). This prompted closer examination of the specimen and discovery that a small hairline crack had appeared on both faces of the web, at roughly 50 mm from the south edge of the specimen and 60 mm above the base of the specimen (Fig. 8.17). Five cycles later, the visible horizontal crack had grown to a length of 12.7 and 11.4 mm on the east and west web faces respectively. Strength degradation of 20% was observed after the 46th cycle (i.e. after 34 cycles at $4.0\delta_y$). By the 51st cycle, crack length had reached 26.6 and 14.5 mm on the east and west faces respectively, and strength had dropped nearly 40%. Upon completion of the first cycle at $\pm 6.0\delta_y$, the crack had grown to a visible length of 270 and 184 mm on the east and west faces, tearing the specimen up to its south edge. Testing was stopped after the 56th cycle, at a ductility of $6.0\delta_y$, with only a 65 mm length of uncracked steel at the web's north edge, and a 80% strength degradation. Largest crack opening was approximately 4 mm (Fig. 8.19).

The specimen was then flipped and a similar procedure was followed for testing the second severely corroded web area, with the difference that a different loading history was programmed to investigate the alternating plasticity resistance of the specimen when subjected to more cycles of lower ductility demand, with 3 cycles at each of displacements of $\pm 0.5\delta_y$, and $\pm 1.0\delta_y$, 30 cycles at each of displacements of $\pm 2.0\delta_y$, and $\pm 3.0\delta_y$, followed by 40 cycles at $\pm 4.0\delta_y$, 20 cycles at $\pm 6.0\delta_y$, and cycling to failure at $\pm 8.0\delta_y$. For this test (SW-II), yield displacement was judged to occur at 11 mm, as per the above definition. The resulting load-displacement hysteretic curves for the second test are shown in Fig. 8.20.

The specimen was very closely inspected throughout testing and a small 40 mm-long hairline crack was first observed on the east face 150 mm from the south edge of the specimen at the 83rd cycle (corresponding to the 17th cycle at $\pm 4.0\delta_y$) as shown in Fig. 8.17. First visible crack on the west face was only observed at the 88th cycle; it was 20 mm long and located 135 mm from the south face, at 40 mm above the base of the specimen. Cracks rapidly grew in length and width upon further cycling, as shown in Fig. 8.21, with lengths of 65, 75 and 194 mm on the east face,

and 132, 140, and 165 mm on the west face at the 90th, 98th and 102th cycles respectively. Strength degradation of 20% was observed after the 96th cycle (i.e. after 30 cycles at $4.0\delta_y$). Cracking reached the south edge of the specimen on both the east and west faces simultaneously at the 105th cycle (still at a displacement of $4.0\delta_y$), and reached the north edge on the west face at the 108th cycle (at a displacement of $6.0\delta_y$ since the 107th cycle), with 40 mm left of uncracked steel on the east face. Testing was stopped after the 110th cycle, after a strength loss of 80%.

To provide further perspective on the results of these tests, displacement ductility, hysteretic energy and cumulative hysteretic energy per cycle, as well as corresponding normalized energy ($E_H/P_y\delta_y$) values are presented in Table 8.3. It is notable that the definitions of yield strength and displacement have a considerable impact on all normalized quantities presented in this study, such as ductilities and normalized energies, particularly given the difficulty in defining this yield point, both experimentally and analytically, for the type of rusted specimens under consideration. Since the 0.2% rule was found to be impracticable here, yield was generously defined as the onset of nonlinear behavior. If, in hindsight, yield point was defined by the intersection of the asymptotes to the experimentally obtained initial stiffness and stiffness at maximum resistance, to represent behavior by a bilinear model with strain hardening as frequently done in earthquake engineering, yield displacements would typically become approximately 20 and 17 mm for SW-I and SW-II, making all calculated ductilities considerably smaller (with failures occurring at the same number of cycles, but typically at $2.5\delta_y$ rather than at $4.0\delta_y$, with considerably more alarming consequences).

8.5 Some Observation on Analytical Predictions of Monotonic Load-Displacement Curve

An attempt was made to model the force-deformation curve of the rusted coupon specimen subjected to monotonic loading, relying solely on the availability of a limited number of thickness measurements taken with a micrometer and the theoretical stress-strain curve for the specified

steel. The model considered treats the tension member as a piece-wise sequence of elements each having a cross-section equal to that measured across specimen width using linear thickness variation between the cross-width readings. For this purpose, the flange coupon was selected, and subdivided into 8 such segments of 25 mm length (considering the segments along the gage length).

Following this segmental procedure, as the load on the specimen is progressively increased, the corresponding stress, strain, and elongation is calculated for each segment (using the theoretical stress-strain relationship), and total elongation is obtained by adding the individual segment elongations.

To explore sensitivity of the results to the assumed length of the yield plateau, these calculations were repeated three times, with yield plateau respectively ending at strains of 10, 15 or $20\epsilon_y$ for each segment considered (true length of yield plateau length for A7 steel is approximately $12\epsilon_y$). Results, shown in Fig. 8.22 in terms of force versus total elongation, compare well up to an elongation of 4 mm, corresponding to a strain elongation of 2%. This adequately covers the strain range of engineering significance for seismic-related problems. Beyond that, the model gives a more rapid strength rise, a lower failure elongation, and thus a far worse match against the experimental results. These differences can be attributed to unavoidable errors in obtaining a precise map of coupon thickness along the entire gage length and width, particularly due to limitations in the number of measurements taken, variations and irregularities in the rusted surface texture, and limited accuracy of the data collected using a micrometer with a head of 6 mm diameter on a surface with small asperities. Failing the availability of an accurate continuous measurement technique, it is difficult to improve this model. As for the model's lower elongation past the point of maximum strength, it is simply a consequence of assuming that necking develops in the critical segment having the minimum average thickness without further strain increases in the other segments. A more sophisticated model accounting for true strain (as opposed to engineering strain) and multi-dimensional plasticity interaction could lead to further improvements.

Given the above difficulties in replicating the behavior of a specimen as simple as the tension coupon, further refinements to the model were not attempted. However, it is noteworthy that, in this case, the simple model used confirmed that all segments could yield prior to attainment of the ultimate strength along a given segment, because the ratio of maximum to minimum segment areas over the gage length of the coupon (A_{max}/A_{min}=335/270 = 1.24) was lower than the ratio of tensile to yield strength for this specimen (F_u/F_y = 1.83).

8.6 Rivet Tests

Some riveted pieces were extracted from a few available rusted components to experimentally investigate the impact of corrosion on the tension and shear properties of rivets. By visual assessment of lost head area, rivets judged having most suffered from corrosion were selected among those available. Note that the head diameters of the rivets chosen among those available were approximately 28 mm, considerably less than the 32 mm head diameter customary for these 19 mm (3/4") diameter rivets (Ketchum 1924).

8.6.1 Tension Test

For the tension test, a rivet and its connected plates were isolated and cut out from horizontal bracing rusted double-angle members. Then, using a technique similar to that used by Sarraf and Bruneau (1996) to test undisturbed rivets, two segments of a circular HSS 51x51x3.8 were welded on each side of the specimen, surrounding without contact the rivet heads, and filled with a solid cylindrical steel segment to prevent crushing at the ends inserted in the grips of a universal testing machine. The tensile capacity of the HSS and the tensile strength of fillet weld were provided greater than the maximum tensile capacity of the rivet. The HSS segments were selected 200 mm long to be properly placed into the gripping device of the testing machine.

With the HSS pulling on the connected plates, in turn pulling on the rivet, a tensile strength of 159 kN was obtained for this rivet, corresponding to an ultimate stress of 475 MPa when considering the rivet filled the entire 20.6 mm (13/16") diameter hole when hot driven. Failure occurred by necking at the middle of the rivet's shank. This, as well as the experimentally obtained force-elongation curve, indicates no loss of strength due to corrosion for this rivet.

8.6.2 Shear Test

A similar piece of rivet and connected pieces were isolated and cut out for a double-shear test. As presented in Fig. 8.23, a special set-up was also built to create pure shear test conditions and insertion into an uniaxial testing machine. The bearing capacity of the connected angles and the compression capacity of load applicator plate were checked to be larger than the maximum shear capacity of the rivet. The specimen was finally loaded until shear failure occurred in the rivet. An experimentally obtained ultimate shear strength of 240 kN (in double shear, or 120 kN in single shear) was obtained for the rivet, with a corresponding shear deformation of 8 mm at failure (Fig 8.24a). This is comparable to results reported by Kulak et al. (1987) for unrusted rivets.

Closer inspection of the failed rivets and surfaces revealed that corrosion had not progressed to significantly attack the shank of the rivets (Fig. 8.24b), in spite of the severe rust visible on the rivet heads. That condition can be attributed to the fact that hot rivets expand to fill their holes when driven during construction, and produce a clamping action as they cool and shrink after their installation. These mechanisms help confine the extent of severe corrosion to the rivet heads, and thus effectively prevent degradation of strength and ductility for rivets in similar condition to those considered here, at least as long as a sufficient amount of rivet head remains to allow development of the rivet's tension resistance under that type of loading.

8.7 Summary of Findings

A limited test program was conducted to investigate the effect of severe uniform corrosion on the hysteretic energy dissipation capacity of structural steel. Initial tests confirmed that the non-cyclic ductility of the few corroded structural steel specimens considered here was not significantly affected by the presence of rust, in spite of severe area loss, when subjected to a monotonic tension loading condition. The few available rivets tested in tension or shear did not exhibit any degradation of strength nor ductility, in-spite of being judged severely rusted upon visual inspection before failure of the rivets. However, cyclic flexural tests on structural members revealed that, while stable hysteretic behavior comparable to that of unrusted specimens is possible, premature fracture under alternating plasticity (i.e. low-cycle fatigue) will typically develop. These fractures may be conceptually explained by the presence of irregularities along the rusted surface that may act as crack initiators and precipitate crack propagation throughout the section.

A considerable cumulative hysteretic energy can be dissipated prior to the development of fatal cracking, and it is sufficient to provide adequate seismic resistance in most applications. However, the observed reduced ductile behavior could be an issue in some specialty applications, such as with the types of passive energy dissipation devices considered in the earlier chapters in which steel plates can be subjected to very high local flexural ductility demands; in such cases, preliminary findings in this research suggest that rust protection or replacement of the devices after severe earthquakes would be warranted. In particular, members having large corrosion notches or more severe level and types of corrosion than considered here may be even more significantly affected, and deserve further experimental study. Moreover, considerable reduction in load carrying capacity due to cross-sectional loss should be compensated.

Modeling of the observed behavior, without an accurate and continuous map of thickness variations along and across structural elements, is particularly difficult. Nonetheless, the use of minimum average thickness was reasonably effective in predicting yield and ultimate resistance,

and a proposed segmental model based on a large number of discrete thickness measurements was able to replicate the monotonic force-elongation behavior over an elongation range of approximately 2% (practical range of engineering interest).

Findings from these explorative tests are largely qualitative, based on a small number of specimens, and obviously not in a format usable in design. It is noteworthy that only behavior in bending has been studied, and that the effects of severe corrosion on the cyclic ductility of members subjected to other stress conditions (e.g. axial, or combined axial and bending) may be different. However, this research provides some much needed preliminary data, and hopefully some guidance for future research in that direction.

CHAPTER 9

CONCLUSIONS AND DESIGN RECOMMENDATIONS

9.1 Conclusions

Based on the results from analytical and experimental investigations reported in this thesis, the following major conclusions may be reached:

- Analytical studies demonstrate that a small end-diaphragm stiffness in slab-on-girder steel bridges is sufficient to make the entire superstructure behave as a unit in the elastic range. However, the above results also illustrate that a dramatic shift in seismic behavior could occur once rupture of the end-diaphragms occurs, with a sizeable period elongation, considerably larger lateral displacements and higher propensity to damage due to instability and P-Δ effects based on nonlinear inelastic analyses.

- Results from two analytical models developed to determine period and elastic response in slab-on-girder steel bridges with and without diaphragm, compare well with those obtained

from elastic computer analyses. It is also found that the presence of intermediate diaphragms does not significantly influence the seismic performance of these bridges, both in the elastic and inelastic range whether end-diaphragms are present or not.

- Moreover, these analyses confirmed that effective end-diaphragms constitute the critical structural elements along the main seismic load path, and that they should be designed accordingly. Therefore, in new bridges, they should be designed to resist in an elastic manner the forces induced by the maximum credible earthquake. Alternatively, they could be designed and detailed as ductile members to preclude brittle member or connections failure. This is not warranted for intermediate diaphragms. Non-ductile end-diaphragm members and connection details in existing steel bridges should be retrofitted, recognizing their impact on seismic response.

- For seismic retrofit of slab-on-girder steel bridges, an innovative strategy has been proposed. Taking advantage of the presence of a steel superstructure, the existing end-diaphragms of these bridges are replaced by new ductile diaphragms incorporating stable seismic energy dissipation devices. Per capacity design principles, these devices act as structural fuses calibrated to yield before the strength of the substructure is reached, thus protecting that substructure from undesirable damage. Although targeted for implementation as part of a retrofit strategy, ductile diaphragms should be equally effective in new bridges.

- A simple procedure suitable for hand calculation has been proposed to design the above ductile diaphragms. It uses a trilinear load-displacement relationship and a strength-versus-ductility relationship based on equal energy concepts. Nonlinear inelastic analyses suggest that the resulting designs will exhibit an appropriate ultimate cyclic seismic behavior.

- The impact of intermediate diaphragms and web stiffeners on bridges having ductile diaphragms is minor unless they are closely spaced along the girders particularly around the supports.

- Longer bridges having properly designed ductile end-diaphragms absorb more earthquake energy and more effective retrofits are obtained for these bridges having a smaller number of girders.

- The stiffened girders in slab-on-girder bridges may resist a significant portion of the lateral loads at high inelastic transverse drifts of the deck. In cases where the existing girders are very stiff laterally, the proposed ductile end-diaphragms might be less effective, and other seismic retrofits (like base isolation for example), might be more appropriate to protect the substructure elements. It is noteworthy that the ductile seismic retrofit strategy proposed here works better for steel bridges having relatively weak lateral stiffness.

- Results from testing of the TADAS, EBF and SPS specimens illustrate their large initial elastic stiffness, high strength and capacity to dissipate hysteretic energy. Ductile end-diaphragms eventually fail at high inelastic lateral drifts, mainly due to rupture of the triangular plates in flexure (TADAS), fracture and rupture of link web in shear and/or local buckling of the link beam's flanges. The full scale tests conducted without providing lateral support for the ductile devices, created a rotational capacity of 0.2 rad (TADAS) and link distortion angles of 0.08 to 0.11 rad (EBF and SPS), corresponding to average ductilities of 8 to 10 before failure.

- Ductile end-diaphragms having bolted members may highly exhibit slippage that leads to pinched hysteretic curves. Welding significantly improves the seismic behavior of these ductile systems. All welded connections develop the full capacity of the device, and must possess enough ductility to preclude abrupt connection failure.

- The specimens without any diaphragm (i.e. with stiffened girders only), dissipate some hysteretic energy maybe sufficient to resist small to moderate earthquakes, but their strength and stiffness degradation occur early due to buckling of the web stiffeners and fracture of their welds.

- To investigate the effect of severe uniform corrosion on the hysteretic energy dissipation capacity of structural steel, a limited test program was conducted. These few tests confirmed that the non-cyclic ductility of corroded steel is not significantly affected by the presence of rust, in spite of severe area loss, when subjected to a monotonic tension loading condition. However, cyclic flexural tests on structural members revealed that, while stable hysteretic behavior comparable to that of unrusted specimens is possible, premature fracture under alternating plasticity (i.e. low-cycle fatigue) will typically develop. These fractures may be conceptually explained by the presence of irregularities along the rusted surface that may act as crack initiators and precipitate crack propagation throughout the section.

- A considerable cumulative hysteretic energy can be dissipated prior to the development of fatal cracking, and it may be sufficient to provide adequate seismic resistance, except maybe for large earthquakes of long duration that would excite structures into numerous cycles of severe inelastic deformations.

- The use of minimum average thickness is reasonably effective in predicting the yield and ultimate resistance of corroded members, and a proposed segmental model based on a large number of discrete thickness measurements is able to replicate the monotonic force-elongation behavior over an elongation range of approximately 2%.

9.2 Practical Design Recommendations

The following design recommendations are made to help bridge engineers design ductile end-diaphragms:

- For short to medium span steel bridges, only one diaphragm should be used at each bridge end, since inserting end-diaphragms between all girders makes it difficult to find an

appropriate structural shape from the available section and thus stronger sections may have to be used instead.

- The bearing stiffeners at the support of the girders should be trimmed (or replaced) to have only the minimum width necessary to satisfy their strength and stability requirements. This would also produce flexural yielding in girders' web stiffeners at larger drifts, ensuring better energy dissipation in the ductile diaphragms.

- For the TADAS design, a plate height of 1/10 to 1/12 of the girder height with height to width ratio between 1 and 1.5 is recommended. A larger number of thinner plates is preferable to mitigate potential problems due to the plastic interaction of flexure and shear forces.

- A link length, e, of 1/8 to 1/12 of the girder spacing, L_s, is recommended for the EBF design. Deeper link beams are also preferred as their larger flexural stiffness enhances the overall stiffness of the ductile device, ensuring that its yield displacements is reached much before the onset of yielding of the stiffened girders.

- For the SPS design, a link height of 1/8 to 1/10 of the girder height is recommended. The preferred detail consists of selecting an available structural shape for the link and fully weld it to the bottom beam.

- Welding is recommended as much as possible for all connections of ductile end-diaphragms to avoid slippage that cause a less desirable behavior.

- In rusted steel bridges, considerable reduction in load carrying capacity due to cross-sectional loss should be simply compensated by strengthening the corroded members. However, care should be taken for replacement of those rusted energy dissipating devices, that have to sustain many high inelastic cycles in earthquakes.

9.3 Future Research

To further improve the existing knowledge on the seismic performance and retrofit of steel bridges, the following research is needed:

- Although results from this research have demonstrated the probable failure of steel bridges without diaphragm due to P-Δ effects, a simple and reliable model using yield line failure mechanisms would be useful to predict the ultimate lateral resistance of these bridges.

- While the concept of ductile diaphragms is promising and appears satisfactory based on the analyses reported here, more research is needed. In particular, cyclic and pseudodynamic tests should be conducted on small and/or large scale 3-D models of the entire bridge for experimental verification of the concept and expected behavior.

- Although results from the limited study reported here have illustrated the propensity to premature alternating plasticity failure of rusted steel, many questions remain unresolved. Much testing is still necessary to quantitatively correlate the degree and type of severe corrosion with the plastic strains and corresponding normalized hysteretic energy to failure, and generate statistical data that can be used reliably by practicing engineers. Analytical models and measuring tools capable of accounting for accurate and continuous maps of thickness variations along and across structural elements are also needed to permit calculation of the full strength-deformation envelopes of severely corroded members in the inelastic range. Finally, the effect of severe corrosion on welded structures should also be investigated as severe corrosion could potentially worsen the negative impact of lack-of-penetration or lack-of-fusion defects in groove welds, or undercut defects in fillet welds.

REFERENCES

ADINA R & D, Inc. (1995), "Automatic Dynamic Incremental Nonlinear Analysis", *ADINA software and documentations*, Watertown, MA.

Albrecht, P., and Simon, S. (1981). "Fatigue notch factors for structural details.", *J. Struct. Engrg.*, ASCE, 107(7), 1279-1296.

Allahabadi, R. (1987). "DRAIN-2DX, Seismic response and damage assessment for 2D structures.", *Thesis presented to the Dept. of Civ. Engrg.*, Univ. of California, Berkeley, in partial satisfaction of the requirements for the degree of Doctor of Philosophy.

American Association of State Highway Officials (1961). *Standard specifications for highway bridges*, Washington, D.C.

American Institute of Steel Construction, (1953). *Iron and steel beams 1873 to 1952.* AISC, Chicago.

American Society for Metal (1986). *Atlas of fatigue curves*, Edited by H.E. Boyer, Materials Park, Ohio.

American Institute of Steel Construction (1994). "Load and Resistance Factor Design.", *Manual of steel construction*, 2nd edition.

American Assoc. of State Highway and Transp. Officials (1994). *LRFD Bridge Design specification*, Washington, D.C.

American Society for Testing and Materials (1995). *Annual book of ASTM standards*, Philadelphia, PA.

Applied Technology Council (1992). *Guidelines for cyclic seismic testing of components of steel structures*. Publication ATC-24, Palo Alto, California.

Astaneh-Asl, A. (1993). "Seismic retrofit concepts for the East Bay Crossing of the San Francisco-Oakland Bay bridge.", *Proc. 1st US seminar on seismic evaluation and retrofit of steel bridges*, San Francisco, CA.

Astaneh-Asl, A., Shen, J. H. and Cho, S. W. (1993). "Seismic performance and design consideration in steel bridges.", *Proc. 1st US seminar on seismic evaluation and retrofit of steel bridges*, San Francisco, CA.

Astaneh-Asl, A., Bolt, B., Mcmullin, K. M., Donikian, R. R., Modjtahedi, D. and Cho, S. W. (1994). "Seismic performance of steel bridges during the 1994 Northridge earthquake.", *UCB report* CE-STEEL 94/01, Berkeley, CA.

Azizinamini, A., Kathol, S. and Beacham, M. W. (1995). "Influence of cross frames on load resisting capacity of steel girder bridges.", *AISC Engineering Journal*, 32(3), 107-116.

Bridge seismic retrofit study for Southwest Admiral-South bridge (1993). *Final Report*, Seattle Engineering Department, Seattle, Washington.

Brockenbrough, R. L. and Merritt, F. S. (1995). *Structural Steel Designer's Handbook*. 2nd ed., McGraw-Hill Inc., New York.

Bruneau, M. (1990). "Preliminary report of structural damage from the Loma Prieta earthquake of 1989 and pertinence to Canadian structural engineering practice.", *Canadian J. Civ. Engrg.*, 17(1), 198-208.

Bruneau, M., Wilson, J. W. and Tremblay, R. (1996). "Performance of steel bridges during the 1995 Hyogo-ken Nanbu (Kobe, Japan) earthquake.", *Canadian J. Civ. Engrg.*, 23(3), 678-713.

Buckle, I. G., Mayes, R. L. and Button, M. R. (1986). "Seismic design and retrofit manual for highway bridges.", *Computech Engineering Services*, Berkeley, CA., Published also as *Report FHWA-IP-87-6*, U.S. Dept. of Transp., Federal Highway Administration.

Canadian Institute of Steel Construction (1962). *Structural steel material specifications.* Toronto, Ontario.

Canadian Institute of Steel Construction (1995). *Handbook of steel construction.* 6th ed., Willowdale, Ontario.

Canadian Portland Cement Association (1995). "Concrete design handbook.", Ottawa, Ont.

Canadian Standards Association (1994). "Limit states design of steel structures.", *CAN/CSA-S16.1-M89*, Rexdale, Ontario.

Chai, Y. H. (1996). "An analysis of the seismic characteristics of steel-jacketed circular bridge columns.", *Earthquake Engrg. and Struct. Dynamics*, 25(2), 149-161.

Cherry, S. and Filiatrault, A. (1993). "Seismic response control of buildings using friction dampers.", *Earthquake Spectra*, 9(3), 447-466.

Clough, R. W. and Penzien, J. (1993). *Dynamics of structures.* McGraw-Hill, New York.

Cooper, S. E. and Chen, A. C. (1985). *Designing steel structures: methods and cases.* Prentice Hall, New York.

Davis, H. E., Troxell, G. E. and Hauck, G. F.W. (1982). *The testing of engineering materials.* McGraw-Hill, New York.

Dicleli, M., Bruneau, M. (1995). "Seismic performance of single-span simply-supported and continuous slab-on-girder steel highway bridges.", *J. Struct. Engrg.*, ASCE, 121(10), 1497-1506.

Dicleli, M., Bruneau, M. (1996). "Quantitative approach to rapid seismic evaluation of slab-on-girder steel highway bridges.", *J. Struct. Engrg.*, ASCE, 122(10), 1160-1168.

Degenkolb, O. H. (1978). "Retrofitting bridges to increase seismic resistance.", *J. technical councils of ASCE*, 104(TC1), 13-20.

Douglas, M. B. (1979). "Experimental dynamic response investigations of existing highway bridges.", *Proc. a workshop on earthquake resistance of highway bridges*, 497-523.

Earthquake Engineering Research Institute. (1990). "Loma Prieta Earthquake reconnaissance report." *Spectra*, Supplement to vol. 6, Oakland, CA.

Earthquake Engineering Research Institute. (1994). "Northridge Earthquake Jan. 17, 1994, preliminary reconnaissance report." *Earthquake Engrg. Res. Inst.*, Oakland, CA.

Earthquake Engineering Research Institute. (1995). "The Hyogo-Ken Nanbu Earthquake Jan. 17, 1995, preliminary reconnaissance report." *Earthquake Engrg. Res. Inst.*, Oakland, CA.

Engelhardt, M. D. and Popov, E. P. (1989). "On design of eccentrically braced frames.", *Earthquake Spectra*, 5(3), 495-511.

Fehling, E., Pauli, W. and Bouwkamp, J. G. (1992). "Use of vertical shear-link in eccentrically braced frames.", *Proc. 10th world conf. on earthquake engrg.*, Madrid, 8, 4475-4479.

Filiatrault, A., Tremblay, S. and Tinawi, R. (1994). "A rapid seismic screening for existing bridges in Canada.", *Canadian J. Civ. Engrg.*, 21(4), 626-642.

Fisher, J. W., Yen, B. T. and Wang, D. (1990). "Fatigue strength of riveted bridge members.", *J. Struct. Engrg.*, ASCE, 116(11), 2968-2981.

Fisher, J. W., Yen, B. T. and Wang, D. (1991). "Corrosion and its influence on strength of steel bridge members.", A paper presented at Third Bridge Engineering Conference, Denver, Colorado, *Transp. Research Record No. 1290*, 1, 211-219.

Galambos, T. V., and Ravindra, M. K., (1978). "Properties of steel for use in LRFD", *J. Struct. Engrg.*, ASCE, 104(ST9), Proc. Paper 14009, 1459-1468.

Gorman, D. J. (1975). *Free vibration analysis of beams and shafts.* John Wiley & Sons, Toronto.

Guidelines for cyclic seismic testing of components of steel structures (1992). *Report ATC-24*, Applied Technology Council, Stanford, CA.

Hjelmstad, K. D. and Popov, E. P. (1983). "Cyclic behavior and design of link beams.", *J. Struct. Engrg.*, ASCE, 109(10), 2387-2403.

Hjelmstad, K. D. and Popov, E. P. (1984). "Characteristics of eccentrically braced frames.", *J. Struct. Engrg.*, ASCE, 110(2), 340-353.

Horne, M. R. and Morris, L. J. (1981). *Plastic design of low-rise frames.* Granada, London.

Humar, J. L. (1987). *Dynamics of structures*. Prentice Hall, New Jersey.

Imbsen, R. A., Penzien, J. (1984). "Evaluation of energy absorbing characteristic of highway bridges under seismic conditions.", *EERC report* 84/17.

Iron and Steel Beams 1873 to 1952 (1953). Amer. Institute of Steel Construction, Chicago.

Kasai, K. and Popov, E. P. (1986). "Cyclic web buckling control for shear link beams.", *J. Struct. Engrg.*, ASCE, 112(3), 505-523.

Kawashima, K. (1990). "Seismic design, seismic strengthening and repair of Highway bridges in Japan.", *Proc. first US-Japan workshop on seismic retrofit of bridges*, Tsukuba Science City, Japan.

Kayser, J. R. and Nowak, A. S. (1987). "Evaluation of corroded steel bridges.", *Proc. Struct. Congress Related to Bridges and Transmission Line Struct.*, ASCE, 35-46.

Kayser, J. R., Malinski, T. and Nowak, A. S. (1987). "Corrosion damage models for steel girder bridges.", *Proc. on effects of damage and redundancy on structural performance*, ASCE, 9-22.

Kayser, J. R. and Nowak, A. S. (1989). "Capacity loss due to corrosion in steel-girder bridges.", *J. Struct. Engrg.*, ASCE, 115(6), 1525-1537.

Ketchum, M.S. (1924). *Structural Engineer's Handbook*, Mc-Graw Hill Book Co., New York.

Komp, M. E. (1987). "Atmospheric corrosion rating of weathering steel-Calculations and significance.", *Materials Performance*, 26(7), 42-44.

Krawinkler, H., Popov, E. P. (1982). "Seismic behavior of moment connections and joints.", *J. Struct. Engrg.*, ASCE, 108(ST2), 373-391.

Krawinkler, H. (1996). "Cyclic loading histories for seismic experimentation on structural components". *Earthquake Spectra*, 12 (1), 1-12.

Kulak, G. L., Adams, P. F. and Gilmor, M. I. (1990). *Limit states design in structural steel.* Canadian Institute of Steel Construction, Fourth edition, Markham, Ontario.

Kulak, G. L., Fisher, J. W., Struik, J. H. A. (1987). *Guide to design criteria for bolted and riveted joints.* Second edition, John Wiley & Sons, New York.

Kulicki, J. M., Prucz, Z., Sorgenfrei, D. F., Mertz, D. R. and Young, W. T. (1990). "Guidelines for evaluating corrosion effects in existing steel bridges.", *NCHRP Report 333*, Transp. Research Board, National Research Council, Washington, D. C.

Lew, H. S. (1990). "An overview of damage to highway bridges during the Loma Prieta earthquake.", *Proc. first US-Japan workshop on seismic retrofit of bridges*, 111-139, Tsukuba Science City, Japan.

MacRae, G. A., Kawashima, K. and Hasegawa, K. (1990). "Repair and retrofit of steel piers.", *Proc. first US-Japan workshop on seismic retrofit of bridges*, Tsukuba Science City, Japan.

MacRae, G. A., Priestley, M. J. N. and Tao J. (1993). "P-Δ design in seismic regions.", *Report No. SSRP- 93/05*, University of California, San Diego, CA.

Malley, J. O. and Popov, E. P. (1983). "Design considerations for shear links in eccentrically braced frames.", *EERC report 83-24*, Univ. of Calif., Berkeley, CA.

Mander, J.B, Kim, D-K., Chen, S.S. and Premus, G.J. (1996). "Response of steel bridge bearings to reversed cyclic loading.", *National Center for Earthquake Engineering Research Technical Report NCEER-96-0014*, Buffalo, N.Y.

Mayes, R. L., Buckle, I. G., Kelly, T. E. and Jones, L. R. (1992). "AASHTO Seismic isolation design requirements for highway bridges.", *J. Struct. Engrg.*, ASCE, 118(1), 284-304.

Mayes, R. L., Choudhury, D., Crooks, R. S., Jones, D. M. and Knight, R. P. (1993). "Isolation Design: Aid to bridge rehabilitation in low to moderate seismic zones.", *Proc. symposium on practical solutions for bridge strengthening & rehabilitation*, Iowa State Univ., Ames, Iowa, 133-142.

Mayes, R. L., Jones, D. M., Knight R. P., Choudhury, D. and Crooks, R. S. (1994). "Seismically isolated bridges come of age.", *Proc. 4th Intl. Conf. on short and medium span bridges*, Halifax, Nova Scotia, 1095-1106.

Mitchell, D., Sexsmith, R. and Tinawi, R. (1994). "Seismic retrofitting techniques for bridges-a state-of-the-art report.", *Canadian J. Civ. Engrg.*, 21, 823-835.

Mitchell, D., Bruneau, M., Williams, M., Anderson, D., Saatcioglu, M. and Sexsmith, R. (1995). "Performance of bridges in the 1994 Northridge earthquake.", *Canadian J. Civ. Engrg.*, 22, 415-427.

Naeim, F. (1989). *The seismic design handbook.* Van Nostrand Reinhold, New York.

Nakashima, M., Akazawa, T. and Igarashi, H. (1995). "Pseudo-dynamic testing using conventional testing devices.", Earthquake Engrg. and Struct. Dynamics, 24(10), 1409-1422.

Nakashima, M. (1995). "Strain-hardening behavior of shear panels made of low-yield steel. I: Test.", *J. Struct. Engrg.*, ASCE, 121(12), 1742-1749.

Nakashima, M., Akazawa, T. and Tsuji, B. (1995). "Strain-hardening behavior of shear panels made of low-yield steel. II: Model.", *J. Struct. Engrg.*, ASCE, 121(12), 1750-1757.

National Building Code of Canada (1990). Associate committee on the National Building Code, *National Research Council of Canada*, Ottawa.

Newmark, N. M. and Hall, W. J. (1982). *Earthquake spectra and design.* Earthquake Engineering Research Institute, Oakland, Ca.

Ontario Highway Bridge Design Code (1991a). *Ministry of Tranp.*, Quality and standards division, Ontario, Canada.

Ontario highway bridge design code-Commentary (1991b). *Ministry of Transp.* Quality and standards division, Ontario, Canada.

Paulay, T. (1977). "Capacity design of reinforced concrete ductile frames.", *Proc. workshop on earthquake resistant reinforced concrete buiding construction*, 3, Technical papers, Berkeley CA.

Penzien, J., Chen, M. (1975). "Seismic response of highway bridges.", *Proc. U.S. national conference on earthquake engineering.*

Prakash, V., Powell, G. H. and Campbell, C. (1993). "DRAIN-2DX base program description and user guide.", *Report No. UCB/SEMM 93/17*, University of California, Berkeley, CA.

Priestley, M. J. N. (1988). "The Whitter Narrows, California earthquake of Oct. 1987, damage to the I-5/I-605 separator.", EERI, *Earthquake Spectra*, 4(2), 389-405.

Priestley, M. J. N., Seible, F. and Chai, Y. H. (1992). "Seismic retrofit of bridge columns using steel jackets.", *Proc. 10th world conf. on earthquake engrg.*, Madrid, 9, 5285-5290.

Priestley, M. J. N., Seible, F. and Calvi, G. M. (1996). "Seismic design and retrofit of bridge.", John Wiley & Sons, Inc. New York.

Riley, E. F. and Zachary, L. (1989). "Introduction to mechanics of materials.", John Wiley & Sons Inc., New York.

Roberts, J. E. (1992). "Sharing California's seismic lessons.", *Modern steel construction*, July issue, 32-37.

Roeder, C. W. and Popov, E. P. (1978). "Eccentrically braced steel frames for earthquakes.", *J. Struct. Engrg.*, ASCE, 104(3), 391-412.

Sarraf, M., and Bruneau, M. (1996). "Cyclic Testing of Existing and Retrofitted Riveted Stiffened-Seat Angle Connections", *J. Struct. Engrg.*, ASCE, 122 (7), 762-775.

Seim, C., Ingham, T. and Rodriguez, S. (1993). "Seismic performance and retrofit of the Golden Gate bridge.", *Proc. 1st US seminar on seismic evaluation and retrofit of steel bridges*, San Francisco, CA.

Seismic design guidelines for highway bridges (1981). *Report ATC-6*, Applied Technology Council, Redwood City, CA.

Seismic retrofitting guidelines for highway bridges (1983). *Report ATC-6-2*, Applied Technology Council, Palo Alto, CA.

Seto W. W. (1983). *Mechanical vibrations*. Schaum's Outline Series, McGraw Hill.

Shirolé, A. M., Malik, A. H. (1993). "Seismic retrofitting of bridges in New York State.", *Proc. symposium on practical solutions for bridge strengthening & rehabilitation*, Iowa State Univ., Ames, Iowa, 123-131.

Tsai, K. C., Chen, H. W., Hong, C. P. and Su, Y. F. (1993). "Design of steel triangular plate energy absorbers for seismic- resistant construction.", EERI, *Earthquake Spectra*, 9(3), 505-528.

Tsai, K. C., Li, J. W. and Wang, T. F. (1994). "Pseudodynamic performance of steel plate energy-dissipating substructures.", *Proc. 5th U.S. national conference on earthquake engineering*, EERI, Chicago, Illinois, 735-744.

Tseng, W. S., Penzien, J. (1973). "Analytical investigations of the seismic response of long multiple-span highway bridges.", *EERC report* 73-12, Univ. of Calif., Berkeley, CA.

Whittaker, A.S., Uang, C.M., and Bertero, V.V. (1990). "Experimental seismic response of steel dual systems", *Proc. Fourth U.S. national conference on earthquake engineering*, Palm Spring, California, 655-664.

Wilson, E. L. and Habibullah, A. (1992). "SAP90 Computer Software for Structural & Earthquake Engineering.", *Comp. and Struct. Inc.*, Berkeley, California.

Xanthakos, P. P. (1994). *Theory and design of bridges*. John Wiley & Sons Inc., New York.

Table 3.1. Geometric and structural characteristics of the steel bridge considered in case studies where I_w, I_b and I_D are the moments of inertia of girder web per unit length about bridge longitudinal axis, girder bottom flange about its strong axis, and superstructure about a vertical axis, respectively

Span (m) (1)	Deck Width (m) (2)	No. of Girders (3)	Girder Spacing (m) (4)	Slab Depth (mm) (5)	Girder Size and Properties (6)	Mass (10^3kg) (7)	I_w ($10^{-6}m^4$) (9)	I_b ($10^{-6}m^4$) (8)	I_D (m^4) (10)
20	8	4	2	200	WWF800x184	126	0.111	56.25	1.322
30	8	4	2	200	WWF1000x262	202	0.229	133.3	1.617
40	8	4	2	200	WWF1200x333	286	0.341	160	1.797
50	8	4	2	200	WWF1400x405	367	0.341	312.5	1.983
60	8	4	2	200	WWF1600x496	465	0.341	485.3	2.212

Table 3.2. Comparison of elastic lateral deck drift and period of steel bridges with and without web bearing stiffeners, subjected to 1g pseudo acceleration (assuming laterally simply-supported)

Bridge Span (m) (1)	Web Stiffeners size (2)	Lateral Drift (mm)		Lateral Period (s)	
		With stiffeners (3)	Without stiffeners (4)	With stiffeners (5)	Without stiffeners (6)
20	2Pl. 100x10	5.3	228	0.11	0.94
30	2Pl. 100x10	16	324	0.17	1.08
40	2Pl. 100x10	30	478	0.26	1.27
50	2Pl. 120x12	37	785	0.26	1.66
60	2Pl. 120x12	56	1195	0.30	2.03

Table 3.3. Lateral periods of braced bridges obtained by proposed method and SAP90 (assuming one laterally fixed end) where ρA is the superstructure mass per unit length

Bridge Span (m) (1)	ρA (kg/m) (2)	I_D (m^4) (3)	X-braces size (4)	T_{SAP90} (s) (5)	$T_{proposed}$ (s) (6)	Difference (%) (7)
20	6300	1.322	2L100x100x10	0.0515	0.047	8%
30	6733	1.617	2L100x100x10	0.076	0.071	7%
40	7150	1.797	2L100x100x10	0.12	0.112	6.6%
50	7340	1.983	2L100x100x10	0.17	0.16	6%
60	7750	2.212	2L100x100x10	0.222	0.213	4%

Table 4.1. Inelastic response of the 40m span slab-on-girder bridge (braced with three EBF end-diaphragm at each end) to three different PGA levels, ξ=2%, R=3 (μ_{demand}=5) and Strain-Hardening Ratio=0.03

Bridge Specifications (1)	T_{model} (sec) (2)	PGA (g) (3)	Scaled Earthquake (4)	Expected Psa (g) (5)	Expected S_d (mm) (6)	δ_{max} (mm) (7)	μ (8)	γ_{max} (mm) (9)	$V_{link,max}$ (kN) (10)	$M_{w,max}$ (kN.m) (11)	$F_{eq,max}$ (kN) (12)
S75x8 Link Beam 2L45x45x5 Braces $V_{elastic}$=258 kN $V_{inelastic}$=86 kN	0.204	0.2g	Pacoima Dam	0.67	7.1	4.9	1.35	0.018	54.8	33.3	188
			El-Centro	0.53	5.6	5.1	1.4	0.019	54.9	34.8	193
			Loma Prieta	0.28	4.8	4.7	1.3	0.017	54.7	32.2	184
			Parkfield	0.46	3.0	2.8	0.8	0.009	39.6	19	123
			Saguenay	0.32	3.3	5.05	1.4	0.019	54.9	34.6	192
W150x14 Link Beam 2L55x55x5 Braces $V_{elastic}$=515 kN $V_{inelastic}$=172 kN	0.154	0.4g	Pacoima Dam	1.04	5.4	4.8	1.55	0.013	111.1	32	284
			El-Centro	0.98	5.1	4.6	1.5	0.012	110.2	30	277
			Loma Prieta	0.73	3.8	4.9	1.6	0.013	111.4	32.8	286
			Parkfield	0.70	3.6	4.3	1.4	0.01	109.4	28.2	271
			Saguenay	0.76	4.0	4.0	1.3	0.009	108.5	26.1	263
W200x15 Link Beam 2L65x65x6 Braces $V_{elastic}$=785 kN $V_{inelastic}$=262 kN	0.136	0.6g	Pacoima Dam	1.42	5.7	5.4	1.8	0.015	152.4	35	365
			El-Centro	1.69	6.8	6.7	2.2	0.021	159	42.5	403
			Loma Prieta	1.17	4.7	7.1	2.4	0.023	161	43.2	412
			Parkfield	0.84	3.4	4.6	1.5	0.012	149	30	344
			Saguenay	0.96	3.9	3.9	1.3	0.008	146	25	324

Table 4.2. Inelastic response of the 60m span slab-on-girder bridge (braced with three EBF end-diaphragms at each end) to three different *PGA* levels ξ=2%, R=3 (μ_{demand}=5) and Strain-Hardening Ratio=0.03

Bridge Specifications (1)	T_{model} (sec) (2)	PGA (g) (3)	Scaled Earthquake (4)	Expected PSa (g) (5)	Expected S_d (mm) (6)	δ_{max} (mm) (7)	μ (8)	γ_{max} (mm) (9)	$V_{link,max}$ (kN) (10)	$M_{w,max}$ (kN.m) (11)	$F_{eq,max}$ (kN) (12)
S75x8 Link Beam 2L45x45x5 Braces $V_{elastic}$=415 kN $V_{inelastic}$=138 kN	0.263	0.2g	Pacoima Dam	0.43	7.5	7.2	2.0	0.017	113	33	219
			El-Centro	0.60	10.3	7.1	1.9	0.016	113	32.1	218
			Loma Prieta	0.53	9.3	7.2	2.0	0.016	113	32.2	219
			Parkfield	0.29	5.0	4.6	1.2	0.007	107	20.4	185
			Saguenay	0.62	10.9	6.0	1.6	0.012	111	26.9	204
W150x14 Link Beam 2L55x55x5 Braces $V_{elastic}$=835 kN $V_{inelastic}$=278 kN	0.193	0.4g	Pacoima Dam	0.98	9.3	8.0	2.6	0.019	223	36.7	371
			El-Centro	1.02	10.1	8.6	2.8	0.021	226	38.9	382
			Loma Prieta	1.18	11.0	6.9	2.2	0.015	217	32.5	352
			Parkfield	0.51	4.7	5.4	1.7	0.01	209	27.0	326
			Saguenay	0.69	6.4	7.1	2.3	0.016	218	33.3	356
W200x15 Link Beam 2L65x65x6 Braces $V_{elastic}$=1278 kN $V_{inelastic}$=426 kN	0.168	0.6g	Pacoima Dam	1.22	8.7	7.7	2.6	0.015	336	40.4	515
			El-Centro	1.63	11.5	10.7	3.6	0.025	367	44.8	572
			Loma Prieta	1.84	12.8	8.8	2.9	0.019	347	42.0	536
			Parkfield	0.94	6.6	6.9	2.3	0.013	328	39.3	498
			Saguenay	1.38	9.6	6.4	2.1	0.011	323	37.9	486

Table 4.3. Geometric and structural characteristics of the steel bridge examples

Span (m)	Deck Width (m)	No. of Girders	Girder Spacing (m)	Slab Depth (mm)	Girder Size and Properties	I_D (m^4)	Mass (10^3kg)	m^* (10^3kg)	K^* (10^8N/m)
(1)	(2)	(3)	(4)	(5)	(6)	(7)	(8)	(9)	(10)
40+	8	4	2	200	WWF1200x333	1.797	286	143	2.831
60-90-60	15	2	11.6	250	1000x45 Flanges	23.5	2156	1425	5.14
3-span					& 5000x20 Web++				

+ For bridge spans on abutments or piers.

++ Excluding the 1.5 m tall truss at the upper level of girders.

Table 4.4. Design procedure for 40 m simply supported span bridge examples with target R of 3.75

Trial No. (1)	V_c (kN) (2)	V_{incl} (kN) (3)	$n_g V_g$ (kN) (4)	V_d (kN) (5)	Diaphragm Design				$n_d K_{DD}$ (N/mm) (10)	δ_y (mm) (11)	$n_g K_g$ (N/mm) (12)	K_{total} (N/mm) (13)	δ_c (mm) (14)	δ'_y (mm) (15)	$n_g V_g$ (kN) (16)	V_{incl} (kN) (17)	R (18)
					Device (6)	h_l (SPS) e (EBF) t_T(TADAS) (mm) (7)	Braces (8)	Bot. Beam (9)									
1 SPS	880	234	70	164	W150x14 (l_l=230mm)	150	2L65x65x5	W150x22	90500	1.8	13280	103780	6.8	11	92	256	3.44
2	880	234	92	142	W150x14 (l_l=200mm)	150 St. Pl.45x6	2L65x65x5	W150x22	86120	1.7	13280	99400	7.0	11	96	238	3.7
T=0.22 s < 0.33 s, μ=7.3, δ_{max}=12.4 mm < 24 mm, γ_{max}=0.08 < 0.09																	
1 EBF	880	234	70	164	W150x14 (V_l=106kN)	300	2L65x65x6	---	73650	2.4	13280	86930	8.1	11	112	289	3.04
2	880	234	112	122	Web 120x4 (V_l=90kN)	300 Fl.Pl.150x8	2L65x65x5	built-up section	78770	1.9	13280	92050	7.6	11	104	254	3.46
T=0.23 s < 0.33 s, μ=6.5, δ_{max}=12.4 mm < 24 mm, γ_{max}=0.07 < 0.09																	
1 TADAS	880	234	92	142	4Pl.125x95 (b_T=95mm)	25	2L65x65x5	W150x22	55620	2.55	13280	68900	10.1	11	138	280	3.14
2	880	234	138	96	4Pl.100x70 (b_T=70mm)	25	2L65x65x5	W150x22	75940	1.75	13280	89220	7.8	11	106	237	3.7
T=0.24 s < 0.33 s, μ=7.3, δ_{max}=12.8 mm < 24 mm																	

Table 4.5. Design procedure for support diaphragms of the center 90 m span of three-span bridge examples with target R of 3

Trial No. (1)	V_e (kN) (2)	V_{incl} (kN) (3)	$n_g V_g$ (kN) (4)	V_d (kN) (5)	Diaphragm Design				$n_d K_{DD}$ (N/mm) (10)	δ_y (mm) (11)	$n_g K_g$ (N/mm) (12)	K_{total} (N/mm) (13)	δ_t (mm) (14)	δ'_y (mm) (15)	$n_g V_g$ (kN) (16)	V_{incl} (kN) (17)	R (18)
					Device (6)	h_l (SPS) e (EBF) t_T(TADAS) (mm) (7)	Braces (8)	Bot. Beam (9)									
1 SPS	5075	1692	254	1438	W360x179 (l_l=580mm)	368	2L200x 200x20	W360x122	177000	8.1	1340	178340	28.5	90	51	1489	3.4
2	3960	1320	51	1269	W360x179 (l_l=520mm)	368	2L200x 200x20	W410x85	139060	8.7	1340	140400	28.2	90	50	1255	3.1
T=0.50 s > 0.33 s, μ=5.3, δ_{max}=46 mm <100 mm, γ_{max}=0.098																	
1 EBF	5075	1692	254	1438	W460x67 (V_l=636kN)	1000	2L200x 200x20	---	139860	10.3	1340	141200	47.9	90	86	1539	3.3
2	3860	1287	64	1223	W460x52 (V_l=564kN)	1000	2L200x 200x20	---	144200	9.0	1340	145540	26.5	90	48	1356	2.85
T=0.50 s > 0.33 s, μ=4.5, δ_{max}=40 mm <100 mm, γ_{max}=0.093																	
1 TADAS	5075	1692	254	1438	9Pl.300x250 (b_T=250mm)	50	2L200x 200x20	W410x132	128200	11.0	1340	129540	39.2	90	70	1476	3.4
2	3852	1284	70	1214	8Pl.300x250 (b_T=250mm)	50	2L200x 200x20	W410x132	122730	10.2	1340	124070	31.0	90	55.4	1305	3.0
T=0.52 s > 0.33 s, μ=5, δ_{max}=51 mm <100 mm																	

Table 4.6. Nonlinear inelastic response of 40 m span bridges with ductile diaphragms, using Strain-Hardening ratio of 0.01 (relative displacements are reported)

Case (1)	Period (s) (2)	Time-History Analysis												
		El-Centro		Parkfield		Pacoima Dam		Saguenay		Loma Prieta		Average EQs		
		δ_{max} (mm) (3)	γ_{max} (4)	δ_{max} (mm) (5)	γ_{max} (6)	δ_{max} (mm) (7)	γ_{max} (8)	δ_{max} (mm) (9)	γ_{max} (10)	δ_{max} (mm) (11)	γ_{max} (12)	δ_{max} (mm) (13)	μ_{max} (14)	γ_{max} (15)
SPS	0.236	12.0	0.060	19.5	0.106	8.1	0.038	15.6	0.081	8.9	0.042	12.8	6.7	0.065
EBF	0.238	10.1	0.039	14.6	0.059	7.9	0.030	11.4	0.045	7.8	0.030	10.4	5.0	0.041
TADAS	0.245	12.9	--	23.1	--	8.7	--	19.0	--	11.2	--	15.0	7.5	--
SPS[+]	0.274	11.1 (2.1)	0.055	22.6 (2.6)	0.123	8.4 (1.8)	0.039	18.5 (2.5)	0.098	12.1 (2.2)	0.060	14.5	7.6	0.075
EBF[+]	0.275	9.0 (2.1)	0.034	18.3 (2.7)	0.077	7.4 (1.9)	0.027	15.2 (2.6)	0.063	7.5 (1.9)	0.027	11.5	5.5	0.046
TADAS[+]	0.35	8.9 (15.2)	--	20.2 (17.8)	--	8.4 (14.9)	--	15.5 (17.4)	--	7.2 (13.9)	--	12.0	6.0	--
SPS[++]	0.48	31.1 (26.6)	0.171	38.1 (27.7)	0.210	8.6 (16.6)	0.040	31.1 (26.2)	0.173	26.8 (24.7)	0.148	27.1	14.2	0.148
EBF[++]	0.48	28.5 (28.1)	0.128	36.8 (29.5)	0.158	8.9 (18.3)	0.033	24.5 (26.9)	0.111	10 (19.4)	0.039	21.7	10.4	0.094
TADAS[++]	0.86	23 (155)	--	4.7 (100)	--	2.7 (79)	--	3.5 (95)	--	27 (160)	--	12.2	6.1	--

[+] Multi-span simply-supported 40 m span bridge on concrete bents each having four 900 mm diameter columns (5 m tall).

[++] Multi-span simply-supported 40 m span bridge on concrete bents each having four 600 mm diameter columns (6 m tall). Note that due to flexibility of the piers in this case, the generalized mass and stiffness would be different, i.e. worse results might be obtained indicating the weakness of the proposed design procedure for the bridges on flexible piers.
Numbers in brackets refer to the drifts of the pier caps.

Table 5.1. Bill of materials for TADAS specimen

Quantity (No.)	Items and Dimensions	Drawing Details
2 4 20	Girder Segments including: (WWF1200x333), 500mm long (Pl. 1140x100x10) Plate Stiffeners (3/4"ϕ Stud Shear Connector), 130mm tall	See Detail 1 (Bolts holes and cut as per detail 1)
2	Braces (L65x65x5*) x1218mm	See Detail 7
2	Brace Segment (L65x65x5*) x200mm	See Detail 7
2	Braces (L65x65x5*) x1218mm	See Detail 8
2	Brace Segment (L65x65x5*) x200mm	See Detail 8
1 1 2 1 4 4 8	Special TADAS Assembly including: (Pl. 330x140x10) Gusset plate (Pl. 250x80x8) Top Plate (Pl. 220x50x10) Side Plates (Pl. 280x120x25) Bottom Plate (Pl. 110x80x25) Triangular Plates 20ϕ Steel Rods, 60mm 40ϕ Steel Washers, 5mm thick	For special detailing See Detail 9 Cut as per detail 9C
1 4	Bottom Beam including: (W150x22) x1964mm (Pl. 138x50x6) web stiffeners	See Detail 6
8	Anchor Bolts (#30), each 930mm	See Detail 13
28	Bolts (M20 A325M Grade), each 50mm long	

* L65x65x5 can be replaced with L2-1/2x2-1/2x3/16 (equivalent imperial section).

Typical Instructions:

1) Steel material: Grade CAN/CSA G40.21-M 350W (No substitute)
2) Weld material: E480XX (Electrode classification)
3) All welds shall be accomplished by certified welder.
4) All edges shall be rolled, sawn or gas-cut (not sheared). Bolt holes can be drilled or sheared.
5) Besides the numbered details, additional drawings are provided to show intended erected structure.
6) Detail number shall be written on long braces for easy identification.

Table 5.2. Bill of materials for EBF specimen

Quantity (No.)	Items and Dimensions	Drawing Details
2 4 20	Girder Segments including: (WWF1200x333), 500mm long (Pl. 1140x100x10) Plate Stiffeners (3/4"ϕ Stud Shear Connector), 130mm tall	See Detail 1 (Bolts holes and cut as per detail 1)
2	Braces (L65x65x6*) x1192mm	See Detail 10
2	Brace Segment (L65x65x6*) x200mm	See Detail 10
2	Braces (L65x65x6*) x1192mm	See Detail 11
2	Brace Segment (L65x65x6*) x200mm	See Detail 11
2 2 1 4 4 4	Special EBF Assembly including: (Pl. 160x150x10) Gusset plates (Pl. 60x60x6) Stiffener Plate (W150x14) x1964mm Link Beam (Pl. 138x45x8) Stiffener Plates (Pl. 138x45x6) Stiffener Plates (Pl. 70x45x8) Stiffener Plates	For special detailing See Detail 12
8	Anchor Bolts (#30), each 930mm	See Detail 13
24	Bolts (M20 A325M Grade), each 50mm long	

* L65x65x6 can be replaced with L2-1/2x2-1/2x1/4 (equivalent imperial section).

Typical Instructions:

1) Steel material: Grade CAN/CSA G40.21-M 350W (No substitute)
2) Weld material: E480XX (Electrode classification)
3) All welds shall be accomplished by certified welder.
4) All edges shall be rolled, sawn or gas-cut (not sheared). Bolt holes can be drilled or sheared.
5) Besides the numbered details, additional drawings are provided to show intended erected structure.
6) Detail number shall be written on long braces for easy identification.

Table 5.3. Bill of materials for SPS specimens

Quantity (No.)	Items and Dimensions	Drawing Details
2 4 20	Girder Segments including: (WWF1200x333), 500mm long (Pl. 1140x100x10) Plate Stiffeners (3/4"ϕ Stud Shear Connector), 130mm tall	See Detail 1 (Bolts holes and cut as per detail 1)
2	Braces (L65x65x5*) x1218mm	See Detail 2
2	Brace Segment (L65x65x5*) x200mm	See Detail 2
2	Braces (L65x65x5*) x1218mm	See Detail 3
2	Brace Segment (L65x65x5*) x200mm	See Detail 3
1 1 1 2 1 4	Special Shear Panel Assembly including: (W200x15) x140mm (Pl. 280x140x10) Gusset plate (Pl. 200x100x10) Top Plate (Pl. 190x45x6) Stiffeners (W150x22) x1964mm Bottom Beam (Pl. 138x50x8) Web Stiffeners	For special detailing See Detail 4
1	(W200x15) x500mm, stub taken from same stock	No Detail Provided
1 1 1 1 4 2	Build-up Shear Panel Assembly including: (Pl. 280x140x10) Gusset Plate (Pl. 175x100x10) Top Plate (Pl. 175x130x5) Web Plate (Pl. 280x120x10) Bottom Plate (Pl. 130x45x8) Stiffeners (Pl. 148x45x6) Stiffeners	For special detailing See Detail 5
1	(Pl. 400x100x5) from same stock as Pl.175x130x5 shown on Detail ⑤	No Detail Provided
1 4	Bottom Beam including: (W150x22) x1964mm (Pl. 138x50x6) web stiffeners	See Detail 6
8	Anchor Bolts (#30), each 930mm	See Detail 13
32	Bolts (M20 A325M Grade), each 50mm long	

* L65x65x5 can be replaced with L2-1/2x2-1/2x3/16 (equivalent imperial section).

Table 5.4. Bill of materials for foundation, deck slabs and test set-up

Quantity (No.)	Items and Dimensions	Drawing Details
	Foundation Reinforcement including: ($W_{St.}$=270kg)	See Detail 14
7	(#25 Rebars) x2950mm	
8	(#25 Rebars) x1000mm	
8	(#25 Rebars) x1320mm	
4	(#20 Rebars) x2900mm	
4	(#20 Rebars) x1100mm	
4	(#20 Rebars) x1370mm	
15	(#10 Rebars) x4150mm	
3	(#10 Rebars) x2070mm	
1	Concrete x2.2 m^3	
	Actuators Connection to Foundation including:	See Detail 15
2	(Pl. 1100x580x50) Actuators Base Plates with special countersink holes	(1098mm c/c as per Detail 15)
2	(C380x50) x2880mm	
2	(C380x50) x1730mm with special 30mm holes	Welds as Detail 15
6	(64mm Rods) x1300mm with threaded ends	(Strong Bolts)
	Top Connection to Slab Assembly including:	See Detail 16
1	(Pl. 500x500x25) with 6x 40mm holes	
1	(Pl. 480x200x40) Stiffener Plate	
2	(Pl. 480x40x40) Stiffener Plate	
1	(Pl. 500x240x10) End Plate with 2x 40mm holes	
2	(ABC Pipe) x2500mm with internal Diameter of 40mm	
2	(1½" Rods) x2650mm with threaded ends	(400 Mpa Steel)
2	(Corresponding A325 Nuts) W=60mm, H=37mm	
	Slab Reinforcement Including: (W_{Steel} =85kg)	For special detailing See Detail 16
	(#20 Rebars) x2540mm	
12	(#10 Rebars) x1380mm	
12	Concrete x0.25 m^3	
1		

	Build-up Test Set-up Assembly including:	See Detail 17
1	(Built-up Box of 25 & 20mm Plates) x1700mm	(Existing)
2	(W410x85) x2250mm, Large Beams	
6	(Pl. 380x120x8) Baten Plates	
8	(Pl. 380x80x8) Web Stiffeners	
2	(W200x59) x500mm, Load Applicators	
4	(Pl. 181x80x8) Stiffeners	
8	(1" A325 Bolts)	
16	(A325 M20 Bolts)	

Table 5.4. Continued (Bill of materials for foundation, deck slabs and test set-up)

Typical Instructions:

1) Steel material for W sections and plates: Grade CAN/CSA G40.21-M 350W
2) Steel material for rods and rebars: with strength of at least 400 MPa
3) Weld material: E480XX (Electrode classification)
4) All welds shall be accomplished by certified welder.
5) Concrete with strength of 30 MPa (f_c').

Table 6.1. Test program for experiments 1 to 8 of the end-diaphragm specimens

Experiment	Specimen	Original Test	Retest	Type of Diaphragm					Gravity Loads	Lateral Support*	Test Type	
				TADAS	EBF	SPS	Channel	None			Cyclic	PDT
1	1 (TADAS)	A		x					x	x	x	
2	1		B					x	x		x	
3	2 (EBF1)	A			x				x		x	
4	2 (EBF2)		B		x				x		x	
5	2		C					x				x
6	3 (SPS1)	A				x			x	x	x	
7	3 (SPS2)		B			x			x	x	x	
8	3 (Channel)		C				x		x		x	

* Lateral support was present during the experiment, to be provided if required. However, as per LVDTs fixed to measure the sideway movement of the ductile devices, these lateral deflections were mostly negligible.

Table 7.1. Comparison of experimental results with those predicted by the proposed analytical model for the specimens having ductile diaphragms

Specimen (1)	Analytical predictions			Test Results						
	δ_y (mm) (2)	P_y (kN) (3)	P_u^* (kN) (4)	δ_y^{**} (mm) (5)	Slippage of Connections (mm)				P_y (kN) (10)	P_u (kN) (11)
					(Estimated)	(Measured)		Total (9)		
					Braces (6)	Device (7)$^+$	Girder (8)$^{++}$			
TADAS	3.0	239	436	16.5	7.0	3.5	1.0	13.0$^{\square}$	280	450
EBF1	3.4	316	495	20	14	--	2.0	16.0	390	600
EBF2	3.4	316	495	5.5	--	--	1.5	1.5	350	630
SPS1	2.1	220	439	12	7.5	--	1.6	9.1	295	500
SPS2	2.1	220	439	16	8.1	3.5	1.5	13.1	290	440

* Corresponding to the failure of the specimens

** Including slippage, when strain gages on ductile device showed evidence of yielding

$^+$ Measured from revealed unpainted surface

$^{++}$ As per LVDTs fixed to the foundation to measure girders slippage

$^{\square}$ Including a gap of 1.5 mm at the grooves of TADAS

Table 7.2. Hysteretic energy values for the TADAS and the first specimen without diaphragm.

Experiment #1 (TADAS specimen)						Experiment #2 (without diaphragm)					
Cycle (1)	Drift (mm) (2)	Drift (%) (3)	Load (kN) (4)	E_H (kN-mm) (5)	ΣE_H (kN-mm) (6)	Cycle (7)	Drift (mm) (8)	Drift (%) (9)	Load (kN) (10)	E_H (kN-mm) (11)	ΣE_H (kN-mm) (12)
1-3	2.4	0.2	90	0	0	1-3	6	0.5	60	0	0
4-6	4.7	0.4	125	300	900	4-6	12	1	115	275	825
7-9	10.5	0.9	220	1580	5640	7-9	18	1.52	150	2030	6915
10	14	1.2	260	2790	8430	10-12	24	3	160	3570	17625
11-13	18	1.5	340	5500	24930	13-15	36	4	170	7860	41205
14-16	24	2	380	9640	53850	16	48	4	175	12090	53295
17-19	34	2.8	440	21235	117560	17-18	48	5	160	10440	74175
20	44	3.7	460	35390	152950	19	60	6	150	13740	87915
21	44	3.7	400	30120	183070	20	72	6	140	17310	105225
						21-22	72	8	120	11000	127225
						23	96	8	100	18680	145905
						24	96	8	90	12090	158000
						25	96		80	11000	167000

Table 7.3. Hysteretic energy values for the EBF1 and EBF2 specimens

Experiment #3 (EBF1 specimen)						Experiment #4 (EBF2 specimen)					
Cycle (1)	Drift (mm) (2)	Drift (%) (3)	Load (kN) (4)	E_H (kN-mm) (5)	ΣE_H (kN-mm) (6)	Cycle (7)	Drift (mm) (8)	Drift (%) (9)	Load (kN) (10)	E_H (kN-mm) (11)	ΣE_H (kN-mm) (12)
1-3	1.5	0.13	80	140	420	1-3	2.0	0.17	150	0	0
4-6	3	0.25	110	550	2070	4-6	4.5	0.38	300	380	1140
7-9	4.5	0.38	135	820	4530	7-9	6.0	0.5	370	1200	4740
10-12	6	0.5	150	1360	8610	10-12	8.0	0.67	420	2830	13230
13-15	12	1	260	2380	15750	13-15	12	1	500	7660	36210
16	18	1.5	390	6060	21810	16-18	16	1.3	570	13680	77250
17-18	18	1.5	370	5520	38370	19-21	24	2	640	28860	163830
19	24	2	480	9670	48040	22	32	2.7	400	29810	193640
20-21	24	2	450	8990	66020						
22	36	3	600	27650	93670						
23	36	3	600	25900	119570						
24	36	3	590	24800	144370						

Table 7.4. Hysteretic energy values for the SPS1 and SPS2 specimens

Experiment #6 (SPS1 specimen)						Experiment #7 (SPS2 specimen)					
Cycle (1)	Drift (mm) (2)	Drift (%) (3)	Load (kN) (4)	E_H (kN-mm) (5)	ΣE_H (kN-mm) (6)	Cycle (7)	Drift (mm) (8)	Drift (%) (9)	Load (kN) (10)	E_H (kN-mm) (11)	ΣE_H (kN-mm) (12)
1-3	1.5	0.13	60	0	0	1-3	3	0.25	60	60	180
4-6	2.8	0.23	95	120	360	4-6	6	0.5	100	480	1620
7-9	6	0.5	180	480	1800	7-9	9	0.75	140	840	4140
10-12	9	0.75	250	1200	5400	10-12	12	1	200	1320	8100
13-15	12	1	310	2510	12930	13-15	15	1.25	280	2100	14400
16-18	18	1.5	400	6570	32640	16-18	18	1.5	340	3460	24780
19	21	1.75	420	9850	42490	19	21	1.75	360	5670	30540
20-22	24	2	450	13140	81910	20-22	24	2	400	7760	53730
23-25	30	2.5	480	21610	146740	23-25	30	2.5	440	13250	93480
26-27	36	3	500	30570	207880	26	36	3	450	21850	115330
28	36	3	450	29250	237130	27	36	3	370	19110	134440
29	36	3	350	22090	259220						

Table 7.5. Hysteretic energy values for the Channel diaphragm specimen and the specimen without diaphragm tested pseudodynamically.

Experiment #8 (Channel diaphragm specimen)						Experiment #5 (pseudodynamic)		
Cycle (1)	Displ. (mm) (2)	Displ. (%) (3)	Load (kN) (4)	E_H (kN-mm) (5)	ΣE_H (kN-mm) (6)	Cycle (7)	E_H (kN-mm) (8)	ΣE_H (kN-mm) (9)
1-3	1.5	0.125	25	0	0	1	0	0
4-6	3	0.25	40	70	210	2	1040	1040
7	4.5	0.325	55	140	350	3	15600	16640
8-10	6	0.5	70	210	980	4	12800	29440
11	9	0.75	100	350	1330	5	8200	37640
12-14	12	1	125	490	2800	6	2840	40480
15-17	18	1.5	175	1580	7540	7	9200	49680
18-20	24	2	220	3920	19300	8	8800	58480
21-23	30	2.5	235	6950	40150	9	3200	61680
24-26	36	3	250	9790	69520	10	7200	68880
27-28	48	4	220	12630	107410	11	600	69480
29	48	4	190	9480	116890			
30	72	6	180	18320	135210			
31	72	6	160	10740	145950			

Table 8.1. Thicknesses along the gage length for rusted coupon specimens

Location (1)	Flange Coupon		Web 1 Coupon		Web 2 Coupon	
	Thickness (mm) (2)	t_{ave} (mm) (3)	Thickness (mm) (4)	t_{ave} (mm) (5)	Thickness (mm) (6)	t_{ave} (mm) (7)
1	7.87		9.53		11.3	
2	7.49	7.47	8.64	8.07	11.58	11.35
3	7.04		6.05		11.18	
4	8.18		9.65		11.18	
5	7.32	7.18	8.46	8.37	11.38	11.2
6	6.05		7.01		11.05	
7	9.65		8.89		11.05	
8	7.92	7.93	8	8.13	10.92	11.05
9	6.22		7.49		10.18	
10	7.42		8.38		11.13	
11	8.26	7.77	7.37	7.58	11.18	11.12
12	7.62		6.99		11.05	
13	8.89		9.02		11.1	
14	8.69	8.82	7.92	8.19	11.15	11.18
15	8.89		7.62		11.3	
16	8.13		8.38		11.51	
17	8.76	8.45	7.67	7.65	11.35	11.48
18	8.46		6.91		11.58	
19	8.05		8.33		11.18	
20	6.91	7.1*	7.26	7.37*	11.23	11.16
21	6.35**		6.53**		11.07	
22	7.92		9.07		10.6**	
23	7.87	7.48	8.2	8.13	10.8	10.8*
24	6.65		7.11		11	
25	8.56		10.41		10.69	
26	7.52	7.31	8.81	8.88	11.43	11.01
27	5.84		7.42		10.92	
28	8.26		10.54		11	
29	6.81	7.22	9.53	9.72	10.8	10.87
30	6.6		9.09		10.8	

* Minimum average thickness

** Minimum thickness at the critical section

Table 8.2. Thicknesses along rusted lacing plates

Location (1)	Lacing Plate Specimen 1		Lacing Plate Specimen 2	
	Thickness (mm) (2)	t_{ave} (mm) (3)	Thickness (mm) (2)	t_{ave} (mm) (3)
1	6.4		7.6	
2	6.0		7.2	
3	6.2	6.5	6.4	6.8
4	6.4		7.0	
5	7.5		5.9	
6	6.1		6.7	
7	5.2		6.9	
8	7.1	6.7	7.1	6.6
9	7.3		6.5	
10	7.9		5.9	
11	8.5		5.8	
12	8.5		6.2	
13	8.5	8.5	6.4	6.1
14	8.6		5.9	
15	8.2		6.2	

Table 8.3. Displacement Ductility and hysteretic energy values for SW-I and SW-II specimens

S-shape Web 1 (SW-I) Test						S-shape Web 2 (SW-II) Test					
Cycle (1)	Displ. (mm) (2)	Displ. (δ_y) (3)	Load (kN) (4)	E_H (kN-mm) (5)	ΣE_H (kN-mm) (6)	Cycle (7)	Displ. (mm) (8)	Displ. (δ_y) (9)	Load (kN) (10)	E_H (kN-mm) (11)	ΣE_H (kN-mm) (12)
1-3	6.3	0.5	3.0	0	0	1-3	5.5	0.5	2.0	0	0
4-6	12.5	1	6.2	14.7	44	4-6	11	1	3.3	11	33
7-9	25	2	9.0	243	773	7-36	22	2	4.7	109	3300
10-12	37.5	3	10.0	823	3242	37-66	33	3	5.5	272	11460
13-41	50	4	11.2	1045	33547	67-89	44	4	6.1	479	22477
42-43	50	4	11.0	960	35467	90-91	44	4	5.8	435	23347
44	50	4	10.8	914	36381	92-94	44	4	5.5	418	24601
45	50	4	9.8	874	37255	95	44	4	5.0	395	24996
46	50	4	8.4	800	38055	96-98	44	4	4.5	366	26094
47	50	4	8.2	725	38780	99-100	44	4	3.9	340	26774
48-52	50	4	7.5	663	42095	101-103	44	4	3.6	306	27692
53	75	5	7.7	1170	43265	104-105	44	4	3.1	278	28248
54	75	5	6	1114	44379	106	44	4	2.7	253	28501
55	75	5	4.6	1028	45407	107	55	5	2.4	397	28898
56	75	5	2.6	857	46264	108-109	55	5	2	376	29650
						110	55	5	1.3	350	30000
$\Sigma E_H/Py\delta y=600$						$\Sigma E_H/Py\delta y=820$					

Fig. 2.1. Restraining cables added to older existing bridges to prevent girders from falling off of their supports during earthquakes (Roberts 1992).

Fig. 2.2. A typical buckling of the X-configuration diaphragms on the Vun Duzen River bridge after the 1992 Mendecino earthquake (Roberts 1992).

Fig. 2.3. Severe buckling of diaphragm members on the same bridge (Roberts 1992).

Fig. 2.4. The north girder span of the same bridge (restrainer cables on the left side of the girder are slack while in the right side they are taut, showing a movement to the left; Roberts 1992).

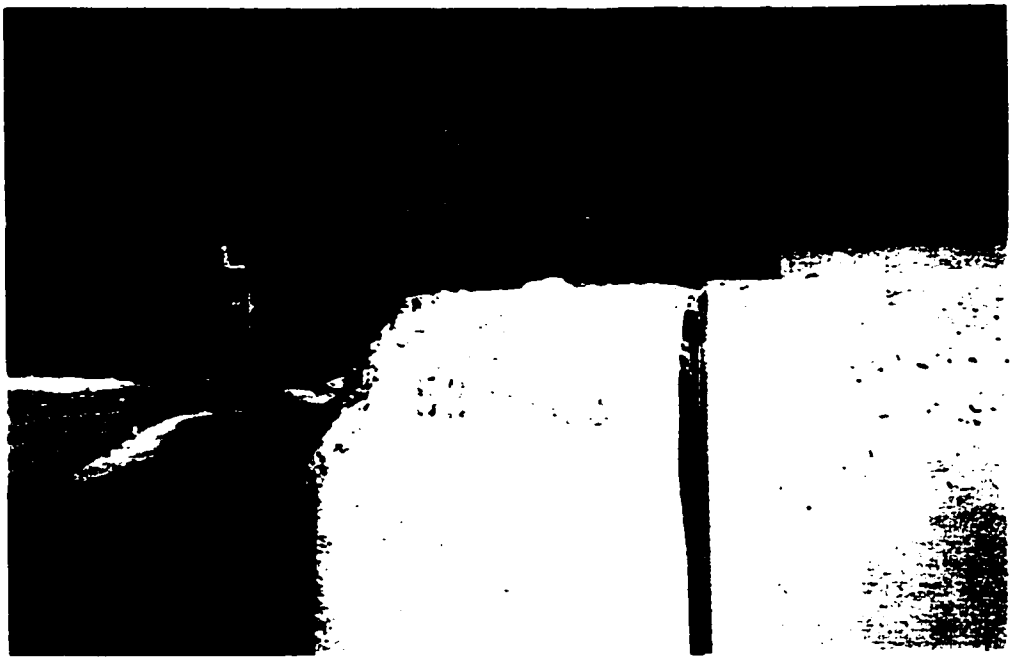

Fig. 2.5. Damage to seismic restrainer angle at roller bearing of the Southern bridge in the 1994 Nothridge earthquake (Astaneh-Asl et al. 1994).

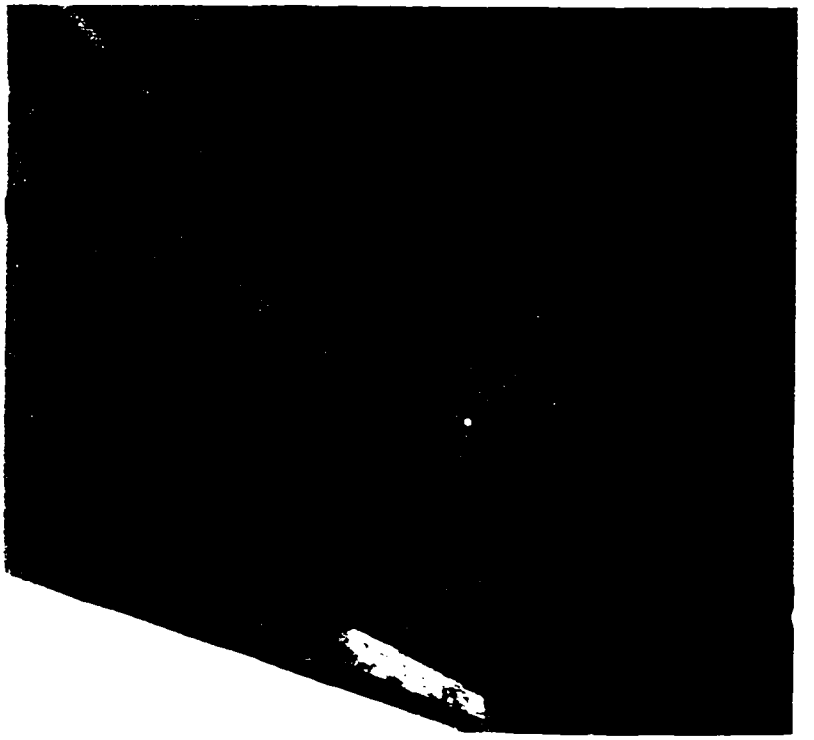

Fig. 2.6. Bending of web stiffener at the end-diaphragm of the Northern bridge damaged in the Northridge earthquake (Astaneh-Asl et al. 1994).

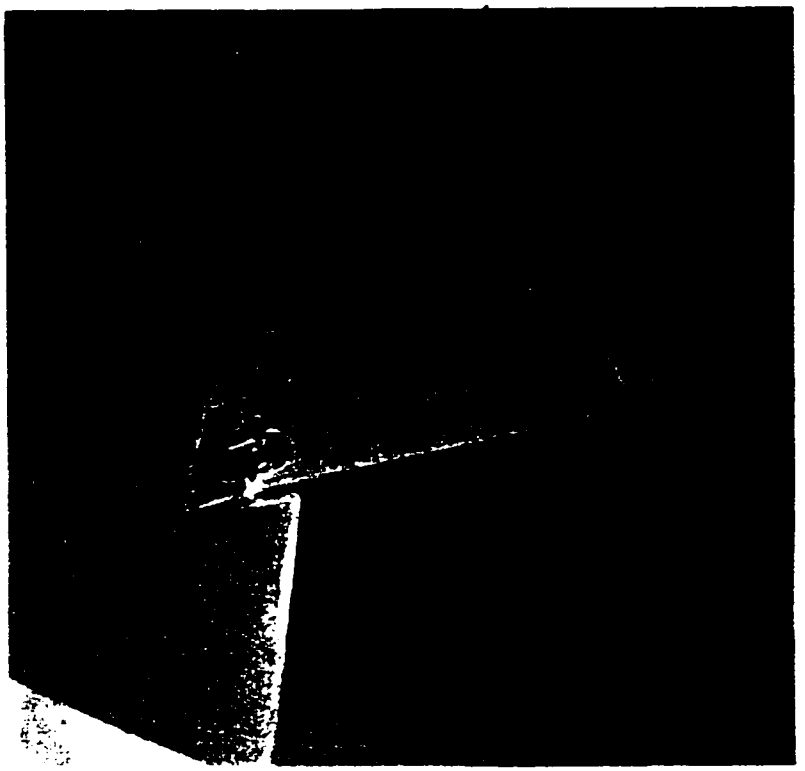

Fig. 2.7. Fracture of diaphragm gusset plate at the east abutment of the Northern bridge damaged in the Northridge earthquake (Astaneh-Asl et al. 1994).

Fig. 2.8. Deformed shape of end-diaphragm due to buckling of the braces and bending of the lower horizontal member on the Old Road bridge damaged in the Northridge earthquake (Astaneh-Asl et al. 1994).

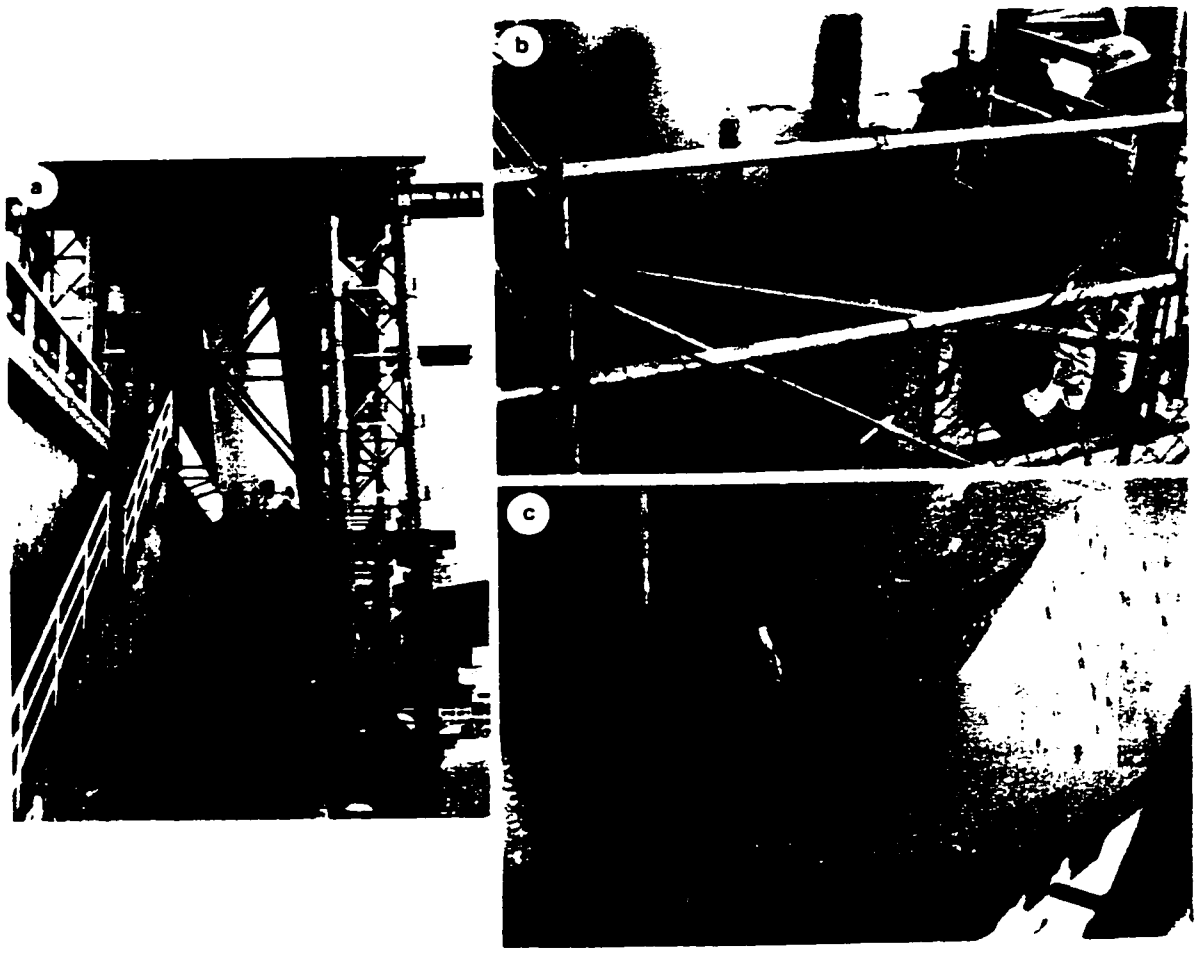

Fig. 2.9. Typical severe local buckling of circular steel columns after the 1995 Kobe earthquake: (a) elevation of a damaged column, (b) location of buckling and (c) close-up of fractured steel (Bruneau et al. 1996).

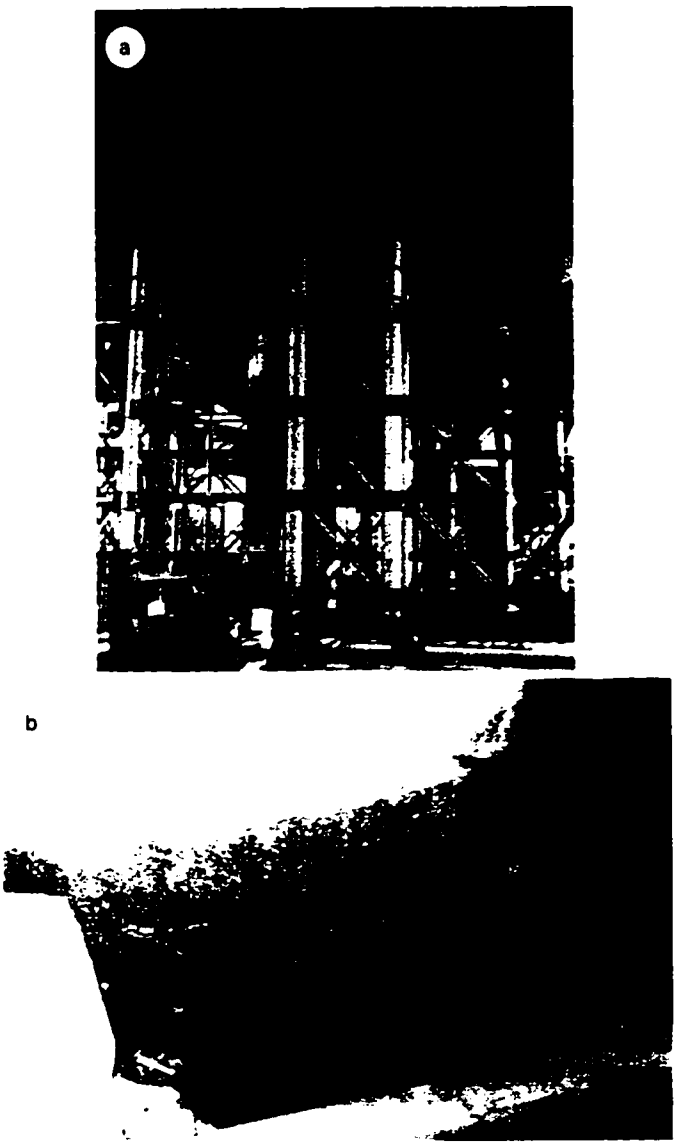

Fig. 2.10. Fracture in a rectangular steel column damaged in the Kobe earthquake: (a) global view of the column and (b) close-up view of fractured steel (Bruneau et al. 1996).

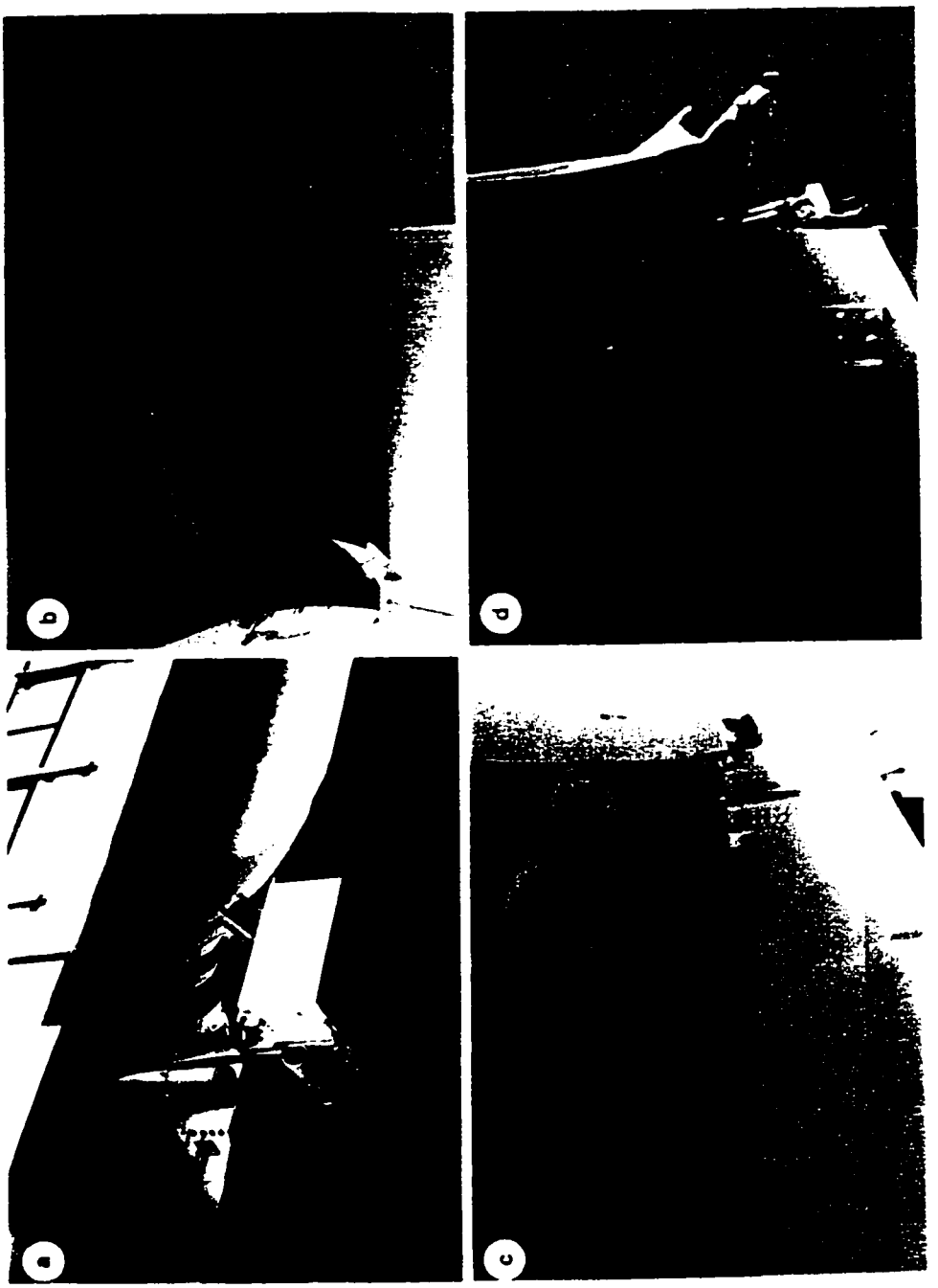

Fig. 2.11. Large transverse movements due to bearing failures on the Hanshin Expressway after the Kobe earthquake: (a) severe damage at the end of girders. (b) underside view showing tear-up of diaphragm members, (c) damage at the other end of same pier and (d) close-up view indicative of lateral movement (Bruneau et al. 1996).

Fig. 2.12. Strengthening of diaphragm by doubling braces in a pedestrian overpass in San Francisco (Mitchell et al. 1994).

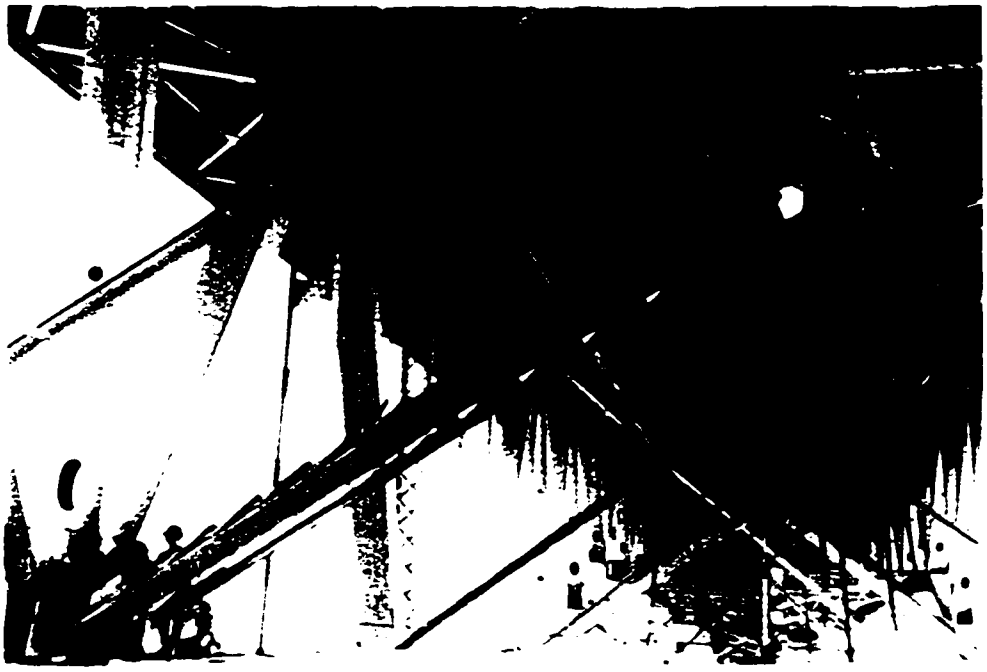

Fig. 2.13. Seismic retrofit of the Granville bridge in Vancouver by adding truss members (Mitchell et al. 1994).

Pier E1 is strengthened by adding reinforced concrete or composite jacket and its foundation is tied down to rock.

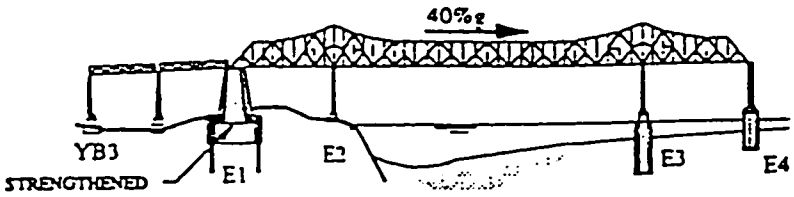

Strength Added While Original Articulation Maintained

Add semi-rigid connections to the base of Pier E9 to permit slight rocking during severe earthquakes. Reinforce bottom chord eyebars of trusses.

Add semi-rigid connections to the base of Pier E17 to permit slight rocking during severe earthquakes. Bottom chords of trusses may need strengthening.

Add semi-rigid connections to the truss shoes of each span.

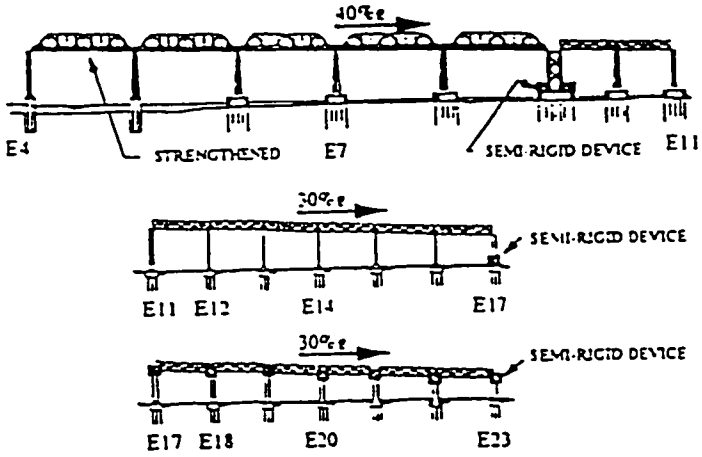

Fig. 2.14. Retrofit concepts proposed for the East Bay Crossing of the Bay bridge (Astaneh-Asl 1993).

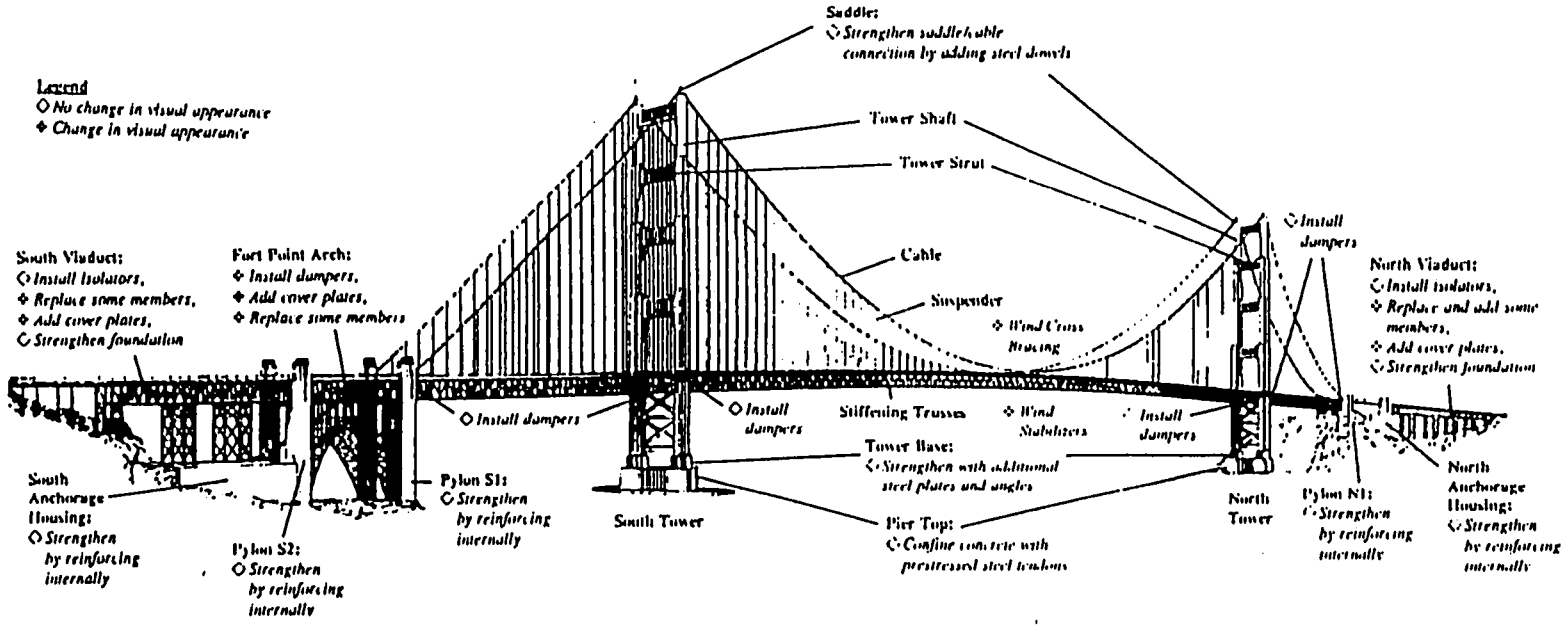

Fig. 2.15. Seismic retrofit measures for the Golden Gate bridge (Seim et al. 1993).

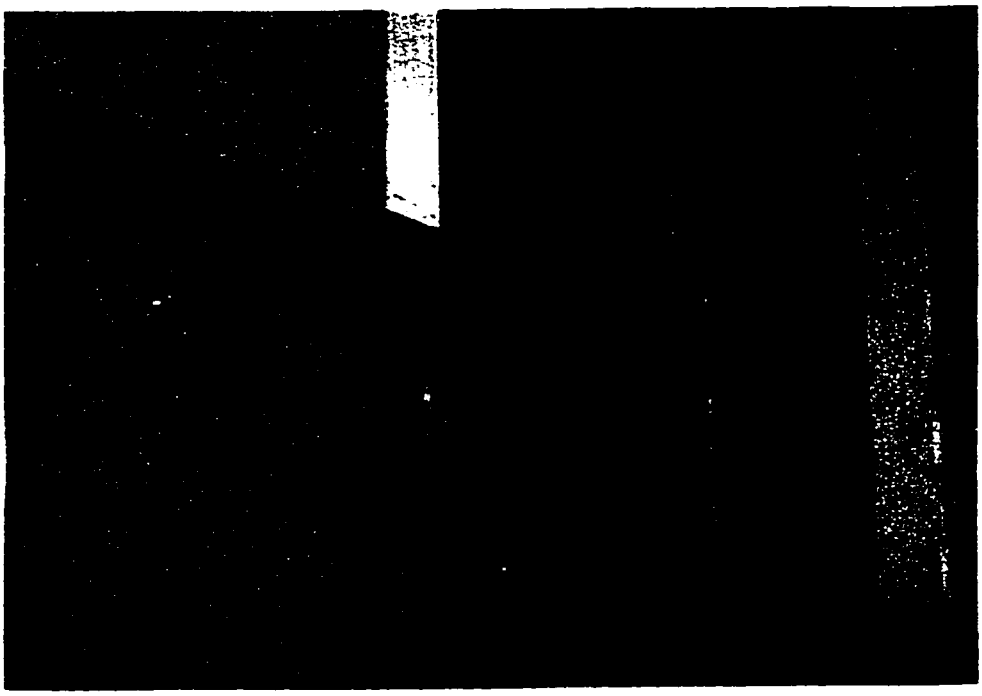

(a)

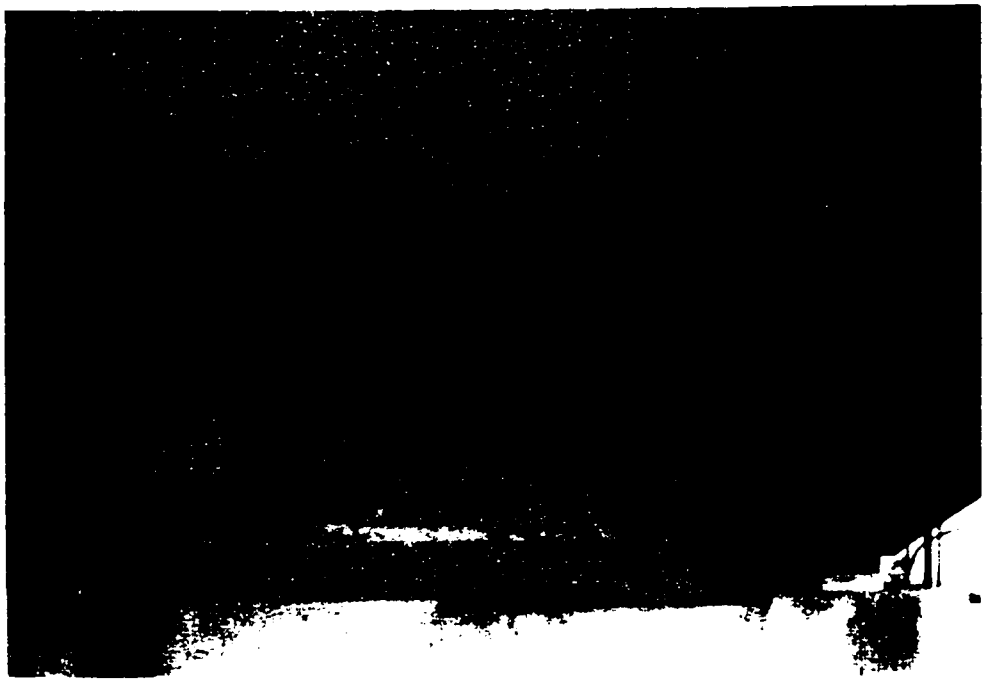

(b)

Fig. 3.1. Nominal end-diaphragms in existing slab-on-girder steel bridges: (a) close-up view of channel diaphragm used in a skew bridge in Ottawa, Ontario; (b) the same for another bridge in Quebec.

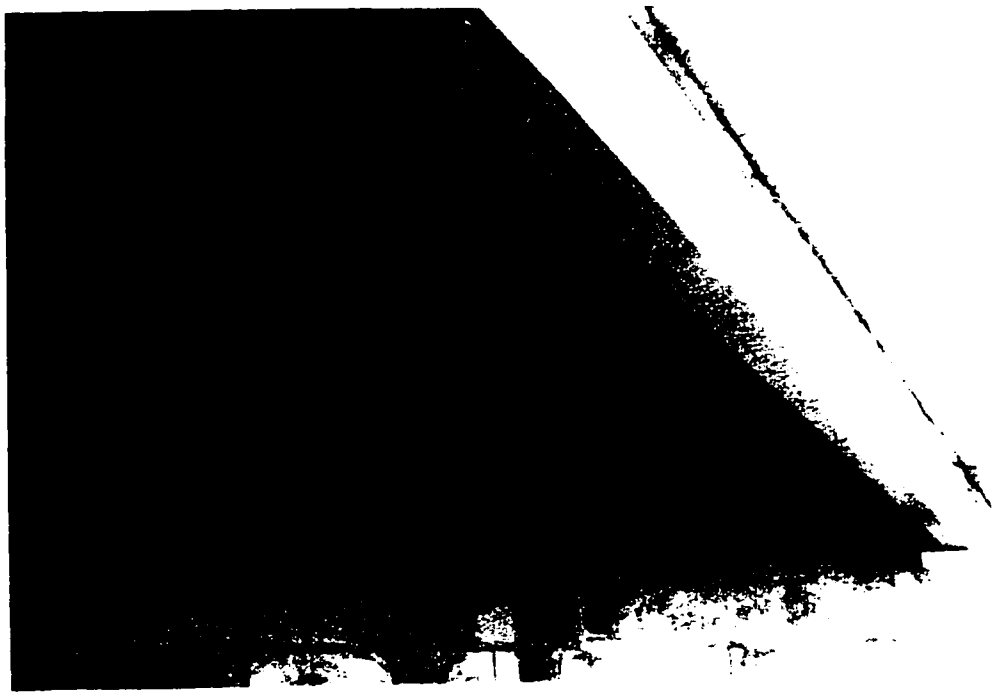

Fig. 3.2. Nominal intermediate diaphragms used in a bridge in Ottawa, Ontario.

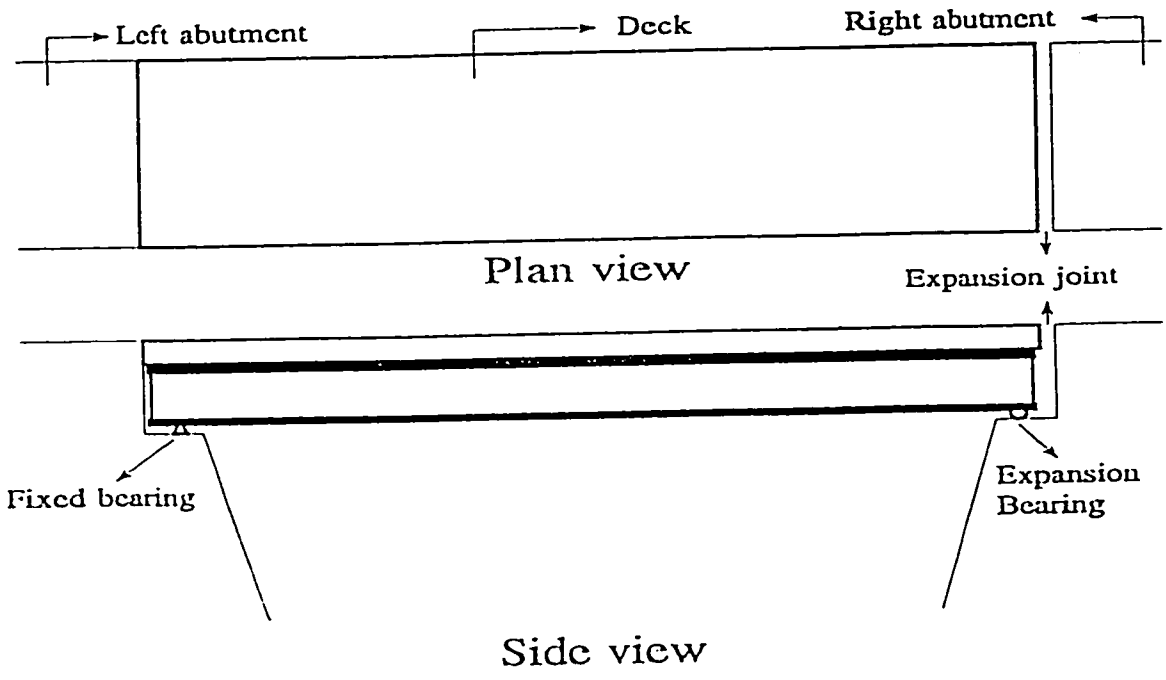

Fig. 3.3. Schematic of a single span simply supported bridge.

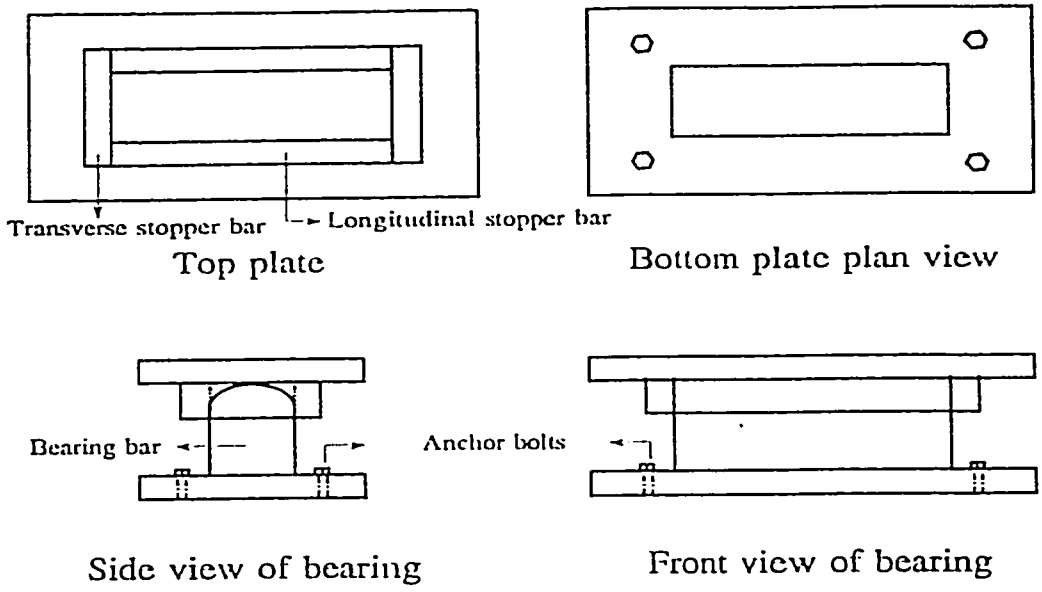

(a)

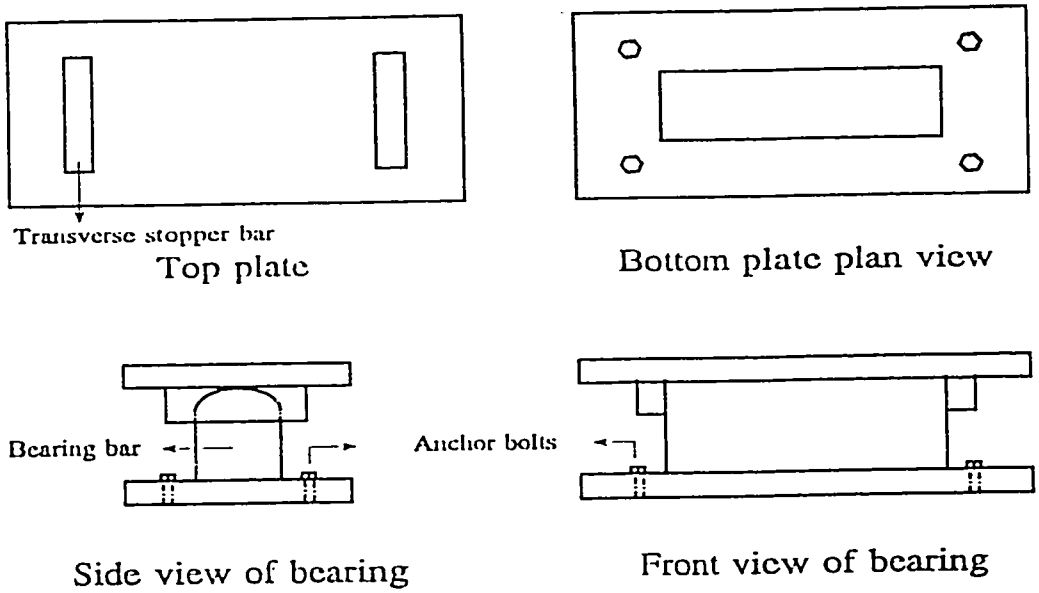

(b)

Fig. 3.4. Typical sliding bearings: (a) fixed bearing; (b) expansion bearing.

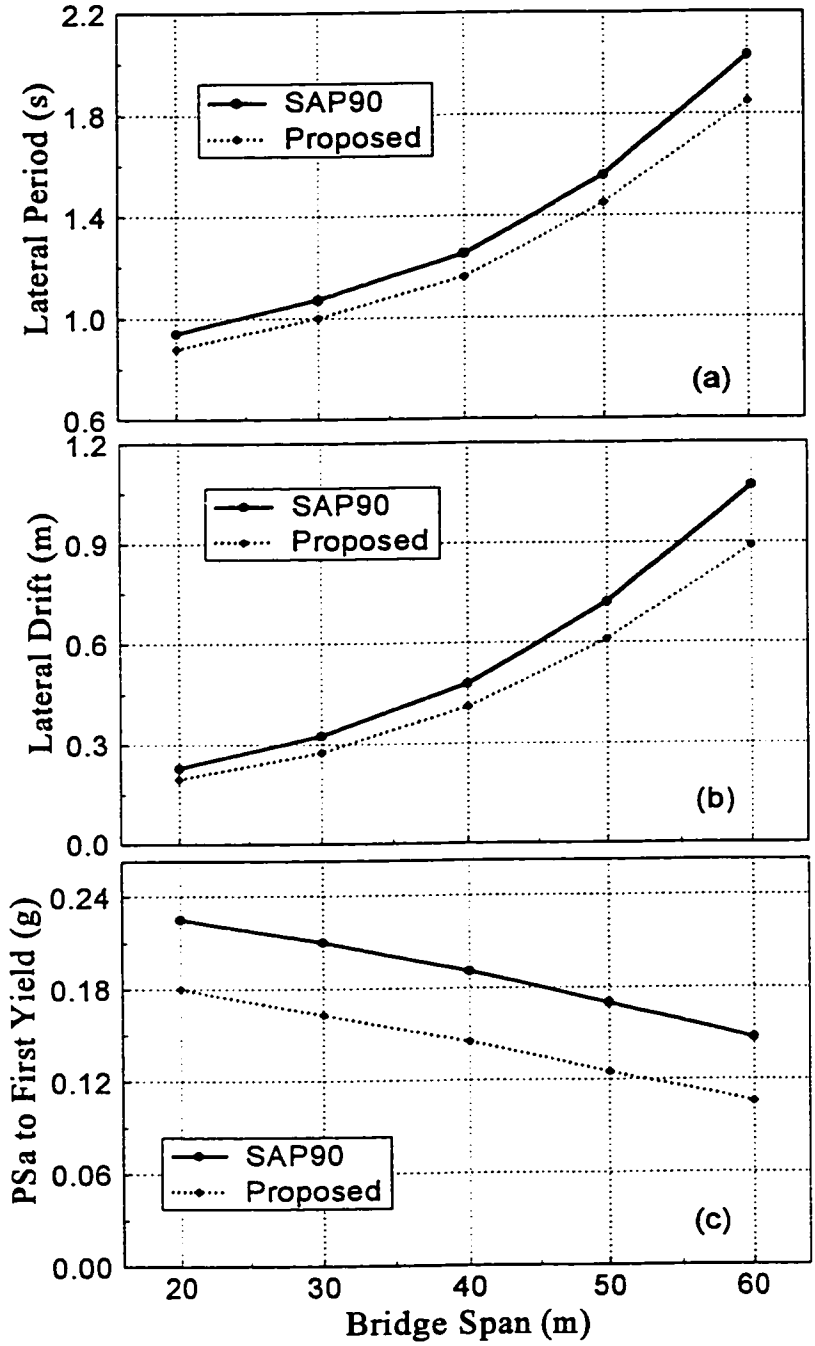

Fig. 3.5. Comparison of results for different bridges (laterally simply supported) obtained by SAP90 and proposed model: (a) lateral period; (b) lateral drift; (c) required *Psa* to bring the bridge to first yield.

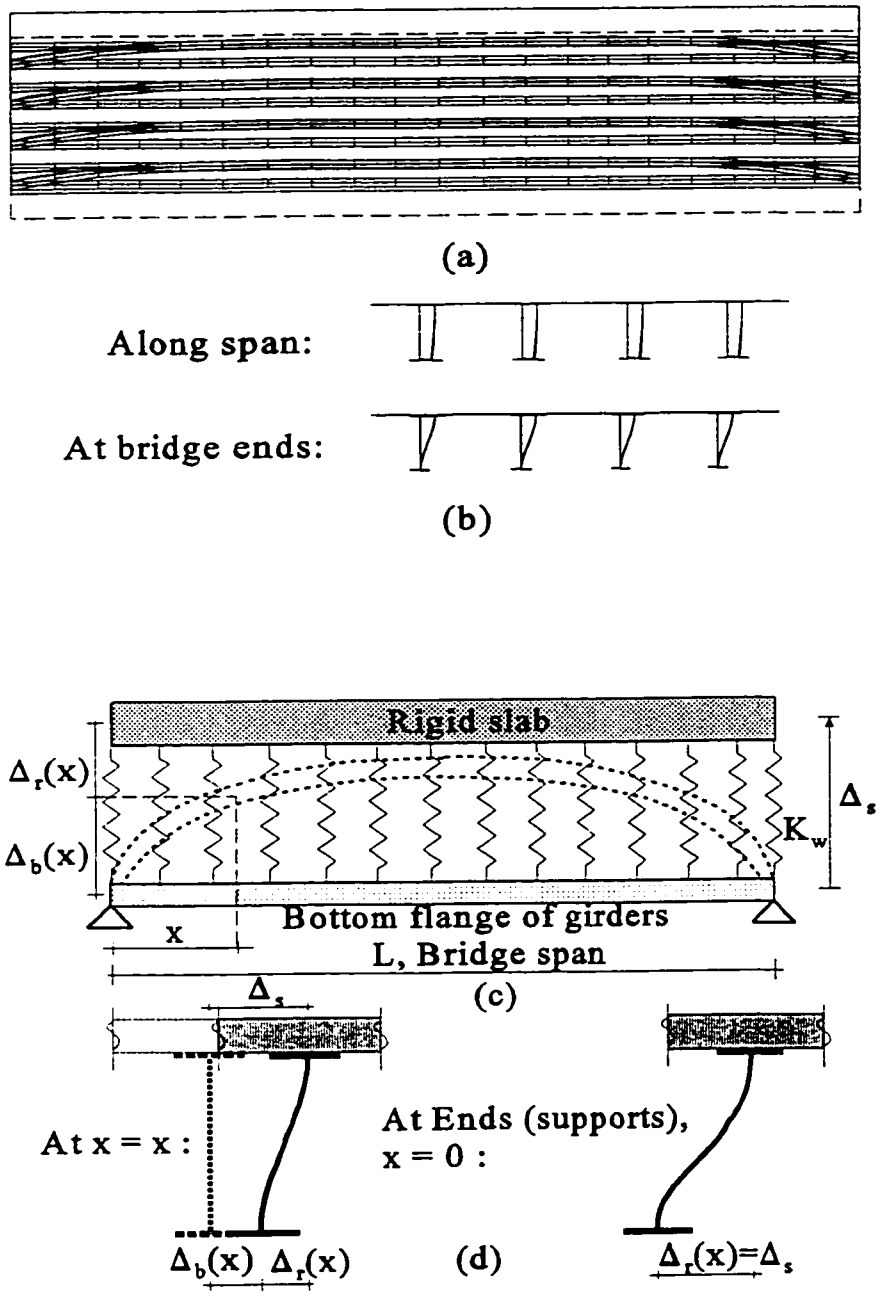

Fig. 3.6. SAP90 deformed shapes for typical bridges without diaphragm: (a) plan view; (b) side view; and schematic of simplified model without diaphragm: (c) plan view; (d) side view.

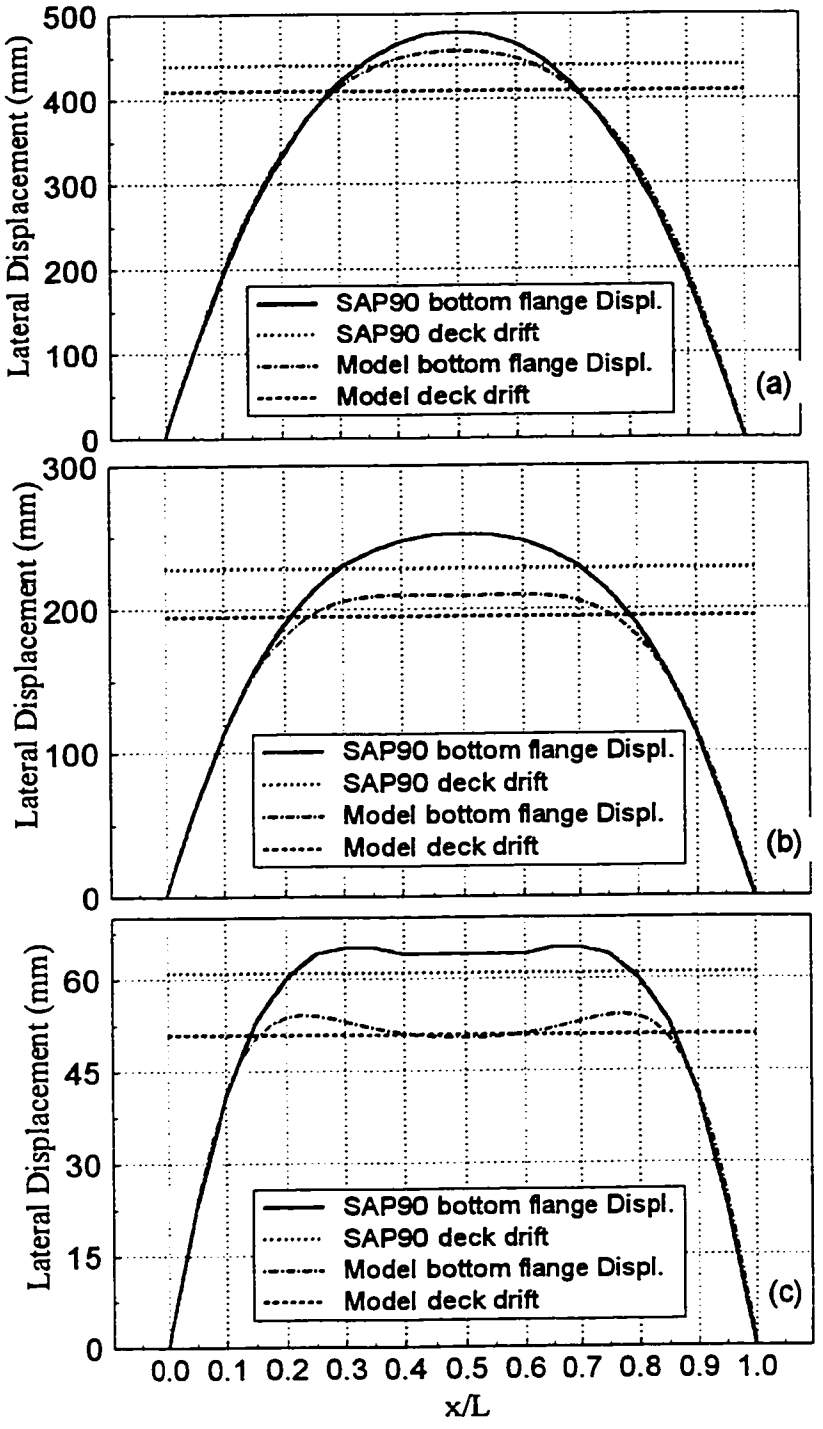

Fig. 3.7. Comparison of girder bottom flange displacements obtained by SAP90 and proposed model for a 20 m span bridge (simply supported laterally), respectively for girder web thickness of: (a) 8 mm; (b) 11 mm corresponding to the WWF800x184 in the original design; and (c) 20 mm.

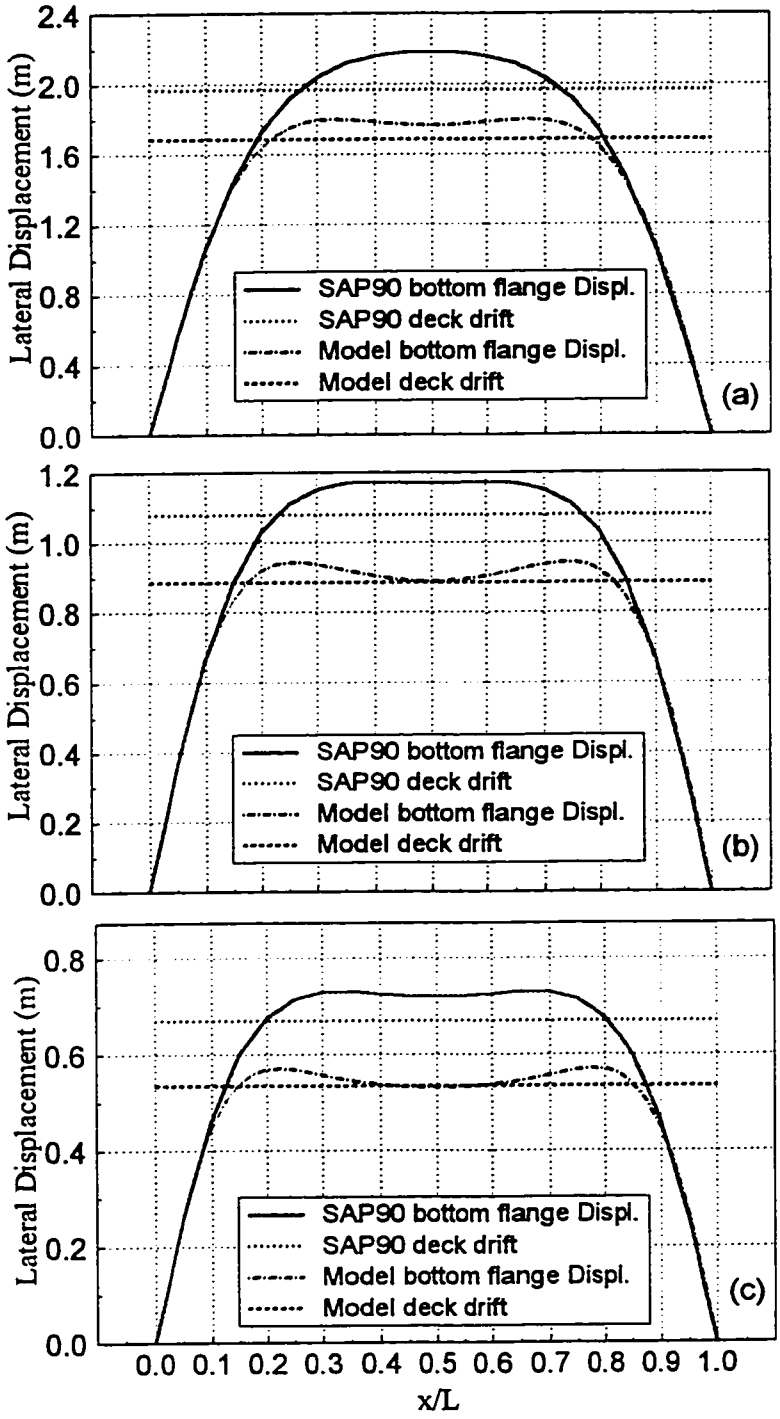

Fig. 3.8. Comparison of girder bottom flange displacements obtained by SAP90 and proposed model for a 60 m span bridge (simply supported laterally), respectively for girder web thickness of: (a) 12 mm; (b) 16 mm corresponding to the WWF1600x496 in the original design; and (c) 20 mm.

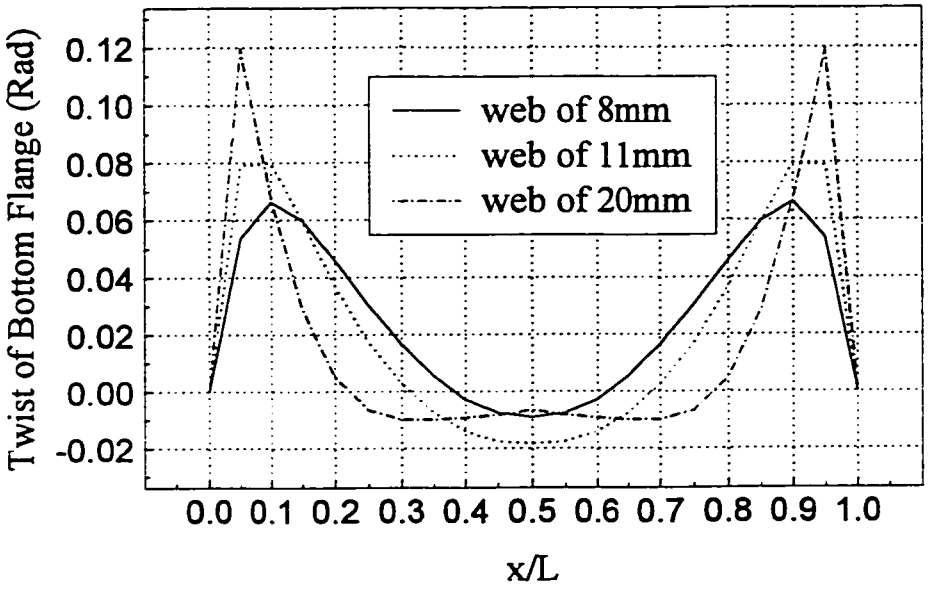

Fig. 3.9. Rotation of girder bottom flange for the 20 m span bridge (simply supported laterally), for a normalized 100 mm of maximum transverse displacement.

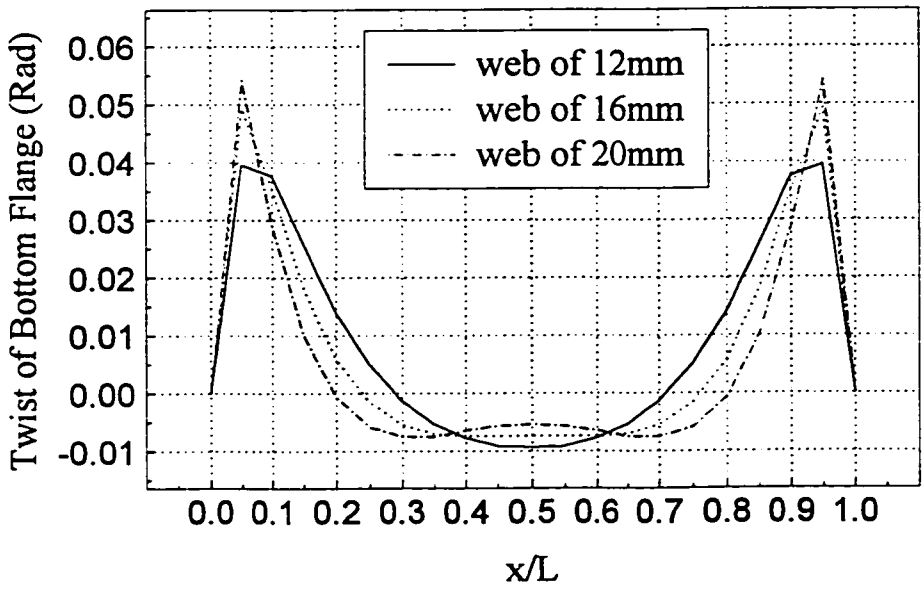

Fig. 3.10. Rotation of girder bottom flange for the 60 m span bridge (simply supported laterally), for a normalized 100 mm of maximum transverse displacement.

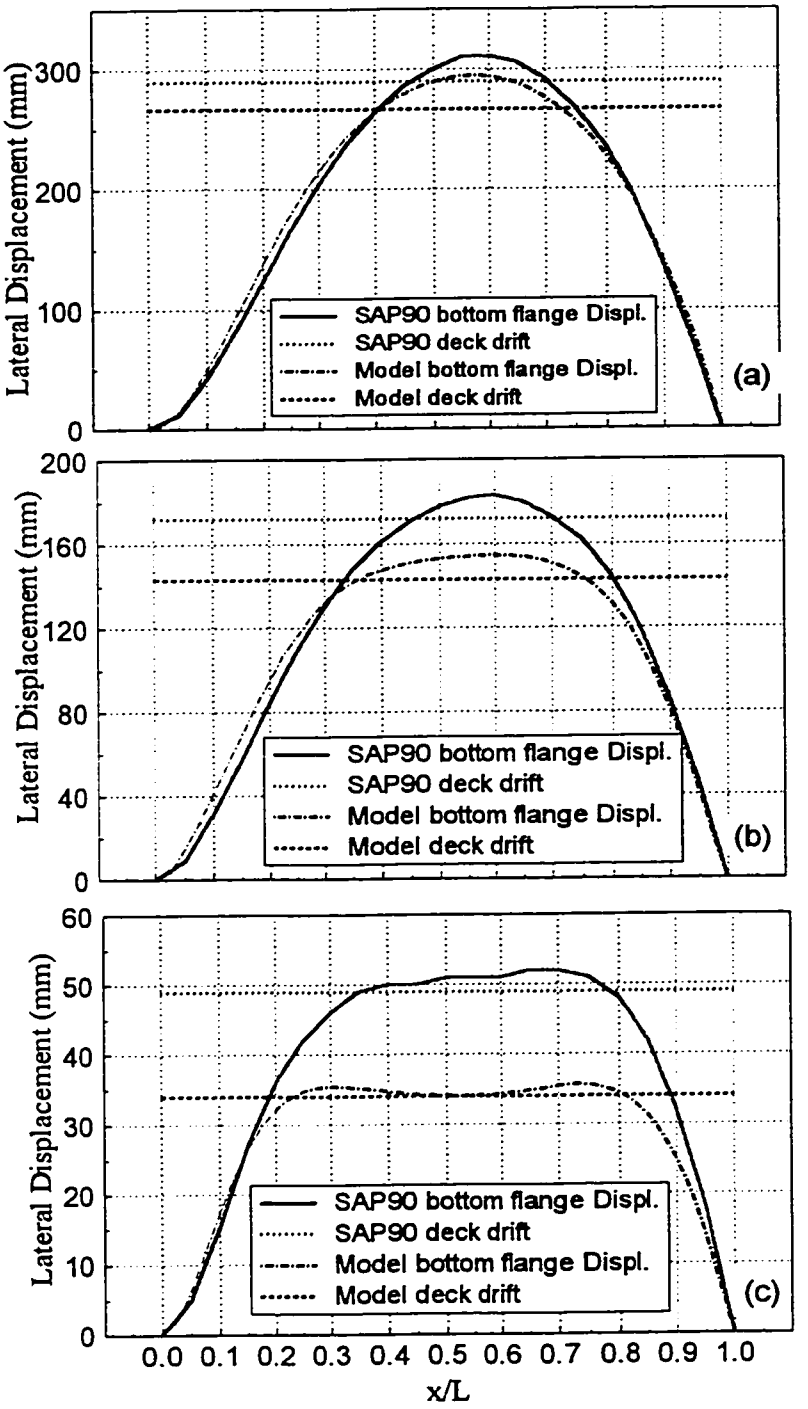

Fig. 3.11. Comparison of girder bottom flange displacements obtained by SAP90 and proposed model for a 20 m span bridge (laterally fixed at one end), respectively for girder web thickness of: (a) 8 mm; (b) 11 mm corresponding to the WWF800x184 in the original design; and (c) 20 mm.

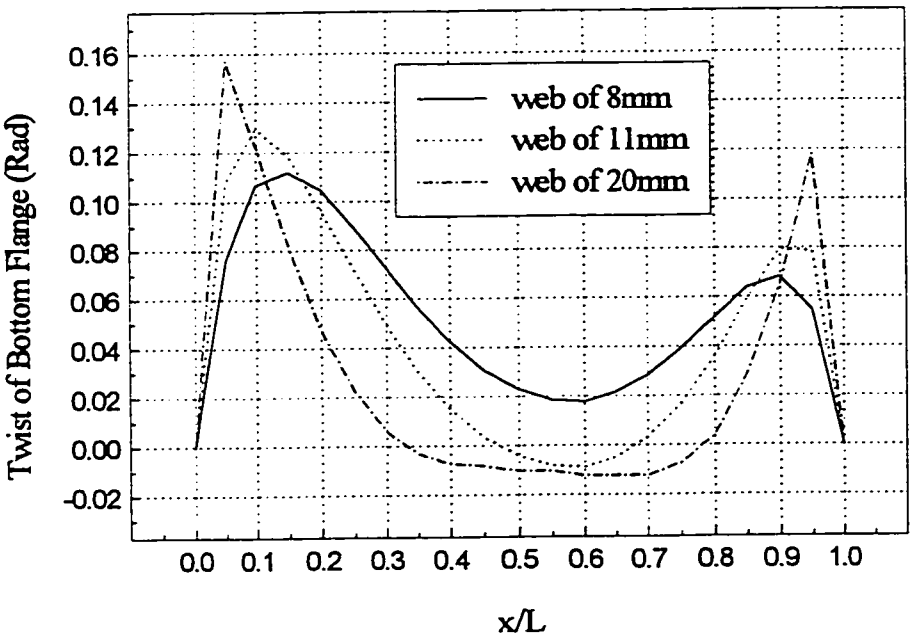

Fig. 3.12. Rotation of girder bottom flange for the 20 m span bridge (laterally fixed at one end), for a normalized 100 mm of maximum transverse displacement.

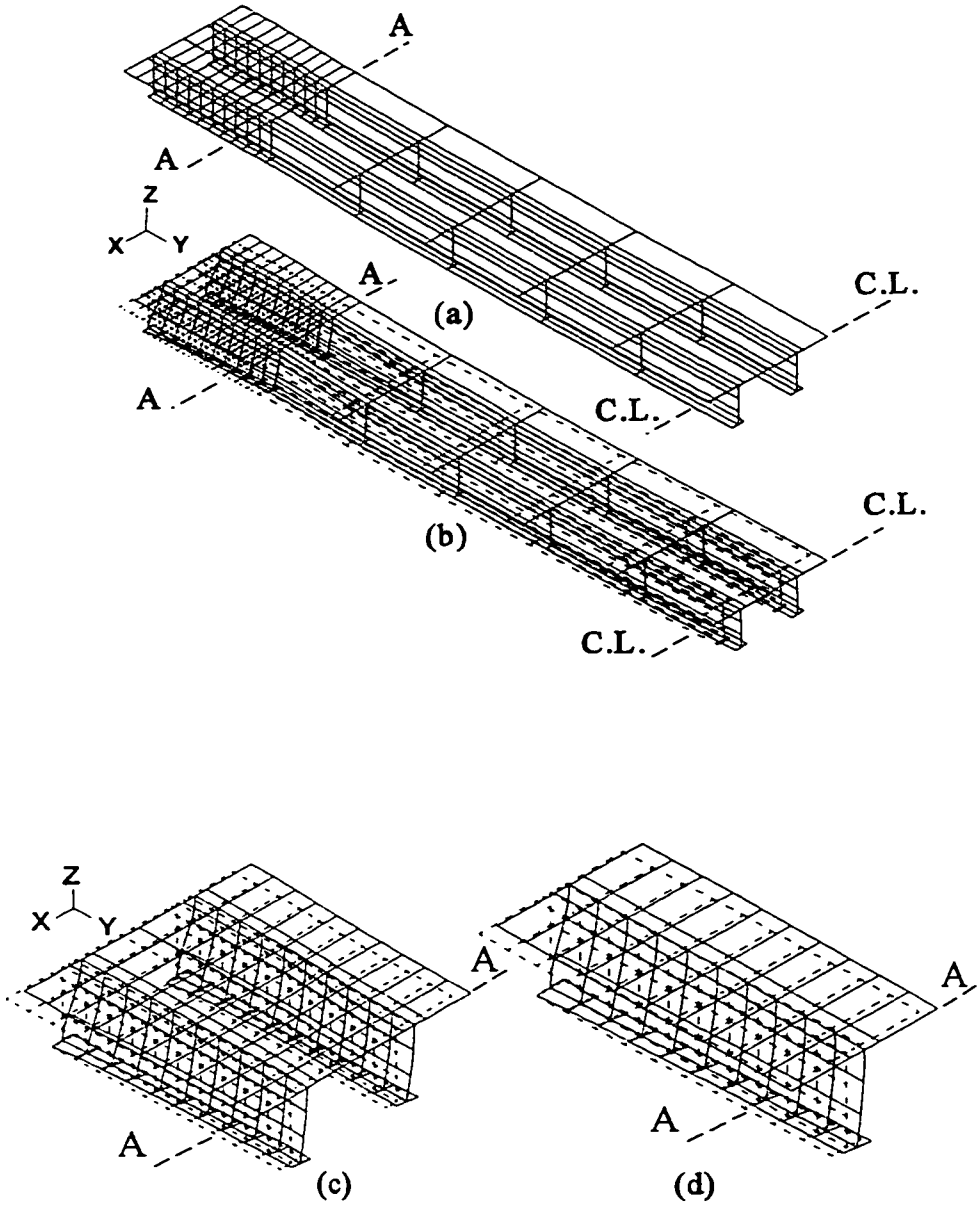

Fig. 3.13. ADINA modeling and deflected shapes for a 40 m span bridge without any diaphragm or web stiffeners: (a) undeformed shape (a quarter of the bridge is shown); (b) deflected shape; (c) close-up view of deformed shape near supports; (d) close-up of web deformation.

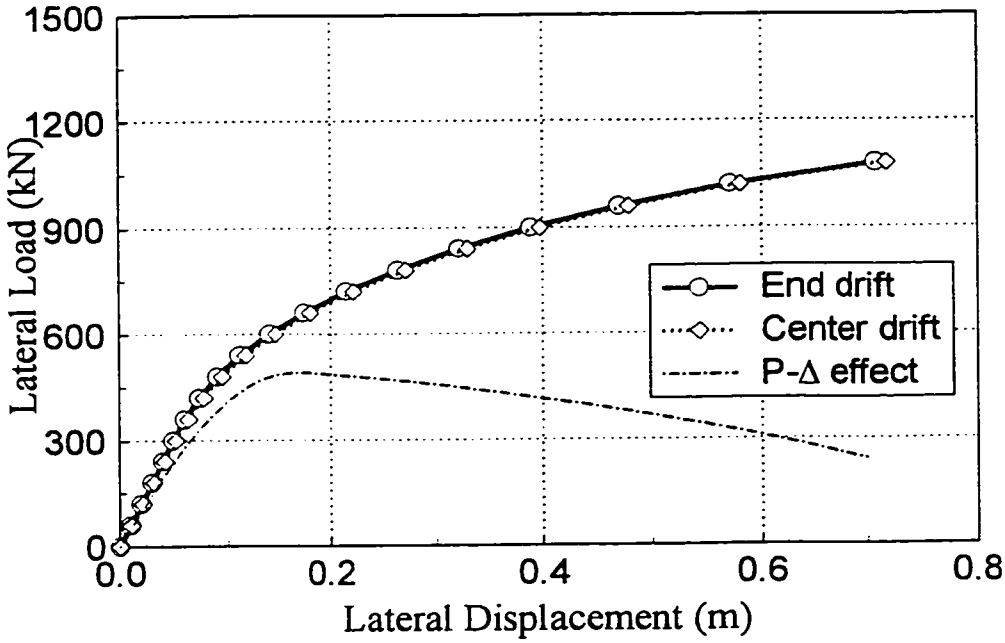

Fig. 3.14. Load-displacement curve for the 40 m span bridge with and without consideration of P-Δ effects.

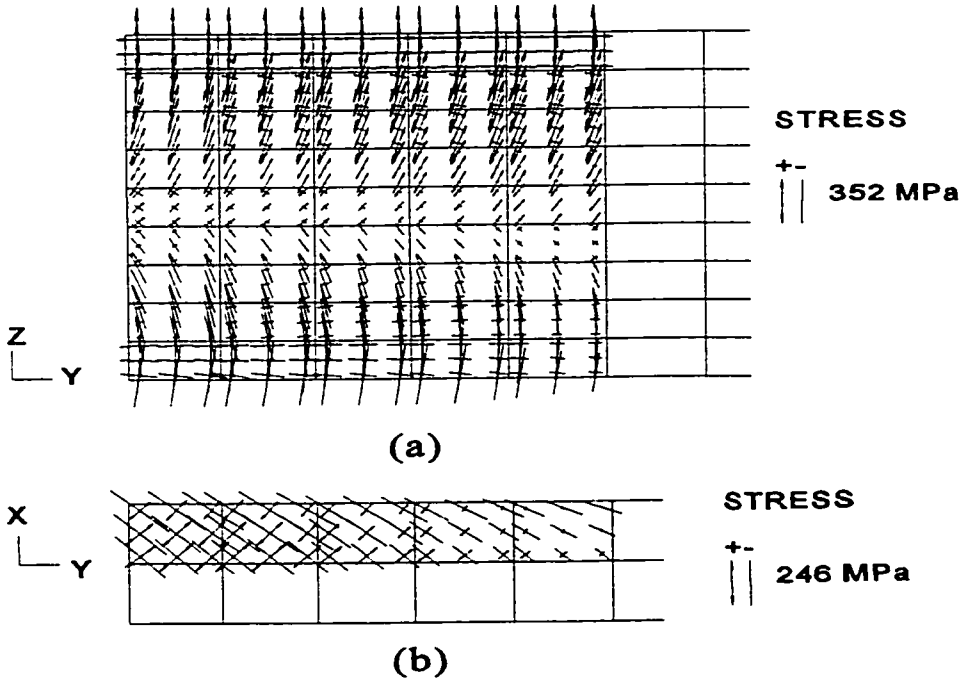

Fig. 3.15. Stress vectors for the steel girders of the 40 m span bridge near end support, obtained by ADINA: (a) in the web; (b) in the flange.

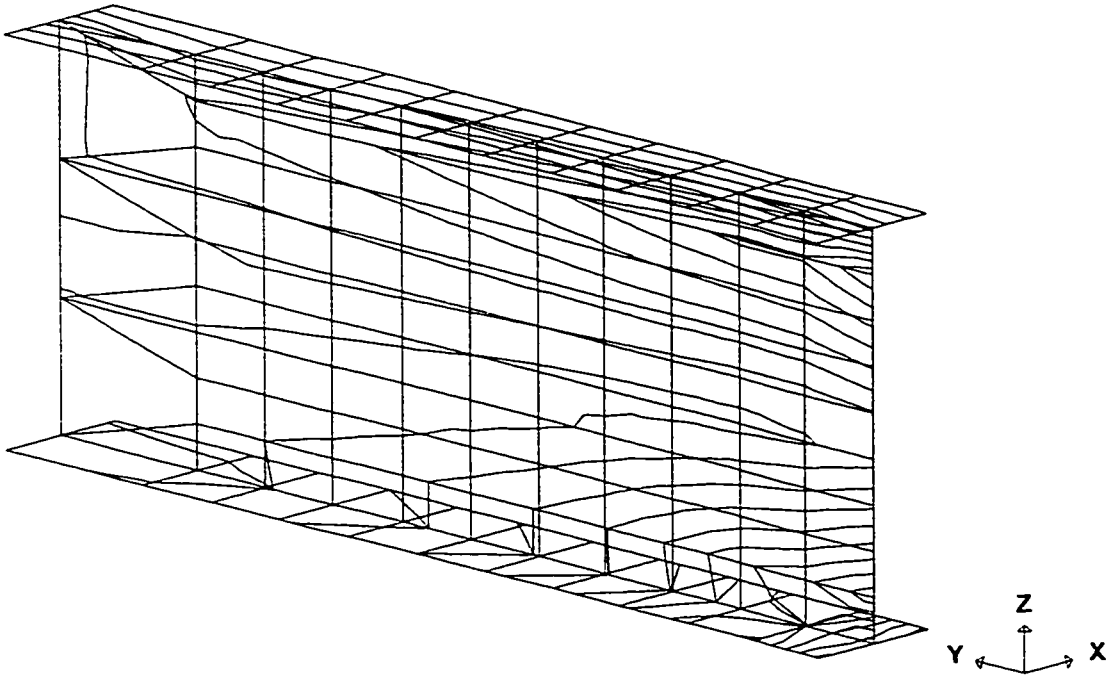

Fig. 3.16. Stress contours for the steel girder of the 40 m span bridge near end support, obtained by SAP90. Yield lines are in agreement with the ADINA results.

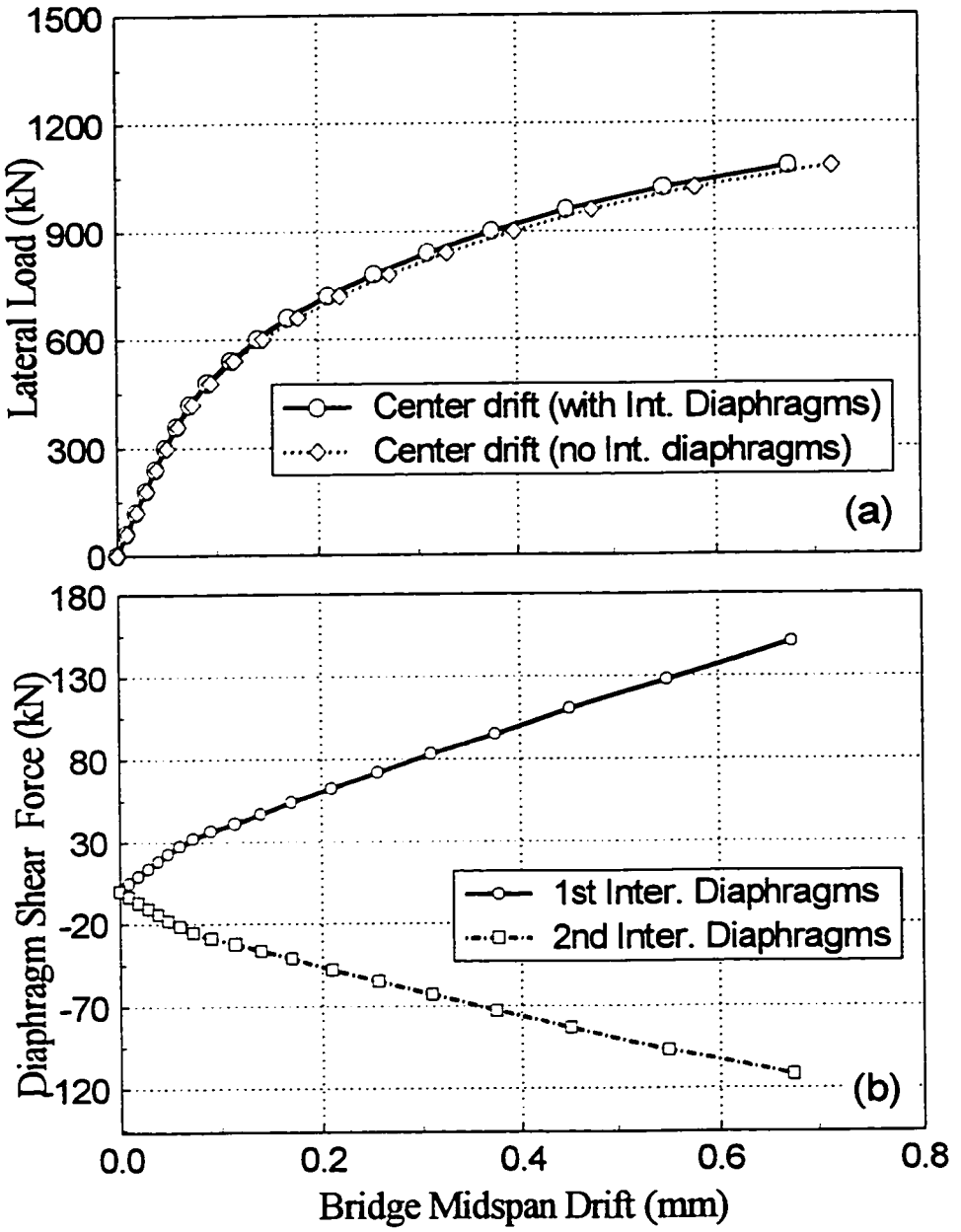

Fig. 3.17. Impact of intermediate diaphragms on the 40 m span bridge without end-diaphragm: (a) lateral load versus midspan drift; (b) horizontal shear force in the first and second intermediate diaphragms from bridge end.

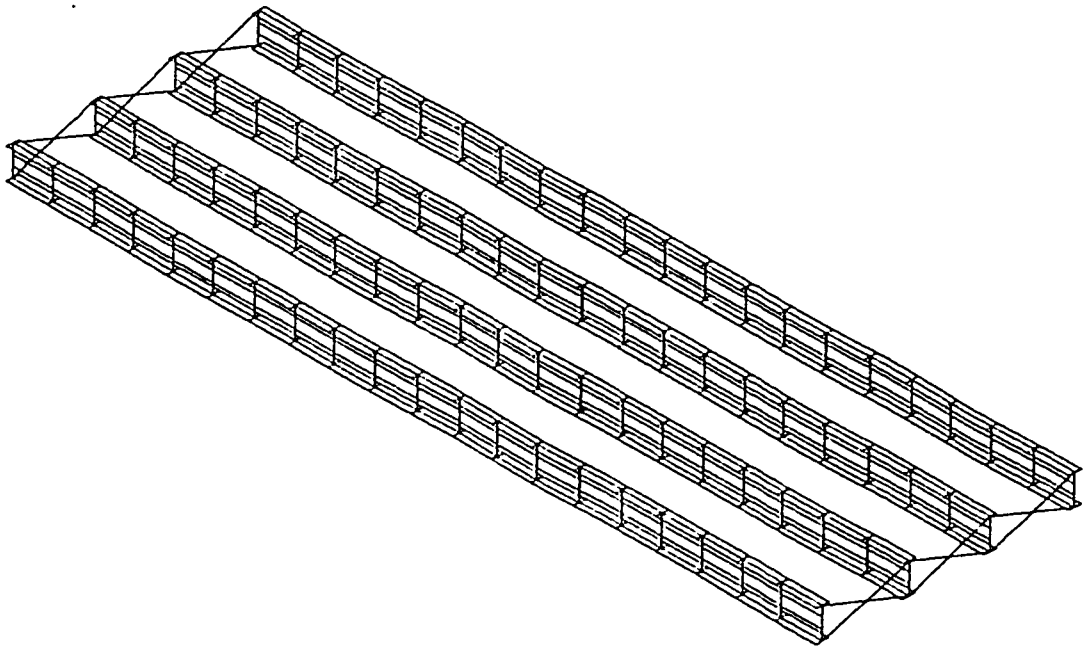

(a)

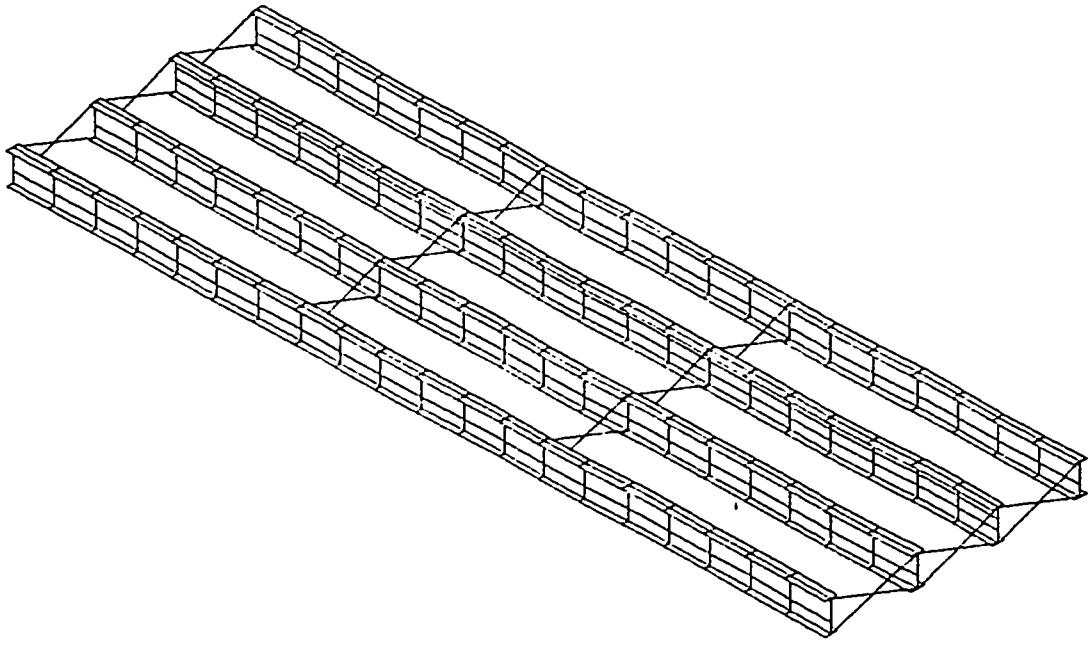

(b)

Fig. 3.18. Typical model (SAP90 modeling) of bridges with: (a) X-bracing at both ends; (b) intermediate X-bracing are present as well. Deck slab not shown.

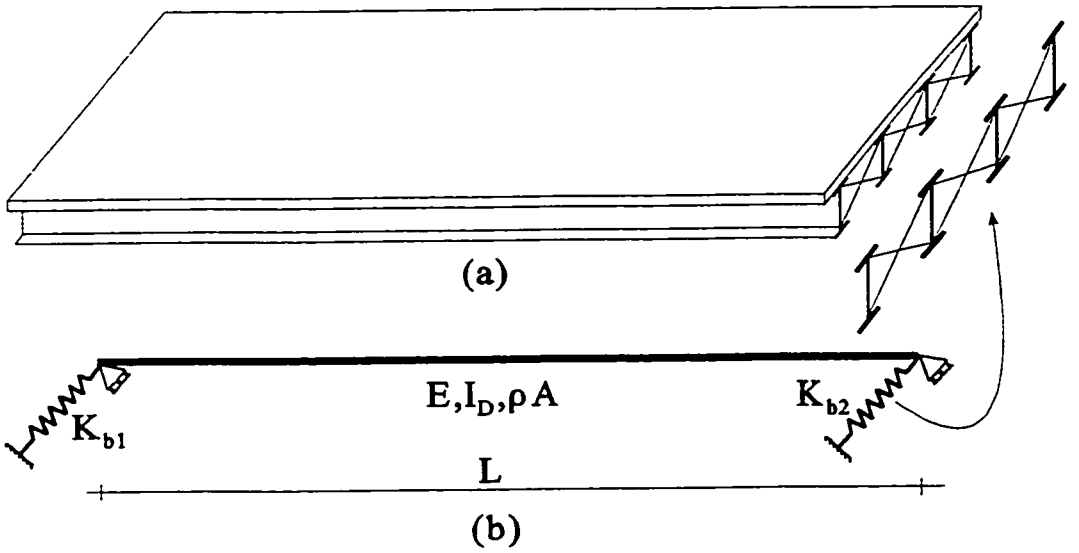

Fig. 3.19. Schematical simplified model for bridges with end-diaphragms.

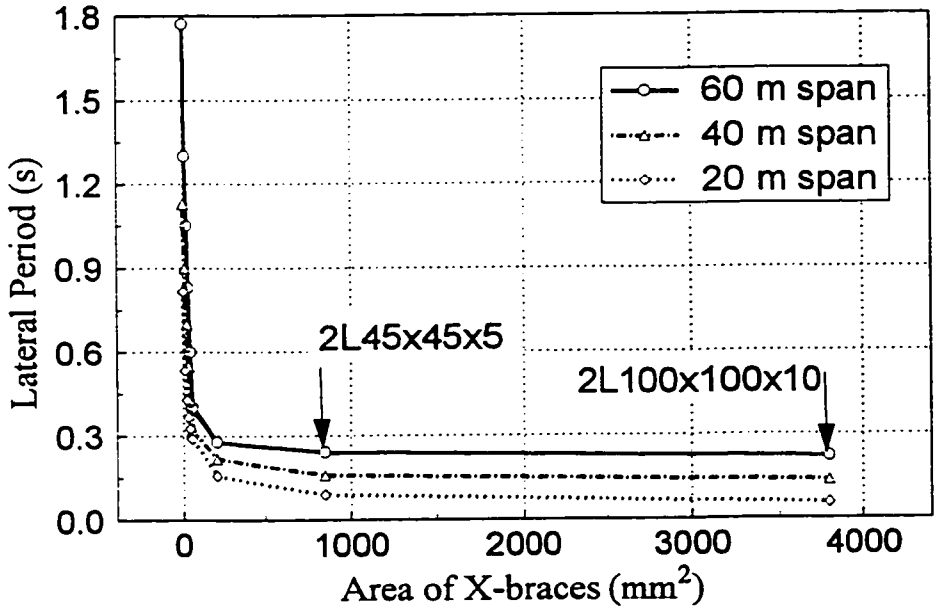

Fig. 3.20. Lateral period versus cross-sectional area of braces for 20 m, 40 m and 60 m span bridges (laterally fixed at one end).

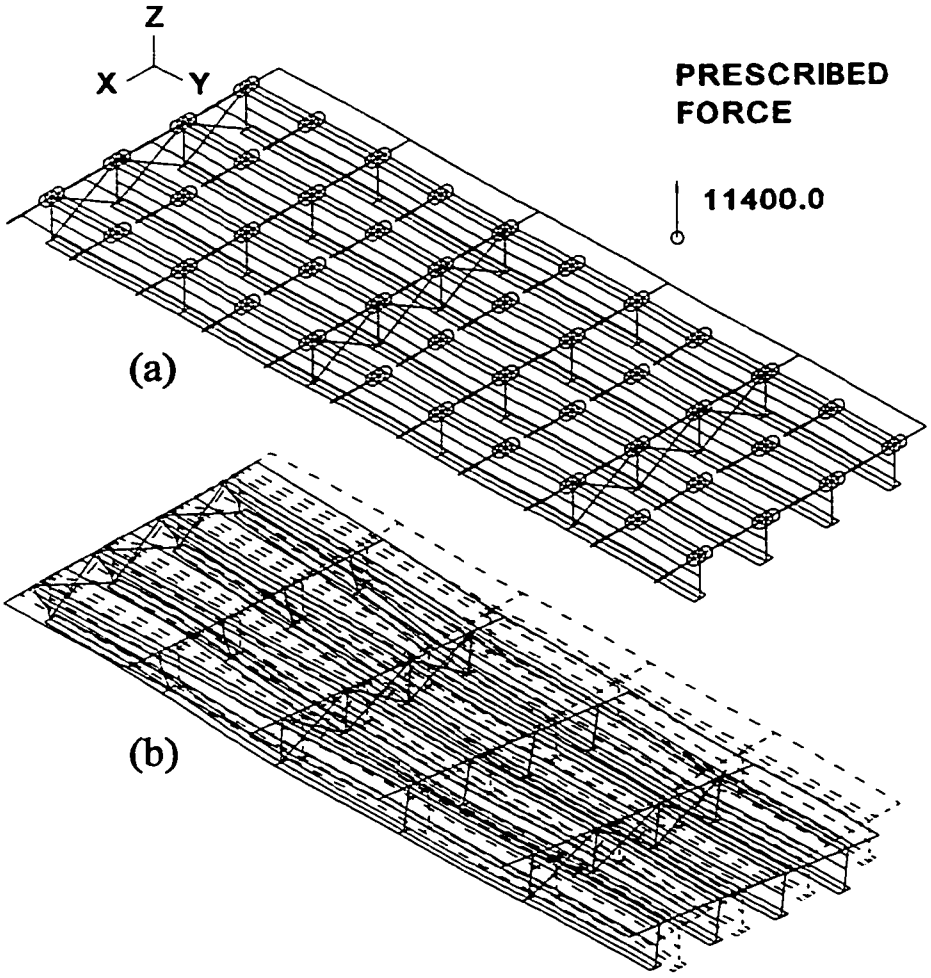

Fig. 3.21. ADINA modeling and deflected shape for a 40 m span bridge with effective diaphragms: (a) undeformed shape (half model is shown); (b) deflected shape.

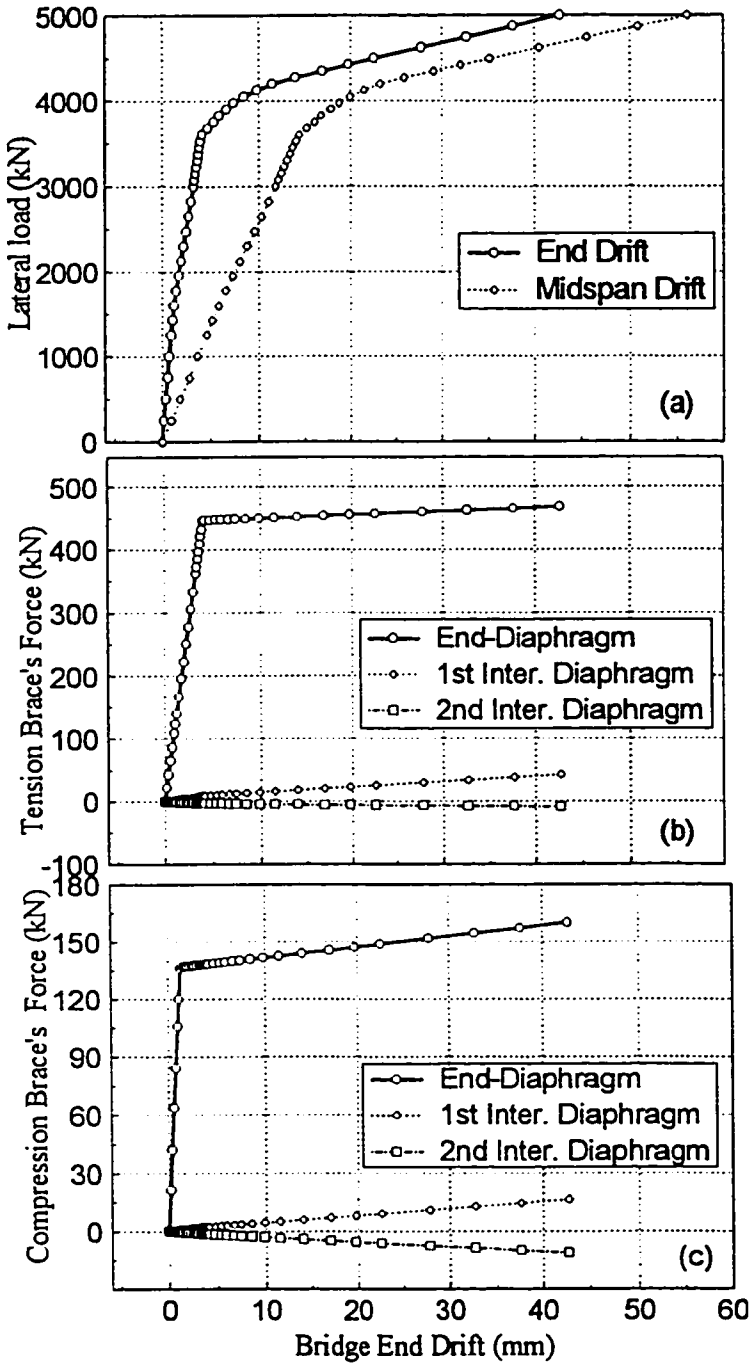

Fig. 3.22. Inelastic results for a 40 m span bridge: (a) lateral load versus end and midspan drifts; (b) and (c) tension and compression axial forces in one pair of the diaphragm braces, respectively. Contribution resisted by flexure of the stiffened girders (per Eq. 3.26) not shown.

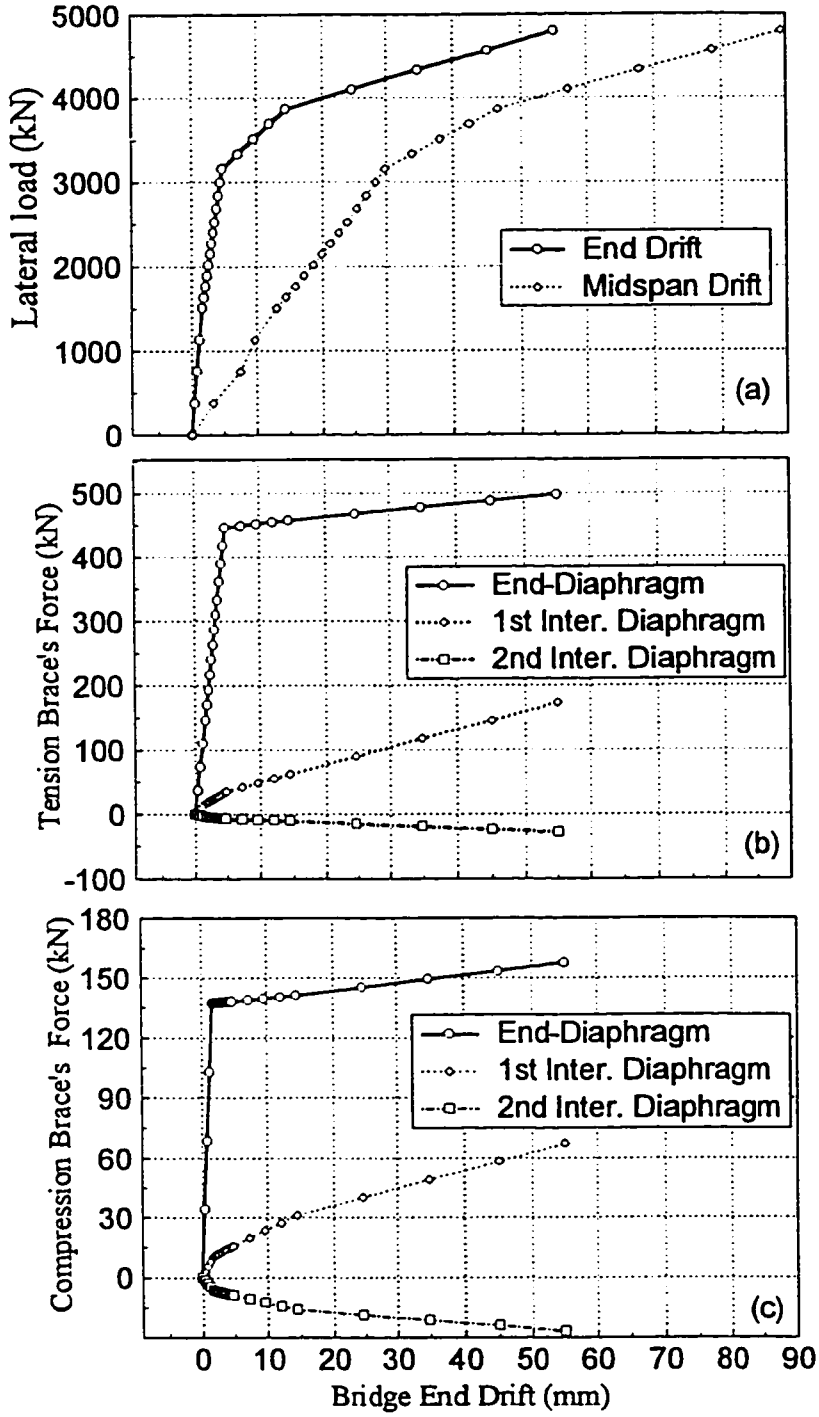

Fig. 3.23. Inelastic results for a 60 m span bridge: (a) lateral load versus end and midspan drifts; (b) and (c) tension and compression axial forces in one pair of the diaphragm braces, respectively. Contribution resisted by flexure of the stiffened girders (per Eq. 3.26) not shown.

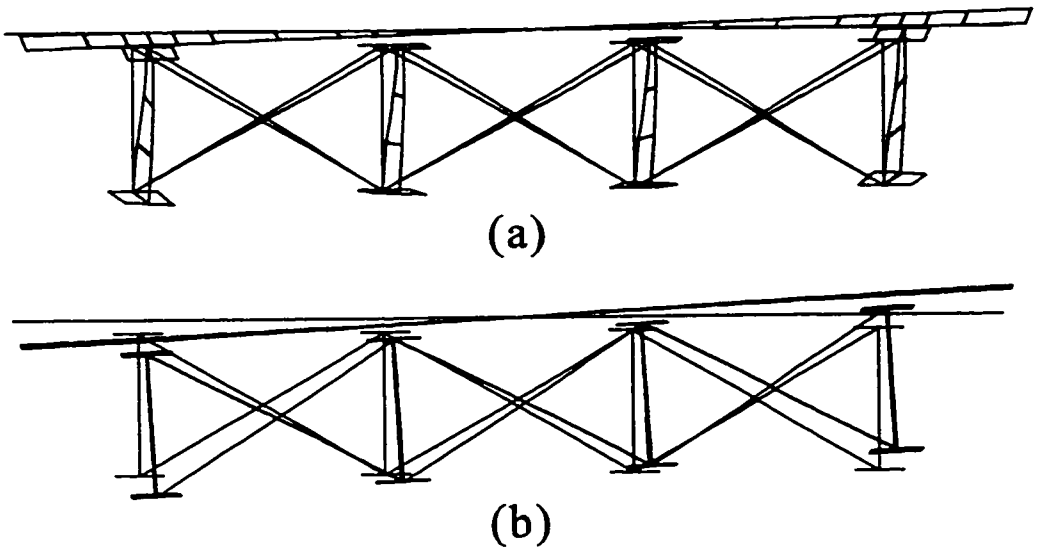

Fig. 3.24. End views of deformed shapes for the 40 m span bridge at: (a) one end; and (b) a distance of 8 m from bridge end.

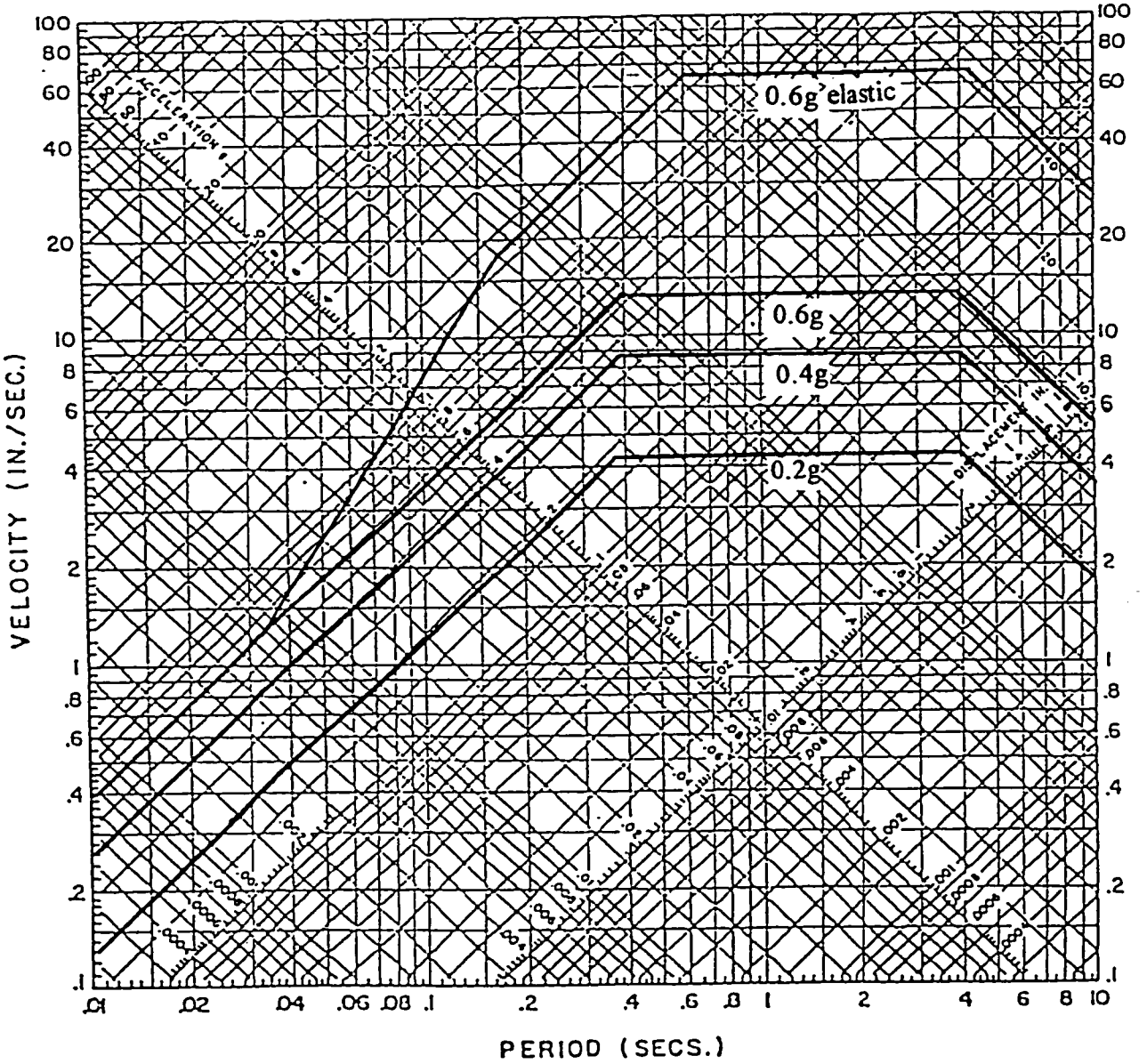

Fig. 4.1. Inelastic Newmark-Hall design spectra obtained for peak ground accelerations of 0.2g, 0.4g and 0.6g with 2% damping (elastic response spectra for *PGA* of 0.6g shown for comparison).

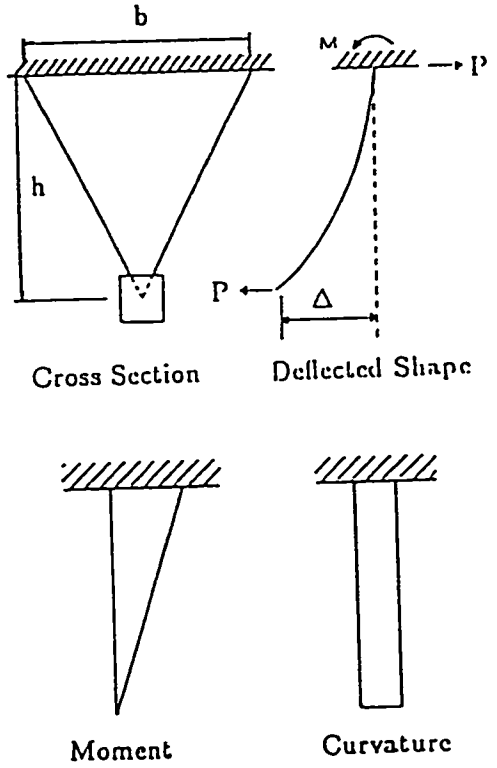

Fig. 4.2. Basic behavior of triangular steel plates under lateral loading (Tsai et al. 1993).

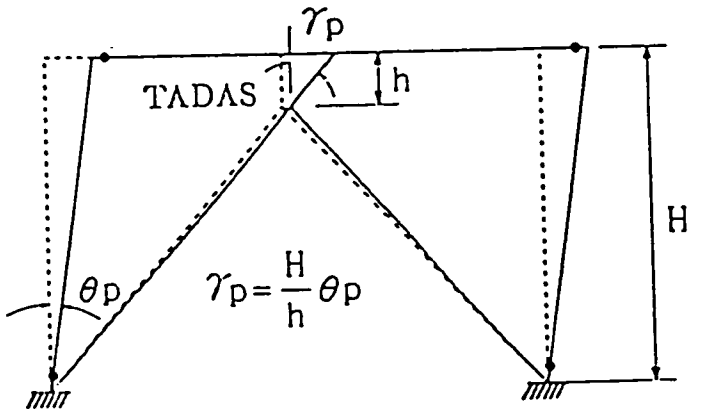

Fig. 4.3. Plastic failure mechanism for a frame having Triangular-plate Added Damping And Stiffness Device (TADAS) (Tsai et al. 1993).

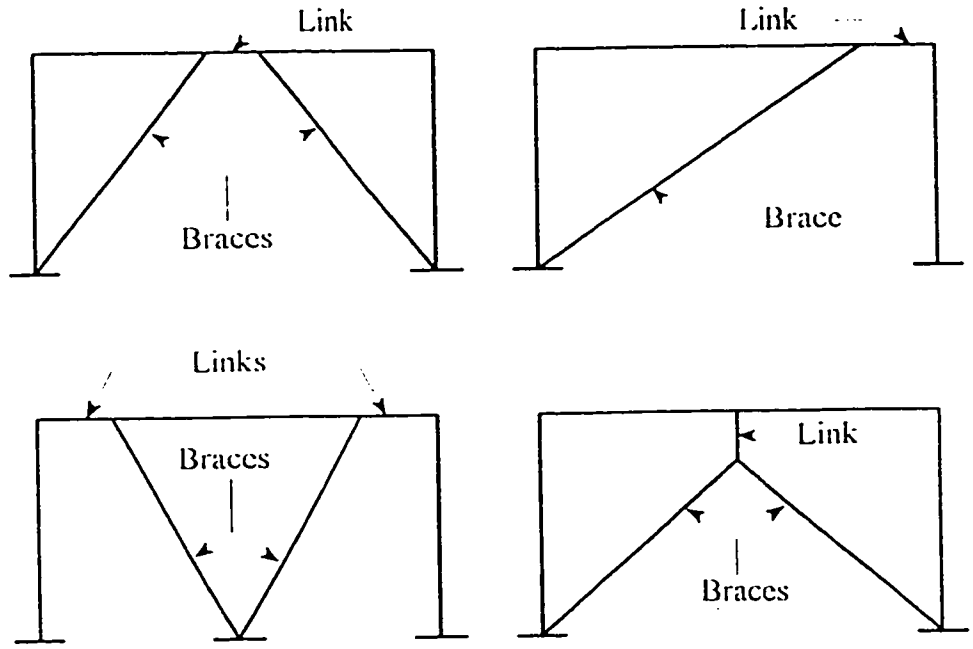

Fig. 4.4. Common configurations of Eccentrically Braced Frames (EBF).

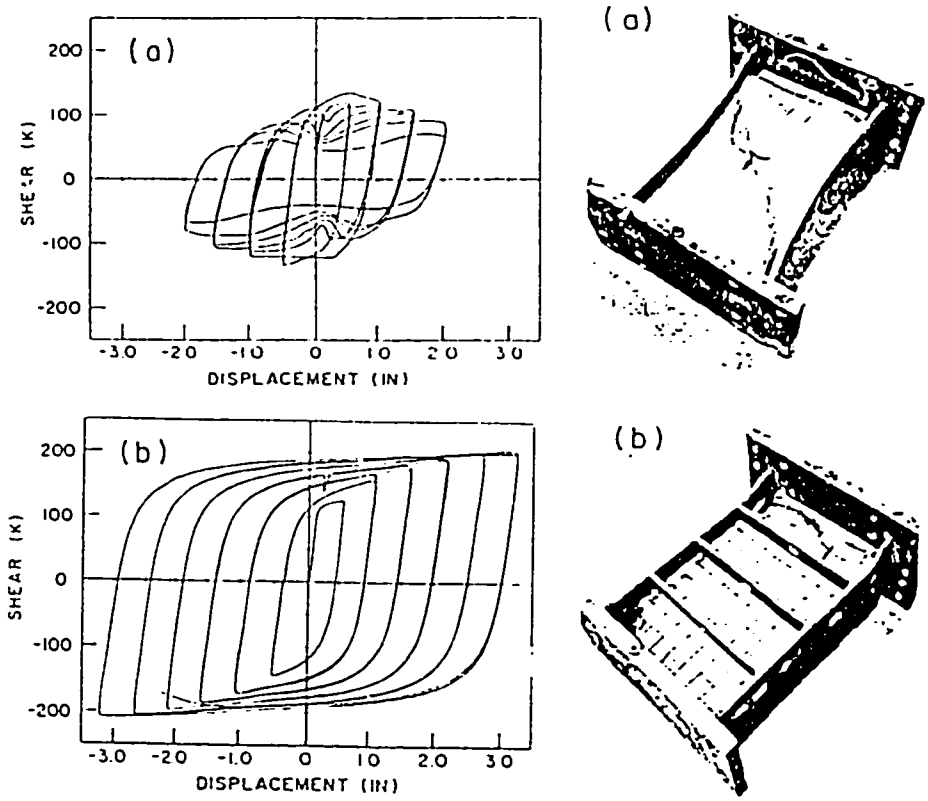

Fig. 4.5. Hysteretic behavior and failure pattern of: (a) shear link without web stiffeners; (b) stiffened shear link (Kasai and Popov 1986).

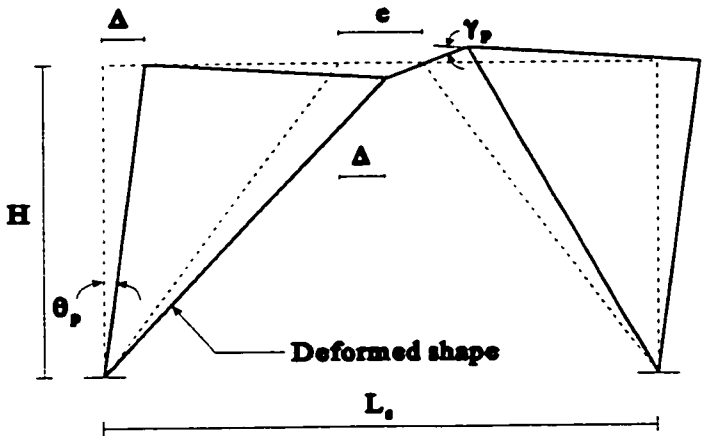

Fig. 4.6. Shear plastic mechanism for an EBF.

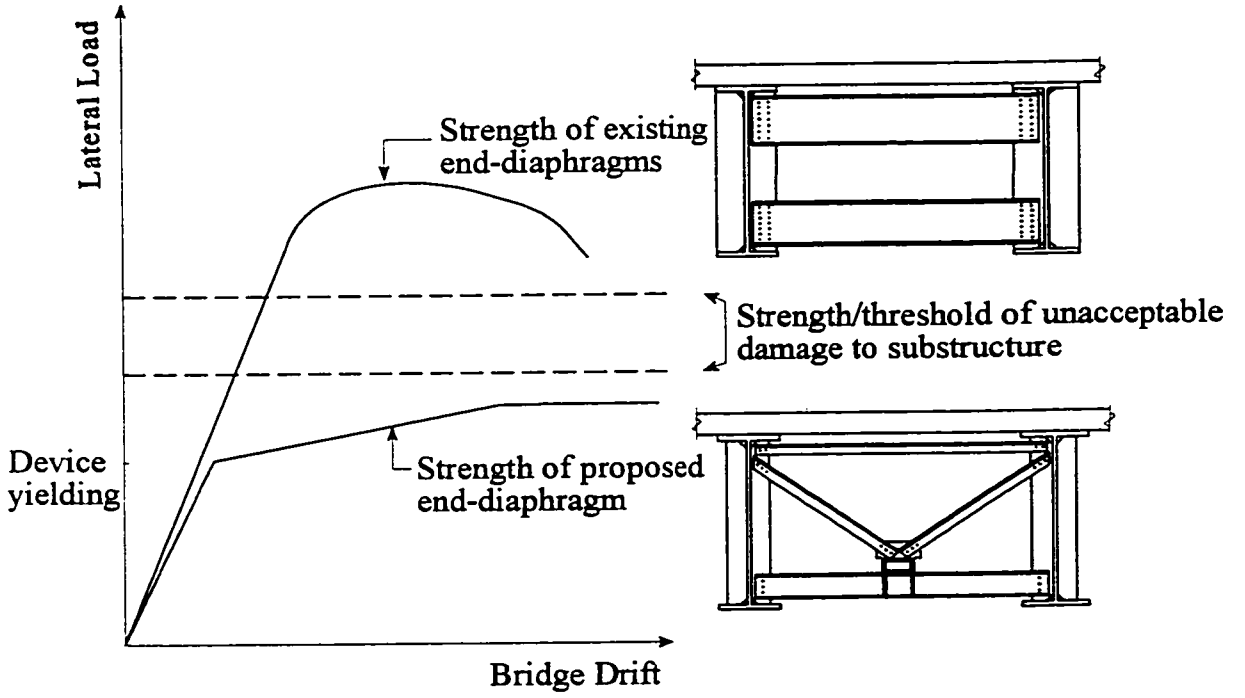

Fig. 4.7. Inelastic behavior of proposed ductile end-diaphragms compared to that of existing steel bridges.

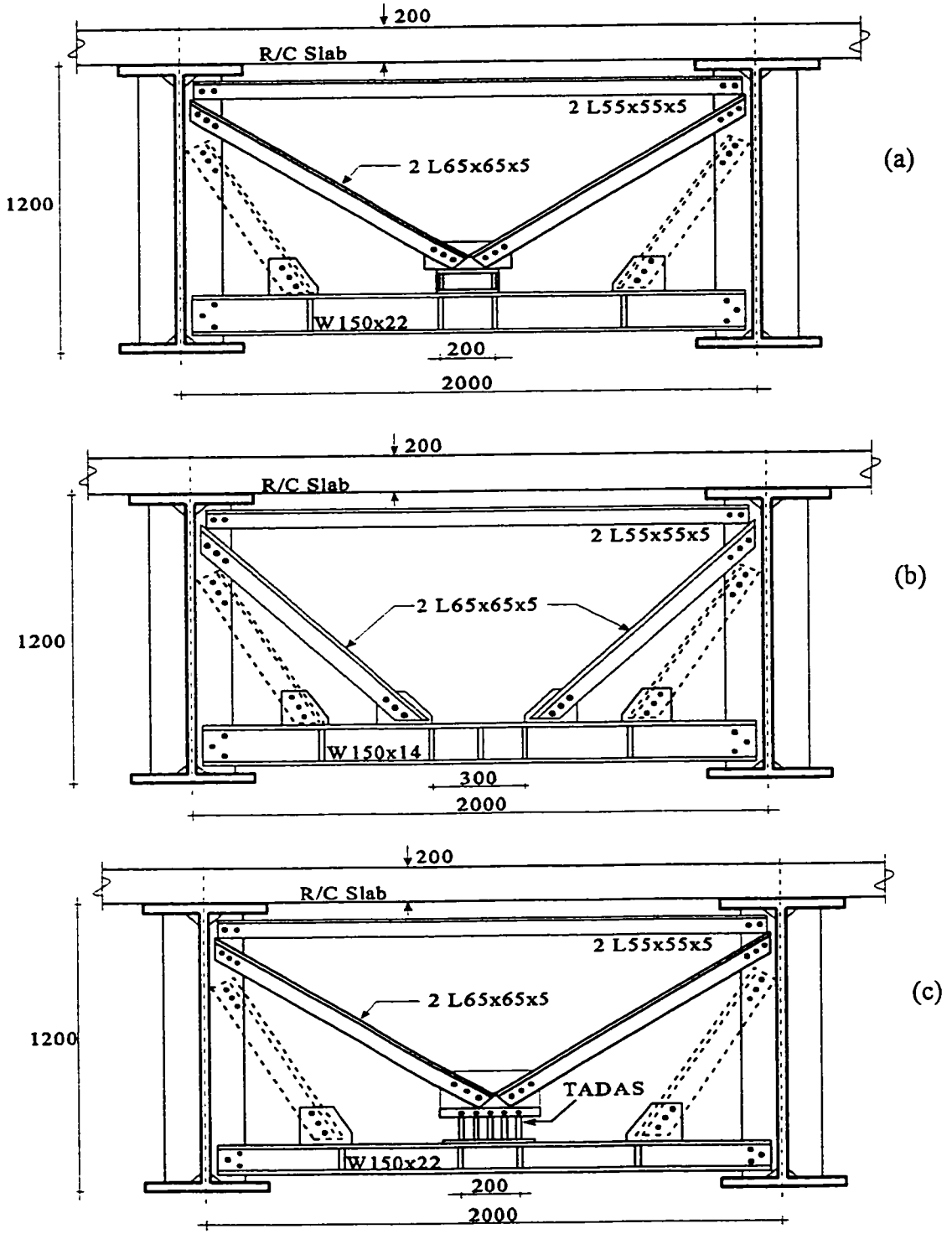

Fig. 4.8. Proposed ductile end-diaphragms of a typical 40 m span bridge with: (a) TADAS; (b) EBF; (c) SPS (other unbraced girders not shown); dotted members only if required for jacking purposes for non-seismic reasons).

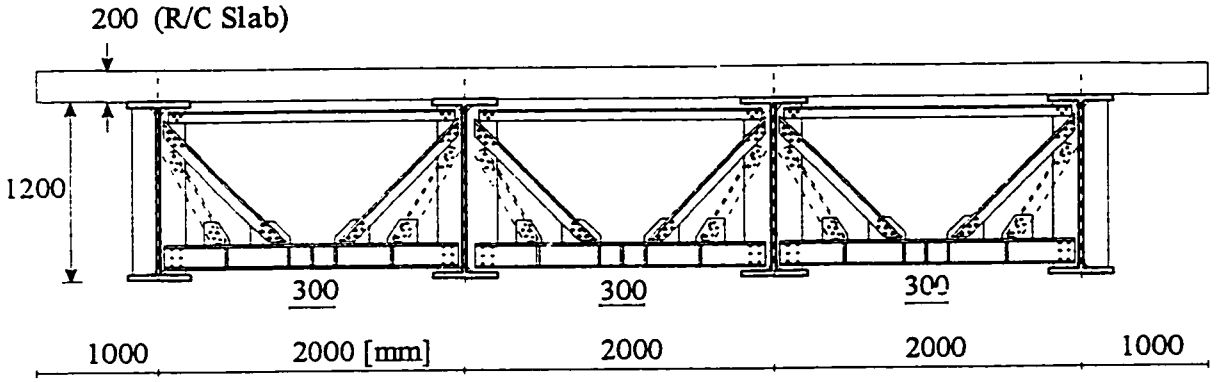

Fig. 4.9. Ductile end-diaphragms inserted between all girders for preliminary case studies.

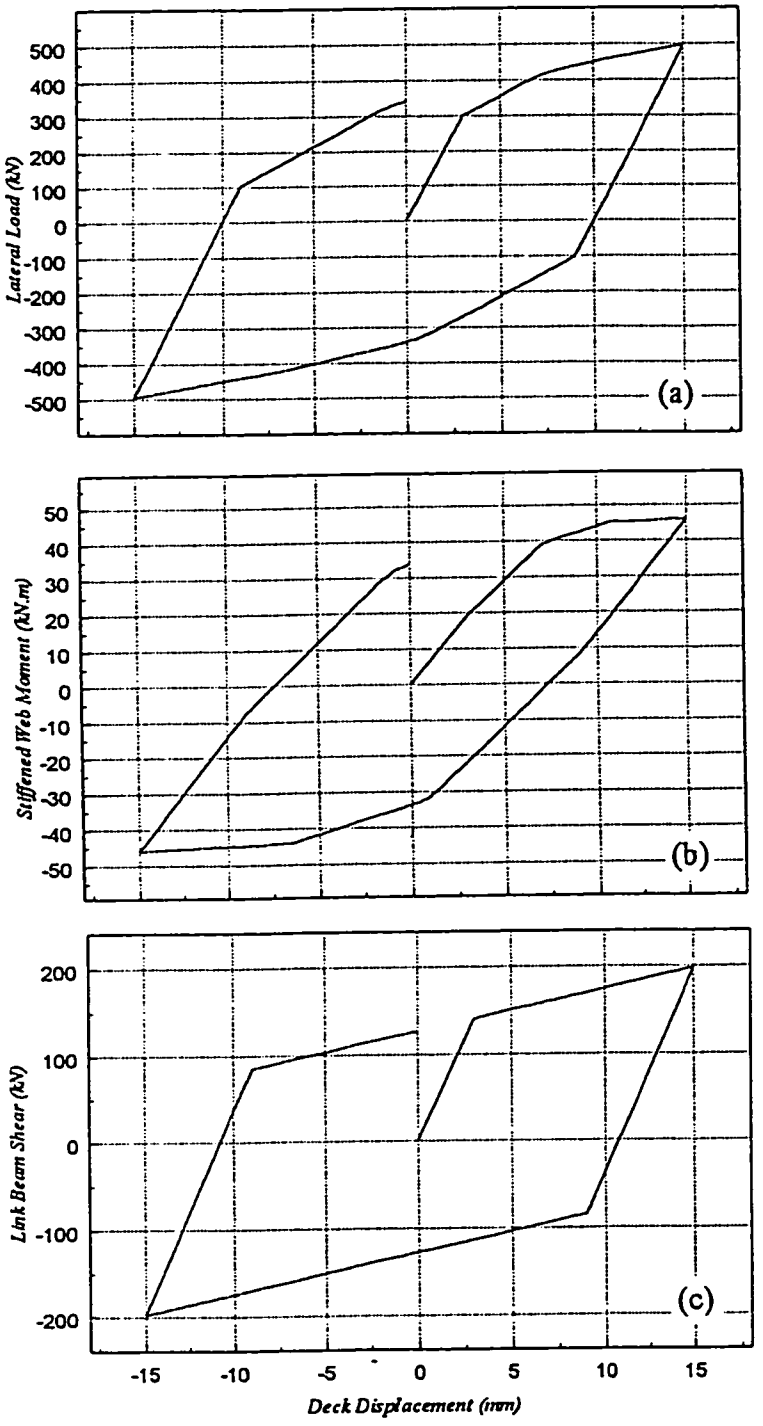

Fig. 4.10. Inelastic results for the 40 m span bridge having EBF between all girders, i.e. three panel each end, by DRAIN-2DX: (a) Lateral load; (b) bending moment in one web stiffener at bridge end; (c) link shear force, versus deck displacement. Results for one panel shown.

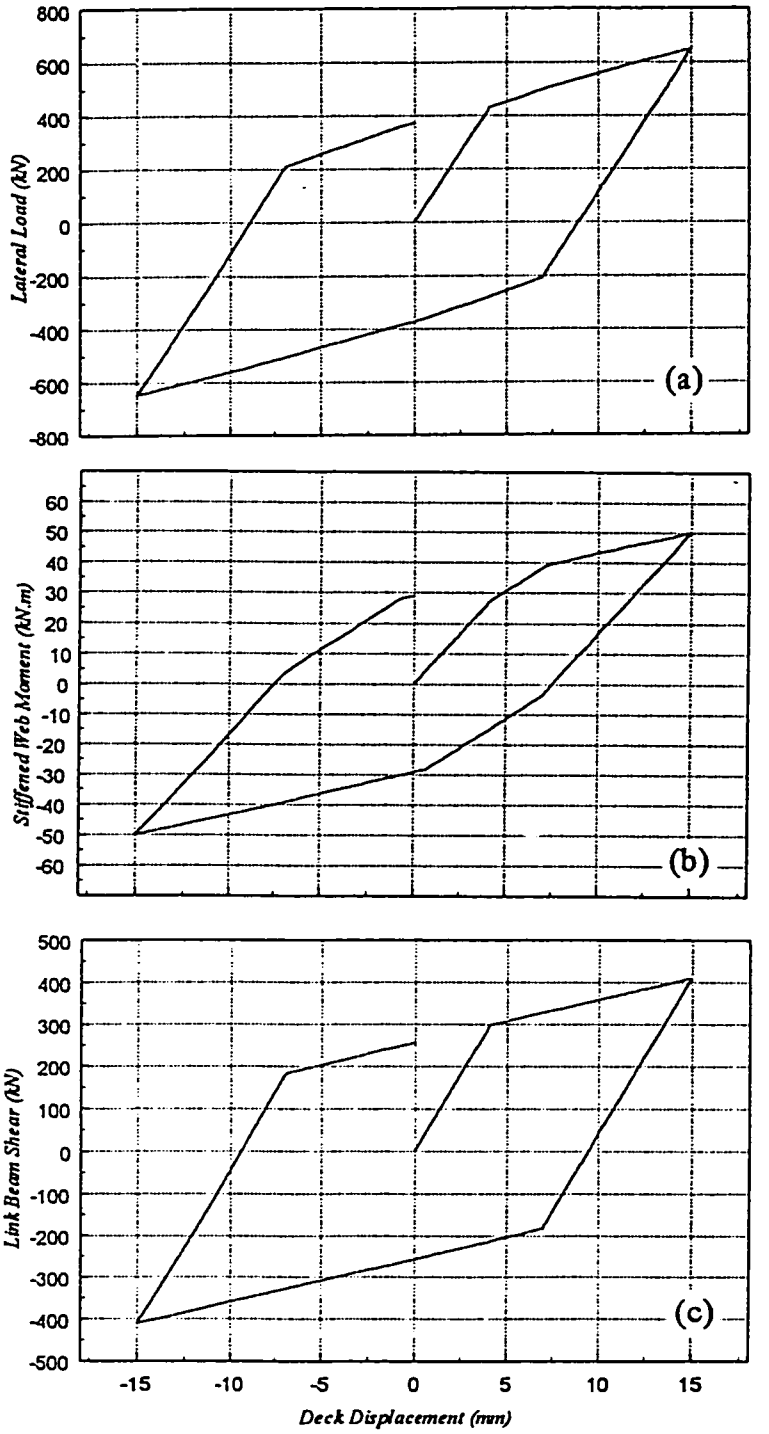

Fig. 4.11. Inelastic results for the 60 m span bridge having EBF between all girders, i.e. three panel each end, by DRAIN-2DX: (a) Lateral load; (b) bending moment in one web stiffener at bridge end; (c) link shear force, versus deck displacement. Results for one panel shown.

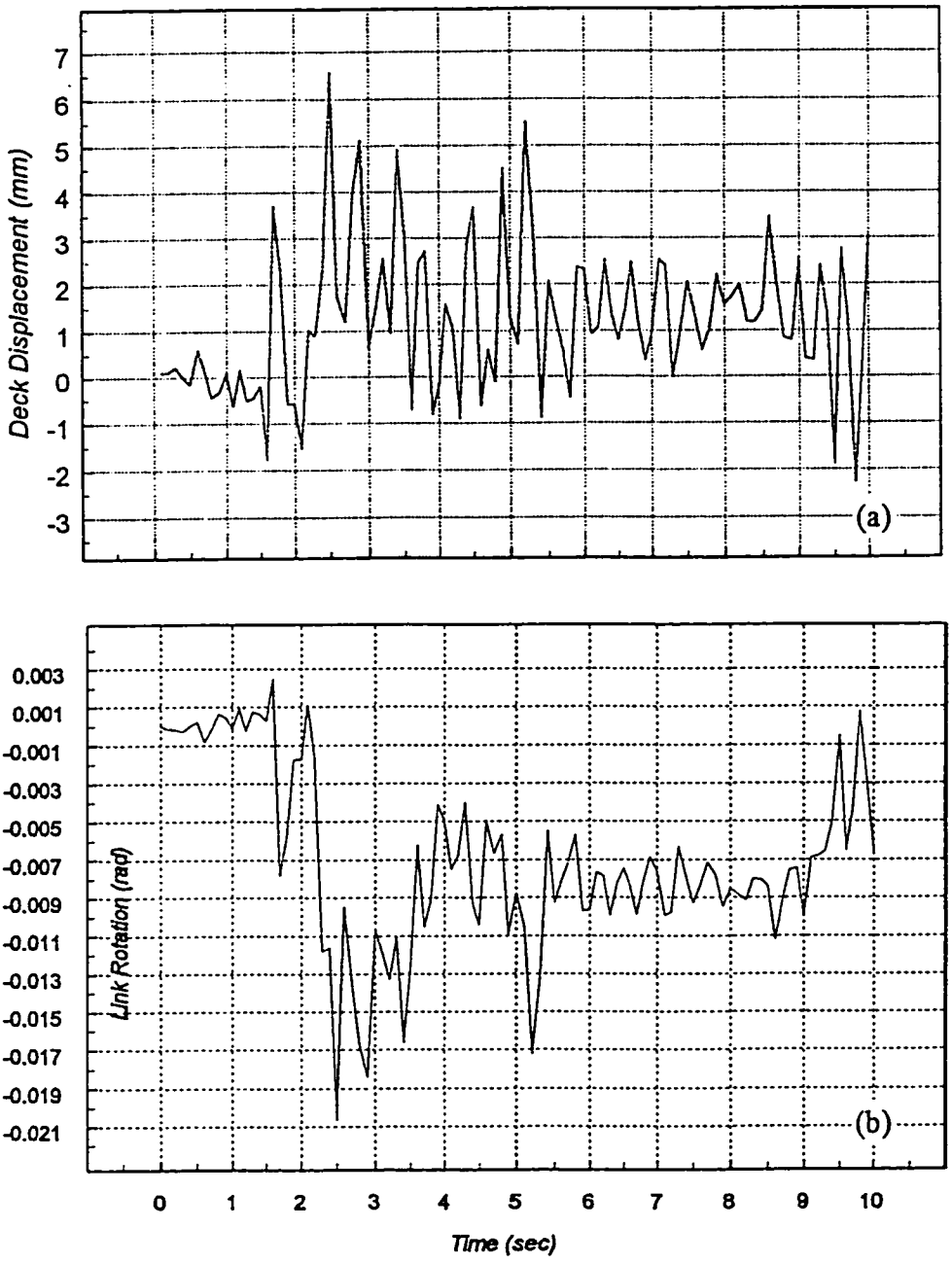

Fig. 4.12. Inelastic time-history analysis results by DRAIN-2DX for the 40 m span bridge having EBF subjected to the El-Centro earthquake scaled to a *PGA* of 0.6g: (a) deck drift and (b) link distortion versus time.

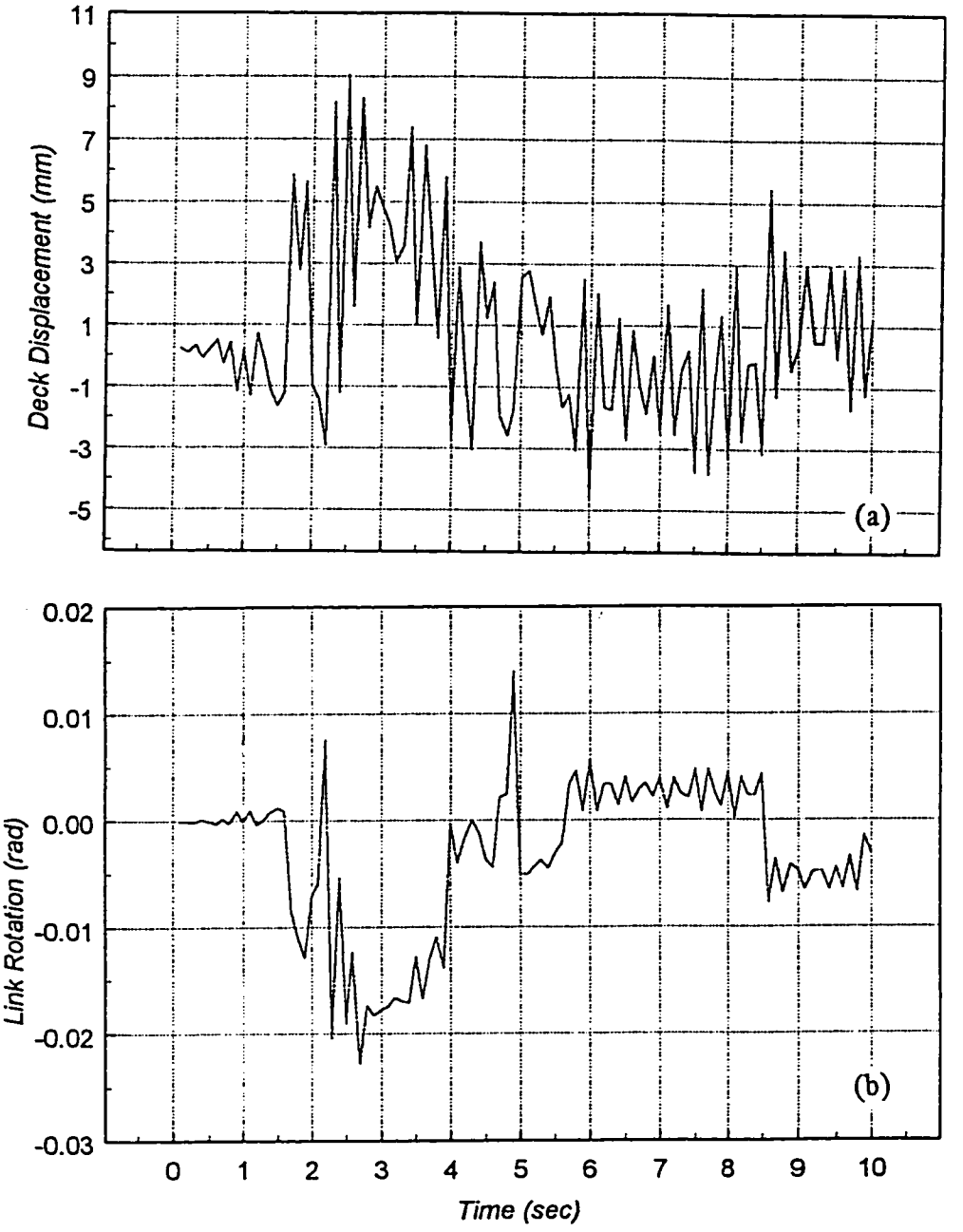

Fig. 4.13. Inelastic time-history analysis results by DRAIN-2DX for the 60 m span bridge having EBF subjected to the El-Centro earthquake scaled to a *PGA* of 0.6g: (a) deck drift and (b) link distortion versus time.

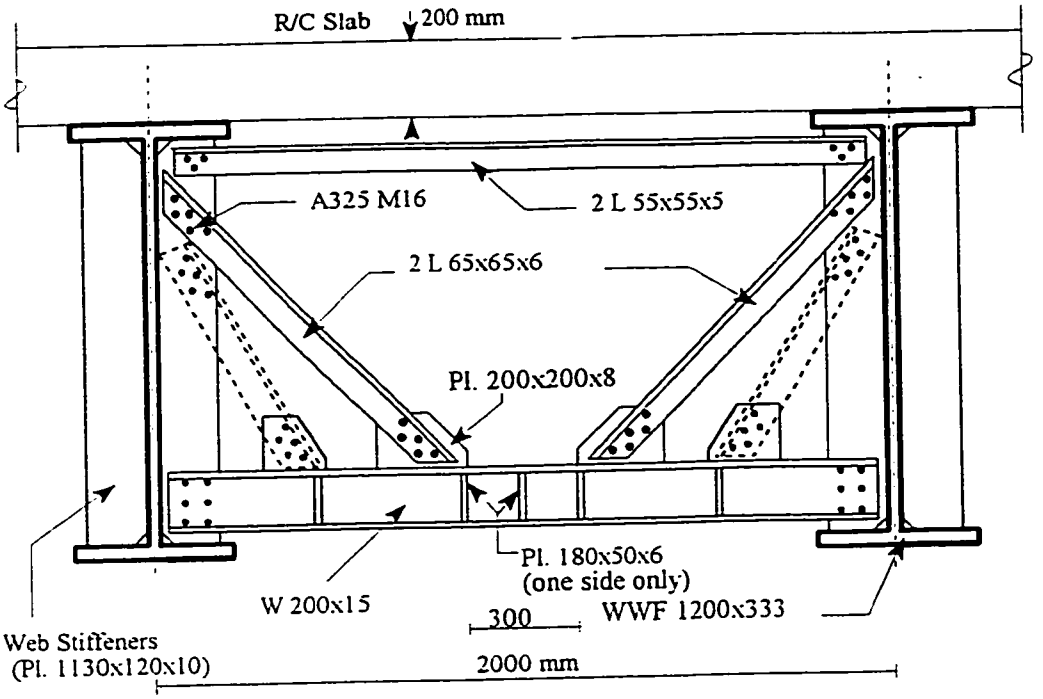

(a)

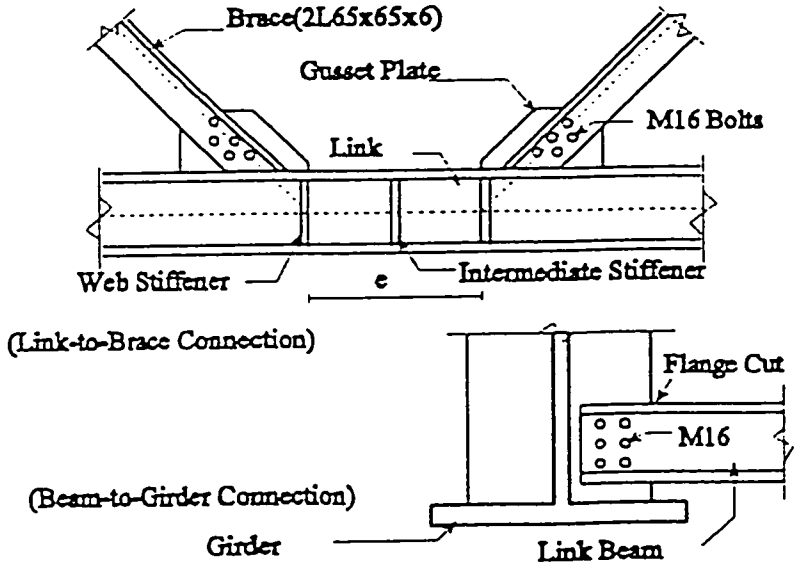

(b)

Fig. 4.14. Ductile end-diaphragm designed for the 40 m span bridge to resist a *PGA* of 0.6g: (a) one of panels having EBF, (b) some typical connection detailing.

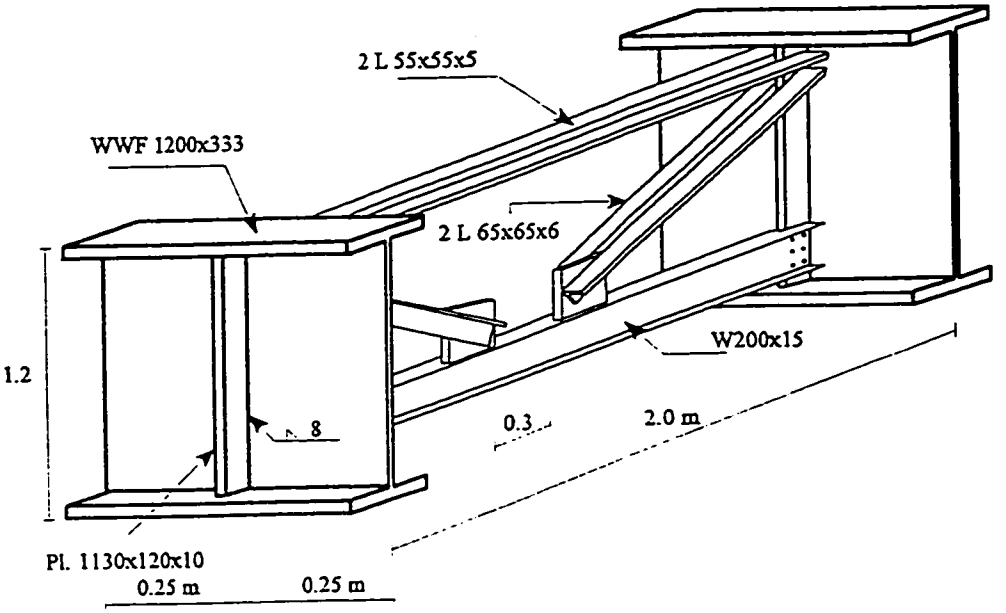

Fig. 4.15. Schematic 3-D view of the ductile end-diaphragm proposed for 2-D analytical analysis.

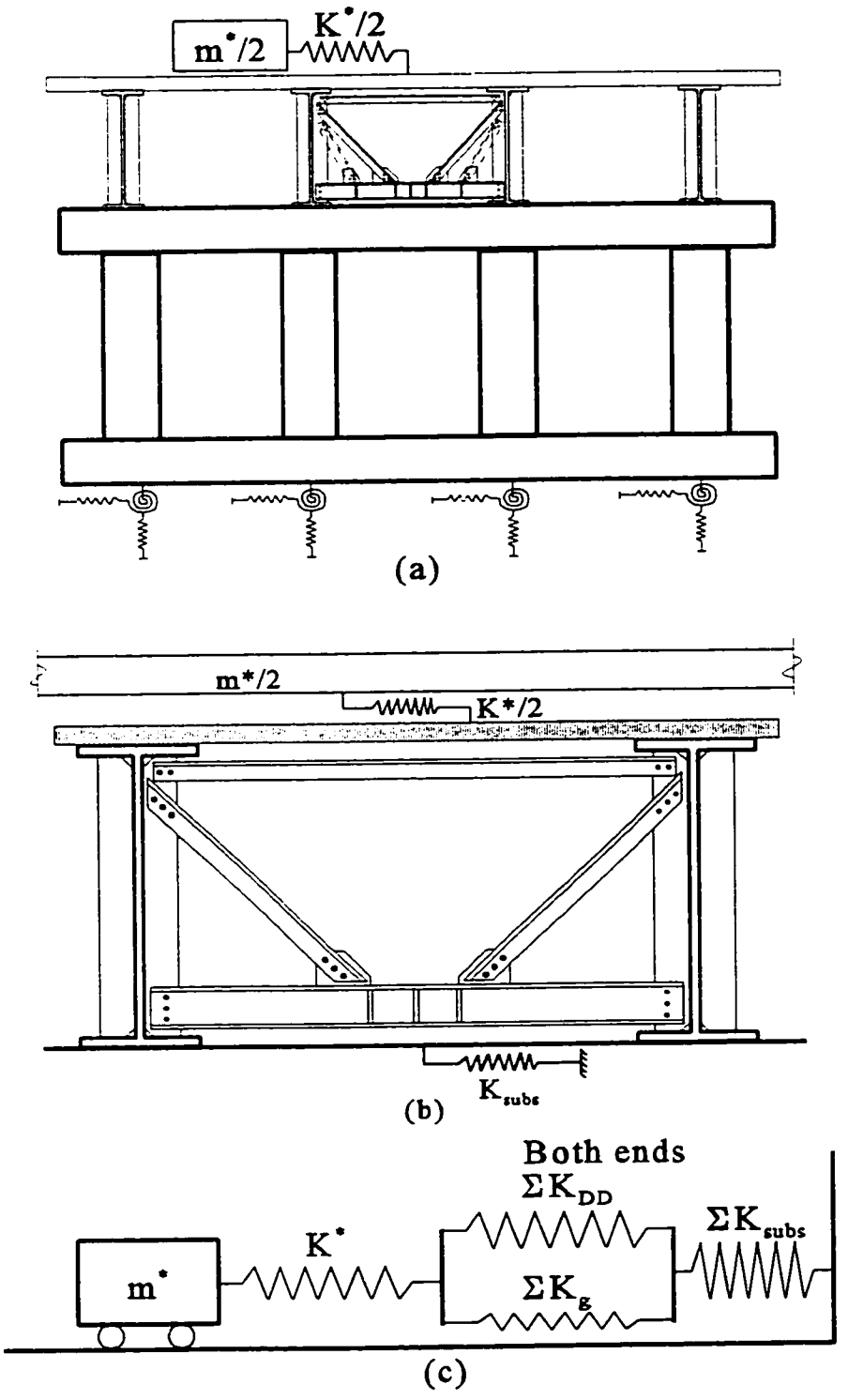

Fig. 4.16. Spring modeling: (a) schematic of a typical bridge supported by a substructure including piers and foundations; (b) spring modeling of the bridge in the transverse direction at one end; (c) simple spring model of the dual system in entire bridge superstructure.

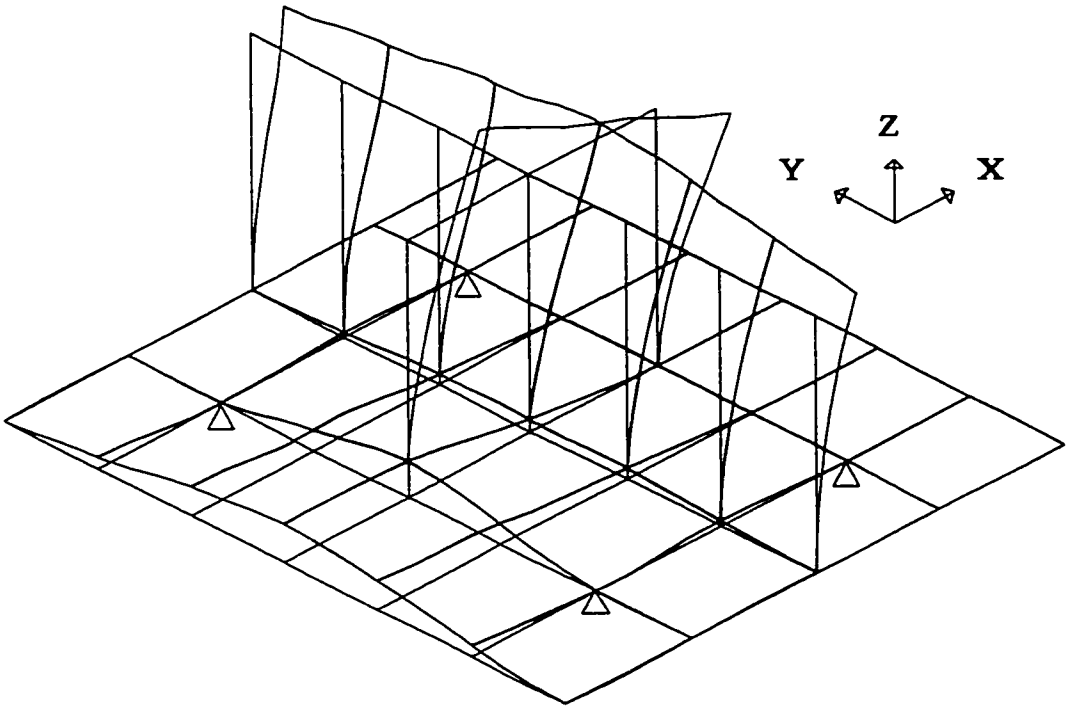

Fig. 4.17. Flexibility of the girder's bottom flange in modeling the level of fixity, based on SAP90 analyses (the rest of girders and web stiffeners not shown).

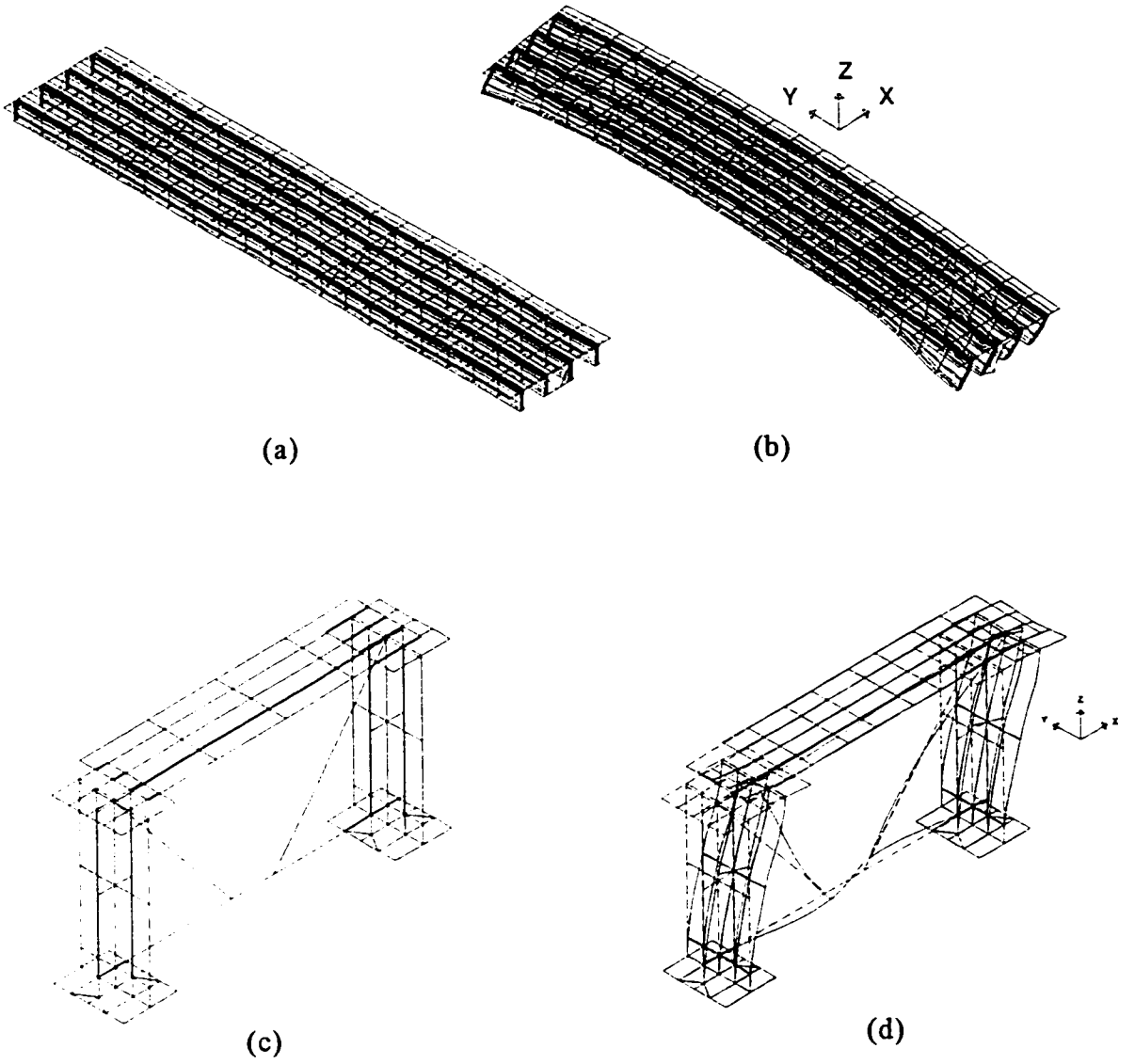

Fig. 4.18. Modeling of a typical slab-on-girder steel bridge using SAP90: (a) 3-D model; (b) 3-D deformed shape; (c) 2-D model; and (d) 2-D deformed shape (deformed shapes are greatly magnified for illustration purposes).

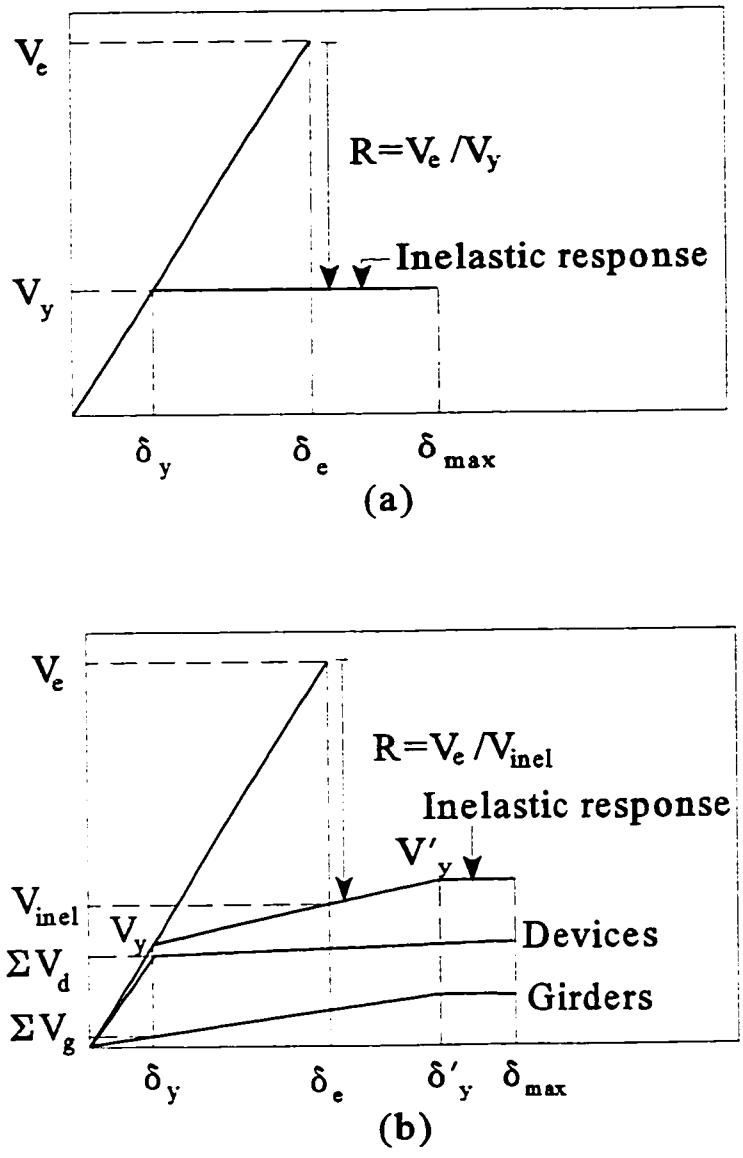

Fig. 4.19. Hysteretic modeling of seismic resistant systems: (a) bilinear model; (b) trilinear model.

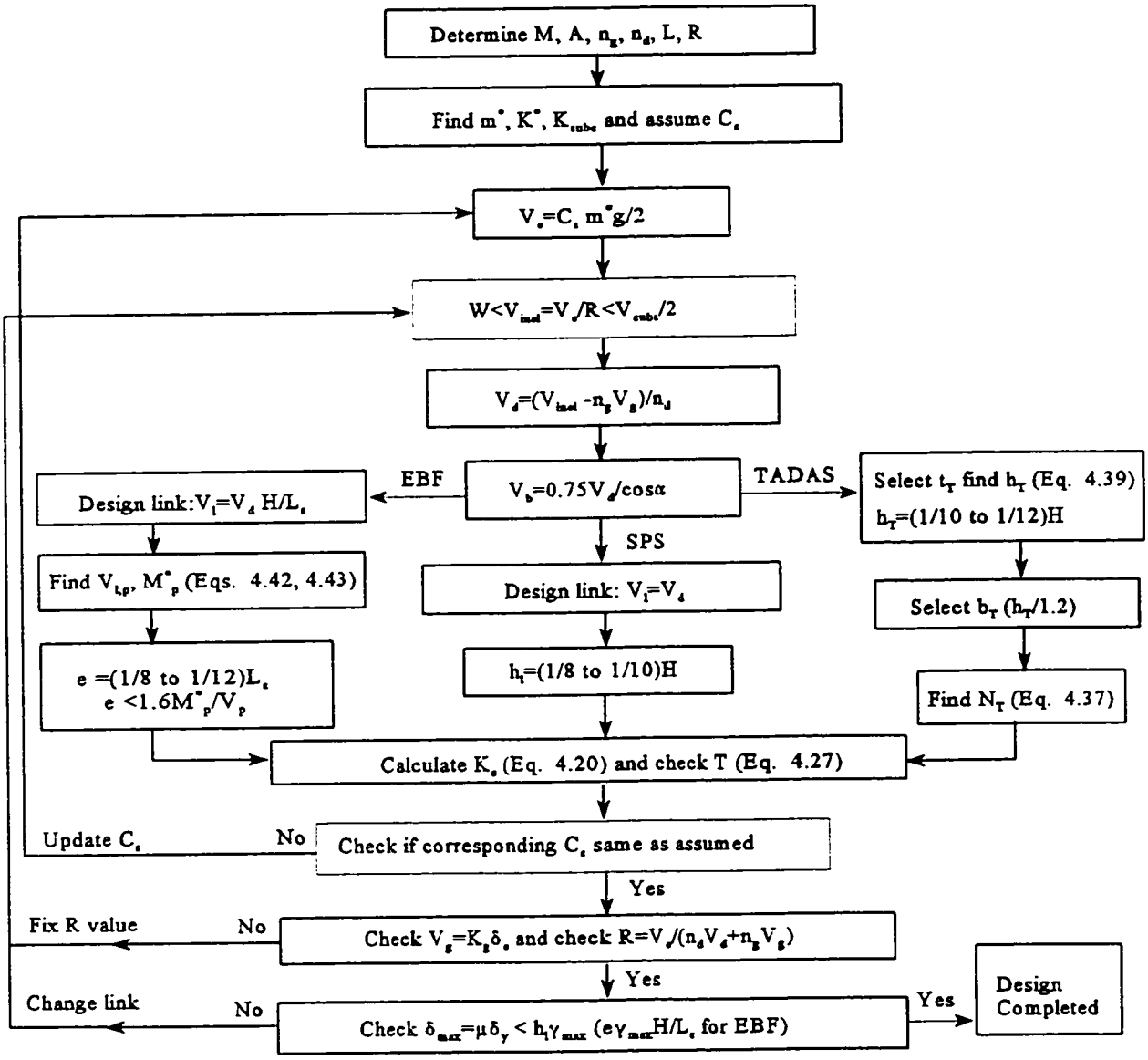

Fig. 4.20. Simple folw chart for proposed design procedure.

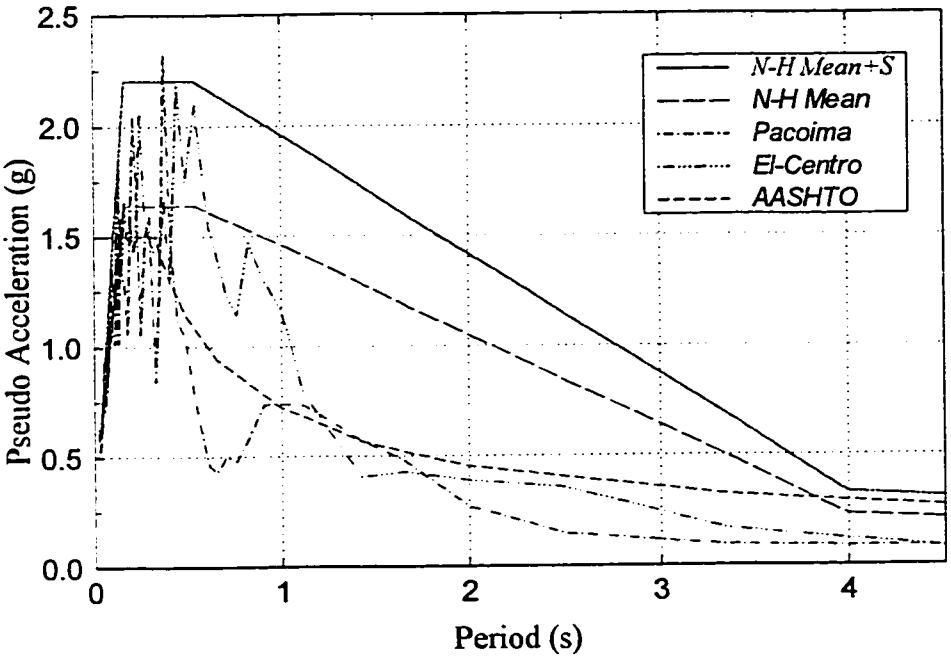

Fig. 4.21. Newmark-Hall and AASHTO design spectra versus the response spectra for two earthquakes, scaled to a *PGA* of 0.6g.

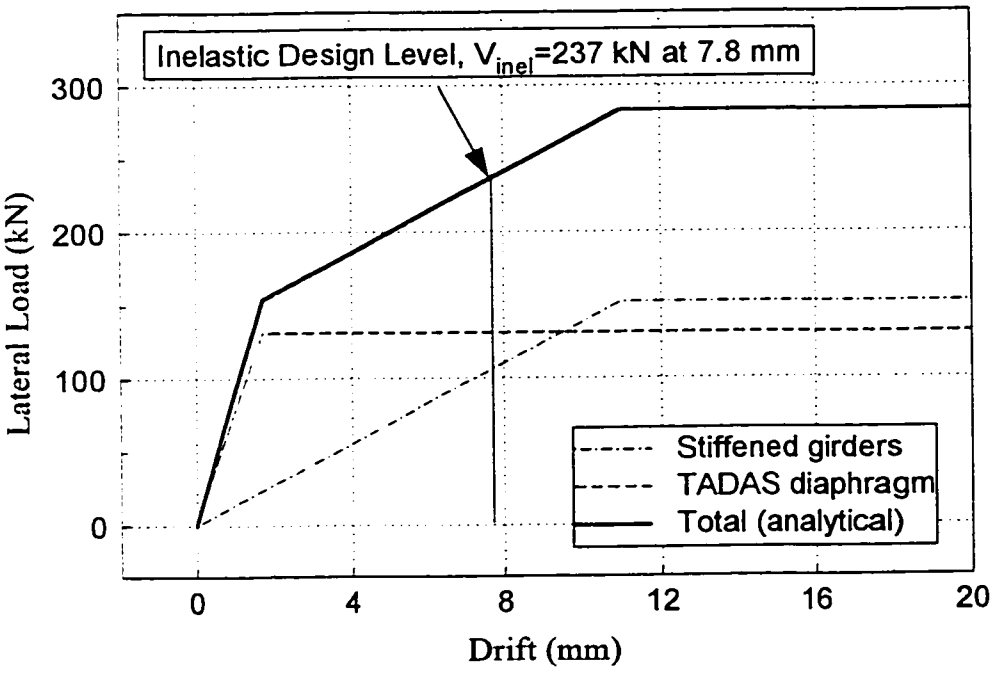

Fig. 4.22. Proposed trilinear curve for design of the TADAS for a 40 m span bridge.

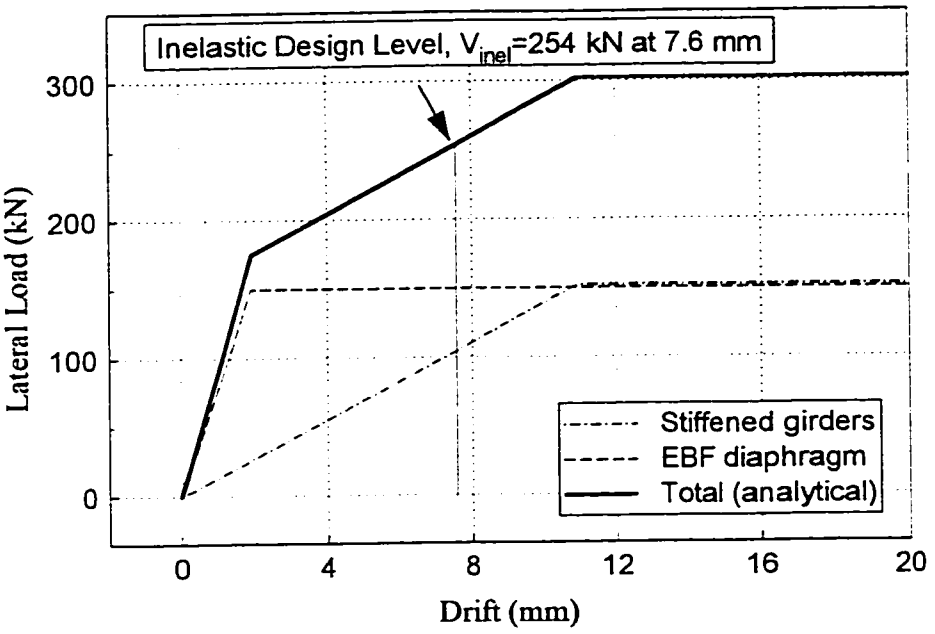

Fig. 4.23. Proposed trilinear curve for design of the EBF for a 40 m span bridge.

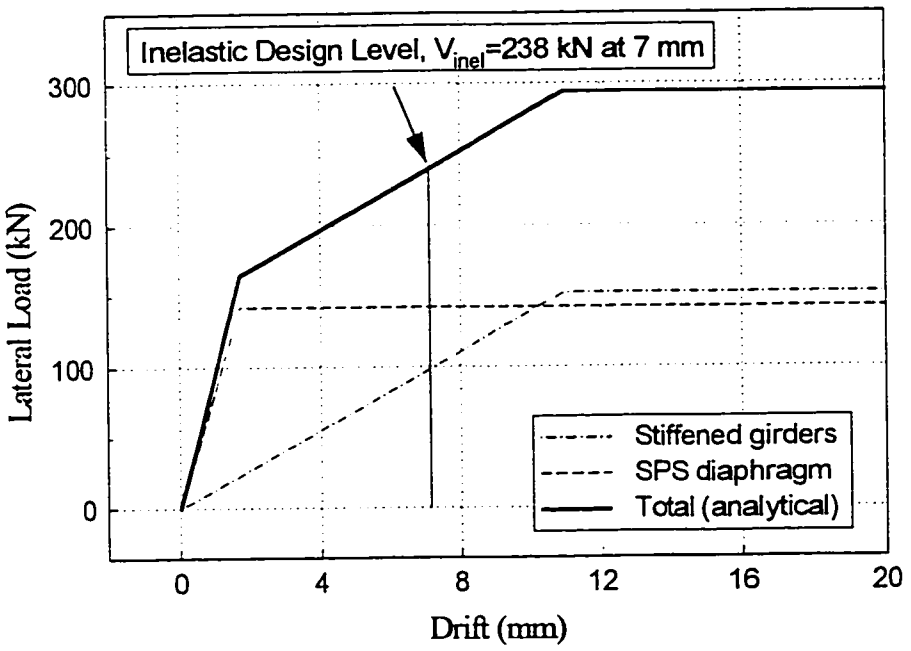

Fig. 4.24. Proposed trilinear curve for design of the SPS for a 40 m span bridge.

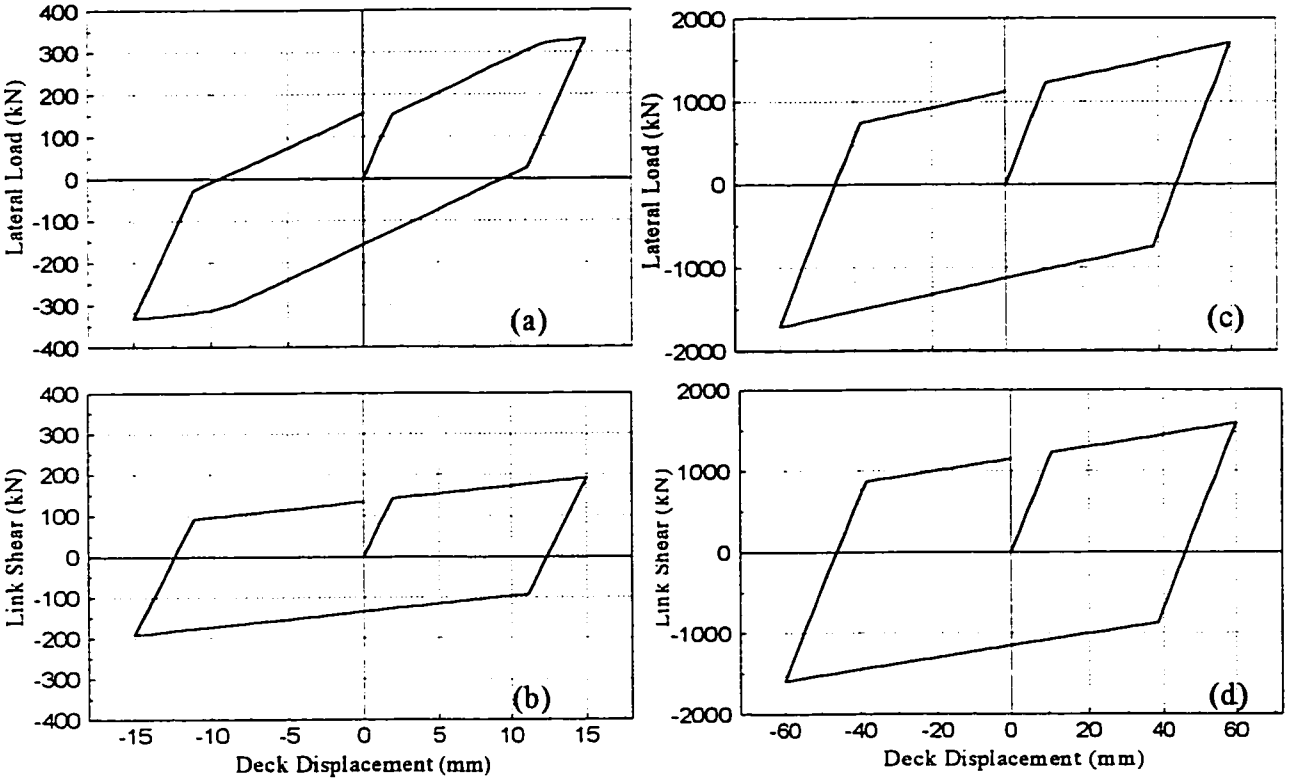

Fig. 4.25. Lateral load and link shear force versus deck displacement respectively: (a) and (b) for the 40 m single span bridge; (c) and (d) for support diaphragm of the three span bridge (side span of 60 m and center span of 90 m), with SPS diaphragms. Note that the link shear force is, in fact, the lateral load resisted by the link.

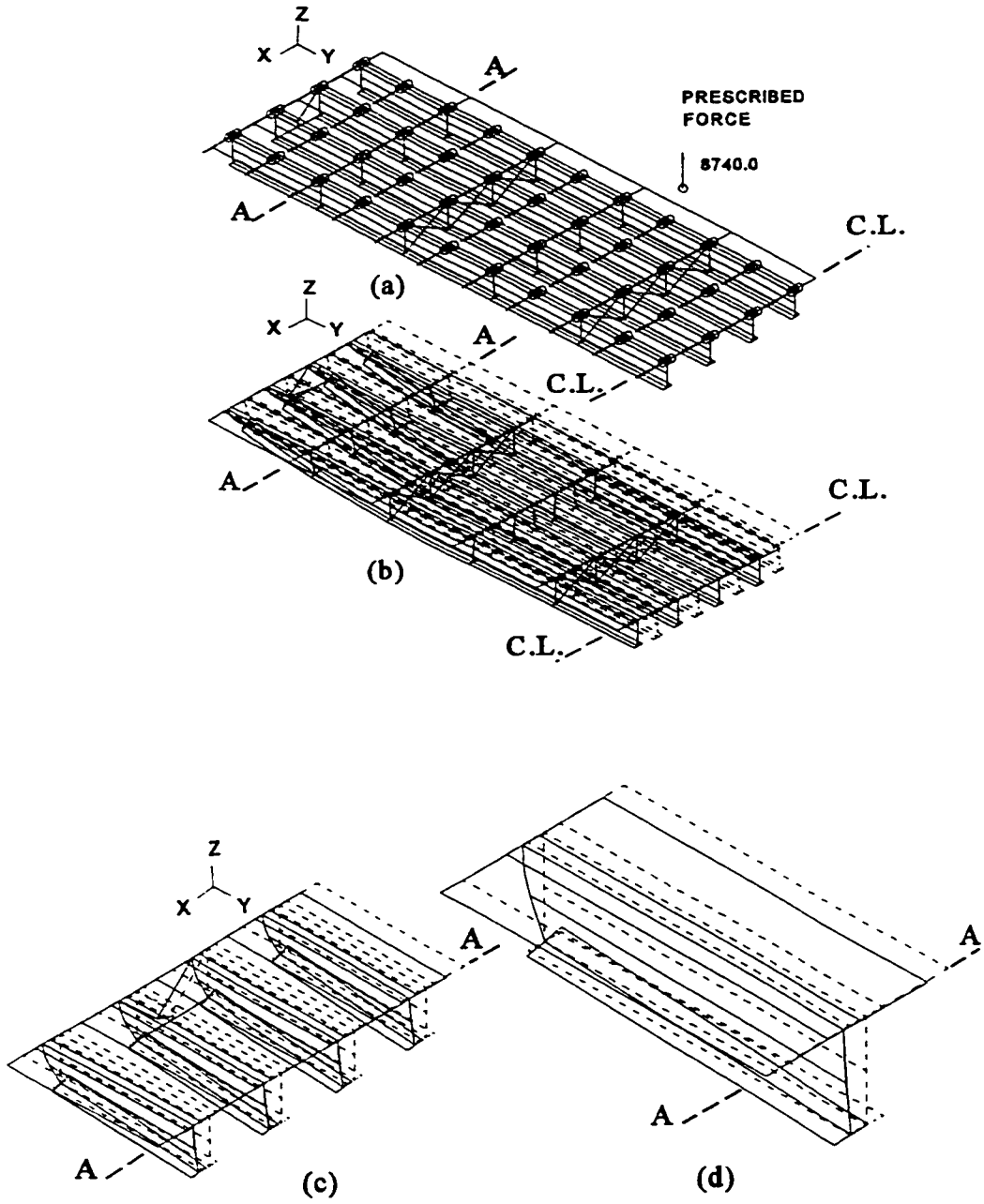

Fig. 4.26. ADINA modeling and analysis: (a) undeformed shape; (b) deformed shape (with magnified deformations for illustration purposes); (c) and (d) close-up of deformations.

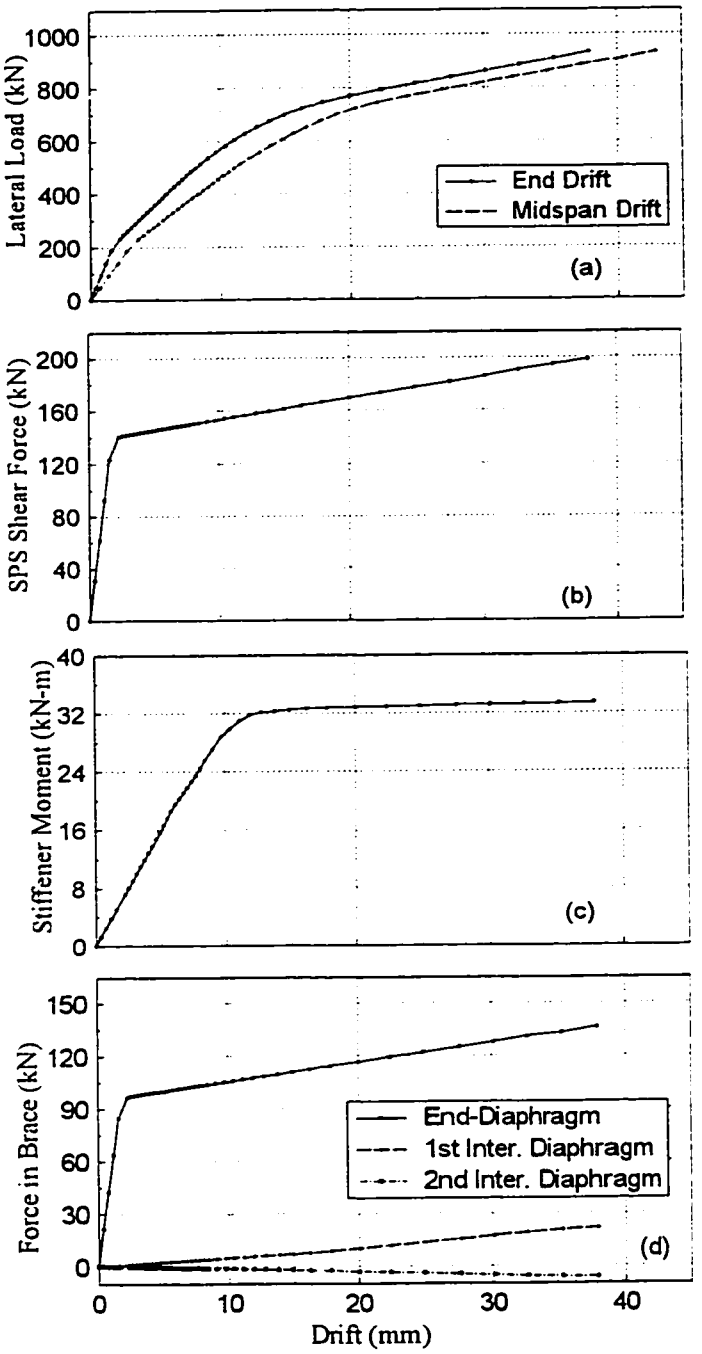

Fig. 4.27. Inelastic 3-D analysis results for a 40 m span bridge having SPS end-diaphragms by ADINA (web stiffeners only at supports): (a) lateral load versus end and center drifts; (b) shear force in the SPS; (c) bending moment in web stiffener and (d) axial forces in braces, versus end drift.

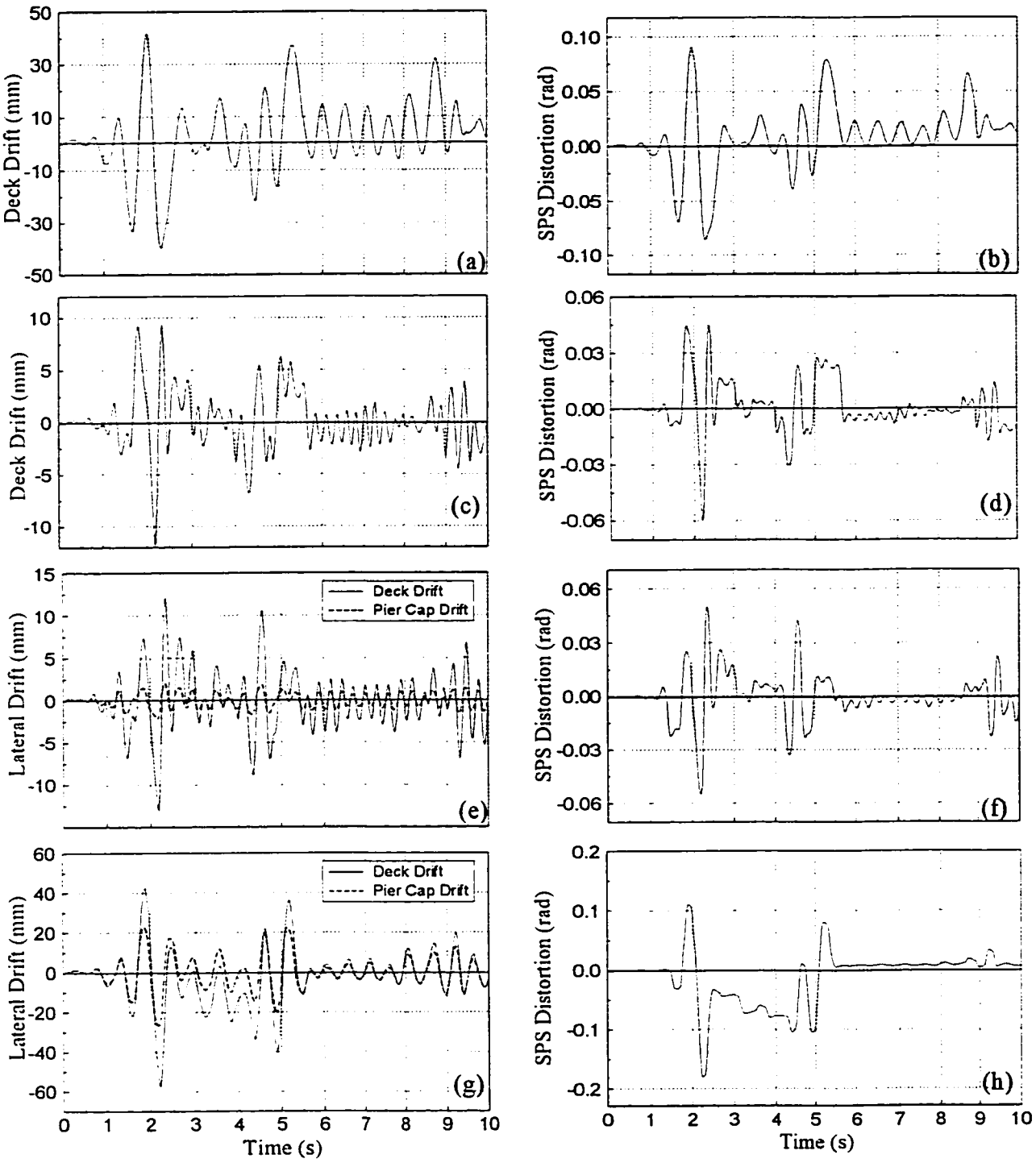

Fig. 4.28. Inelastic time-history analyses for the bridges subjected to the El-Centro earthquake scaled to 0.4g (for first 10 seconds) by DRAIN-2DX: (a) deck displacement and (b) link distortion for the three span bridge with 90 m center span; (c) deck displacement and (d) link distortion for the 40 m span bridge; (e) and (f) same for the 40 m multi-span bridge on stiff piers (four columns of 900 mm diameter and 5 m tall at each bent); (g) and (h) same for the 40 m multi-span bridge on flexible piers (four columns of 600 mm diameter and 6 m tall at each bent).

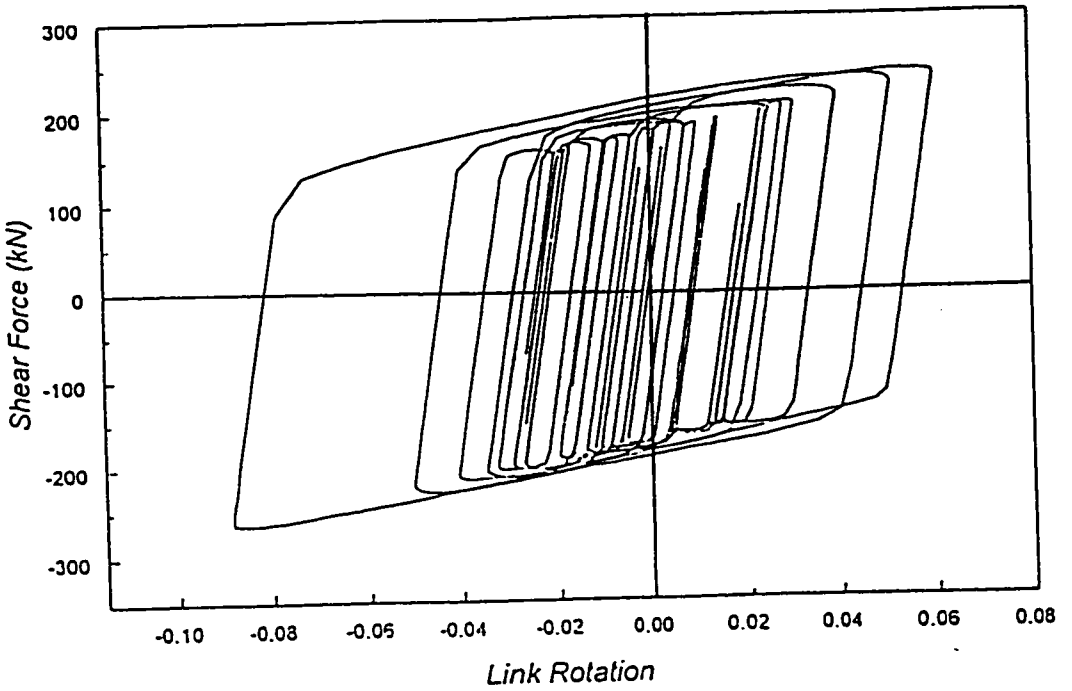

Fig. 4.29. Analytical hysteretic curves for the SPS implemented in the 40 m span bridge subjected to the El-Centro earthquake scaled to a *PGA* of 0.4g.

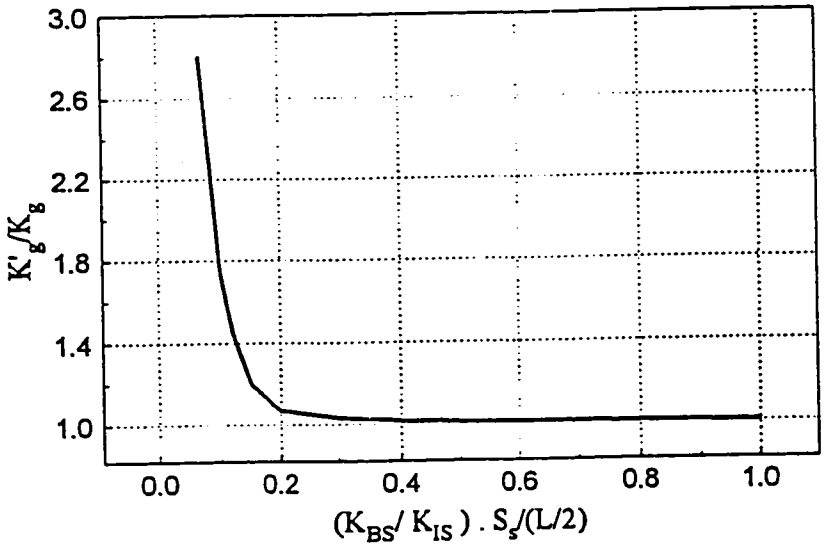

Fig. 4.30. Impact of intermediate web stiffeners on the proposed design procedure.

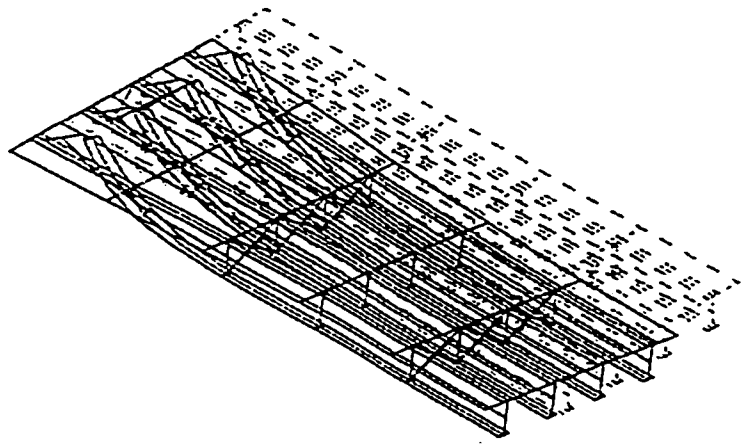

(a)

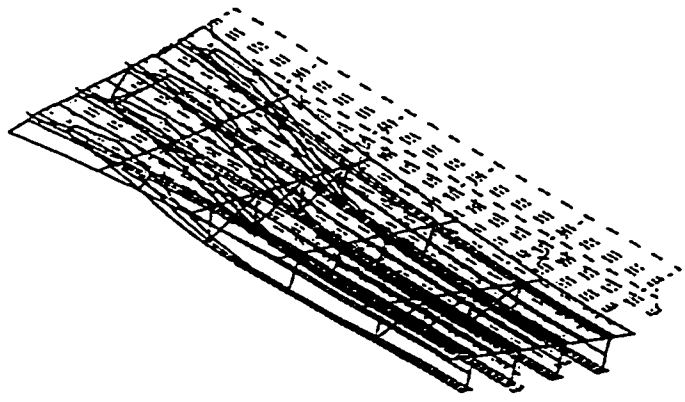

(b)

Fig. 4.31. Deflected shapes by ADINA for a 40 m span bridge having transverse web stiffeners at every: (a) 4 m; (b) 2 m, along the girders.

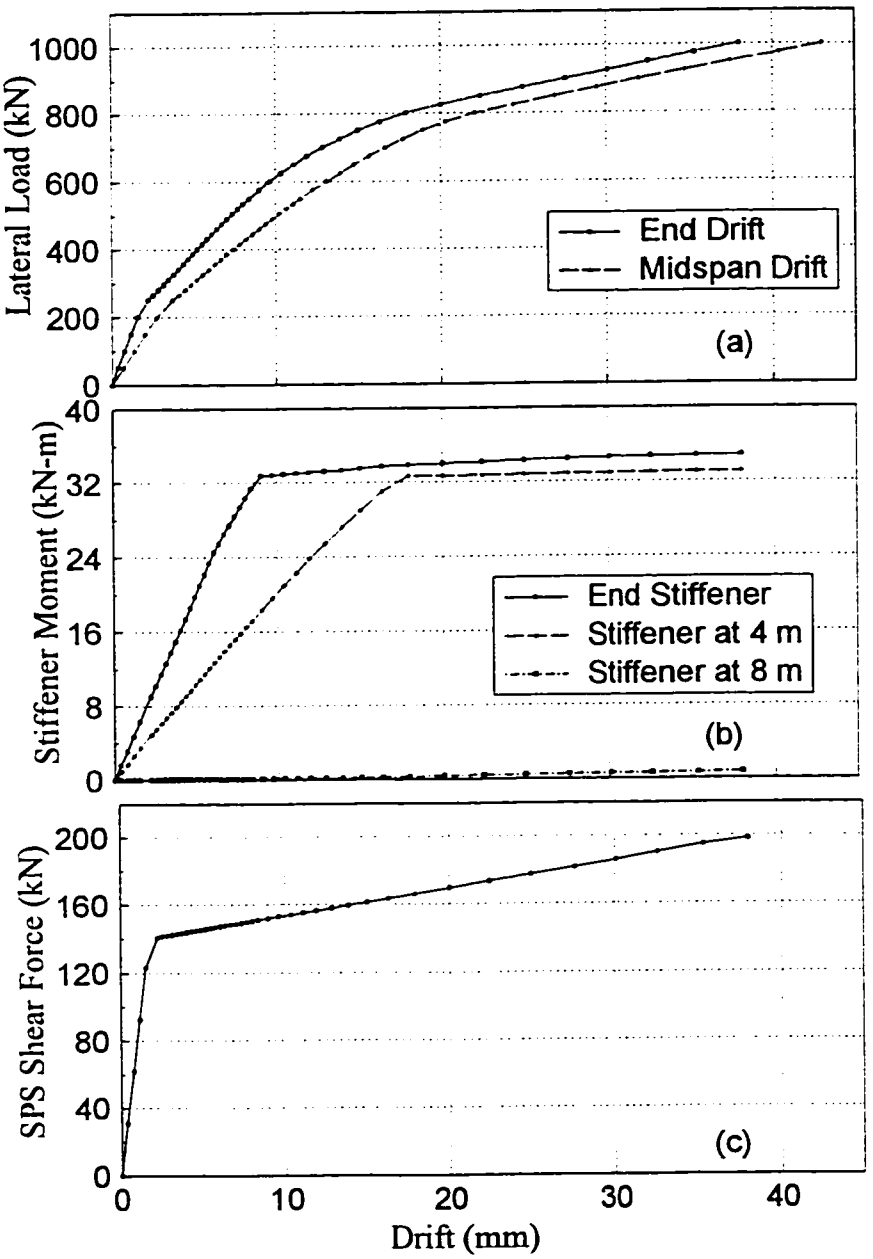

Fig. 4.32. Inelastic 3-D analysis results for the 40 m span bridge having SPS end-diaphragms by ADINA (web stiffeners at every 4 m): (a) lateral load versus end and center drifts; (b) bending moment in web stiffeners and (c) axial forces in braces, versus end drift.

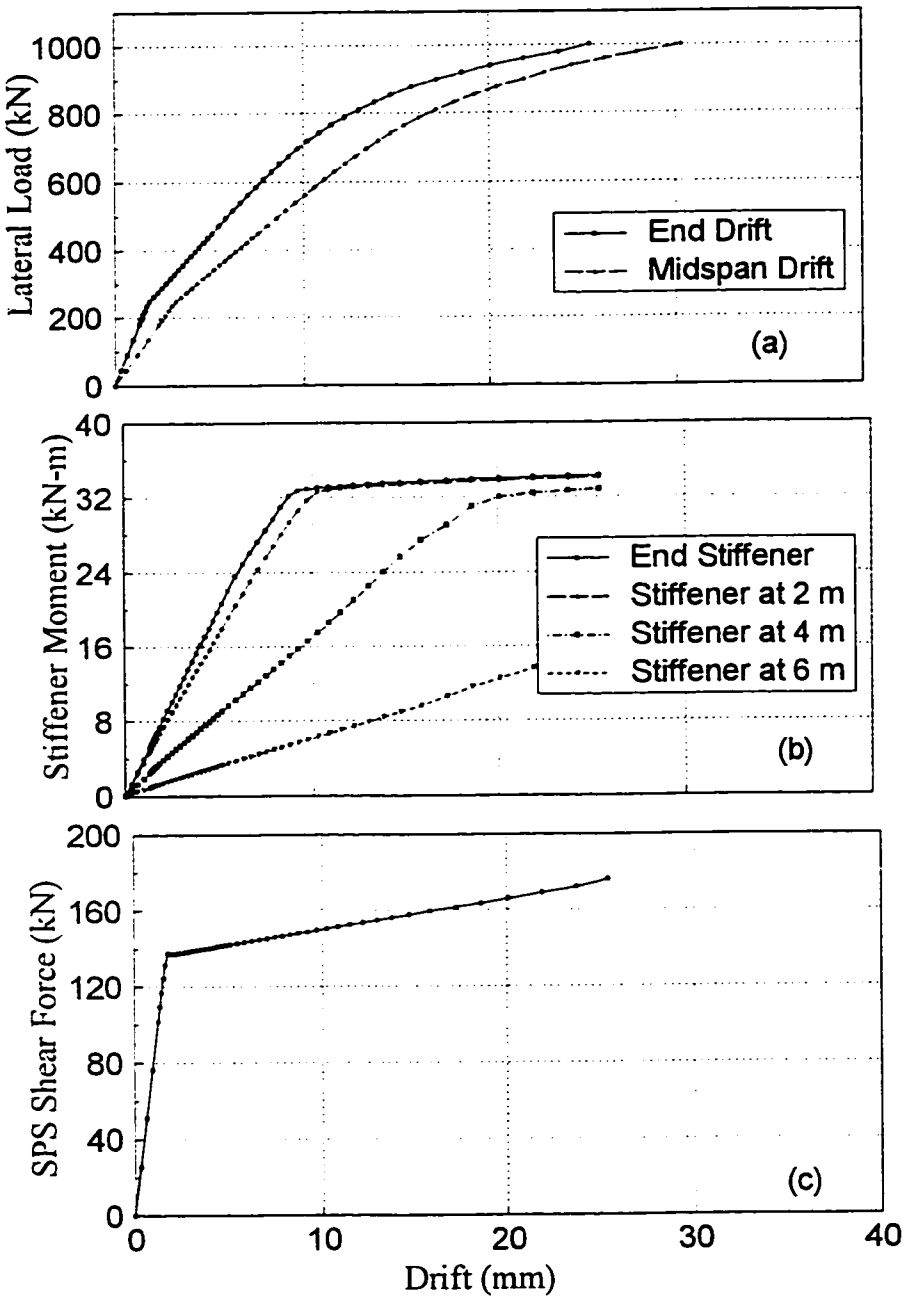

Fig. 4.33. Inelastic 3-D analysis results for a 40 m span bridge having SPS end-diaphragms by ADINA (web stiffeners at every 2 m): (a) lateral load versus end and center drifts; (b) bending moment in web stiffeners and (c) axial forces in braces, versus end drift.

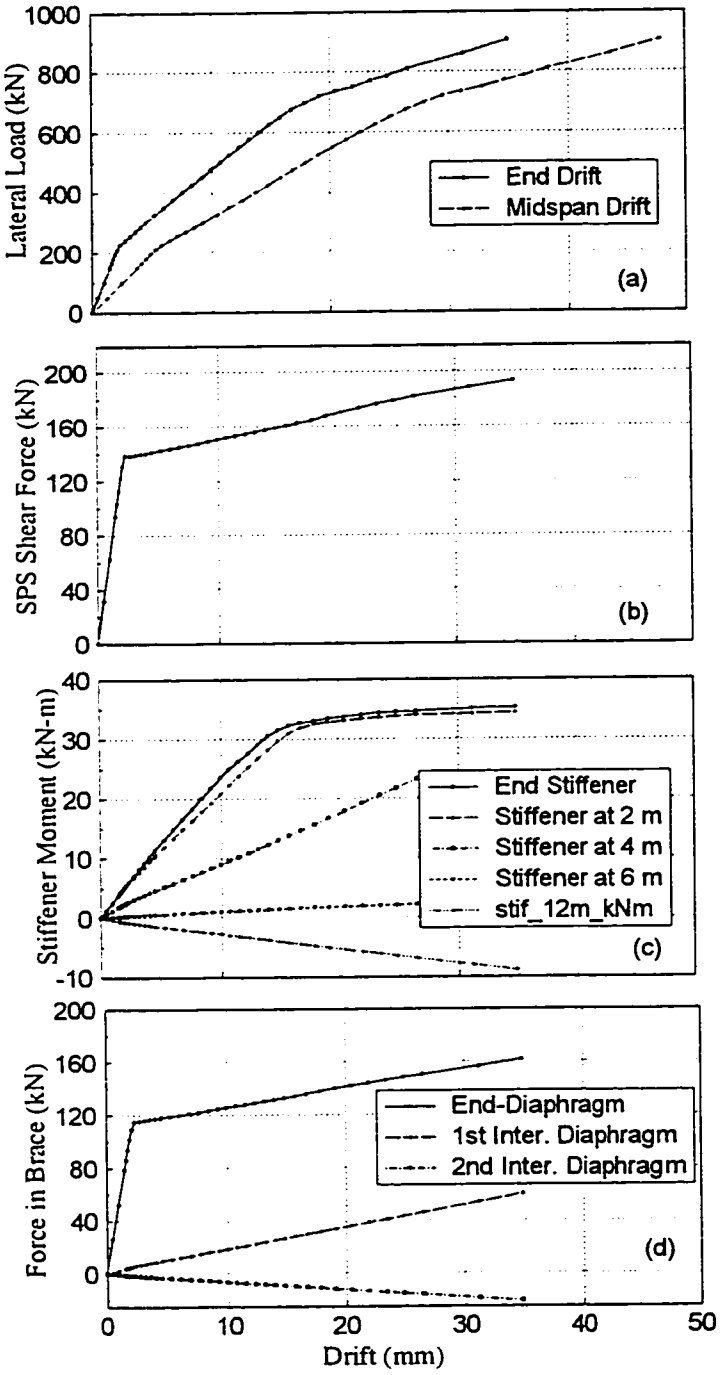

Fig. 4.34. Inelastic 3-D analysis results for a 60 m span bridge having SPS end-diaphragms by ADINA (web stiffeners every 3 m): (a) lateral load versus end and center drifts; (b) shear force in the SPS; (c) bending moment in web stiffeners and (d) axial forces in braces, versus end drift.

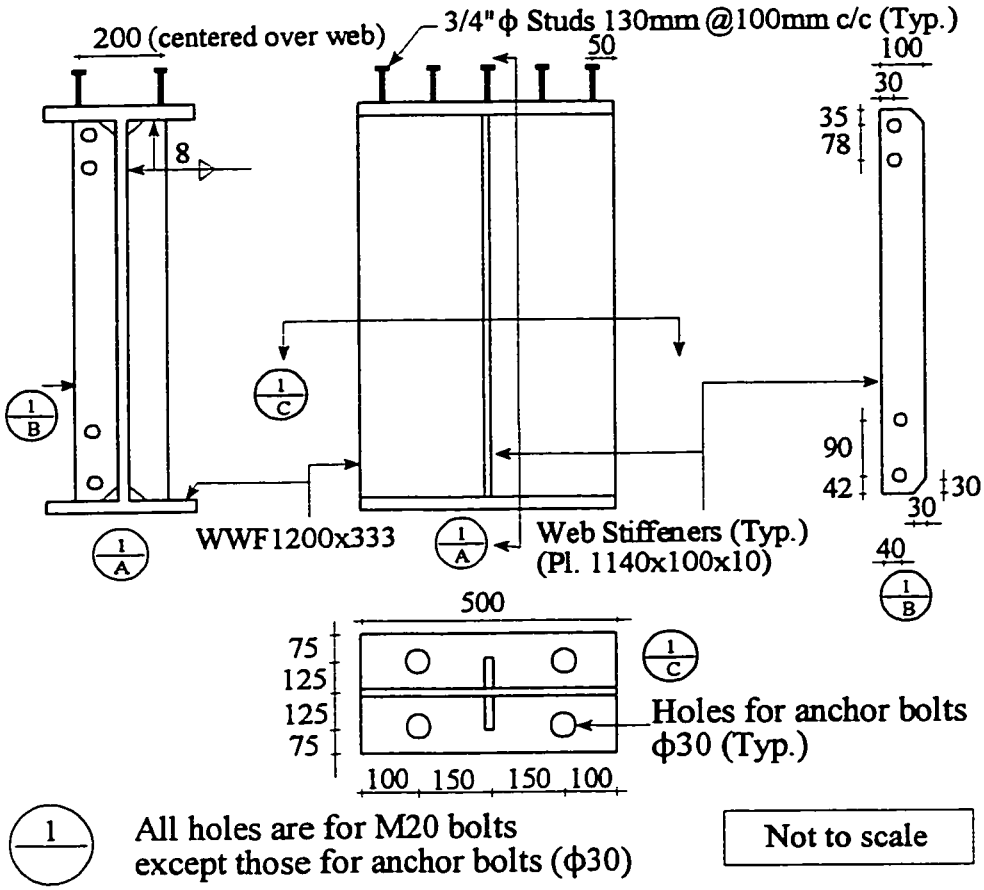

Fig. 5.1. Drawing details for stub-girders of the specimens.

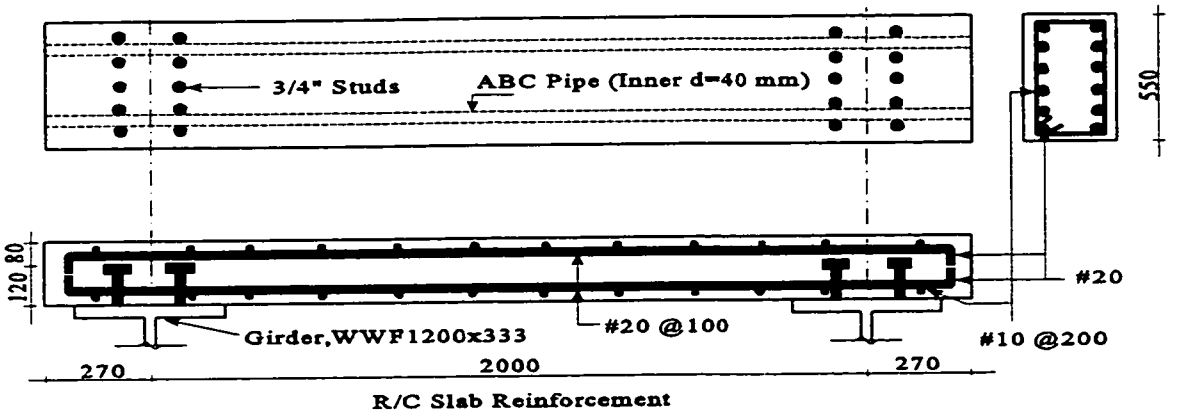

Fig. 5.2. Deck slab reinforcement for the designed specimens.

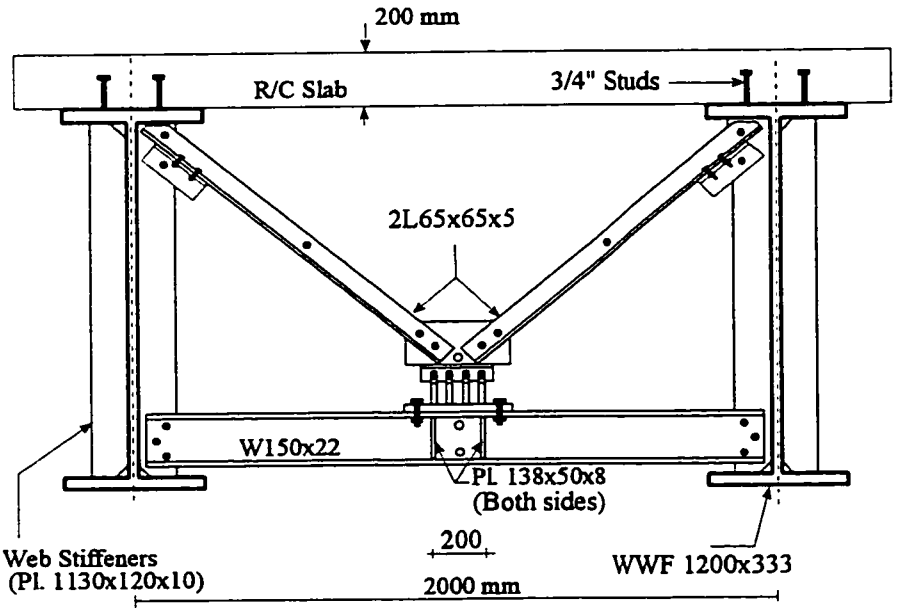

Fig. 5.3. Elevation of ductile end-diaphragm specimen having TADAS.

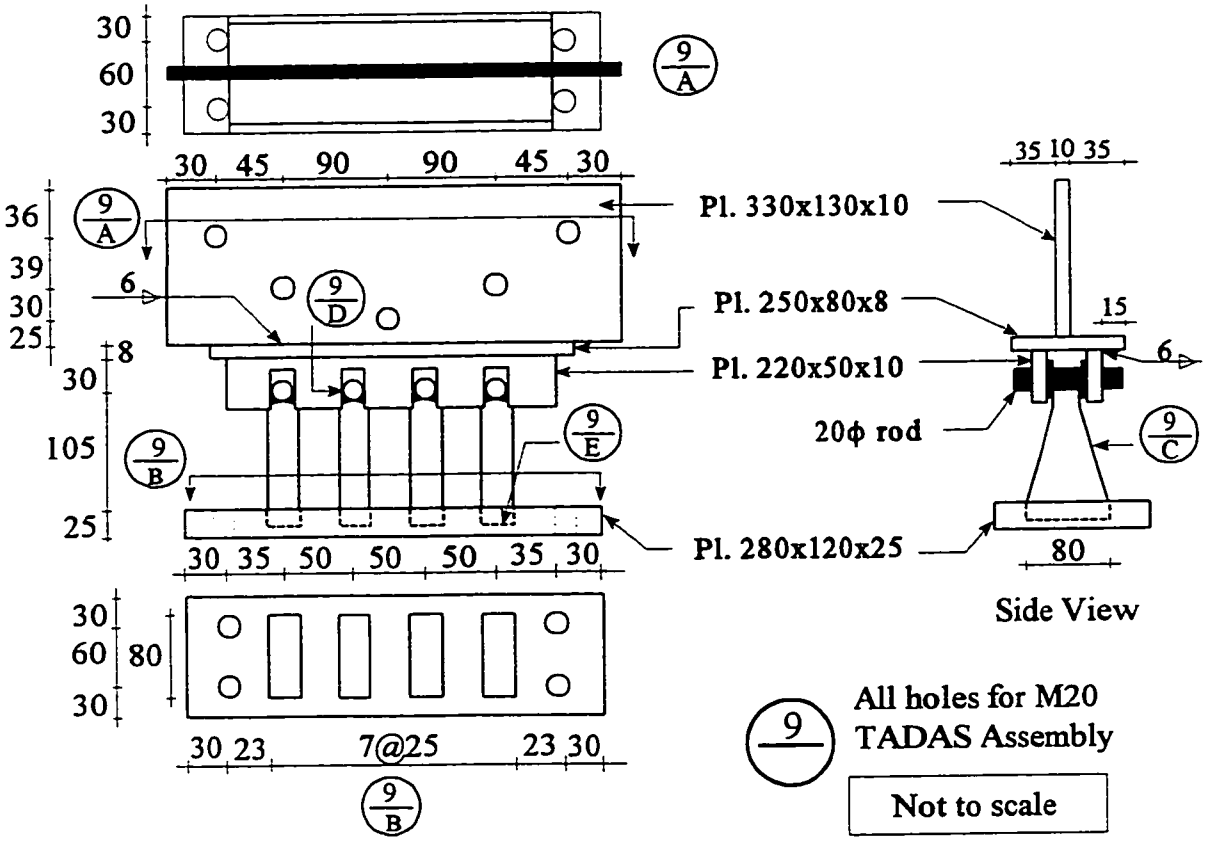

Fig. 5.4. TADAS assembly designed for the TADAS specimen.

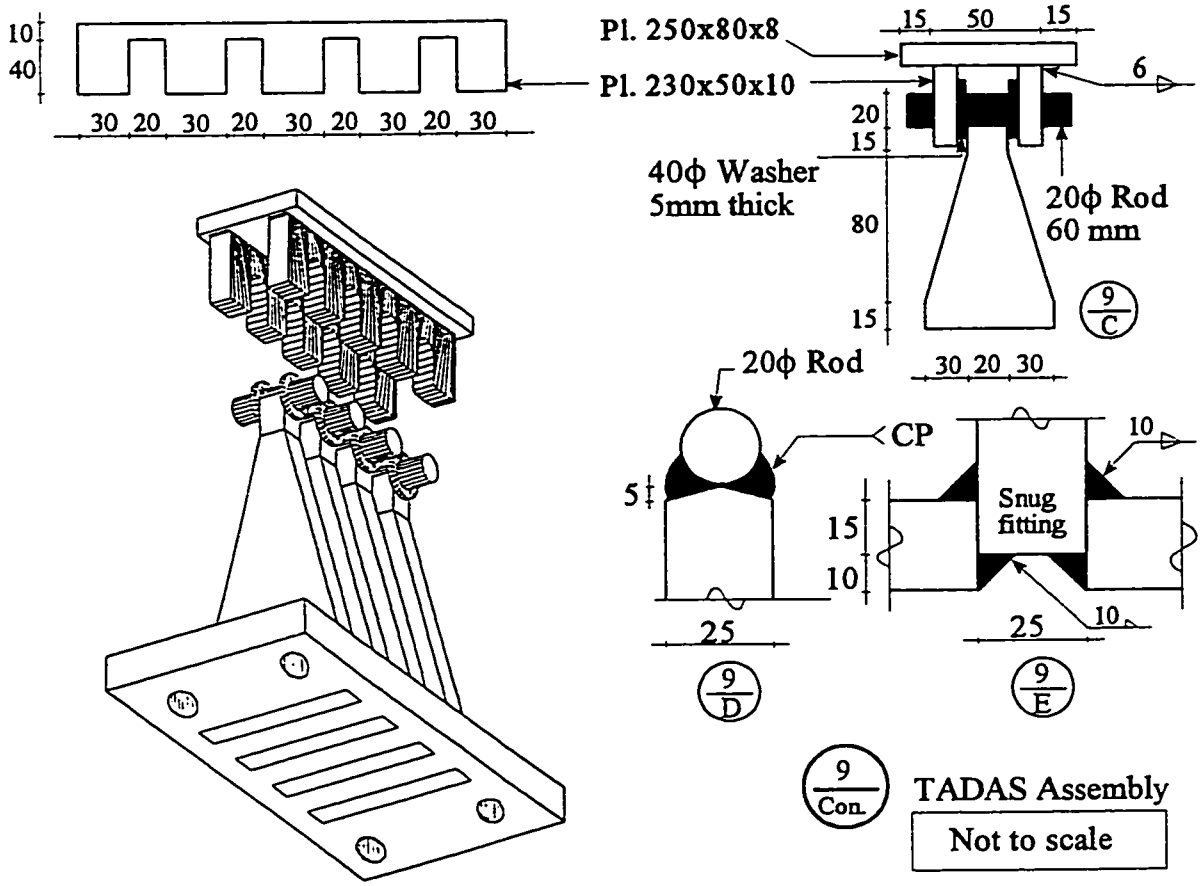

Fig. 5.5. Design detailing for TADAS.

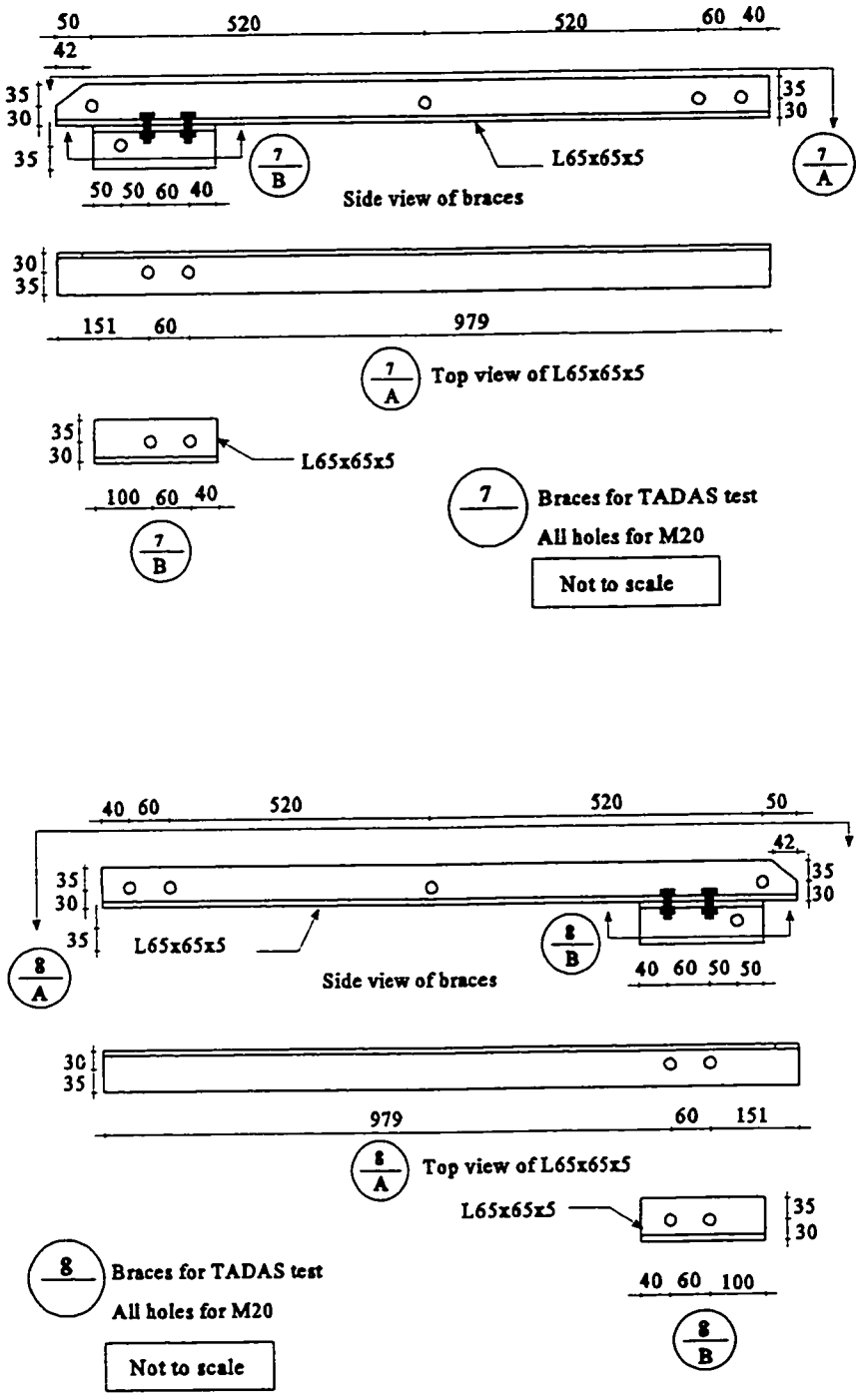

Fig. 5.6. Bracing members for the TADAS specimen.

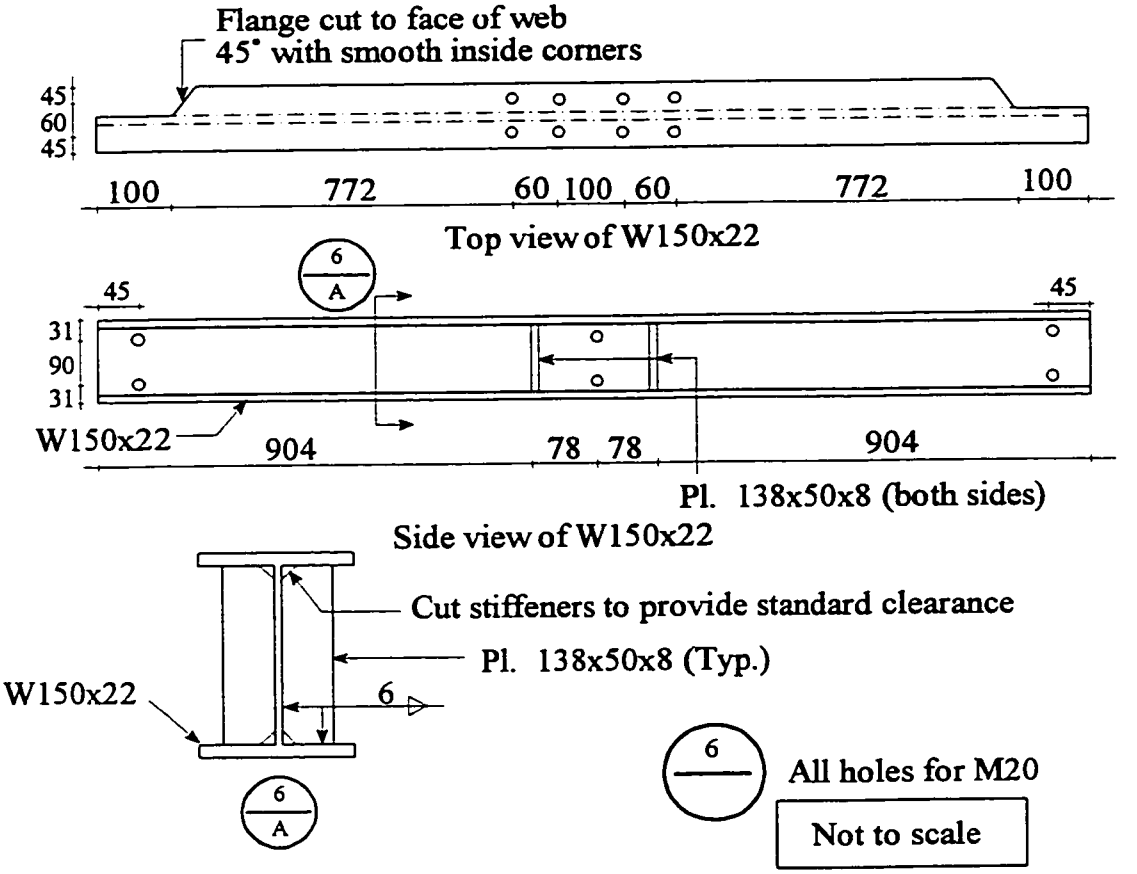

Fig. 5.7. Bottom beam and its detailing for the TADAS specimen.

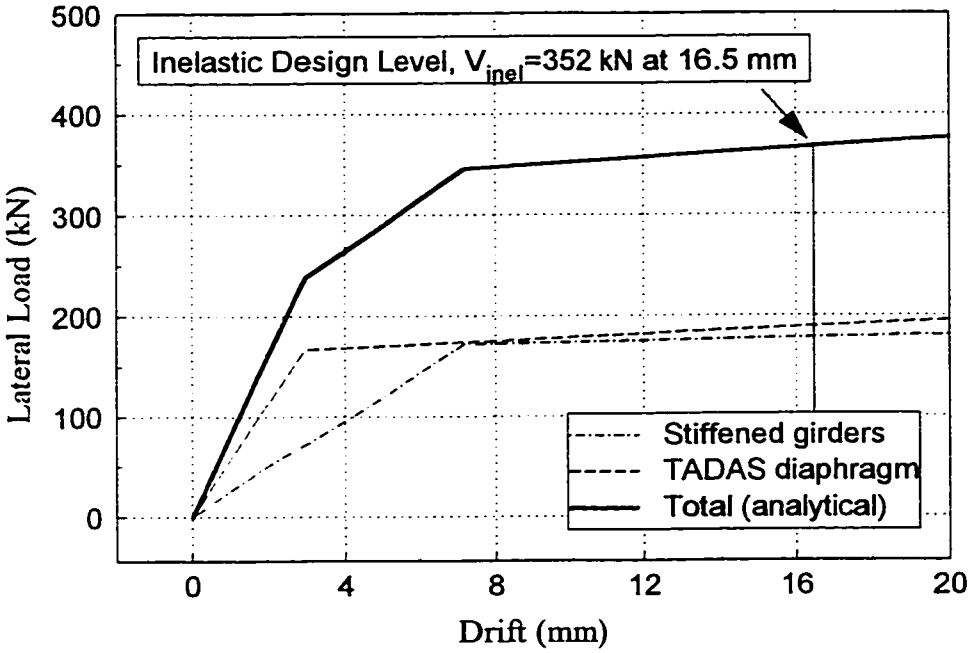

Fig. 5.8. Trilinear curve for the TADAS specimen following the proposed design procedure..

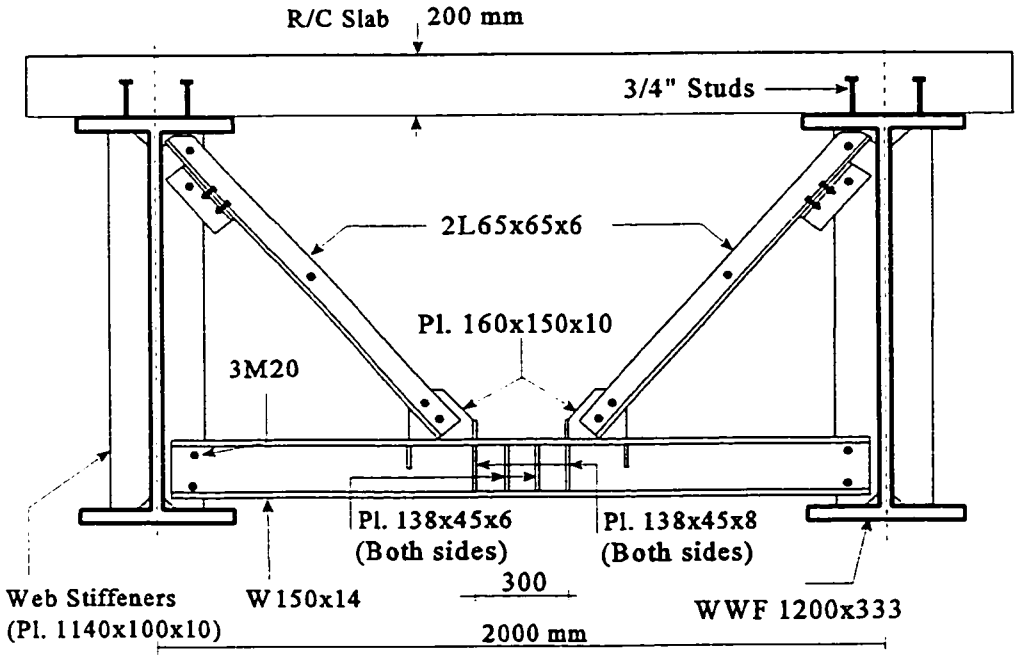

Fig. 5.9. Elevation of ductile end-diaphragm specimen having EBF.

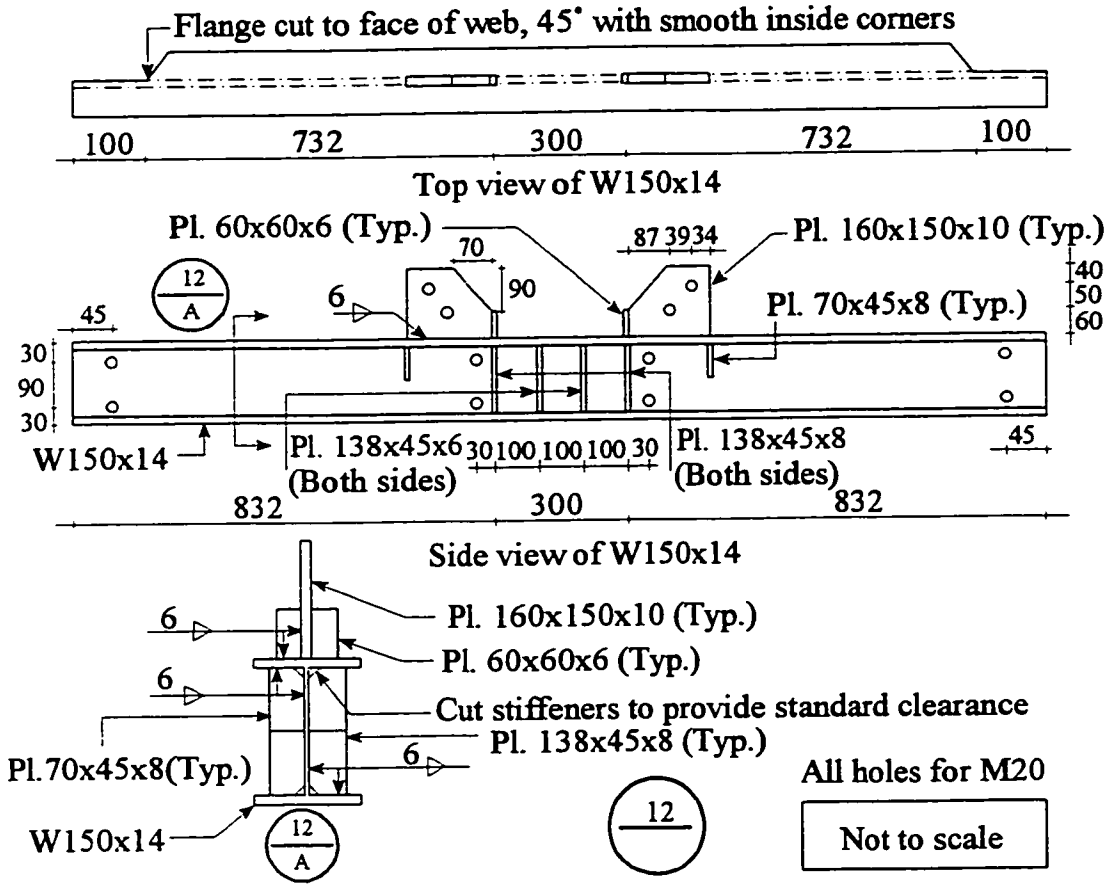

Fig. 5.10. Drawing details for the link beam in the EBF specimen.

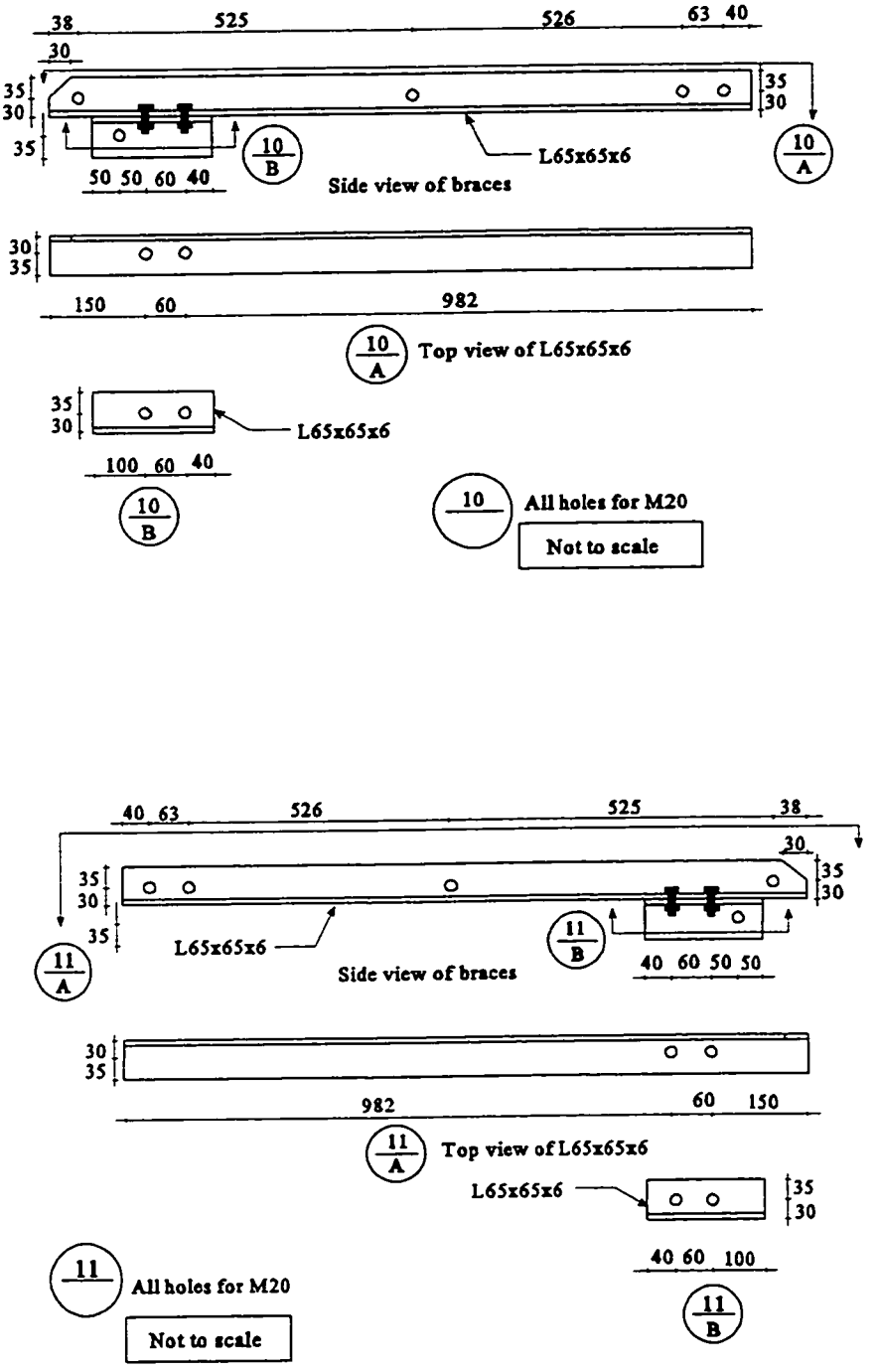

Fig. 5.11. Bracing members for the EBF specimen.

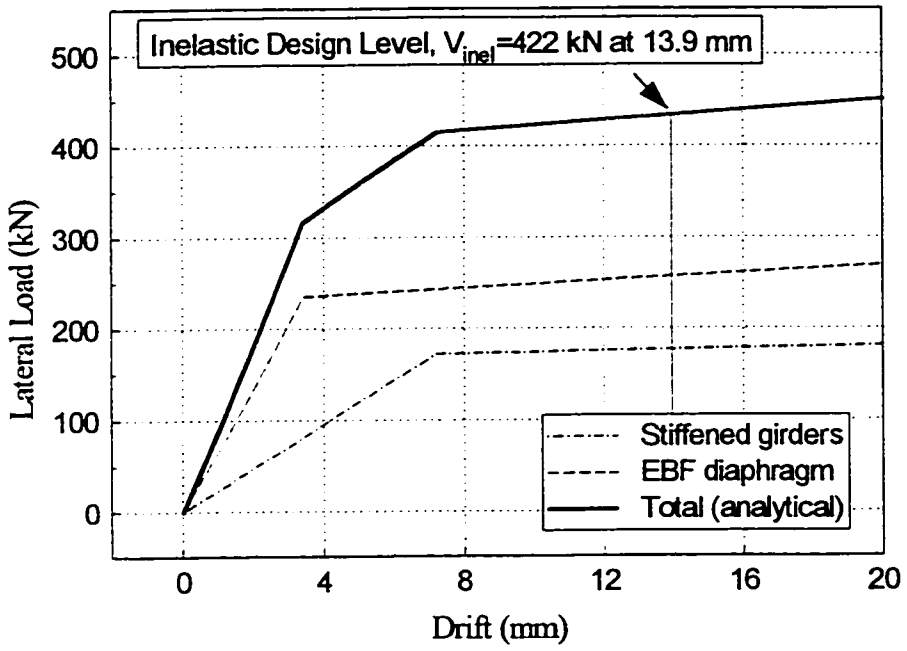

Fig. 5.12. Trilinear curve for EBF specimen following the proposed design procedure.

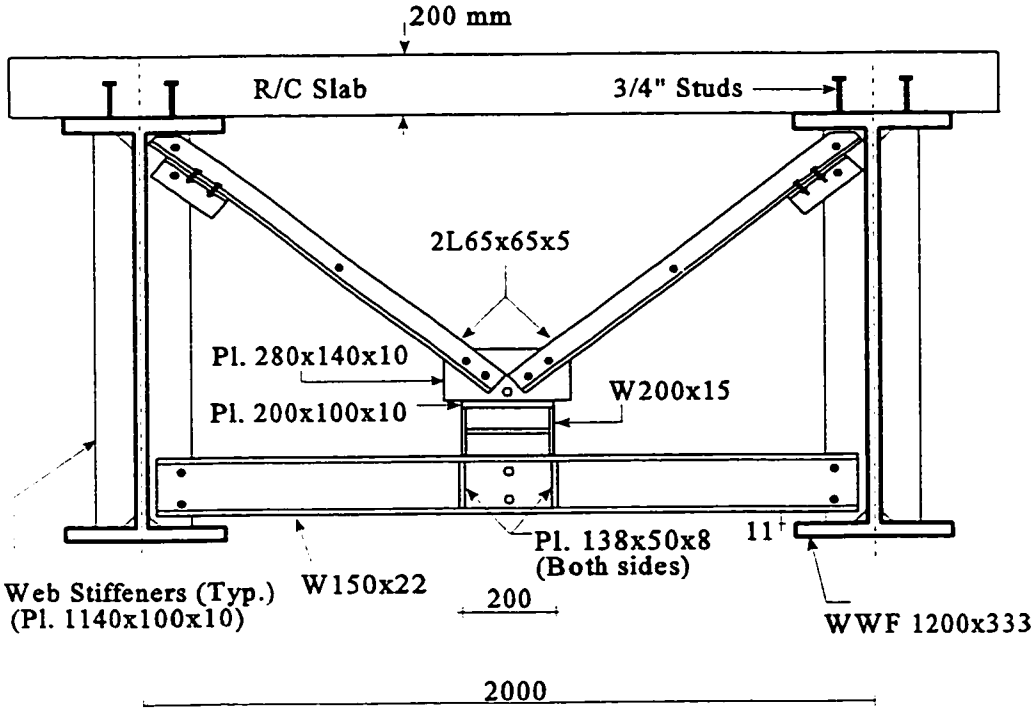

Fig. 5.13. Elevation of ductile end-diaphragm SPS specimen with a W200x15.

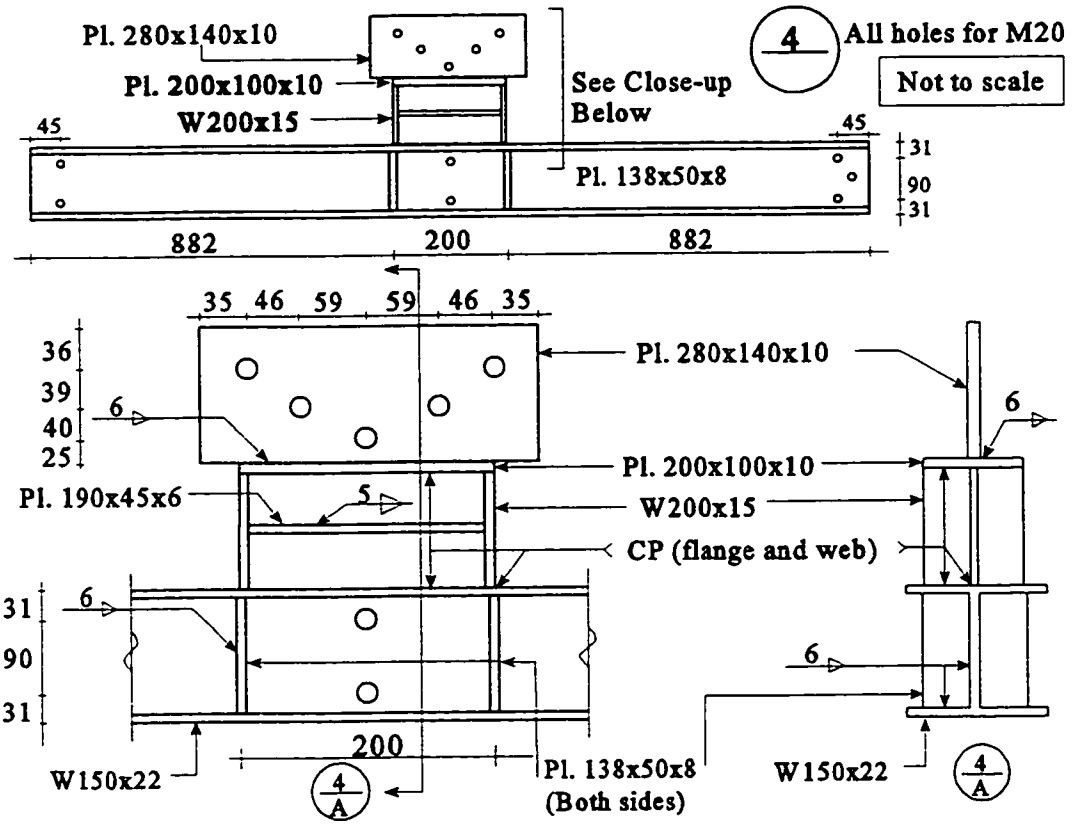

Fig. 5.14. Details of the first alternative SPS and its bottom beam.

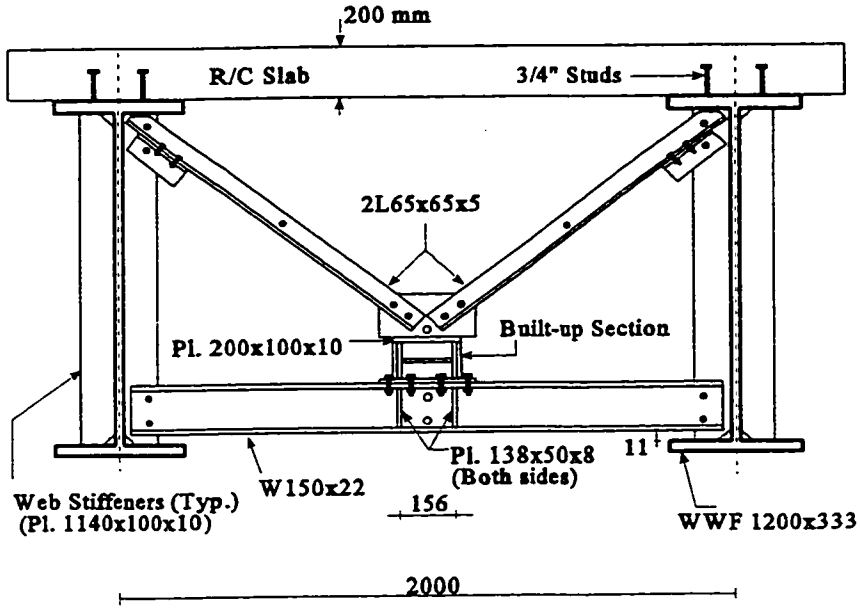

Fig. 5.15. Elevation of ductile end-diaphragm SPS specimen with built-up section.

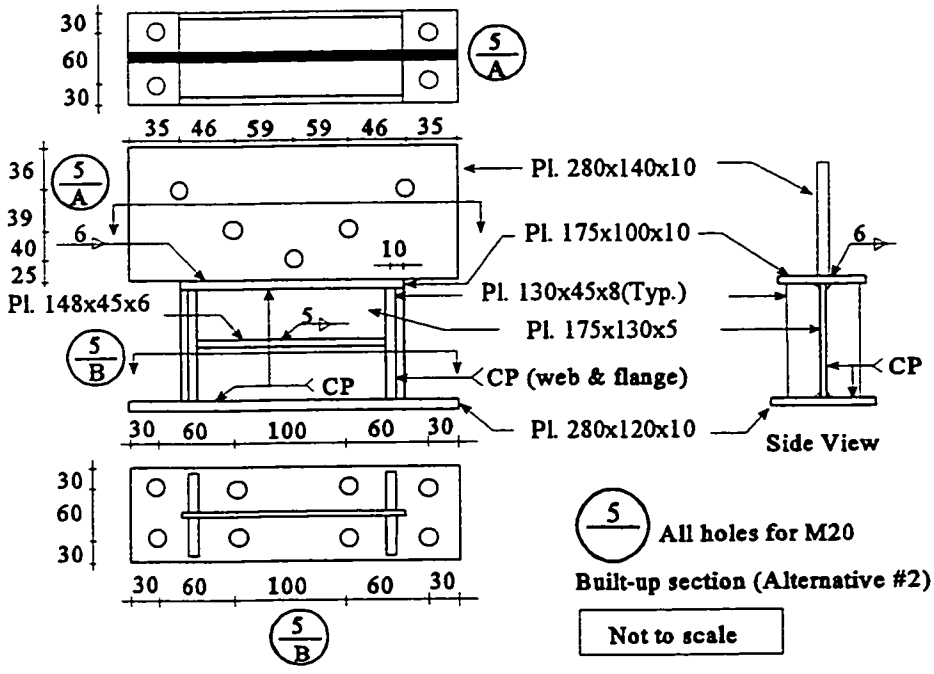

Fig. 5.16. Details for the 2nd SPS alternative (bolted to the bottom beam).

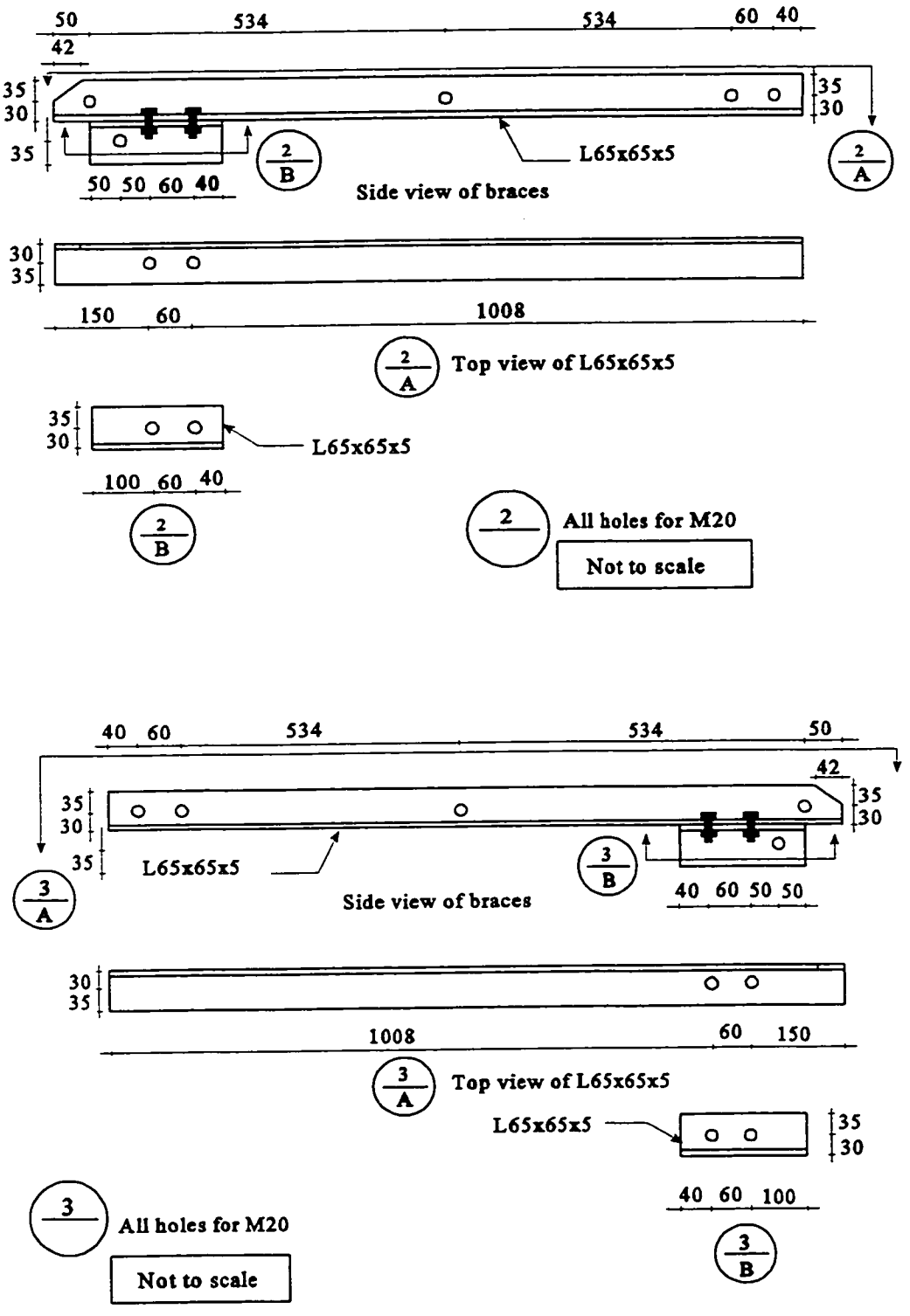

Fig. 5.17. Bracing members for the SPS specimens.

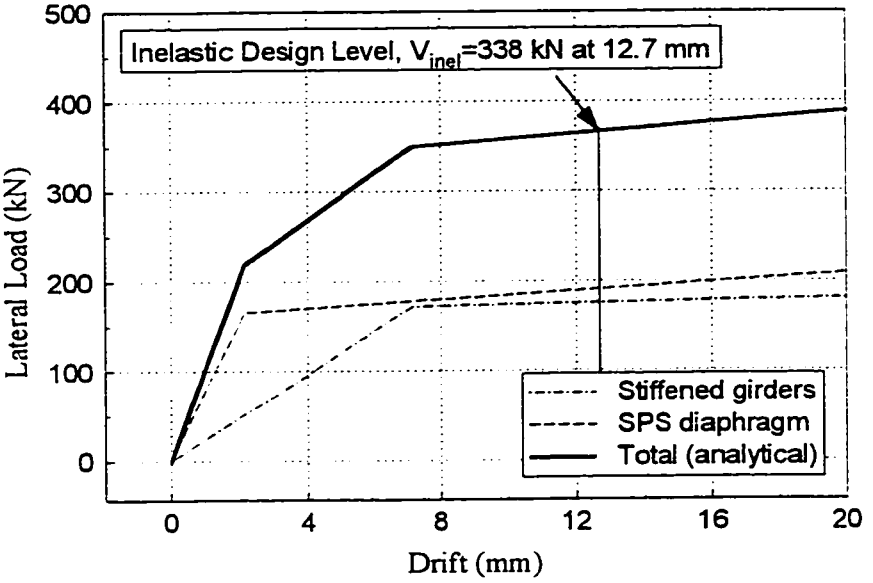

Fig. 5.18. Trilinear curve for the SPS specimen following the proposed design procedure.

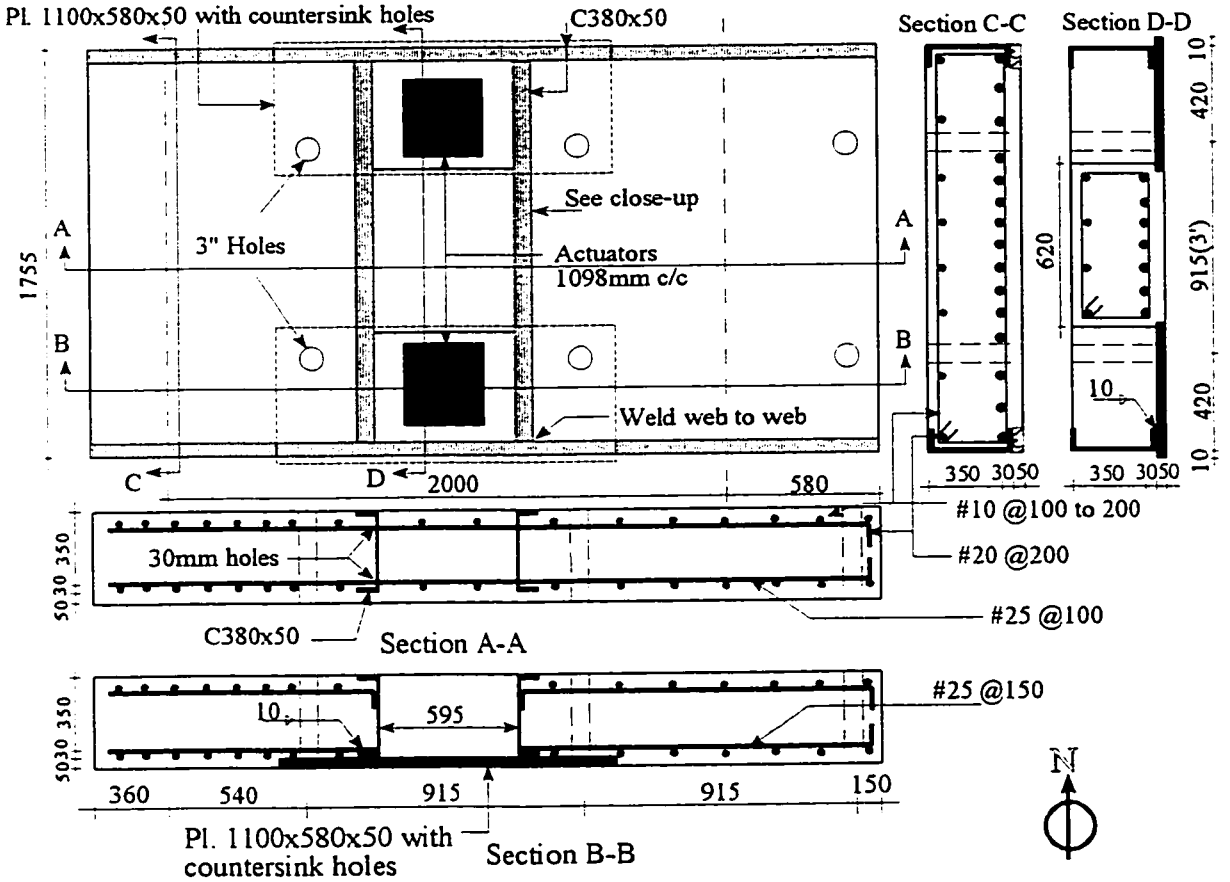

Fig. 5.19. Reinforcements for the foundation designed for testing of the specimens.

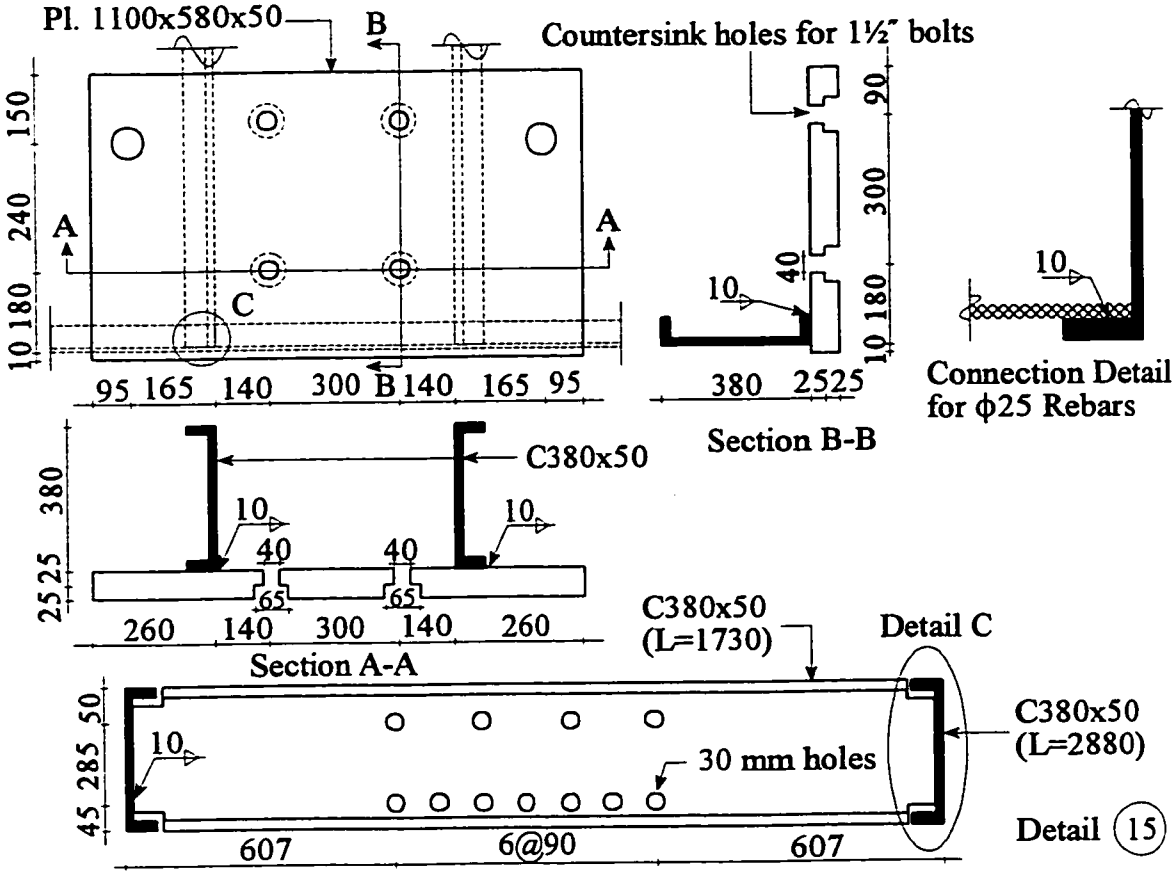

Fig. 5.20. Details for holes and connections of base plates and channel sections in foundation.

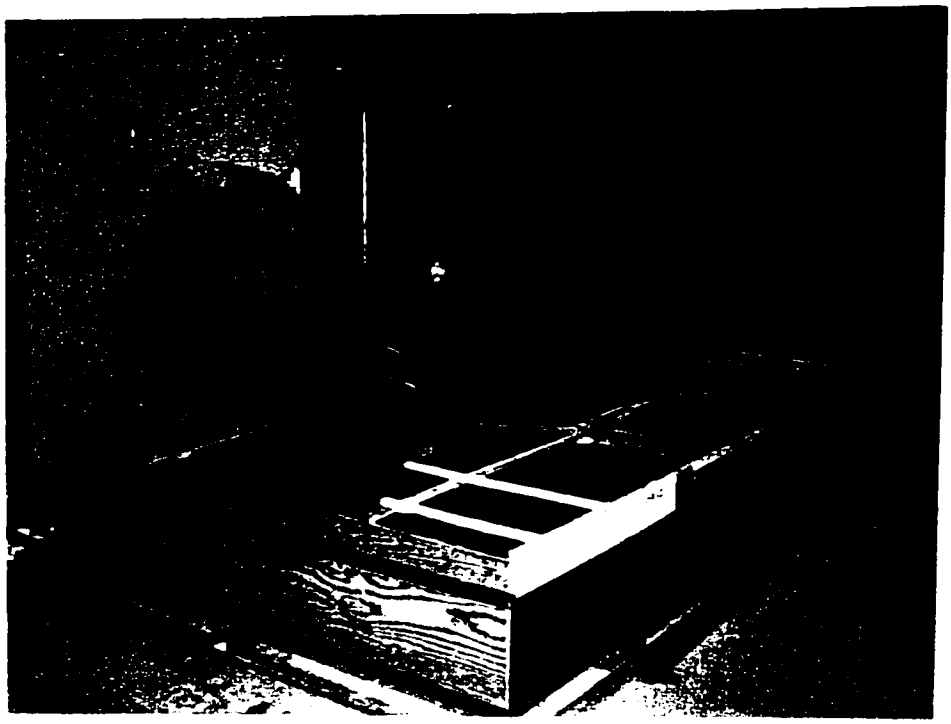

Fig. 5.21. Foundation cage and its formwork, note that one of the specimens is located in place to accurately position the anchor bolts inside the reinforced concrete foundation.

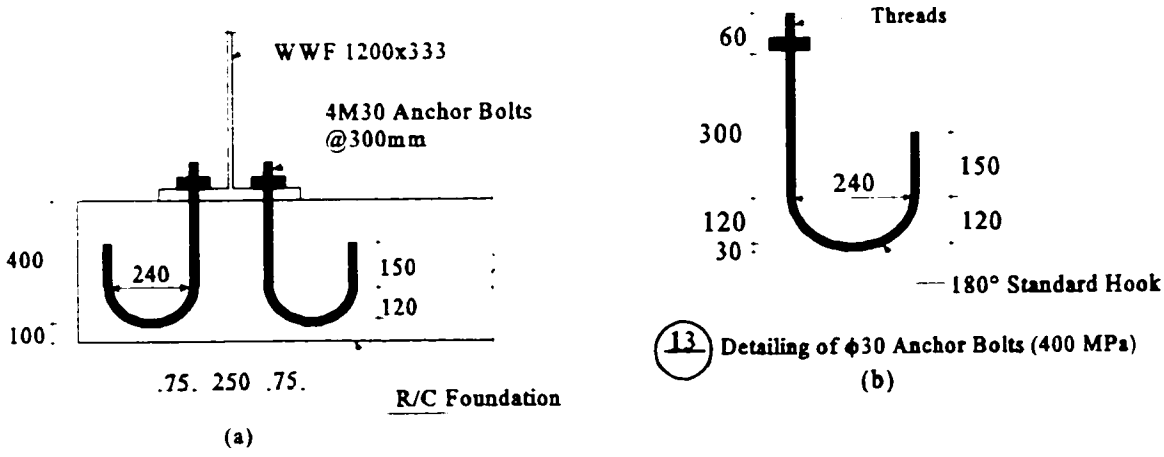

Fig. 5.22. Details on anchor bolts.

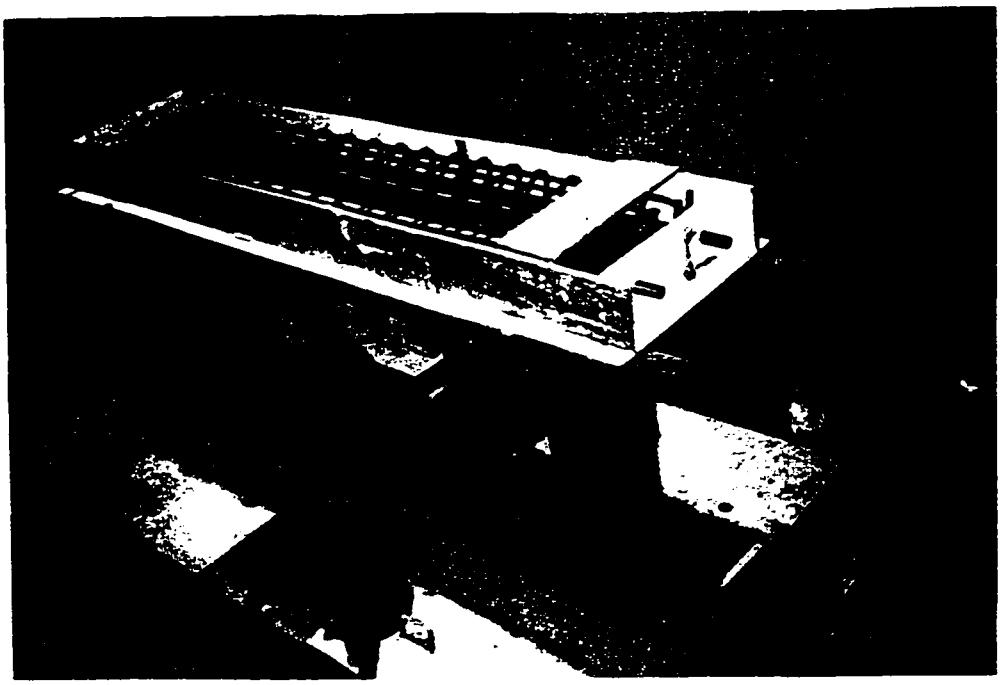

Fig. 5.23. Deck slab cage and its formwork before pouring the concrete. Four bolts are placed each side of the deck slab to be connected to load applicator beams.

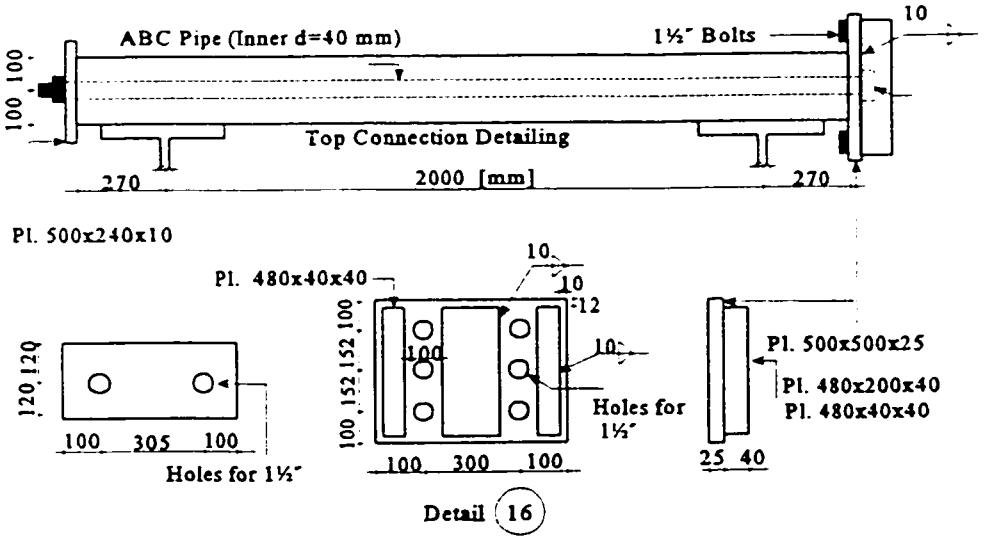

Fig. 5.24. End plates to connect the specimen deck to the horizontal actuator.

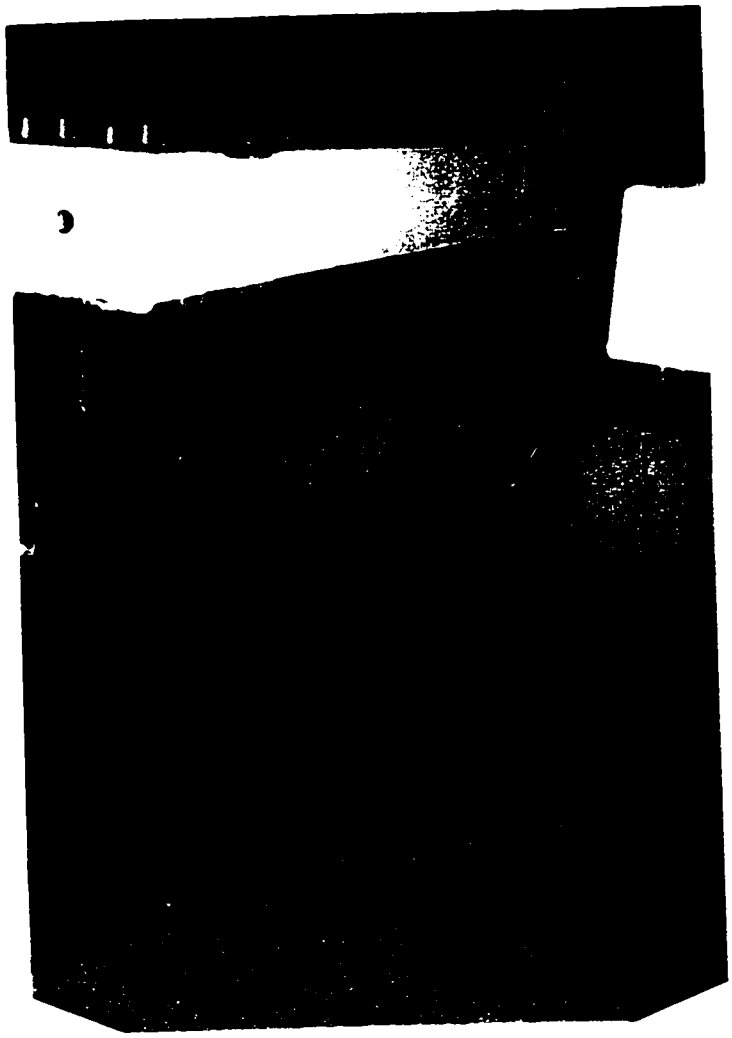

Fig. 5.25. Test specimens after construction.

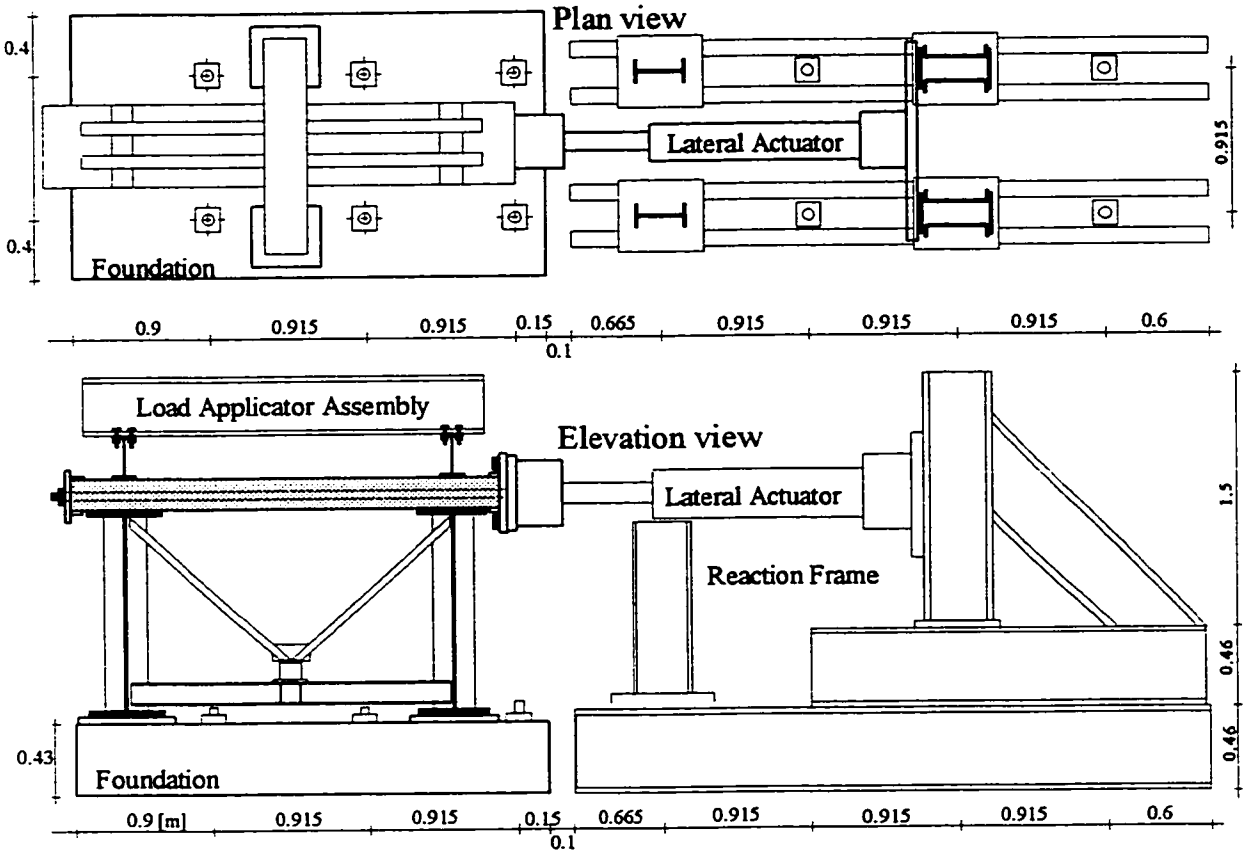

Fig. 5.26. Plan and elevation schematical views of test set-up prepared for experiments.

Fig. 5.27. Photo of test set-up and load applicator beam assembly.

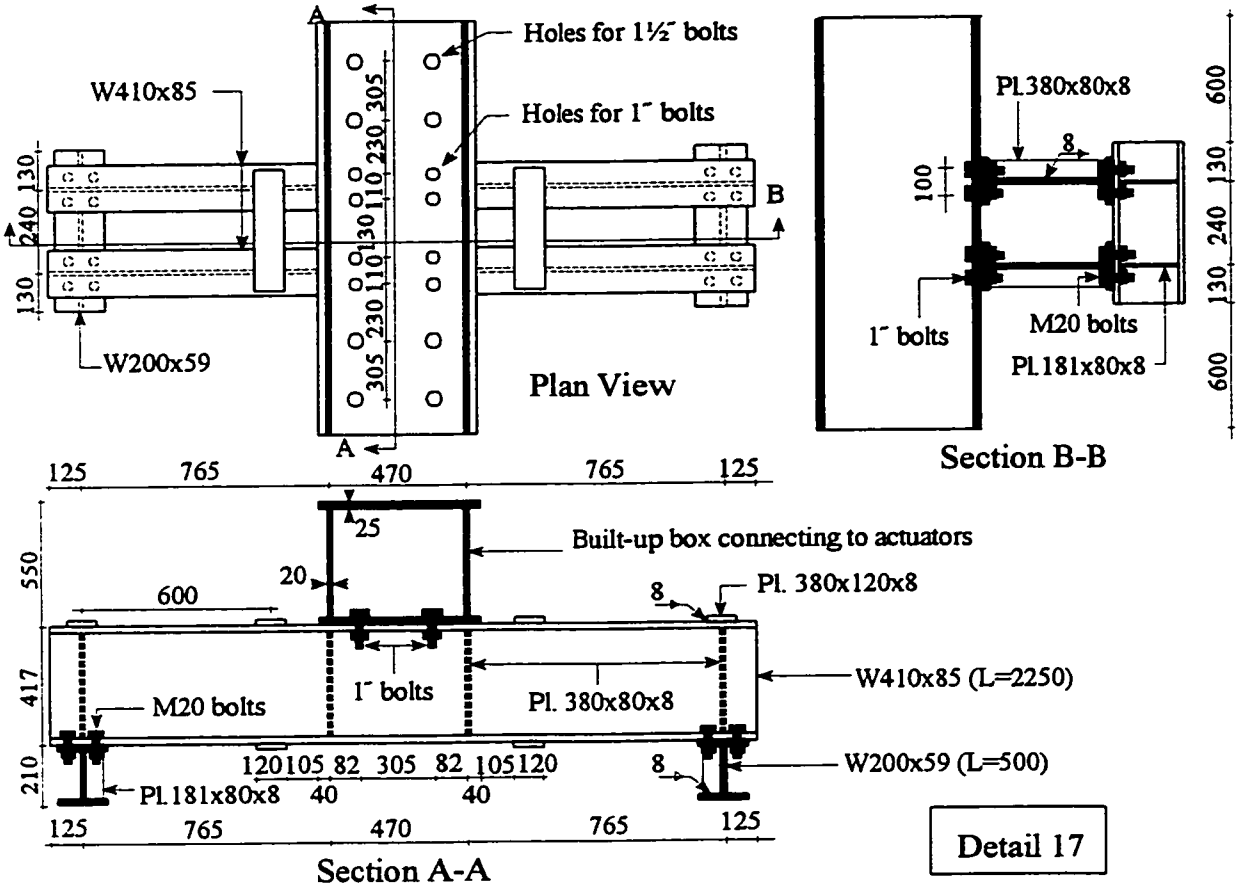

Fig. 5.28. Drawing details for load applicator beams.

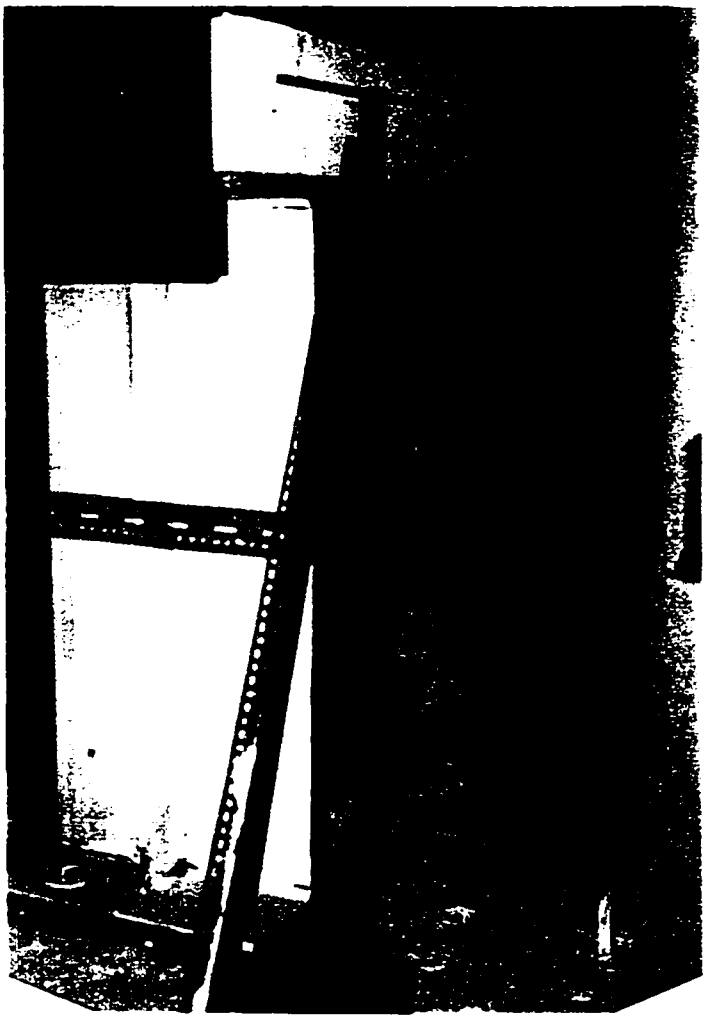

Fig. 5.29. Light frame built with slotted angles to support Temposonic transducers and LVDTs.

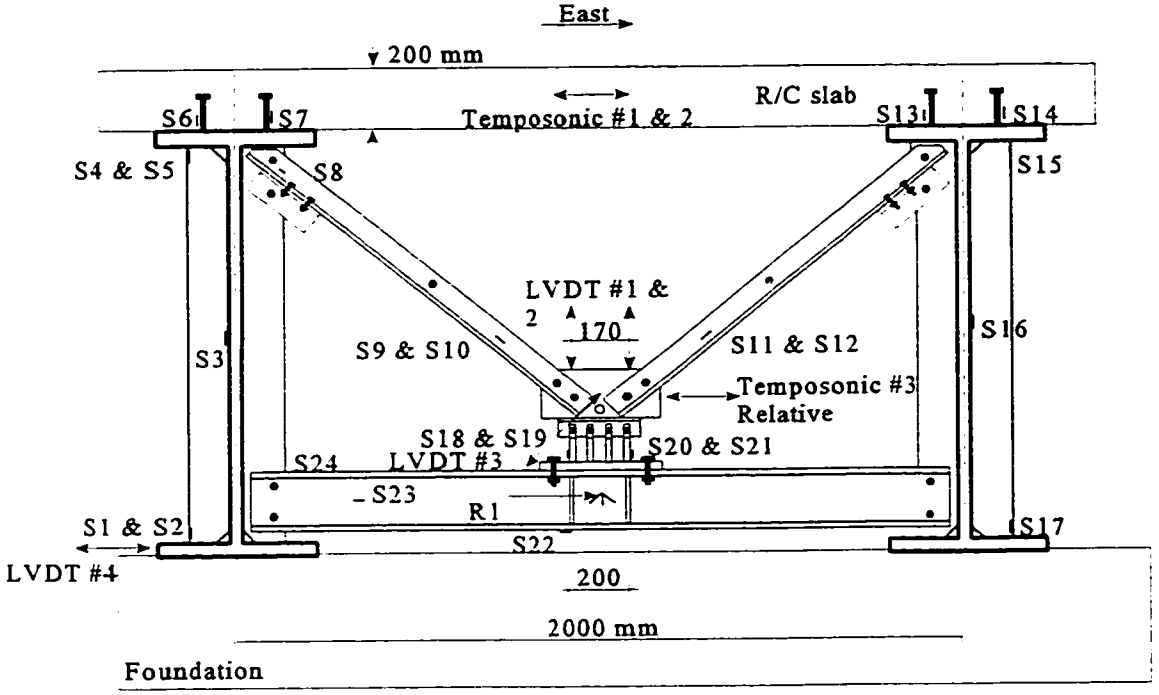

Fig. 5.30. Instrumentation of the TADAS specimen.

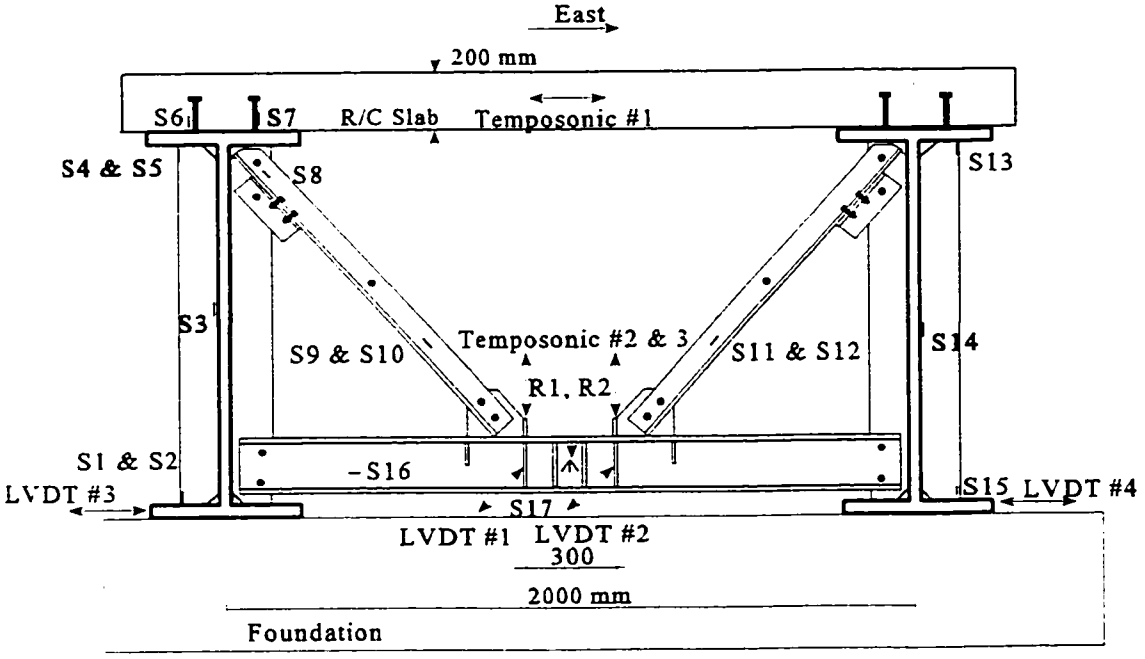

Fig. 5.31. Instrumentation of the EBF specimen.

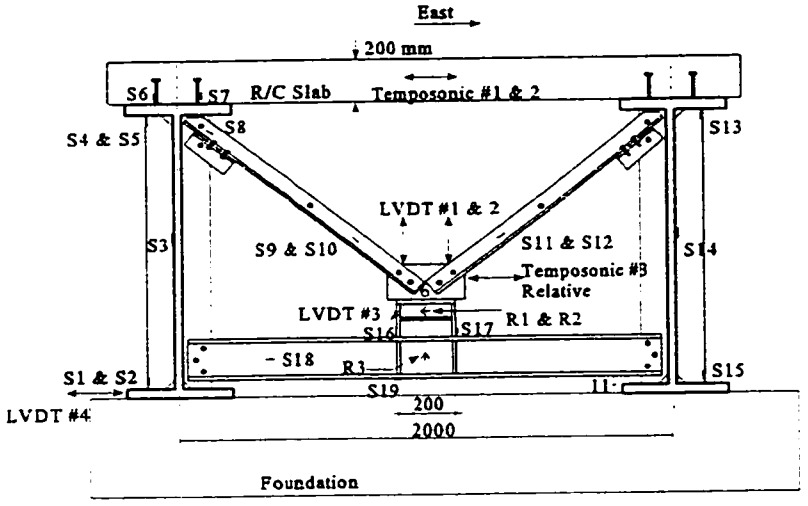

(a)

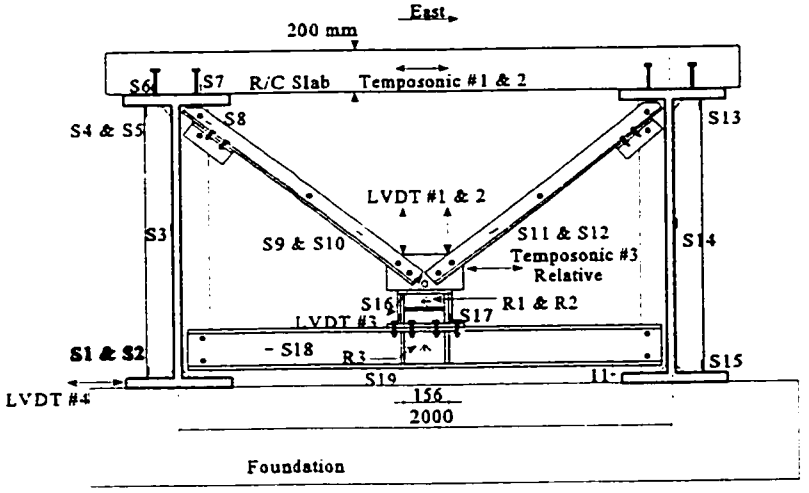

(b)

Fig. 5.32. Instrumentation of: (a) the SPS1 specimen; (b) the SPS2 specimen.

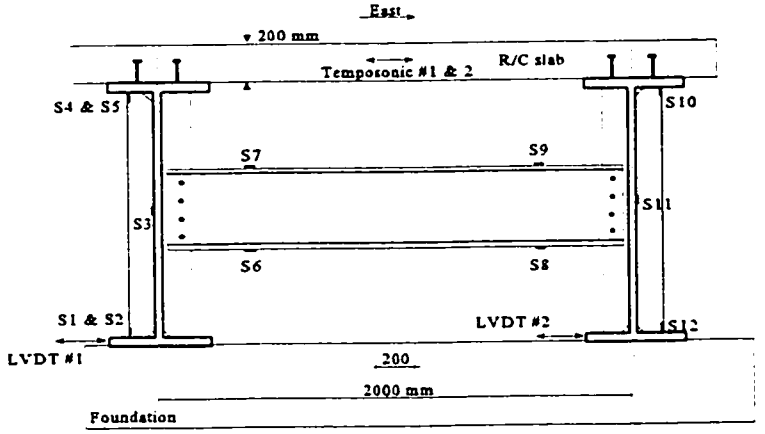

Fig. 5.33. Instrumentation of the Channel specimen

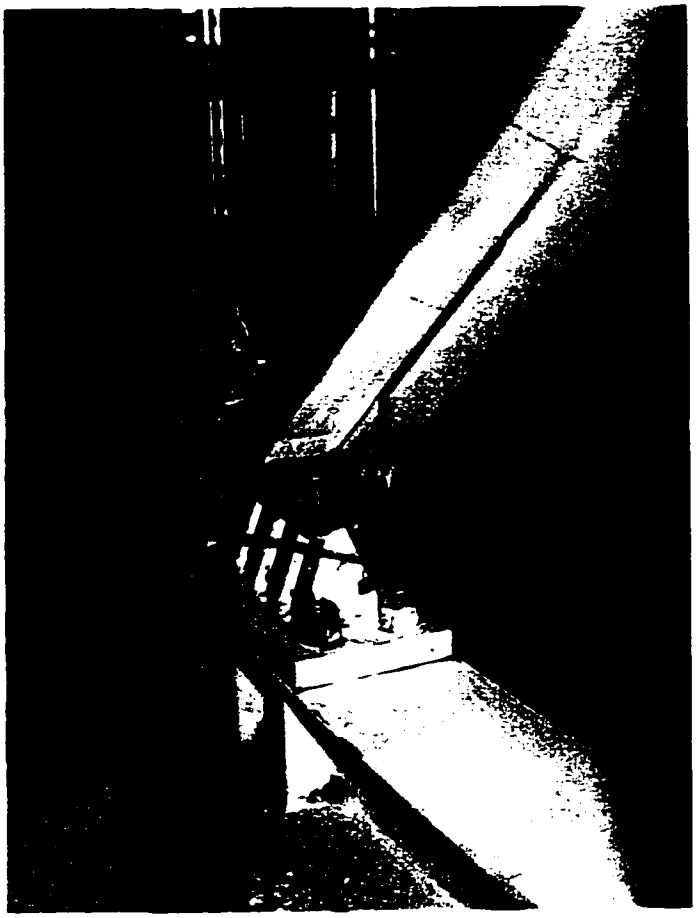

Fig. 5.34. LVDTs and Temposonic tranducer to measure deformations of the TADAS plates and rotation of bottom beam.

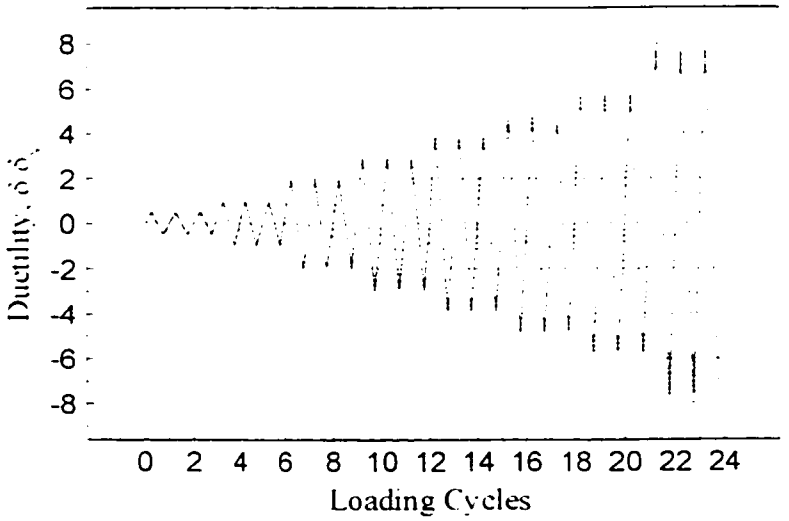

Fig. 5.35. Cyclic displacement history imposed to the specimens.

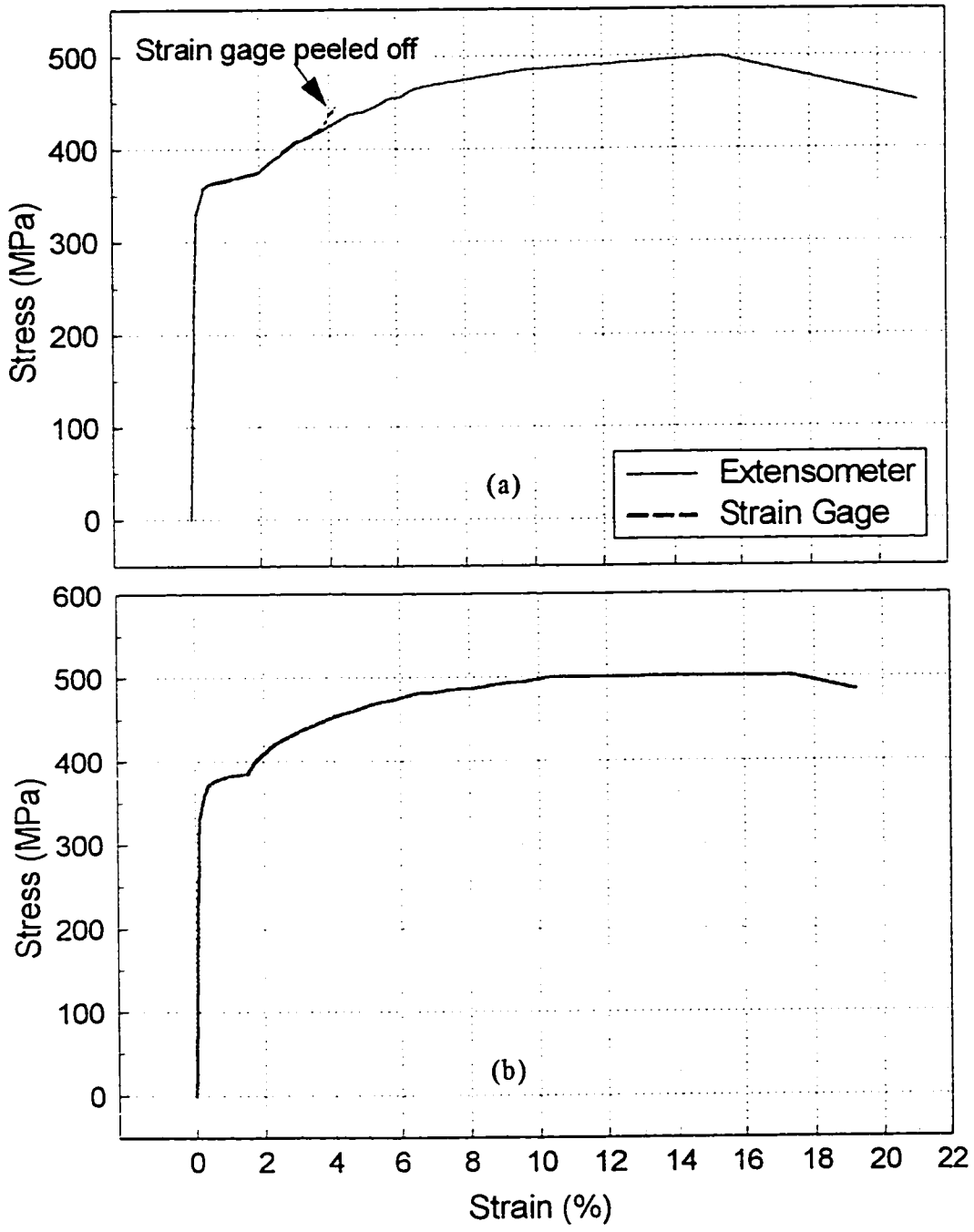

Fig. 6.1. Preliminary tests on coupons taken from same stock as web of first SPS (W200x15), to determine the strength and ductility of provided steel: (a) first coupon; (b) second coupon.

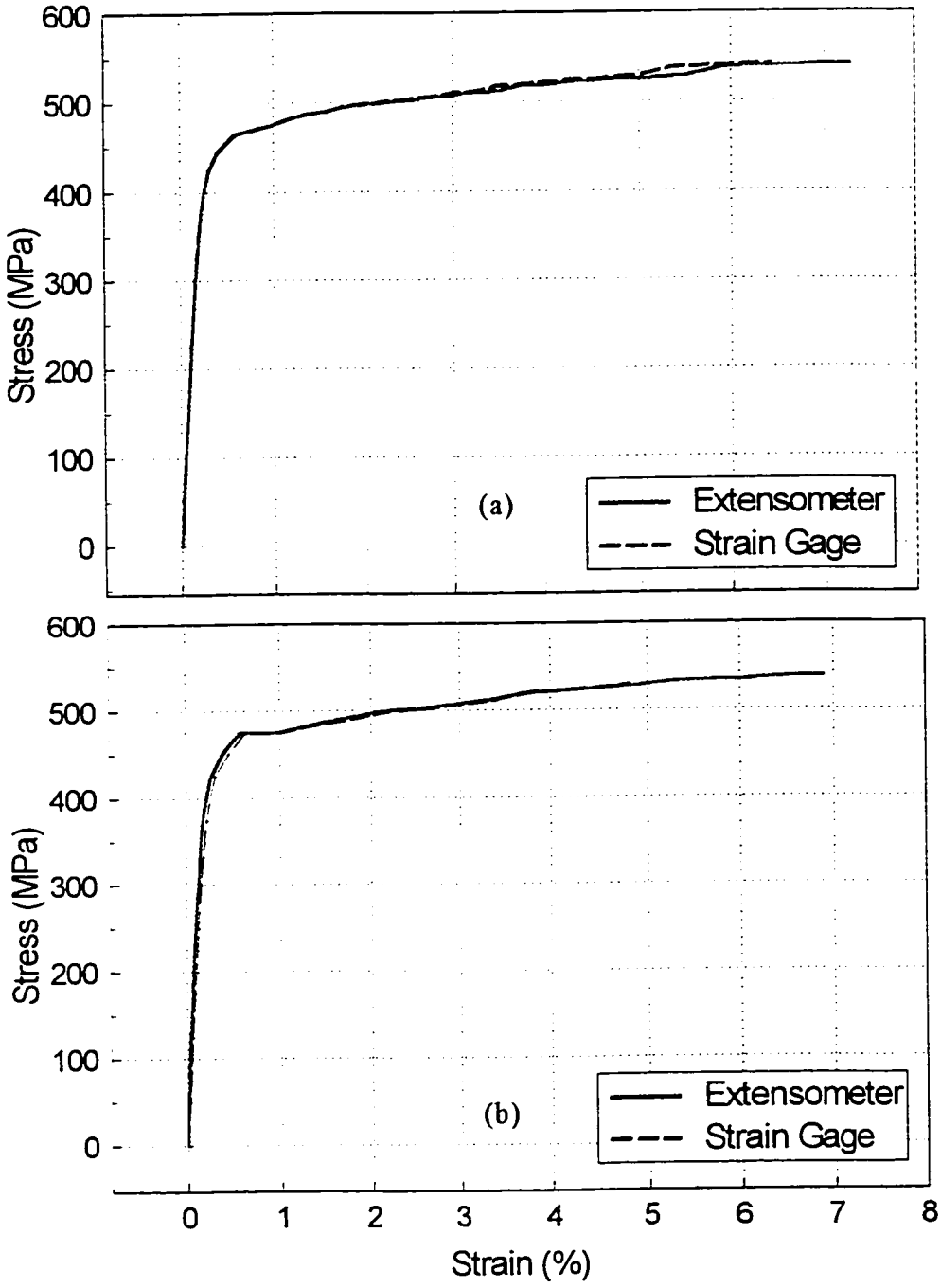

Fig. 6.2. Preliminary tests on coupons taken from same stock as web of second SPS (built-up), to determine the strength and ductility of provided steel: (a) first coupon; (b) second coupon.

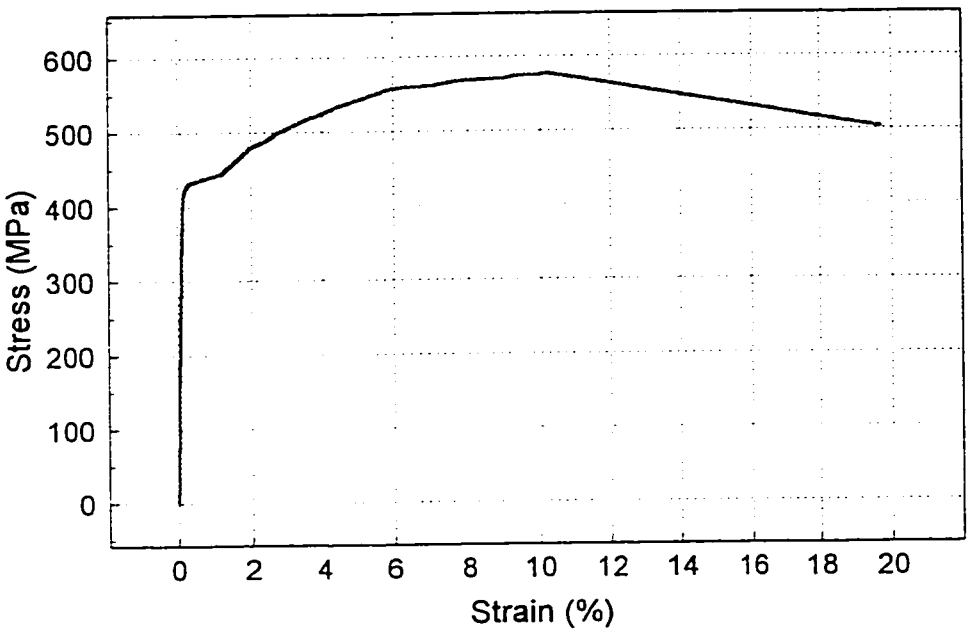

Fig. 6.3. Preliminary tests on coupons taken from link web of EBF, to determine the strength and ductility of provided steel.

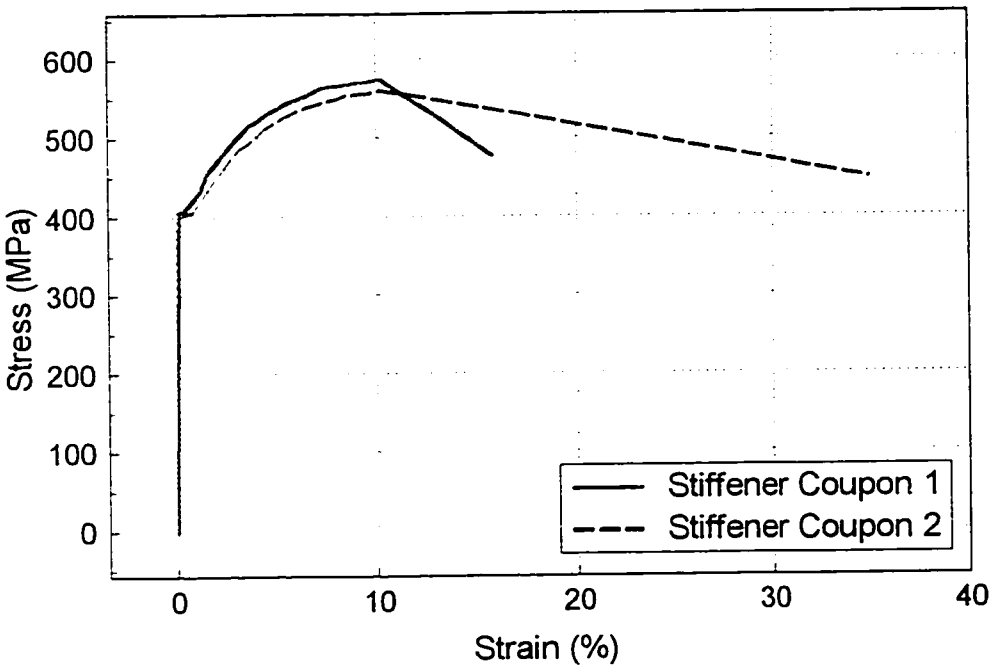

Fig. 6.4. Preliminary tests on coupons taken from girder web stiffeners, to determine the strength and ductility of provided steel.

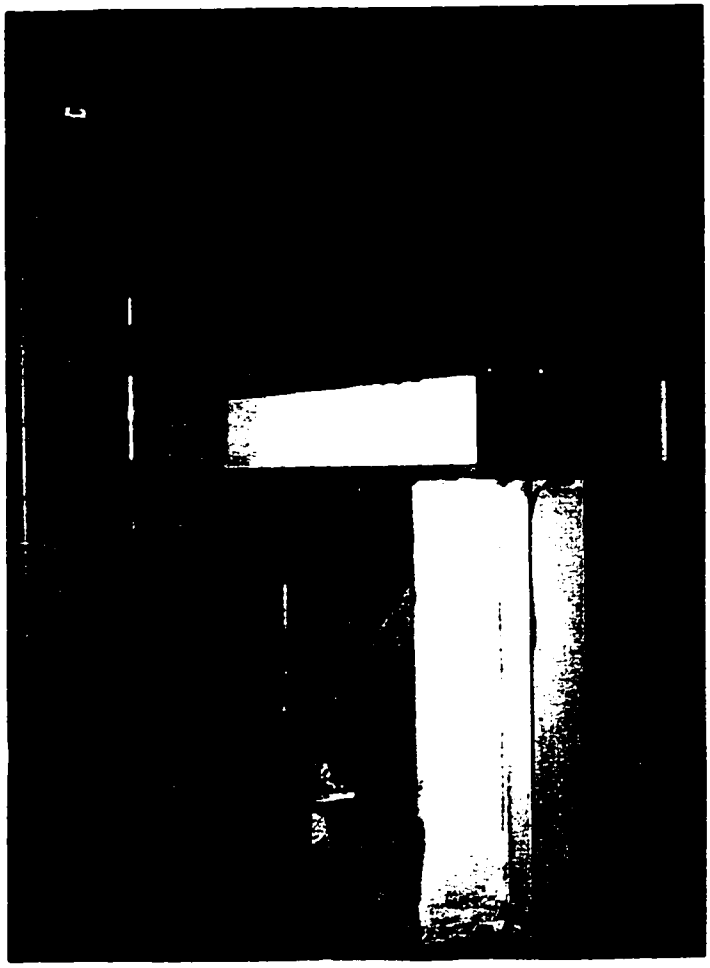

Fig. 6.5. The TADAS specimen under testing.

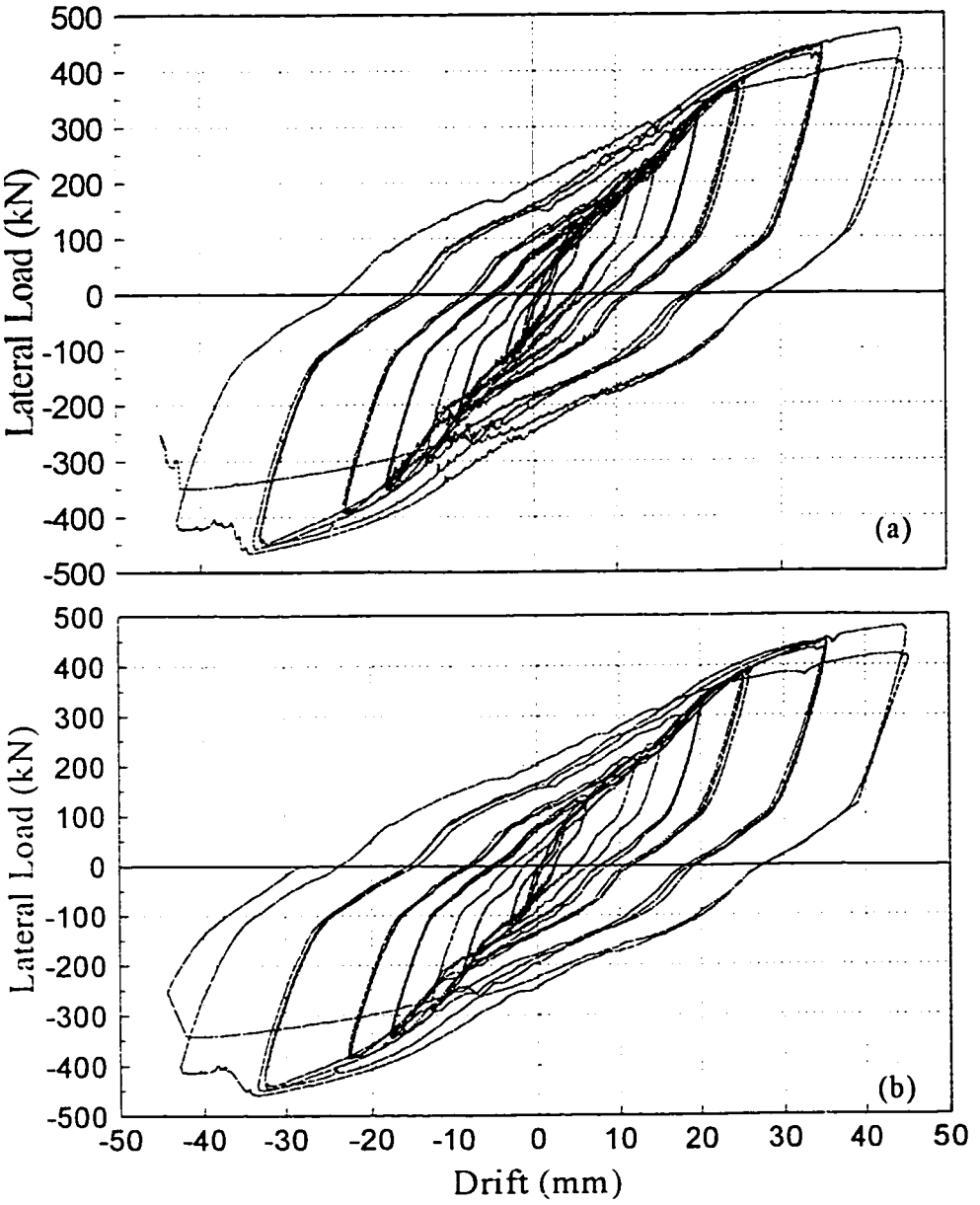

Fig. 6.6. Hysteretic curves for the TADAS specimen: (a) recorded by MTS Testar; (b) recorded by Vishay data aquisition system after data reduction.

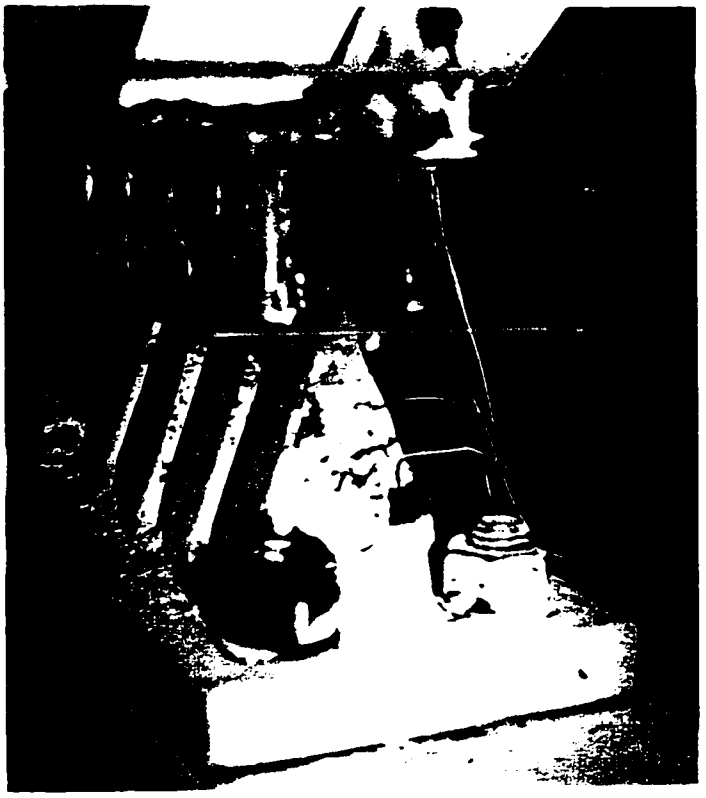

Fig. 6.7. Slippage of the TADAS device base plate, also showing cracks on the whitewash of the plates particularly near the top.

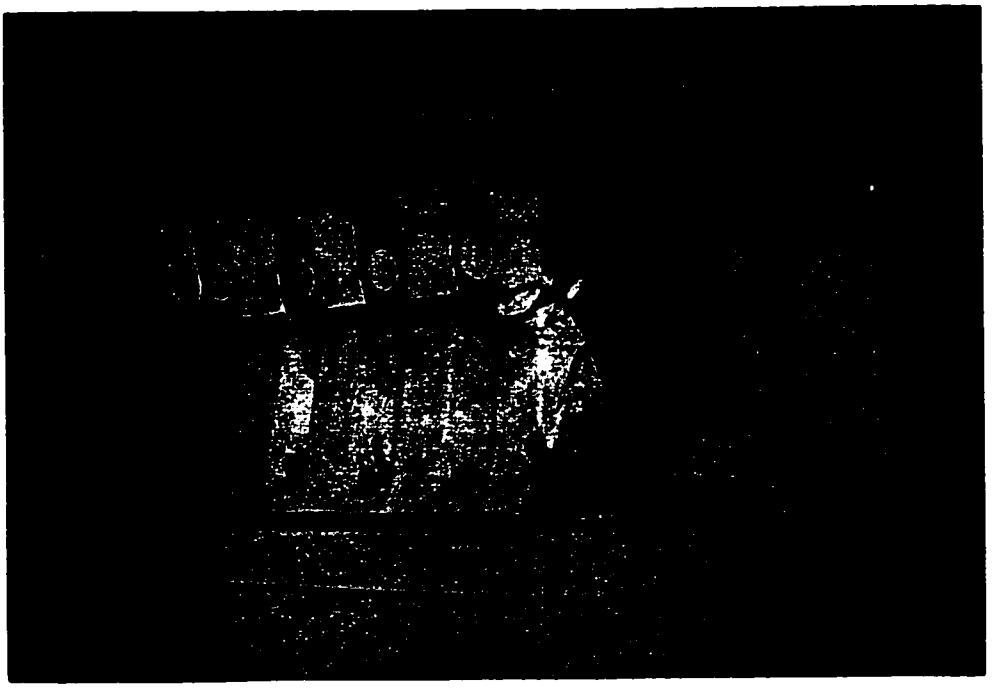

Fig. 6.8. Small gap under the TADAS base plate on the lifted side.

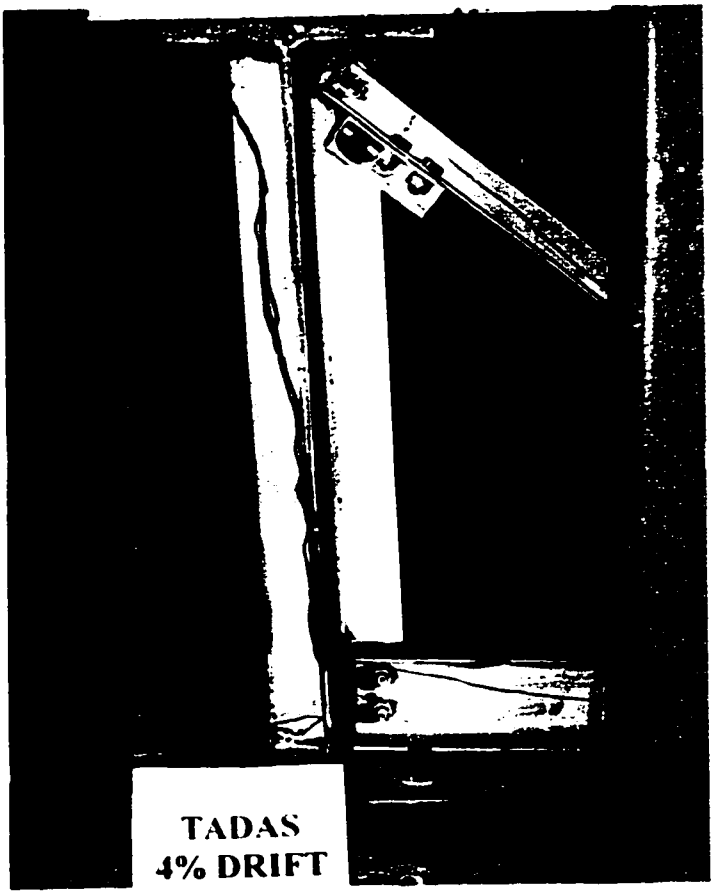

Fig. 6.9. TADAS specimen subjected to a drift of 4%.

Fig. 6.10. Significant slippage at the connection of the braces to the web stiffeners.

Fig. 6.11. Local buckling observed at the bottom of the west bearing stiffener of the west girder.

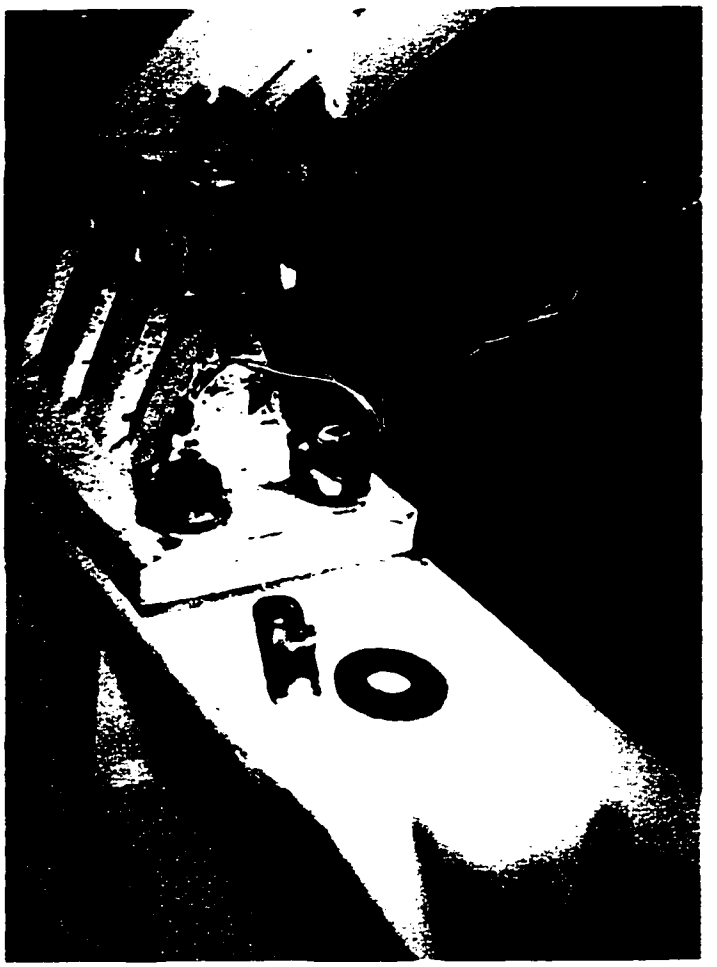

Fig. 6.12. Rupture of the first TADAS plate near its top.

Fig. 6.13. More severe buckling on the west stiffener of the west girder of TADAS specimen.

Fig. 6.14. Ruptures in two other TADAS plates indicative of the end of testing.

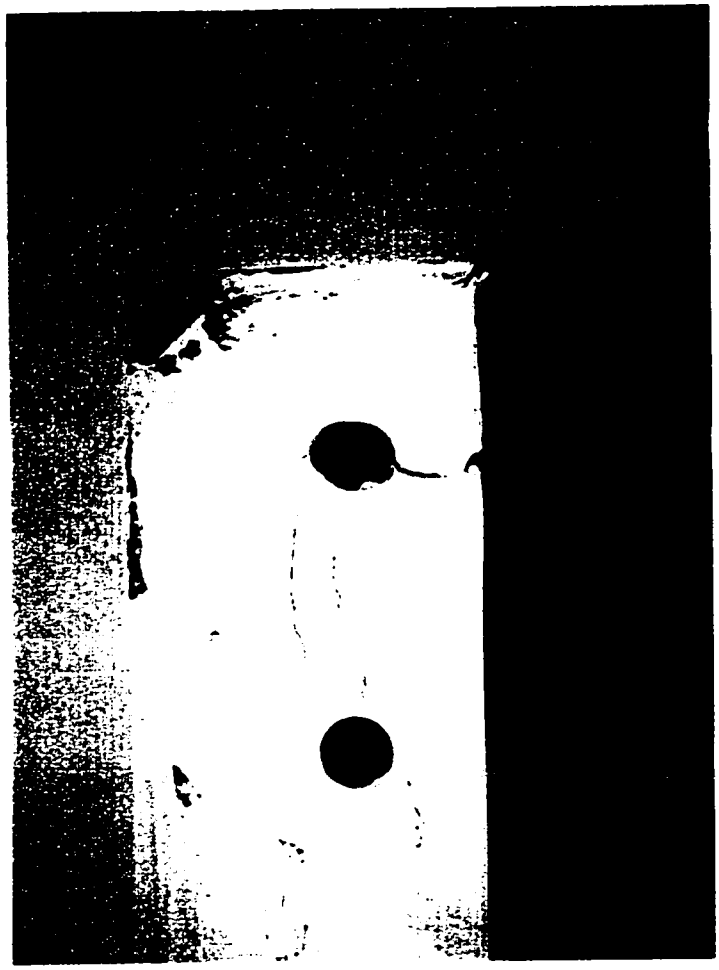

Fig. 6.15. Cracks in web stiffeners propagating from their holes to the free edge of the stiffeners. induced during the TADAS experiment.

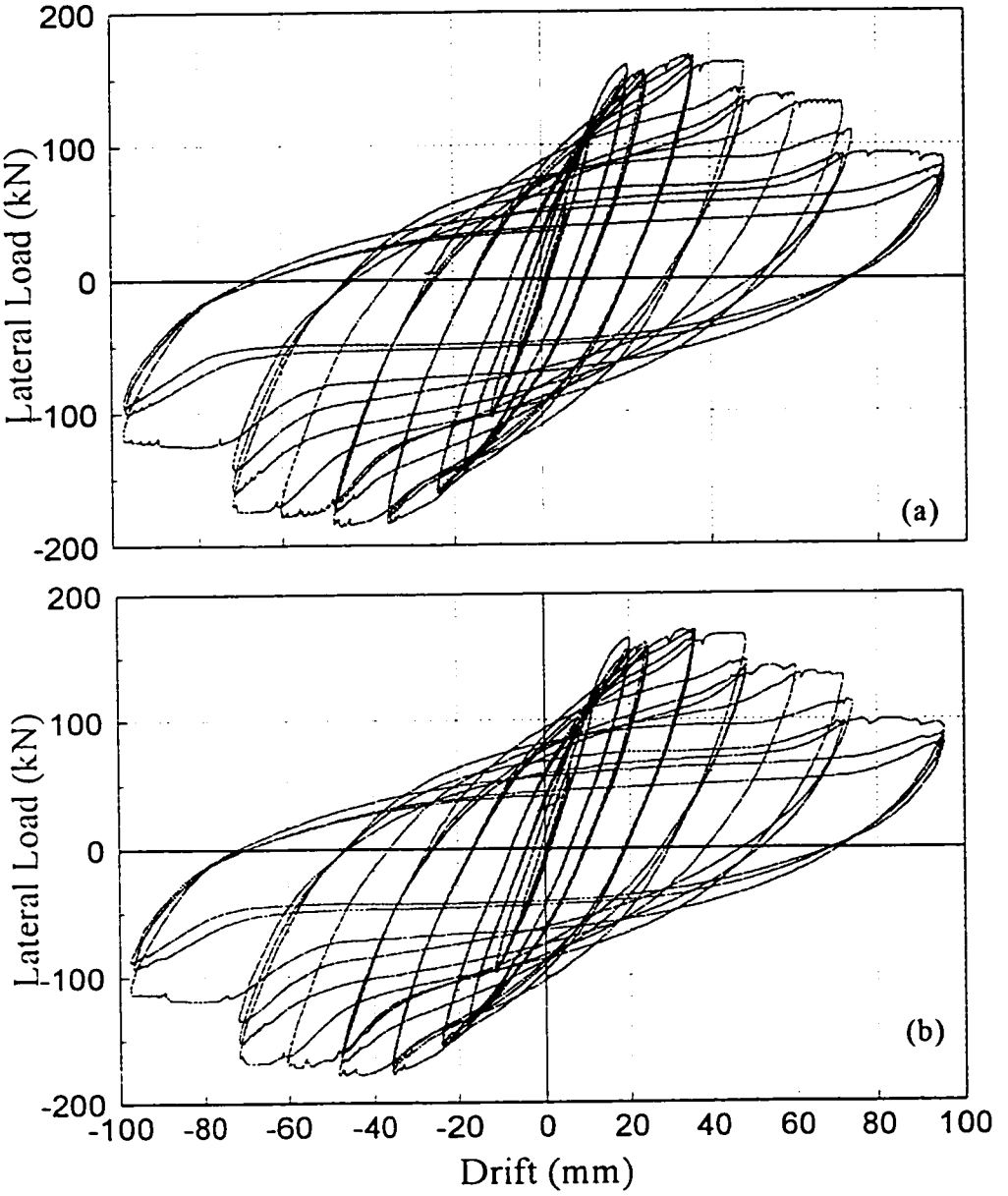

Fig. 6.16. Hysteretic curves for the first specimen without diaphragm: (a) recorded by MTS Testar; (b) recorded by Vishay data aquisition system after data reduction.

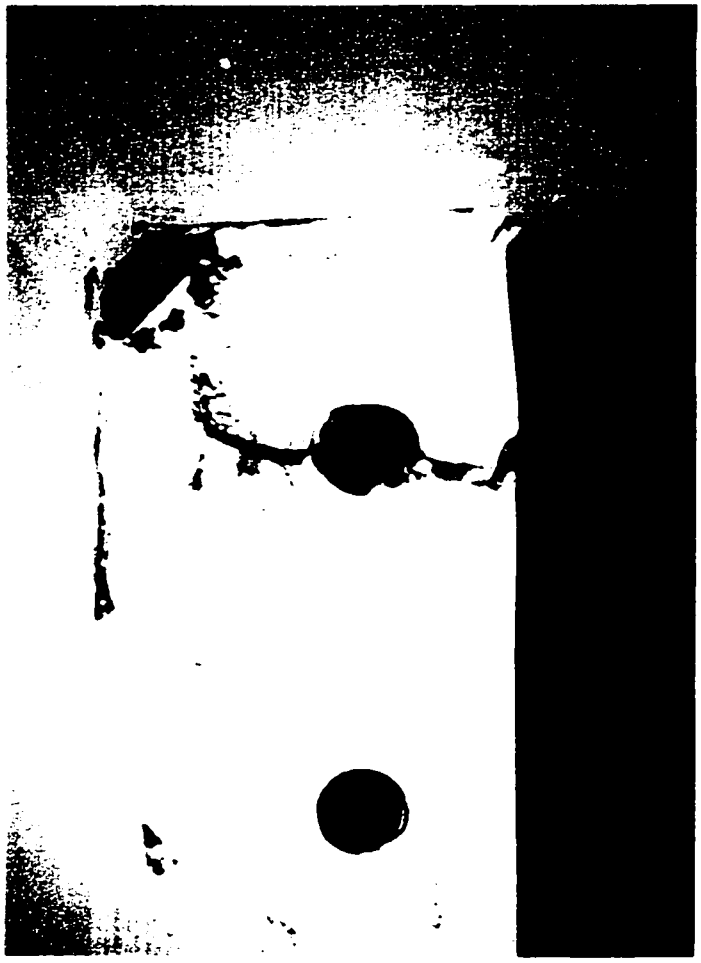

Fig. 6.17. Expanded and widened cracks at the stiffener holes.

Fig. 6.18. Fracture of the full penetration weld at the base of the west web stiffener.

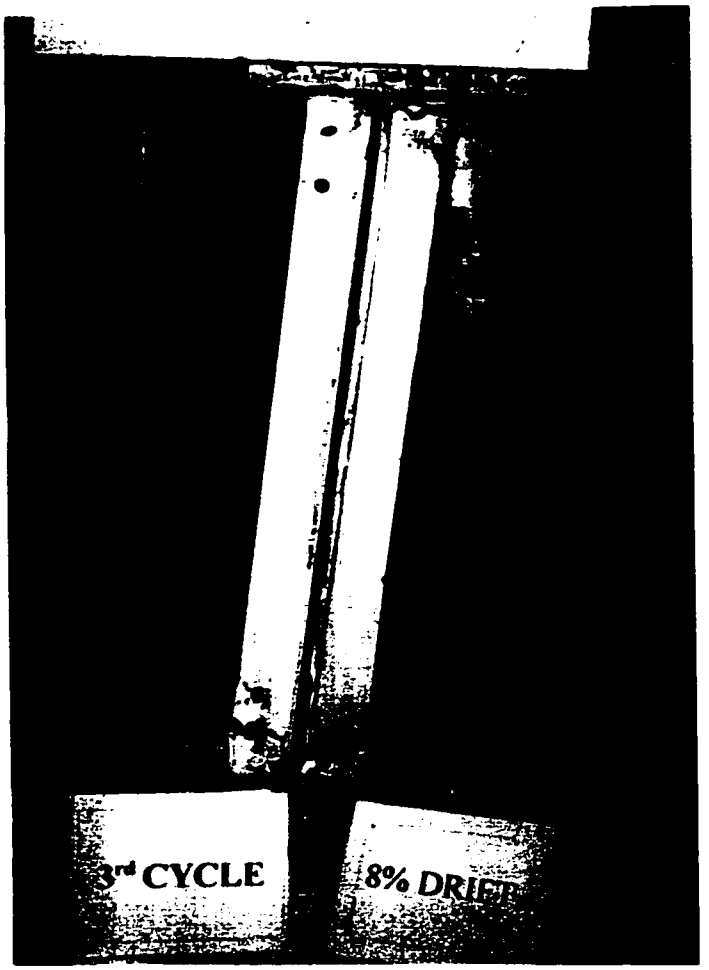

Fig. 6.19. The specimen without diaphragm subjected to a drift of 8%.

Fig. 6.20. Another fracture of full penetration welds at the bottom of the girder bearing stiffeners. Experiment ended at this time when all full penetration welds were fractured.

Fig. 6.21. The 300 mm long stiffened shear link of the EBF end-diaphragm.

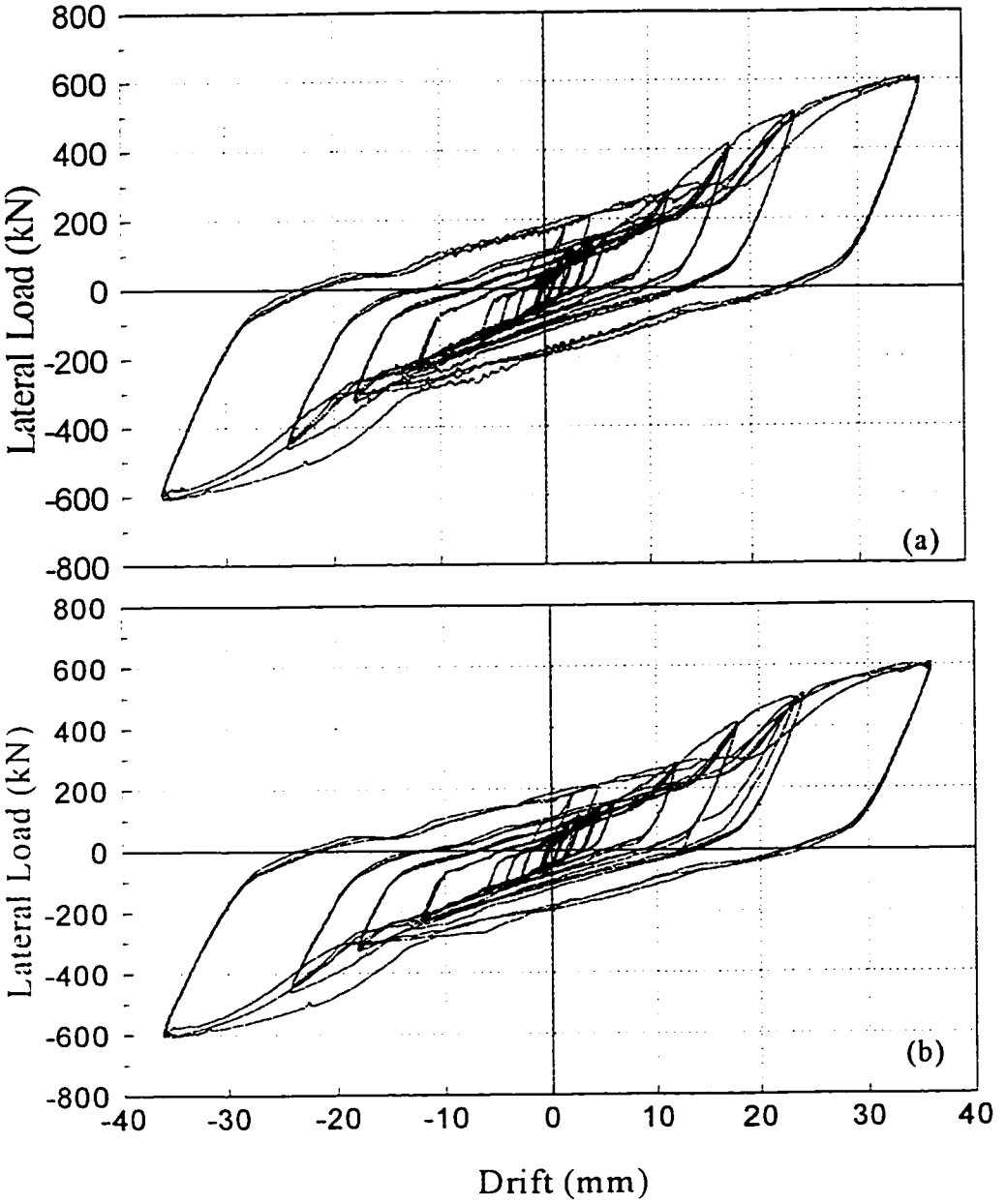

Fig. 6.22. Hysteretic curves for the first EBF specimen: (a) recorded by MTS Testar; (b) recorded by Vishay data aquisition system after data reduction.

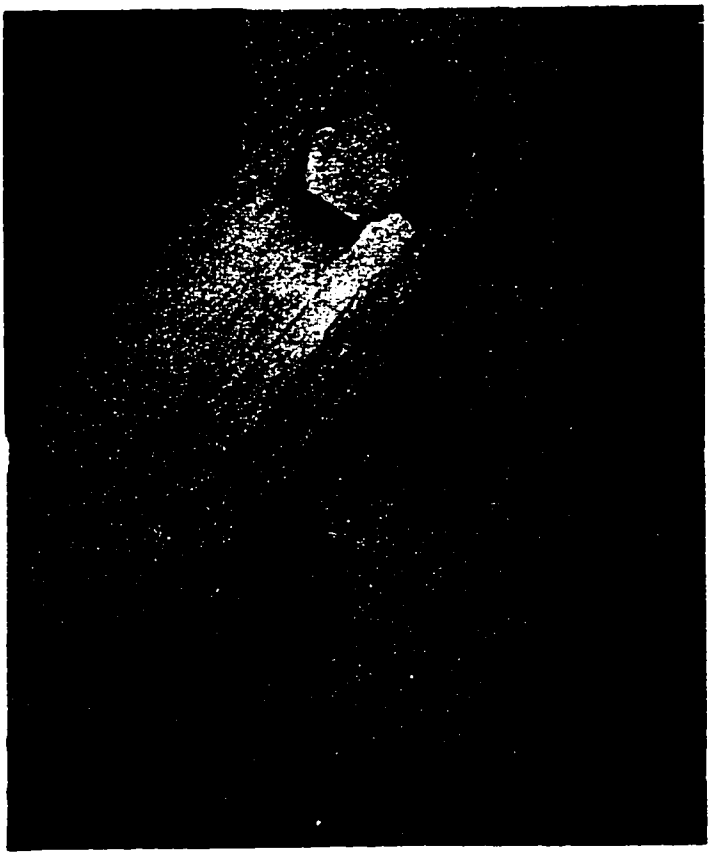

Fig. 6.23. large percentage of the applied displacements to the EBF1 specimen taken up by slip at the bolted connection of braces.

Fig. 6.24. Deformation of the shear link into a parallelogram bounded by the end stiffener plates and flanges of the link beam.

Fig. 6.25. The more severe cracks and flakes in the whitewash in the link beam web, mostly in the end panels.

Fig. 6.26. One of the welded connection before Experiment 4 (the EBF2 specimen).

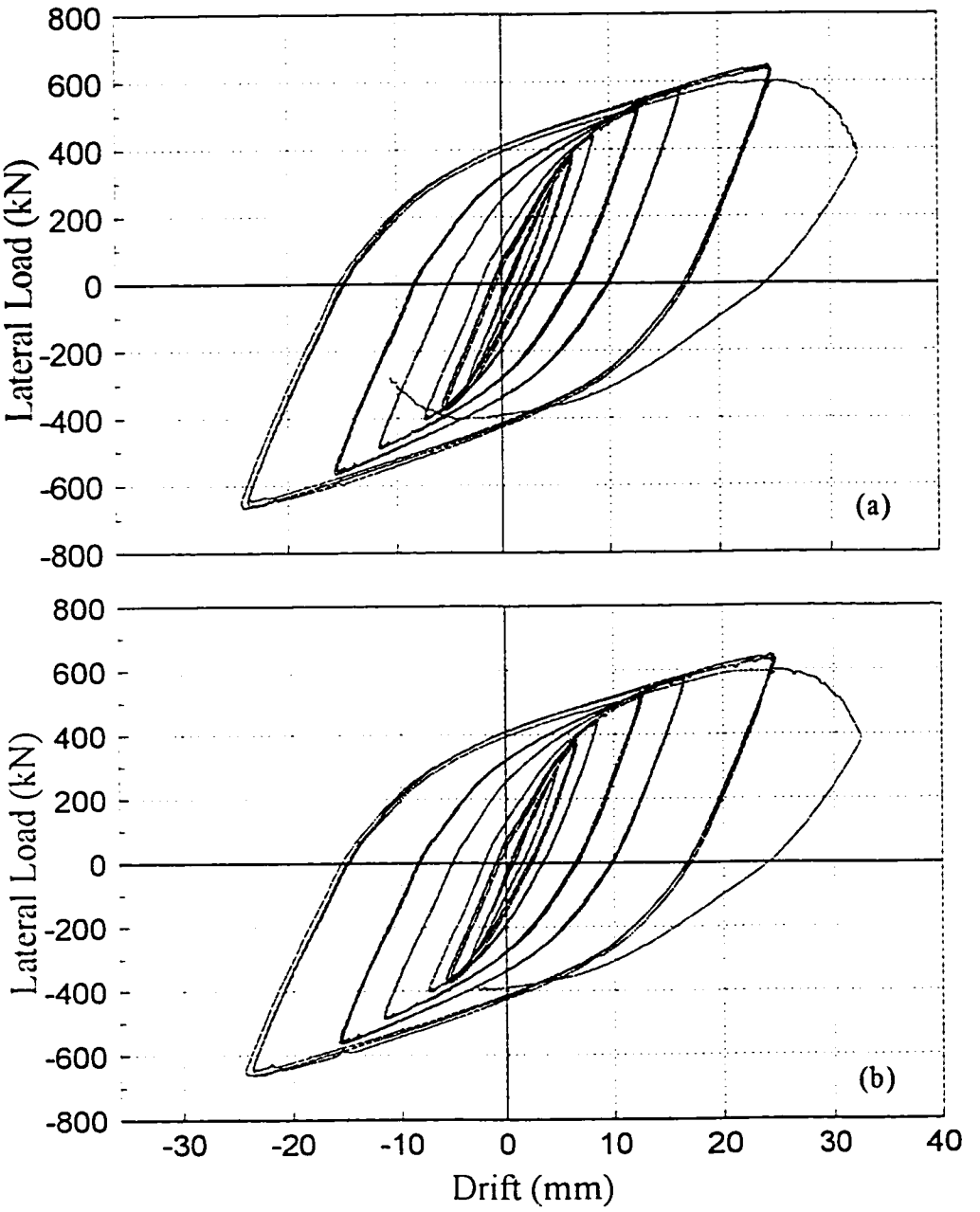

Fig. 6.27. Hysteretic curves for the EBF2 specimen: (a) recorded by MTS Testar; (b) recorded by Vishay data aquisition system after data reduction.

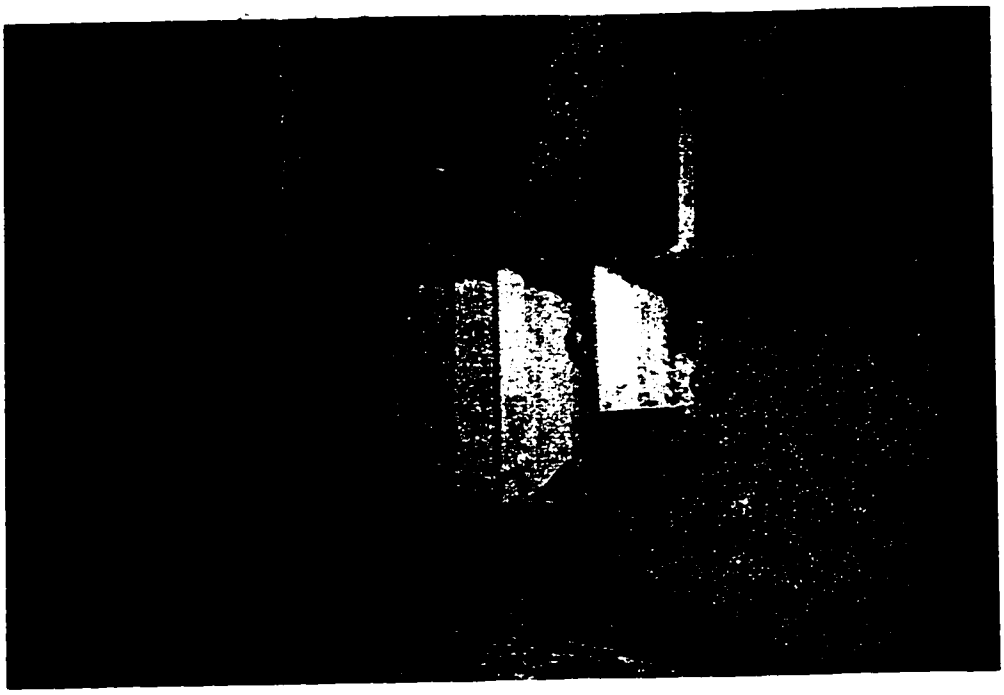

Fig. 6.28. Large shear distortions of the link of the welded EBF specimen.

Fig. 6.29. Significant visible local buckling at the north side of the east end panel of the link.

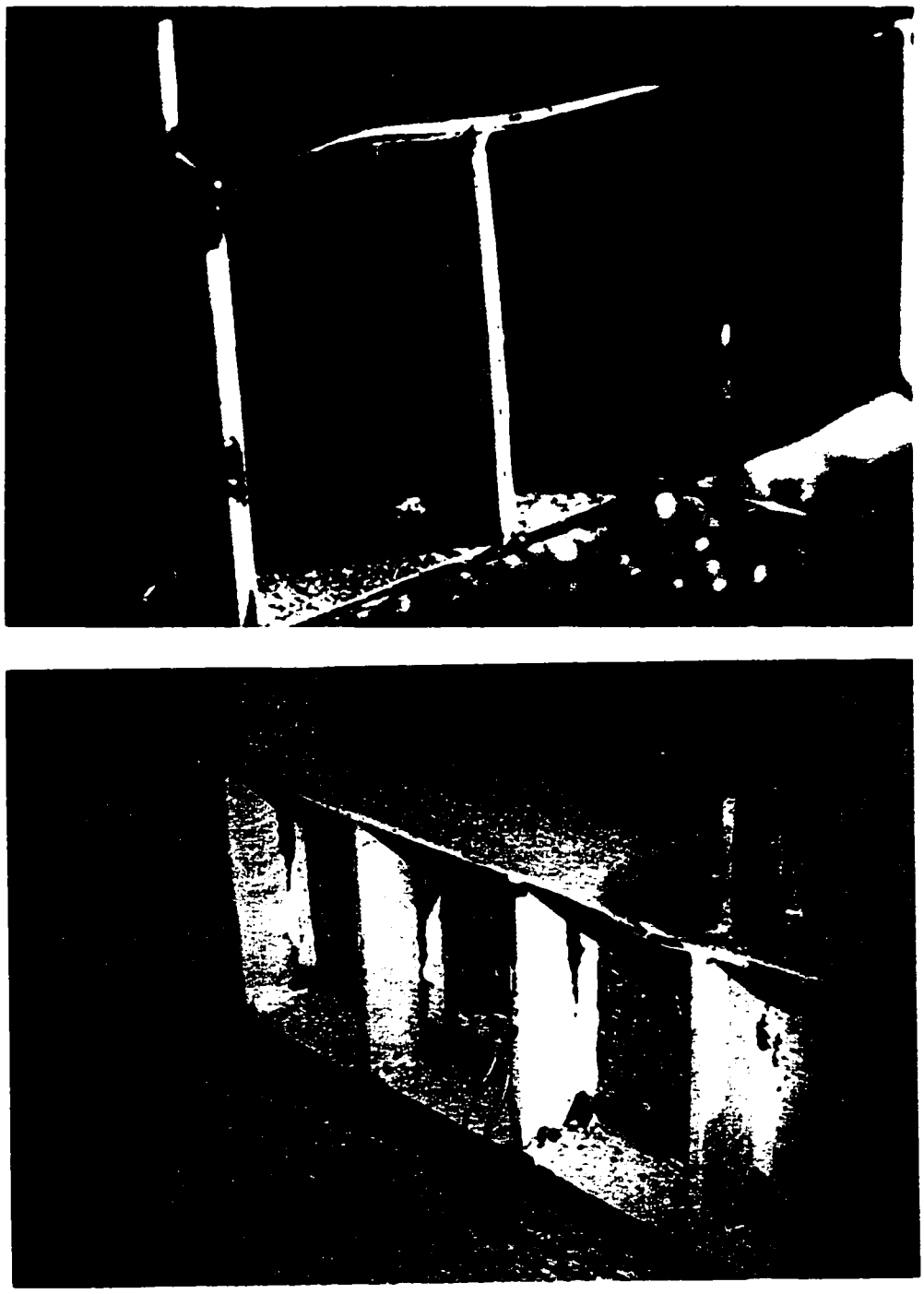

Fig. 6.30. Severe flange distortion in the shear link of the EBF2 specimen.

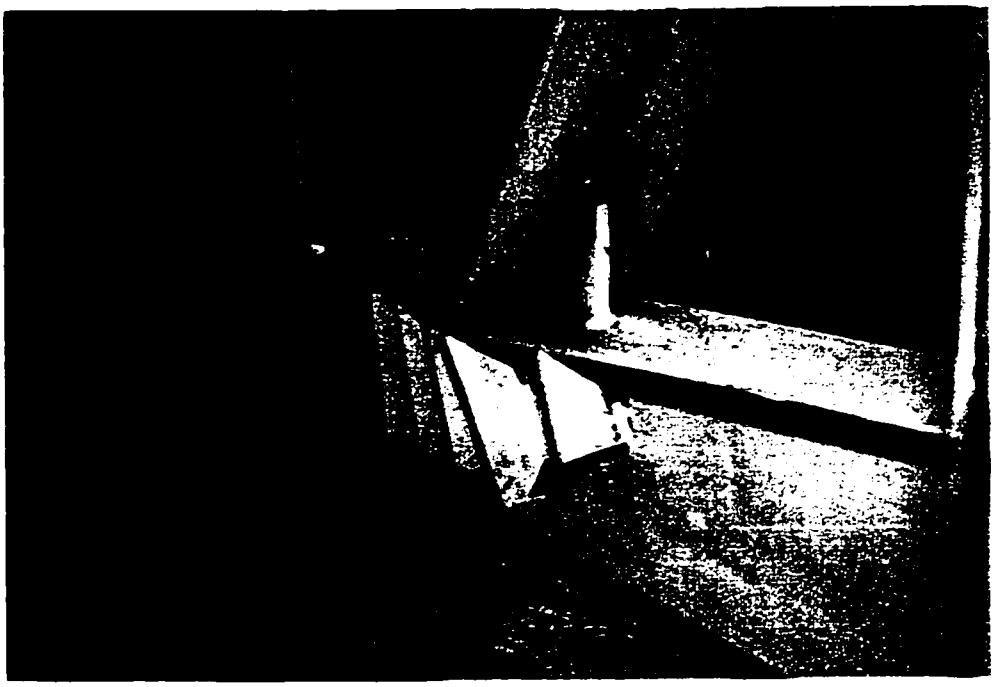

Fig. 6.31. Sudden twisting of the link beam of the welded EBF specimen.

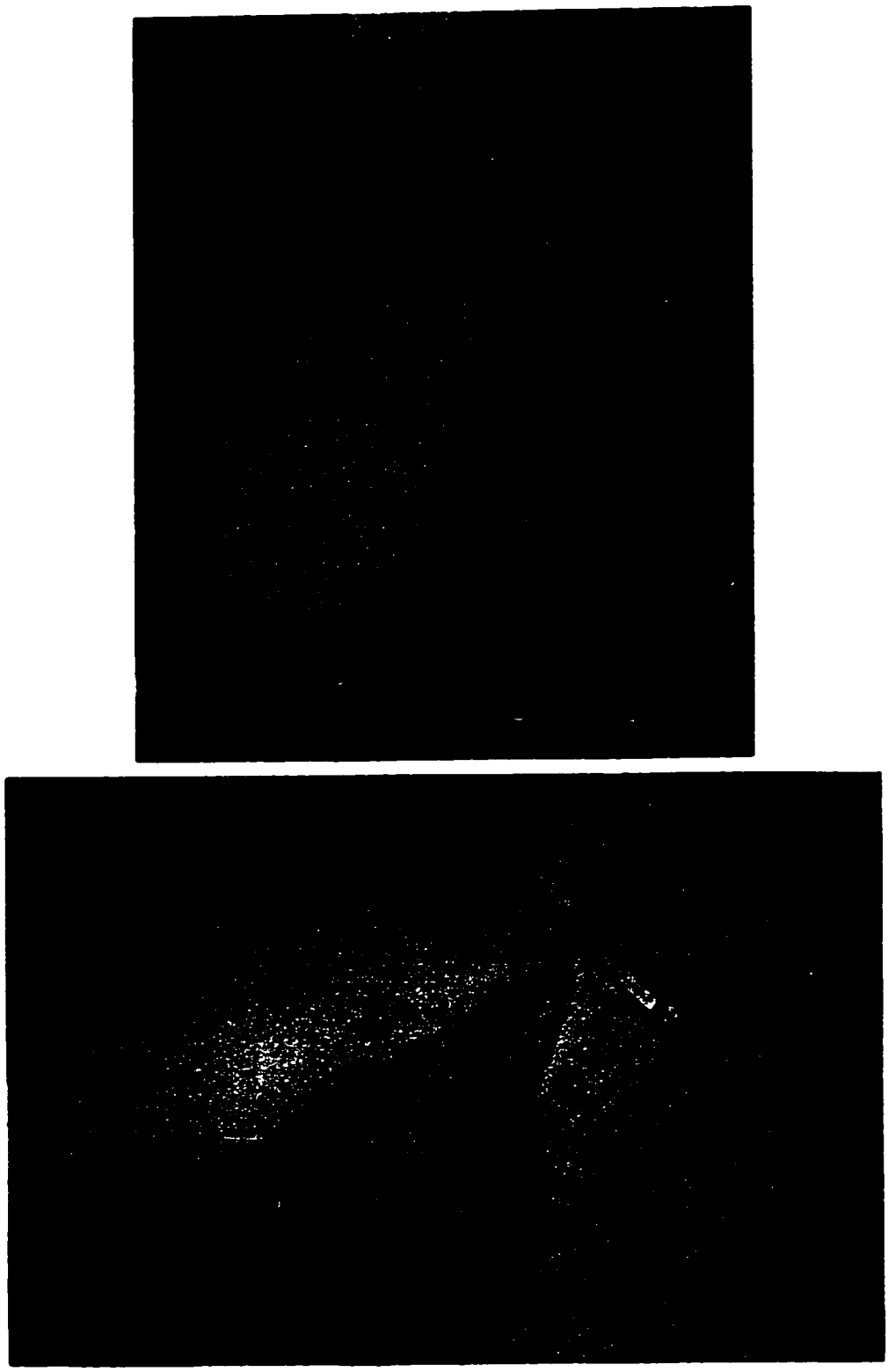

Fig. 6.32. Fracture of the west end of the link (most visible at the top flange) due to excessive lateral deformations.

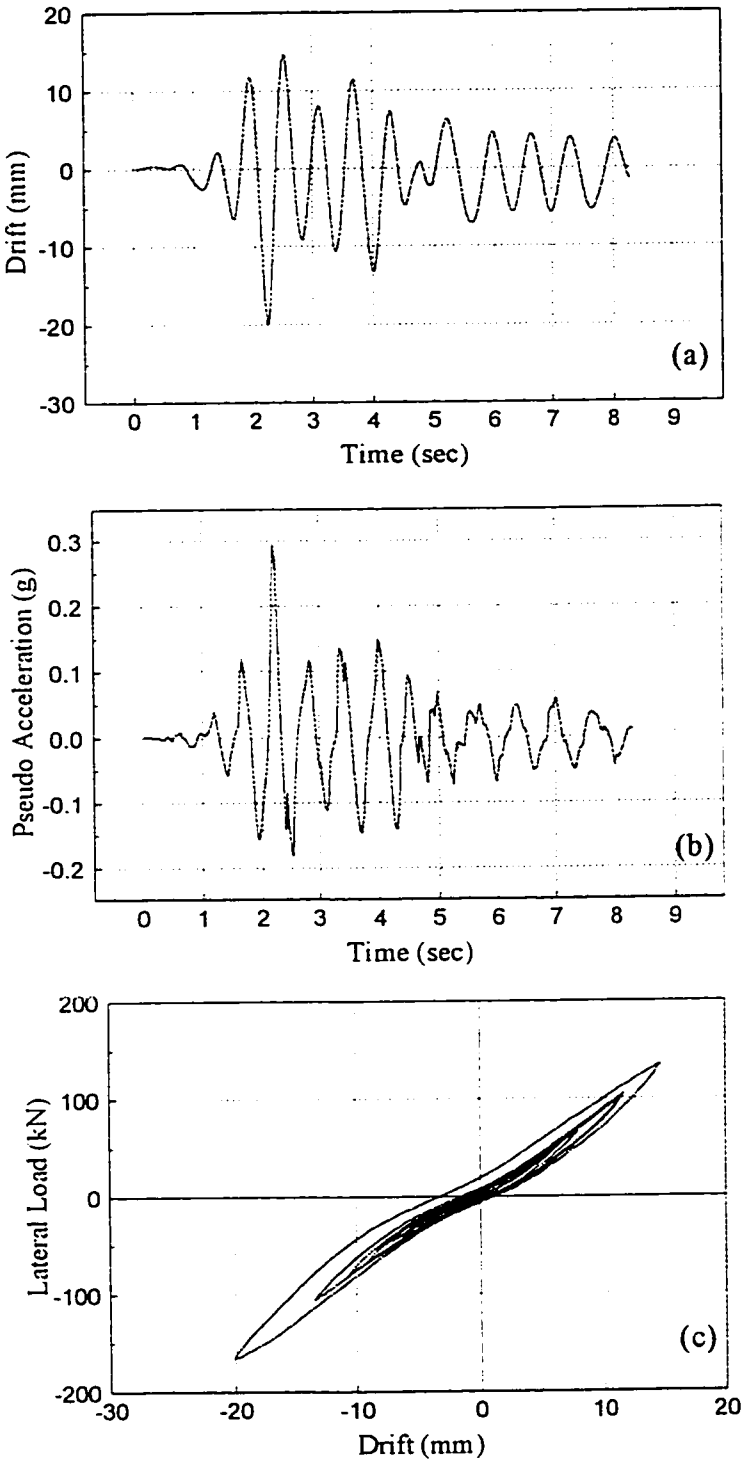

Fig. 6.33. Results of the pseudodynamic test of the second specimen without diaphragm subjected to the El-Centro earthquake scaled to a *PGA* of 0.085g: (a) lateral drift and (b) *PSa*, versus time; (c) hysteretic curves.

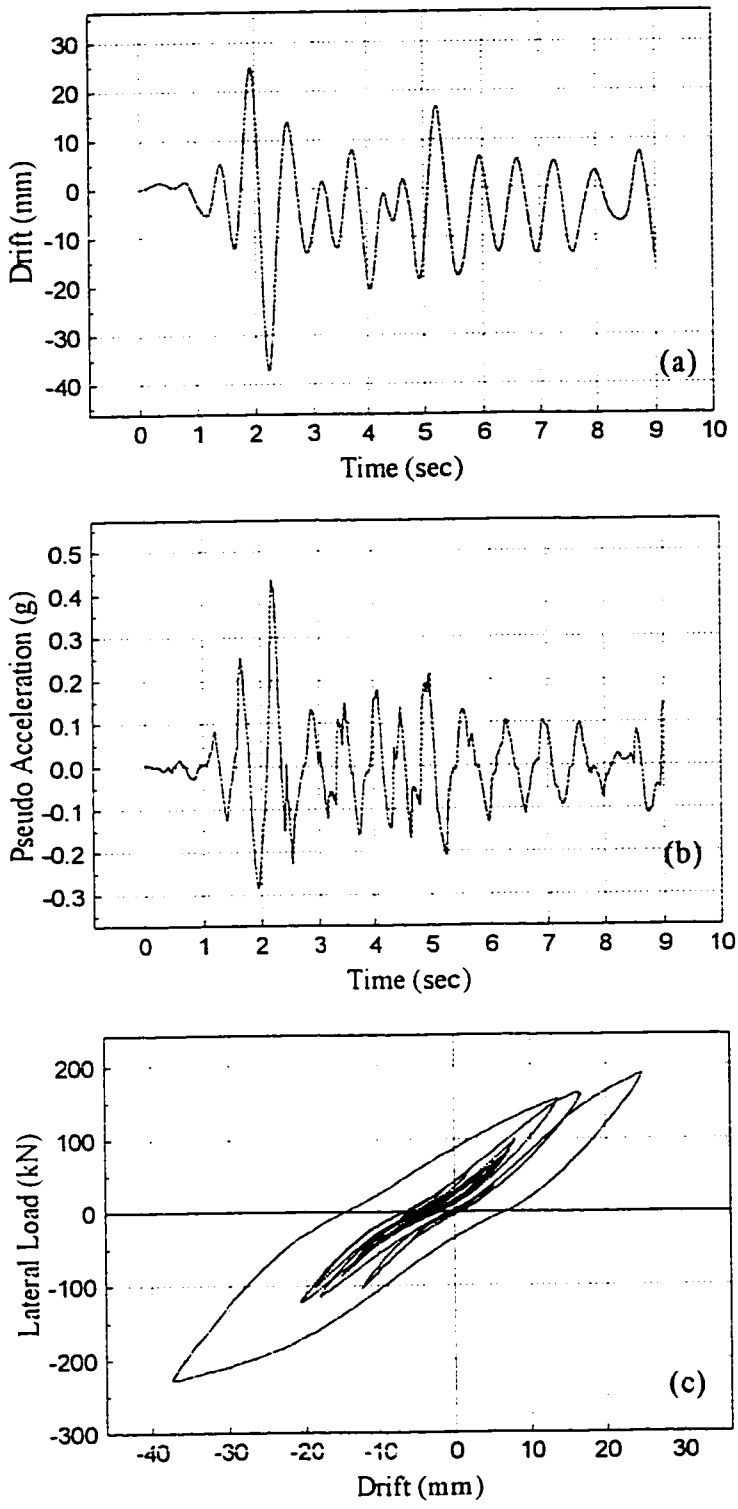

Fig. 6.34. Results of the pseudodynamic test of the second specimen without diaphragm subjected to the El-Centro earthquake scaled to a *PGA* of 0.17g: (a) lateral drift and (b) *PSa*, versus time; (c) hysteretic curves.

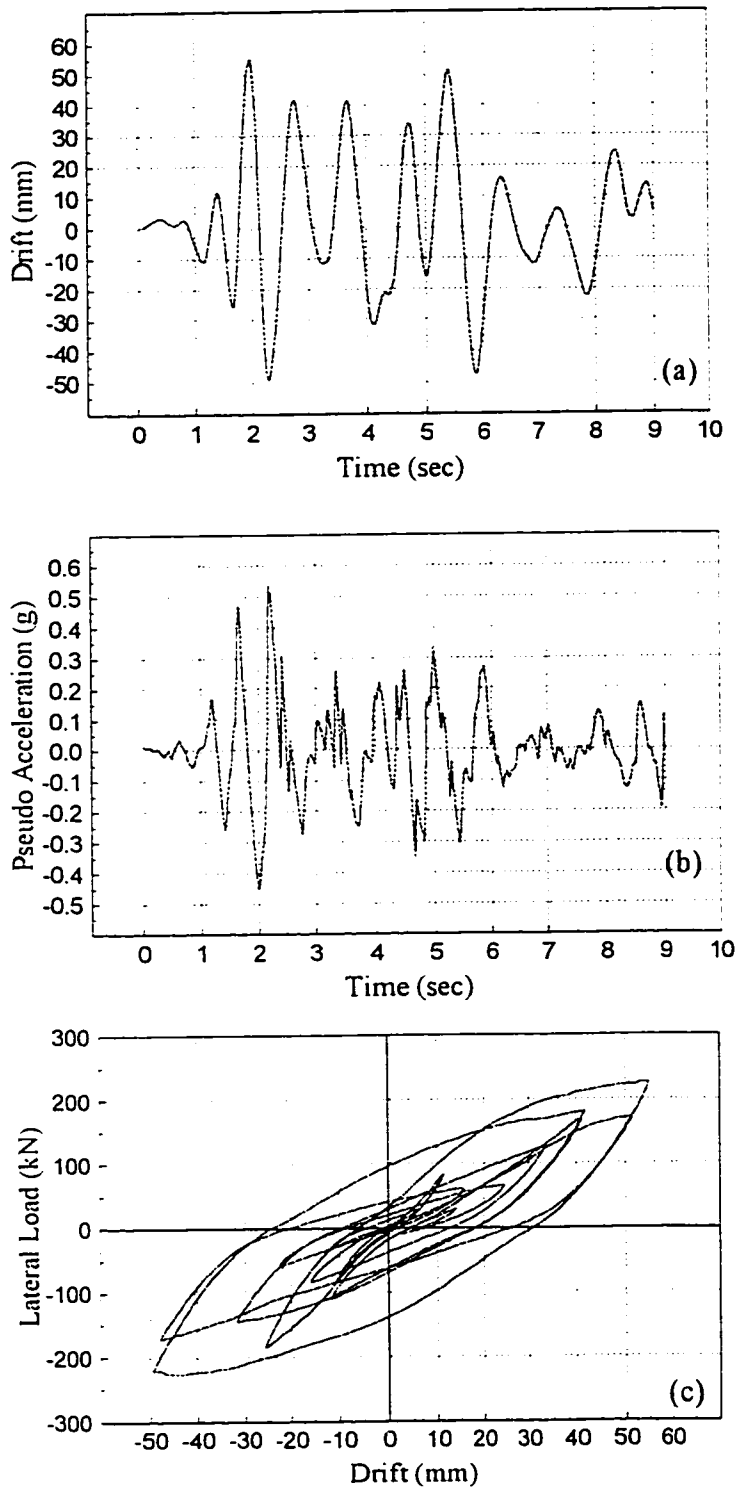

Fig. 6.35. Results of the pseudodynamic test of the second specimen without diaphragm subjected to the actual El-Centro earthquake, i.e. scaled to a *PGA* of 0.34g: (a) lateral drift and (b) *PSa*, versus time; (c) hysteretic curves.

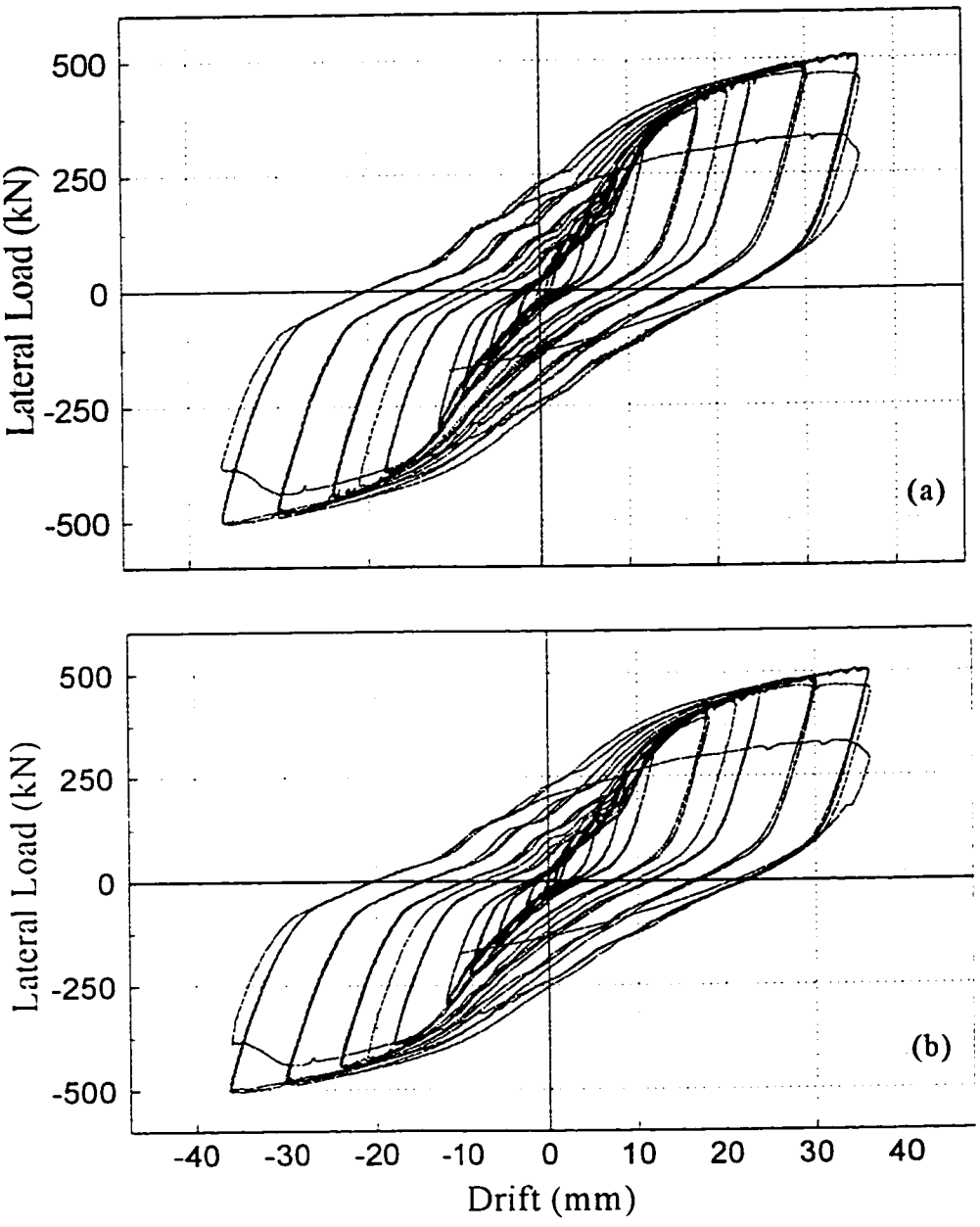

Fig. 6.36. Hysteretic curves for the SPS1 specimen: (a) recorded by MTS Testar; (b) recorded by Vishay data aquisition system after data reduction.

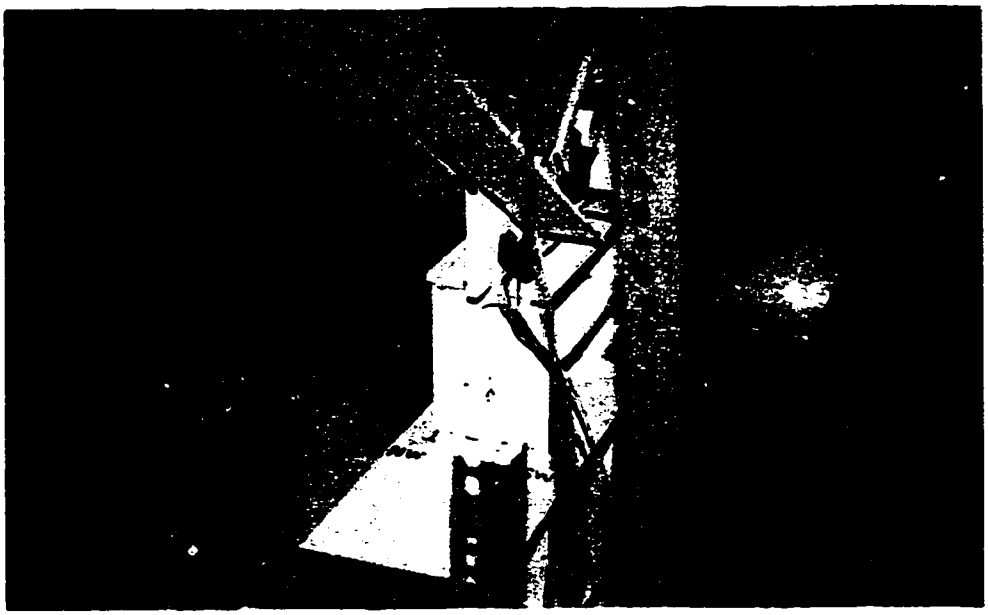

Fig. 6.37. lateral support of the ductile device is present but not effective as the threaded rods provided to act as lateral braces are intentionally felt loose; they are to be tied during testing if needed

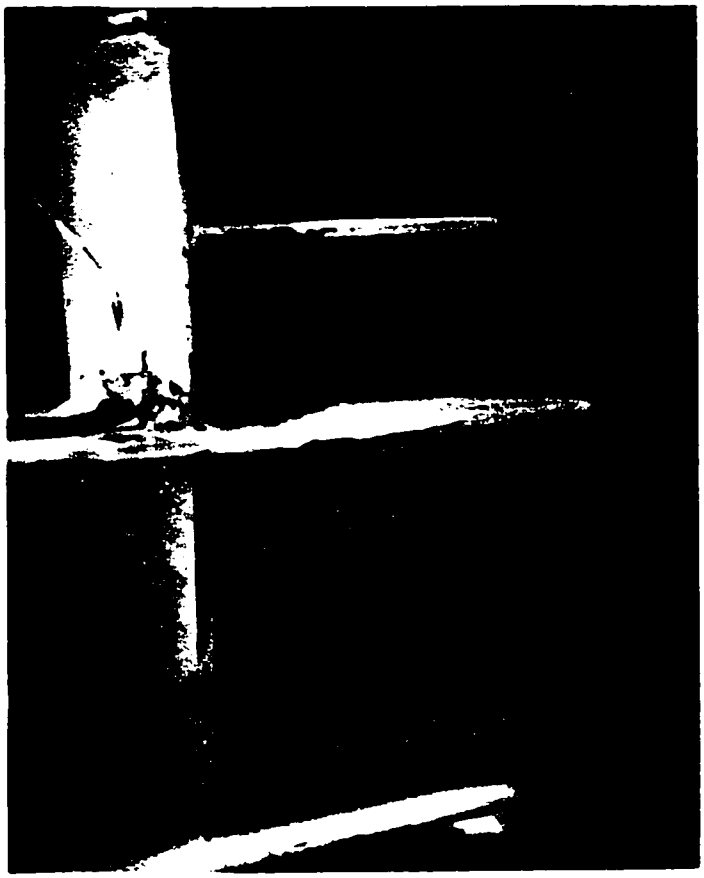

Fig. 6.38. The first SPS shear link visible deformation as a parallelogram bounded by the end plates and flanges.

Fig. 6.39. Visible buckling in the SPS1 flanges.

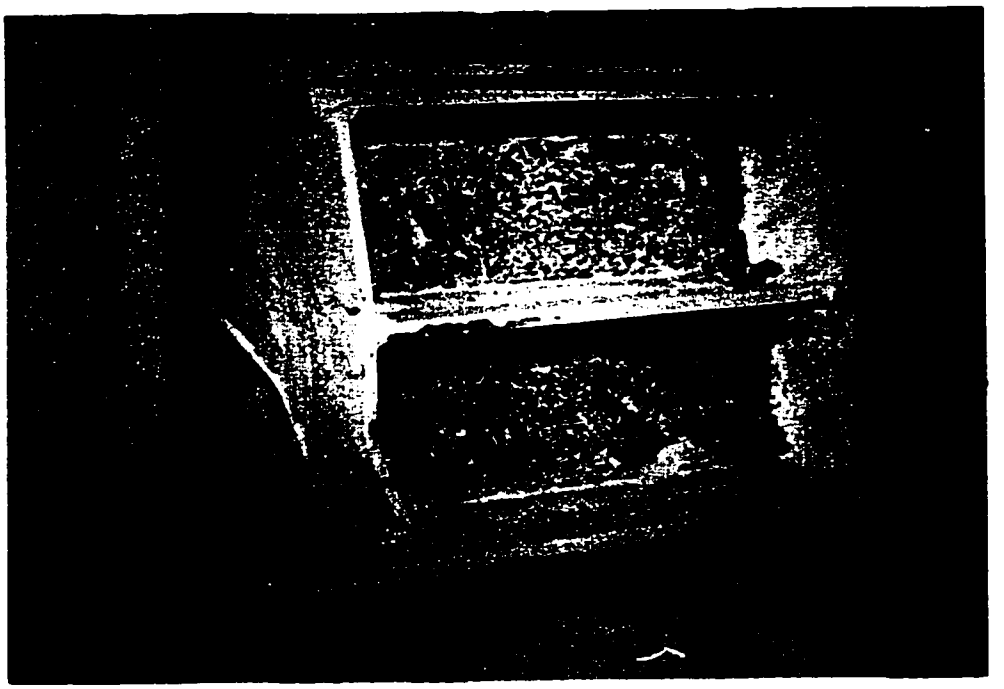

Fig. 6.40. Fracture at the base of the SPS on its north-east side and severe buckling of the SPS flange at the base on the north-west side of the panel.

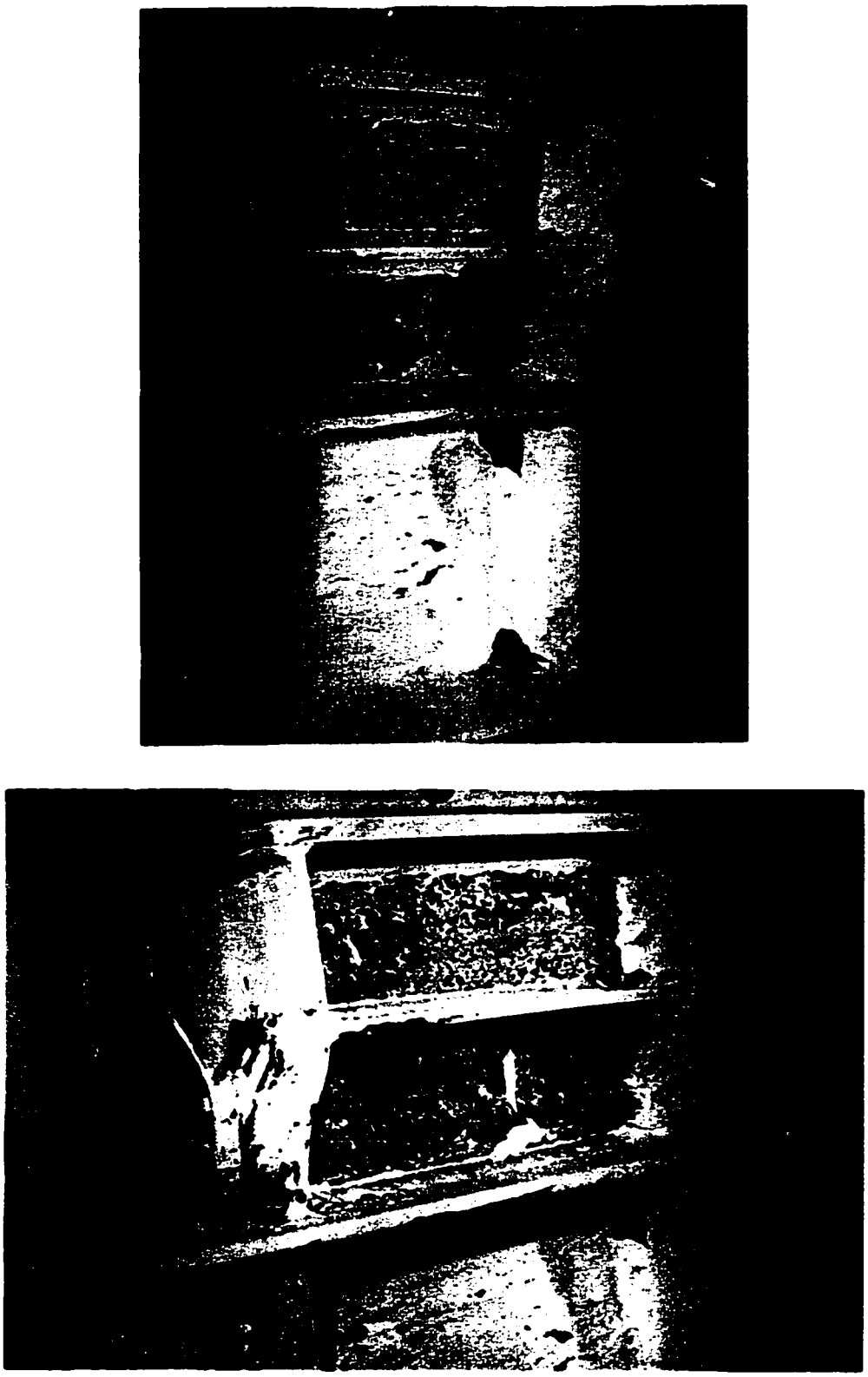

Fig. 6.41. Fracture propagation through the web of the SPS1 specimen.

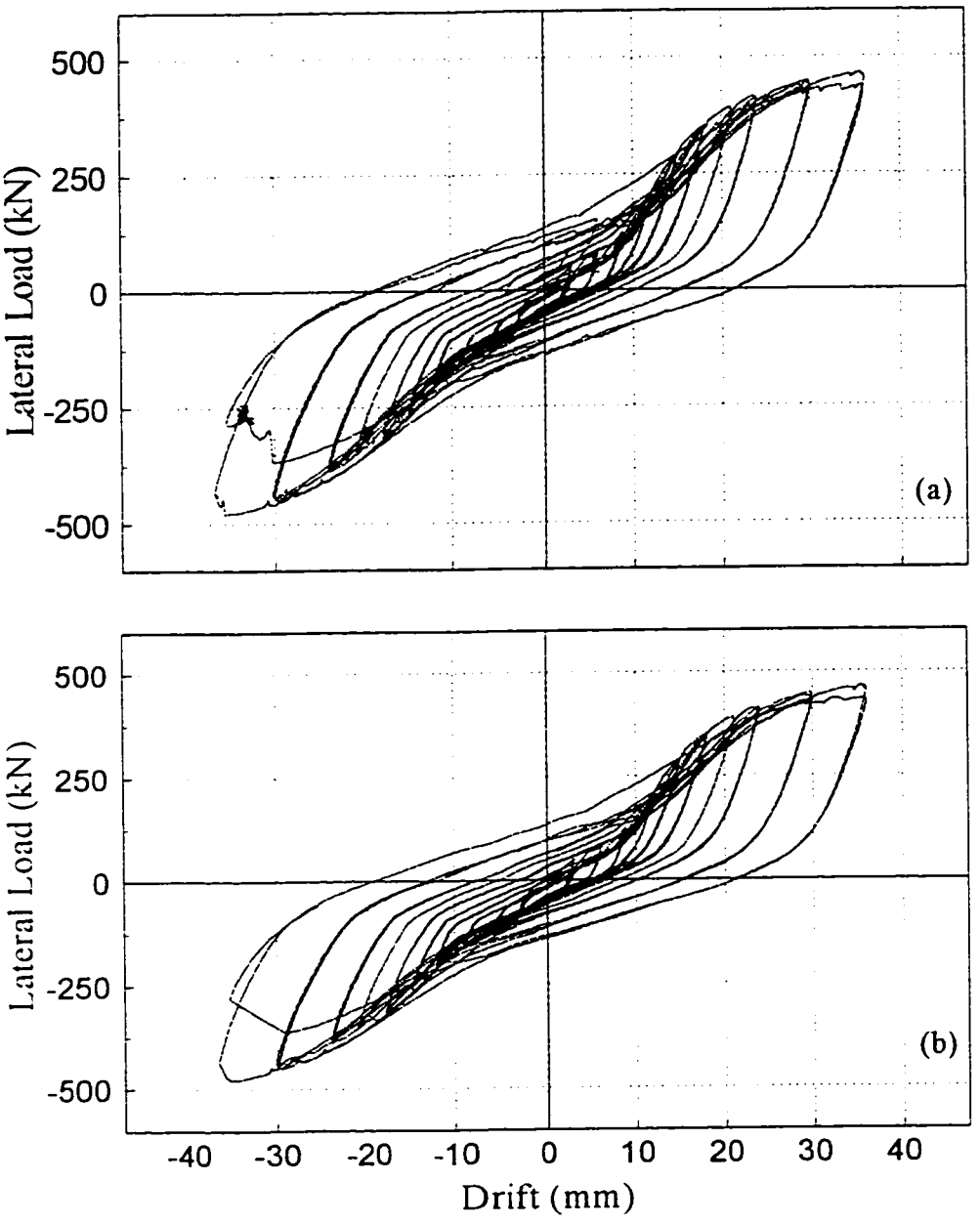

Fig. 6.42. Hysteretic curves for the SPS2 specimen: (a) recorded by MTS Testar; (b) recorded by Vishay data aquisition system after data reduction.

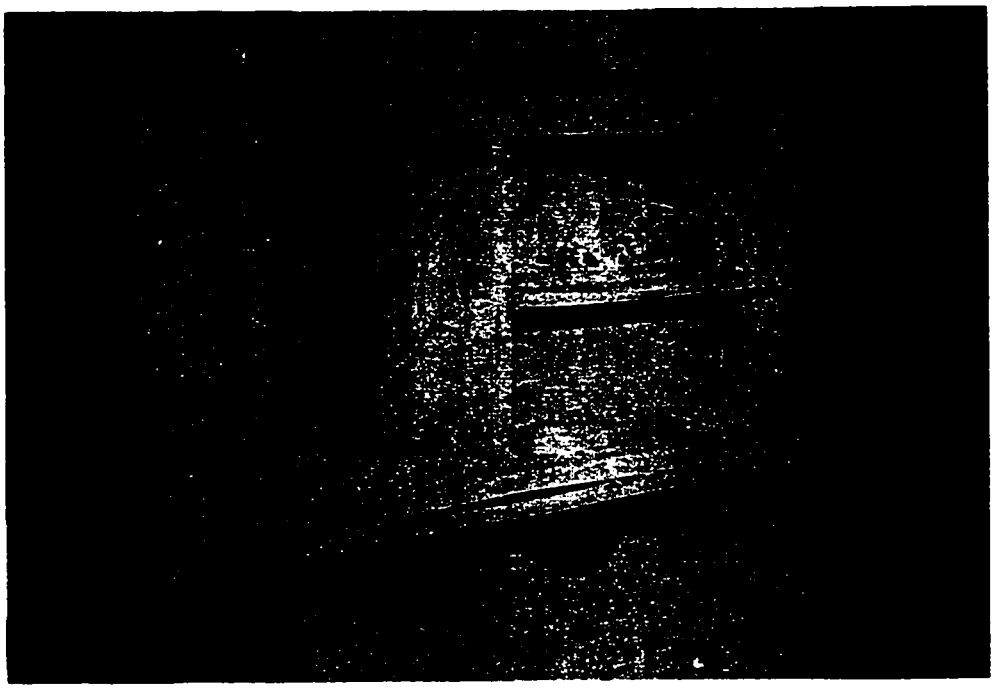

Fig. 6.43. Cracks found in the whitewash of the SPS2 web a few cycles after its yielding.

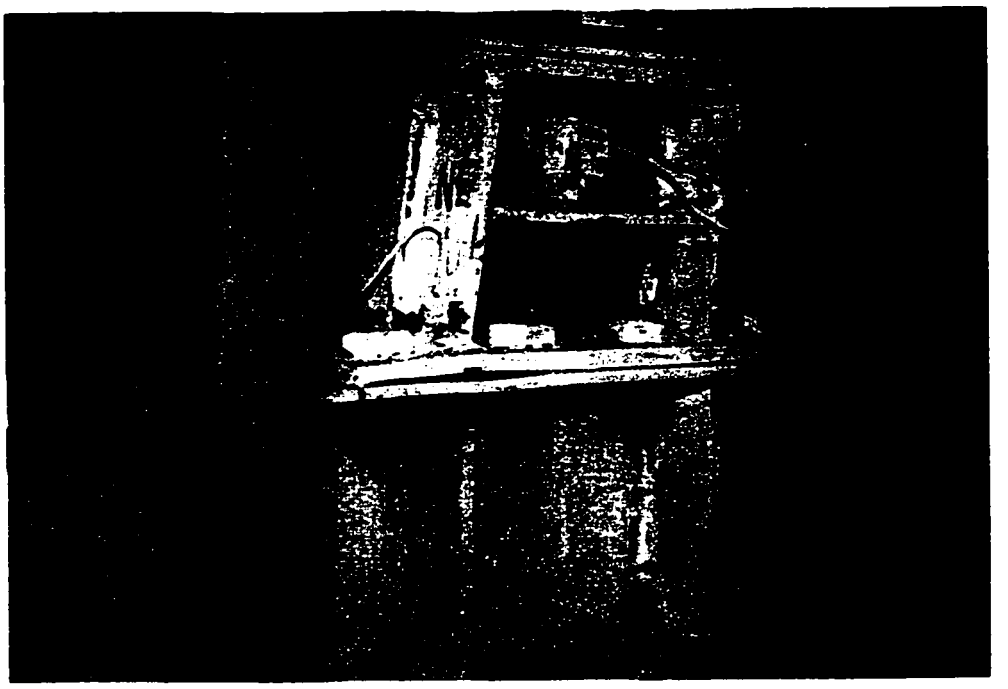

Fig. 6.44. Little whitewash left on the SPS2 web.

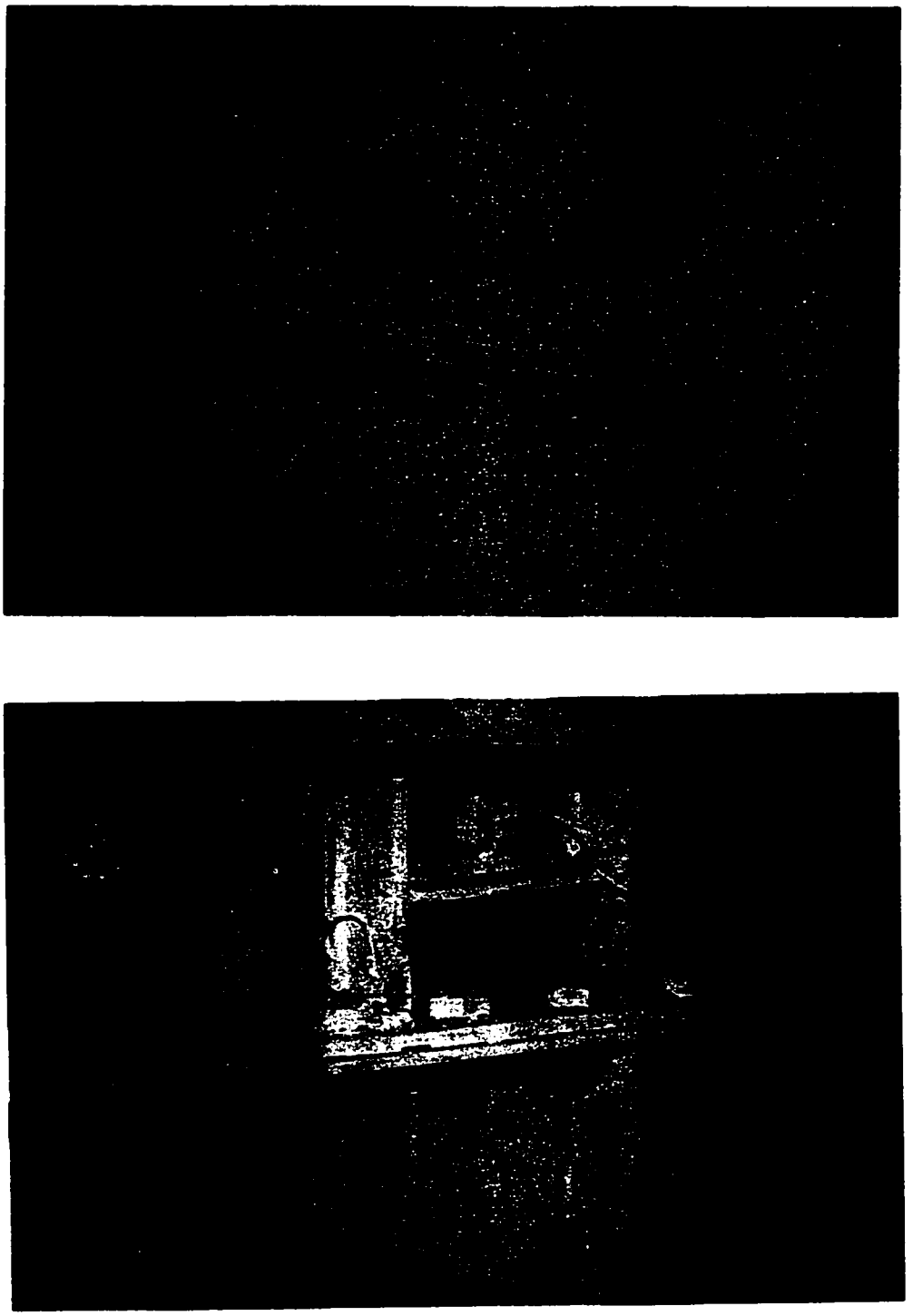

Fig. 6.45. Fracture progressed through the entire SPS web after fracture of flange weld on the west side of the SPS2.

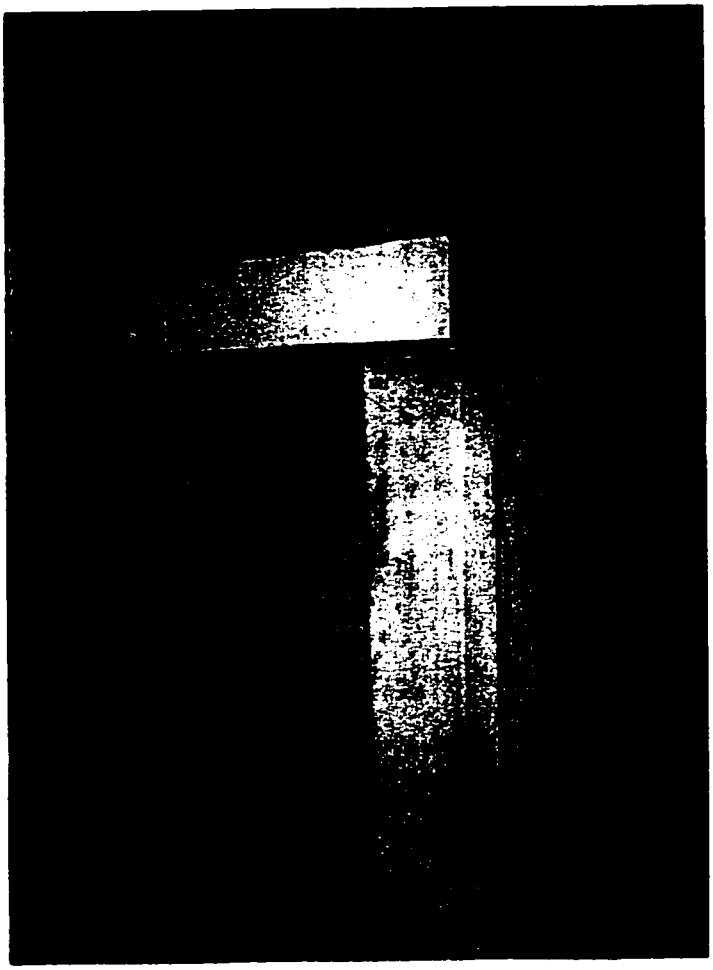

Fig. 6.46. A relatively deep channel placed at mid-height between the stub-girders (location with maximum rotation).

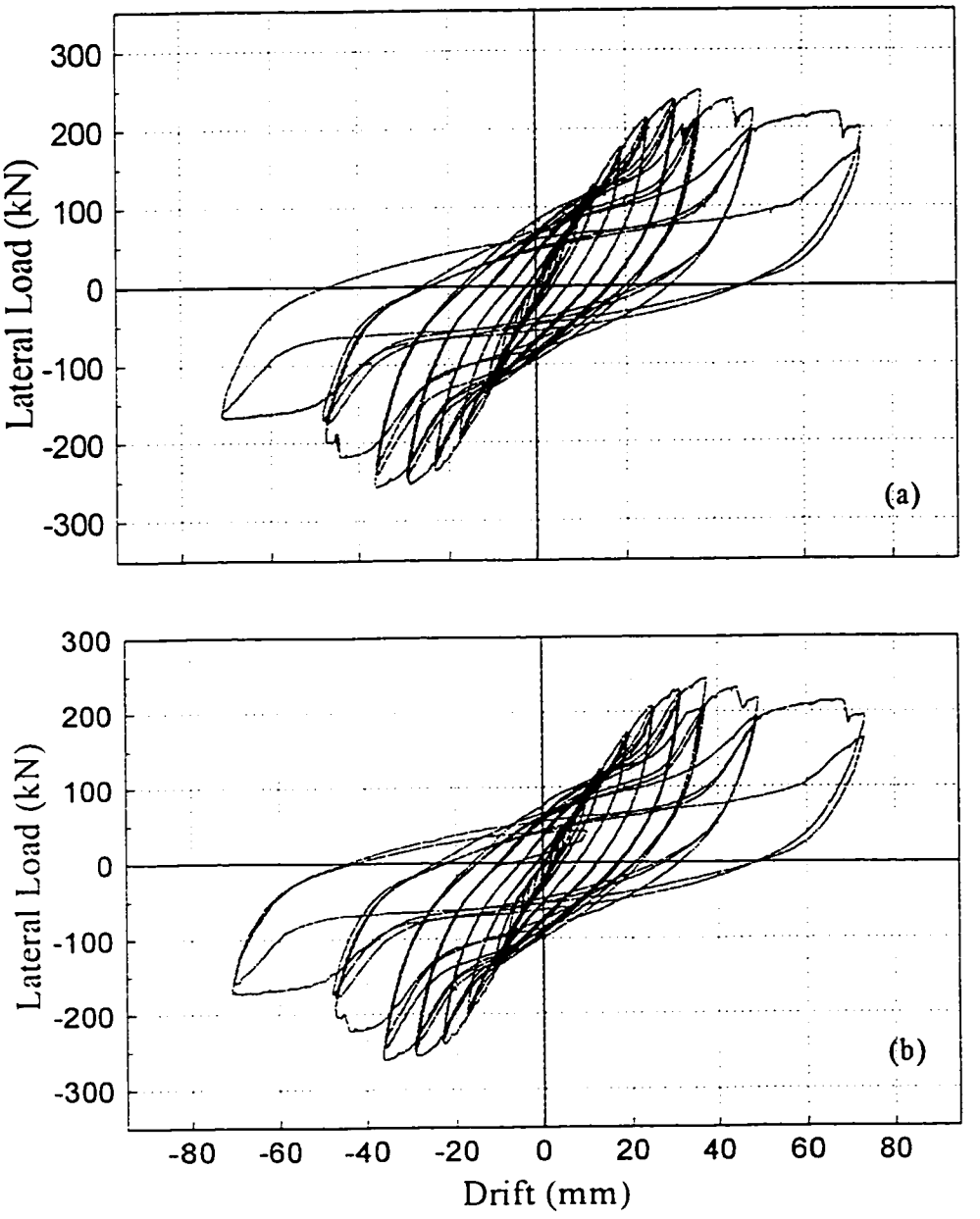

Fig. 6.47. Hysteretic curves for the Channel specimen: (a) recorded by MTS Testar; (b) recorded by Vishay data aquisition system after data reduction.

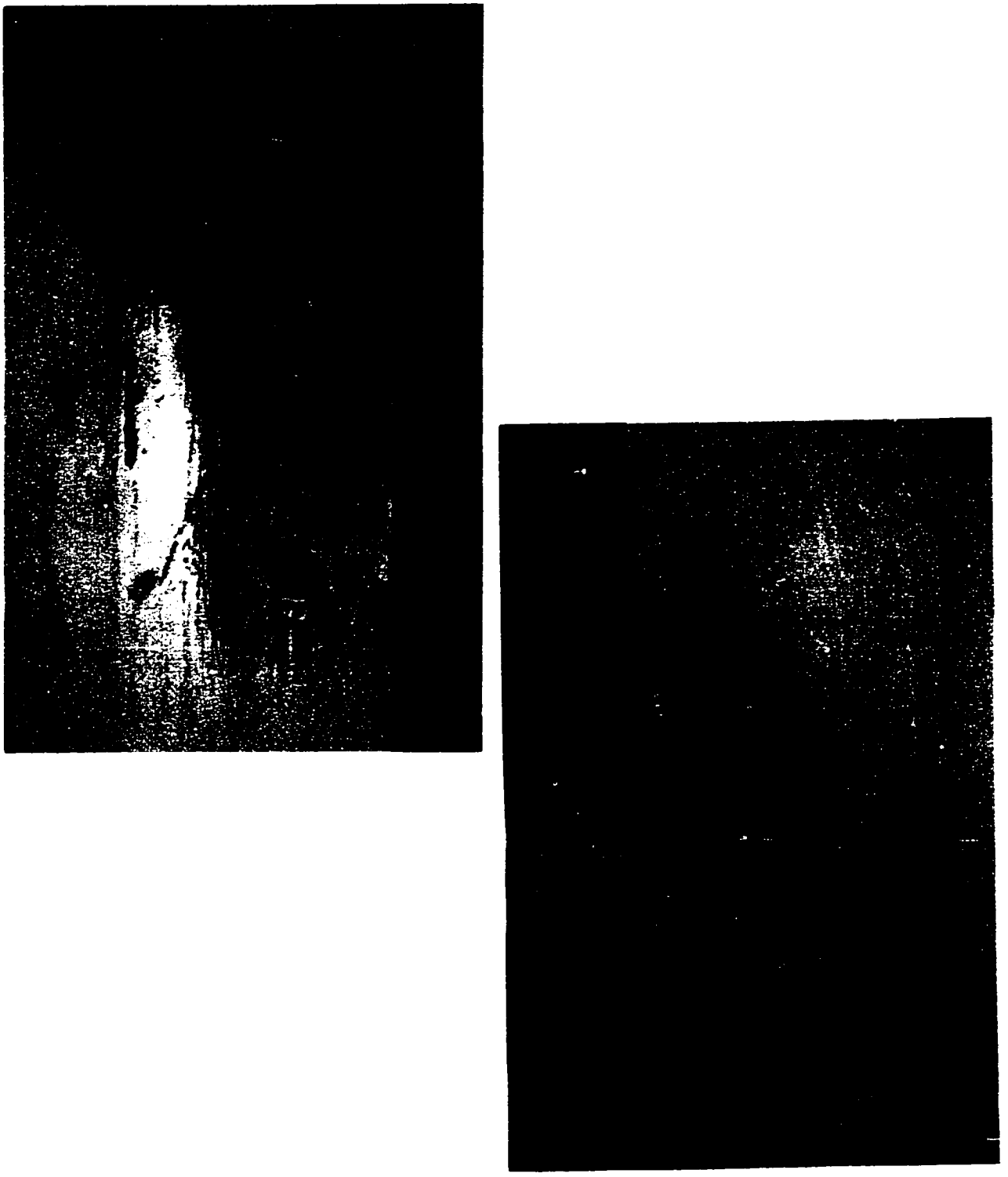

Fig. 6.48. Breakage beginning at the welds near the holes on the stiffener at the east top end and west lower end locations.

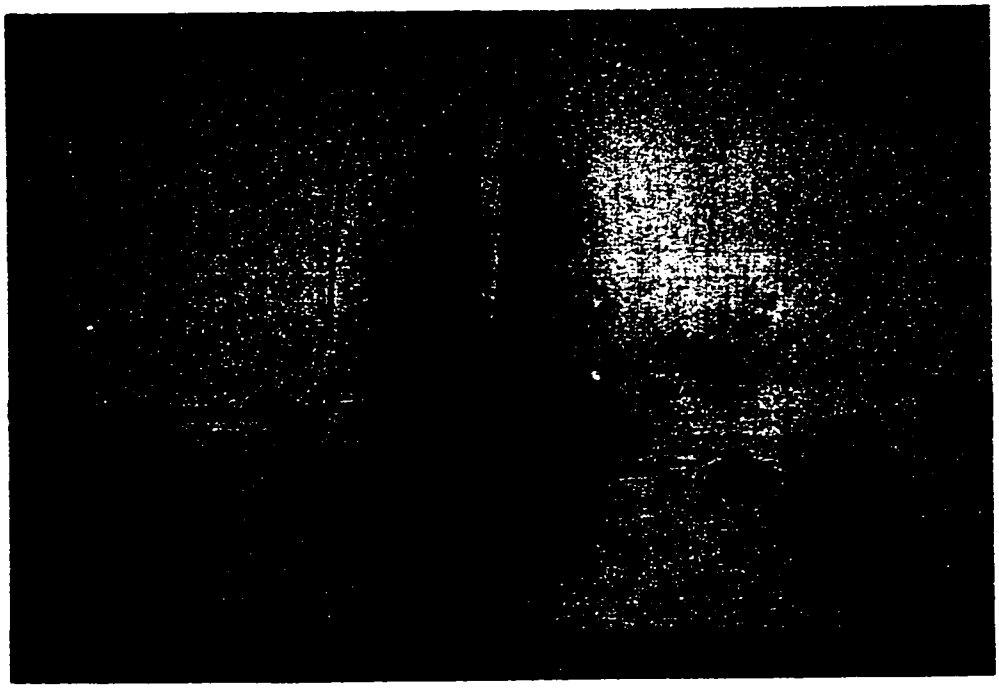

Fig. 6.49. Fractured of the weld at the bottom end of exterior stiffener on east girder of the channel specimen.

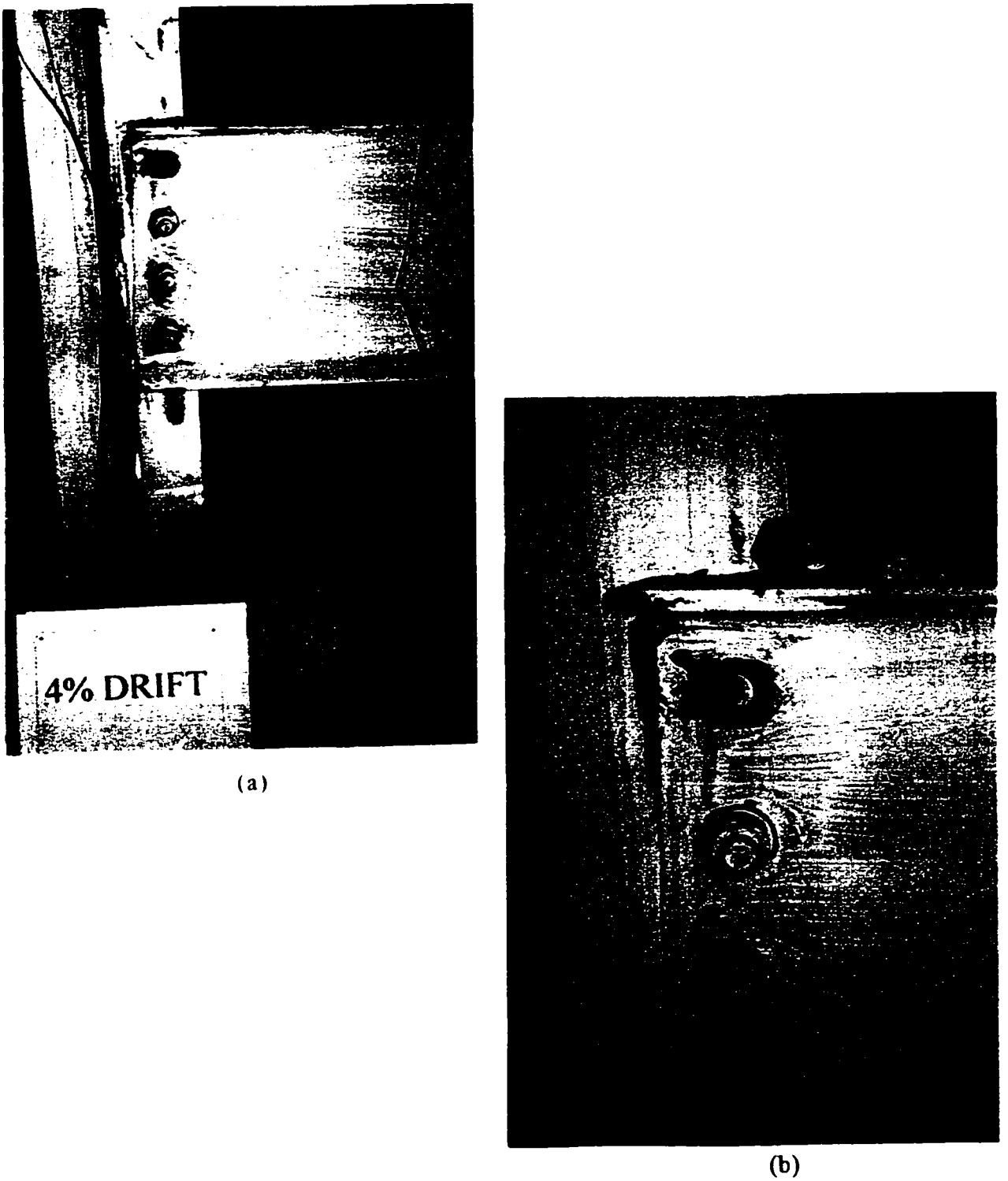

(a)

(b)

Fig. 6.50. Rupture of top bolt on the west side channel connection, accompanied by a huge "bang": (a) the specimen subjected to 4% drift; (b) close-up view of the ruptured bolt.

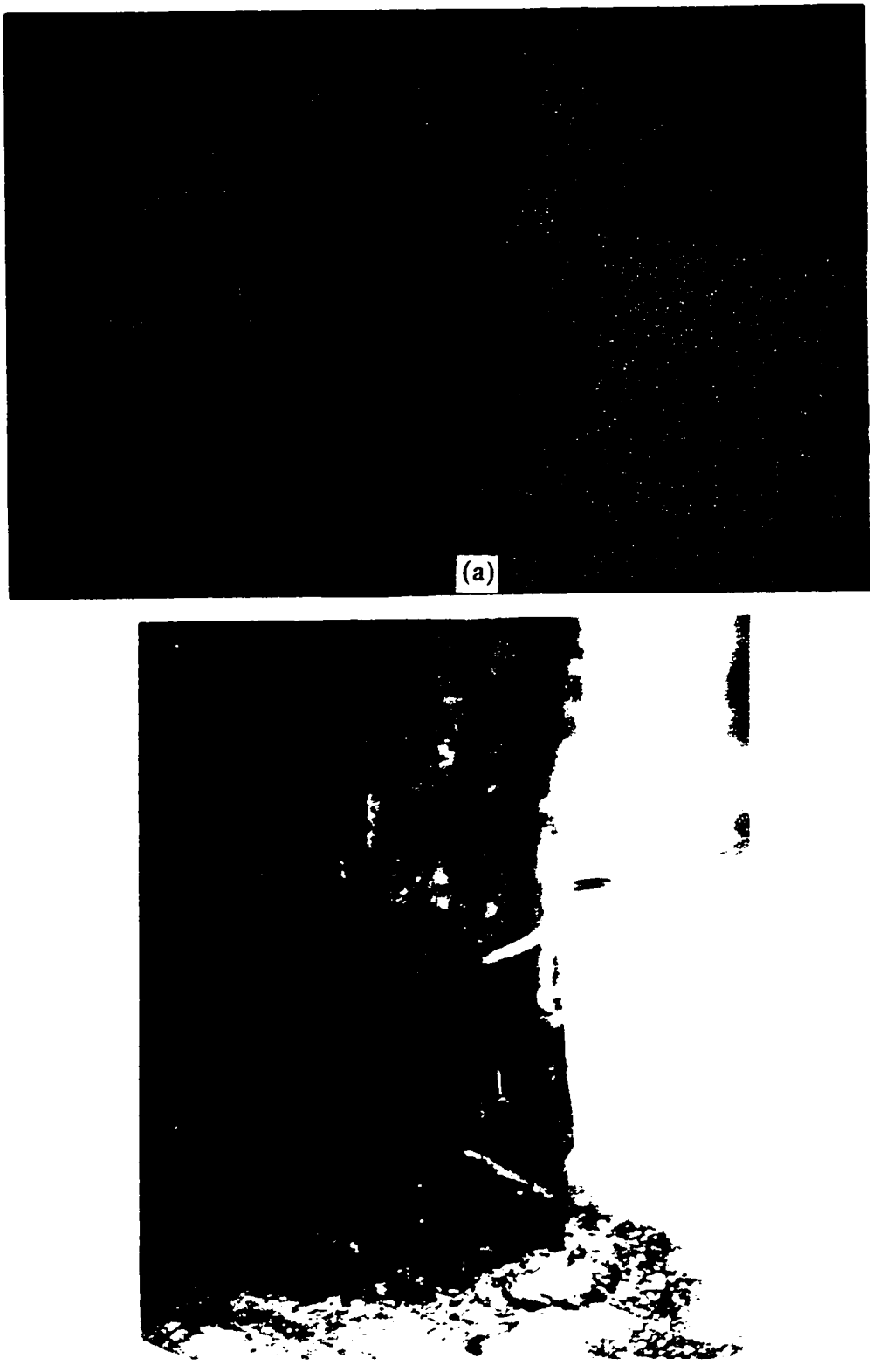

Fig. 6.51. Fracture of the weld at the west exterior stiffener of the channel specimen: (a) severe buckling from previous cycles; (b) close-up view of the weld rupture.

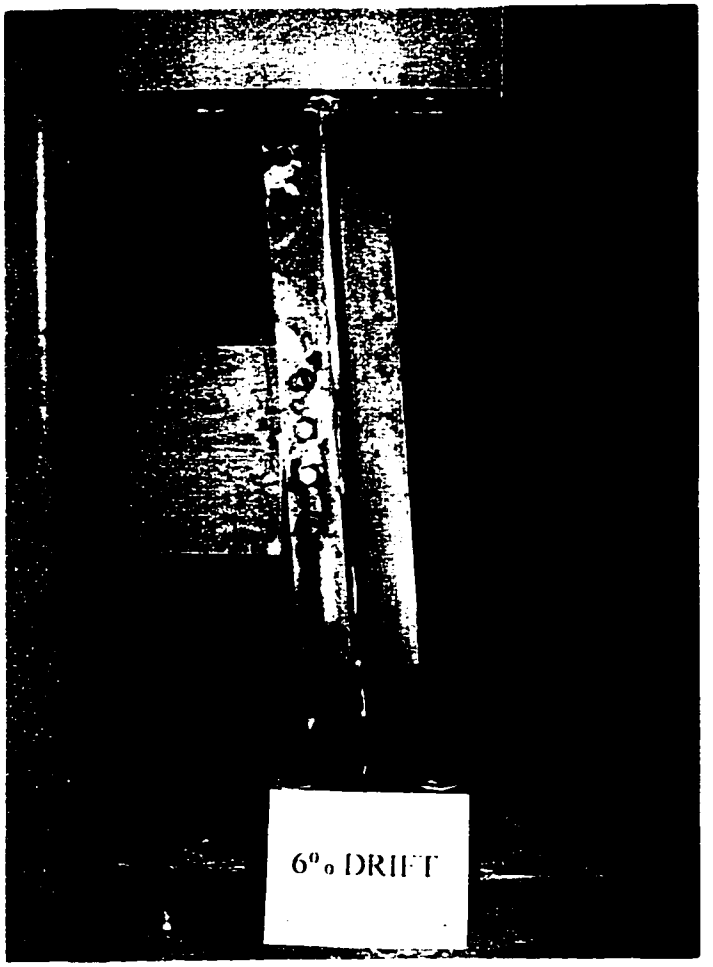

Fig. 6.52. The channel specimen subjected to a drift of 6%, inducing rupture of two other bolts.

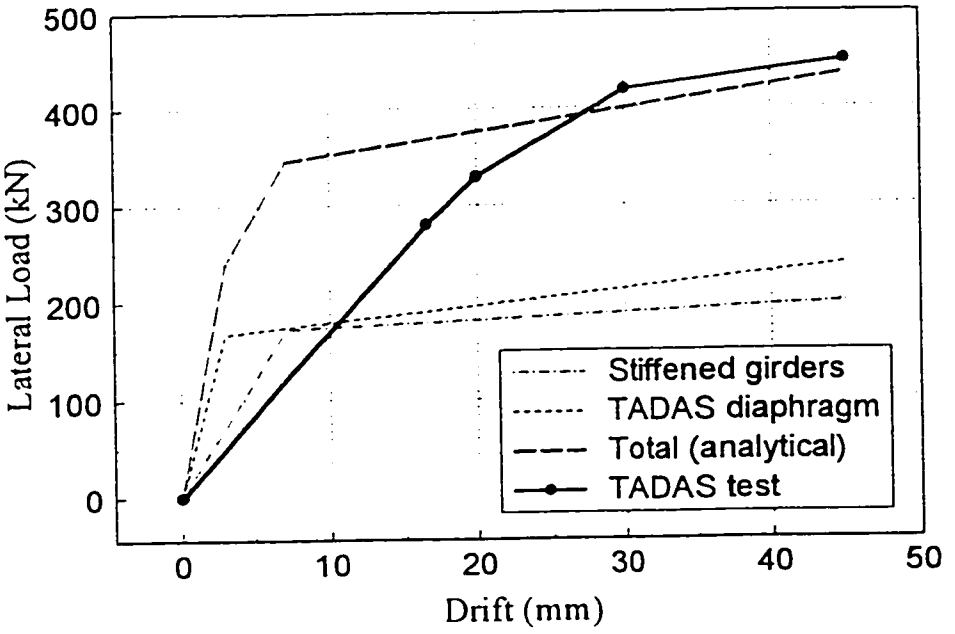

Fig. 7.1. The predicted trilinear load-drift curve for the TADAS specimen compared to an envelope of the TADAS hysteretic curves obtained from testing.

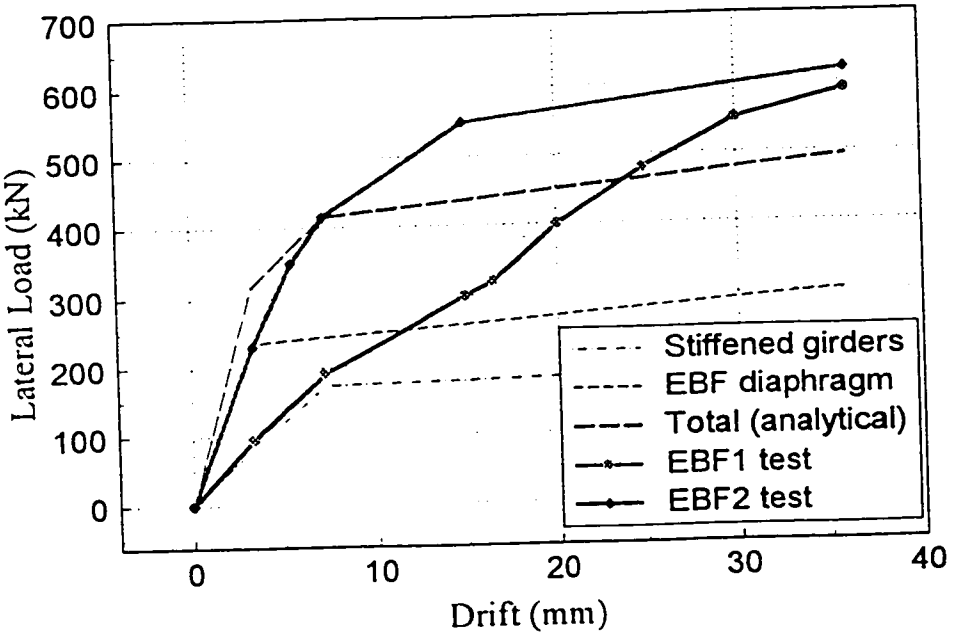

Fig. 7.2. The predicted trilinear load-drift curve for the EBF1 and EBF2 specimens compared to envelopes of the EBF1 and EBF2 hysteretic curves obtained from testing.

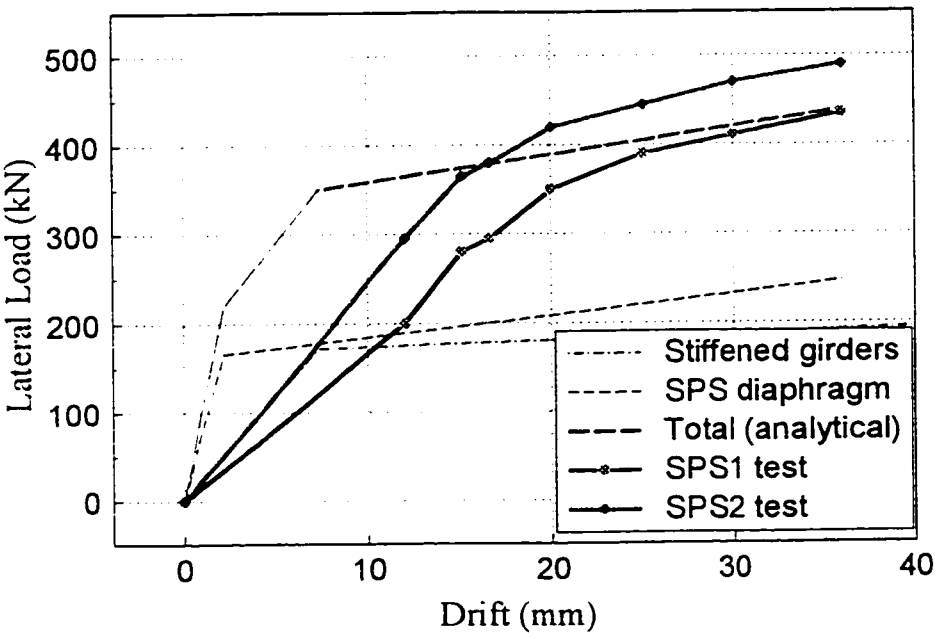

Fig. 7.3. The predicted trilinear load-drift curve for the SPS1 and SPS2 specimens compared to envelopes of the TADAS hysteretic curves obtained from testing.

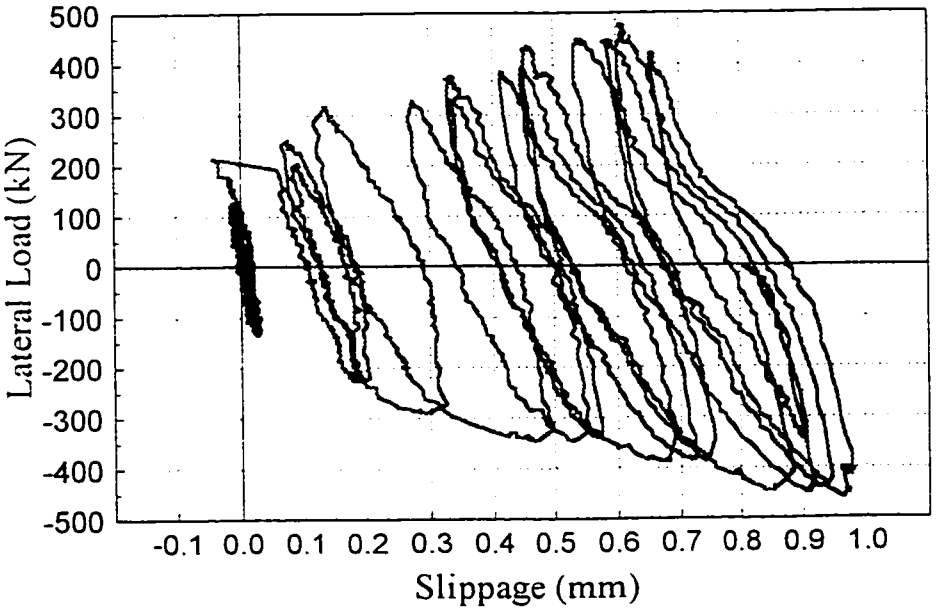

Fig. 7.4. Slippage of the stub-girders of the TADAS specimen during testing.

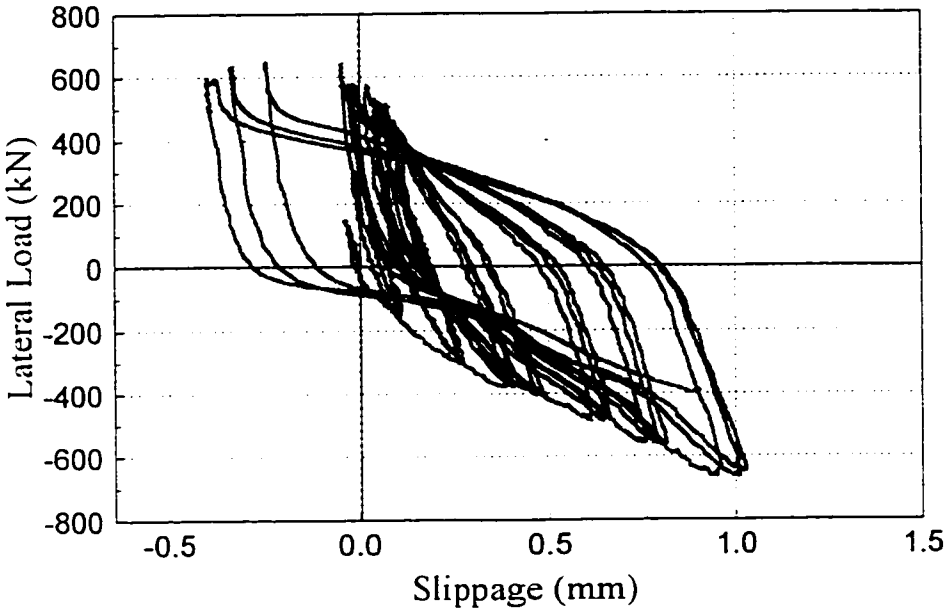

Fig. 7.5. Typical slippage of the stub-girders of the EBF specimens during testing.

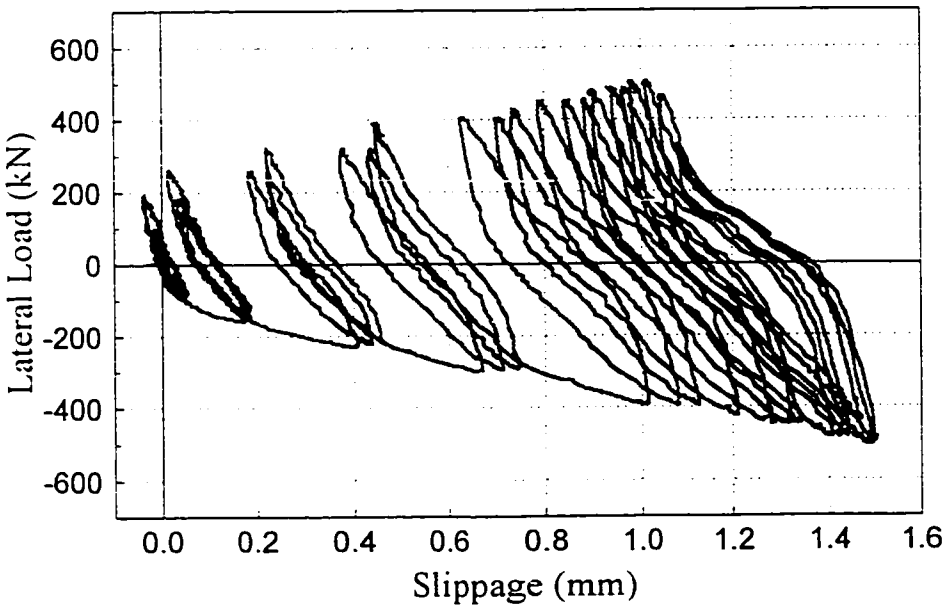

Fig. 7.6. Typical slippage of the stub-girders of the SPS specimens during testing.

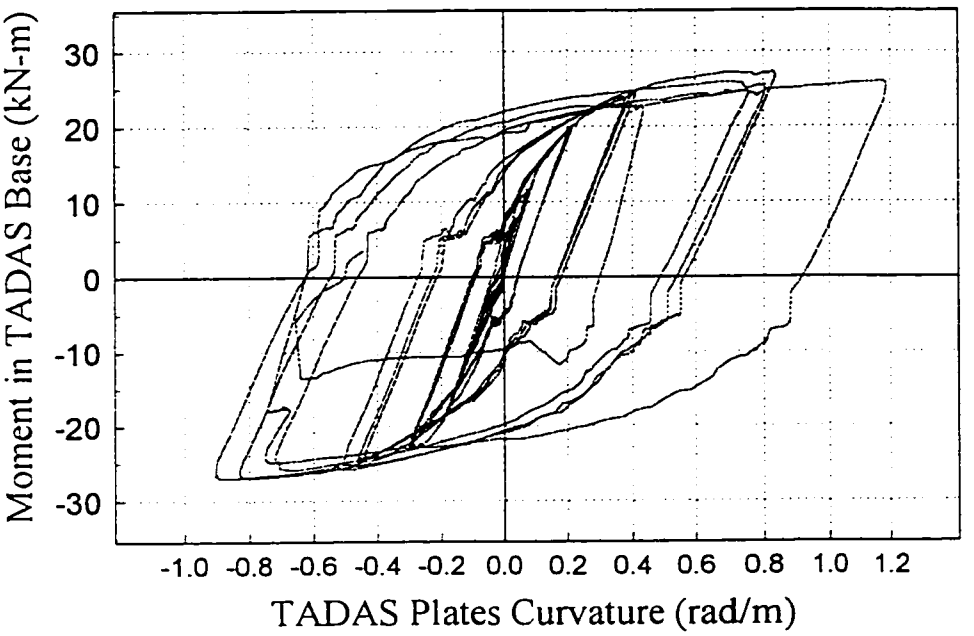

Fig. 7.7. Moment-curvature curves at the base of the TADAS device.

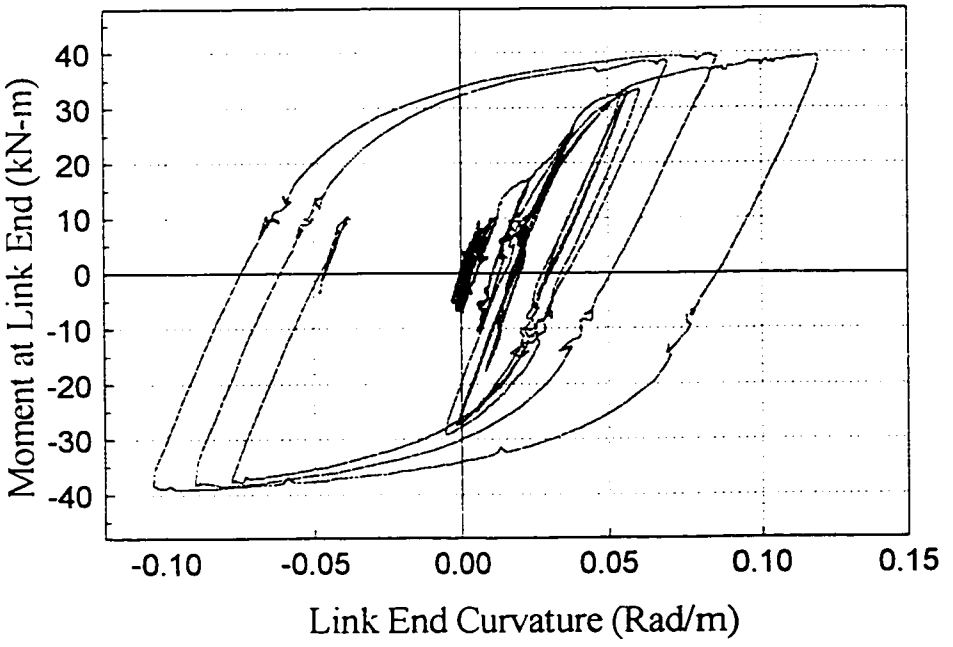

Fig. 7.8. Moment-curvature curves at the end of shear link in the EBF1 specimen.

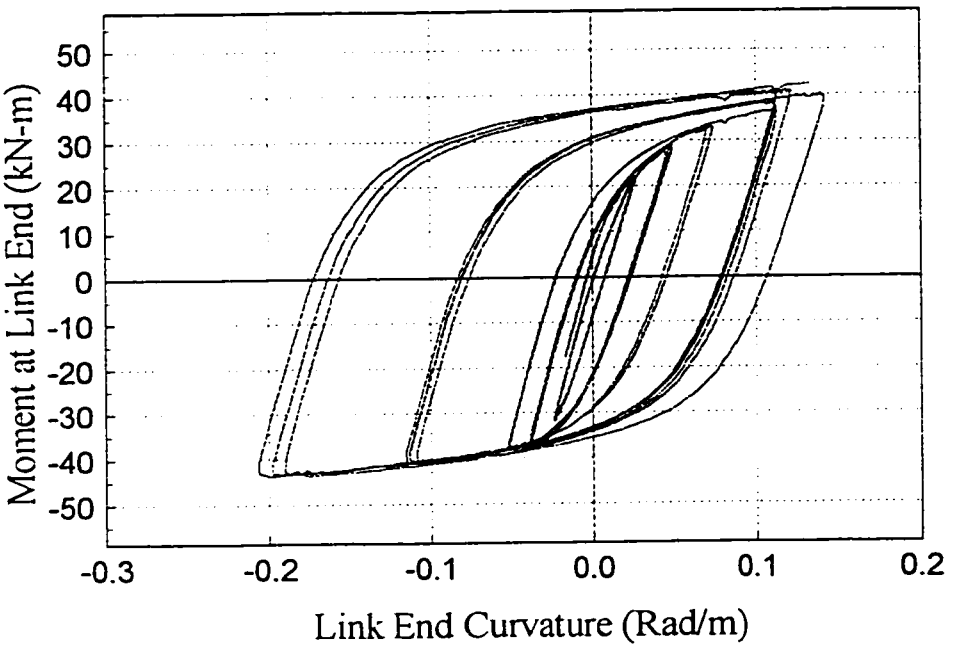

Fig. 7.9. Moment-curvature curves at the ends of shear link in the EBF2 specimen.

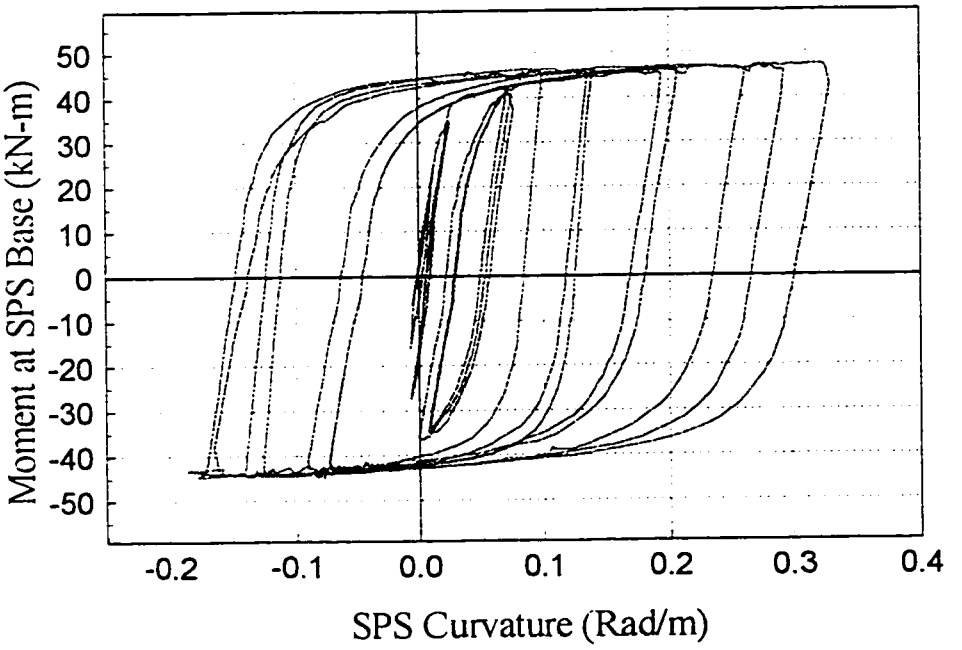

Fig. 7.10. Moment-curvature curves at the base of the SPS1 shear link.

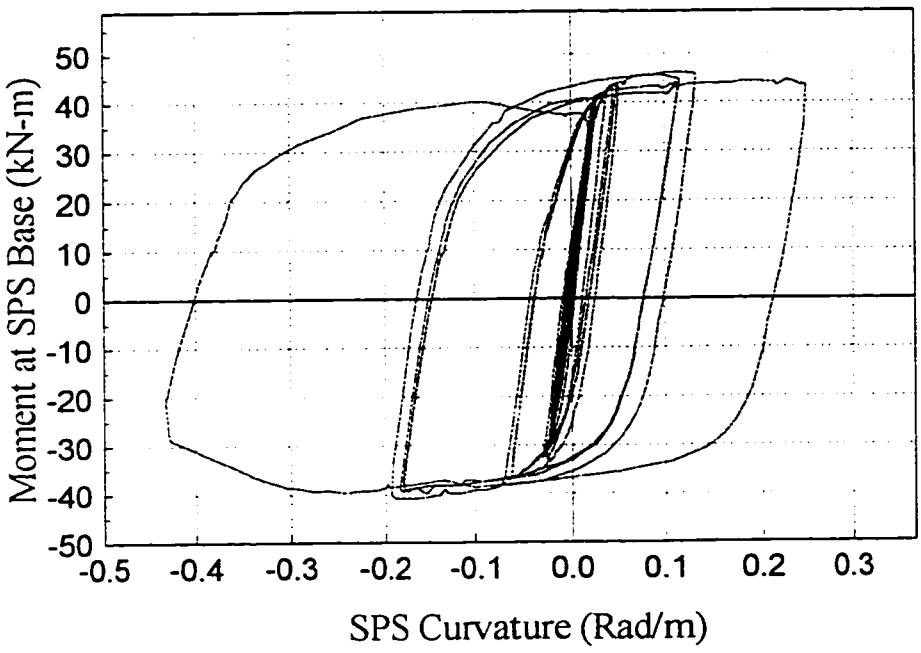

Fig. 7.11. Moment-curvature curves at the base of the SPS2 shear link.

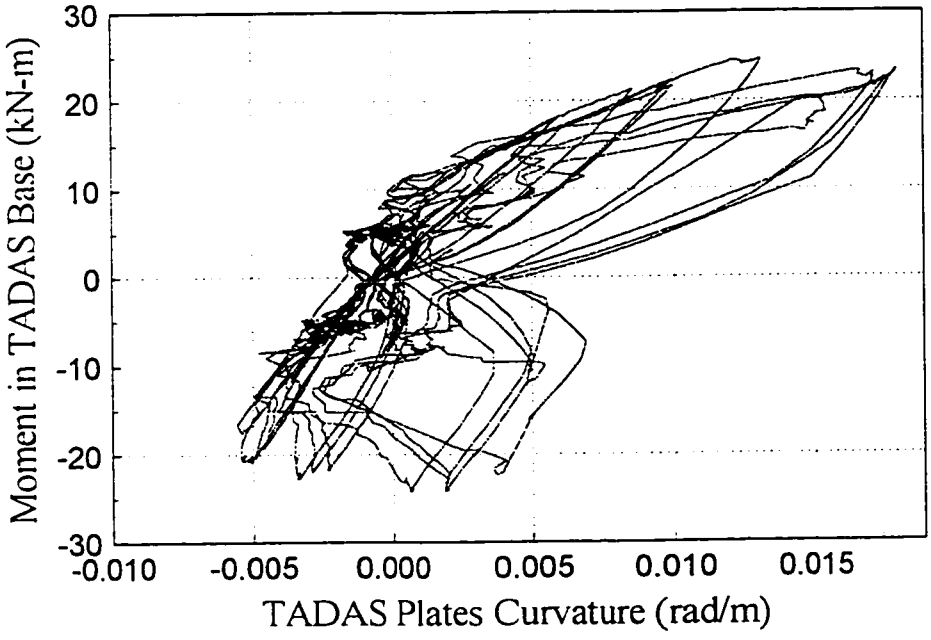

Fig. 7.12. Moment-curvature curves for the bottom beams (at the location of its web stiffeners) of the TADAS specimen.

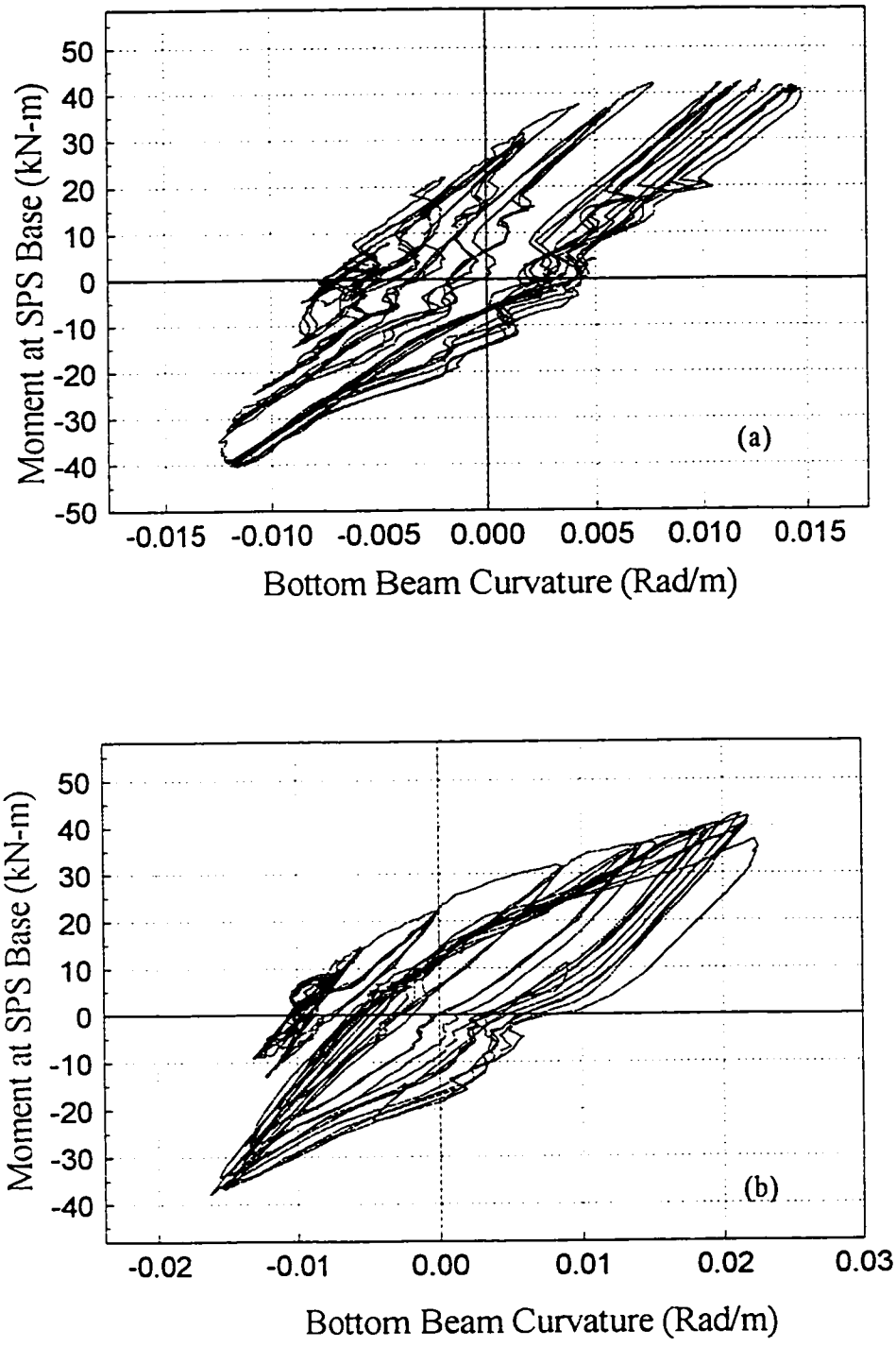

Fig. 7.13. Moment-curvature curves for the bottom beams (at the location of its web stiffeners) of: (a) the SPS1 specimen; (b) the SPS2 specimen.

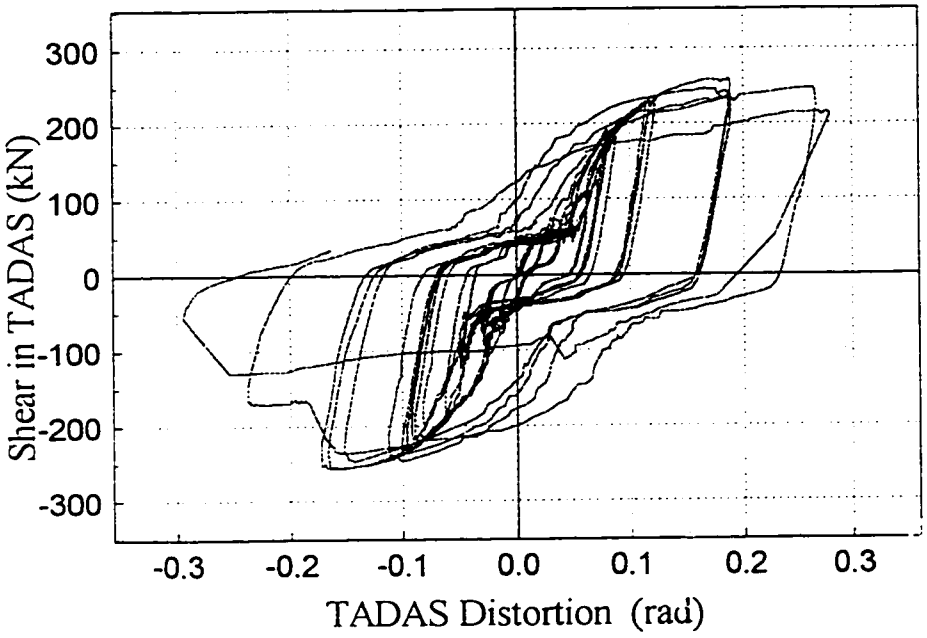

Fig. 7.14. Shear-distortion curves for the TADAS device.

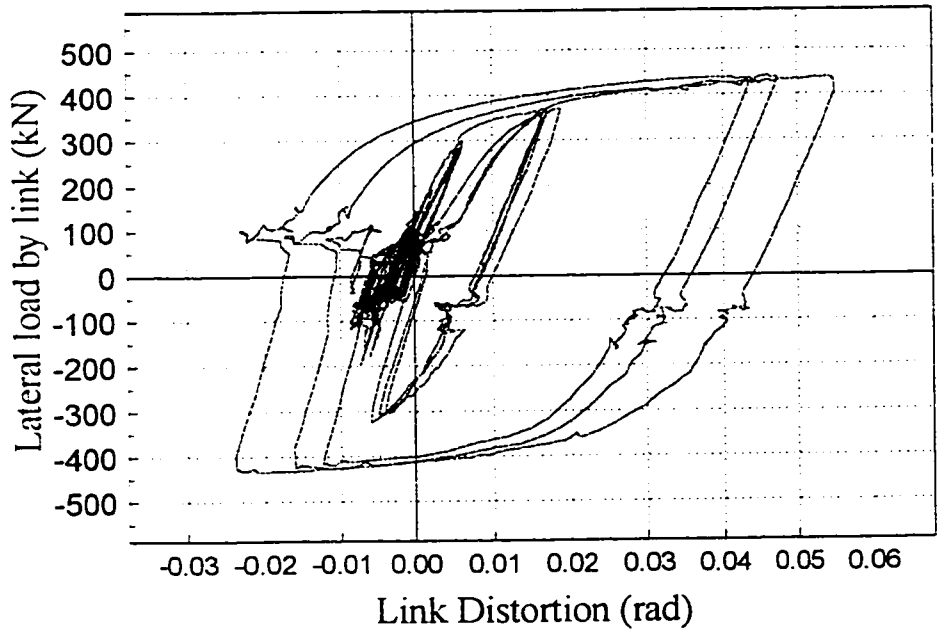

Fig. 7.15. Shear-distortion curves for the EBF1 shear link.

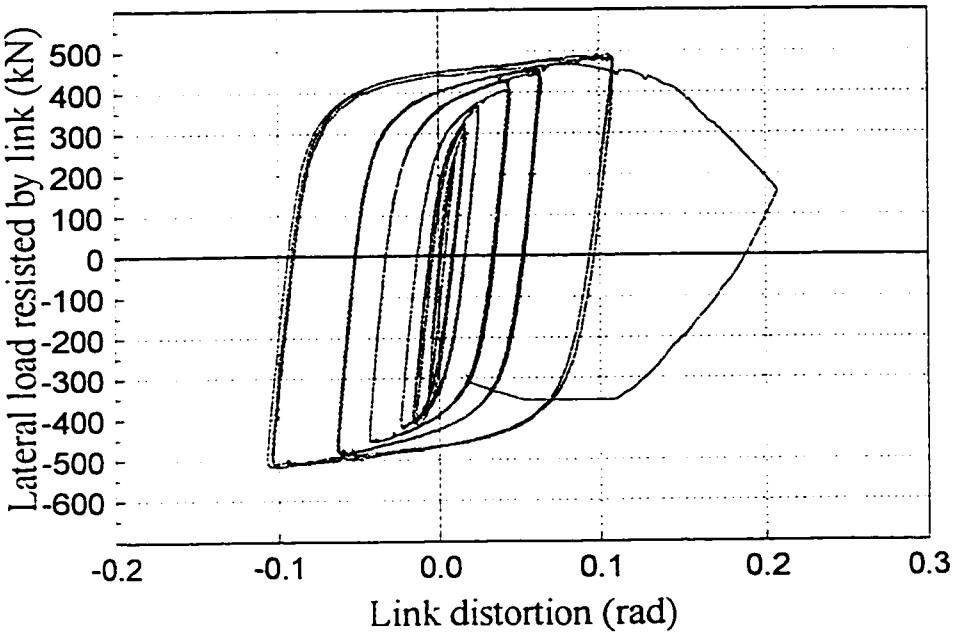

Fig. 7.16. Shear-distortion curves for the EBF2 shear link.

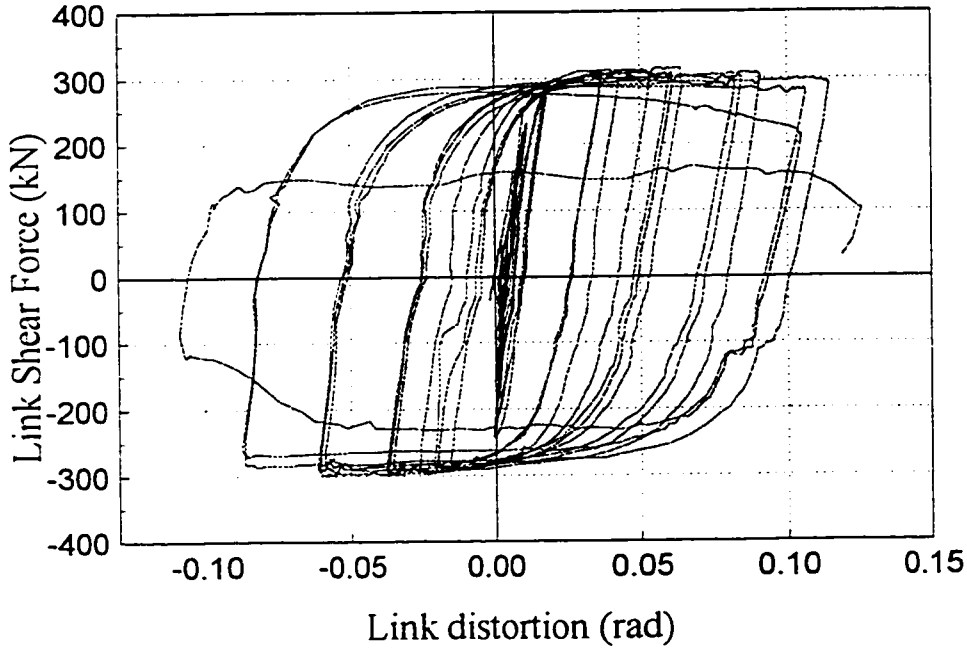

Fig. 7.17. Shear-distortion curves for the SPS1 shear link.

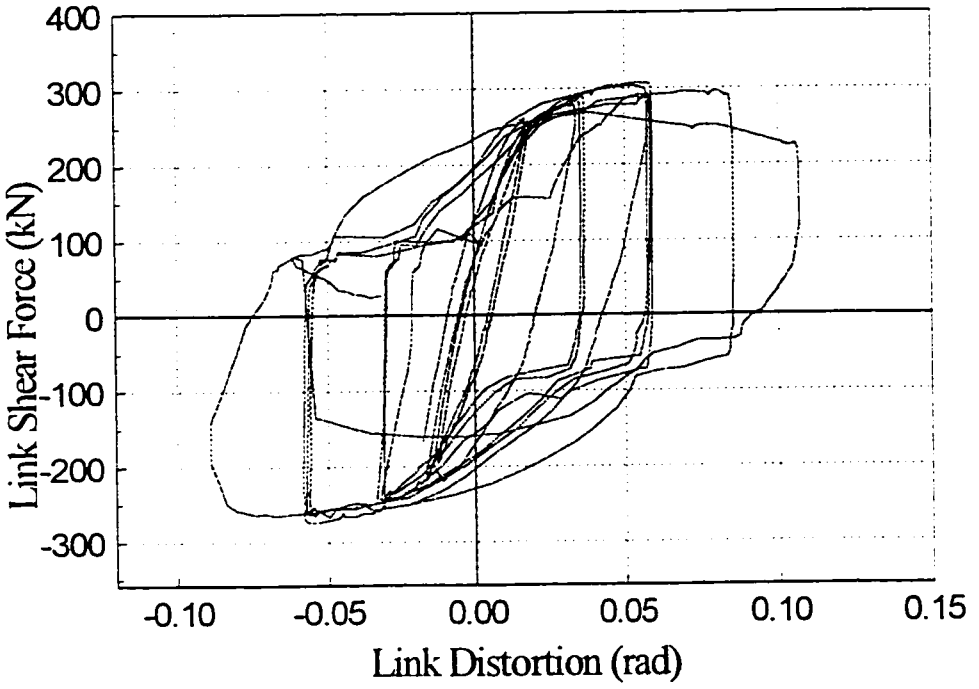

Fig. 7.18. Shear-distortion curves for the SPS2 shear link.

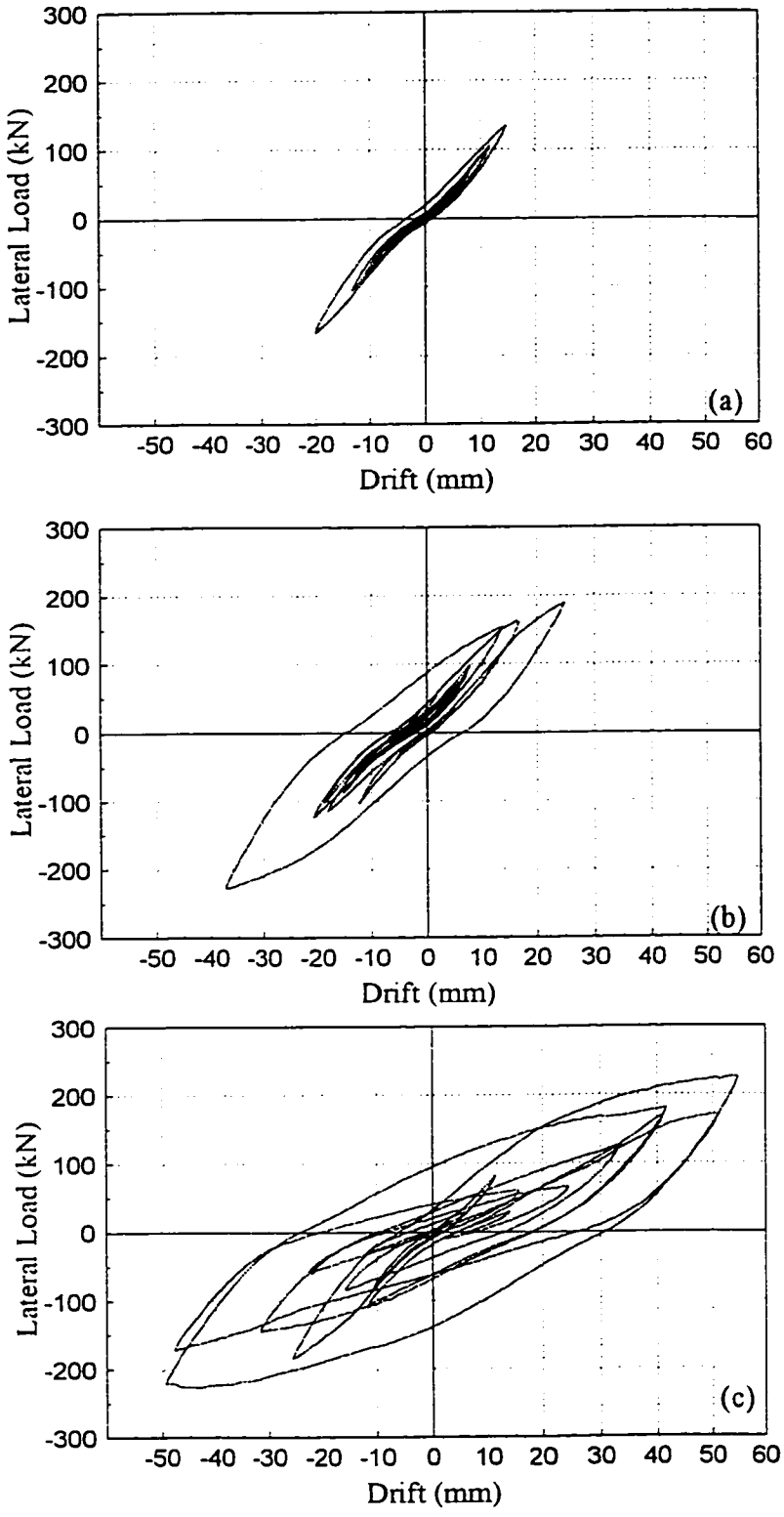

Fig. 7.19. Comparison of the hysteretic curves for the specimen without diaphragm subjected to the El Centro earthquake scaled to *PGAs* of 0.085g, 0.17g and 0.34g.

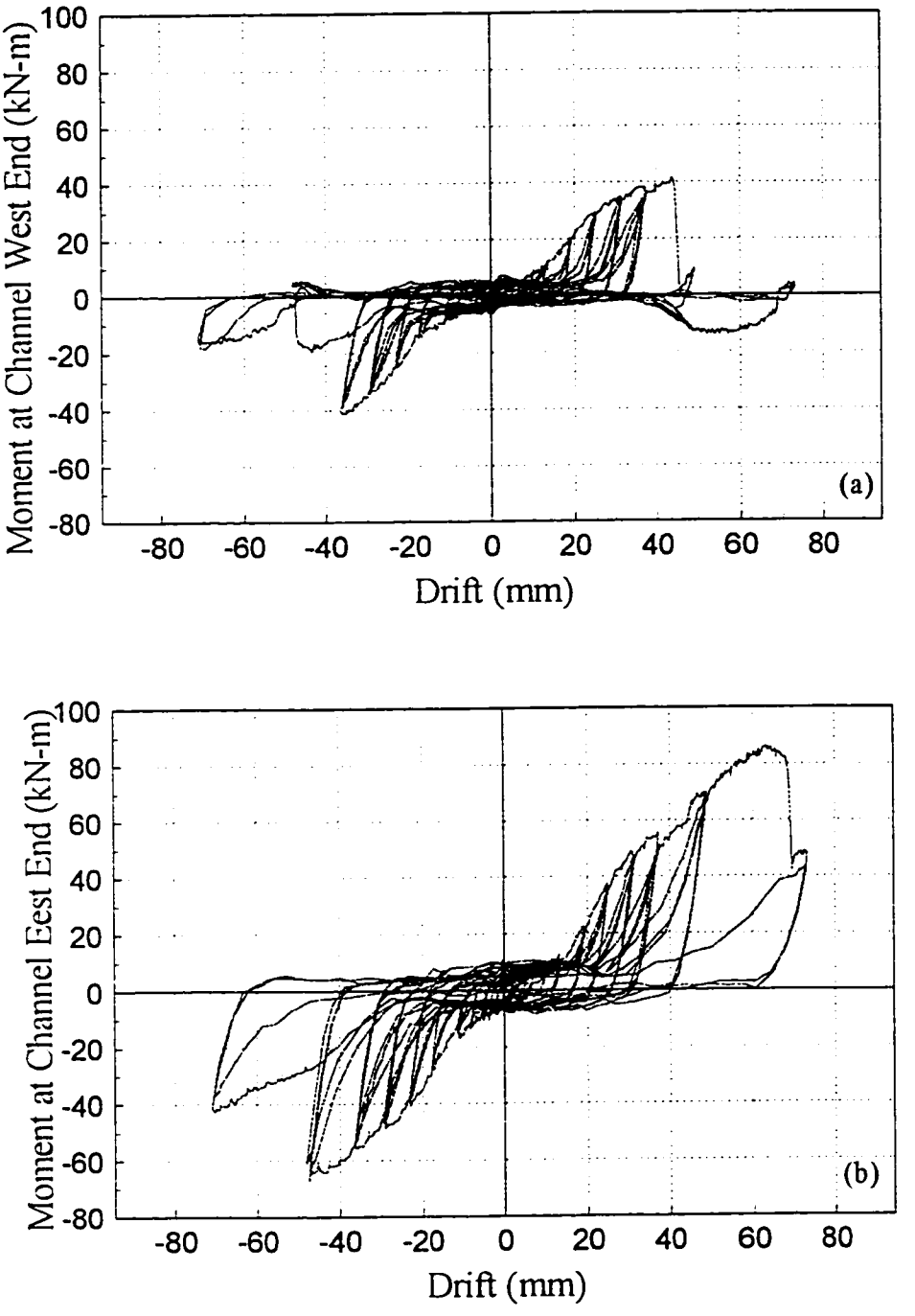

Fig. 7.20. End bending moments of the channel versus drift imposed to the channel specimen: (a) at the west connection; and (b) at the east connection.

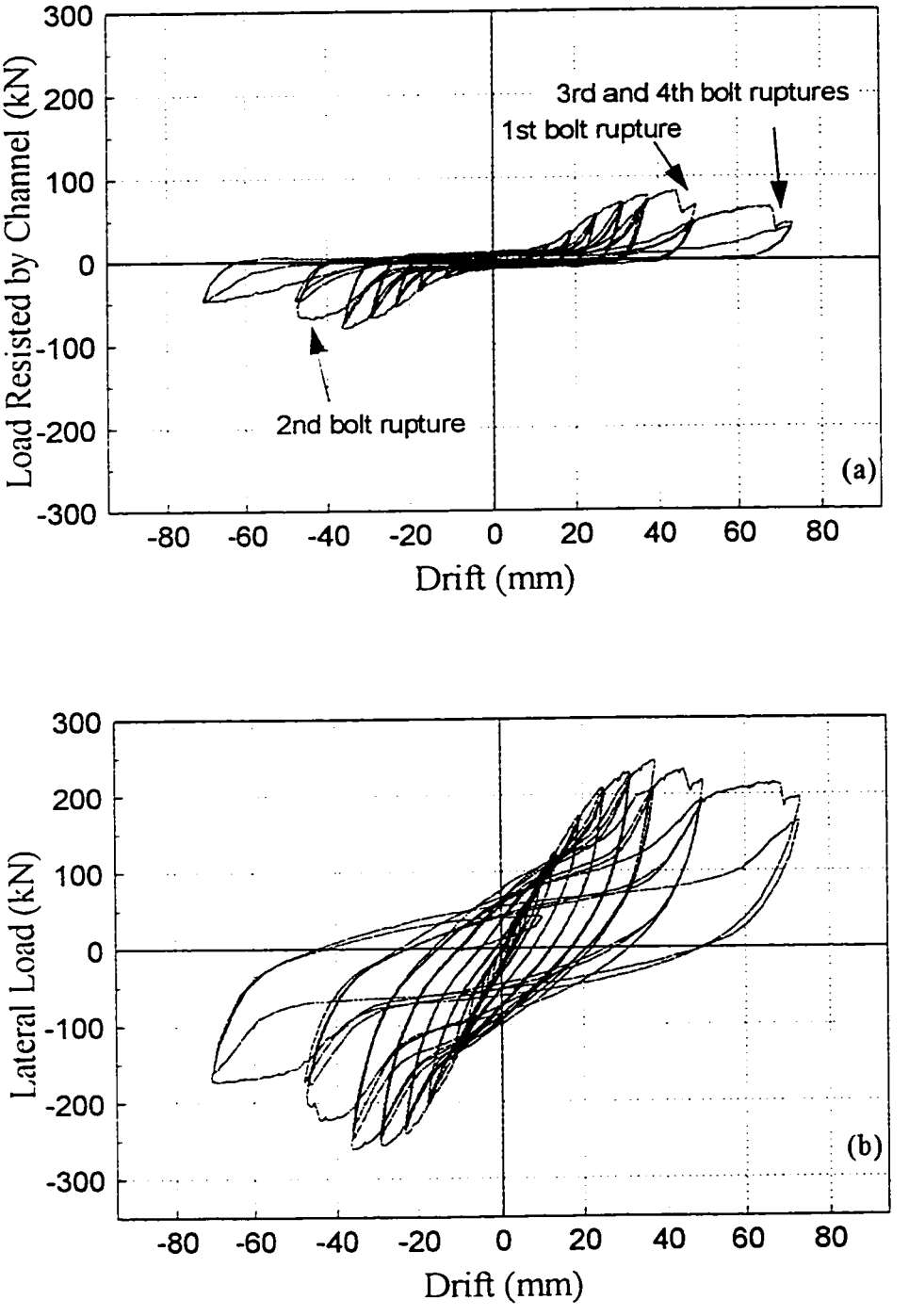

Fig. 7.21. Hysteretic lateral load-drift curves for: (a) the channel section only, i.e. based on its resistance to the lateral load; (b) the channel specimen.

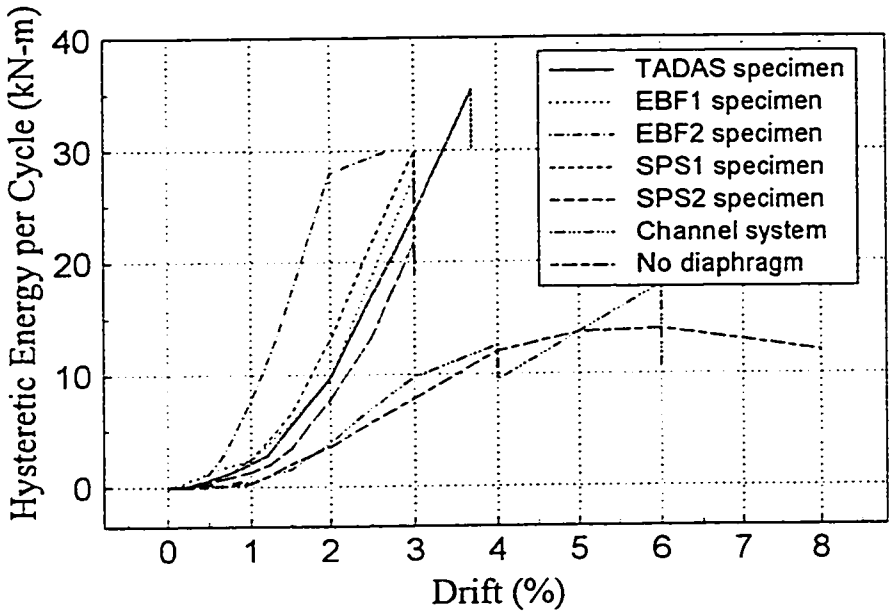

Fig. 7.22. Hysteretic energies per cycle dissipated by the various specimens at different drifts.

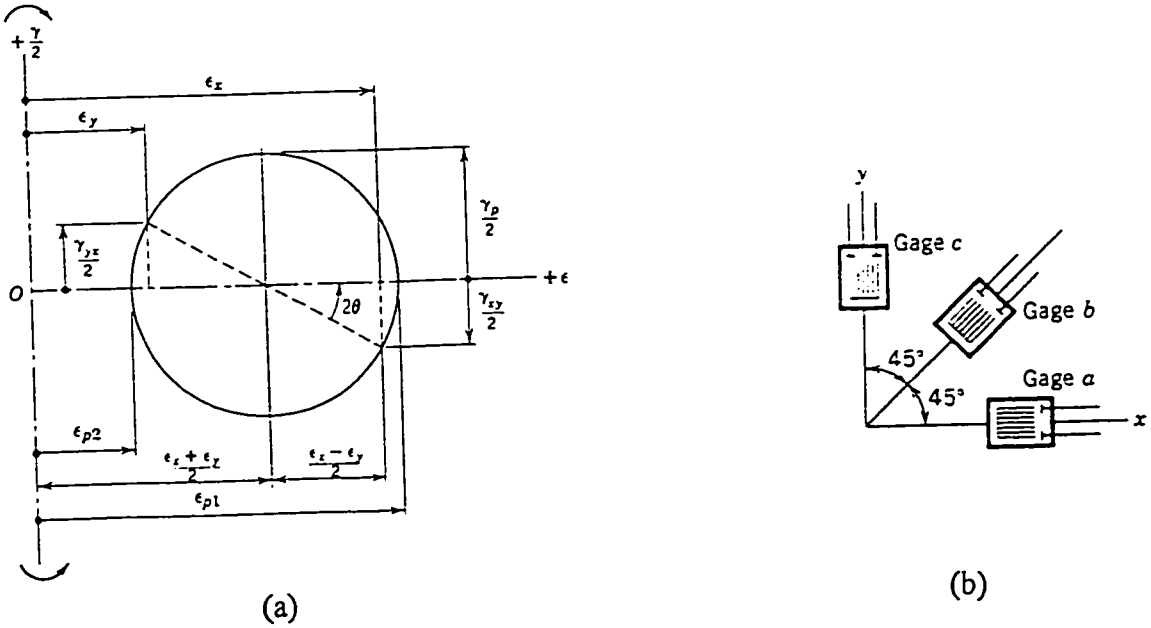

Fig. 7.23. Using data from strain rosettes: (a) Mohr's circle for the strains to find the principal and maximum shear strain; (b) strain rosettes with 45° between the gages used in experiments.

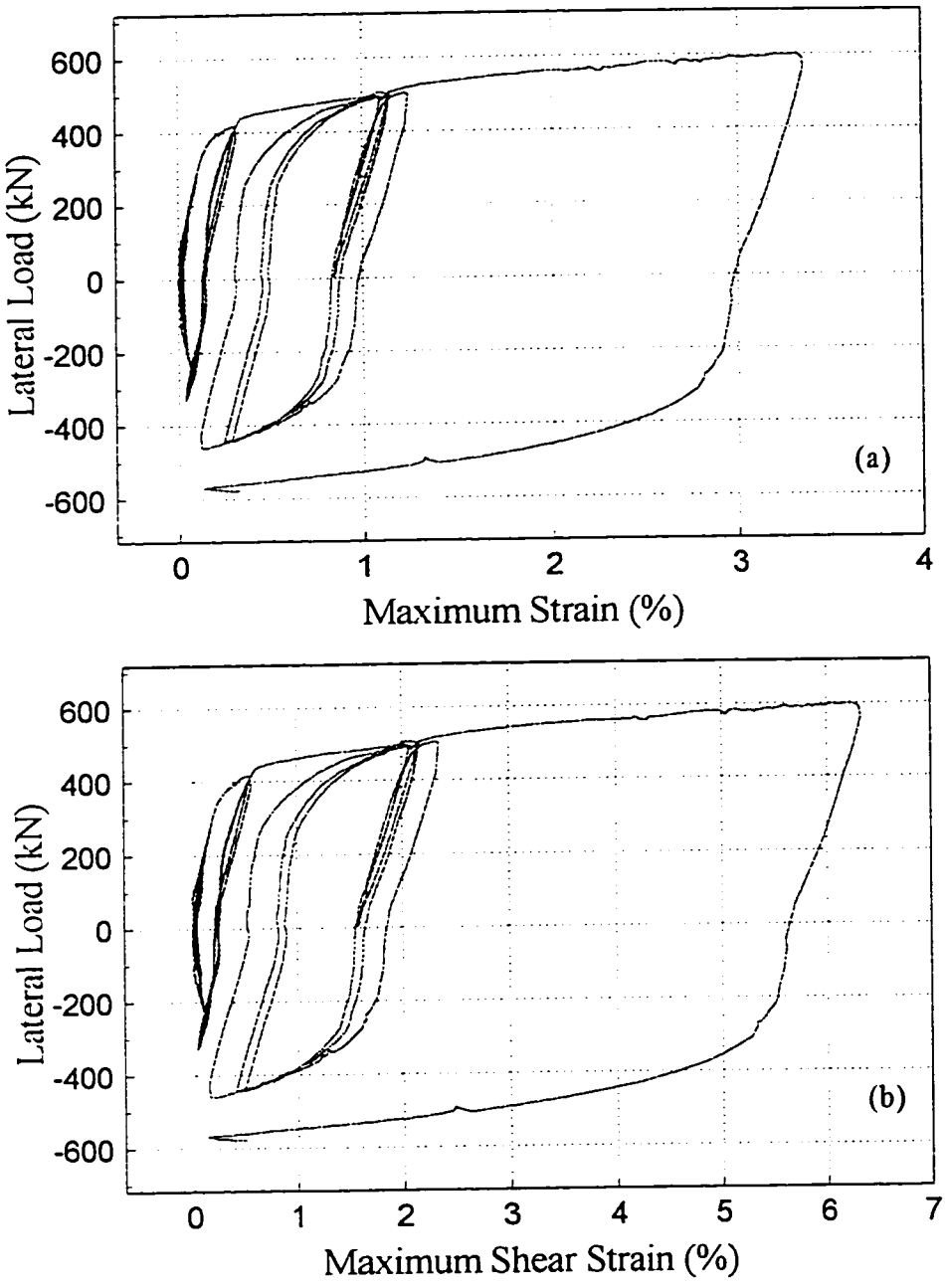

Fig. 7.24. lateral load versus: (a) the maximum principal strain; and (b) maximum shearing strain, for the link beam of the EBF1 specimen.

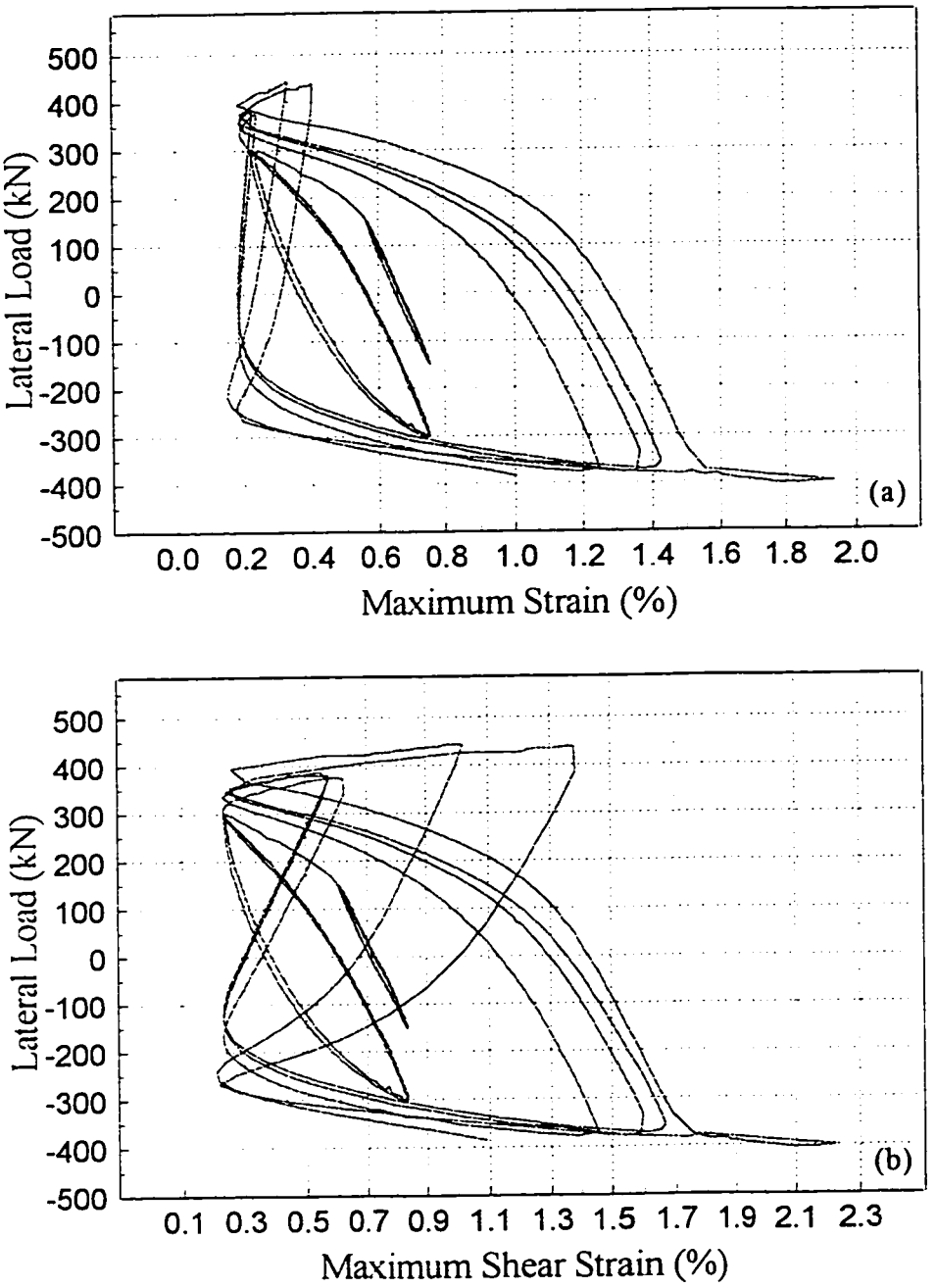

Fig. 7.25. lateral load versus: (a) the maximum principal strain; and (b) maximum shearing strain, for the link beam of the EBF2 specimen.

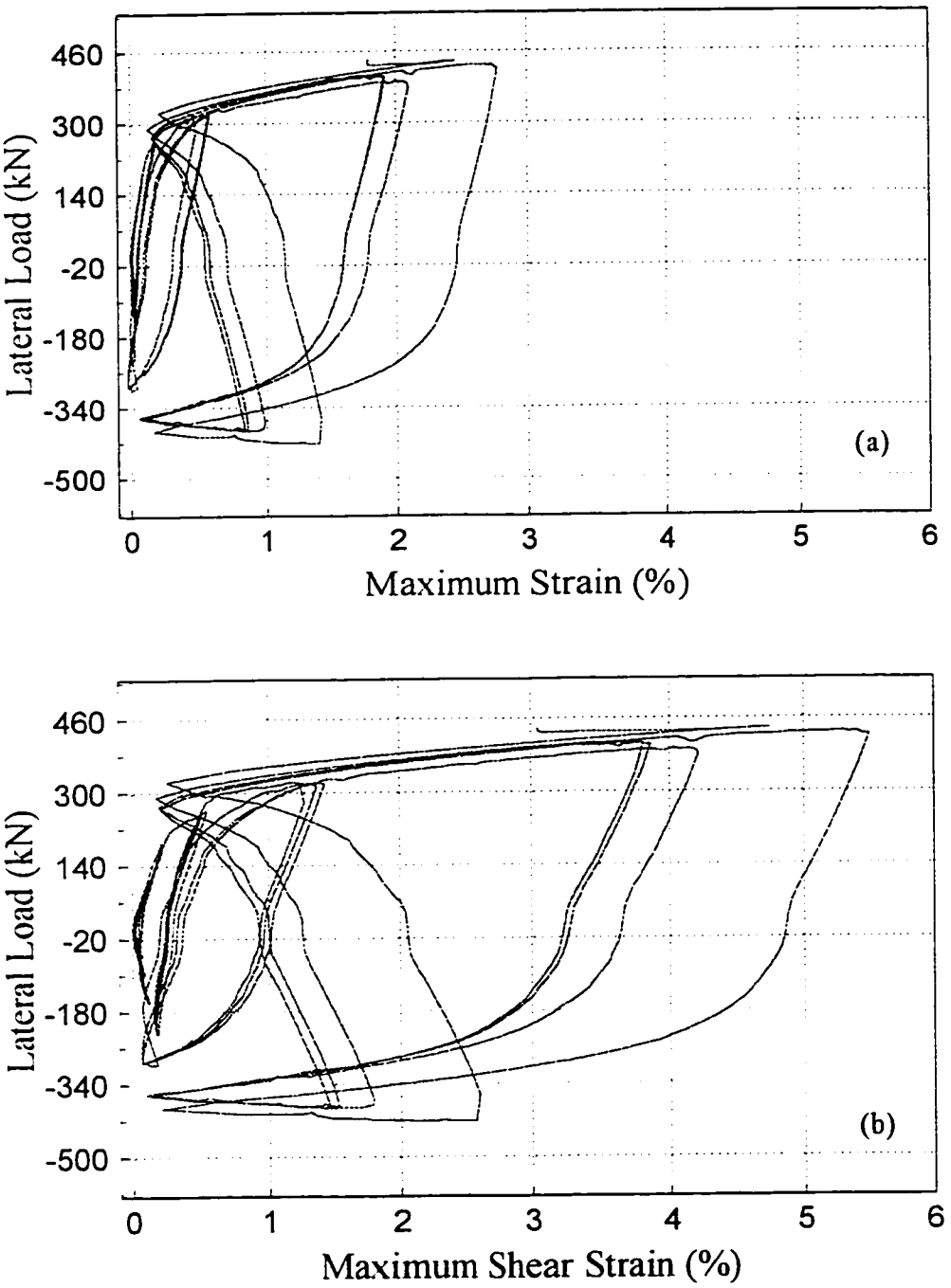

Fig. 7.26. lateral load versus: (a) the maximum principal strain; and (b) maximum shearing strain, for the link beam of the SPS1 specimen.

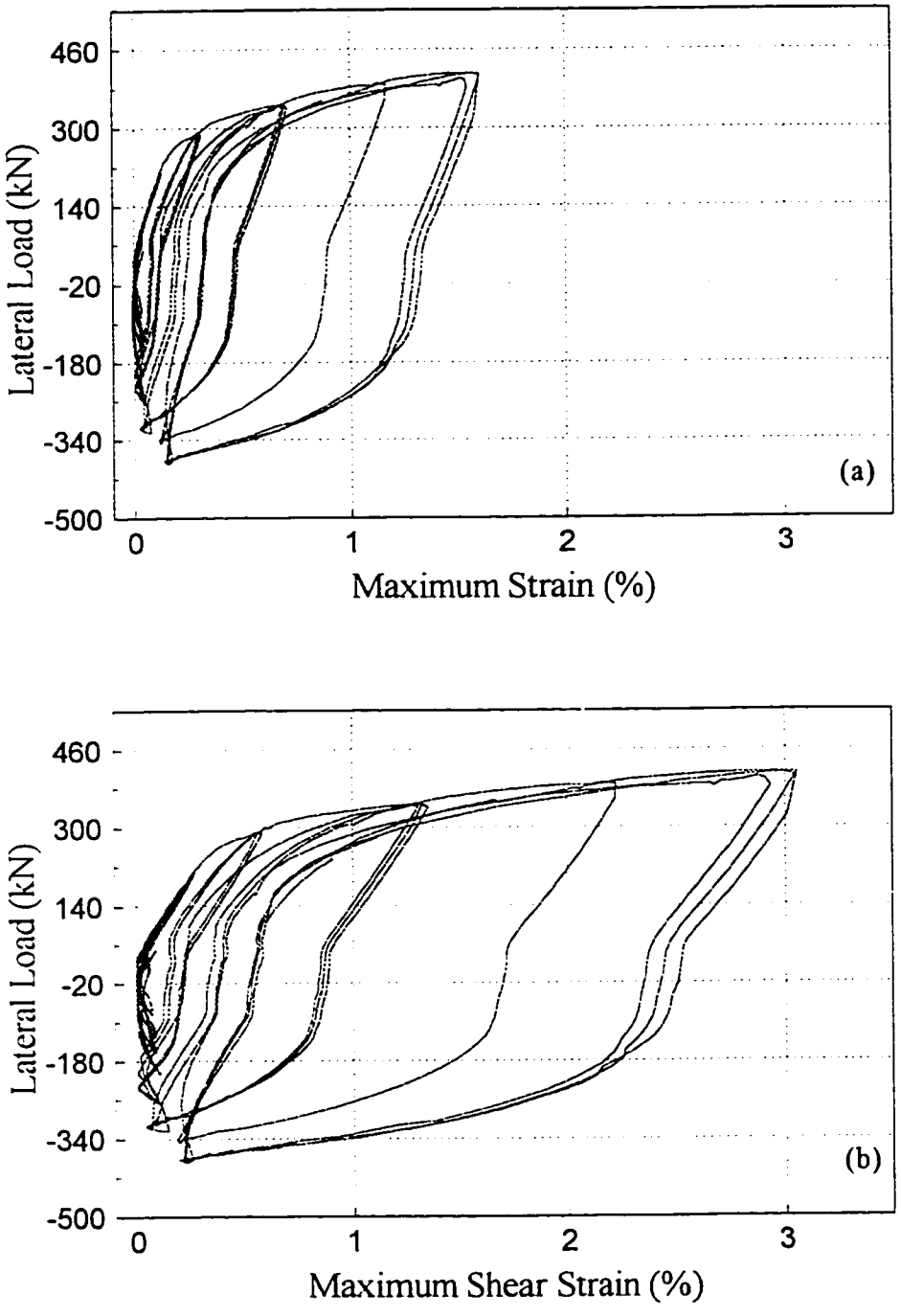

Fig. 7.27. lateral load versus: (a) the maximum principal strain; and (b) maximum shearing strain, for the link beams of the SPS2 specimens.

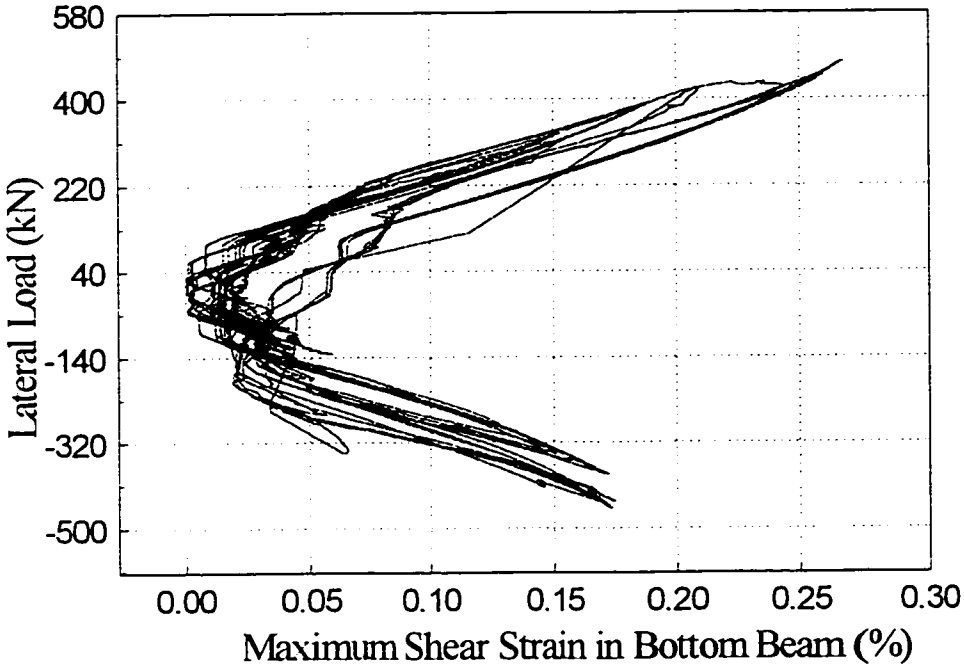

Fig. 7.28. Maximum shearing strain in bottom beam of the TADAS specimen.

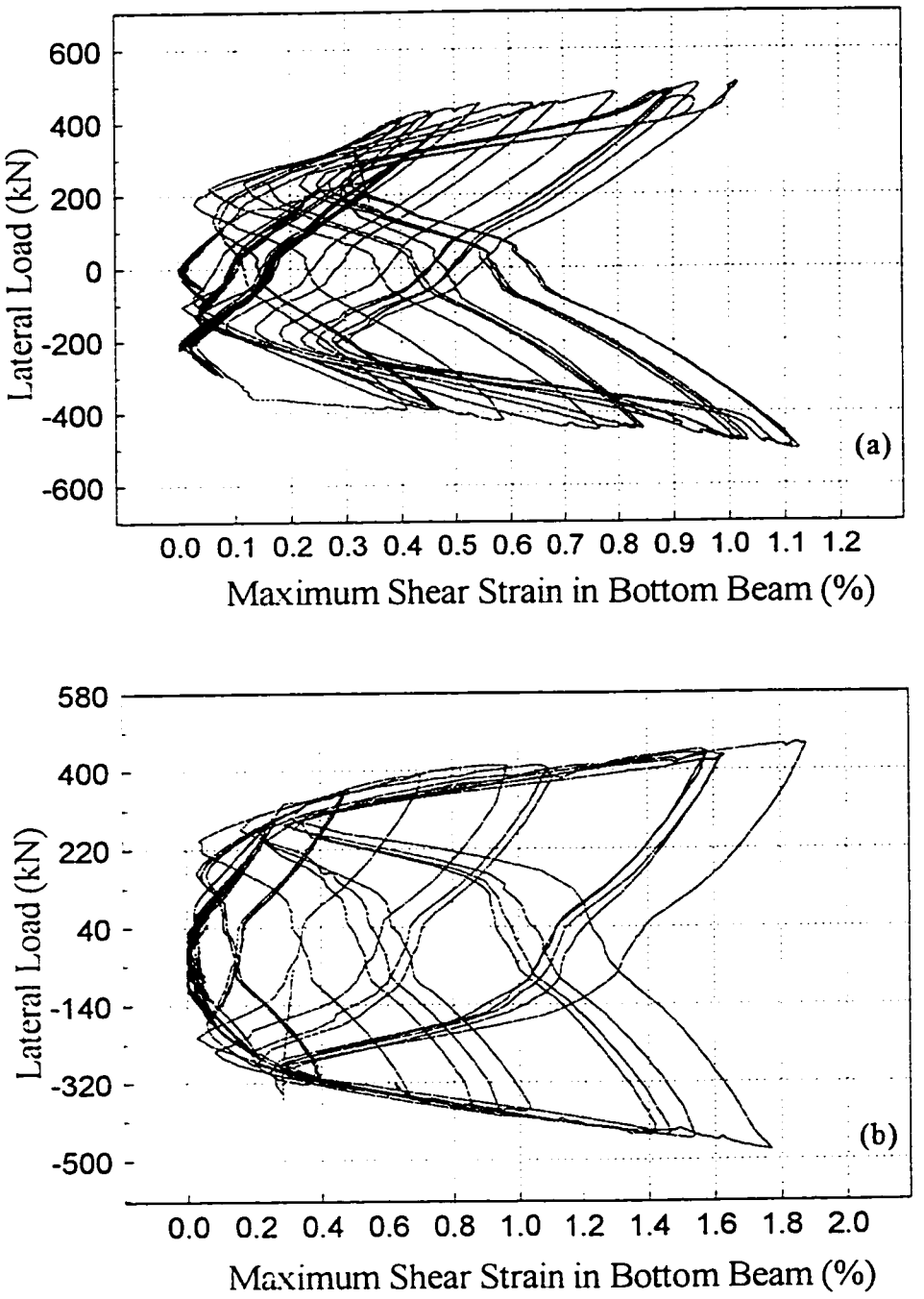

Fig. 7.29. Maximum shearing strain in bottom beam of: (a) the SPS1; and (b) the SPS2 specimens.

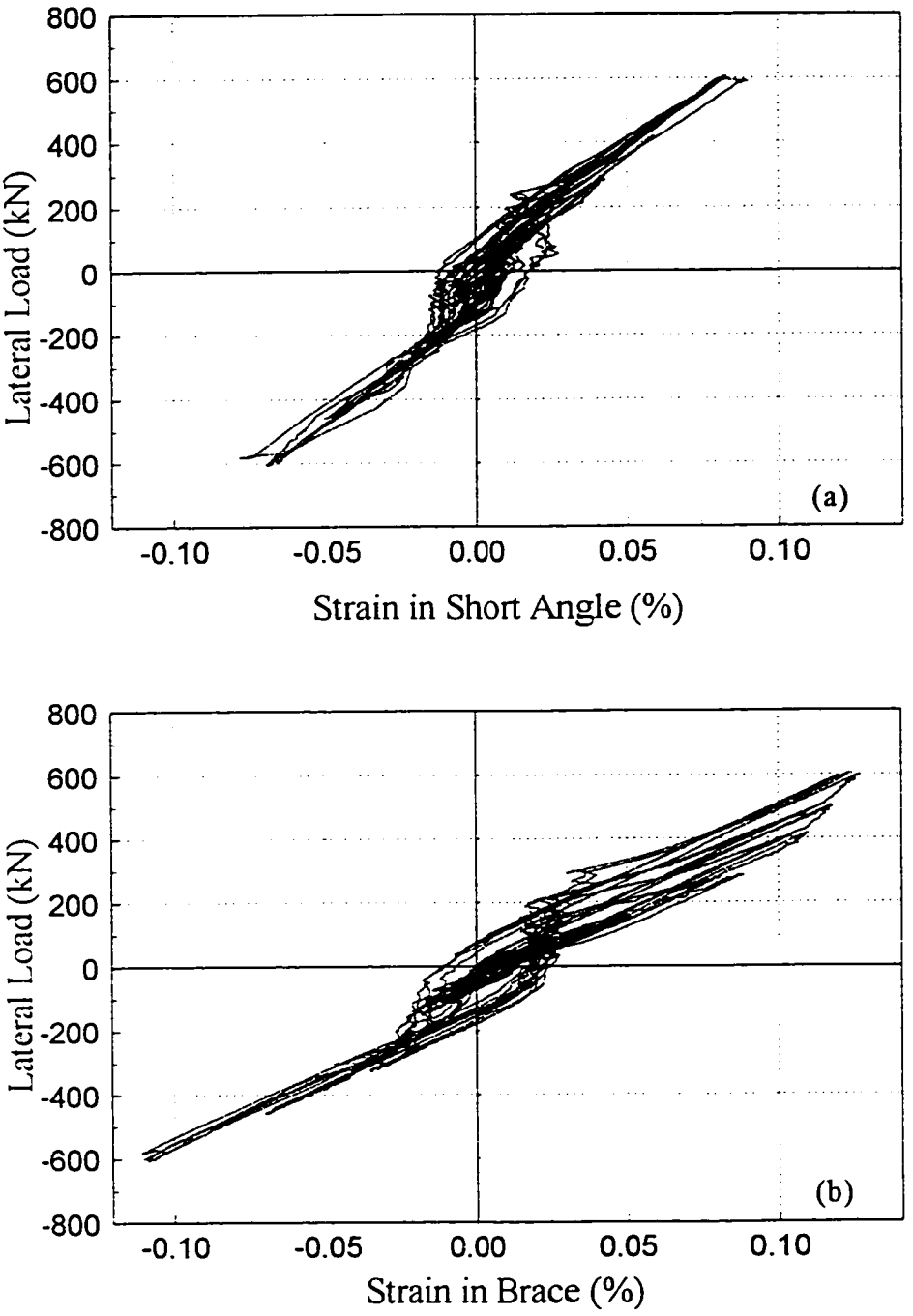

Fig. 7.30. Strain data for: (a) one of the short angles added at the connection to the web stiffeners, (b) one of braces.

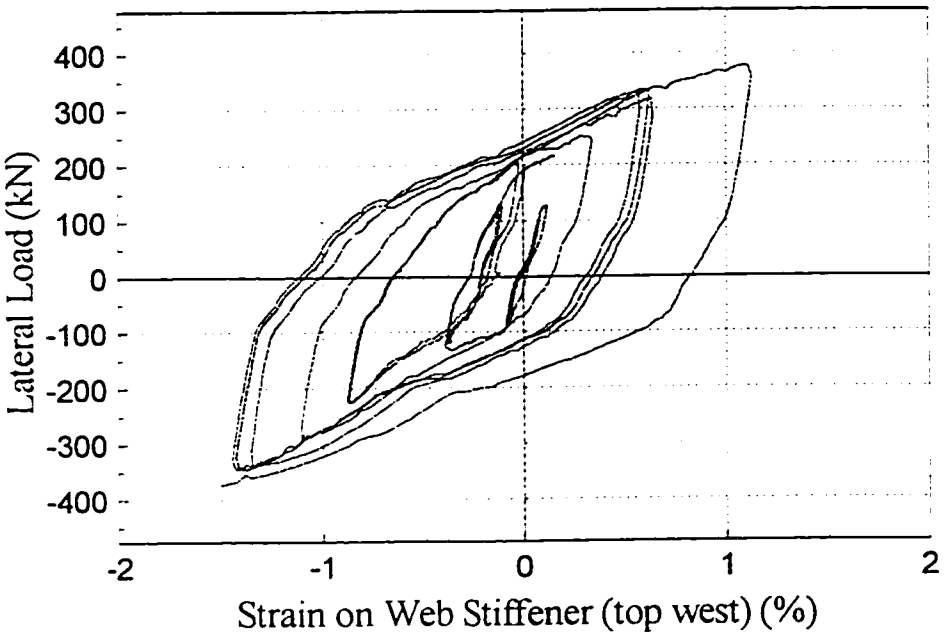

Fig. 7.31. Typical results for strain gages on the web stiffeners of the TADAS specimen.

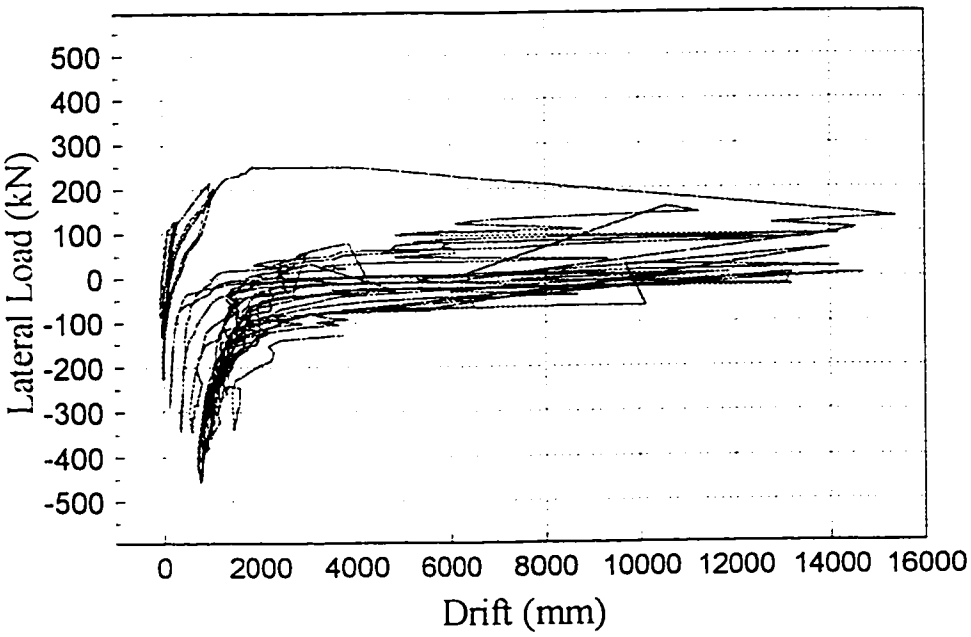

Fig. 7.32. Typical results from strain gages on the shear studs.

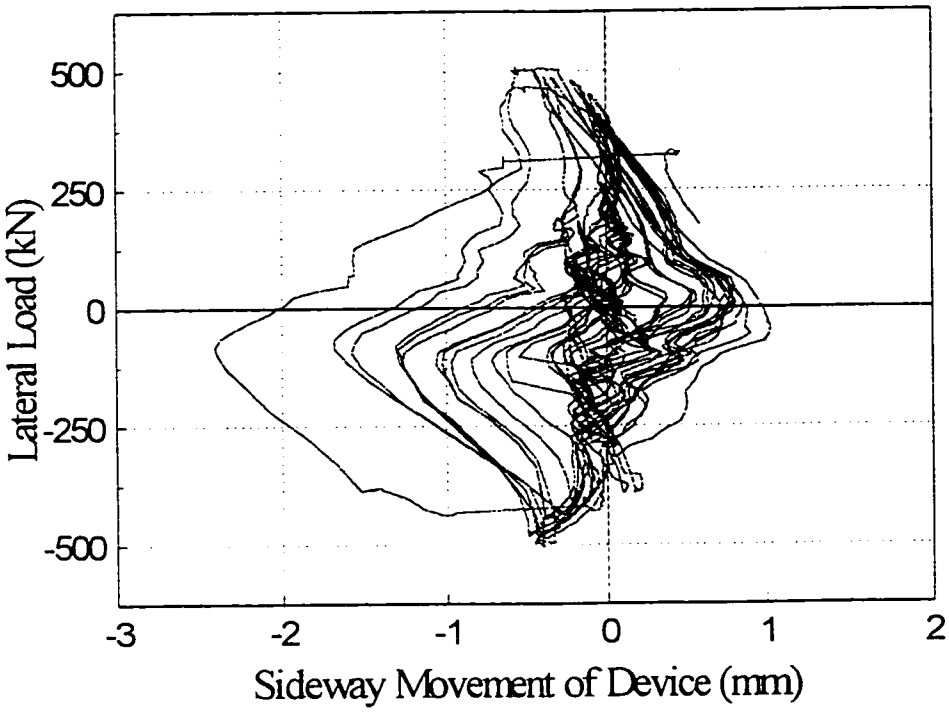

Fig. 7.33. Typical small sideway movements for the ductile devices in the TADAS specimen.

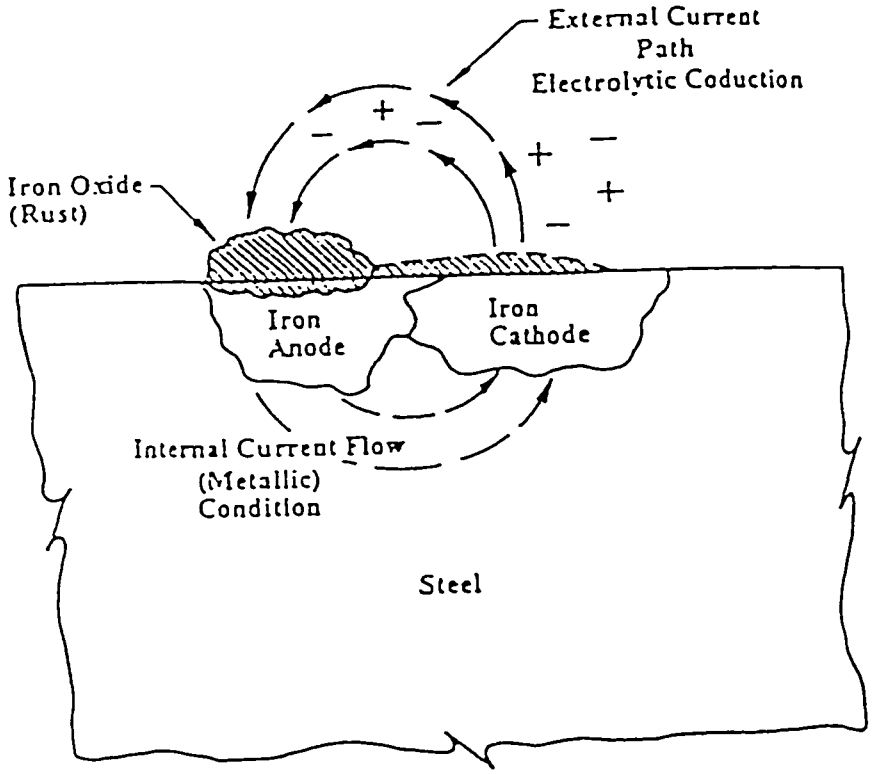

Fig. 8.1. Schematic of corrosion process (Fisher et al. 1991).

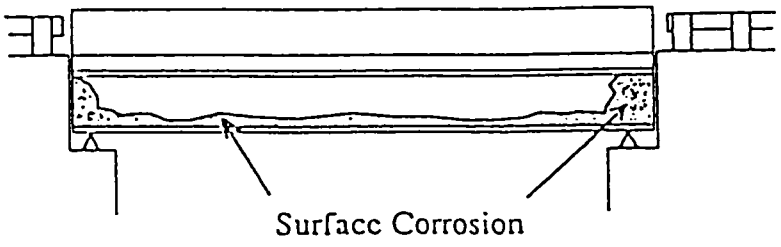

Fig. 8.2. Corrosion pattern for typical steel bridges (bridge ends are mostly vulnerable to corrosion) (Kayser et al. 1987).

Fig. 8.3. Typical areas of section loss to the flanges and web of stringers (Kulicki et al. 1990).

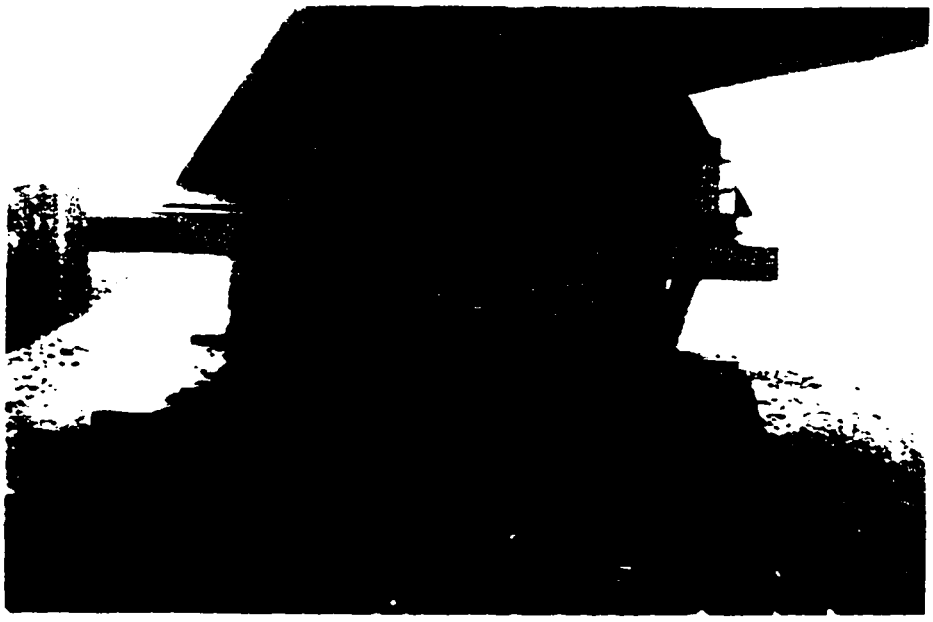

Fig. 8.4. Typical condition of expansion bearings, many bolts have bent or sheared off (Kulicki et al. 1990).

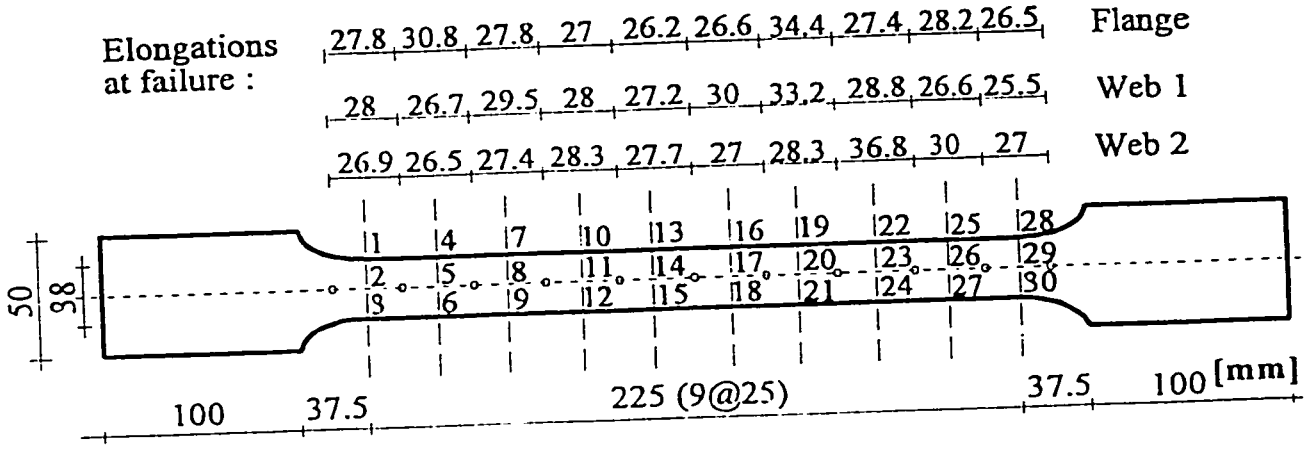

Fig. 8.5. ASTM E8M rusted coupon specimens.

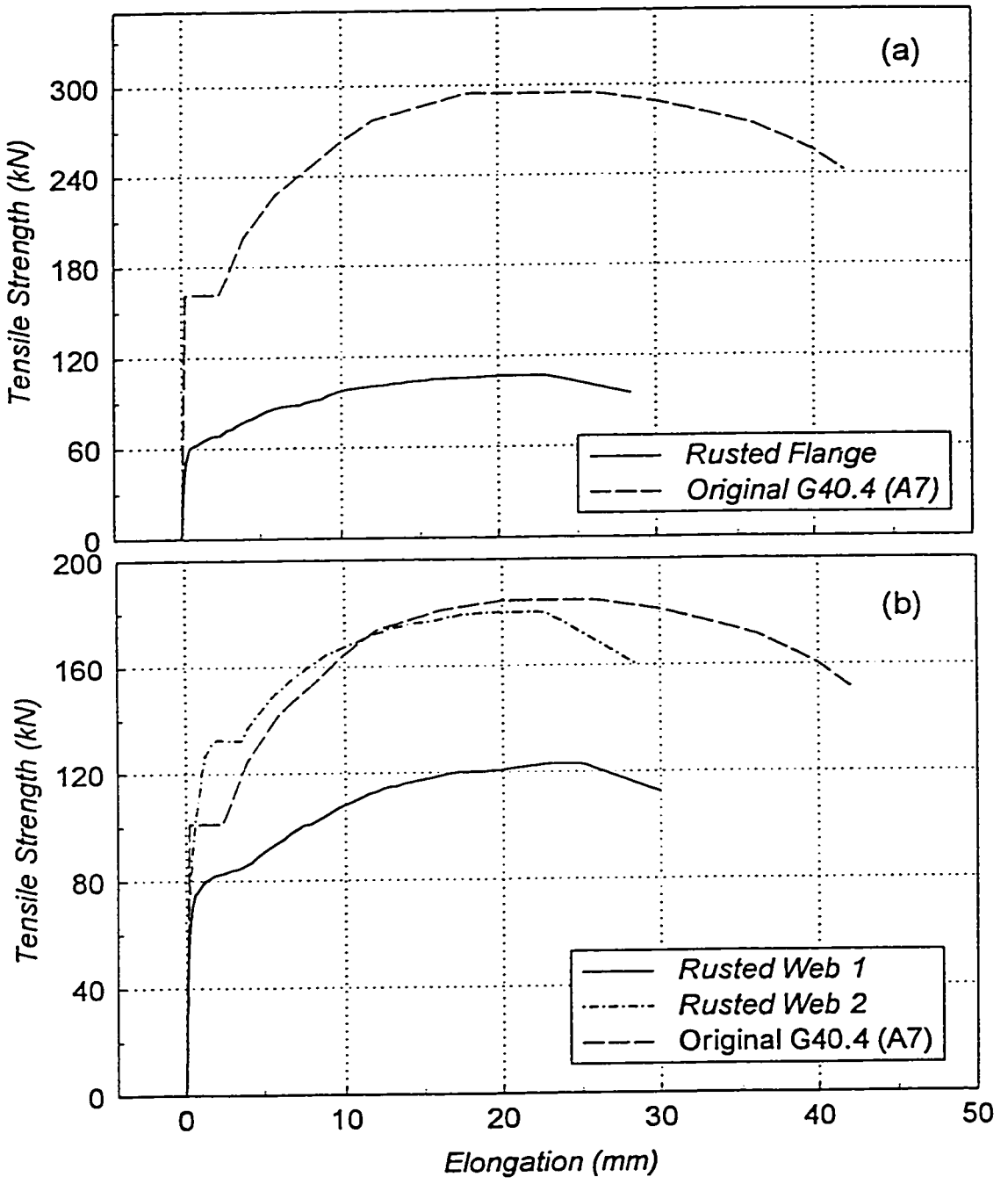

Fig. 8.6. Experimentally obtained tensile strength of rusted coupons compared to typical strength of unrusted A7 steel: (a) flange coupon; (b) web coupons.

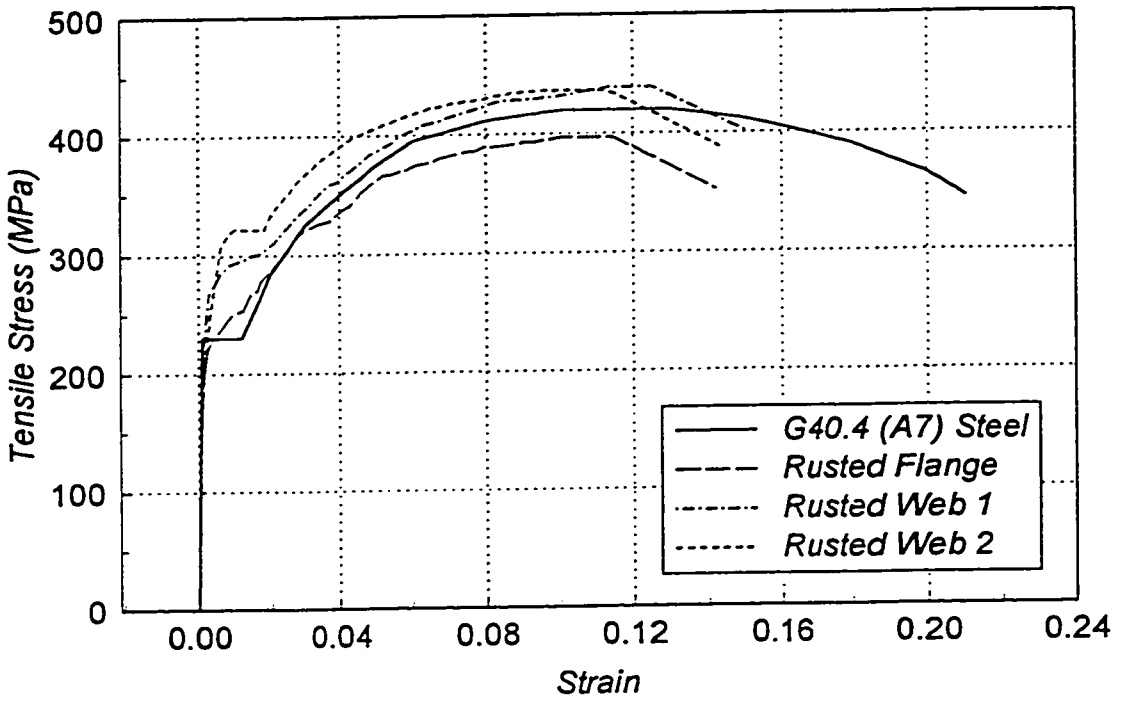

Fig. 8.7. Experimentally obtained stress-strain relationship for rusted coupons compared to typical stress-strain curve for unrusted A7 steel.

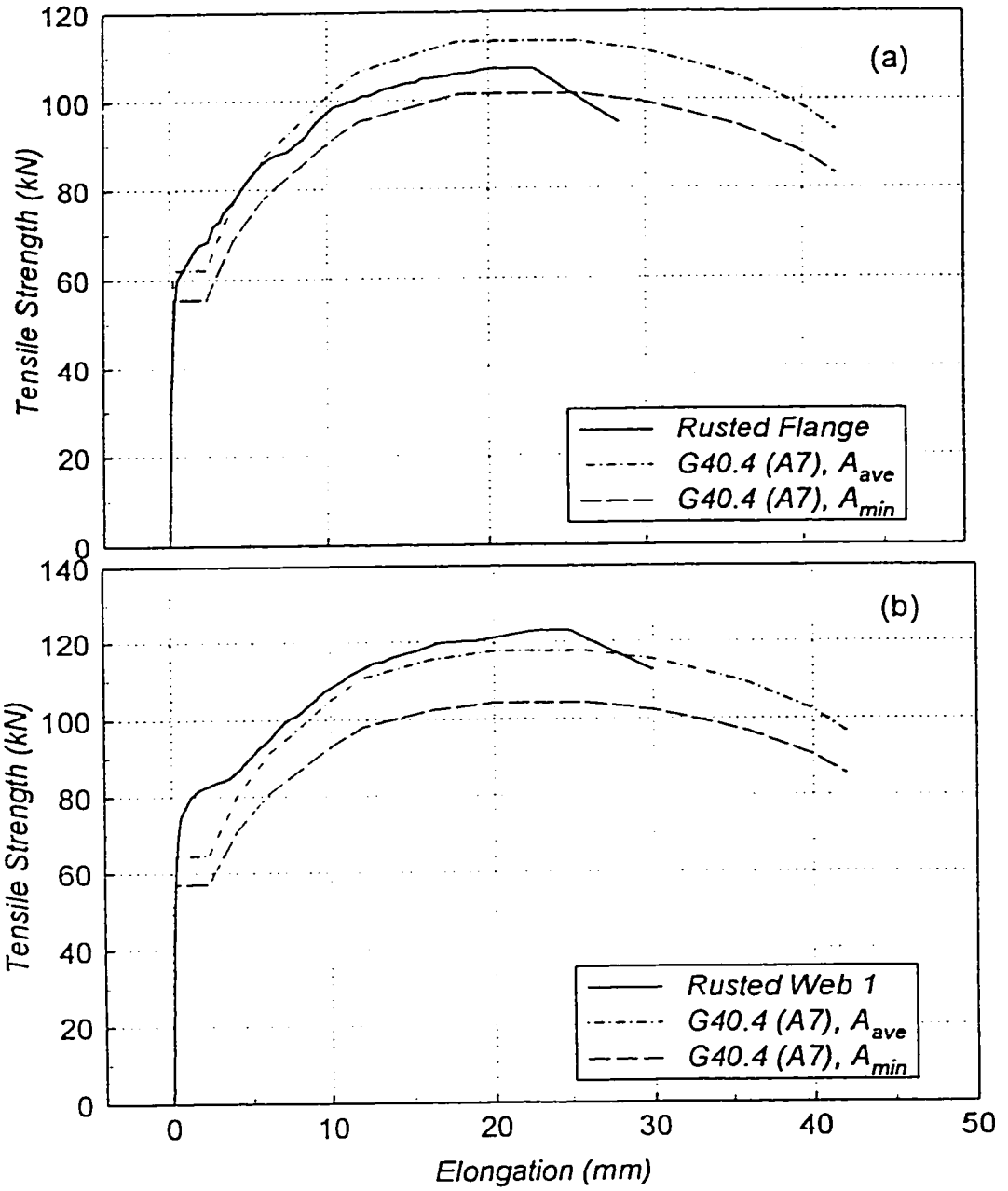

Fig. 8.8. Experimentally obtained tensile strength of rusted coupons compared to their theoretical strength normalized using average and minimum thicknesses at the critical cross-section: (a) flange coupon; (b)web 1 coupon.

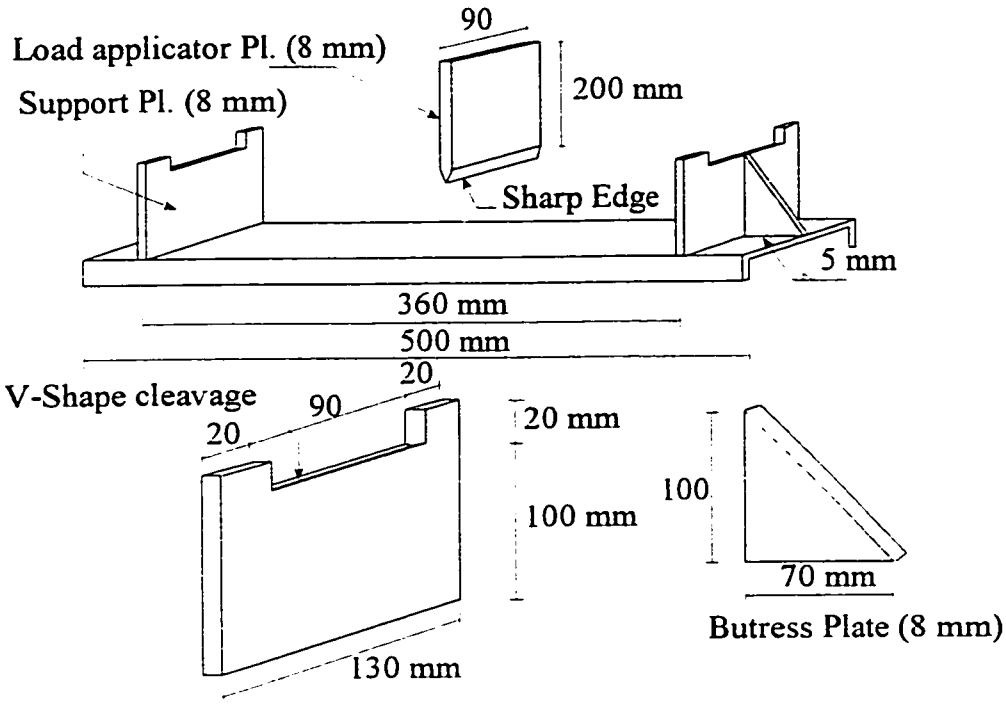

Fig. 8.9. Test set-up for 3-point bending test.

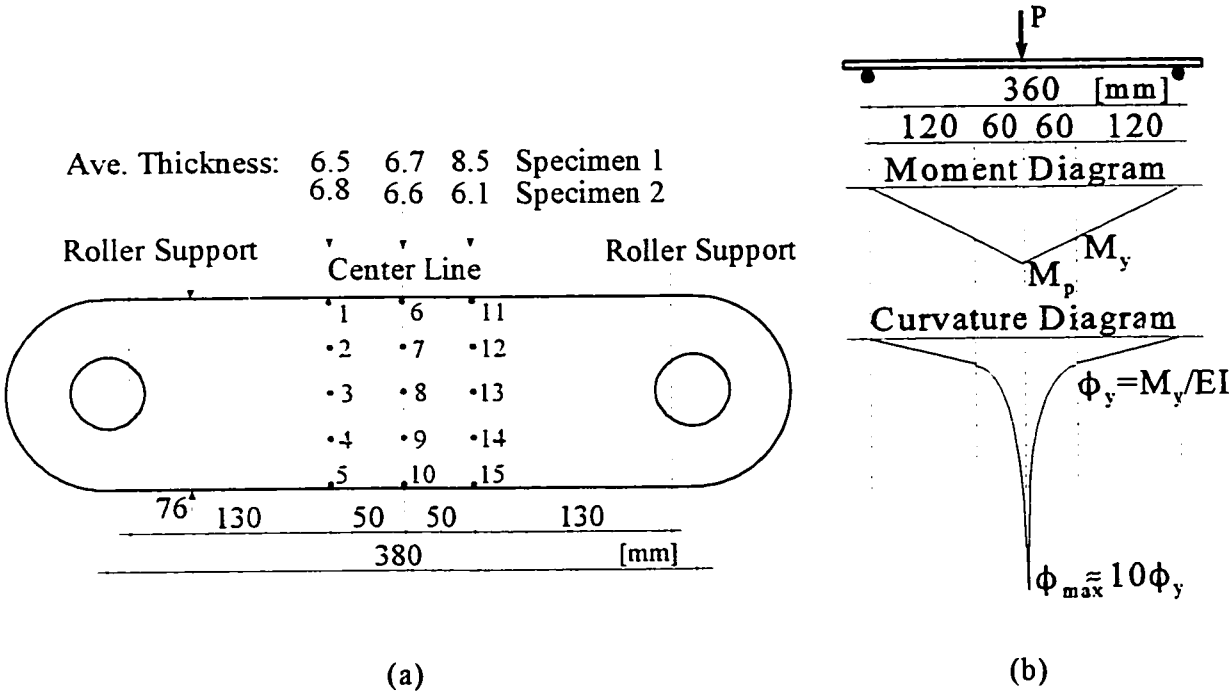

Fig. 8.10. Lacing plate specimen subjected to cyclic loading: (a) location of measurements; (b) loading and corresponding moment and curvature diagrams.

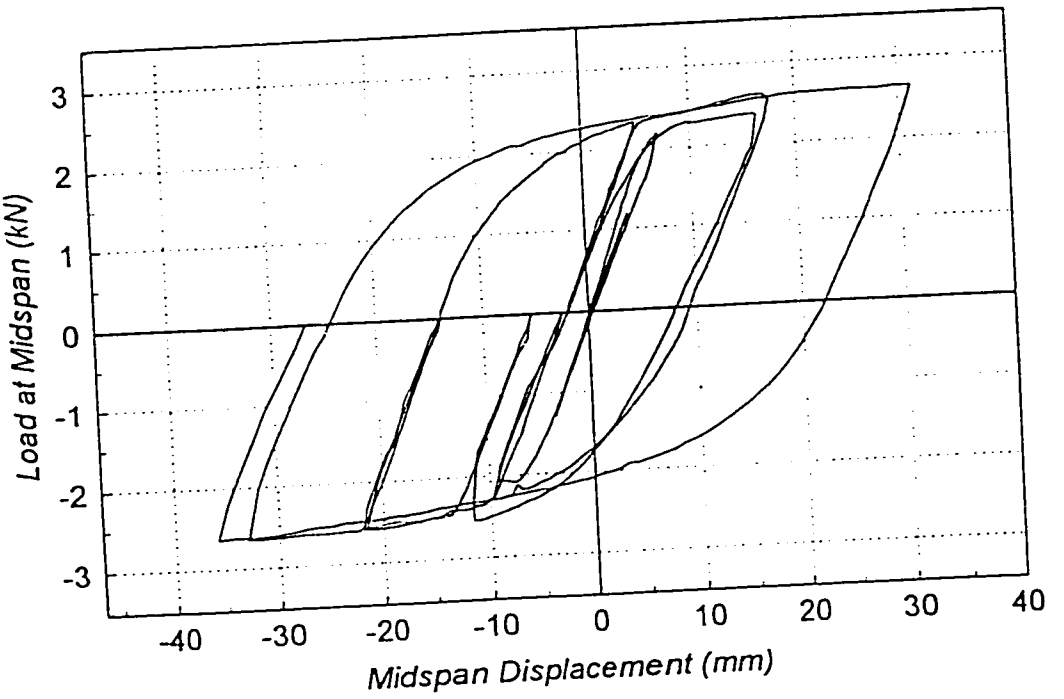

Fig. 8.11. Cyclic load-displacement relationship for plate specimen 1, first 5 cycles.

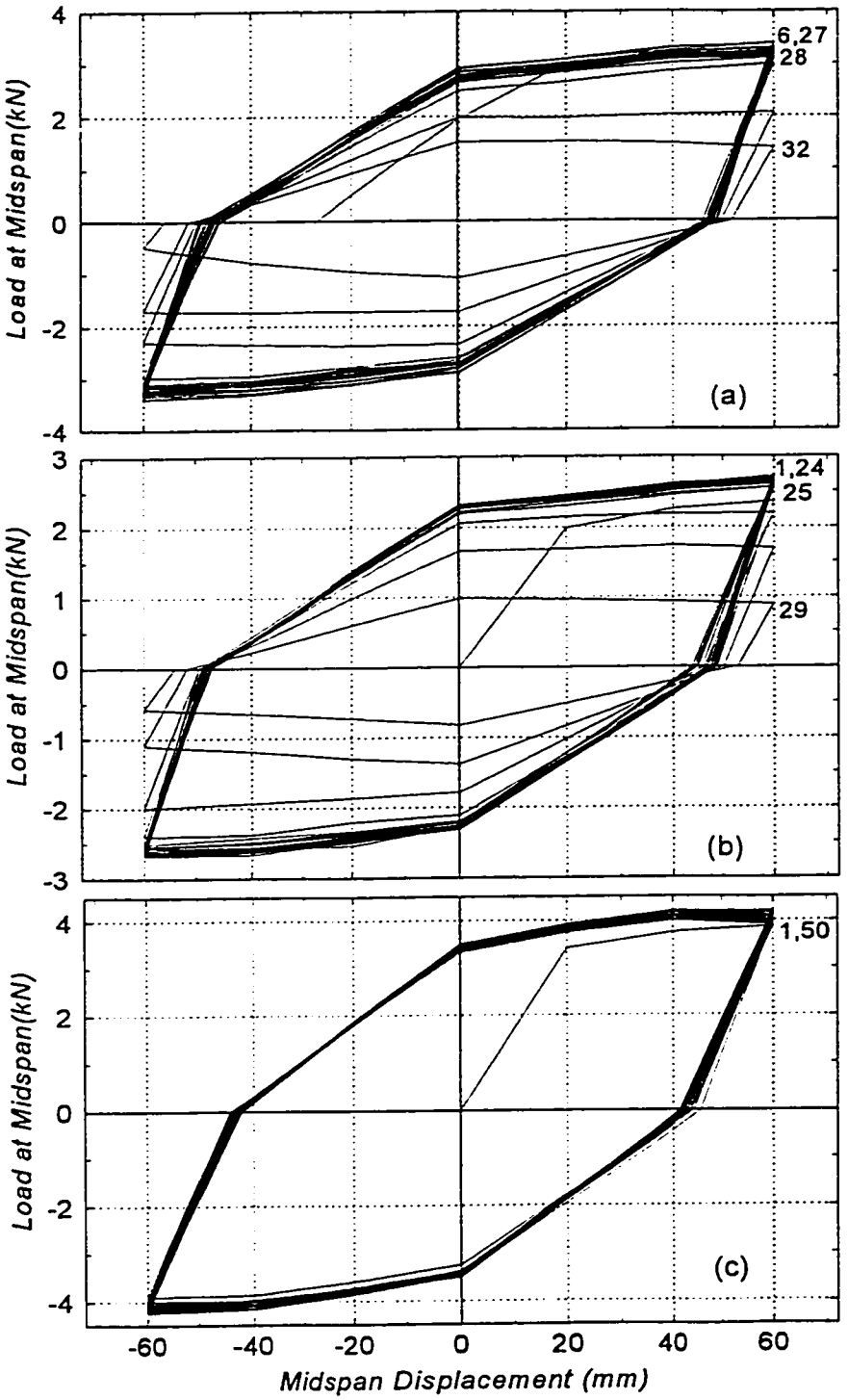

Fig. 8.12. Simplified hysteretic behavior of the plate specimens: (a) rusted specimen 1, for cycles 6 to failure; (b) rusted specimen 2, all cycles; (c) unrusted specimen, all cycles.

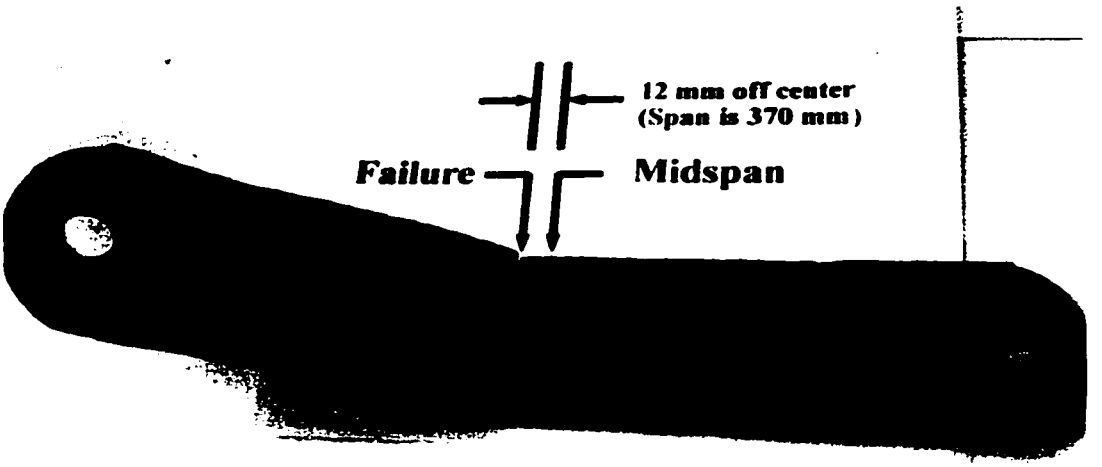

(a)

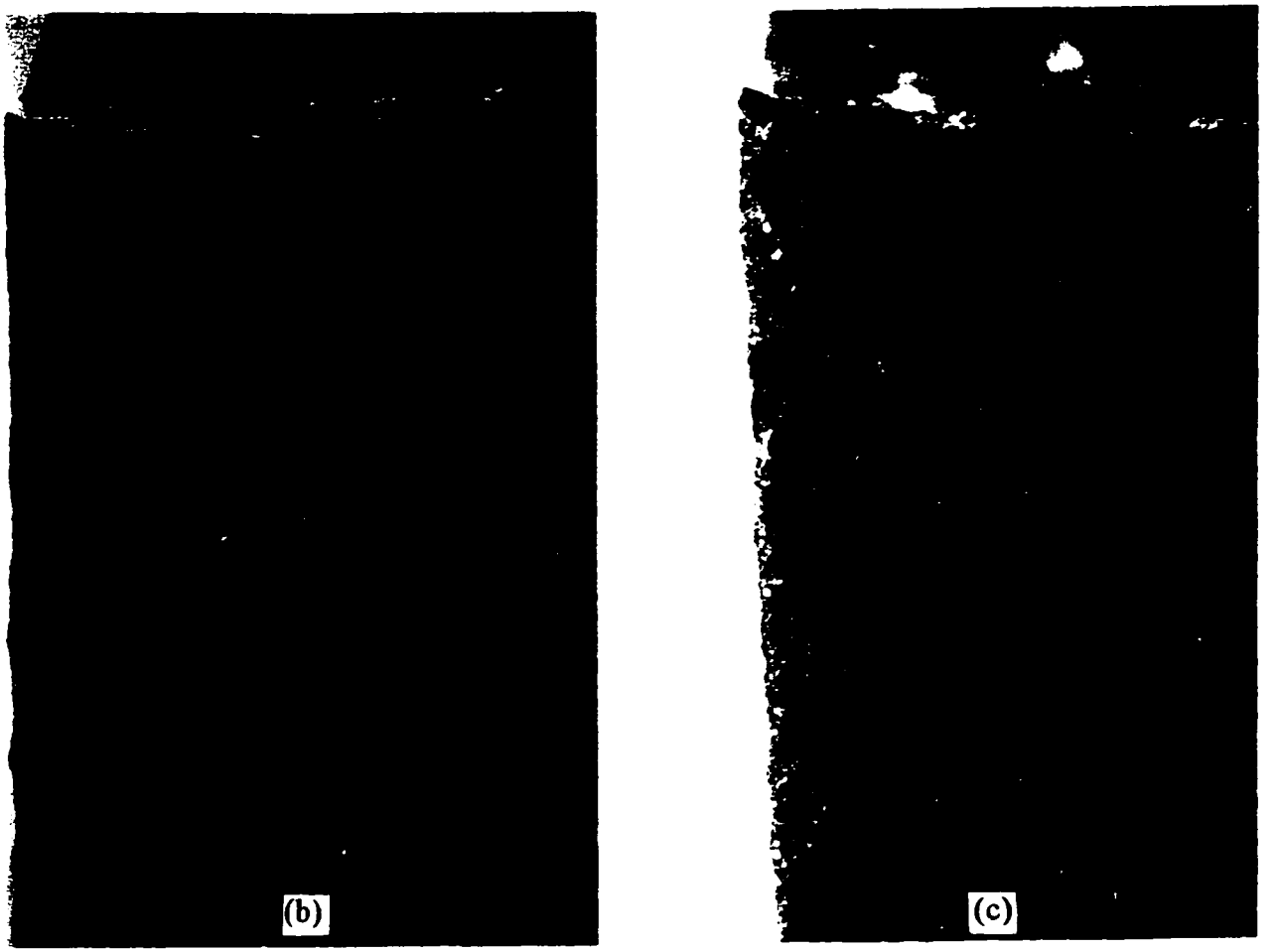

Fig. 8.13. Final state of the plate specimens and cross-width cracks: (a) global view of specimen 1 after the test; (b) cross-width cracking for specimen 1; (c) cross-width cracking for specimen 2.

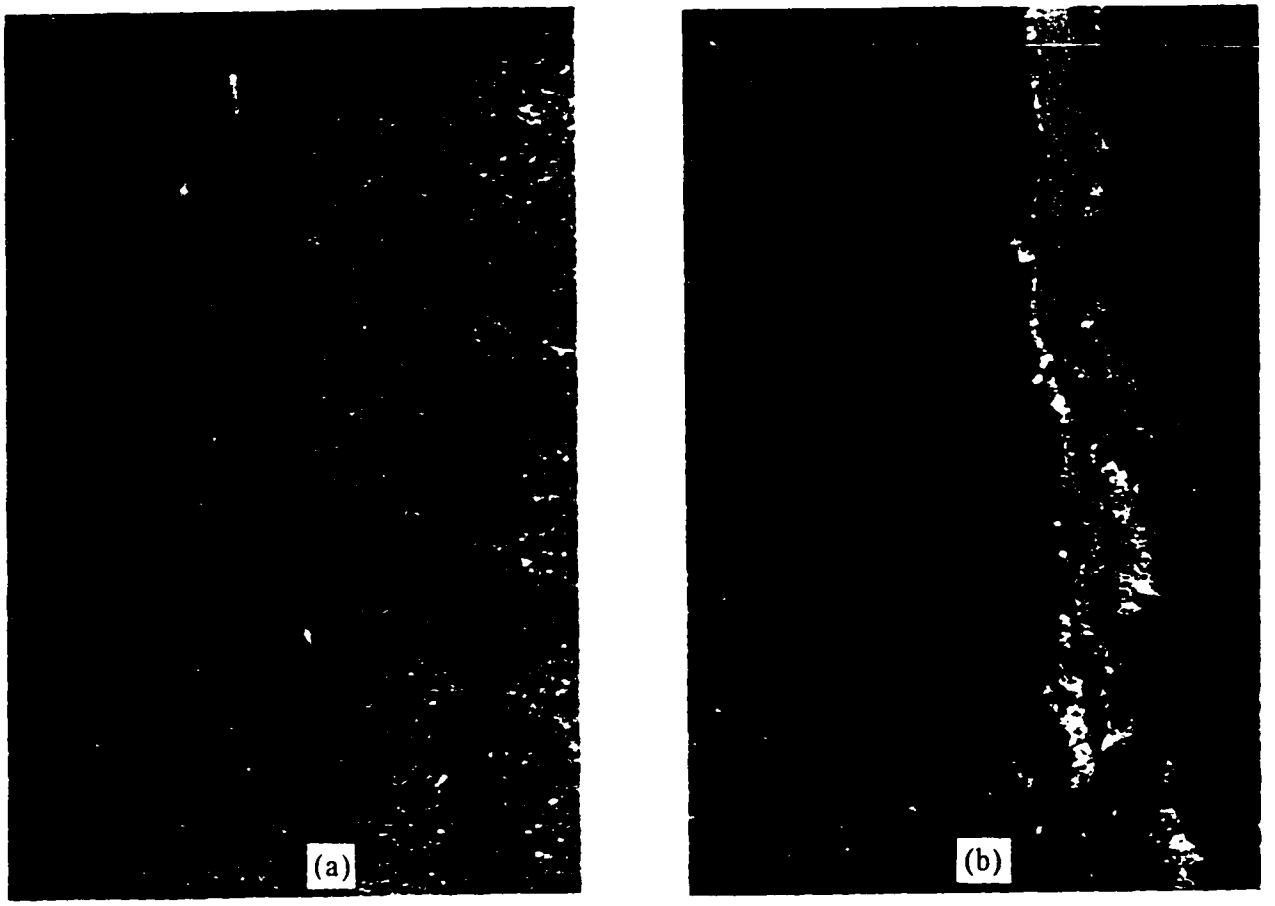

Fig. 8.14. Close-up view of surface texture for three-point bending specimens: (a) first cracking side of specimen 1; (b) last ruptured side of specimen 2.

Fig. 8.15. Close-up view of other cracks of finite length parallel to the failure surface.

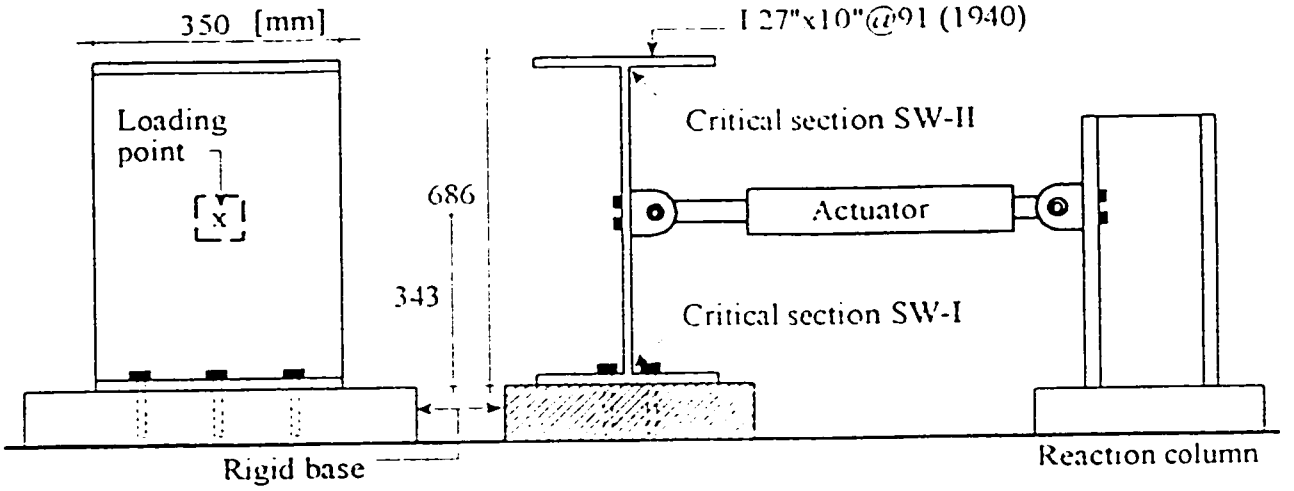

(a)

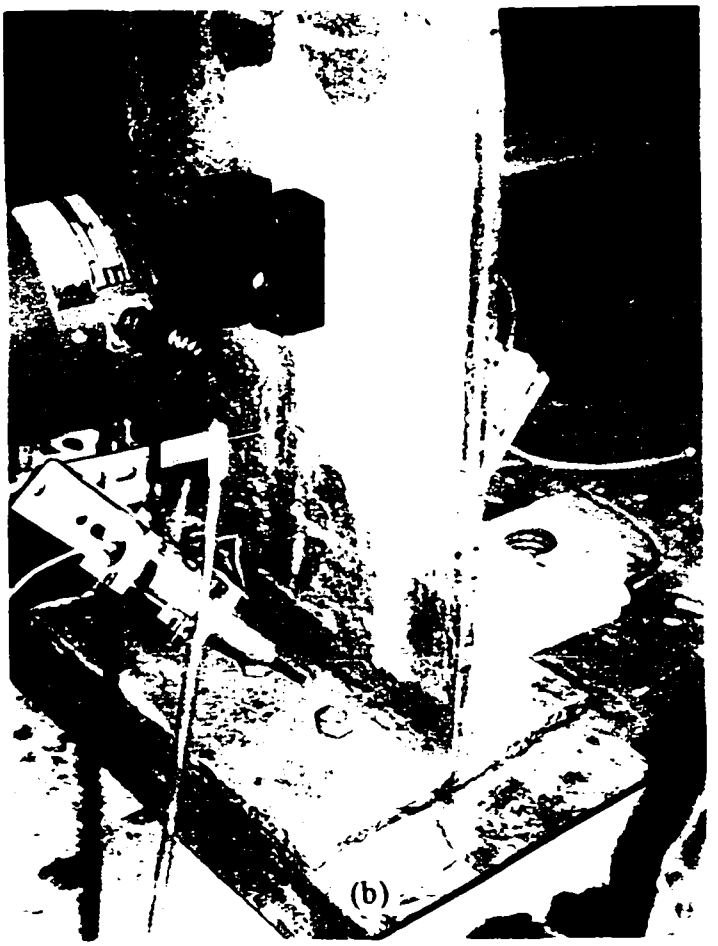

Fig. 8.16. Test set-up for weak-axis bending of floorbeam's rusted web: (a) schematic view showing the set-up including the reaction column; (b) Close-up of test set-up and instrumentation.

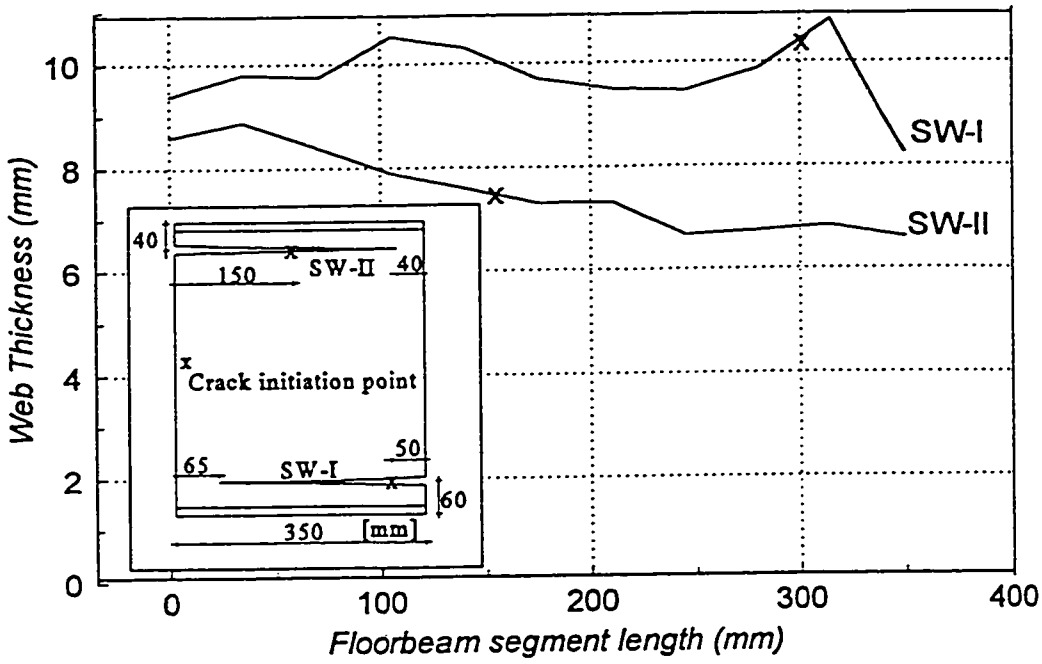

Fig. 8.17. Web thickness in the critical areas where cracking happened for two specimens.

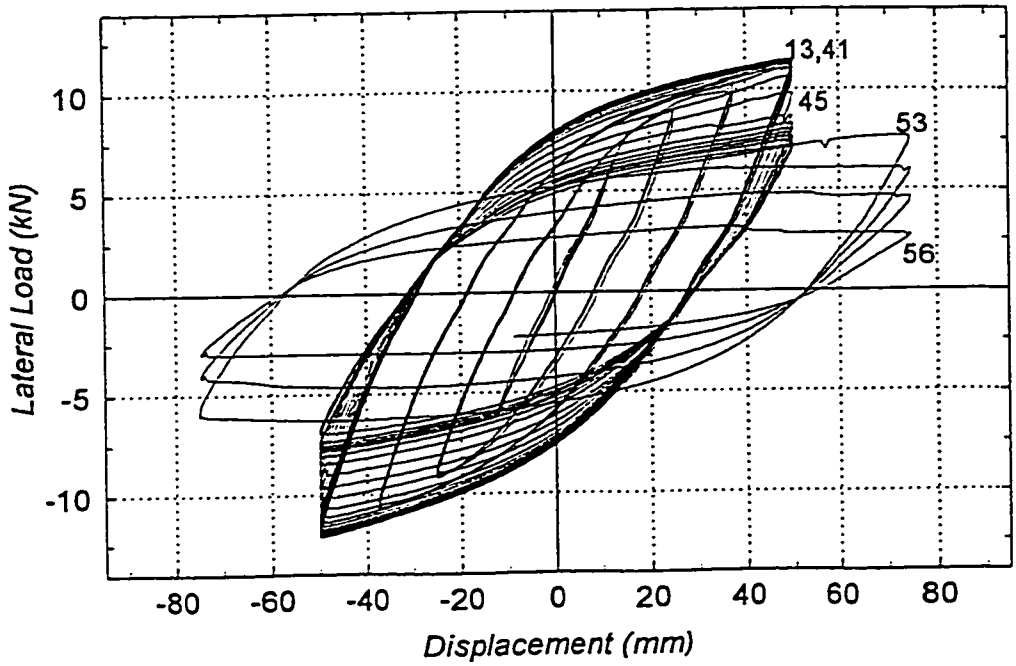

Fig. 8.18. Hysteretic curves for floorbeam web specimen 1 (SW-I).

Fig. 8.19. Specimen SW-I after testing (upside down), showing final crack length and opening.

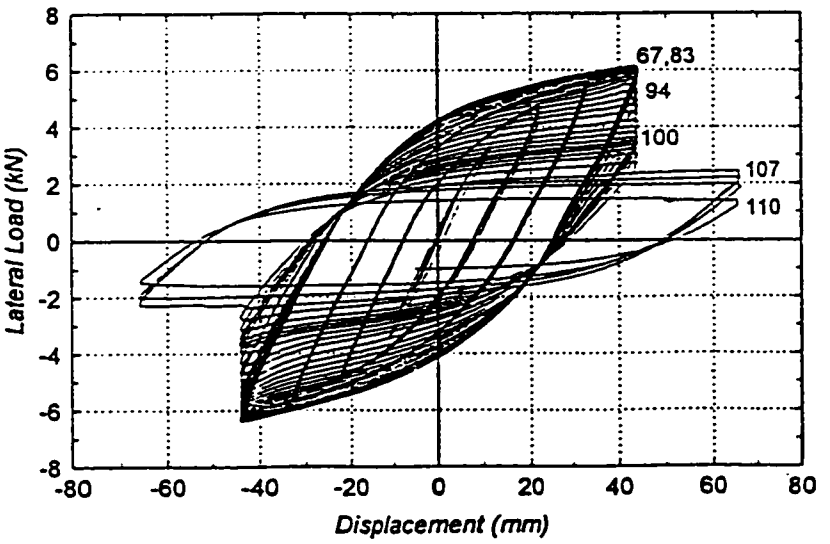

Fig. 8.20. Hysteretic load-displacement curves for floorbeam web specimen 2 (SW-II).

Fig. 8.21. Progression of cracking in specimen SW-II: (a) early cracking on east face; (b) same on west face; (c) significant crack propagation on west face.

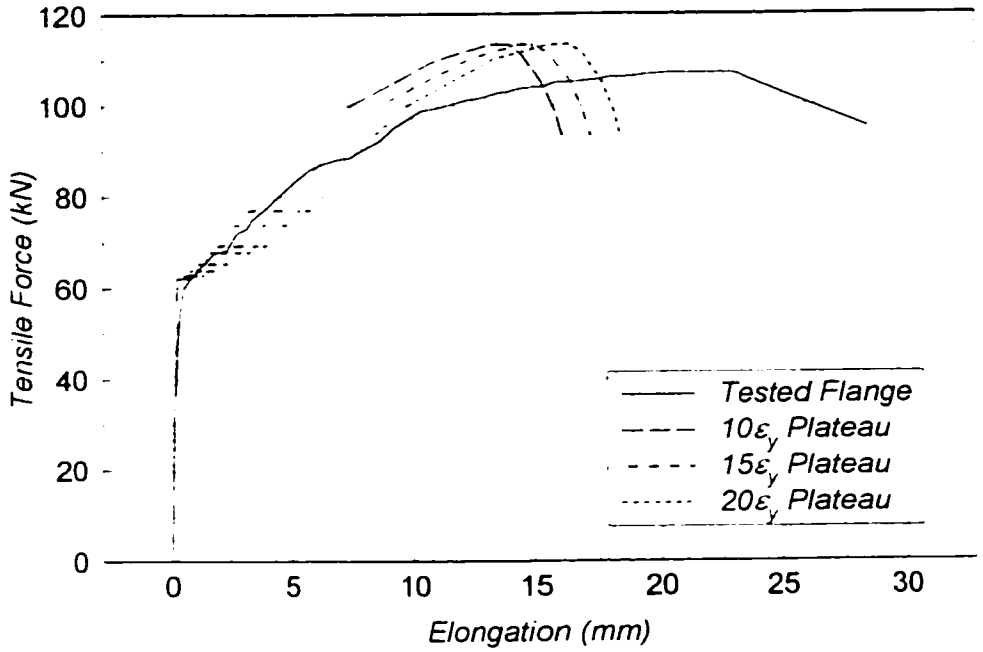

Fig. 8.22. Analytical prediction of monotonic load-elongation curve for flange coupon.

Fig. 8.23. Special set-up to create pure shear test conditions and insertion into an uniaxial testing machine.

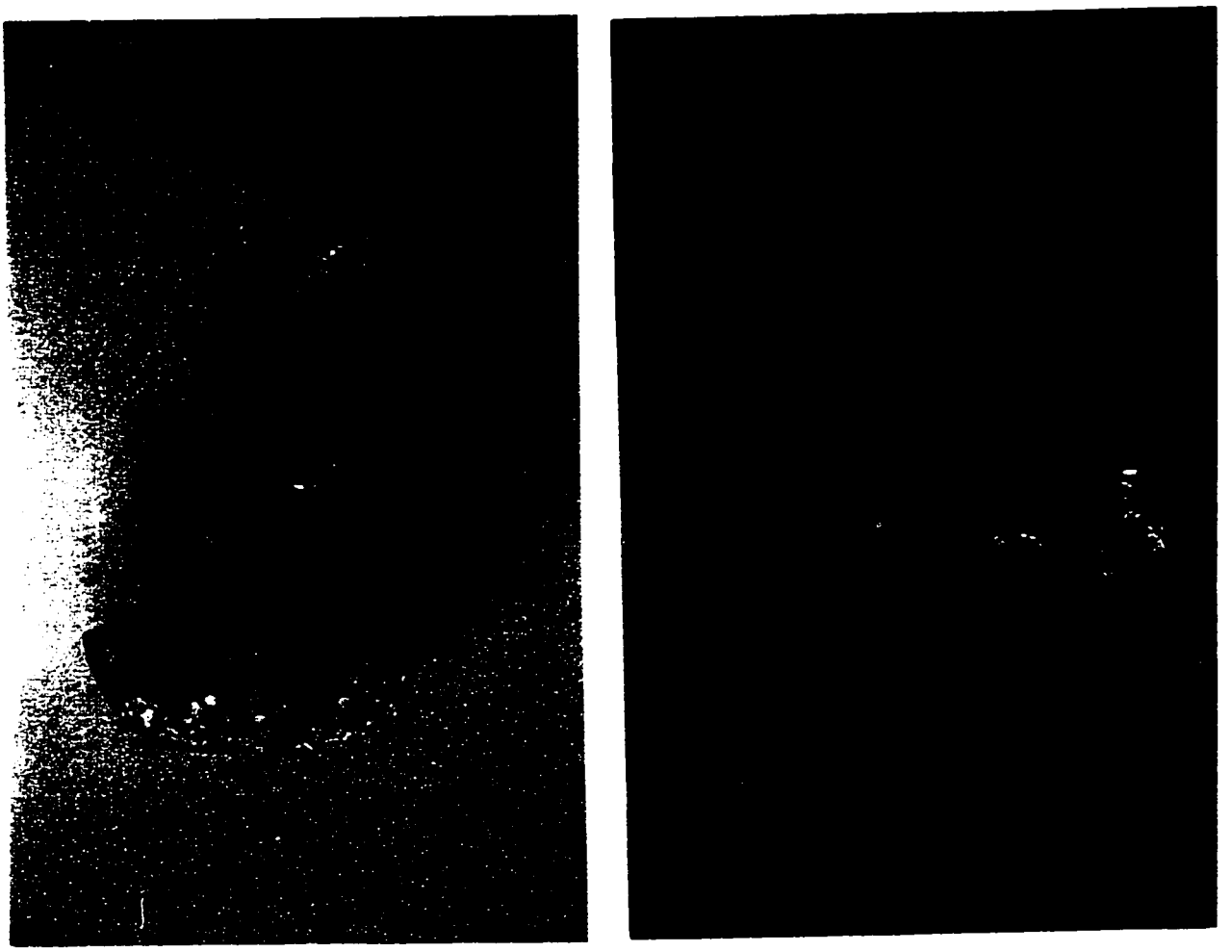

(a) (b)

Fig. 8.24. Rivet tested in shear: (a) deformed shape of rivet at rupture (broken pieces put back together for this photo); (b) view of rupture surface and minor corrosion on shank of rivet.

APPENDIX A

PLASTIC FAILURE MECHANISMS — FOR STEEL BRIDGES WITHOUT DIAPHRAGM

A few possible yielding failure mechanisms are studied here for slab-on-girder bridges without diaphragm to analytically evaluate their ultimate strength. Nonlinear inelastic analyses by ADINA were used in Chapter 4 to investigate the seismic performance of these bridges. Stress vectors in the girder web obtained by ADINA for a 40 m span bridge (Fig. 3.15) indicate that yield lines form to some extent in the web at the top and bottom of the steel girders, while the web at mid-height remains elastic. Also as mentioned earlier, stress contours in the girders of the same bridge in the elastic range by SAP90 analysis, shown in Fig. 3.16, compare fairly with the stress vectors from ADINA results.

Since the bridge supprot reactions can be cosidered as point lateral loads applied to the corners of steel girders, the first plastic failure mechanism, as shown in Fig. A.1, is simply considered with a yield line of limited length in the web near bottom flange of each girder and an inclined yield line in the web. Following yield line theory, two plastic hinges are assumed in the girder bottom flange and at the top and bottom of girder web (for that limited length). Since the bridge, in such a case without any diaphragm or stiffeners, laterally moves as a rigid body along its span length, a uniform lateral load, w_p, can be applied to the concrete deck to reach the failure mechanism. Imposing a drift of Δ_s to the bridge slab deck, the external and internal work

expressions for one steel girder, $W_{external}$ and $W_{internal}$ respectively, corresponding to the plastic failure mechanism can be written as:

$$W_{external} = \frac{w_p L}{2} \Delta_s \tag{A.1}$$

$$W_{internal} = M_{p,w} x \theta_p + M_{p,w} (x \theta_p + d_w \alpha_p) + 2M_{pf} \alpha_p \tag{A.2}$$

where $M_{p,w}$ and M_{pf} are respectively the plastic moment capacities of the web and bottom flange (about strong its axis) of the bridge girders, θ_p and α_p are the plastic rotations in the girder web and bottom flange respectively, x is the length of horizontal yield line (Fig. A.1) and d_w is the height of girder web between the flanges. On the other hand,

$$\theta_p = \frac{\Delta_s}{d_w} \quad , \quad \alpha_p = \frac{\Delta_s}{x} \tag{A.3}$$

Substituting the above θ_p and α_p into Eq. A.2 and equating the external and internal work expressions, w_p for one girder can be obtained from:

$$w_p = \frac{2M_{p,w}}{L} \left(\frac{2x}{d_w} + \frac{d_w}{x} \right) + \frac{4Mp,f}{xL} \tag{A.4}$$

To find the lowest upper bound, the derivative of w_p with respect to x should be zero, or:

$$\frac{\partial w_p}{\partial x} = 0 \tag{A.5}$$

This would lead to a solution for the length of horizontal yield line considered for the plastic failure mechanism:

$$x = d_w \sqrt{\frac{M_{pf}}{d_w M_{p,w}} + 0.5} \tag{A.6}$$

The ultimate lateral load corresponding to this failure mechanism can be obtained by substituting the above yield line length in Eq. A.4. For a 40 m span bridge (with geometry characteristics given in Table 3.1), $M_{p,w}$ and M_{pf} can be obtained as 19.2 kN-m per unit length and 360 kN-m, respectively, giving a value of 4.75 m for x and finally 15.6 kN/m for the uniform lateral load, w_p, applied to one girder. This would then translate to an ultimate lateral load of about 2500 kN for the entire bridge with four steel girders.

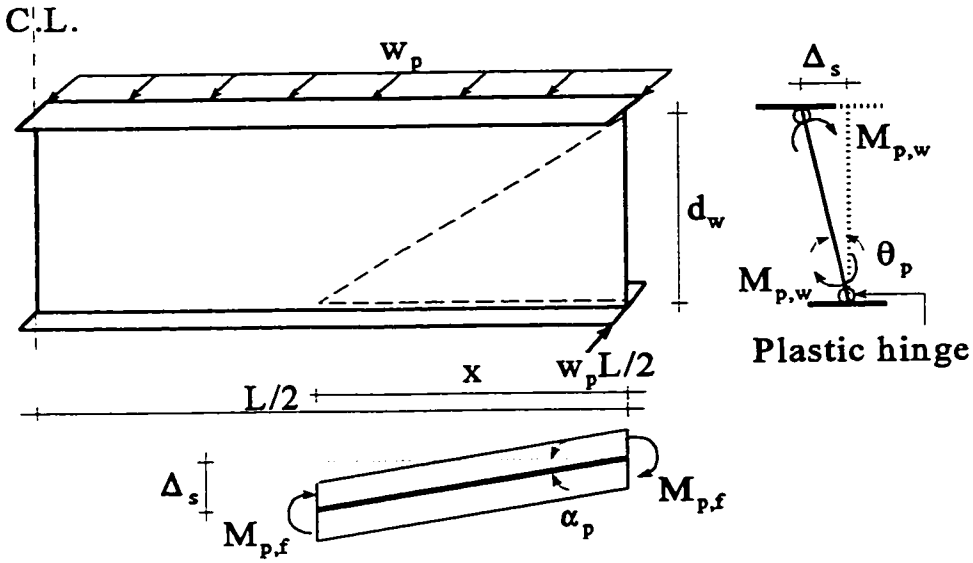

Fig. A.1. Main yield line pattern for slab-on-girder bridges

If the bottom flange of girder rotates during lateral movement of the deck, a plastic hinge against the weak axis of bottom flange should be considered at the interior end of the horizontal yield line. In other words, the plastic moment capacity of the bottom flange, m_{pf}, should be used in Eq. A.2 for that location, thus in such a case, w_p can be obtained from:

$$w_p = \frac{2M_{p,w}}{L}\left(\frac{2x}{d_w} + \frac{d_w}{x}\right) + \frac{2M_{pf} + 2m_{pf}}{xL} \qquad \text{(A.7)}$$

Similarly, the length of horizontal yield line in this case is:

$$x = d_w \sqrt{\frac{M_{pf} + m_{pf}}{2 d_w M_{p,w}}} + 0.5 \qquad \text{(A.8)}$$

For example, following this less conservative failure mechanism, the yield line length and ultimate lateral load per girder for the same 40 m span bridge with m_{pf} of 27 kN-m can be calculated as 3.5 m and 11.6 kN/m respectively, corresponding to a total lateral load of 1855 kN applied to the entire bridge.

Similar results can be obtained for other yield line mechanisms (e.g. assuming a horizontal yield line in the web at its connection to the top flange as shown in Fig. A.2). Although these proposed simplified models offer capacity results close to those obtained by the ADINA inelastic push-over analyses presented in Chapter 4, the yield line patterns obtained by ADINA differs from those expected from the yield lines assumed in the plastic collapse mechanisms. Therefore, more complex plastic failure mechanisms are desired to predict the structural collapse of these bridges more reliably.

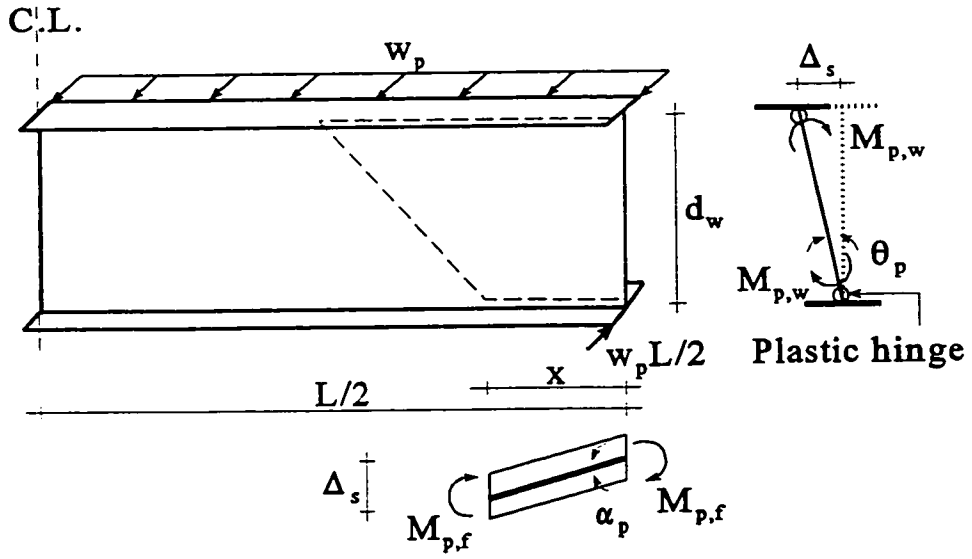

Fig. A.2. Another yield line pattern for slab-on-girder bridges

APPENDIX B

DESIGN DETAILS OF TEST FOUNDATION

The design and construction of the foundation was briefly explained in Chapter 5. However, since this foundation is supposed to be used for other probable experiments, some details are provided in the following.

A large rectangular shape (2.9 m x 1.7 m) with a depth of 0.45 m was considered for the test foundation, pretensioned to the strong floor of the structural laboratory by six 1.8 m long bolts of 64 mm, to provide support for the two stub-girders of the specimens. For space constraints in the laboratory, the foundation's west end was designed to behave as a cantilever under uplifting forces from the west girder. Lateral and gravity loads applied to the specimens were considered as shown in Fig. B.1. A safety factor of 2 was used to keep the foundation in the elastic range.

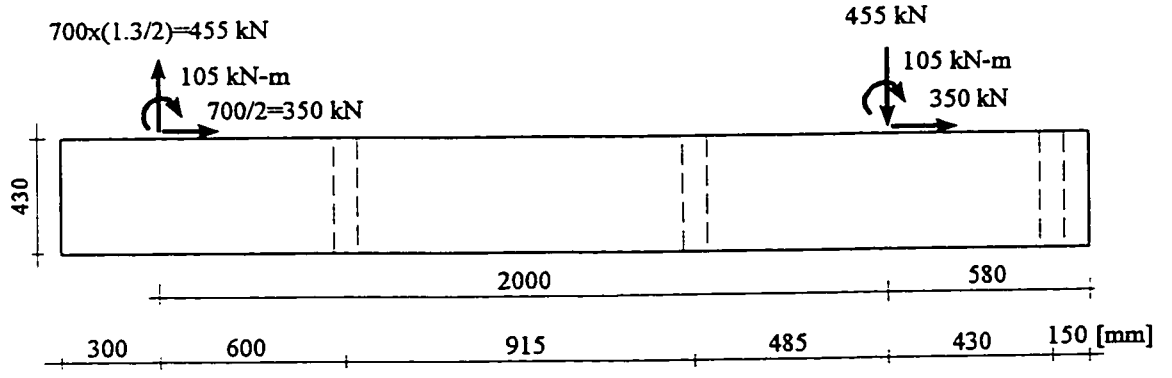

Fig. B.1. Critical loading for the foundation design (cantilever part)

The middle longitudinal strip of the reinforced concrete foundation with an effective width of 0.7 m was conservatively designed for shear and flexure due to uplift forces of the vertical actuators. Two 1100x580x50 mm base plates were designed as support for vertical actuators. C380x50 sections sitting on these plates and spanning across the width of the foundation were designed to transfer the vertical actuator uplift forces to the foundation in addition to act as formwork. The potential flexural contribution of side channels was conservatively ignored. Refer to Figs. 5.19 and 5.20 for reinfocing details of the foundation.

In addition to six ABS tubes with inside diameter of 76 mm (3") to allow the connection of the base to the laboratory strong floor using six 64 mm diameter strong bolts, sixteen 40 mm diameter ABS tubes were placed in the base, as shown in Fig. B.2, to provide a grid for 1.5" diameter anchor bolts for future experiments. Small wooden pieces were put at the bottom of these tubes to provide a recess to accommodate bolt heads.

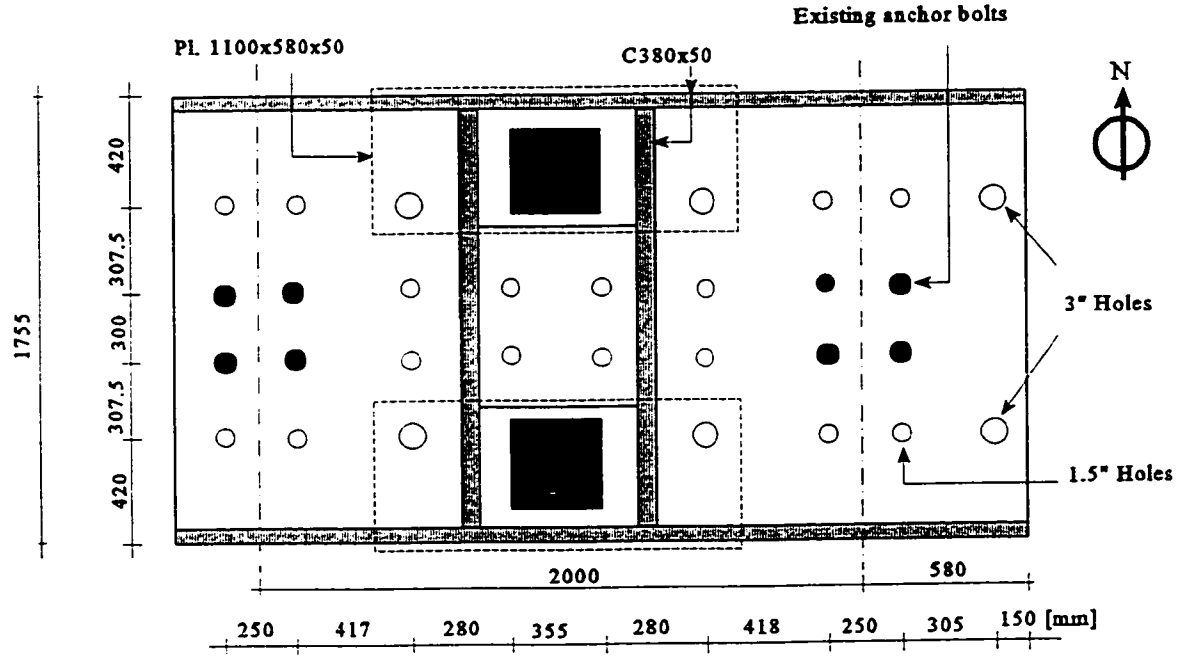

Fig. B.2. Location of different holes provided for the test foundation

APPENDIX C

TO SCALE DRAWING DETAILS OF DUCTILE SYSTEMS

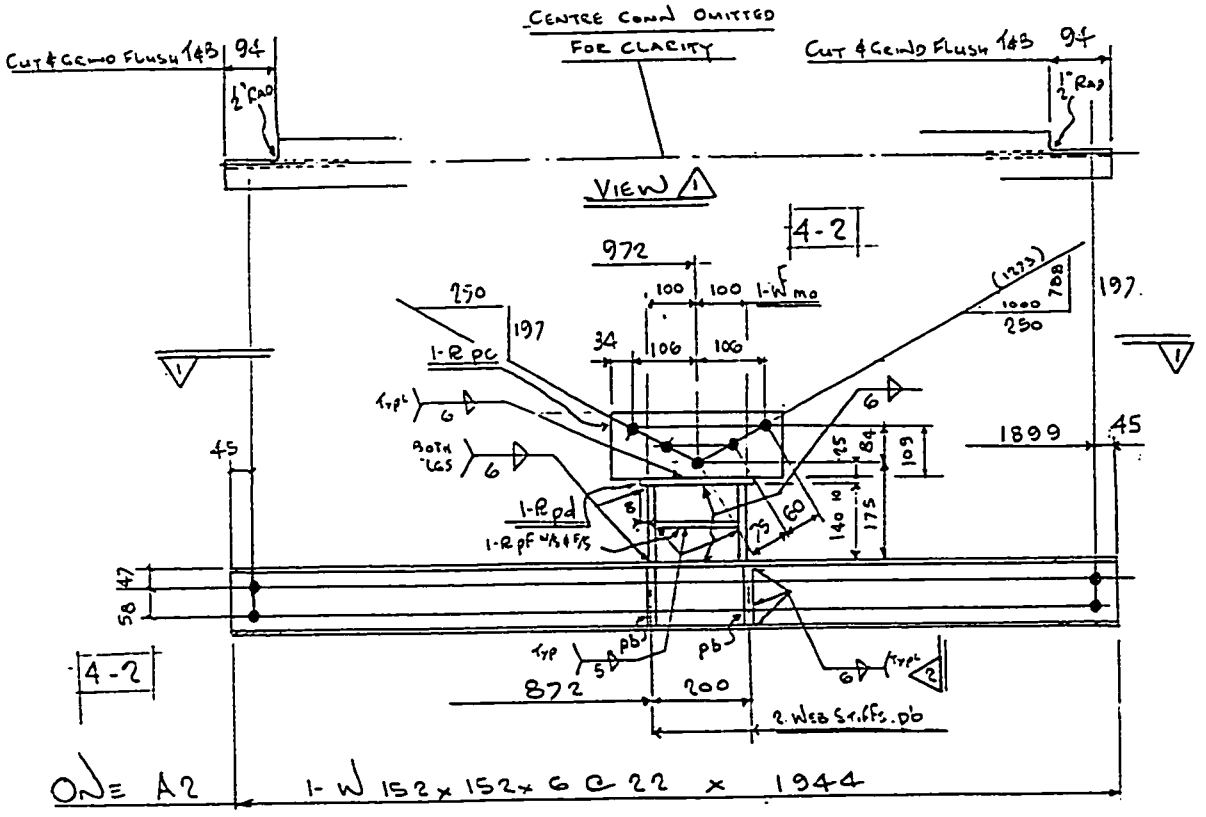

Fig. C.1. To scale drawing of SPS - W section

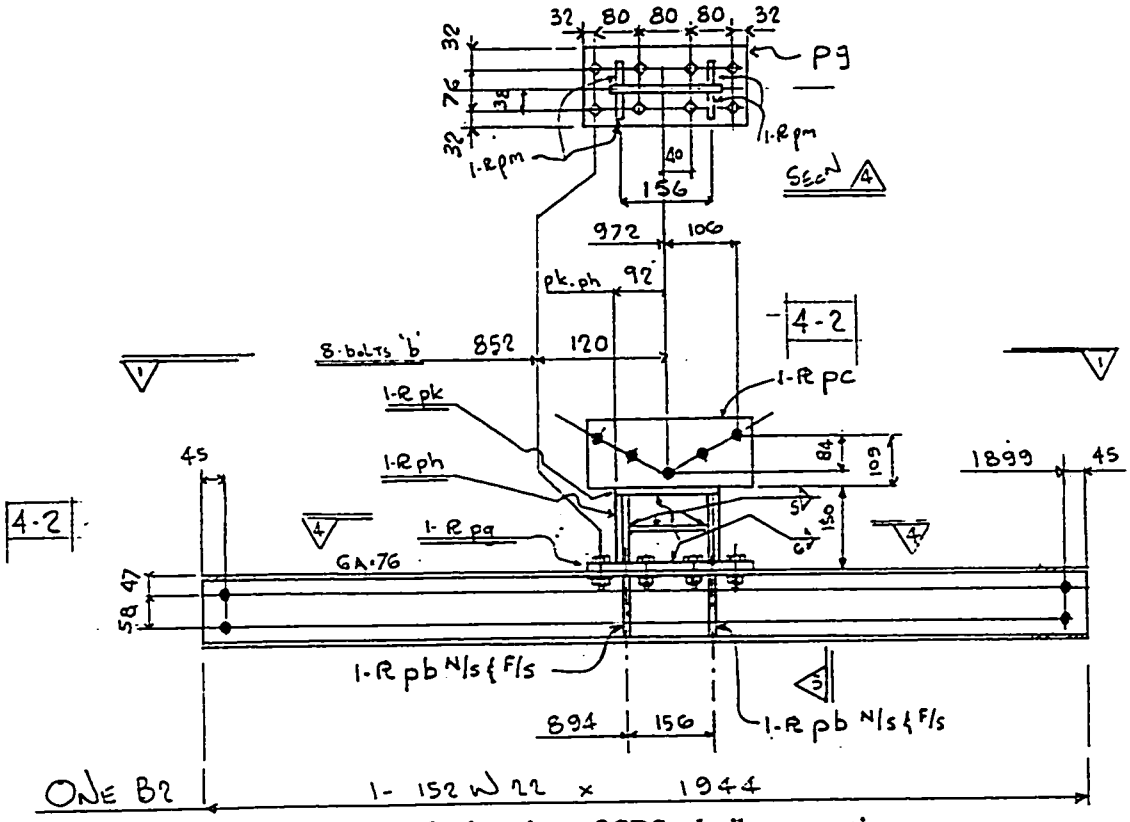

Fig. C.2. To scale drawing of SPS - built-up section

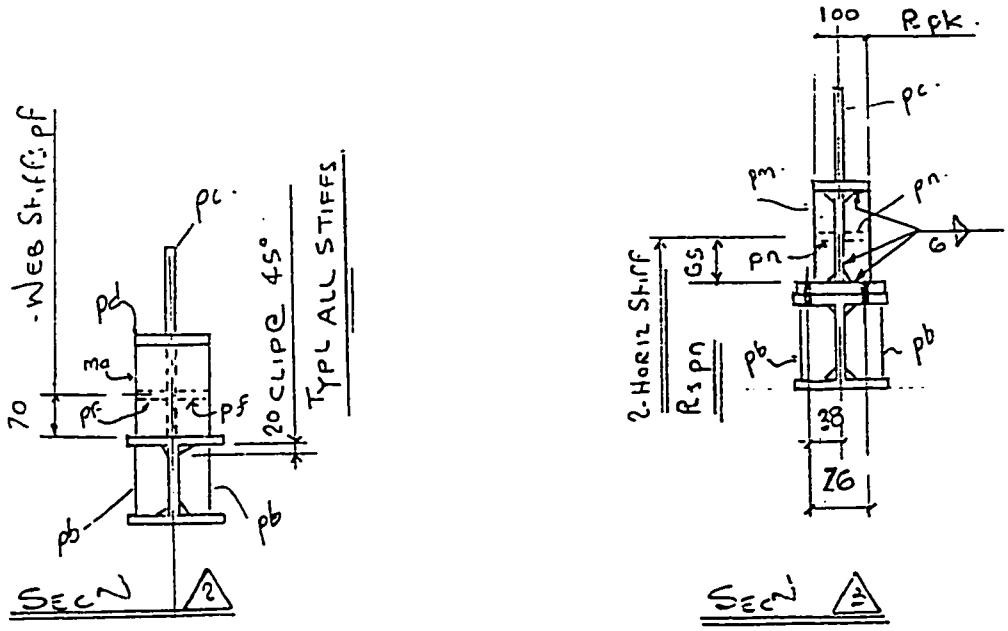

Fig. C.3. Section views of the SPS devices

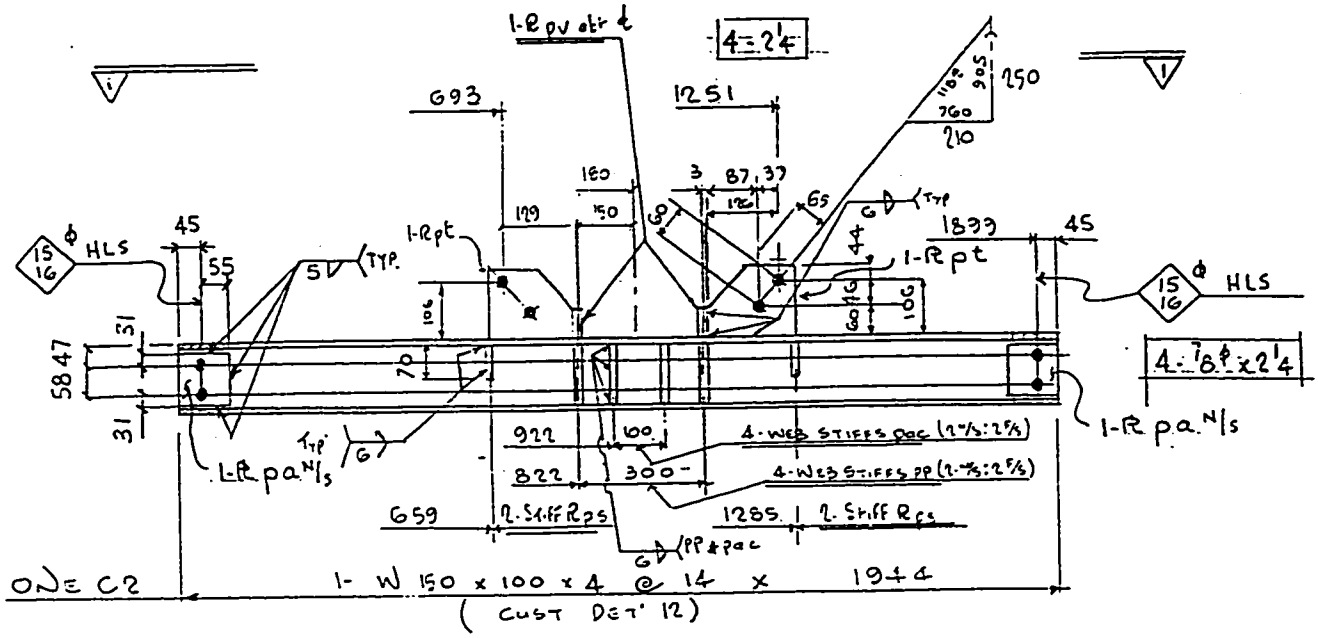

Fig. C.4. To scale drawing of EBF system

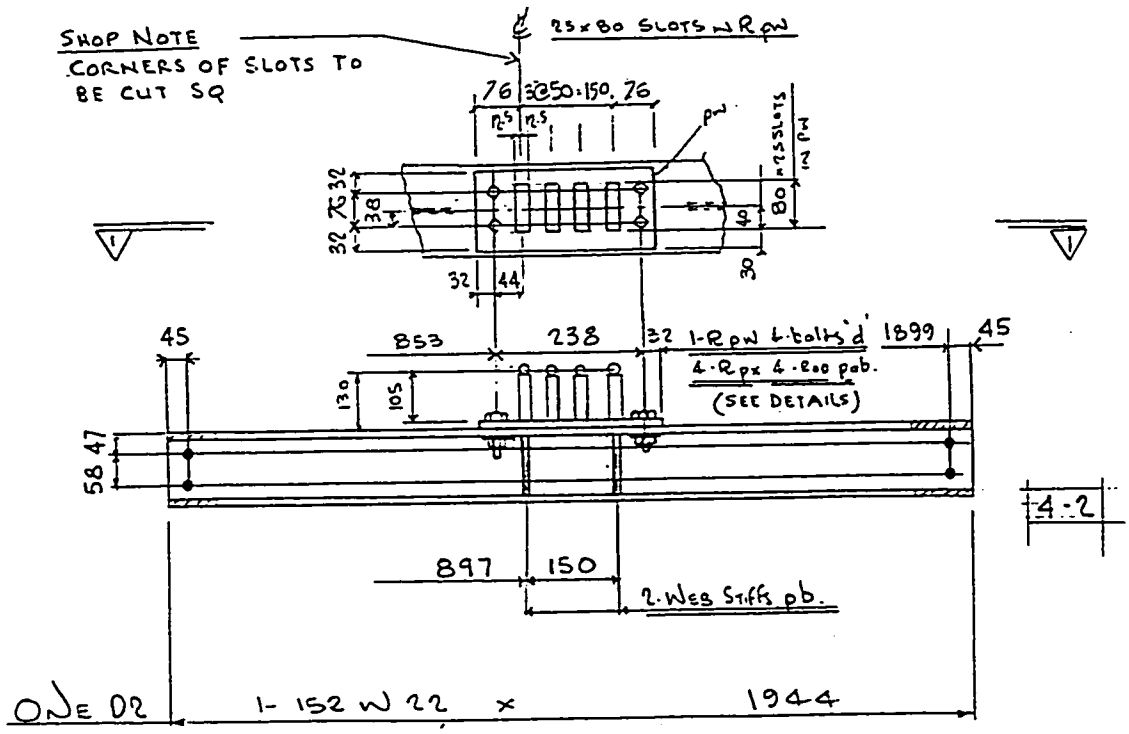

Fig. C.5. To scale drawing of TADAS device

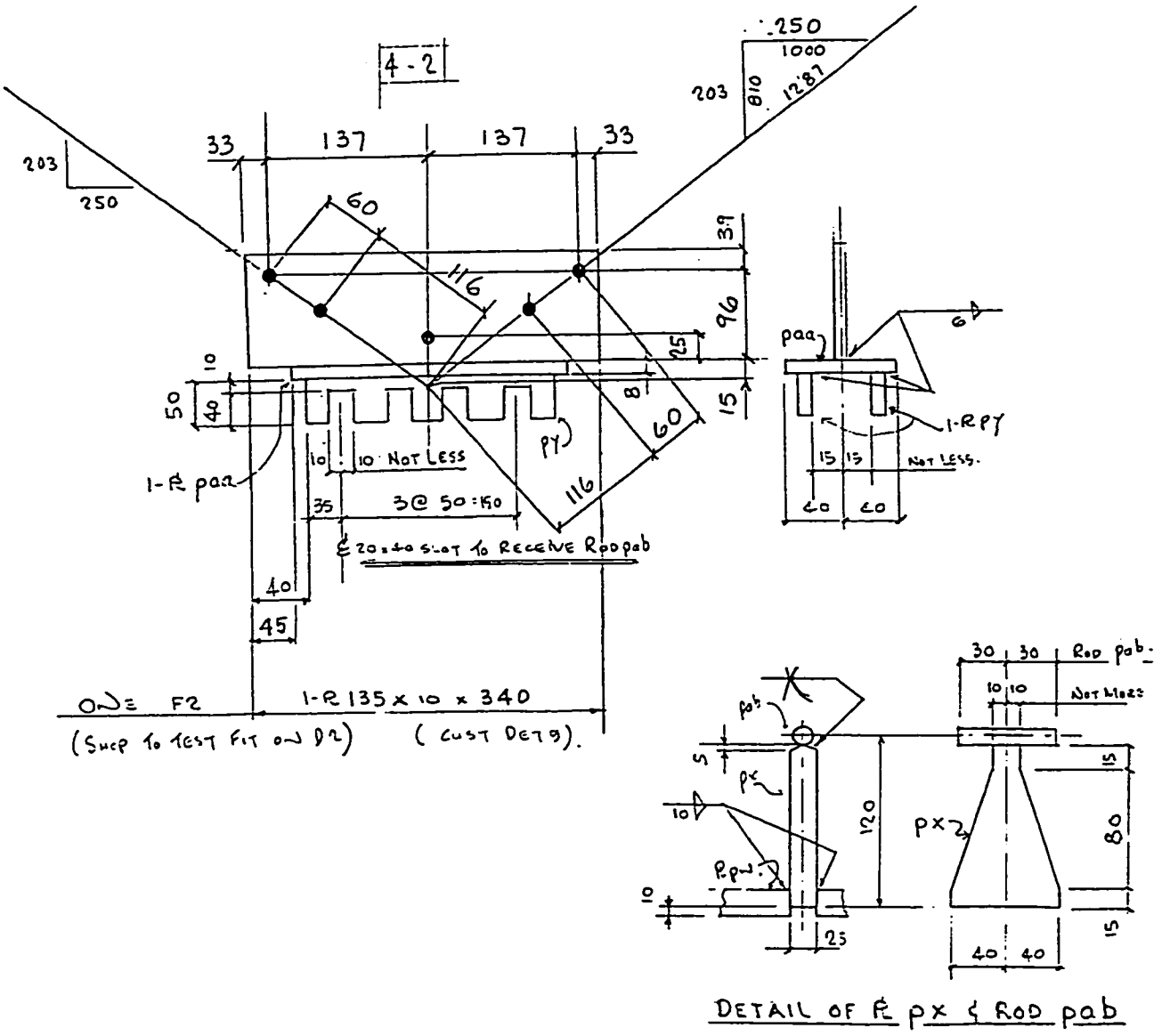

Fig. C.6. Details of TADAS Device

BILL OF MATERIAL

ALL CATEGORY NO. _____ U/N

MATERIAL SPEC. G40 21 300W U/N

CONTRACT NO. 96-2848

DRAWING NO. 2

NO. OF PCS	MARK	SIZE	SHAPE	WT. LB/FT. MASS KG/M	LENGTH FT.	LENGTH IN.	LENGTH MM 000	LENGTH MM 000	WT LB MASS KG	ADV BILL ITEM NO.	CATEGORY	BLOCK QTY/BLK	REMARKS			
1	A2	150 W				1	9	144	52			1				1
1		150	W	22		1	9	144					SUB W6x15			2
																3
4	pb	50 x 8	R					138					SUB 5/16			4
1	pc	142 x 10	R					280					SUB 3/8			5
1	pd	100 x 10	R					216					SUB 3/8			6
2	pf	45 x 6	R					130					SUB 1/4			7
1	ma	200 x 100 x 5	W	15				140					A36. SUB W15x10			8
ONE	A2X	200	W	15				500	7.50			1	PLAIN MATL CUT FROM SAME	STOCK	Asma	9
																10
1	B2	150 W				1	9	144	56			1				11
1		150	W	22		1	9	144					SUB W6x15			12
																13
4	pb		R													14
1	pc		R													15
1	pa	140 x 10	R					304					SUB 3/8			16
1	pn	130 x 5	R					184					SUB 5/16			17
1	pk	100 x 10	R					184					SUB 3/8			18
4	pm	49 x 8	R					130					SUB 5/16			19
2	pn	45 x 6	R					148					SUB 1/4			20
8	b	3/8 ABCS	Bolt					132								21
ONE	B2X	100 x 5	PL					400	1.56			1	PLAIN MATL CUT FROM SAME	STOCK	Asph	22
																23
1	C2	150W				1	9	144	56			1				24
1		150	W	14		1	9	144					A36 SUB 6W9			25
2	pa	100 x 6	R					120					SUB 1/4			26
4	pf	45 x 8	R					138					SUB 5/16			27
1	ps	45 x 8	R					70					SUB 5/16			28
2	pt	150 x 10	R					160					SUB 3/8			29
2	pv	60 x 6	R					60					SUB 1/4			30
4	pac	45 x 6	R					138					SUB 1/4			31
																32
1	D2	150 W				1	9	144	62			1				33
1		150	W	22		1	9	144					SUB W6x15			34

Table C.1. Bill of material provided by fabrication shop

4	pb													35
1	ow	140 x 25	R			302					SUS 1"			36
														37
4	d	¾ ϕ A325	BOLT			22								38
4	pb	20 ϕ				60								39
4	px	80 x 25	R			110					{ SHAPE & RECP.			40
											{ SUB 1			41
														42
1	F2	BRKT					58			1				43
1		135 x 10	R			340					SUB 3B			44
2	PY	50 x 10	R			220					SUB 3B			45
1	pao	80 x 8	R			250					SUB 5B			46
														47
		G T			14	000	5							48
		5 T			1	400	1							49
		10 T			1	300	1							50
		⊣				80	1							51
		8 ⊼				720	1	4						52

WT/MASS OF PAINT & / OR GALVANIZING

TOTAL WEIGHT / MASS (NOT INCLUDING FIELD BOLTS) ____ WT/LB MASS / KG

FOR CALCULATOR USE

WT. REC

110-115

FIELD BOLT SUMMARY (INCH / MM)

QTY	Ø & TYPE	LGTH.	QTY/BLK.		QTY	Ø & TYPE	LGTH	QTY/BLK.	
24	¾ϕ A325	2							
4	¾ϕ A325	2¼							
8	¾ϕ WASH								

TOTAL FIELD BOLT WT/LB MASS KG

HOLES: $13/16$ ϕ U/N

SHOP PAINT: NONE

W

BILL NO: 2a

NOTES: WELD ELECTRODES E480 xx

Δ	DATE	REVISION	X NO.	S. C. NO.
1	APR 11/96	REV TO SUIT APP.	—	—

CANRON INC. EASTERN STRUCTURAL DIVISION TORONTO

Table C.1. Bill of material provided by fabrication shop (Cont'd)

APPENDIX D

ADDITIONAL PLOTS OF RAW RESULTS

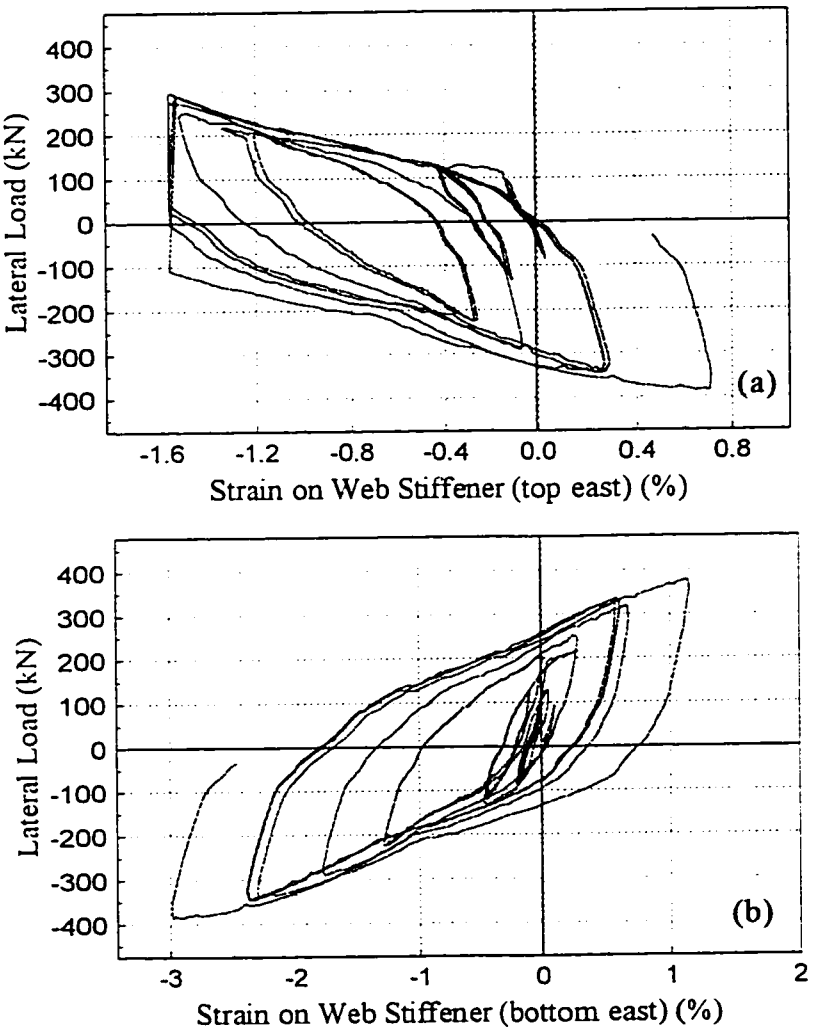

Fig. D.1. Lateral load versus strain close to the free edge at: (a) top; and (b) bottom of the web stiffeners of the east girder of the TADAS specimen.

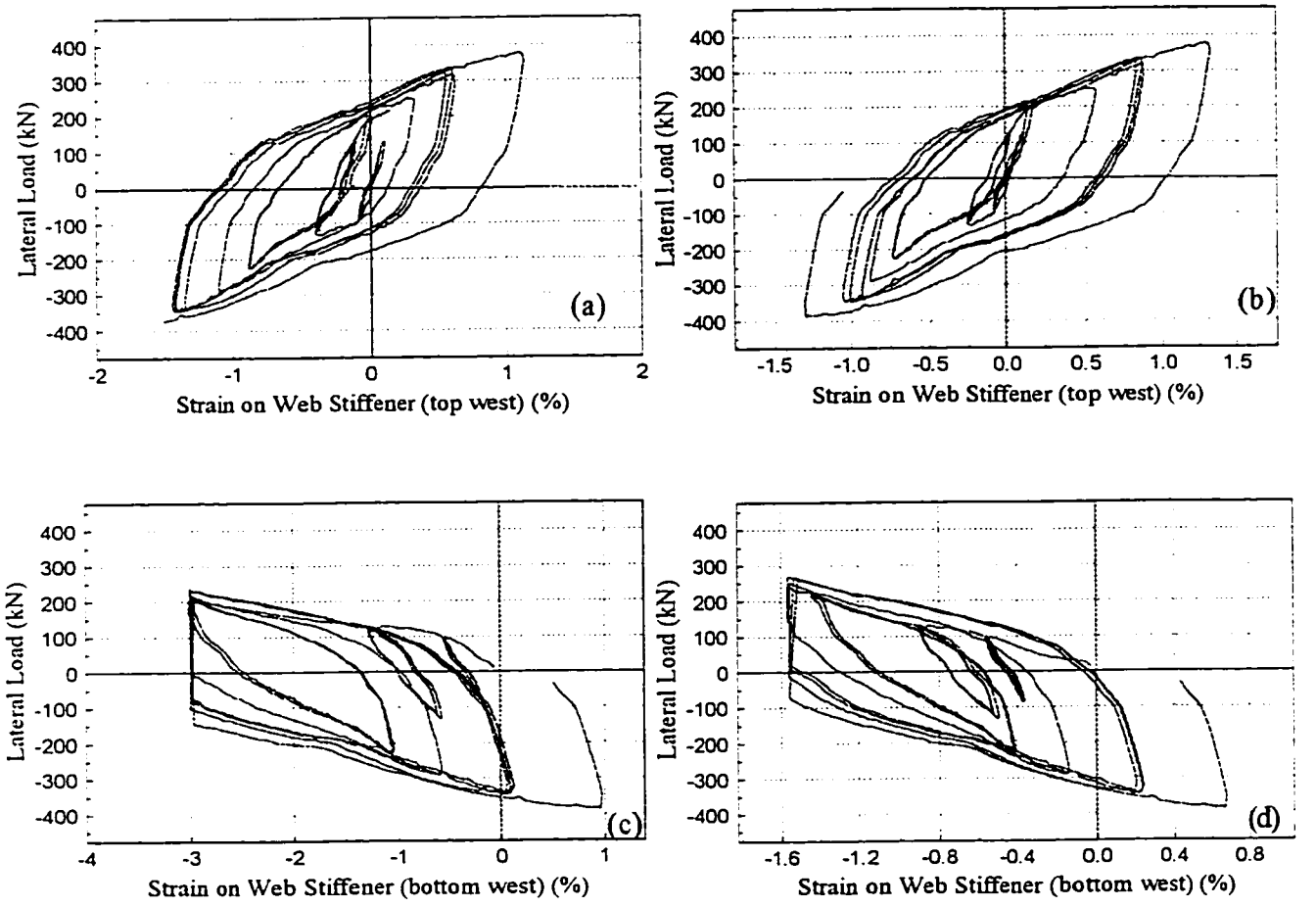

Fig. D.2. Lateral load versus strain close to the free edge at: (a) and (b) top (two sides); and (c) and (d) bottom (two sides) of the web stiffeners of the east girder of the TADAS specimen.

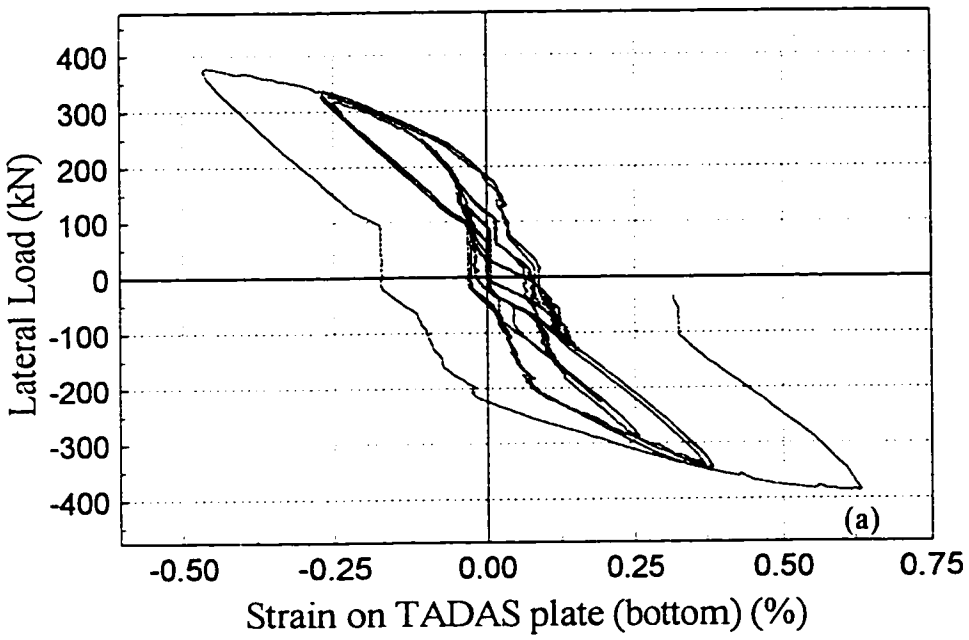

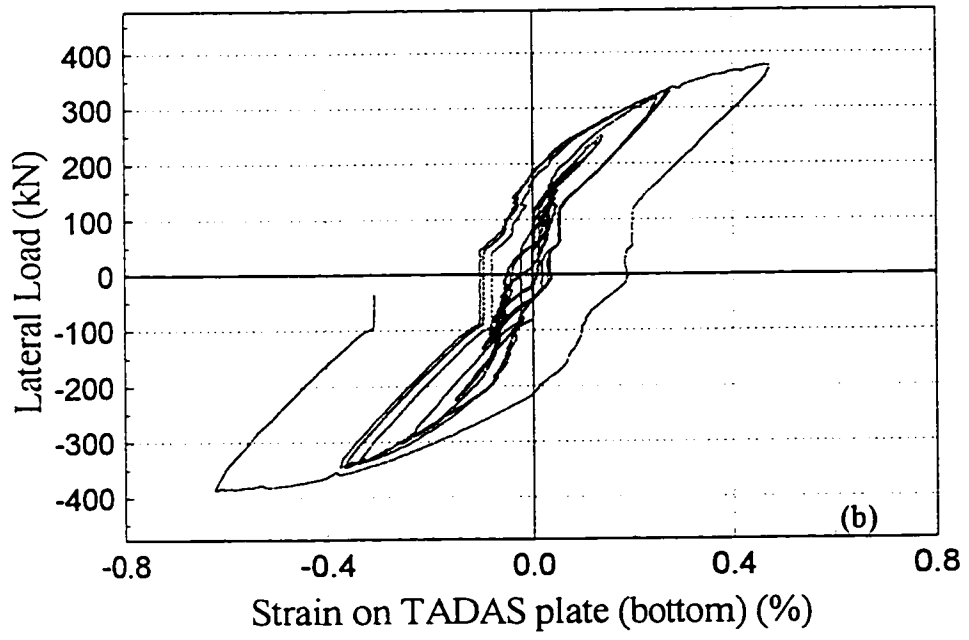

Fig. D.3. Lateral load versus strain at the bottom of: (a) and (b) two sides of a TADAS plate in the TADAS specimen.

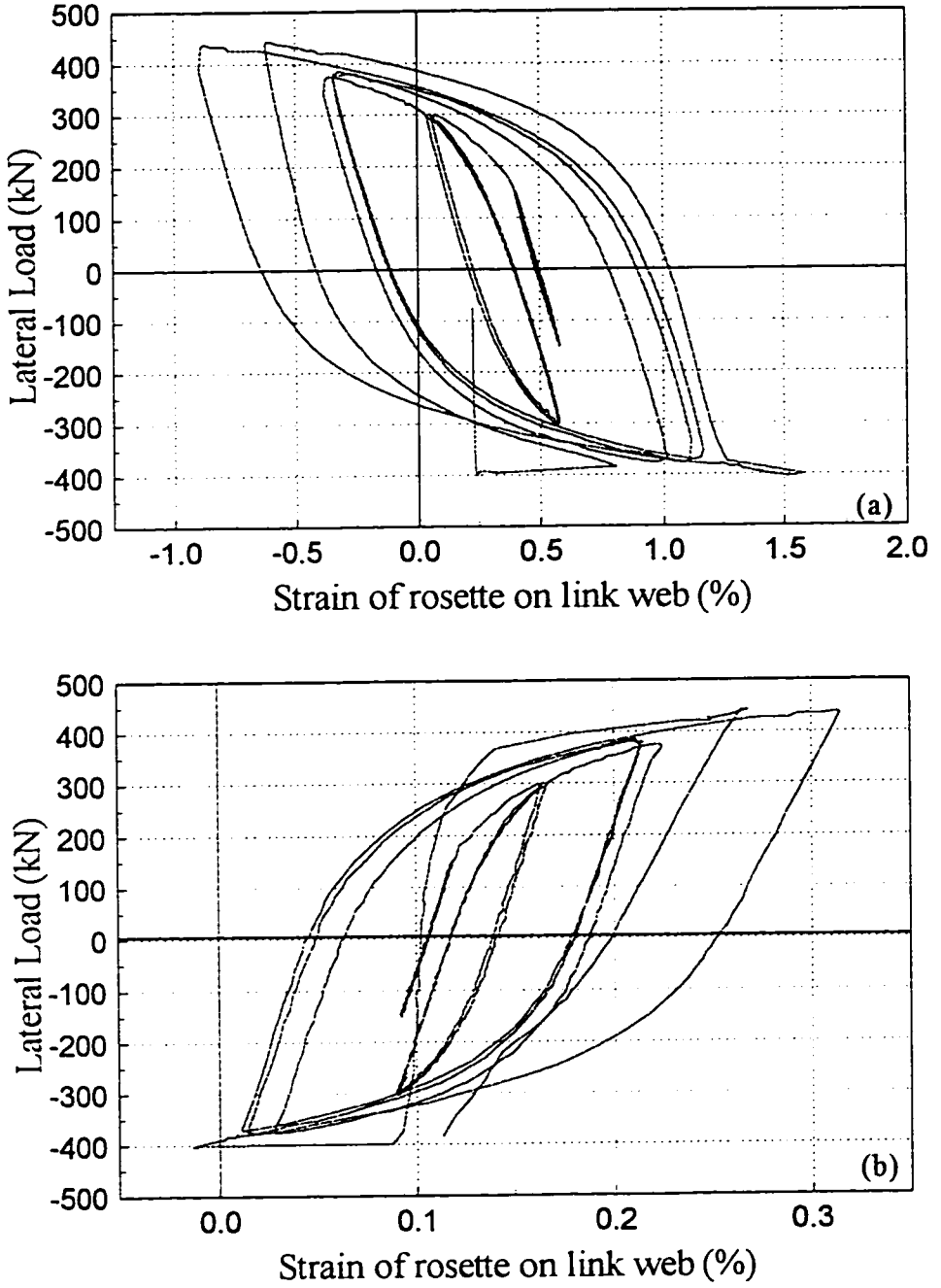

Fig. D.4. Lateral load versus strain of: (a) and (b) the 45° rosettes attached to the link beam web in the EBF2 specimen.

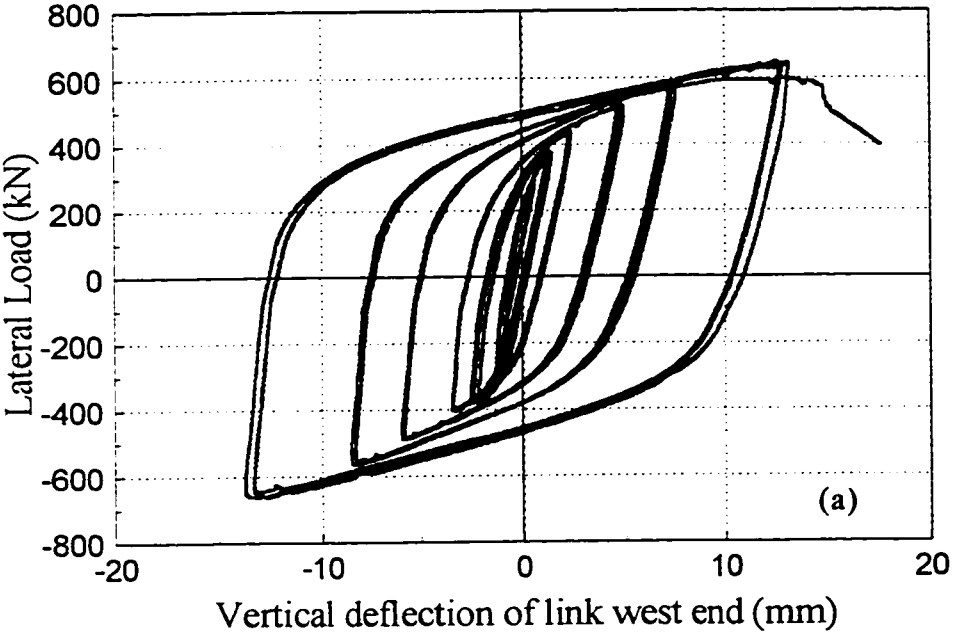

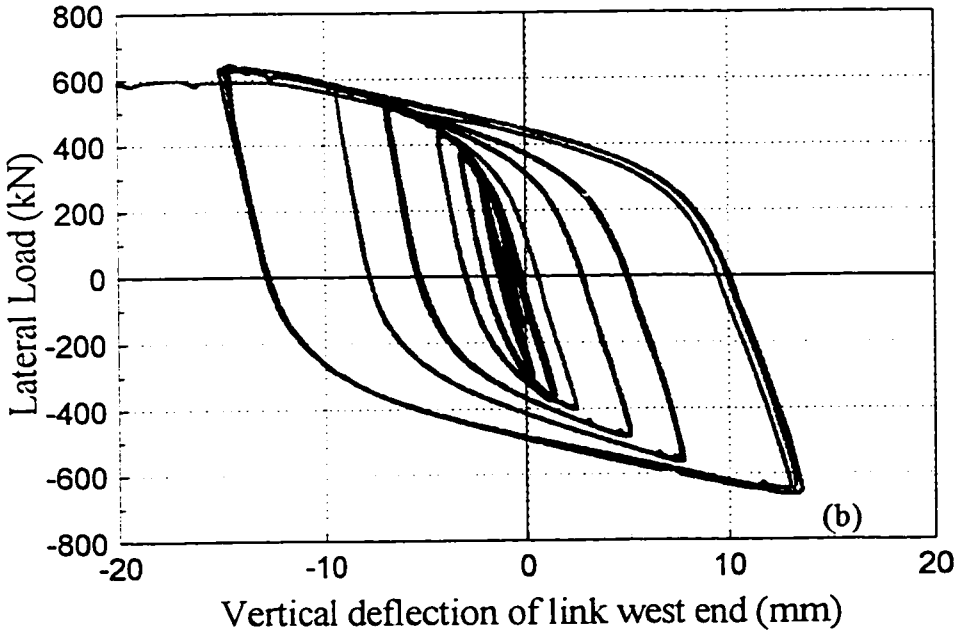

Fig. D.5. Lateral load versus vertical deflection of: (a) west; and (b) east end of the link beam of the EBF2 specimen.

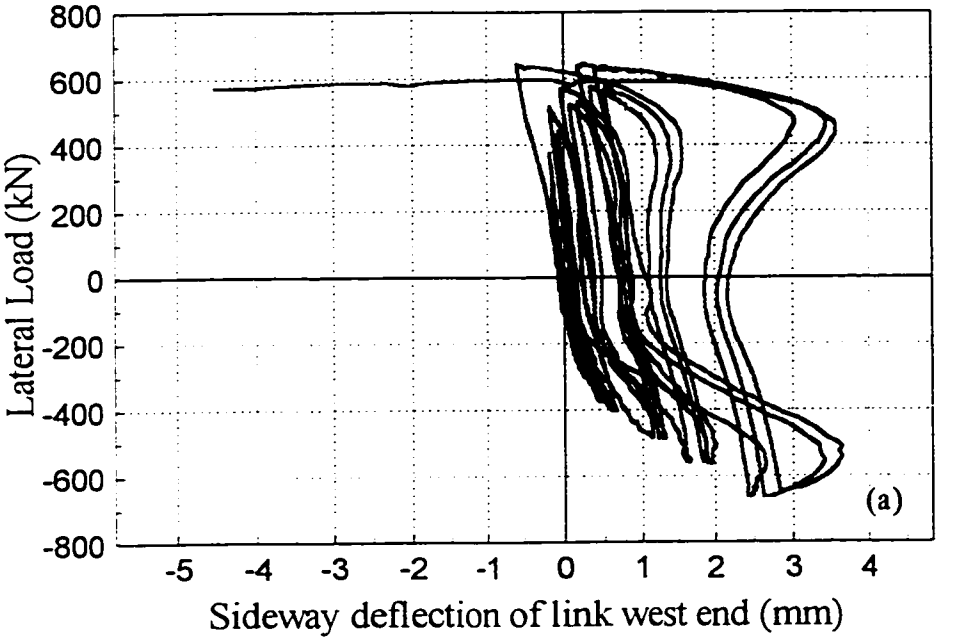

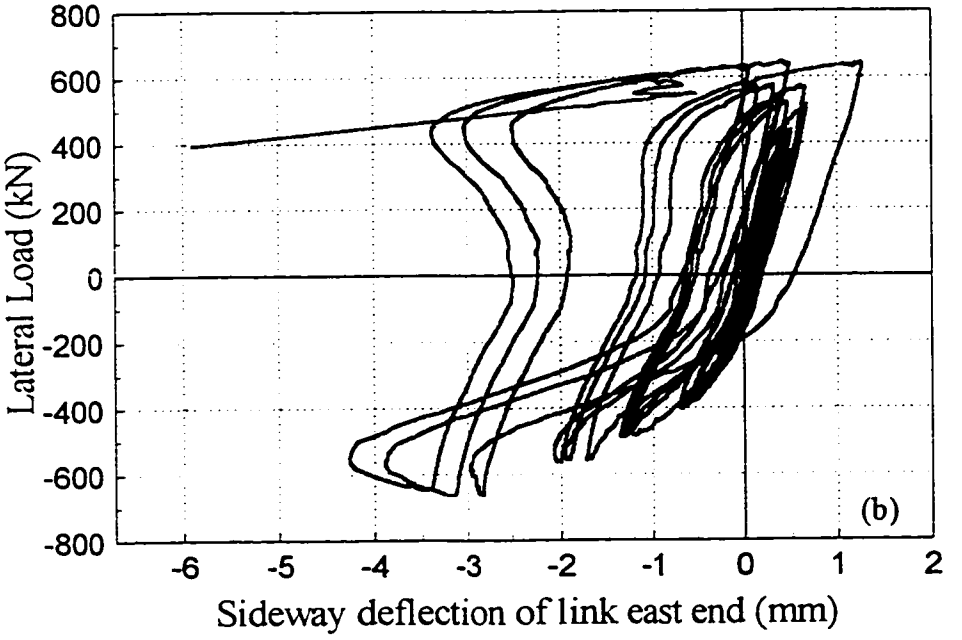

Fig. D.6. Lateral load versus sideway deflection of: (a) west; and (b) east ends of the link beam of the EBF2 specimen.

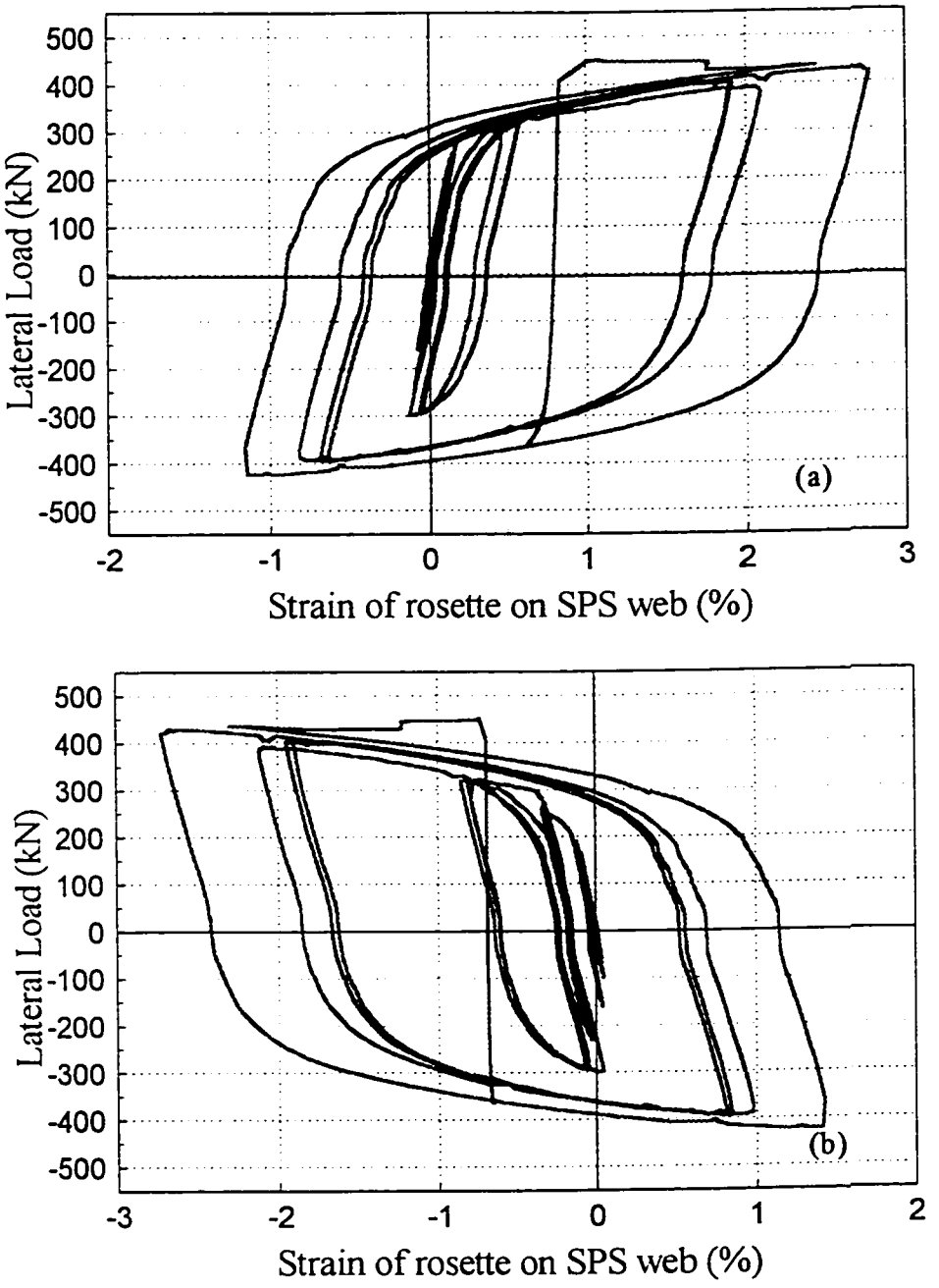

Fig. D.7. Lateral load versus strain of: (a) and (b) the 45° rosettes attached to the vertical link beam web of the SPS1 specimen.

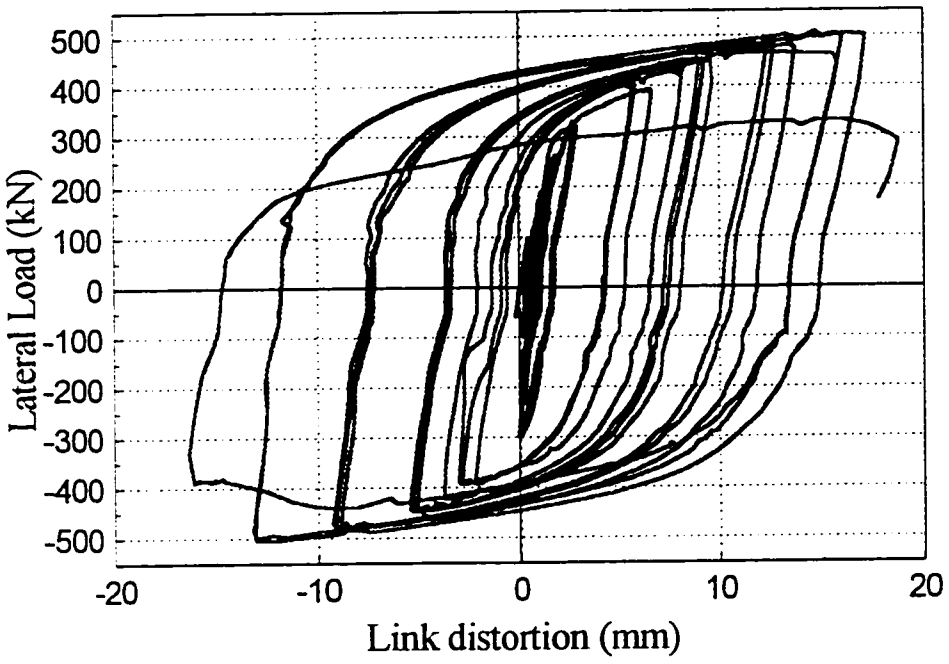

Fig. D.8. Lateral load versus link beam distortion in the SPS1 specimen.

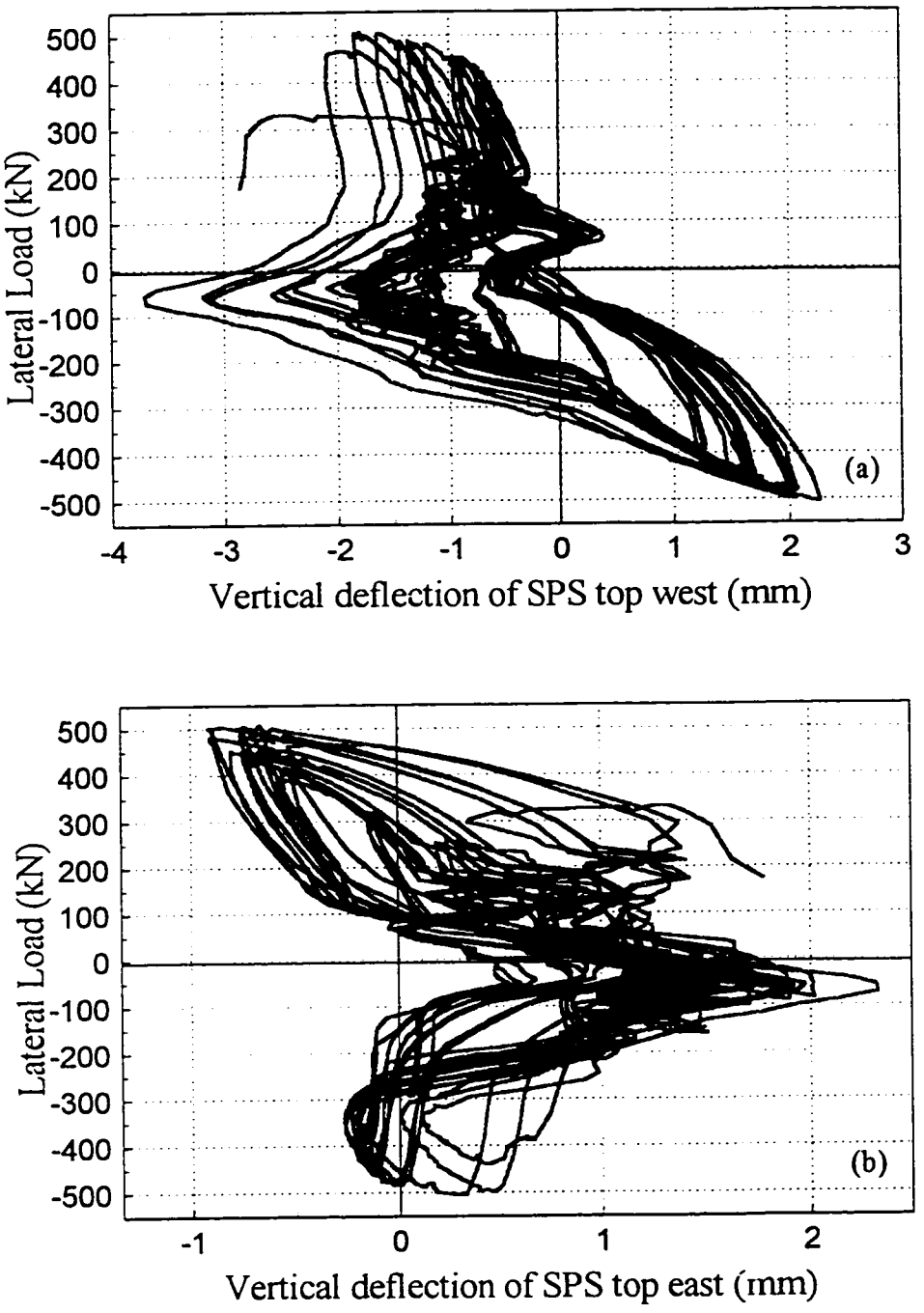

Fig. D.9. Lateral load versus vertical deformation at: (a) top west; and (b) top east of the vertical link beam of the SPS1 specimen.

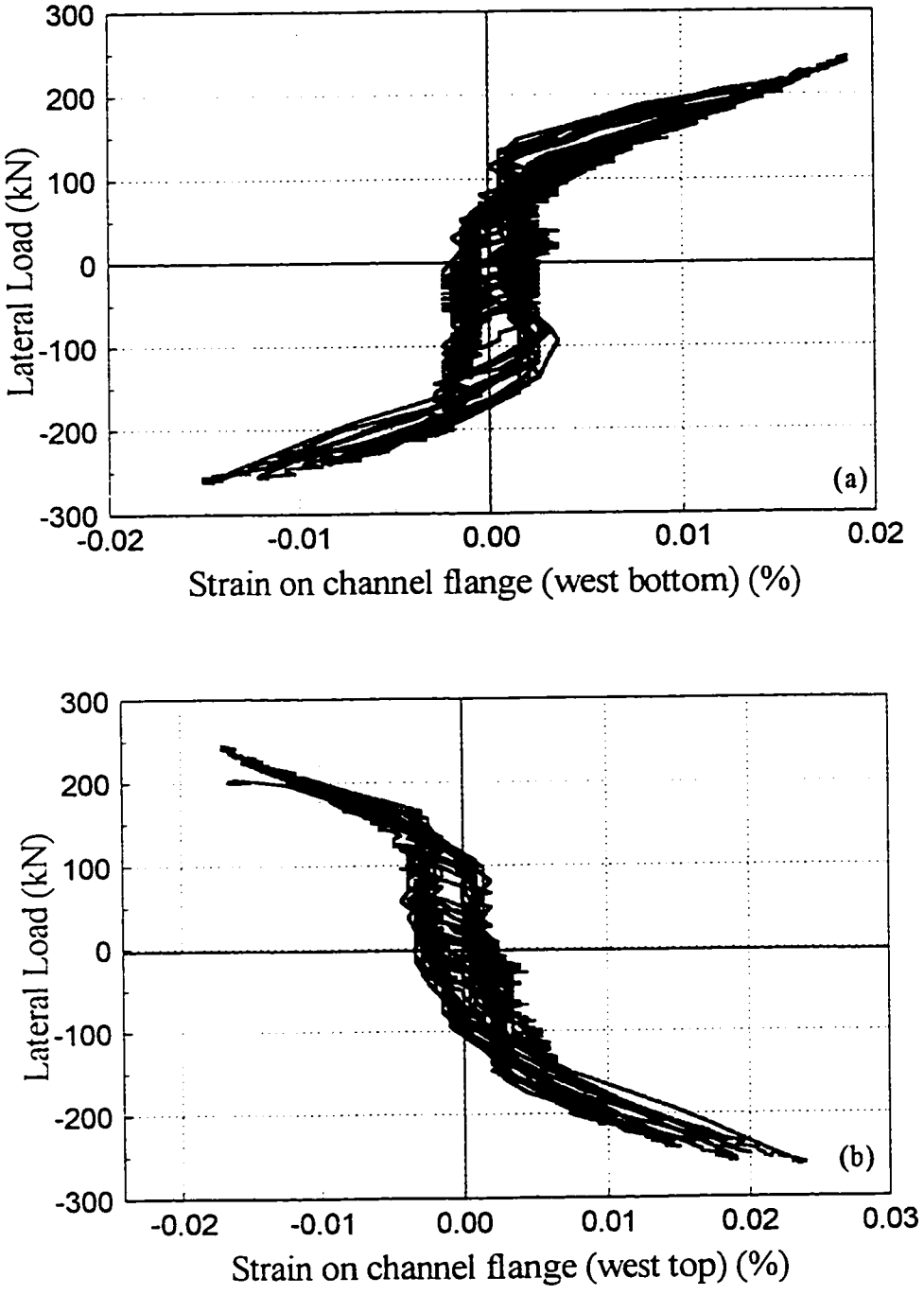

Fig. D.10. Lateral load versus strain of: (a) bottom flange; and (b) top flange of the channel section of the Channel specimen at a distance of the channel depth from each end.

IMAGE EVALUATION
TEST TARGET (QA-3)

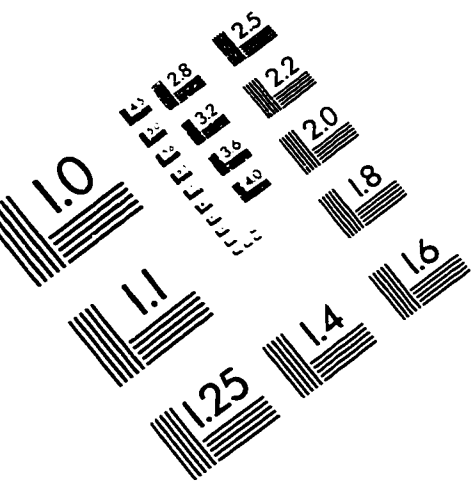

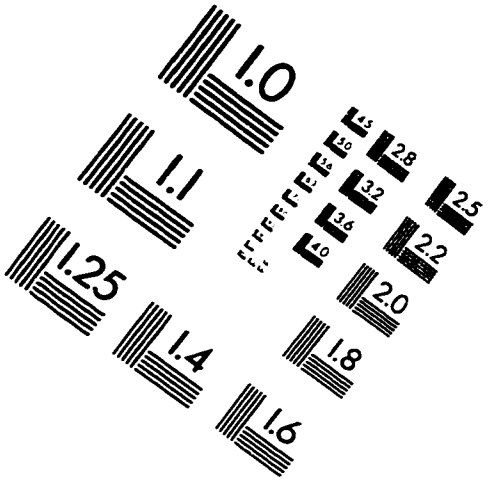

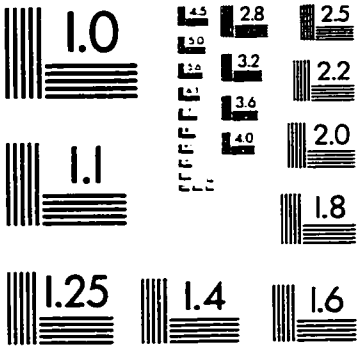

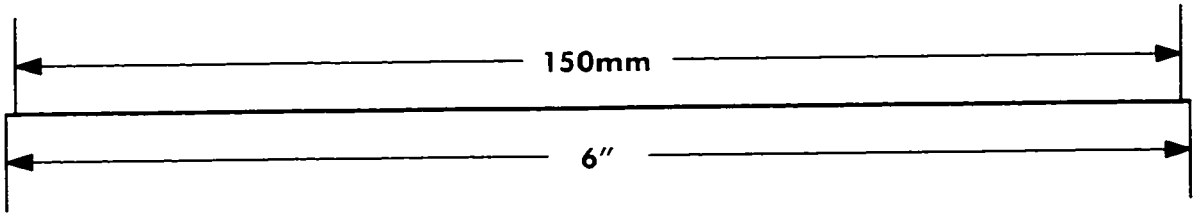

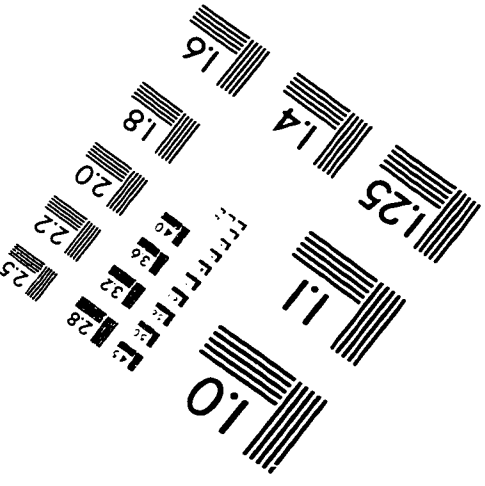

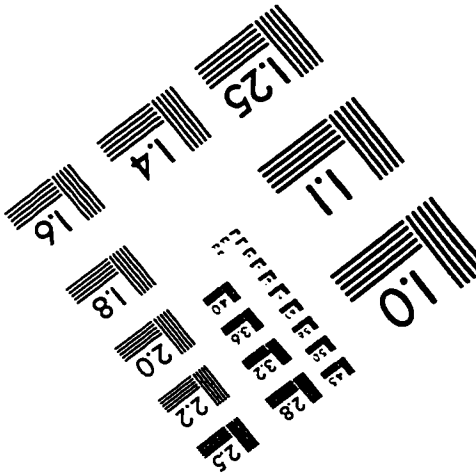

APPLIED IMAGE, Inc
1653 East Main Street
Rochester, NY 14609 USA
Phone: 716/482-0300
Fax: 716/288-5989